

Springer Series in Materials Science 247

Wolfgang Grellmann
Beate Langer *Editors*

Deformation and Fracture Behaviour of Polymer Materials

 Springer

Springer Series in Materials Science

Volume 247

Series editors

Robert Hull, Troy, USA

Chennupati Jagadish, Canberra, Australia

Yoshiyuki Kawazoe, Sendai, Japan

Richard M. Osgood, New York, USA

Jürgen Parisi, Oldenburg, Germany

Tae-Yeon Seong, Seoul, Republic of Korea (South Korea)

Shin-ichi Uchida, Tokyo, Japan

Zhiming M. Wang, Chengdu, China

The Springer Series in Materials Science covers the complete spectrum of materials physics, including fundamental principles, physical properties, materials theory and design. Recognizing the increasing importance of materials science in future device technologies, the book titles in this series reflect the state-of-the-art in understanding and controlling the structure and properties of all important classes of materials.

More information about this series at <http://www.springer.com/series/856>

Wolfgang Grellmann · Beate Langer
Editors

Deformation and Fracture Behaviour of Polymer Materials

 Springer

Editors

Wolfgang Grellmann
Centre of Engineering,
Martin-Luther-University Halle-Wittenberg
Halle, Saxony-Anhalt
Germany

Wolfgang Grellmann
Polymer Service GmbH Merseburg,
Associated An-Institute of University of
Applied Sciences Merseburg
Merseburg, Saxony-Anhalt
Germany

Beate Langer
Department of Engineering and Natural
Sciences
University of Applied Sciences Merseburg
Merseburg, Saxony-Anhalt
Germany

Beate Langer
Polymer Service GmbH Merseburg,
Associated An-Institute of University of
Applied Sciences Merseburg
Merseburg, Saxony-Anhalt
Germany

ISSN 0933-033X

ISSN 2196-2812 (electronic)

Springer Series in Materials Science

ISBN 978-3-319-41877-3

ISBN 978-3-319-41879-7 (eBook)

DOI 10.1007/978-3-319-41879-7

Library of Congress Control Number: 2017938288

© Springer International Publishing AG 2017

This work is subject to copyright. All rights are reserved by the Publisher, whether the whole or part of the material is concerned, specifically the rights of translation, reprinting, reuse of illustrations, recitation, broadcasting, reproduction on microfilms or in any other physical way, and transmission or information storage and retrieval, electronic adaptation, computer software, or by similar or dissimilar methodology now known or hereafter developed.

The use of general descriptive names, registered names, trademarks, service marks, etc. in this publication does not imply, even in the absence of a specific statement, that such names are exempt from the relevant protective laws and regulations and therefore free for general use.

The publisher, the authors and the editors are safe to assume that the advice and information in this book are believed to be true and accurate at the date of publication. Neither the publisher nor the authors or the editors give a warranty, express or implied, with respect to the material contained herein or for any errors or omissions that may have been made. The publisher remains neutral with regard to jurisdictional claims in published maps and institutional affiliations.

Printed on acid-free paper

This Springer imprint is published by Springer Nature

The registered company is Springer International Publishing AG

The registered company address is: Gewerbestrasse 11, 6330 Cham, Switzerland

Preface

The growing demands on the reliability, safety and lifetime of machines, equipment and components made of polymers and composites make it necessary to develop meaningful test methods for the assessment of fracture properties. For this purpose, polymer-specific evaluation methods and concepts of the field of technical fracture mechanics and polymer diagnostics/polymer testing are used. Within polymer sciences, these areas of research have emerged as separate disciplines over recent years, evidenced by curricula of polymer engineering programmes at universities and universities of applied sciences.

The present status report on the current state of knowledge of technical fracture mechanics of polymers and composites with polymer matrix has been supplemented by revised presentations from the 14th discussion conference on “Deformation and Fracture Behaviour of Polymers” and by contributions describing our own research. By including additional contributions dealing with the investigation into the toughness of polymers with time-dependent fracture mechanical characteristics and the use of crack resistance concepts for polymers and elastomers, we aim to provide a comprehensive overview of the current state of knowledge.

The discussion conference on “Deformation and Fracture Behaviour of Polymers” has been taking place every two years in Merseburg for more than 30 years and has become a recognised scientific conference.

The 2014 conference was held jointly with the international scientific congress “PolyMerTec 2014”, which was organised by the Merseburg University of Applied Sciences and focused on engineering topics for the first time.

The conferences aim at showcasing the progress in fundamental research and applied research in this scientific discipline. This is accomplished by means of plenary talks, short contributions and lively discussions among the large number of expert colleagues.

Essential topics are as follows:

- Polymer testing, damage analysis and polymer diagnostics of components
- Toughness characterisation of polymers with fracture mechanics concept

- Hybrid methods for polymer testing and diagnostics
- Non-destructive polymer testing (ultrasound)
- Long-term static behaviour and ageing

The conference programme also includes exhibitions of equipment used for non-destructive and destructive material testing, polymer analytics and elastomer and film testing.

This book follows the status reports that have already been published by Springer:

- Deformation und Bruchverhalten von Kunststoffen
Hrsg: W. Grellmann und S. Seidler
1998, ISBN 3-540-63671-4
- Deformation and Fracture Behaviour of Polymers
Eds.: W. Grellmann and S. Seidler
2001, ISBN 3-540-41247-6

A comprehensive compilation of mechanical and fracture mechanical properties from the literature and own research is documented in the following encyclopaedia:

- Mechanical and Thermomechanical Properties of Polymers
Group VIII Advanced Materials and Technologies Volume VIII/6A3
Eds.: W. Grellmann and S. Seidler
2014, ISBN 978-3-642-55165-9

In addition to the aforementioned books on the deformation and fracture behaviour of polymers, the Merseburg School edited the textbooks *Polymer Testing* for students at universities and universities of applied sciences. These textbooks were published by Hanser in German (2005, 2011, 2015) and English (2007, 2013). A Russian translation appeared in 2010.

These textbooks on polymer testing and diagnostics and on technical fracture mechanics of polymers and composites with polymer matrix also form the basis of an online encyclopaedia on “polymer testing and diagnostics”. This online encyclopaedia follows the wiki system known from Wikipedia and is available for free at <http://wiki.polymerservice-merseburg.de> in Version 4.0 (2014).

With the edition of this status report, we hope to contribute to an enhanced understanding of specific problems of the discipline among colleagues from different research institutes and the polymer industry.

The editors would like to express their special thanks to Dr.-Ing. Ralf Lach, Polymer Service GmbH Merseburg, Associate Institute of the Merseburg University of Applied Sciences, for his comprehensive support and critical advice.

Halle and Merseburg, Germany
Merseburg, Germany
September 2016

Wolfgang Grellmann
Beate Langer

Contents

Part I Modern Aspects of Fracture Mechanics in the Industrial Application of Polymers

1	Time-Dependent Fracture Behaviour of Polymers at Impact and Quasi-Static Loading Conditions	3
	R. Lach and W. Grellmann	
1.1	Comparison of Methods for the Determination of R-Curves for Polymers at Impact Loading	4
1.2	Material Samples	5
1.2.1	Semicrystalline Polymers with Particle–Matrix Structure: PP/EPR/PE Copolymers	5
1.2.2	Short-Glass Fibre (GF)-Reinforced Semicrystalline Polymers: PP/GF	6
1.2.3	Nanophase-Separated Amorphous Polymers: Binary Blends of PS–PB Block Copolymers	7
1.2.4	CTOD Rate Under Quasi-Static Test Conditions: PP/EPR Blends	10
1.2.5	Influence of the Temperature: Amorphous Polycarbonate (PC)	11
1.3	Crack Propagation Kinetics of Polymers at Impact Loading Conditions	12
1.4	Discussion of Literature on Crack Propagation Kinetics	15
1.5	Stable Crack Propagation as Kinetic Phenomenon—An Outlook	19
	References	20
2	Fatigue Crack Growth Behaviour of Epoxy Nanocomposites—Influence of Particle Geometry	23
	M.H. Kothmann, G. Bakis, R. Zeiler, M. Ziadeh, J. Breu and V. Altstädt	

2.1	Introduction	23
2.2	Experimental.	25
	2.2.1 Materials	25
	2.2.2 Preparation of Nanocomposites	26
	2.2.3 Characterisation Methods.	26
2.3	Results and Discussion	27
	2.3.1 Organophilisation of Nanoparticles	27
	2.3.2 Morphology.	27
	2.3.3 Fatigue Crack Propagation Behaviour	28
2.4	Conclusion	30
	References.	31
3	Fracture Mechanics Methods to Assess the Lifetime of Thermoplastic Pipes	33
	F. Arbeiter, G. Pinter, R.W. Lang and A. Frank	
3.1	Failure Behaviour of Polymer Pipes	34
3.2	Fracture Mechanics Approach for Pipe Lifetime Calculations	36
3.3	Crack Growth in Polyethylene	39
3.4	Extrapolation to Static Crack Growth Behaviour from Fatigue Tests	41
3.5	Lifetime Calculation of PE Pipe Grades	44
3.6	Lifetime Calculation of a PE Pipe Grade at 80 °C Using Cyclic CRB Tests	45
3.7	Conclusion and Outlook	48
	References.	49
4	Thermographic Characterisation of the Deformation and Fracture Behaviour of Polymers with High Time and Spatial Resolution	55
	M. Stein and K. Schneider	
4.1	Introduction	55
4.2	Experimental.	56
	4.2.1 Materials	56
	4.2.2 Methods.	57
4.3	Results	59
	4.3.1 Thermomechanical Characterisation of PET	59
	4.3.2 Thermomechanical Characterisation of PC.	65
4.4	Discussion.	67
	4.4.1 Polycarbonate—Affine Deformation with Uniform Energy Dissipation.	68
	4.4.2 Poly(Ethylene Terephthalate)—Localised Deformation and Complex Influence of Two Phases	68

4.5	Conclusion	71
	References	71
5	Mechanical and Fracture Mechanical Properties of Polymorphous Polypropylene	73
	A. Monami, B. Langer, J. Sadilek, J. Kučera and W. Grellmann	
5.1	Introduction	73
5.2	Experimental Part	75
5.3	Results and Discussion	77
	5.3.1 Degree of Crystallinity	77
	5.3.2 Influence of Cooling Rate on the Resistance Against Stable Crack Initiation and Crack Growth	78
5.4	Conclusion	80
	References	80
6	Numerical Modelling of Damage Initiation and Failure of Long Fibre-Reinforced Thermoplastics	83
	L. Schulenberg, D.-Z. Sun and T. Seelig	
6.1	Introduction	83
6.2	Problem Formulation	84
	6.2.1 Experimental Observation	84
	6.2.2 Microscopic Observation	84
	6.2.3 Numerical Microstructural Model	86
6.3	Numerical Results	87
	6.3.1 Single-Fibre Unit Cell Under Uniaxial Tension	87
	6.3.2 Unit Cells Containing Three Fibres	88
	6.3.3 Variations of the Fibre Overlapping Length and Load Direction	90
6.4	Discussion	91
6.5	Summary	91
	References	92
 Part II Advanced Structure-Sensitive Methods for Analysing Cracks and Fracture Surfaces		
7	Characterisation of Polymers in the Scanning Electron Microscope—From Low-Voltage Surface Imaging to the 3D Reconstruction of Specimens	95
	A. Zankel, M. Nachtnebel, C. Mayrhofer, K. Wewerka and T. Müllner	
7.1	Introduction	95
7.2	Low-Voltage Mode of the SEM	96
7.3	Low-Vacuum Mode of the ESEM	97
7.4	The ESEM Mode	100

7.5	Artefacts and Beam Damage.	101
7.6	3D Information Using In Situ Ultramicrotomy	103
7.7	Conclusions	106
	References.	107
8	3D Reconstruction of Cracks in Polymers—New Insight into the Fracture Behaviour?	109
	M. Nachtnebel, A. Zankel, C. Mayrhofer, M. Gahleitner and P. Pölt	
8.1	Introduction	109
8.2	Preparation and Image Processing.	111
8.3	Results and Discussion	112
8.4	Conclusion	117
	References.	118
9	Determination of the Stable Crack Growth by Means of the Fluorescence Adsorption-Contrast Method (3D-FAC Method)	121
	M. Kroll, B. Langer and W. Grellmann	
9.1	Introduction	122
9.2	Experimental.	123
	9.2.1 Materials	123
	9.2.2 <i>J</i> - <i>R</i> -Curve Determination.	124
9.3	Development of a Fluorescence Microscopy Procedure for Δa Measurement.	125
	9.3.1 Fluorescent Penetration Dye Colouring	125
	9.3.2 Optimisation of the Fluorescent Application Process	126
	9.3.3 Fluorescence Adsorption-Contrast Method (3D-FAC Method)	129
9.4	Results and Discussion	133
9.5	Conclusions	135
	References.	136
10	Acoustic Emission Analysis for Assessment of Damage Kinetics of Short-Glass Fibre-Reinforced Thermoplastics—ESEM Investigations and Instrumented Charpy Impact Test	139
	M. Schoßig, A. Zankel, C. Bierögel, P. Pölt and W. Grellmann	
10.1	Introduction	140
10.2	Theoretical Background	141
	10.2.1 Acoustic Emission (AE) Analysis	141
	10.2.2 Frequency Analysis—Wavelet Transform (WT)	144
10.3	Experimental Details.	145
	10.3.1 In Situ Tensile Tests in ESEM Coupled with AE Measurement	145
	10.3.2 Coupling ICIT and AE Analysis	147

10.4	Results	149
10.4.1	ESEM Investigations—Coupling the In Situ Tensile Test with AE Analysis	149
10.4.2	AE Measurements During ICIT	157
10.5	Summary	161
	References	162
11	The Fractography as a Tool in Failure Analysis—Possibilities and Limits	165
	I. Kotter and W. Grellmann	
11.1	Introduction	165
11.2	Fractography—Fracture Surface Structures	166
11.2.1	Waves and Grid Lines	166
11.2.2	Fracture Parabola Respectively U- or V-Shaped Ramps	167
11.2.3	Ramps, Bars or Steps	169
11.2.4	Example: Fracture of a Multi-Layer Pipe	169
11.3	Limits of Validity of the Fractography for Filled and Reinforced Plastics	171
11.4	Summary	173
	References	174
 Part III Fracture Mechanics and Related Methods for Analysing the Fracture Safety and Lifetime of Plastic Pipe Materials		
12	Slow Crack Growth of Polyethylene—Accelerated and Alternative Test Methods	177
	B. Gerets, M. Wenzel, K. Engelsing and M. Bastian	
12.1	Introduction	177
12.2	Slow Crack Growth	178
12.3	Test Methods to Determine Slow Crack Growth Behaviour of PE	178
12.3.1	Conventional Test Methods	178
12.3.2	Accelerated Test Methods: (Accelerated) Full Notch Creep Test (FNCT and aFNCT)	179
12.3.3	Alternative Test Methods: Strain Hardening Test (SHT)	182
12.3.4	Alternative Test Methods: Cracked Round Bar Test—CRB Test	185
12.4	Conclusions	186
	References	187
13	Polypropylene for Pressure Pipes—From Polymer Design to Long-Term Performance	189
	L. Boragno, H. Braun, A.M. Hartl and R.W. Lang	

13.1	Introduction PP Market Overview.	189
13.2	Morphology and Polymorphism of PP	191
13.3	Short-Term Properties—Charpy and Pipe Falling Weight.	192
13.4	From Microstructure to Final Properties	194
13.5	Influence of Processing.	196
13.6	Long-Term Behaviour—Pressure Resistance and Slow Crack Growth in PP Materials	197
13.7	Conclusions	199
	References.	200
14	Lifetime of Polyethylene (PE) Pipe Material—Prediction Using Strain Hardening Test.	203
	E. Nezbedová, J. Hodan, J. Kotek, Z. Krulis, P. Hutař and R. Lach	
14.1	Introduction	203
14.2	Conventional Assessment of Long-Term Performance and Lifetime: The Pennsylvania Edge Notch Tensile Test and the Tensile Full Notch Creep Test	205
14.3	Accelerated Assessment of Long-Term Performance and Lifetime: The Strain Hardening Test.	206
14.4	Results	207
14.5	Conclusions	209
	References.	210
15	Influence of Welding and Composition on the Short-Term Stable Crack Propagation Through Polyolefin Single- and Bilayered Structures.	211
	R. Lach, T. Krolopp, P. Hutař, E. Nezbedová and W. Grellmann	
15.1	Introduction	212
15.2	Experimental.	212
	15.2.1 Materials and Specimen Preparation	212
	15.2.2 Equipment and Data Analysis	214
15.3	Results and Discussion	215
	15.3.1 Influence of Specimens Shape, Orientation, Welding and Loading Speed on Stable Crack Initiation and Propagation Behaviour in Single- Layer Pipes Made from PE 100, PE 80 and PP Materials	215
	15.3.2 Influence of Interlayers and Crack Propagation Direction on Stable Crack Initiation and Propagation Behaviour in Bilayer Pipes Made from PP Materials	220
15.4	Summary	224
	References.	226

16	Influence of Different Welding Conditions of Polyolefin Pipes on Creep Crack Growth	229
	J. Mikula, P. Hutař, M. Ševčík, E. Nezbedová, R. Lach, W. Grellmann and L. Náhlík	
16.1	Introduction	230
16.2	Welding of Polyolefin Pipes	230
16.3	Material Properties of the Welded Region	231
16.4	Numerical Model Description	233
16.5	Location of Crack Initiation	234
16.6	Stress Intensity Factors for Different Configurations	235
	16.6.1 Influence of Material Inhomogeneity	235
	16.6.2 Influence of the Weld Bead Radius	236
	16.6.3 Influence of Different Weld Bead Shape	236
16.7	Crack Trajectories for Different Welds	238
16.8	Lifetime Prediction	239
16.9	Conclusion	239
	References.	240
17	Epoxy Modifications—A Novel Sealing Material for Rehabilitation of Pipe Joints.	243
	C. Schoberleitner, T. Koch and V.-M. Archodoulaki	
17.1	Introduction	244
17.2	Experimental Section	245
17.3	Results and Discussion	247
17.4	Conclusion	251
	References.	252
Part IV Deformation Behaviour and Fracture Mechanics		
Characteristics of Polymer Films and Adhesive Systems		
18	Approaches to Characterise the Mechanical Properties of Films and Elastomers	257
	K. Reincke and W. Grellmann	
18.1	Introduction	257
18.2	Experimental Opportunities of Mechanical Films and Elastomers Testing	258
	18.2.1 Conventional Tensile and Notched Impact Test After ISO 8256	258
	18.2.2 Instrumented Notched Tensile Impact Test	259
	18.2.3 Instrumented Puncture Impact Test	260
	18.2.4 Tear Test	261
	18.2.5 Peel Tests	262
18.3	Examples of Use.	264
	18.3.1 Assessment of the Toughness Properties of Elastomers	264

18.3.2	Influence of Chemical Loading on the Mechanical Properties of a Thermoplastic Film	265
18.3.3	Influence of Chemical Loading on the Toughness Properties of Elastomers	266
18.3.4	Evaluation of a PE/PB-1 Peel System	267
18.4	Conclusions	269
	References.	269
19	Fracture Mechanics Characterisation of Peelfilms	271
	M. Nase, M. Rennert, S. Henning, A. Zankel, K. Naumenko and W. Grellmann	
19.1	Introduction	272
19.2	Experimental.	274
19.3	Results and Discussion	276
	References.	280
20	Fracture Mechanics Characterisation of Low-Adhesive Stretch Films.	283
	M. Rennert, M. Nase, K. Reincke, R. Lach and W. Grellmann	
20.1	Introduction	284
20.2	Experimental.	286
20.2.1	Material and Composition of the Films	286
20.2.2	Cling Test According to ASTM D 5458	287
20.3	Results and Discussion	291
20.4	Conclusion	295
	References.	295
21	Thermal Stability and Lifetime Prediction of an Epoxide Adhesive System	297
	R. Tiefenthaller, R. Fluch, B. Strauß and S. Hild	
21.1	Introduction	297
21.2	Materials and Methods	299
21.2.1	Material and Samples	299
21.2.2	Spectroscopic Techniques and Mechanical Analyses	299
21.2.3	T-Peel Test and Tensile Lap-Shear Test	300
21.3	Results and Discussion	300
21.3.1	Thermomechanical Analysis	300
21.3.2	ATR-IR Spectroscopy	301
21.3.3	Raman Spectroscopy and Thermogravimetric Analysis.	304
21.3.4	Lifetime Prediction: T-Peel Test and Tensile Lap-Shear Test.	304
21.4	Conclusions	309
	References.	309

Part V Fatigue Crack Propagation, Lifetime and Long-Term Mechanical Behaviour of Thermoplastics and Elastomers

22 Morphology and Fatigue Behaviour of Short-Glass Fibre-Reinforced Polypropylene 315
 M. Palmstingl, D. Salaberger and T. Koch
 22.1 Introduction 315
 22.2 Analysis of Morphology of SFRP. 316
 22.3 Determination of Fatigue Behaviour 323
 References. 331

23 Characterisation of the Deformation and Fracture Behaviour of Elastomers Under Biaxial Deformation 335
 K. Schneider, R. Calabrò, R. Lombardi, C. Kipscholl, T. Horst, A. Schulze, S. Dedova and G. Heinrich
 23.1 Introduction 335
 23.2 Concept of the Biaxial Test Stand 336
 23.3 Upgrading of a Biaxial Testing Method 338
 23.3.1 New Clamping System for High Biaxial Deformation. 339
 23.3.2 Specimen Geometry. 340
 23.3.3 Crack Propagation with the New Specimen. 341
 23.4 Material 341
 23.5 Results 342
 23.5.1 Material Behaviour Under Biaxial Load 342
 23.5.2 Strain Amplification at the Crack Tip of a SENT Sample. 343
 23.5.3 Crack Propagation Under Biaxial Load 344
 23.5.4 Crack Propagation and Estimation of the Tearing Energy 345
 23.6 Conclusion 348
 References. 348

24 Influence of Thermal Ageing Process on the Crack Propagation of Rubber Used for Tire Application 351
 R. Stoček, O. Kratina, P. Ghosh, J. Maláč and R. Mukhopadhyay
 24.1 Introduction 351
 24.2 Theoretical Background 354
 24.2.1 Dynamic-Mechanical Analysis (DMA) 354
 24.2.2 Fracture Crack Growth (FCG). 355
 24.3 Experimental Details. 356
 24.3.1 Material Preparation. 356
 24.3.2 Ageing. 356
 24.3.3 DMA 357
 24.3.4 FCG. 357

24.4	Results and Discussion	358
24.4.1	DMA	358
24.4.2	FCG	360
24.5	Conclusion	362
	References.	363
25	Development of Magnetorheological Elastomers (MREs) for Strength and Fatigue Resistance	365
	J. McIntyre and S. Jerrams	
25.1	Introduction	366
25.2	Preparation of Materials	368
25.3	Experimental Methodology	369
25.4	Results and Discussion	371
25.5	Summary and Conclusions	373
	References.	374
26	Fibre-Reinforced Polyamides and the Influence of Water Absorption on the Mechanical and Thermomechanical Behaviour	377
	P. Guttman and G. Pilz	
26.1	Introduction and Objectives	378
26.2	Experimental.	378
	26.2.1 Materials	378
	26.2.2 Experimental Procedure.	379
26.3	Results and Discussion	380
	26.3.1 Water Absorption	380
	26.3.2 Dynamic-Mechanical Analysis (DMA)	381
	26.3.3 Monotonous Tensile Tests	382
	26.3.4 Media Creep Tests.	385
26.4	Summary and Outlook	387
	References.	388
27	Accelerated Measurement of the Long-Term Creep Behaviour of Plastics	389
	F. Achereiner, K. Engelsing and M. Bastian	
27.1	Introduction	389
27.2	Principle of the Stepped Isothermal Method	391
27.3	Creep Testing Using SIM	392
27.4	Construction of a Master Curve	395
27.5	Assessment of the Method	397
27.6	Applications of SIM	398
27.7	Conclusions	400
	References.	401

Part VI Influence of Ageing on Mechanical and Fracture Mechanics Performance of Thermoplastics and Elastomers

28	Hygrothermal Ageing of Injection-Moulded PA6/GF Materials Considering Automotive Requirements	405
	T. Illing, M. Schoßig, C. Bierögel, B. Langer and W. Grellmann	
28.1	Introduction	405
28.2	Material and Experiments	407
28.3	Results and Discussion	408
28.4	Summary and Conclusion	416
	References.	417
29	Ageing of Polymer Materials—Testing, Modelling and Simulation Considering Diffusion	421
	H. Baaser	
29.1	Introduction	421
29.2	Test Method	423
	29.2.1 Change in Stiffness Over a Long Period of Time	423
	29.2.2 <i>Diffusion</i>	423
29.3	Mechanical Model and Numerical Application	425
29.4	Computational Results	426
	29.4.1 O-Ring Application	426
	29.4.2 Compression Test Specimen—Surface–Volume Ratio	426
29.5	Conclusions and Discussion	428
	References.	429
30	Investigations of Elastomeric Seals—Low-Temperature Performance and Ageing Behaviour	431
	M. Jaunich, A. Kömmling and D. Wolff	
30.1	Introduction	431
30.2	Behaviour at Low Temperatures	432
30.3	Methodology for the Ageing of Elastomeric Seals	435
30.4	Conclusion	442
	References.	442

Part VII Mechanical Properties and Fracture of Elastomers— Influence of Composition, Reinforcement and Crosslinking

31	Mechanical Reinforcement in a Polyisoprene Rubber by Hybrid Nanofillers	447
	S. Agnelli, V. Cipolletti, S. Musto, M. Coombs, L. Conzatti, S. Pandini, M.S. Galimberti and T. Riccò	
31.1	Introduction	447
31.2	Experimental.	449

31.3	Results and Discussion	451
31.3.1	Transmission Electron Microscopy Analyses	451
31.3.2	Mechanical Behaviour	452
31.4	Conclusions	458
	References.	458
32	Structure–Property Correlations of SSBR/BR Blends	461
	K. Reincke, W. Grellmann, S. Ilisch, S. Thiele and U. Ferner	
32.1	Introduction	462
32.2	Experimental.	462
32.3	Results	464
32.3.1	Influence of the Composition on the Processing- Related Properties	464
32.3.2	Influence of Composition of the Rubber Mixture on the Physical Properties.	467
32.4	Structure–Property Correlation	470
32.5	Conclusions	472
	References.	473
33	Comparison Between Peroxide and Radiation Crosslinking of Nitrile Rubber	475
	K. Bandzierz, D.M. Bielinski, G. Przybytniak, M. Jaszczak and A. Marzec	
33.1	Introduction	475
33.2	Experimental.	477
33.2.1	Materials and Samples Preparation	477
33.2.2	Radiation Crosslinking.	477
33.2.3	Peroxide Thermal Crosslinking	478
33.2.4	Crosslink Density Determination	478
33.2.5	Chain Scission and Crosslinking Ratio Determination	479
33.2.6	Mechanical Properties Test	480
33.3	Results and Discussion	480
33.4	Conclusion	482
	References.	482
34	Wood Flour as a Filler of Natural and Epoxidised Natural Rubber	485
	A. Smejda-Krzewicka, W.M. Rzymiski and P. Dmowska-Jasek	
34.1	Introduction	485
34.2	Materials and Methods	486
34.2.1	Materials	486
34.2.2	Sample Preparation	486
34.2.3	Testing Methods	487

34.3	Results and Discussion	487
34.3.1	Effect of Wood Flour Derived from Coniferous Trees (CF) on Properties of NR and ENR	487
34.3.2	Effect of Wood Flour Derived from Deciduous Coniferous Trees (DF) on Properties of NR and ENR	489
34.4	Conclusion	491
	References.	491
35	Characterisation of the Ultimate Tensile Properties of Elastomers by a Dimensionless Hooke Number—A New Approach to Failure Envelopes	493
	N. Rennar and P. Kirchner	
35.1	Introduction	493
35.2	Theoretical Background	494
35.3	Experimental Part	497
35.3.1	Selection of Polymers and Recipes of Test Compounds	497
35.3.2	Mixing Procedure, Crosslinking and Testing	497
35.4	Results and Discussion	498
35.5	Summary and Conclusions	505
	References.	506
36	Thermomechanical Analysis Strategies for Elastomer Components Under Dynamic Loading	507
	R. Behnke and M. Kaliske	
36.1	Introduction and Overview	507
36.2	Simultaneous Solution Scheme	509
36.3	Sequential Solution Scheme	511
36.4	Conclusion and Outlook	515
	References.	516
37	Influence of Selected Silica Fillers on the Properties of Vulcanised Rubber Blends	517
	W.M. Rzymiski, A. Smejda-Krzewicka, J. Rogoża and A. Ochendusko	
37.1	Introduction	517
37.2	Materials and Methods	518
37.3	Results and Discussion	519
37.4	Conclusion	524
	References.	524

List of Authors

F. Achereiner SKZ—German Plastics Center, Würzburg, Germany

S. Agnelli Department of Mechanical and Industrial Engineering, University of Brescia, Brescia, Italy

V. Altstädt Department of Polymer Engineering, University of Bayreuth, Bayreuth, Germany

F. Arbeiter Department Polymer Engineering and Science, Montan University Leoben, Leoben, Austria

V.-M. Archodoulaki Institute of Materials Science and Technology, Vienna University of Technology, Vienna, Austria

H. Baaser Freudenberg Technology Innovation, FTI, Weinheim, Germany; Professor for Engineering Mechanics & FEM, University of Applied Sciences, Bingen, Germany

G. Bakis Department of Polymer Engineering, University of Bayreuth, Bayreuth, Germany

K. Bandzierz Faculty of Chemistry, Institute of Polymer & Dye Technology, Łódź University of Technology, Łódź, Poland

M. Bastian SKZ—German Plastics Center, Würzburg, Germany

R. Behnke Faculty of Civil Engineering, Institute for Statics and Dynamics of Structures, Dresden University of Technology, Dresden, Germany

D.M. Bielinski Faculty of Chemistry, Institute of Polymer & Dye Technology, Łódź University of Technology, Łódź, Poland; Division of Elastomers & Rubber Technology, Institute for Engineering of Polymer Materials & Dyes, Piastow, Poland

C. Bierögel Centre of Engineering, Martin-Luther-University Halle-Wittenberg, Halle/Saale, Germany; Polymer Service GmbH Merseburg, Associated An-Institute of University of Applied Sciences Merseburg, Merseburg, Germany

L. Boragno Borealis Polyolefine GmbH, Linz, Austria

H. Braun Borealis Polyolefine GmbH, Linz, Austria

J. Breu Department of Inorganic Chemistry I, University of Bayreuth, Bayreuth, Germany

R. Calabrò Department of Chemistry, Materials and Chemical Engineering, Polytechnic University of Milan, Milan, Italy

V. Cipolletti Department of Chemistry Materials and Chemical Engineering, Polytechnic University of Milan, Milan, Italy

L. Conzatti Institute for Macromolecular Studies, National Research Council, Genova, Italy

M. Coombs Pirelli Tyre, Milan, Italy

S. Dedova Leibniz Institute for Polymer Research Dresden e.V., Dresden, Germany; Dresden University of Technology, Dresden, Germany

P. Dmowska-Jasek Faculty of Chemistry, Institute of Polymer & Dye Technology, Łódź University of Technology, Łódź, Poland

K. Engelsing SKZ—German Plastics Center, Würzburg, Germany

U. Ferner Trovotech GmbH, Bitterfeld-Wolfen, Germany

R. Fluch voestalpine Stahl GmbH, Linz, Austria

A. Frank Polymer Competence Center Leoben GmbH, Leoben, Austria

M. Gahleitner Borealis GmbH, Linz, Austria

M.S. Galimberti Department of Chemistry Materials and Chemical Engineering, Polytechnic University of Milan, Milan, Italy

B. Gerets SKZ—German Plastics Center, Würzburg, Germany

P. Ghosh Hari Shankar Singhanian Elastomer & Tyre Research Institute, Kankroli, Rajasthan, India

W. Grellmann Centre of Engineering, Martin-Luther-University Halle-Wittenberg, Halle/Saale, Germany; Polymer Service GmbH Merseburg, Associated An-Institute of University of Applied Sciences Merseburg, Merseburg, Germany

P. Guttman Department Polymer Engineering and Science, Montan University Leoben, Leoben, Austria

A.M. Hartl Institute of Polymeric Materials and Testing, Johannes Kepler University Linz, Linz, Austria

G. Heinrich Leibniz Institute for Polymer Research Dresden e.V., Dresden, Germany; Faculty of Mechanical Science and Engineering, Dresden University of Technology, Dresden, Germany

S. Henning Fraunhofer Institute for Microstructure of Materials and Systems (IMWS), Halle/Saale, Germany

S. Hild Institute of Polymer Sciences, Johannes Kepler University Linz, Linz, Austria

J. Hodan Institute of Macromolecular Chemistry, Academy of Sciences of the Czech Republic, Prague, Czech Republic

T. Horst Faculty of Automobile and Mechanical Engineering, University of Applied Sciences Zwickau, Zwickau, Germany

P. Hutař Institute of Physics of Materials, Academy of Sciences of the Czech Republic, Brno, Czech Republic

T. Illing Valeo Schalter und Sensoren GmbH, Bietigheim-Bissingen, Germany

S. Ilisch Trinseo Deutschland GmbH, Schkopau, Germany

M. Jaszczak Faculty of Chemistry, Institute of Polymer & Dye Technology, Łódź University of Technology, Łódź, Poland

M. Jaunich BAM—Federal Institute for Material Research and Testing, Berlin, Germany

S. Jerrams Centre for Elastomer Research, Dublin Institute of Technology, Dublin, Ireland

M. Kaliske Faculty of Civil Engineering, Institute for Statics and Dynamics of Structures, Dresden University of Technology, Dresden, Germany

C. Kipscholl Coesfeld GmbH & Co. KG, Dortmund, Germany

P. Kirchner Plastics and Elastomer Technology, University of Applied Sciences Würzburg-Schweinfurt, Würzburg, Germany

T. Koch Institute of Materials Science and Technology, Vienna University of Technology, Vienna, Austria

A. Kömmling BAM—Federal Institute for Material Research and Testing, Berlin, Germany

J. Kotek Institute of Macromolecular Chemistry, Academy of Sciences of the Czech Republic, Prague, Czech Republic

M.H. Kothmann Department of Polymer Engineering, University of Bayreuth, Bayreuth, Germany

I. Kotter Polymer Service GmbH Merseburg, Associated An-Institute of University of Applied Sciences Merseburg, Merseburg, Germany

O. Kratina Centre of Polymer Systems, Tomas Bata University in Zlín, Zlín, Czech Republic; Department of Polymer Engineering, Faculty of Technology, Tomas Bata University in Zlín, Zlín, Czech Republic

M. Kroll BASF Leuna GmbH, Leuna, Germany; Institute of Macromolecular Chemistry, Academy of Sciences of the Czech Republic, Prague, Czech Republic

T. Krolopp Polymer Service GmbH Merseburg, Associated An-Institute of University of Applied Sciences Merseburg, Merseburg, Germany

Z. Kruliš Institute of Macromolecular Chemistry, Academy of Sciences of the Czech Republic, Prague, Czech Republic

J. Kučera Polymer Institute Brno, Brno, Czech Republic

R. Lach Polymer Service GmbH Merseburg, Associated An-Institute of University of Applied Sciences Merseburg, Merseburg, Germany

R.W. Lang Institute of Polymeric Materials and Testing, Johannes Kepler University Linz, Linz, Austria

B. Langer Department of Engineering and Natural Sciences, University of Applied Sciences Merseburg, Merseburg, Germany; Polymer Service GmbH Merseburg, Associated An-Institute of University of Applied Sciences Merseburg, Merseburg, Germany

R. Lombardi Leibniz Institute for Polymer Research Dresden e.V., Dresden, Germany; University of Naples Federico II, Naples, Italy; Bridgestone Technical Center Europe, Rome, Italy

J. Maláč Centre of Polymer Systems, Tomas Bata University in Zlín, Zlín, Czech Republic; Department of Polymer Engineering, Faculty of Technology, Tomas Bata University in Zlín, Zlín, Czech Republic

A. Marzec Faculty of Chemistry, Institute of Polymer & Dye Technology, Łódź University of Technology, Łódź, Poland

C. Mayrhofer Austrian Centre for Electron Microscopy and Nanoanalysis, Graz, Austria; Institute for Electron Microscopy and Nanoanalysis, Graz University of Technology, Graz, Austria

J. McIntyre DKI—The German Institute of Rubber Technology, Hanover, Germany

J. Mikula Institute of Physics of Materials, Academy of Sciences of the Czech Republic, Brno, Czech Republic; Brno University of Technology, Brno, Czech Republic

A. Monami Polymer Service GmbH Merseburg, Associated An-Institute of University of Applied Sciences Merseburg, Merseburg, Germany

R. Mukhopadhyay Hari Shankar Singhania Elastomer & Tyre Research Institute, Kankroli, Rajasthan, India

T. Müllner Department of Chemistry, Philipps University, Marburg, Germany

S. Musto Department of Chemistry Materials and Chemical Engineering, Polytechnic University of Milan, Milan, Italy

M. Nachtnebel Institute for Electron Microscopy and Nanoanalysis, Graz University of Technology, Graz, Austria

L. Náhlik Institute of Physics of Materials, Academy of Sciences of the Czech Republic, Brno, Czech Republic

M. Nase University of Applied Sciences Hof, Hof, Germany

K. Naumenko Institute of Mechanics, Otto Von Guericke University Magdeburg, Magdeburg, Germany

E. Nezbedová Polymer Institute Brno, Brno, Czech Republic

A. Ochenduszko Synthos S.A., Oświęcim, Poland

M. Palmstingl Institute of Materials Science and Technology, Vienna University of Technology, Vienna, Austria

S. Pandini Department of Mechanical and Industrial Engineering, University of Brescia, Brescia, Italy

G. Pilz Department Polymer Engineering and Science, Montan University Leoben, Leoben, Austria

G. Pinter Department Polymer Engineering and Science, Montan University Leoben, Leoben, Austria; Polymer Competence Center Leoben GmbH, Leoben, Austria

P. Pöhl Institute for Electron Microscopy and Nanoanalysis, Graz University of Technology, Graz, Austria

G. Przybytniak Institute of Nuclear Chemistry and Technology, Warsaw, Poland

K. Reincke Centre of Engineering, Martin-Luther-University Halle-Wittenberg, Halle/Saale, Germany; Polymer Service GmbH Merseburg, Merseburg, Germany

N. Rennar Plastics and Elastomer Technology, University of Applied Sciences Würzburg-Schweinfurt, Würzburg, Germany

M. Rennert Polifilm Extrusion GmbH, Südliches Anhalt, Germany; University of Applied Sciences Hof, Hof, Germany

T. Riccò Department of Mechanical and Industrial Engineering, University of Brescia, Brescia, Italy

J. Rogoża Synthos S.A., Oświęcim, Poland

W.M. Rzymiski Institute of Polymer & Dye Technology, Łódź University of Technology, Łódź, Poland

J. Sadilek Polymer Institute Brno, Brno, Czech Republic

D. Salaberger University of Applied Sciences of Upper Austria, Wels, Austria

K. Schneider Leibniz Institute for Polymer Research Dresden e.V., Dresden, Germany

C. Schoberleitner Institute of Materials Science and Technology, Vienna University of Technology, Vienna, Austria

M. Schoßig Polymer Service GmbH Merseburg, Associated An-Institute of University of Applied Sciences Merseburg, Merseburg, Germany

L. Schulenberg Fraunhofer Institute for Mechanics of Materials (IWM), Freiburg, Germany

A. Schulze Leibniz Institute for Polymer Research Dresden e.V., Dresden, Germany; Chemnitz University of Technology, Chemnitz, Germany

T. Seelig Institute of Mechanics, Karlsruhe Institute of Technology (KIT), Karlsruhe, Germany

M. Ševčík Institute of Physics of Materials, Academy of Sciences of the Czech Republic, Brno, Czech Republic

A. Smejda-Krzewicka Institute of Polymer & Dye Technology, Łódź University of Technology, Łódź, Poland

M. Stein Institute of Processing Machines and Mobile Machinery, Dresden University of Technology, Dresden, Germany

R. Stoček PRL Polymer Research Lab s.r.o., Zlín, Czech Republic; Centre of Polymer Systems, Tomas Bata University in Zlín, Zlín, Czech Republic

B. Strauß voestalpine Stahl GmbH, Linz, Austria

D.-Z. Sun Fraunhofer Institute for Mechanics of Materials (IWM), Freiburg, Germany

R. Tiefenthaller Institute of Polymer Science, Johannes Kepler University Linz, Linz, Austria; voestalpine Stahl GmbH, Linz, Austria

S. Thiele Trinseo Deutschland GmbH, Schkopau, Germany

M. Wenzel SKZ—German Plastics Center, Würzburg, Germany

K. Wewerka Institute for Electron Microscopy and Nanoanalysis, Graz University of Technology, Graz, (Austria)

D. Wolff BAM—Federal Institute for Material Research and Testing, Berlin, Germany

A. Zankel Institute for Electron Microscopy and Nanoanalysis, Graz University of Technology, Graz, Austria; Austrian Centre for Electron Microscopy and Nanoanalysis, Graz, Austria

R. Zeiler Department of Polymer Engineering, University of Bayreuth, Bayreuth, Germany

M. Ziadeh Department of Inorganic Chemistry I, University of Bayreuth, Bayreuth, Germany

Abbreviations

2NCT	Double Notch Creep Test
3D-FAC	Fluorescence adsorption contrast method
ABS	Acrylonitrile–butadiene–styrene
ACN	Acrylonitrile
ACT	Accelerated Creep Test
AE	Acoustic emission
AFM	Atomic force microscopy
aFNCT	Accelerated Full Notch Creep Test
ALE	Arbitrary Lagrangian Eulerian
ATBN	Amine-terminated butadiene–acrylonitrile copolymer
BET	Brunauer–Emmett–Teller
BIIR	Brominated poly(isobutylene-co-isoprene)
BOPET	Biaxial oriented poly(ethylene terephthalate)
BR	Butadiene rubber
BSE	Backscattered electrons
C(T)OD	Crack-(tip)-opening displacement
CA	Coupling agent
CB	Carbon black
CCG	Creep crack growth
CD	Particle distance
CEG	Cation exchange capacity
CF	Coniferous trees
CIP	Carbonyl iron powder
CNT	Carbon nanotubes
CRB specimen	Cracked round bar specimen
CRB test	Crack Round Bar Test
CS	Compression set
CSEM	Conventional scanning electron microscopy
CT specimen	Compact tension specimen
CT	Computed tomography

CTOA	Crack-tip-opening angle
DCP	Dicumyl peroxide
DENT specimen	Double-edge-notched tension specimen
DGEBA	Diglycidyl ether of bisphenol-A
DI	Macro dispersion index
DIC	Digital image correlation
DIE	Digital image elaboration
DMA	Dynamic-mechanical-analysis
DMTA	Dynamic-mechanical-thermal analysis
DSC	Differential scanning calorimetry
EB	Electron beam
EDS	Energy-dispersive X-ray Spectrometry
EDZ	State of plane strain
EFTEM	Energy-filtered transmission electron microscopy
ENR	Epoxidised natural rubber
EPDM	Ethylene-propylene-diene rubber
EPFM	Elastic-plastic fracture mechanics
EPR	Ethylene-propylene rubber
ESEM	Environmental scanning electron microscopy
ETD	Everhart-Thornley detector
EVA	Ethylene(vinyl acetate)
FBA	Formerly bonded area
FCG	Fatigue crack growth
FCP	Fatigue crack propagation
FE	Finite element
FEA	Finite element analysis
FEG	Field-emission gun
FEM	Finite element method
FKM	Fluorocarbon rubber
FNCT	Full Notch Creep Test
FSBR	Styrene-butadiene-butylacrylate mix polymer
FTIR	Fourier transform infrared spectroscopy
FT-model	Folgar-Tucker model
FW	Impact falling weight
GF	Short glass fibre-reinforced
GPC	Gel permeation chromatography
HNBR	Hydrogenated nitrile butadiene rubber
ICIT	Instrumented Charpy impact test
IR	cis-1,4-polyisoprene; synthetic rubber
IRHD	International rubber hardness degree
LEFM	Linear elastic fracture mechanics
LFT	Long fibre-reinforced thermoplastics
LVSEM	Low-voltage scanning electron microscopy
MAH	Maleic anhydride
micro-CT	Microcomputer tomography

MR	Magnetorheological
MRE	Magnetorheological elastomer
MTS criterion	Maximum tangential stress criterion
nanoG	Nano-graphite
NBR	Nitrile-butadiene rubber
NCTL Test	Notched Constant Tensile Load Test
NIS	Notched impact strength
NPT	Notch Pipe Test
NR	cis-1,4-polyisoprene; natural rubber
PA	Polyamide
PA6	Polyamide 6
PA66	Polyamide 66
PB-1	Polybutene-1
PC	Polycarbonate
PDMS	Polydimethylsiloxane
PE	Polyethylene
PE-HD	High-density polyethylene
PE-LD	Low-density polyethylene
PE-LLD	Linear low-density polyethylene
PE-MD	Medium-density polyethylene
PENT Test	Pennsylvania Edge Notch Tensile Test
PES	Polyethersulfone
PET	Poly(ethylene terephthalate)
PLT	Point Load Test
PMMA	Poly(methyl methacrylate)
PNR	Polynorbornene
PP	Polypropylene
PPA	Polyphthalamide
PS specimen	Pure-shear specimen
PVC	Poly(vinyl chloride)
PXRD	Powder X-ray Diffraction
R-curve	Crack resistance curve
RH	Relative humidity
RSC model	Modified model of Wang and Jin
SBEM	Serial block face scanning electron microscopy
SBR	Styrene-butadiene rubber
SCG	Slow crack growth
SE	Secondary electrons
SEM	Scanning electron microscopy
SENB specimen	Single-edge-notched bending specimen
SENT specimen	Single-edge-notched tension specimen
SF	Single fibre
SFRP	Short fibre-reinforced polymers
SHT	Strain Hardening Test
SIM	Stepped Isothermal Method

SMART	Small accelerated reliable test
SZH	Stretch zone height
SZW	Stretch zone width
TEM	Transmission electron microscopy
TGA	Thermogravimetric analysis
THF	Tetrahydrofuran
TMT	Thermomechanical treatment
TOR	Polyoctenamer
TPE	Thermoplastic elastomer
TPU	Thermoplastic polyurethane
TTSP	Time–temperature superposition principle
UD	Unidirectional
VPSEM	Variable pressure scanning electron microscopy
WF	Wood flour
WLF	Williams-Landel-Ferry
WOL	Wedged open loading
WT	Wavelet transform
X-CT	X-ray computed tomography

Part I
**Modern Aspects of Fracture Mechanics in
the Industrial Application of Polymers**

Chapter 1

Time-Dependent Fracture Behaviour of Polymers at Impact and Quasi-Static Loading Conditions

R. Lach and W. Grellmann

Abstract Based on the crack resistance (R) concept of elastic fracture mechanics the crack propagation kinetics at impact and quasi-static loading conditions was analysed both from the experimental and analytical point of view. For blends composed of polyurethane (TPU) and an acrylonitrile–butadiene–styrene copolymer (ABS), it has been shown that the stop block method in multiple-specimens technique is the most suitable method for determining R-curves at impact loading conditions. As shown for a couple of thermoplastic materials such as polypropylene (PP)/ethylene–propylene rubber (EPR)/polyethylene(PE) copolymers, short-glass fibre-reinforced PP, binary blends of polystyrene(PS)–polybutadiene(PB) block copolymers and PP/EPR blends, the crack-tip-opening displacement (CTOD) rate (limit value) relates exclusively to the deformations that occur in the matrix or the major phase, not, however, to those that occur inside the particles or the minor phase, or near interfaces. That means that the CTOD rate is not affected by the glass fibre fraction or the particle distance. Furthermore the CTOD rate is not influenced by the temperature (polycarbonate) and proportional to the loading speed (PP materials). For most of the polymers investigated, such as PC (> 40 °C), PP/EPR/PE, PP, PP/glass fibre composites, PE, ABS, TPU/ABS blends and SB block copolymer blends, a 3-phase process the crack propagation kinetics could be found, with the CTOD rate as a function of the stable crack growth (or of time) quickly converging against a limit value. Here, this stationary crack propagation (Phase III) is preceded by crack-tip blunting/crack initiation (Phase I) and non-stationary stable crack growth (Phase II).

R. Lach (✉) · W. Grellmann
Polymer Service GmbH Merseburg, Merseburg, Germany

W. Grellmann
Centre of Engineering, Martin Luther University Halle-Wittenberg, Halle/Saale, Germany

1.1 Comparison of Methods for the Determination of R-Curves for Polymers at Impact Loading

Based on irreversible thermodynamics, the J -integral is a parameter that describes the energy field around a propagating crack for the case of stationary stable crack propagation [1]. Assuming that the coordinate system moves with the crack, that is, the coordinate origin is located at the tip of the crack, any acceleration dependence during crack propagation can be excluded entirely. This means that (i) the strain field at the crack tip is time-independent and (ii) the crack propagation speed is constant. The requirement (i) is comparable to a constant crack-tip-opening angle or a constant CTOD rate, because the CTOD (crack-tip-opening displacement) is a measure of the elongation of materials close to the crack tip. The quality of experimental R-curve routines is generally determined through the fulfilment of the above-mentioned conditions (i) and (ii). Any changes in the energy field as a result of local relaxation caused by stable crack growth are already considered by correction terms in the determination of J -values. In the following, the results of different procedures for the determination of R-curves will be compared for one material system.

For TPU/ABS blends, which consist of a thermoplastic elastomer based on polyurethane (TPU) and an acrylonitrile–butadiene–styrene terpolymer (ABS), and other polymer systems [3], it has been shown that the stop block method in multiple specimens technique is the most suitable method for determining R-curves (Fig. 1.1a) and that it is associated with the kinetics of stable crack propagation. This means that the crack-tip-opening displacement rate $\dot{\delta}$ ($d\delta/dt$) is constant except for small Δa values, consistent with condition (i) above (Fig. 1.1b).

Compared with the low blow method, the stop block method leads to smaller values for the resistance against crack initiation and against crack propagation (Fig. 1.1a). The $\dot{\delta}$ values determined by means of the low blow method increase as the Δa values increase, corresponding to the increasing impact testing speed v_H (Fig. 1.1b), because the ratio $\dot{\delta}/v_H$, as shown below (see Figs. 1.10 and 1.13), is material-specific, in contrast to the ratio of the crack speed \dot{a}/v_H (see Fig. 1.12).

Owing to the growth of the crack-tip blunting zone with the number of loading cycles, using the quasi single-specimen method the crack-tip-opening displacement rate $\dot{\delta}$ (Fig. 1.1d) decreases because it is a measure of the local strain rate close to the crack tip. Compared with the multiple-specimens technique, this behaviour (decreasing strain rate) is related to a higher dissipation of energy as a function of Δa (Fig. 1.1c).

In conclusion, only the stop block method in multiple-specimens technique fulfils the criterion (i) of the “time-independent” strain field.

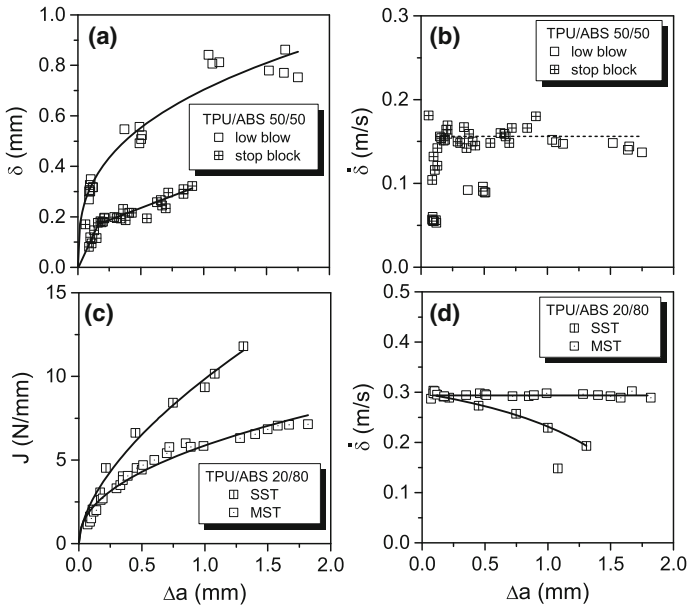


Fig. 1.1 δ -R- (a) and J -R-curves (c), measured with different methods (*SST* single-specimen technique, *MST* multiple-specimens technique) and relating to the CTOD rate for TPU/ABS blends (b, d) (Fig. 1.1a, b as well as Fig. 1.1c, d are related to each other) [2]

1.2 Material Samples

1.2.1 Semicrystalline Polymers with Particle–Matrix Structure: PP/EPR/PE Copolymers

Ethylene–propylene copolymers (in the following referred to as PP/EPR/PE copolymers) that have a matrix–particle structure (Fig. 1.2) with different centre-to-centre particle distances (CD) ranging from 2.0 to 4.1 μm were used to determine the R-curve (Fig. 1.3a; $v_H = 1 \text{ m/s}$; room temperature). Crack-tip blunting and crack initiation were not influenced by the morphology, so that the crack initiation resistance was the same as that of pure matrix material (PP). In contrast, the crack propagation resistance, for example in form of rising R-curves, is sensitive to morphological changes.

It could be observed that the value of the crack-tip-opening displacement (CTOD) rate $\dot{\delta}$ (Fig. 1.3b) quickly converges against a material-specific limit (stationary crack propagation, that is, an equilibrium state, state III in Fig. 1.3d) after crack tip-blunting/stable crack initiation (state I in Fig. 1.3d) and non-stationary crack growth (state II in Fig. 1.3d) which is independent of the particle distance (Fig. 1.3b, c). As shown in Fig. 1.3d, both conditions (i) and (ii) (Sect. 1.1) are fulfilled for times greater than 0.45 ms. Since both $\dot{\delta}$ and \dot{a}

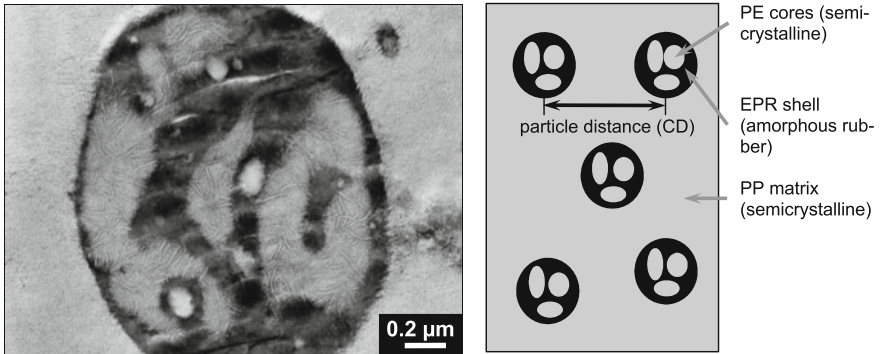


Fig. 1.2 Morphology of a PP/EPR/PE copolymer (matrix-particle structure) [2]

remain constant, the J -integral is the parameter that is used for describing the energy balance around a propagating crack in PP/EPR/PE. The maximum CTOD rate (80 mm/s) lies within the range of pure PP (Fig. 1.3c), with CTOD being a measure of the plasticity close to the crack tip. Accordingly, the CTOD rate relates exclusively to the deformations that occur in the matrix or the major phase, not, however, to those that occur inside the particles or the minor phase, or near interfaces.

1.2.2 Short-Glass Fibre (GF)-Reinforced Semicrystalline Polymers: PP/GF

While in ethylene-propylene copolymers the crack propagation resistance (slope of R-curves)—correlating with impact modification—rises with increasing rubber content, the crack propagation resistance in short-glass fibre (GF)-reinforced propylene (PP/GF; GF content: 0–26%) decreases with increasing GF content (Fig. 1.4a; $v_H = 1$ m/s; room temperature). This is caused by the increasing deformation constraint of the polymer matrix because of the fibres. Hence, the crack propagation resistance of PP/GF and PP/EPR/PE (see Sect. 1.2.1) is a good indicator of morphological changes.

Independent of the GF content (Fig. 1.4b, c), the CTOD rate converges against a limit of 80 mm/s (Fig. 1.4b), related to stationary crack propagation, which lies within the range of pure PP, as it does in PP/EPR/PE. Hence, the statements made in Sect. 1.2.1 on the interpretation of the CTOD and CTOD rate also apply to PP/GF.

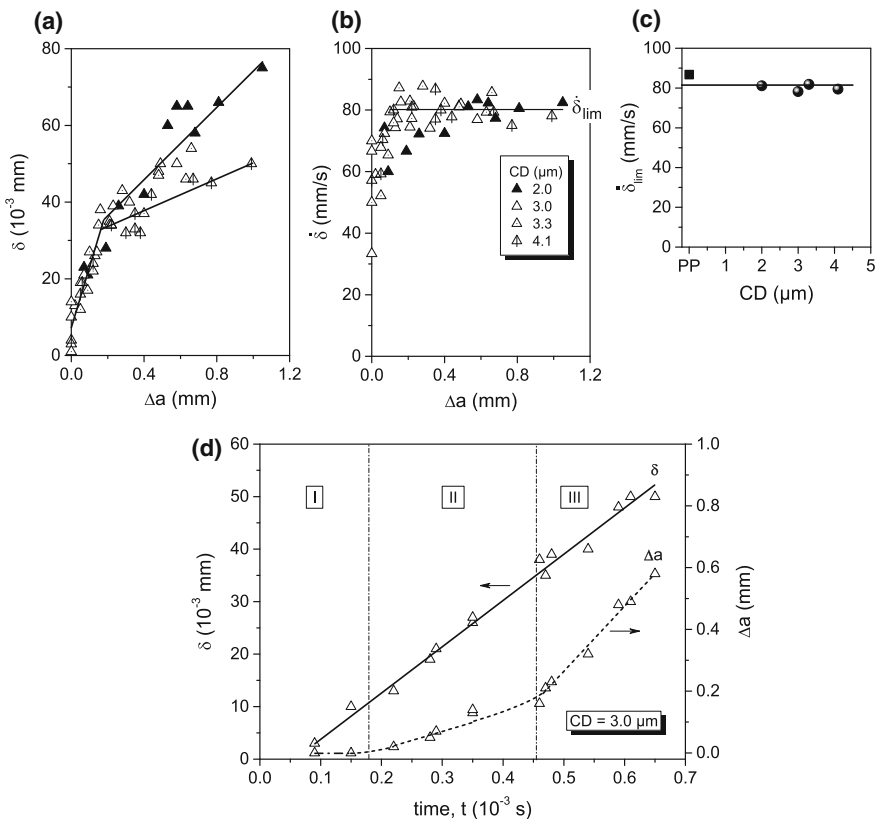


Fig. 1.3 δ -R-curves (a) (with crack-tip blunting lines from the beginning of the fracture process up to $\Delta a = 0.2$ mm for all copolymers and two crack propagation lines for $CD = 2.0$ μm and $CD = 4.1$ μm), CTOD rate $\dot{\delta}$ depending on stable crack growth Δa (b), dependence of the maximum $\dot{\delta}$ values on particle distance CD (c), δ and Δa as a function of time ($CD = 3.0$ μm) (d) for PP/EPR/PE (for I-III: see text) [2]

1.2.3 Nanophase-Separated Amorphous Polymers: Binary Blends of PS–PB Block Copolymers

In addition to the multiple-phase semicrystalline polymers with particle–matrix structure, such as PP/EPR/PE, in which the heterogeneities are formed by particles in the range of micrometres and crystallites in the nanometre range, new classes of self-structuring nanoscale polymers, such as binary blends made of block copolymers, receive growing interest. In this study, we examine amorphous blends that are based on a relatively brittle star block copolymer and a triblock copolymer (a thermoplastic elastomer) as impact modifier, while both block copolymers are based on styrene and butadiene (Fig. 1.5).

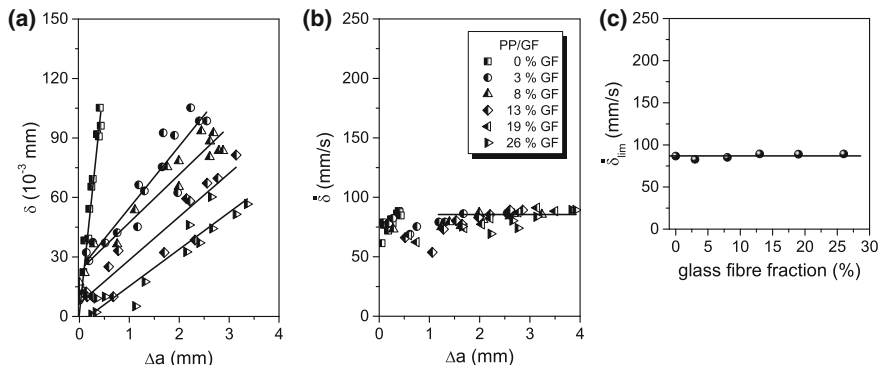


Fig. 1.4 δ -R-curves (a), CTOD rate values $\dot{\delta}$ dependent on stable crack growth Δa (b), dependence of the maximum $\dot{\delta}$ values on glass fibre content (c) for PP/short-glass fibre (GF) composites

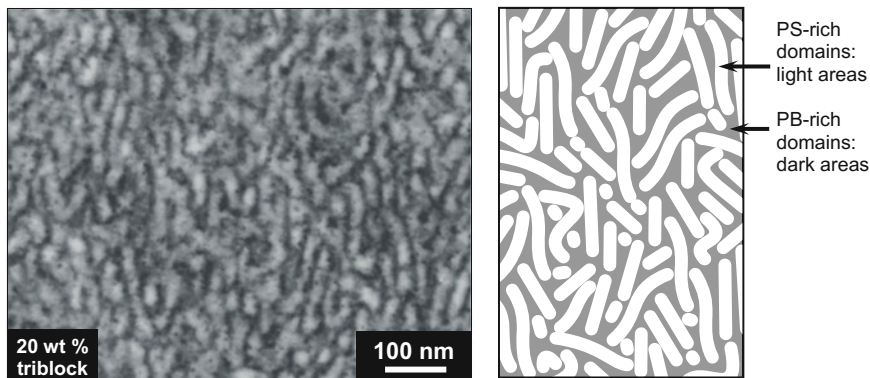


Fig. 1.5 Morphology of polystyrene block copolymer blends of a triblock and a star block copolymer [2]

The δ - Δa -curves of star block/triblock copolymer blends depend on the triblock content, as shown in Fig. 1.6a ($v_H = 1$ m/s; room temperature). The R-curves slope increases significantly with increasing triblock copolymer content.

For this polymer system, three stages of the crack propagation were observed as well (Fig. 1.6a, b). Stage I correlates with crack-tip blunting and stable crack initiation, corresponding with a considerable increase in the $\dot{\delta}$ -values. In Stage II, the crack propagation continues to be stable but in a non-stationary way, which correlates with a further increase in the $\dot{\delta}$ -values. In Stage III, the crack propagation process reaches a stationary stage, that is, an equilibrium state, with the $\dot{\delta}$ -values remaining constant. Corresponding to the statements about PP/EPR/PE in Sect. 1.2.1 (Fig. 1.3c), conditions (i) and (ii), that is, that $\dot{\delta}$ and \dot{a} are constant

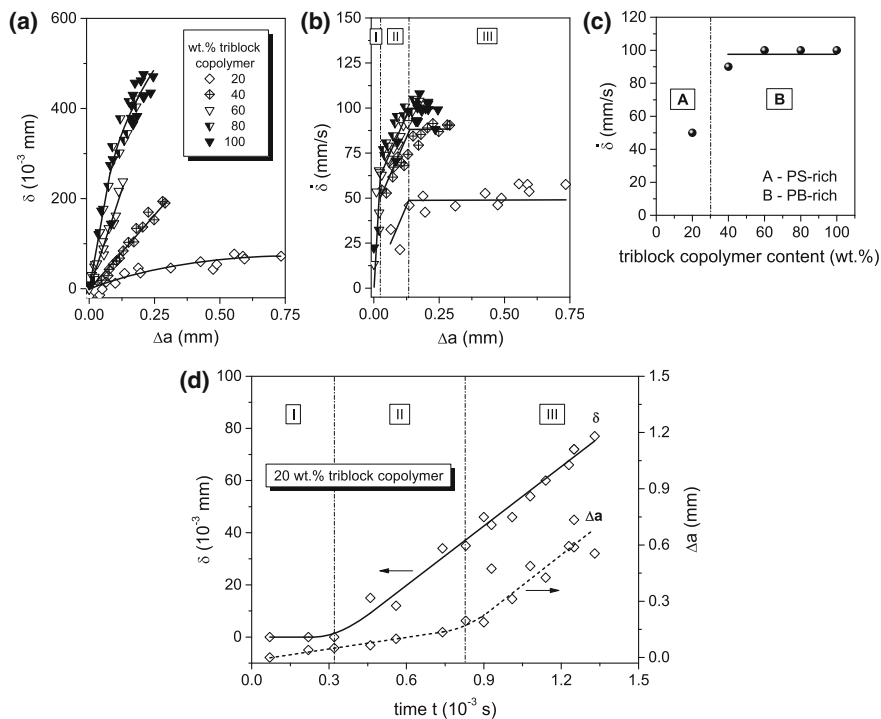


Fig. 1.6 δ -R-curves (a) and CTOD rate $\dot{\delta}$ (b) as a function of stable crack growth Δa , dependence of the maximum $\dot{\delta}$ values on the triblock copolymer content (c) and δ and Δa as a function of time (20% triblock copolymer) (d) for binary SB block copolymer blends (for I–III: see text) [2]

(see Sect. 1.1: the J -integral is a parameter that describes the energy field around a propagating crack for the case of stationary stable crack propagation), are also fulfilled for the copolymer blends (for times greater than 0.8 ms, see Fig. 1.6c). The maximum $\dot{\delta}$ -values increase with increasing triblock copolymer content of up to 100 mm/s for 60 wt% triblock copolymers. This morphological dependency of the limits can be explained by the fact that the plastic deformations occur primarily during the main phase initiated either by PS-rich ($\dot{\delta} = 50$ mm/s) or by PB-rich domains ($\dot{\delta} = 90$ – 100 mm/s), corresponding to a triblock copolymer content of 20 and 40–100 wt% respectively. This deformation behaviour can be understood on the basis of a rheological model with the phase geometry as parameter [4].

1.2.4 CTOD Rate Under Quasi-Static Test Conditions: PP/EPR Blends

The crack resistance of PP/EPR blends—consisting of PP as matrix polymer and individually distributed EPR as impact modifier—was determined by means of a single-specimen in situ method described in [5] under quasi-static test conditions (crosshead speed of the universal testing machine: 10 mm/min, room temperature). For this purpose, the stable crack growth Δa and the crack-tip-opening displacement δ were determined video optically at different times while simultaneously recording the load and displacement (Fig. 1.7) and—based thereupon—constructing the R-curves (Fig. 1.8a).

The time dependencies of the crack growth and CTOD (Fig. 1.7) determined for PP/EPR at quasi-static load do not differ in quality from those that were determined

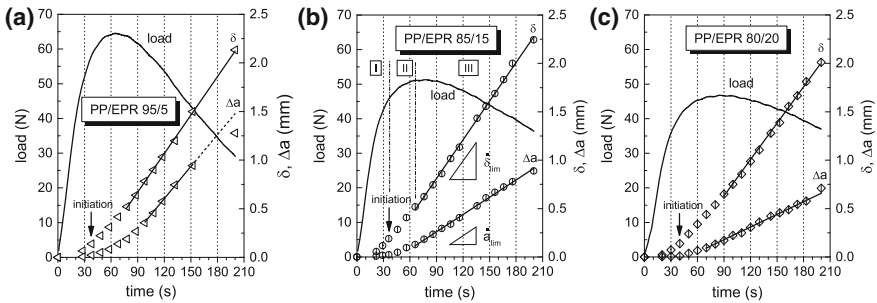


Fig. 1.7 Load, δ and Δa as a function of time for PP/EPR blends with 5% (a), 15% (b) and 20% (c) of EPR (for I–III: see text)

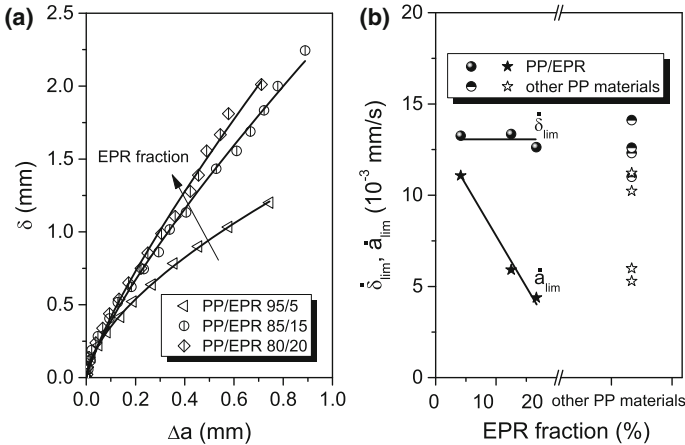


Fig. 1.8 δ -R-curves for PP/EPR blends (a), CTOD rate $\dot{\delta}_{lim}$ and crack speed \dot{a}_{lim} for PP/EPR blends as a function of the EPR content and other PP polymers for comparison's purposes (b)

at impact loading (see Figs. 1.3d and 1.6c). It can be observed that the CTOD rate converges against the same value, independent of the EPR content (see also Fig. 1.8b), therefore being matrix-specific (compare Sect. 1.3). In contrast, the maximum crack speed decreases with increasing EPR content because of the increasing crack propagation stability, which is reflected by a steadily increasing slope of the R-curves (Fig. 1.8a). Under quasi-static test conditions, the three-phase process (Phases I–III) discussed above can also be found for stable crack propagation (Fig. 1.7). Figure 1.8b provides an overview of the limits for $\dot{\delta}$ and \dot{a} ($\dot{\delta}_{lim}$ and \dot{a}_{lim}) of PP/EPR in comparison to other PP polymers investigated under quasi-static test conditions. The values for $\dot{\delta}_{lim}$ are on the same level independent of the material because they are influenced only by the matrix—in this case, PP. In contrast, the values for \dot{a}_{lim} cover a large area because the individual polymers have different phase morphologies and different crack propagation stabilities, that is, resistance against stable crack propagation.

1.2.5 Influence of the Temperature: Amorphous Polycarbonate (PC)

If the maximum CTOD rate $\dot{\delta}_{lim}$ is indeed exclusively a measure of the strain rate of the polymer matrix—immediately in front of the crack tip, it should be independent of the temperature provided that there is a specified load speed and a temperature-independent activation mechanism for plastic deformations. This could be shown for the amorphous homopolymer polycarbonate (PC), because the stable crack propagation process is dominated by the same shear flow process stimulated by the β relaxation at temperatures ranging between 60 and 90 °C but is not

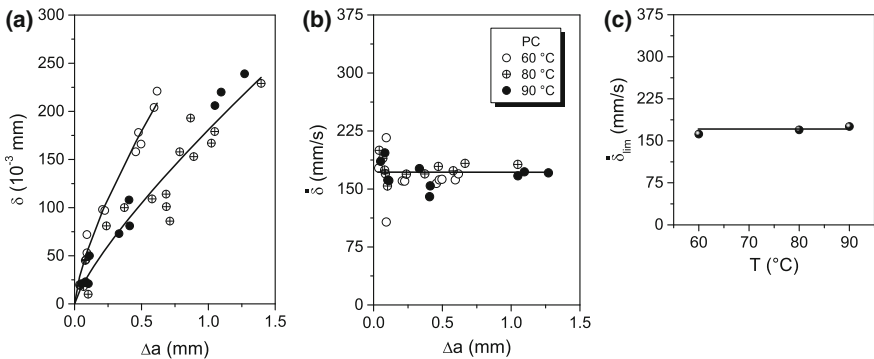


Fig. 1.9 δ -R-curves (a), CTOD rate values $\dot{\delta}$ dependent on stable crack growth Δa (b), dependence of temperature on the maximum $\dot{\delta}$ values (c) for PC

influenced by the crack propagation that decreases with increasing temperature (Fig. 1.9a): $\dot{\delta}_{\text{lim}}$ is temperature-independent (Fig. 1.9b, c).

1.3 Crack Propagation Kinetics of Polymers at Impact Loading Conditions

For most of the polymers investigated, such as PC ($T > 40$ °C), PP/EPR/PE, PP, PP/glass fibre blends, PE-HD, ABS, TPU/ABS blends and SB block copolymer blends, a 3-phase process could be found under test conditions (Fig. 1.10), with the CTOD rate $\dot{\delta}$ as a function of Δa (or of time) quickly converging against a limit $\dot{\delta}_{\text{lim}}$.

As shown in Fig. 1.11a for SB block copolymer blends, this stationary crack propagation (Phase III) is preceded by crack-tip blunting/crack initiation (Phase I) and non-stationary stable crack growth (Phase II). A more general model for the crack propagation kinetics of polymers under moderate impact-loading conditions is shown in Fig. 1.11b. Relative brittle materials, such as PC for $T \leq 40$ °C [1], show a transition to unstable crack propagation without passing through Phase III. In contrast, for highly ductile materials (e.g. some PP materials impact-modified with EPR) the plastic zone during crack-tip blunting increases to such an extent that they come in contact with the specimen's edge ("full-scale yielding"). In this case, the crack propagation behaviour can no longer be described by J and stationary crack propagation does not occur. It could be shown that the normalised stationary CTOD rate $\dot{\delta}_{\text{lim}}/v_{\text{H}}$ (v_{H} —impact testing speed and crosshead speed) for specific polymer groups, such as PE-HD, ABS and polymer systems with a PP matrix (Figs. 1.3b and 1.10b), has typical values (Fig. 1.10a) that only depend on the matrix or the major phase. For PP materials, the same $\dot{\delta}_{\text{lim}}/v_{\text{H}}$ values were found, independent of the loading speed, since the CTOD rate is dominated by the matrix. Hence, for quasi-static test conditions (10 mm/min), $\dot{\delta}_{\text{lim}}/v_{\text{H}}$ takes on values of $(7.6 \pm 0.5) \times 10^{-2}$ and for impact-loading test conditions (1 m/s) values of $(8.5 \pm 0.4) \times 10^{-2}$. Furthermore, for PC it could be shown that $\dot{\delta}_{\text{lim}}/v_{\text{H}}$ is temperature independent within the chosen temperature range (Fig. 1.10c, compare with Fig. 1.13). Also, for PC the crack propagation speed \dot{a} , except for initially stable crack growth, is independent of Δa , corresponding to condition (ii) in Sect. 1.1, although the limits of the normalised crack propagation $\dot{a}_{\text{lim}}/v_{\text{H}}$ are temperature-dependent (Fig. 1.12).

The constancy of $\dot{\delta}_{\text{lim}}/v_{\text{H}}$ has an analogy with the crack propagation under static loading (creep), during which the product of the deformation speed of stationary creep $\dot{\epsilon}$ and fracture time t_{B} is constant [6]. Both $\dot{\delta}_{\text{lim}}/v_{\text{H}} = \text{const.}$ and $\dot{\epsilon} \cdot t_{\text{B}} = \text{const.}$ indicate that the fracture—as is typical of polymers—occurs during a critical deformation.

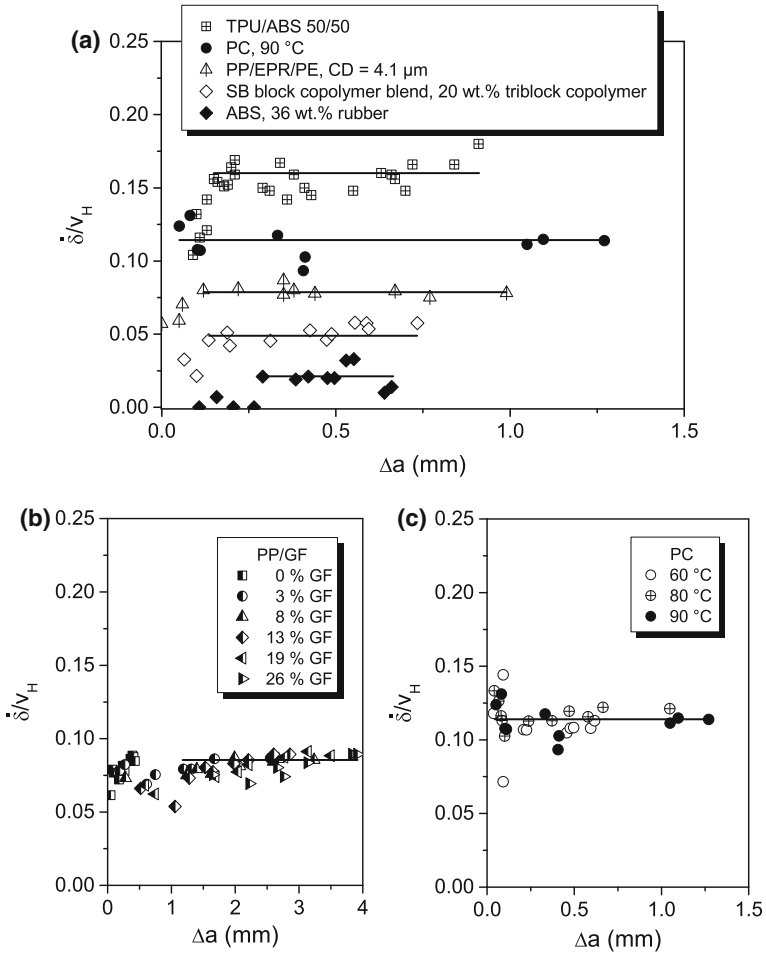


Fig. 1.10 Normalised CTOD rate $\dot{\delta}/v_H$ for different polymers (a) and as a function of the glass fibre (GF) content for PP/GF (b) and the temperature for PC (c) [2]

The crack speed (see Fig. 1.12) is a measure of the stiffness of the entire mechanical system, which depends on the intrinsic brittleness of the notched specimen (shape and size of the specimen, material), the stiffness of the test equipment and the kind of loading (stress- or strain-controlled loading, bending or tensile load, etc.). The CTOD rate (see Fig. 1.10) refers to the deformation processes of the “matrix”, since the CTOD is a measure of the elongation close to the crack tip. For this reason, the limit of the CTOD rate (see Fig. 1.13) as the time sensitivity of the stable crack propagation process depends on the type of plastic deformation and provides an insight into the micromechanics and the activation mechanisms of the fracture process.

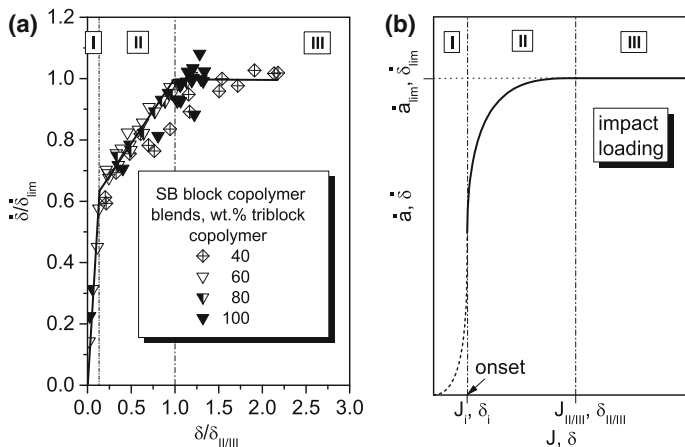


Fig. 1.11 Crack propagation kinetics for SB block copolymer blends (a) and as generalised model for polymers at moderate impact loading (b) (for I-III: see text) [2]

Fig. 1.12 Normalised crack speed \dot{a}/v_H for PC as a function of the temperature [2]

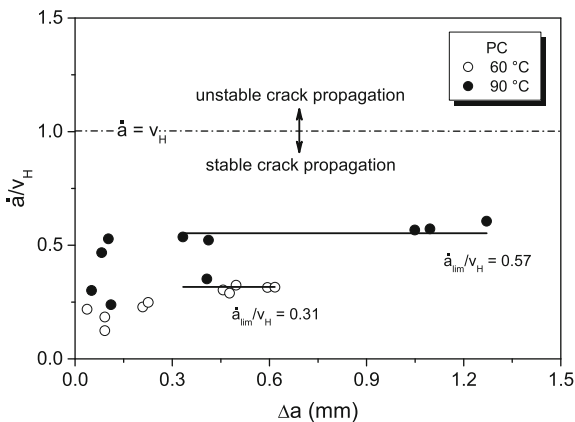
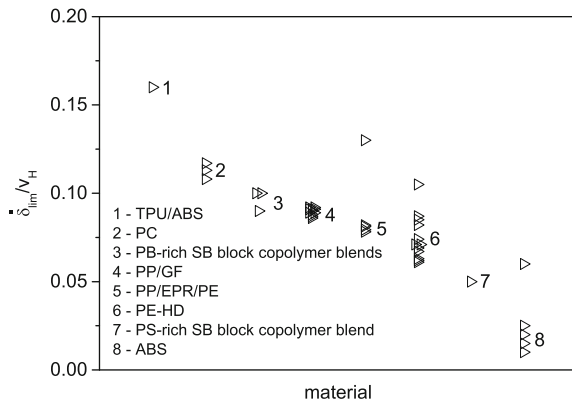


Fig. 1.13 Material dependence of normalised CTOD rate $\dot{\delta}_{lim}/v_H$ for stationary stable crack propagation (each point represents a separate R-curve) [2]

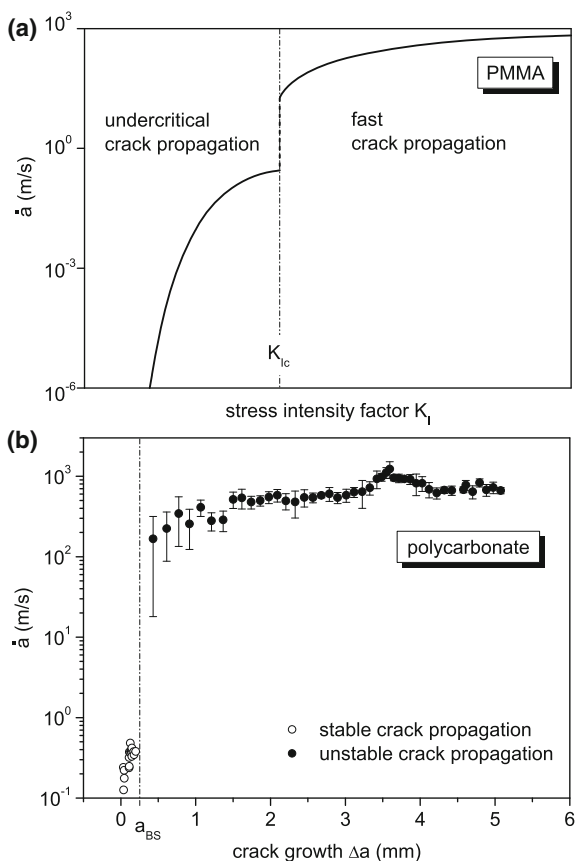


1.4 Discussion of Literature on Crack Propagation Kinetics

For brittle polymers, such as PC at low temperatures and PMMA, the phase of stationary stable crack propagation (Phase III) is not reached. Instead, when fracture toughness K_{Ic} is reached, unstable crack propagation immediately follows, with the crack speed escalating by one or two magnitudes (Fig. 1.14). This has been shown by both studies on the subcritical and fast crack growth of PMMA presented in the literature [7–9] and our own studies on the stable and unstable crack growth of PC (for further information on dynamic crack propagation in polymers, references to the relevant literature are provided).

According to Anderson [11], under the condition that the elastic unloading area and the zone of non-proportional plastic loading (plastic zone) are surrounded by a J -dominated elastic zone at all times during stable crack propagation, the J -integral concept should maintain its validity. With increasing stable crack elongation

Fig. 1.14 Crack propagation speed \dot{a} as a function of stress intensity factor K_I (schematic) for PMMA (after [8, 9], see also [7]) **a** crack propagation speed \dot{a} dependent on crack growth Δa for PC **b** \dot{a} in the range of stable crack growth was determined on the basis of investigations on crack resistance behaviour; the estimate of a mean crack speed \dot{a} for the unstable crack propagation was calculated by analysing beach marks on the fracture surface caused by oscillation of the crack tip following the calibration to the maximum crack speed of 700 m/s [10] (maximum load speed: 1.5 m/s, room temperature, a_{BS} —stable crack growth)



Δa and assuming crack-tip blunting, it should be possible to observe crack initiation and stable crack propagation, which is strongly influenced by the crack-tip blunting process, as well as stationary crack growth, which is independent of the crack-tip blunting process. In principle this corresponds to the 3-phase process described in this study and based on results of investigations on polymers; however, the statements on the shape of the J - Δa crack resistance curves made in [11] contradict the experimental observations and thermodynamic considerations. According to heuristic arguments and based on the results of a mathematical analysis (Rice-Drugan-Sham analysis [12]), the R-curves of stationary crack propagation should be “flat”, that is, they should show a slope dJ/da of $dJ/da = 0$ after [11]. Reasons for this include that for sufficient Δa -values the crack propagation process does no longer depend on the initial conditions and the local material properties are not dependent on the location. During the stationary crack propagation process, a plastic area of consistent width forms along the crack. In this area, constant energy dissipation occurs per unit of the crack progression because of the constant crack propagation speed and constant local material properties. The tearing modulus T_J with $T_J = (dJ/da) \times (E/\sigma_y^2)$ as a measure of the crack propagation resistance indicates (E —modulus of elasticity, σ_y —yield stress) how much energy is converted per unit of the crack progression. A tearing modulus of nearly zero corresponding to a flat R-curve and thus very small crack propagation stability suggests negligible energy dissipation. (Note: According to the first law of thermodynamics, the principle of the conservation of energy, $T_J \leq 0$ is not possible.) Since low crack propagation stability and high crack propagation speed correlate with each other (see Fig. 1.8 for PP/EPR and Figs. 1.9a and 1.12 for PC), it is only possible that $T_J \approx 0$ is associated with unstable crack propagation and not, as Anderson assumes, with stationary stable crack propagation. Rather, for stationary stable crack growth owing to the time constancy of energy dissipation, the following is true: $T_J \rightarrow \text{const.} > 0$, which corresponds with the experimental results (see e.g. R-curves in [3]). This can also be shown by a mathematical analysis. Rice, Drugan and Sham found the following correlation, based on the analysis of the local strains and displacements around a growing crack [12]:

$$\dot{\delta} = \alpha \frac{\dot{J}}{\sigma_y} + \beta \frac{\sigma_y}{E} \dot{a} \cdot \ln\left(\frac{R}{r}\right) \quad \text{for } r \rightarrow 0 \quad (1.1)$$

Here, E and σ_y are material constants (E modulus and yield stress) and α , β and R further constants. Corresponding with [13], R is proportional to the size of the plastic zone for small-scale yielding and $\beta = 4/\sqrt{3}(2 - \nu)$ and $\alpha = \sigma_y \cdot \delta_i/J_i$ (ν —Poisson’s ratio; δ_i , J_i —resistance against stable crack initiation). Since it is true that $\dot{a} = \text{const.} > 0$ and $\dot{\delta} = \text{const.} > 0$ for stationary stable crack growth (see conditions (i) and (ii), Sect. 1.1), $\dot{J} = \text{const.} > 0$ results in general for the time derivation of the J -integral, corresponding to (1.1). With tearing modulus T_J (see above) it follows that:

$$\dot{J} = \frac{dJ}{dt} = \frac{\partial J}{\partial a} \frac{\partial a}{\partial t} = T_J \frac{\sigma_y^2}{E} \dot{a} \quad (1.2)$$

And from this equation it follows that T_J converges against a constant value greater than zero in the case of stationary stable crack growth, which is consistent with experimental results and thermodynamic considerations.

Alternatively, the slope of R -curves for large limits, that is, for stationary stable crack growth with $\lim_{t \rightarrow \infty} \dot{a} = \dot{a}_{\text{lim}} > 0$, can also be derived from the assumption of generalised power functions (as assumptions for the R -curves) in the form of

$$\delta(t) = a_{\delta}(t) \cdot \Delta a^{c_{\delta}(t)} \quad \text{and} \quad J(t) = a_J(t) \cdot \Delta a^{c_J(t)}. \quad (1.3)$$

After converting (1.3) for Δa and deriving the time, it follows (here, the derivation is only shown for $\delta(t)$; for $J(t)$ it is analogous):

$$\dot{a} = \frac{1}{c_{\delta}} \cdot \left(\frac{\delta}{a_{\delta}} \right)^{\frac{1}{c_{\delta}} - 1} \cdot \left(\dot{\delta} \cdot \frac{1}{a_{\delta}} - \delta \cdot \frac{1}{a_{\delta}^2} \cdot \frac{da_{\delta}}{dt} \right) \quad (1.4)$$

Now, $\lim_{t \rightarrow \infty} \dot{a} = \dot{a}_{\text{lim}} > 0$ is only possible if both $1/c_{\delta} - 1 \rightarrow 0$, that is, $c_{\delta} \rightarrow 1$, and $da_{\delta}/dt \rightarrow 0$, that is, $a_{\delta} \rightarrow a_{\delta}^{\text{lim}} = \text{const.} > 0$, are true. Hence, it follows:

$$\dot{a}_{\text{lim}} = \dot{\delta}_{\text{lim}}/a_{\delta}^{\text{lim}} \quad \text{and analogous} \quad \dot{a}_{\text{lim}} = \dot{J}_{\text{lim}}/a_J^{\text{lim}}. \quad (1.5)$$

The crack propagation resistance, that is, the slope of the R -curves a_{δ}^{lim} and a_J^{lim} , is smaller the greater the crack propagation speed and converges against a value of zero in the case of unstable crack growth but not in case of stationary stable crack growth. After adding (1.5), whereby a_{δ}^{lim} and a_J^{lim} are replaced through the tearing moduli T_{δ}^{lim} and T_J^{lim} for $t \rightarrow \infty$ with $a_{\delta}^{\text{lim}} = T_{\delta}^{\text{lim}} \cdot \sigma_y/E$ and $a_J^{\text{lim}} = T_J^{\text{lim}} \cdot \sigma_y^2/E$, an equation can be derived which represents the asymptotic form of (1.1) after Rice, Drugan and Sham for large times:

$$\dot{\delta}_{\text{lim}} = 2T_{\delta}^{\text{lim}} \cdot \frac{\sigma_y}{E} \cdot \dot{a}_{\text{lim}} - \frac{T_{\delta}^{\text{lim}}}{T_J^{\text{lim}}} \cdot \frac{1}{\sigma_y} \cdot \dot{J}_{\text{lim}} \quad (1.6)$$

In the present case [see (1.1)], $\alpha = -T_{\delta}^{\text{lim}}/T_J^{\text{lim}}$ and $\beta = 2T_{\delta}^{\text{lim}} \cdot 1/\ln(R/r)$. The ratio R/r is the measure of the deformation constraint and can be compared to the relation of the size of the plastic zone and the size of the process zone, which also converges against a constant value for stationary stable crack growth.

The above statement about the slope of the R -curve for stationary stable crack growth can be confirmed through the introduction of a normalised energy dissipation rate D^* [14] as follows:

$$D^* = \sigma_y \cdot \frac{d\delta_p}{da} \quad (1.7)$$

whereby δ_p is the plastic crack-tip-opening displacement ($\delta = \delta_e + \delta_p$; δ_e —elastic crack-tip-opening displacement) for which $\delta \approx \delta_p$ is true because of $\delta_e \ll \delta_p$. Thus:

$$D^* = \sigma_y \cdot \frac{\partial \delta}{\partial t} \Big/ \frac{\partial a}{\partial t} \quad \text{with} \quad \lim_{t \rightarrow \infty} D^* = \sigma_y \cdot \frac{\dot{\delta}_{\text{lim}}}{\dot{a}_{\text{lim}}} \quad (1.8)$$

where D^* converges against a constant value for large times, that is, in case of stationary stable crack growth. In [14] it was shown that if small-scale yielding, that is, as opposed to full-scale yielding, occurs, D^* is proportional to the product of $T_J \cdot J_i$ (which is analogous to JT_J -dominated crack growth), where J_i is the physical crack initiation value that is almost independent of the specimen configuration in contrast to T_J . Since the normalised energy dissipation rate D^* is always positive—owing to energy conservation— T_J , like D^* (1.8), converges against a constant value greater than zero.

Furthermore, it can be shown that a constant crack-tip-opening displacement speed $\dot{\delta}$ near the stationary stable crack growth—corresponding with the definition of CTOD used here—corresponds to a constant crack-tip-opening angle (CTOA, ϕ). With the introduction of δ_r as a special CTOD in distance r in front of the crack tip, the CTOA results from $\tan \phi = \delta_r/4r$. The relation of δ and δ_r , derived from intercept theorem ($\delta/(\Delta a + r) = \delta_r/2r$), is

$$\delta = \frac{1}{2} \left(\frac{\bar{a}t}{r} + 1 \right) \cdot \delta_r, \quad (1.9)$$

whereby \bar{a} is the crack speed averaged up to time t . Following the derivation of (1.9) after the time for large times ($t \rightarrow \infty$, $\lim_{t \rightarrow \infty} \bar{a} = \dot{a}_{\text{lim}}$, $\lim_{t \rightarrow \infty} \dot{\delta} = \dot{\delta}_{\text{lim}}$), the following correlation is achieved

$$\dot{a}_{\text{lim}} = \frac{2}{\tan \phi|_{t \rightarrow \infty}} \cdot \dot{\delta}_{\text{lim}} \quad (1.10)$$

which corresponds to the first statement for \dot{a}_{lim} in (1.6). It can be observed that the CTOA converges against a constant value with $\lim_{t \rightarrow \infty} \phi = \arctan 2a_\delta^{\text{lim}}$, which is also the smaller the greater the plastic deformation constraint [15] (the constraint also influences the slope of the R-curve). Since \dot{a}_{lim} , in contrast, increases with increasing constraint, $\dot{\delta}_{\text{lim}}$ should be independent of the specimen's configuration, thus being the fracture mechanical material parameter that best describes the stable crack growth of polymer materials. The CTOA values determined experimentally by the slope a_δ^{lim} of the R-curves and numerically on the basis of finite element

(FEM) simulations on PVC reveal a relatively good correspondence [16]. The CTOA is 31° (experimental) and 40° (numerical) for a crosshead speed of 1 mm/min, and it is 22° (experimental) and 30° (numerical) for a speed of 100 mm/min, whereby these CTOA values which are significantly greater than those for metal materials (e.g. $\phi = 4\text{--}9^\circ$ for aluminium alloy [15]) are caused by the high deformation power of polymers including PVC.

Conversely, based on the Rice-Sorenson Model [13], which can be used for polymers (PE-UHMW [17]), it can be shown that the existence of a constant CTOA > 0 in case of stationary stable crack propagation correlates with the existence of a constant tearing modulus $T_J > 0$:

$$T_J = \frac{\phi|_{t \rightarrow \infty}}{\alpha} \frac{E}{\sigma_y} \cdot \ln\left(\frac{\alpha \sigma_y}{\lambda E}\right), \quad (1.11)$$

whereby λ is a non-dimensional constant. Accordingly, $T_J \approx 0$ is the equivalent of CTOA ≈ 0 , as observed during fast unstable crack propagation (without crack-tip blunting).

1.5 Stable Crack Propagation as Kinetic Phenomenon— An Outlook

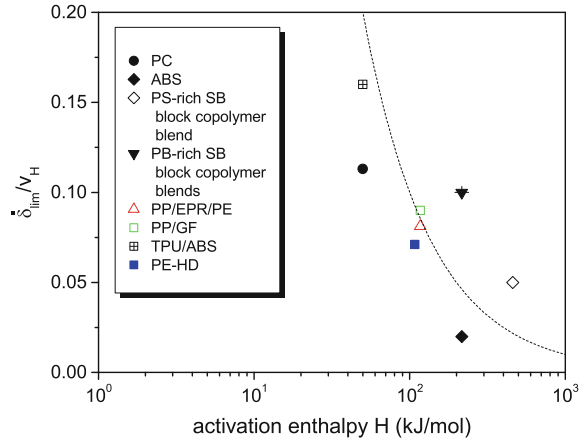
Our own investigations and those of others presented in the literature on numerous polymers (an overview is provided in [18]) have shown that non-linear viscoelastic deformation processes including fracture can be characterised by the same activation enthalpy H as the deformations in the linear response range, despite different deformation amplitudes. On this basis, the results of the dynamic-mechanical analysis (DMA) are also used in this study for determining H . An empirical relationship between the limits $\dot{\delta}_{\text{lim}}/v_H$ and the activation enthalpy was found for deformation H , which is associated with the stable crack propagation process (Fig. 1.15). This relation can be described by (1.12) on the basis of the kinetic theory of fracture.

$$\frac{\dot{\delta}_{\text{lim}}}{v_H} = \frac{H_0}{H} \quad (1.12)$$

H_0 is the activation enthalpy for a fundamental deformation process which is almost independent of the material and lies in the range of ~ 10 kJ/mol.

Depending on the material, the stable crack propagation process is a kinetic phenomenon that can be described by an activation enthalpy that is constant in certain ranges of external loading. This phenomenon is shown especially by the fact that the $\dot{\delta}_{\text{lim}}/v_H$ values are independent of the loading speed ($\dot{\delta}_{\text{lim}}/v_H = 0.08$ for all PP materials) and of the temperature ($\dot{\delta}_{\text{lim}}/v_H = 0.11$ for PC).

Fig. 1.15 Normalised CTOD rate $\dot{\delta}_{\text{lim}}/v_H$ for stationary stable crack propagation as a function of H for different polymers; the dotted line was calculated as $H_0 \sim 10$ kJ/mol, using (1.12)



References

- Horst, T., Heinrich, G.: Modellierung der Rissausbreitung in verstärkten polymeren Werkstoffen. In: Proceedings Polymerwerkstoffe 2004 (Halle, 29.09.–01.10.2004). Halle (2004), PII-45
- Lach, R., Seidler, S., Grellmann, W.: Resistance against the intrinsic rate of fracture mechanics parameters for polymeric materials under moderate impact loading. Mech. Time-Depend. Mater. **9**, 103–119 (2005)
- Grellmann, W., Seidler, S. (eds.): Deformation and Fracture Behaviour of Polymers. Springer, Berlin (2001)
- Lach, R., Adhikari, R., Weidisch, R., Huy, T.A., Michler, G.H., Grellmann, W., Knoll, K.: Fracture toughness behavior of binary styrene-butadiene block copolymer blends. J. Mater. Sci. **39**, 1283–1295 (2004)
- Kotter, I.: Morphologie-Zähigkeits-Korrelationen von EPR-modifizierten Polypropylenwerkstoffen. Mensch & Buch Verlag, Berlin (2003)
- Zhurkov, S.N.: Kinetic concept of the strength of solids. Int. J. Fract. Mech. **1**, 311–323 (1965)
- Hertling, J.: Ausbreitungsgeschwindigkeit von instabilen Rissen in Polymeren bei tiefen Temperaturen. Wissenschaftliche Berichte des Forschungszentrums Karlsruhe (Technik und Umwelt) FZKA 6326 (Ph.D. Thesis, Universität TH Karlsruhe), Forschungszentrum Karlsruhe GmbH, Karlsruhe (1999)
- Döll, W., Seidelmann, U., Könczöl, L.: On the validity of the Dugdale model for craze zones at crack tips in PMMA. J. Mater. Sci. **15**, 2389–2394 (1980). Marshall, G.P., Culver, L.E., Williams, J.G.: Crack and craze propagation in polymers: a fracture mechanics approach. I. Crack growth in polymethyl methacrylate in air. Plast. Polym. **37**, 75–80 (1969)
- Kerkhof, F.: Wave fractography. In: Sik, G.C., Wie, R.P., Erdogan, F. (eds.) Linear Fracture Mechanics. Euro Publisher Company Inc. (1976), pp. 303–321
- Dear, J.P.: Comparison of fast fracture properties of thermoplastics. Polym. Eng. Sci. **36**, 1210–1216 (1996)
- Anderson, T.L.: Fracture Mechanics. Fundamentals and Applications. 2nd ed., CRC Press, Boca Raton (1995)
- Rice, J.R., Drugan, W.J., Sham, T.-L.: Elastic-plastic analysis of growing cracks. In: Proceedings of the 12th National Symposium on Fracture Mechanics (St. Louis, 21.–23.05.1979), pp. 189–221, ASTM Special Technical Publications 700 (1980)

13. Rice, J.R., Sorensen, E.P.: Continuing crack-tip deformation and fracture for plane-strain crack growth in elastic-plastic solids. *J. Mech. Phys. Solids* **26**, 163–186 (1978)
14. Sumpter, J.D.G.: The energy dissipation rate approach to tearing instability. *Eng. Fract. Mech.* **71**, 17–37 (2004)
15. Newman Jr., J.C., James, M.A., Zerbst, U.: A review of the CTOA/CTOD fracture criterion. *Eng. Fract. Mech.* **70**, 371–385 (2003)
16. Grellmann, W., Seidler, S., Jung, K., Che, M., Kotter, I.: Influence of specimen geometry and loading conditions on the crack resistance behaviour of poly(vinyl chloride) and polypropylene. In: Grellmann, W., Seidler, S. (eds.) *Deformation and Fracture Behaviour of Polymers*. Springer, Berlin (2001), pp. 51–70
17. Gomoll, A., Wanich, T., Bellare, A.: J-integral fracture toughness and tearing modulus measurement of radiation cross-linked UHMWPE. *J. Orthop. Res.* **20**, 1152–1156 (2002)
18. Lach, R., Grellmann, W.: Time- and temperature-dependent fracture mechanics of polymers: general aspects at monotonic quasi-static and impact loading conditions. *Macromol. Mater. Eng.* **273**, 555–567 (2008)

Chapter 2

Fatigue Crack Growth Behaviour of Epoxy Nanocomposites—Influence of Particle Geometry

M.H. Kothmann, G. Bakis, R. Zeiler, M. Ziadeh, J. Breu and V. Altstädt

Abstract In this study, surface-modified spherical nano-silica and K-fluoro hectorites (O/K-heckt), characterised by large lateral extensions and aspect ratios, were employed to analyse the effect of geometrical appearance on the fatigue crack growth (FCP) behaviour of an epoxy resin. The addition of nano-silica improved the FCP behaviour by nanoparticle debonding and subsequent plastic void growth. The number of particles contributing to toughening increases remarkably with rising stress intensity factor due to plastic zone enlargement. The improvement in crack propagation resistance by the use of the large O/K-heckt, even at very low amounts (2.2 vol%) has to be highlighted. The main toughening mechanism is crack deflection due to the large lateral extension being in the range of the plastic zone size. Especially in the region of crack initiation and stable crack propagation, the clay tactoids reduce the propagation of the damage zone in front of the crack tip remarkably, resulting in a hugely enhanced crack resistance of the nanocomposites.

2.1 Introduction

The long-term mechanical performance under dynamic loading conditions of polymer matrix composites is of prime concern in their adoption for industrial devices. The failure of these composites originates in the formation and subsequent propagation of microcracks. A profound knowledge of the crack propagation behaviour of the polymer matrix material is of fundamental interest. The enhancement of crack resistance by toughening is improving the fatigue performance. The investigation of the fatigue crack propagation (FCP) rate under varying stress intensity ranges (ΔK) allows for a quantification of the three stages of fatigue crack growth: the threshold value for the initiation of fatigue crack growth, the region of stable crack growth, described by the Paris law ((2.1) [1]), and the critical

M.H. Kothmann (✉) · G. Bakis · R. Zeiler · V. Altstädt
Department of Polymer Engineering, University of Bayreuth, Bayreuth, Germany

M. Ziadeh · J. Breu
Department of Inorganic Chemistry, University of Bayreuth, Bayreuth, Germany

crack growth. A detailed description of the methodology, as well as a schematic diagram, explaining the different regimes of fatigue crack growth, are given by Fischer et al. [2].

$$da/dN = C \cdot \Delta K^m \quad (2.1)$$

In the Paris law a represents the crack length, N the number of cycles, C a material constant and m the slope of the curve on double logarithmic scale. The plastic zone size, ahead of the crack tip, is strongly dependent on the dynamic stress state applied (2.2) [3]. With increasing stress intensity factor, the size of the plastic zone is enlarged. Consequently, the plastic zone is equivalent to a sensor, changing its size, being highly sensitive to all changes in mechanical properties, attributed to the addition of differently shaped nanoparticles and the crack/particle interactions ahead of the crack tip in the nanocomposites.

$$d_p = \frac{1}{3\pi} \left(\frac{K_{\max}}{\sigma_y} \right)^2 \quad (2.2)$$

According to the crack-tip plasticity theory of Irwin [3], in (2.2), d_p represents the diameter of the plastic zone ahead of the crack tip, K_{\max} the maximum stress intensity factor and σ_y the yield stress of the matrix.

In this work the effect of nanoparticle geometry of non-carbon-based filler materials on the FCP behaviour is focused. Commercial spherical nano-silica (average diameter 20 nm) and surface-modified synthetically prepared K-fluoro hectorites characterised by large lateral extensions (up to 8.6 μm) and high aspect ratios (up to 860) were used to examine the effect of particle size and geometry. The good compatibility of the epoxy resin and silica nanoparticles, due to proper surface treatment, is well known [4]. The fluorohectorites were rendered hydrophobically by cation exchange reaction allowing homogeneous particle dispersion. In addition, the synthetic fluorohectorites provide outstanding advantages compared to natural clays like montmorillonite, including larger particle sizes, superb layer charge homogeneity and high phase purity leading to uniform interlamellar reactivity and surface chemistry [5].

The main toughening mechanisms appearing in epoxy-based silica nanocomposites are particle pull-out in combination with plastic void growth on the nano-level involving slight crack deflection on the micro-level [4]. The lack of crack pinning in epoxy-silica nanocomposites is regarded to be due to the small particle sizes in comparison to the crack-tip-opening displacement, respectively plastic zone size [4, 6]. The morphology of the layered silicates is strongly determined by its degree of exfoliation. On the one hand, the exfoliation of smectite clays is accompanied with a high increase in nanocomposites modulus and tensile strength [7]. Whereas, an increase in fracture toughness is mainly reported for intercalated or phase separated morphologies, especially in the case of mica [8] and modified fluorohectorite [9] filled epoxy systems. As stated by Kinloch and Taylor [8], a certain particle size is necessary to achieve an effective interaction between the

dispersed particles and the propagating crack, by provoking crack deflection and crack pinning. The large fluorohectorites, investigated in this study, provide the opportunity to adjust the particle size and render the state of shear stiffness to improve the load bearing ability in layer stacking direction and the flexural rigidity of the tactoids [5].

Although a lot of effort was spent investigating the mechanical properties of epoxy-based nanocomposites [4, 10, 11], the fatigue crack growth behaviour was less discussed. However, it is described, that for epoxy–silica nanocomposites the stress intensity range required for crack initiation is enhanced [6, 12]. Furthermore, the silica nanoparticles lead to an improved FCP behaviour in all three stages of fatigue crack propagation, while the FCP behaviour of the nanocomposites is systematically improved with increasing amount of nano-silica [6]. Hedicke-Höchstötter et al. [13] observed a significantly improved fatigue crack propagation behaviour of polyamide by adding up to 5 wt% exfoliated layered silicates (Nanofil 919). Although several attempts are presented in literature analysing the effect of specific polymer/nanoparticle combinations in terms of fracture toughness and fatigue crack growth propagation, a comprehensive study discussing the effect of particle geometry of differently shaped nanoparticles in the same resin system is missing. This fact clearly shows the high importance of the presented study to analyse fatigue crack growth behaviour by focusing on particle size and shape and discussing the involved toughening mechanisms.

2.2 Experimental

2.2.1 Materials

The epoxy matrix used in this study consists of a diglycidylether of bisphenol-A (DGEBA) epoxy resin, epoxy equivalent weight 172 g/eq (Epikote resin 0162, Momentive Specialty Chemicals, Germany), cured with methylhexahydrophthalic anhydride (Epikure curing agent 868, Momentive Specialty Chemicals, Germany) and additional 1 wt% N,N'-dimethylbenzyl-amine (Sigma-Aldrich, Germany) referred to the liquid matrix to accelerate curing.

Silica nanocomposites were prepared by using nano-silica, kindly provided as colloidal sol in DGEBA by Evonik Hanse GmbH (Nanopox E470, Evonik-Hanse, Germany, 40 wt% SiO₂). The silica nanoparticles are synthesised and surface-modified, with an organosilane, in aqueous solution. The density of the amorphous nano-silica is approx. 2.2 g cm⁻³ [14].

A synthetic Na-fluorohectorite was prepared by melt synthesis with an optimal chemical formula Na_{0.5}[Mg_{2.5}Li_{0.5}]Si₄O₁₀F₂ [15], having a cation exchange capacity (CEC) of 110 meq/100 g as determined by the copper complex method [16]. The aspect ratio of the Na-fluorohectorite was adjusted to maximum 600 and the tactoids were rendered shear stiff by exchanging the intergallery cations with

potassium [5]. Afterwards, the K-fluorohectorites were surface-modified with Dodecylamine (97%, Sigma-Aldrich) using a standard procedure [17]. The density of the organophilised K-fluorohectrite (O/K-lect) is 2.7 g cm^{-3} .

2.2.2 Preparation of Nanocomposites

Epoxy–silica nanocomposites were prepared by simple dilution of the masterbatch with neat DGEBA at $60 \text{ }^\circ\text{C}$. Subsequently, the anhydride hardener and the required amount of N,N'-dimethylbenzylamine was added to the mixture.

The epoxy–clay nanocomposites were prepared according to the following procedure. Subsequent to surface modification in aqueous media, the modified fluorohectorites (O/K-lect) were phase transferred into tetrahydrofuran (THF) without former drying by repeated dispersing and centrifuging for two times with THF. As a general procedure, the nanofiller suspension in THF was mixed with the epoxy resin in a round flask for one hour using mechanical mixing. This was followed by removal of the solvent in a rotary evaporator under vacuum at $80 \text{ }^\circ\text{C}$. Subsequently, the anhydride hardener was added to the epoxy–nanofiller mixture according to its stoichiometric ratio. The mixture was further processed in a three-roll mill Exakt E80 (Exakt Vertriebs GmbH, Germany) for achieving an optimal dispersion prior to curing (3 cycles, 300 rpm, ultimate gap distance $10 \text{ }\mu\text{m}$). Finally the required amount of N,N'-dimethylbenzylamine was added.

The final mixtures were degassed under vacuum at $60 \text{ }^\circ\text{C}$ for 15 min and cured at $140 \text{ }^\circ\text{C}$ for 11 h in a release agent coated aluminium mould.

2.2.3 Characterisation Methods

Powder X-ray diffraction (PXRD) patterns of the final epoxy–clay nanocomposites were recorded to investigate interlamellar spacing of the nanofillers. Samples were fine grinded using cryo-grinding (Pulversiette 14, Fritsch, Germany, 2 mm sieve) and the PXRD patterns were obtained in transmission geometry on a STOE Stadi P powder diffractometer (STOE & Cie GmbH, Germany) equipped with a MYTHEN1K detector using $\text{CuK}\alpha_1$ radiation ($\lambda = 0.154056 \text{ nm}$).

Thermogravimetric analysis (TGA) was applied to determine the amount of the organic modifier of the organo-nanofillers and as well the nanofiller content in the nanocomposites by using a TGA/STDA851e (Mettler Toledo, Germany) under oxygen flow (50 ml/min) at a heating rate of 10 K/min .

The dispersion of the epoxy–silica nanocomposites was characterised using a LEO 922 A energy-filtered transmission electron microscope (EFTEM, Carl Zeiss AG, Germany, 200 kV). Thin sections of 50 nm were cut on a Leica Ultracut microtome (Leica Biosystems GmbH, Germany, 1.5 kV) equipped with a glass knife. Fracture surfaces of selected samples were analysed using a Zeiss 1530 (Carl

Zeiss AG, Germany) scanning electron microscope equipped with a field emission cathode.

Fatigue crack propagation (FCP) experiments were performed at 23 °C and 50% relative humidity employing a servo-hydraulic test machine (Hydropuls MHF, Schenck, Germany) using compact tension (CT) specimens (width 33 mm, thickness 4 mm). The rate of cyclic-fatigue crack growth per cycle, da/dN , was measured as a function of the applied stress intensity factor ratio, ΔK . The loading follows a sinusoidal waveform with a frequency of 10 Hz and an R -ratio (K_{min}/K_{max}) of 0.1. The calculation of the crack length was done considering the specimen's compliance as described in ISO 15850 [18], using an extensometer (632.13F-20, MTS, Germany) fixed to the front face of the CT specimen.

2.3 Results and Discussion

2.3.1 Organophilisation of Nanoparticles

The amount of surface modifier was determined for the organophilised mica-like fluorohectorite (O/K-hect) using thermogravimetric analysis. The resulting values as well as the mean particle sizes and aspect ratios are given in Table 2.1. Silica particles were used as received in the DGEBA matrix.

2.3.2 Morphology

The TEM micrographs presented in Fig. 2.1 clearly reveal the homogeneous dispersion of the nano-silica particles. Furthermore, the morphology of the O/K-hect nanocomposites is characterised by the very large fluorohectorite tactoids, well dispersed in the epoxy matrix. Additionally, the high aspect ratio and equal tactoid thickness of the O/K-hect particles are observable. Furthermore, the intergallery distance of the clay tactoids is analysed by using powder X-ray diffraction measurements, revealing no intercalation during dispersion and curing process (Table 2.1). It is noteworthy that O/K-hect particles are modified solely on the external surfaces, since the internal planes are not accessible due to the collapsed structure of the galleries. Consequently, due to the smaller intergallery distance the

Table 2.1 Nomenclature and properties of the different nanofiller employed

Particle	Amount of surface modifier (wt%)	Mean size (nm)	Intergallery distance (nm)	Mean aspect ratio (μm)
Silica	Not determined	20 [4]	- (Amorphous)	1
O/K-hect	4.4	3800	0.99	380

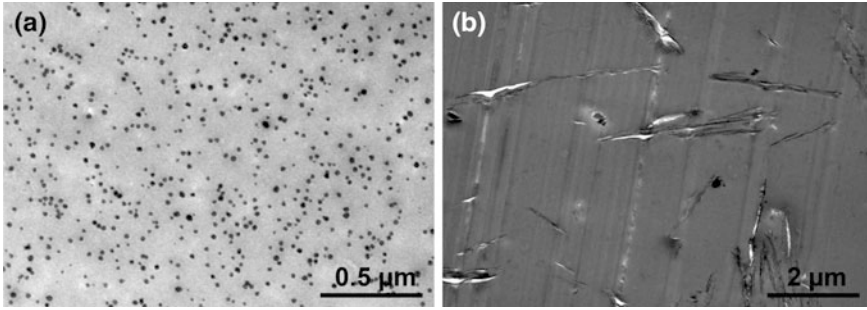


Fig. 2.1 TEM micrographs of the nanocomposites filled with **a** 2.7 vol% SiO₂, and **b** 2.2 vol% O/K-hect

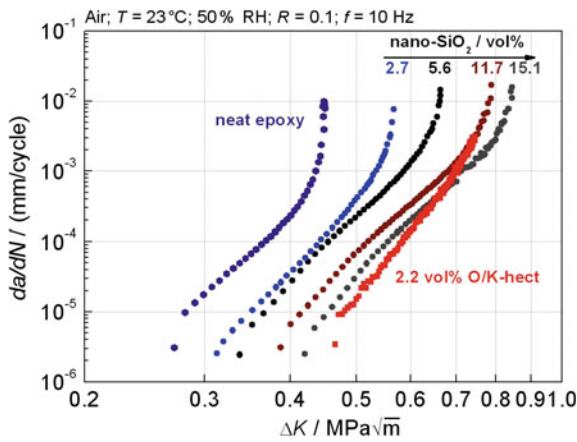


Fig. 2.2 Comparison of the fatigue crack propagation behaviour of nano-silica (2.7–15.1 vol%) and O/K-hect (2.2 vol%) filled epoxy nanocomposites

shear stiffness of O/K-hect is higher as compared to conventional expanded or intercalated organoclays [19].

2.3.3 Fatigue Crack Propagation Behaviour

In Fig. 2.2, the effects of spherical nano-silica and layered O/K-hect on the fatigue crack propagation (FCP) behaviour of epoxy nanocomposites is compared.

An improved crack resistance with increasing nano-silica loading is observed in terms of threshold value of crack propagation (ΔK_{th}) and the material behaviour under critical failure (ΔK_{cf}). At 15.1 vol% an improvement of 66% in ΔK_{th} and 88% in ΔK_{cf} , is obtained. The fracture surfaces of the nanocomposite containing

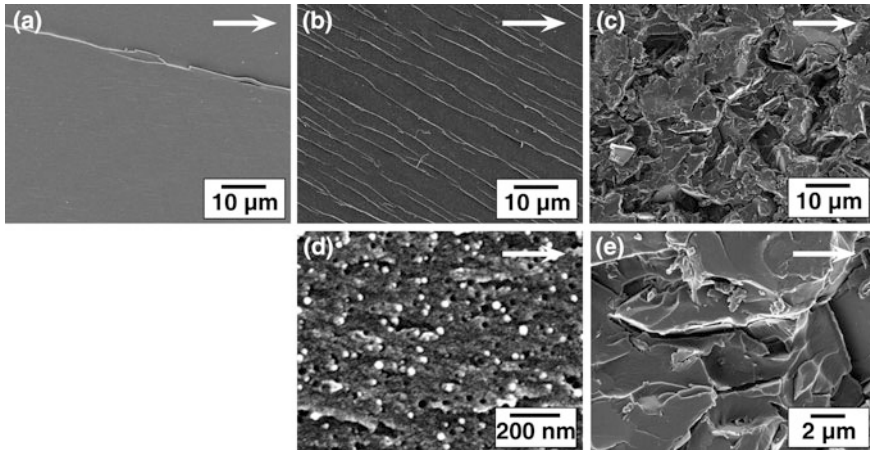


Fig. 2.3 Fracture surfaces (SEM) of the different nanocomposites in the region of stable crack growth, **a** neat epoxy, **b** and **d** nano-SiO₂ nanocomposites, **c** and **e** O/K-hect nanocomposites. The direction of crack propagation is indicated by the *white arrows*

5.6 vol% nano-silica (Fig. 2.3b, d; for the neat epoxy see Fig. 2.3a) reveal particle debonding and plastic void growth as the main toughening mechanisms, combined with an enhanced shear yielding of the matrix. According to the model of Irwin [3], describing the increasing diameter of the cylindrically shaped plastic zone (d_p) with respect of ΔK , respectively K_{\max} [$d_p \sim \Delta K^2$, (2.2)], the number of silica nanoparticles (n) contributing to toughening increases. The number of silica nanoparticles within the plastic zone follows a power law with the exponent of 4 ($n \sim \Delta K^4$), being reflected in the more pronounced FCP improvement at higher crack propagation rates. This is also reflected in the reduction of the slope (m) in the Paris regime (2.1). A detailed description of this correlation is given in [6].

In addition a pronounced improved crack resistance is observed for the O/K-hect-epoxy nanocomposite even at very low amounts of nanofiller. The characteristic values ΔK_{th} and ΔK_{cf} are improved by 73 and 67% by adding 2.2 vol% O/K-hect. The fracture surfaces (Fig. 2.3c, e) of the nanocomposite (2.2 vol% O/K-hect) reveal a very tortuous fracture surface, attributed to strong crack deflection and crack pinning, provoked by the large lateral particle size. Obviously, on a microscopic scale the crack is forced to propagate along the interface between the epoxy resin and the clay tactoids (particle debonding). As a consequence of the specific orientation and the high aspect ratio of the clay tactoids, the crack is deflected locally, increasing the crack path length and leading to an enlargement in the newly formed fracture surface (Fig. 2.3e). Particle cleavage was not observed since the filler-matrix adhesion is regarded being moderate, since the aliphatic dodecyl-tails of the surface modifier show neither entanglements, nor form any covalent crosslinking with the thermosetting matrix.

Comparing the nanocomposites containing comparable nanofiller contents (2.7 vol% nano-silica respectively 2.2 vol% O/K-hect) the dependency of the FCP behaviour on the stress intensity of the nano-silica and the O/K-hect nanocomposites, as expressed by the shape of the FCP curves, is similar. Although the toughening potential of the larger O/K-hect is more prominent, since ΔK_{th} and ΔK_{cf} are improved more significantly. Estimating and comparing the number of particles and their corresponding particle surface area in a reference volume, using the geometrical parameters of the fillers (Table 2.1) reveals a much higher number (33,000 \times) and surface area (1.5 \times) in the case of nano-silica as compared to O/K-hect. Despite the lower number of particles and surface area, the toughening effect is more pronounced in the case of O/K-hect. Leading to the conclusion, toughening dominated by crack deflection as in the case of O/K-hect is more effective as compared to particle debonding, in the case of nano-silica.

In the region of unstable crack growth (ΔK_{cf}), the addition of 11.7 vol% nano-silica exhibits a crack resistance improvement, being comparable to the addition of 2.2 vol% of O/K-hect. Whereas the toughening efficiency of the nano-silica is less pronounced in the region of crack initiation (ΔK_{th}) and stable crack propagation (Paris regime). This phenomenon, accessible by fatigue crack growth experiments cannot be observed by quasi-static fracture toughness experiments investigating solely critical crack growth. In the region of crack initiation, the diameters of the plastic zones, determined according to the theory of Irwin ((2.2), $\sigma_y = 82$ MPa), are approx. 2 and 4 μm in the case of nano-silica (11.7 vol%) and O/K-hect (2.2 vol%) respectively. Due to the large average lateral extension of the O/K-hect (4 μm), the plastic zone can be completely spanned by a single tactoid, decelerating the propagation of the damage zone at the crack tip. Additionally, for complete debonding of an O/K-hect, multiple fatigue cycles are necessary, since the crack propagation per cycle (da/dN) is in the sub-micron range. At higher ΔK , i.e. with increasing plastic zone size, several O/K-hect particles are required for effective crack deflection. Whereas in the case of nano-silica, the effectivity of debonding is multiplied due to the tremendously increased number of particles in the enlarged plastic zone, contributing to toughness enhancement by debonding. These mechanisms clearly explain the distinctive dependencies on ΔK (stages of fatigue crack growth) applied towards the enhancement of crack resistance of the nanofillers, possessing variations in the geometry.

2.4 Conclusion

In this study, surface-modified spherical nano-silica and K-fluorohectorites (O/K-hect), characterised by large lateral extensions and aspect ratios, were employed to analyse the effect of geometrical appearance on the fatigue crack growth (FCP) behaviour of an epoxy resin. The addition of nano-silica improved the FCP behaviour by nanoparticle debonding and subsequent plastic void growth. The number of particles contributing to toughening increases remarkably with

rising ΔK due to plastic zone enlargement. The improvement in crack propagation resistance by the use of the large O/K-lect, even at very low amounts (2.2 vol%) has to be highlighted. The main toughening mechanism is crack deflection due to the large lateral extension being in the range of the plastic zone size. Especially in the region of crack initiation and stable crack propagation, the clay tactoids reduce the propagation of the damage zone in front of the crack tip remarkably, resulting in a hugely enhanced crack resistance of the nanocomposites.

Acknowledgements The authors highly acknowledge the financial support from the German Research Foundation in the frame of the Collaborative Research Center SFB 840: "From particulate nanosystems to mesotechnology", and from the German Federal Ministry for Economic Affairs and Energy (FKZ 0327895E). The authors are grateful towards Mr. Brückner, Mrs. Lang, and Mrs. Förtsch, University of Bayreuth, for their support with the mechanical characterisation and microscopic investigations, respectively.

References

1. Paris, P., Erdogan, F.: A critical analysis of crack propagation laws. *J. Basic Eng.* **85**, 528–533 (1963)
2. Fischer, F., Beier, U., Wolff-Fabris, F., Altstädt, V.: Toughened high performance epoxy resin system for aerospace applications. *Sci. Eng. Compos. Mater.* **18**, 209–215 (2011)
3. Kinloch, A.J., Young, R.J. (eds.): *Fracture Behaviour of Polymers*. Applied Science Publishers, London (1983)
4. Johnsen, B.B., Kinloch, A.J., Mohammed, R.D., Taylor, A.C., Sprenger, S.: Toughening mechanisms of nanoparticle-modified epoxy polymers. *Polymer* **48**, 530–541 (2007)
5. Möller, M.W., Handge, U.A., Kunz, D.A., Lunkenbein, T., Altstädt, V., Brey, J.: Tailoring shear-stiff, mica-like nanoplatelets. *ACS Nano* **4**, 717–724 (2010)
6. Kothmann, M.H., Zeiler, R., Rios de Anda, A., Brückner, A., Altstädt, V.: Fatigue crack propagation behaviour of epoxy resins modified with silica-nanoparticles. *Polymer* **60**, 157–163 (2015)
7. Shi, H., Lan, T., Pinnavaia, T.J.: Interfacial effects on the reinforcement properties of polymer–organoclay nanocomposites. *Chem. Mater.* **8**, 1584–1587 (1996)
8. Kinloch, A.J., Taylor, A.C.: The mechanical properties and fracture behaviour of epoxy-inorganic micro- and nano-composites. *J. Mater. Sci.* **41**, 3271–3297 (2006)
9. Kornmann, X., Thomann, R., Mülhaupt, R., Finter, J., Berglund, L.: Synthesis of amine-cured, epoxy-layered silicate nanocomposites: the influence of the silicate surface modification on the properties. *J. Appl. Polym. Sci.* **86**, 2643–2652 (2002)
10. Dittanet, P., Pearson, R.A.: Effect of silica nanoparticle size on toughening mechanisms of filled epoxy. *Polymer* **53**, 1890–1905 (2012)
11. Zhang, H., Zhang, Z., Friedrich, K., Eger, C.: Property improvements of in situ epoxy nanocomposites with reduced interparticle distance at high nanosilica content. *Acta Mater.* **54**, 1833–1842 (2006)
12. Blackman, B.R.K., Kinloch, A.J., Lee, J.S., Taylor, A.C., Agarwal, R., Schueneman, G., Sprenger, S.: The fracture and fatigue behaviour of nano-modified epoxy polymers. *J. Mater. Sci.* **42**, 7049–7051 (2007)
13. Hedicke-Höchstötter, K., Demchuk, V., Langenfelder, D., Altstädt, V.: Fatigue crack propagation behaviour of polyamide-6 nanocomposites based on layered silicates. *J. Plast. Technol.* **3**, 1–22 (2007)

14. Tang, L.-C., Zhang, H., Sprenger, S., Ye, L., Zhang, Z.: Fracture mechanisms of epoxy-based ternary composites filled with rigid-soft particles. *Compos. Sci. Technol.* **72**, 558–565 (2012)
15. Kalo, H., Möller, M.W., Ziadeh, M., Dolejš, D., Breu, J.: Large scale melt synthesis in an open crucible of Na-fluorohectorite with superb charge homogeneity and particle size. *Appl. Clay Sci.* **48**, 39–45 (2010)
16. Ammann, L., Bergaya, F., Lagaly, G.: Determination of the cation exchange capacity of clays with copper complexes revisited. *Clay Miner.* **40**, 441–453 (2005)
17. Carrado, K.A., Decarreau, A., Petit, S., Bergaya, F., Lagaly, G.: Synthetic clay minerals and purification of natural clay. In: Bergaya, F., Theng, B.K.G., Lagaly, G. (eds.) *Handbook of Clay Science*, pp. 115–139. Elsevier, Amsterdam (2006)
18. ISO 15850 (2014): *Plastics—Determination of tension-tension fatigue crack propagation—Linear elastic fracture mechanics (LEFM) approach*
19. Stefanescu, E.A., Tan, X., Lin, Z., Bowler, N., Kessler, M.R.: Multifunctional PMMA–ceramic composites as structural dielectrics. *Polymer* **51**, 5823–5832 (2010)

Chapter 3

Fracture Mechanics Methods to Assess the Lifetime of Thermoplastic Pipes

F. Arbeiter, G. Pinter, R.W. Lang and A. Frank

Abstract When performing lifetime estimations using extrapolation concepts, it is vital to estimate the uncertainties which always accompany accelerated testing methods. Uncertainties may arise from deviating parameters such as changes in environmental conditions, temperature, different loading ratios, chemicals such as stress cracking agents, etc. Only when these influences are known it is justifiable to go into lifetime calculations. Own studies showed, that fracture mechanics extrapolation concepts for accelerated prediction of PE pressure pipes using short-time fatigue tests provide valid results when compared to pre-notched internal pipe pressure tests. The use of a cracked round bar (CRB) specimen for linear elastic fracture mechanic (LEFM) tests improves the results compared to classical compact tension (CT) specimens, which tend to overestimate lifetimes. This can mainly be attributed to bigger plastic zone sizes which restrict slow crack growth (SCG) in CT specimens. Another advantage is the similarity of constraint and K_I -development between a pipe and CRB specimens. Summarising, the extrapolation concept using short-term fatigue tests on CRB specimens provides a valuable and valid tool to perform lifetime estimations for pipe systems made from high-density polyethylene (PE-HD) pipe materials. Further steps in the development of the approach using cyclic CRB Tests are currently under evaluation. For example, the implementation of influences due to media is an important addition, to be able to cover the area of media and crude oil transportation. The impact of crack growth initiation is also a topic which has yet to be addressed. So far it has often been neglected in lifetime estimations due to complex testing procedures. Also the use of the cyclic CRB Test for different polymeric pipe materials is currently examined. Seeing that only about a third of all thermoplastic pipes is produced from

F. Arbeiter (✉) · G. Pinter

Department Polymer Engineering and Science, Montan University Leoben,
Leoben, Austria

R.W. Lang

Institute of Polymeric Materials and Testing, Johannes Kepler University Linz,
Linz, Austria

G. Pinter · A. Frank

Polymer Competence Center Leoben GmbH, Leoben, Austria

© Springer International Publishing AG 2017

W. Grellmann and B. Langer (eds.), *Deformation and Fracture Behaviour of Polymer Materials*, Springer Series in Materials Science 247,
DOI 10.1007/978-3-319-41879-7_3

PE-HD material this is a logical next step. Besides lifetime estimation, the use of the cyclic CRB Tests at $R = 0.1$ is also discussed for ISO-standardisation for material quality control. Good correlations with established methods support its claim as a precise and fast ranking tool for PE-HD pipe grades.

3.1 Failure Behaviour of Polymer Pipes

The long-term failure of pressurised pipes made from high-density polyethylene (PE-HD) can be characterised by the determination of the long-term hydrostatic strength with internal pressure tests, which is regulated in EN ISO 9080 [1] or ASTM D 2837 [2]. Total testing time of pipes using this method is usually about 1 year. However, pipes that do not fail are removed from testing after a time period of 10^4 h. This means that for modern PE types of the classification of PE 80, PE 100 and PE 100-RC (acc. to PAS 1075) almost no quantitative information concerning the long-term relevant quasi-brittle failure region can be measured as only the ductile failure regime is characterised within testing times. This presents a problem for material developers and grid operators, since no quantitative information regarding failure times of modern material grades can be determined. Therefore, new and faster testing procedures are necessary to provide this vital information.

The typical failure behaviour of PE pipes of internal pressure tests has been well investigated [3–8] and can typically be divided into three different failure regimens depending on the stress level. The regimens are illustrated in Fig. 3.1 [8, 9].

- In Region A, at high internal pressures, the failure is dominated by ductile deformation with the formation of large plastic zones after rather short testing times. This region is mainly controlled by the yield stress of the material and failure usually occurs at the smallest wall thickness or at defects [10].
- With decreasing stresses the failure mechanism passes a ductile brittle transition knee into the quasi-brittle failure (Region B), which exhibits a different slope, compared to Region A. In this region the failure is determined by a combination of crack growth initiation (CGI) and slow crack growth (SCG) with only small-scale plastic deformations adjacent to the crack tip. Due to stress concentrations at small defects in the material, cracks initiate and propagate continuously through the pipe wall until failure. The failure time of the pipe is comprised of both, CGI and SCG time [8, 11–13]. Slow crack growth is significantly influenced by the chemical structure of the polymer, such as the molecular mass as well as the concentration and length of short chain branches [5, 10, 13–18].
- The third failure Region C, where pipes fail nearly independent from the load, becomes essential after very long testing or operational times. It is the result of material ageing and polymer degradation processes. The effect of global ageing of the material leads to the formation of a vast quantity of cracks and small

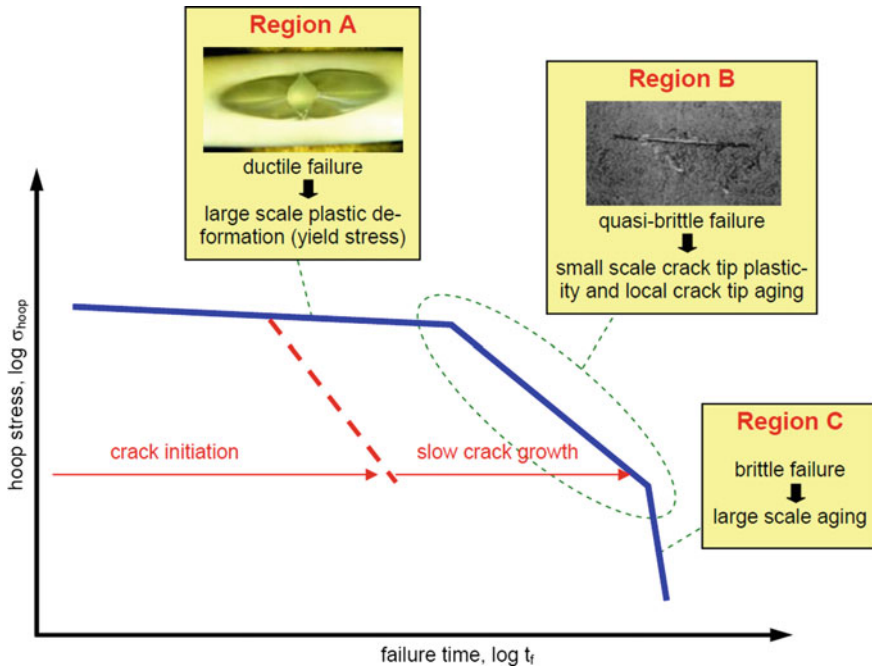


Fig. 3.1 Characteristic failure behaviour Regions A, B and C of PE pressure pipes [9]

stresses may already cause brittle failure of the pipe. The resistance against failure in Region C is mainly controlled by stabilisers [4, 12, 19, 20] which prolong the time before material deterioration.

For long-term application of pressurised pipes (e.g. gas or water distribution) it is an accepted fact, that failure according to Region B is the critical failure mechanism. Slow crack growth usually starts at an initial defect located close to or at the inner pipe wall surface [11–13]. This initial defect creates a stress concentration in which micro-deformations start to nucleate micro-voids. These simultaneously originate crazes. During the formation of crazes a combination of shearing in the amorphous phase and a transformation of the crystalline phase finally lead to highly drawn fibrils. Ensuing quasi-brittle crack growth initiates. Through the rupturing of the highly drawn fibrils a prolonged crack is formed. Simultaneously the stress at the tip of the craze zone increases initiating the formation of new micro-voids and crazes. This ongoing procedure of craze formation and breakdown of drawn fibrils is characteristic for quasi-brittle SCG and has been investigated in numerous studies [5, 21–25]. Chain disentanglement and chain rupture may be assumed to have a contribution to the failure of fibrils [26, 27]. Also local crack-tip ageing can affect the mechanisms of SCG [8, 13, 28, 29]. Concluding that the most important failure mechanism for lifetime of thermoplastic pipes is the Region B failure, this region has been examined closely.

Accelerated test methods, such as internal pipe pressure tests, Notched Pipe Tests (NPT), Full Notch Creep Test (FNCT), Pennsylvania Edge Notch Tensile (PENT) Test etc., were developed to characterise this failure behaviour. For newer materials, these tests are no longer feasible anymore. To estimate long-term behaviour, faster methods are required. Consequently, alternative methods, such as the cyclic Cracked Round Bar Test (CRB Test [30]), or the Strain Hardening Test (SHT [31]) have emerged as promising methodologies to rank materials in regard to their resistance against SCG.

Besides quality control and ranking of materials it is of high interest to estimate actual lifetimes of pipes under application conditions, to schedule service or replacement intervals. For this goal, fracture mechanical concepts such as the linear elastic fracture mechanic (LEFM), on which also aforementioned ranking tests like NPT, FNCT, PENT Test and CRB Test are based, provide promising prospects.

3.2 Fracture Mechanics Approach for Pipe Lifetime Calculations

The LEFM approach used to estimate lifetimes of PE pipe systems is explained in the following section. Alongside, Sect. 3.3 provides the necessary material-specific limitations which have to be considered when using LEFM with thermoplastic pipe grade materials.

The basic idea behind this approach is to use material-specific constants, which can be measured with rather simple experiments, in combination with crack propagation laws based on the stress intensity factor K_I [32] to describe the advance of a crack through any arbitrary structure. A well-known crack propagation law in LEFM is the approach described by Paris and Erdogan in 1963 for cyclic loads [33] and is shown in (3.1), adapted for a static loading case. Even though A and m are material constants, they are dependent on the loading situation and temperature. They have to be measured for the respective loading case and environmental conditions of the actual application. Buried PE-pipes are mainly subjected to static internal pressure. Therefore, A and m are measured using fracture mechanics specimens under static loading. Due to the principle of crack-tip similitude they can then be used for other structures made from the same material subjected to the same loading conditions. For this situation, (3.1) can be applied, where K_I is the stress intensity factor of the examined structure and da/dt the crack extension over a period of time.

$$\frac{da}{dt} = A \cdot K_I^m \quad (3.1)$$

By Integration of this crack propagation law, failure times due to SCG can be estimated. The stress intensity factor K_I used in (3.1) is mainly dependent on the applied stress (σ_I) and the actual crack length (a) [compare (3.2)]. Since cracks

propagate during the lifetime of pipes, the respective values of K_I have to be calculated for each crack length during lifetime. For simple cases, the development of K_I as a function of crack length a and remaining ligament ($f(a/W)$) can be derived via analytical analysis (e.g. [34]). More complex situations or geometries require finite element analysis (FEA) to determine the respective stress field adjacent to the crack tip ([35, 36] et seq.).

$$K_I = \sigma \cdot \sqrt{a} \cdot f\left(\frac{a}{W}\right) \tag{3.2}$$

A schematic illustration of the relationship between crack length a_1 to a_3 in an internally pressurised pipe and the development of K_I is depicted in Fig. 3.2. It can be seen, that K_I usually increases with advances in crack growth through the pipe wall (a/W).

Subsequently, the time for a crack to grow through a component can be calculated by re-arranging (3.1) to the form shown in (3.3). The slow crack growth time (t_{SCG}) is expressed as a function of the parameters A and m , the load dependent stress intensity factor K_I of the structure and the distance of the growing crack in the component starting from the initial crack length a_{ini} to the final crack length a_f .

$$t_{SCG} = \frac{1}{A} \cdot \int_{a_{ini}}^{a_f} \frac{1}{K_I^m} \cdot da \tag{3.3}$$

The total amount of time to failure t_f consists of t_{SCG} and also of the time to crack initiation t_{ini} which can be approximated for PE by the formula given in (3.4) [12], where B and n are again material constants, which are dependent on the test conditions such as temperature, pre-notching or environment [12, 37]. Therefore, the total amount of time to fracture can be summarised as stated in (3.5) [37].

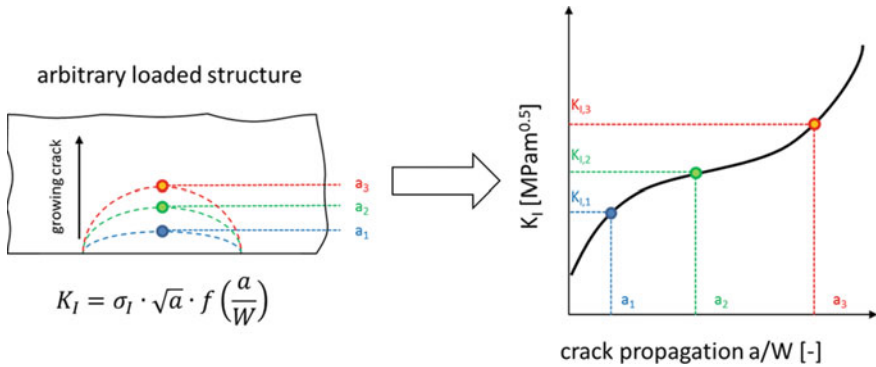


Fig. 3.2 Relation between growing crack length in an arbitrary loaded structure and resulting K_I -values

$$t_{ini} = B \cdot K_{I,ini}^{-n} \quad (3.4)$$

$$t_f = t_{ini} + t_{SCG} = B \cdot K_{I,ini}^{-n} + \frac{1}{A} \cdot \int_{a_{ini}}^{a_f} \frac{1}{K_I^m} \cdot da \quad (3.5)$$

Using this approach, it is possible to estimate lifetimes of pipes as long as the application and loading situation of the pipe, the development of K_I as a function of crack length and the material constants A , m , B and n are known.

The development of K_I as a function of a growing crack in a pipe wall is important for correct estimation of failure times. Literature provides different solutions of K_I under internal pressure [34, 38, 39]. Also FEA can be applied to estimate K_I . In Fig. 3.3 a comparison between different solutions from literature and from FEA is shown. The calculations for the FEA solutions were performed for a semi-elliptical surface crack with the width b of the crack being twice as long as the depth a [12]. The formulations proposed by Anderson [38] and Murakami [34] converge with results of FEA. However, the solution proposed by Krishnamachari [39] delivers significantly different results.

For correct estimation of K_I during a test, not only changes in crack length but also in the actual shape of the crack, which might change the stress field significantly, has to be considered [42–47]. As an example, the difference between a semi-circular and a semi-elliptical crack front is shown in Fig. 3.4 [40]. Even though both cracks have the same initial crack length (a_{ini}), stress distribution around the crack differs quite significantly. For the semi-elliptical crack shape, K_I in point A is significantly higher compared to point C_e which results in a shift to a

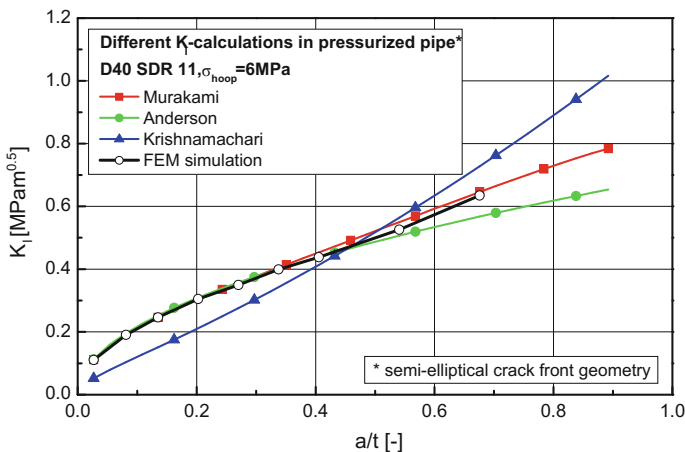


Fig. 3.3 Differences in stress intensity factor development, as proposed by Murakami [34], Anderson [38], Krishnamachari [39] and FEM solution, of a crack growing through the pipe wall of an internal pressurised pipe with a semi-elliptical crack front, in accordance to [40, 41]

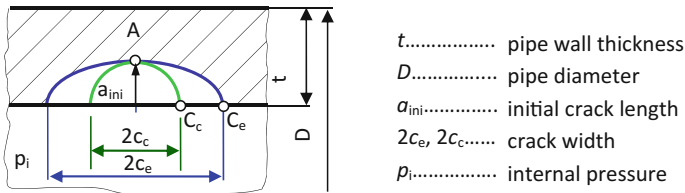


Fig. 3.4 Difference between semi-elliptical and semi-circular crack front for the same initial crack length a_{ini} in an internal pressurised pipe [40]

semi-circular crack front as the crack advances through the pipe wall [13]. If the crack starts out with a semi-circular crack front, K_I is only slightly higher in point C_c than in A. Therefore there is only a small tendency of the crack to change the crack front geometry to a semi-elliptical shape.

Due to the discontinuous crack growth in PE, which consists of a continuous formation of crazes with highly oriented fibrils at the crack tip and their stepwise breakdown [11, 13, 48–51] it is possible to estimate crack front shapes at various testing times from striations on fracture surfaces. In Fig. 3.5 a pipe, which fractured during internal pressure testing, with changing front shape from a semi-circular to a semi-elliptical crack can be seen [40].

Therefore, changes in crack front shape have to be taken into account, when calculating stress intensity factor development for lifetime extrapolation. FEA has proven to be a valid tool in this endeavour, especially since additional influences of outside loads [52] or residual stresses in the material can be included [44].

3.3 Crack Growth in Polyethylene

When using a lifetime concept based on LEFM, applicability and general limitations of the used material have to be verified. The following section focuses on the behavioural details and restrictions of CGI and SCG in polyethylene under similar conditions as in pressurised pipes.

Slow crack growth in polyethylene usually starts due to stress concentrations (e.g. around inclusions, defects, material-inhomogeneity, etc.) or in the case of fracture mechanical tests around notches. Stress concentrations lead to the formation of small plastic zones, which are characterised by the typical properties of crazes in PE [23, 53]. Due to local flow in the amorphous area of the polymer, small voids are created which start to grow, coalesce and form fibrils. Initial crazes start to grow under stress by dragging neighbouring uninfluenced material into the process zone and by disentanglement of tie-molecules between lamellas. Local creep processes can also influence craze formation and propagation (e.g. [54]). As soon as first fibrils start to fracture, CGI followed by SCG takes place. The process of SCG is mainly governed by disentanglement of tie-molecules [13] and up to a certain

Semi-elliptical crack front

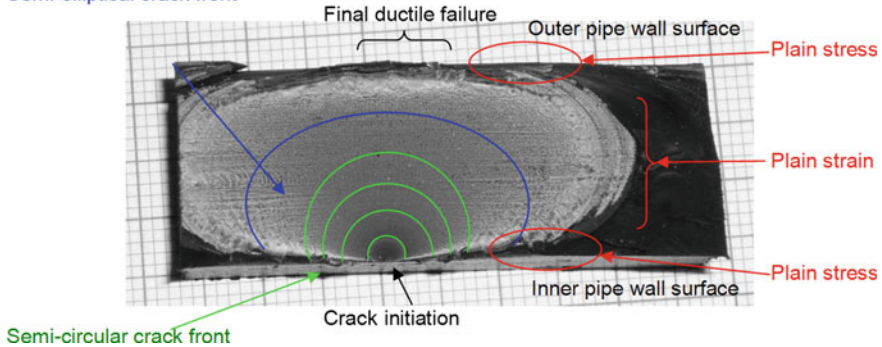


Fig. 3.5 Fracture surface of an internal pressure test with a changing crack front shape from semi-circular to semi-elliptical [40]

amount by fracture of covalent bounds [55]. After first crack initiation and propagation the crack starts to grow by further formation and breakdown of fibrillated zones in front of the crack tip. In PE pipe materials this failure occurs in a step-wise mode, which leads to the formation of discernible markings on the fracture surface of test specimens. These striations were reported for test specimens under constant [13, 56–58] and fatigue load [48, 51, 56, 59–65], as well as internally pressurised pipes [13, 40, 58]. However, this seemingly rather simple process of build-up and break down of material in front of a crack tip is dependent on different aspects which have to be addressed before lifetime estimations can be performed.

Methods based on LEFM are restricted to linear elastic or nearly linear elastic material including small-scale yielding [32, 66]. It was found for polymeric materials that the global loading situation also has to be within the region of linear-viscoelasticity [24]. For PE used in pressurised pipes, this level is usually surpassed [37]. Nevertheless, several authors have successfully shown that failure by SCG in PE pipe materials and several other polymers can be described using LEFM (e.g. [13, 15–17, 56, 57, 67–74]). The group around Brown and Lu was among the first to thoroughly investigate this specific topic from different angles. Influences, such as the transition between ductile and SCG failure [75, 76] as well as the main parameters that govern SCG in polyethylene, like molecular weight [77], density of side branches in copolymers [78, 79], notching [80], stress cracking agents [81] and test temperature and morphology [82] were addressed. Nevertheless, by using the concept of LEFM for lifetime estimations, several simplifications or assumptions have to be made. For example, the size and shape of intrinsic defects in the pipe wall influences calculated lifetimes significantly [12, 37, 40]. A study of fractured pipes from internal pipe pressure tests provided a range between 100 and 400 μm for initial crack length [83]. This margin signifies differences of more than a decade of years for calculated lifetimes. Furthermore, fracture mechanical tests are usually performed at much higher initial K_I values compared to pipes. The power-law correlation between crack kinetics and applied

stress level found in experiments is then simply extrapolated to lower values, neglecting changes of the relation due to short-crack effects or a possible threshold value [37]. Also material deterioration, which is significantly enhanced close to crack tips can influence the behaviour of SCG in PE [19] which is not addressed in a classical LEFM calculation.

Remarkable advances in material development over the last decades also lead to modern PE pipe materials with significantly improved resistance to SCG. While opening up new possibilities for pipe manufacturers and grid operators in regards to service time and applied pressure levels in pipe systems it poses a great challenge for material testing and lifetime estimations using a LEFM approach. The high resistance to SCG has made it virtually impossible to measure the necessary material parameters (e.g. A and m for SCG) without either invalidating the requirements of LEFM, testing at highly elevated temperatures which are far from actual application, using stress cracking agents or resulting in testing times of several years. To accelerate tests without using chemicals or going to elevated temperatures, several authors suggested using cyclic instead of static loads. This proposition was supported by good correlations between results from cyclic and static tests [11, 18, 24, 48, 61–65, 72, 73, 84, 85]. By changing the load situation during tests, material constants used for the LEFM approach do not describe the same process as in a pipe under static load. Therefore, they cannot directly be used for lifetime estimation. To calculate correct CGI and SCG times, material parameters have to be extrapolated to the loading case of the actual application. Additional influences of the cyclic loading also have to be examined in order to produce valid results.

3.4 Extrapolation to Static Crack Growth Behaviour from Fatigue Tests

The basic idea behind this procedure is to calculate synthetic creep crack growth (CCG) curves from tests at different loading conditions (R -ratio = $\sigma_{\min}/\sigma_{\max}$) with short-term tests and extrapolate to a static loading case which would require considerably longer testing times. This approach has been investigated by several authors for PE [48, 56, 86–90] over the last years. Even though different focuses and approaches were chosen in the respective works, authors agree in general that an extrapolation to a static loading case from fatigue tests seems possible as long as several additional influences are considered. For example, whereas static tests are driven by CCG alone, fatigue tests are a combination of creep and fatigue crack growth with different ratios, depending on the specific test configuration. Studies have shown that fatigue tests at R -ratios close to 1 are dominated by creep crack growth than ratios close to 0 where fatigue failure mechanisms are much more dominant [48, 86, 87, 91]. Similar results were found for the influence of testing temperature. For testing temperatures around 23 °C creep crack growth was less

pronounced, compared to tests at higher temperatures (e.g. 80 °C) [70, 86, 87]. Furthermore, choice of frequency can also significantly influence results if not chosen adequately [91–94]. To account for different contributions to failure, Hertzberg et al. [94], Wyzgoski et al. [95] and Pegoretti [96] amongst others proposed a combination of fatigue and creep to describe crack growth behaviour of thermoplastic materials.

However, it has been shown, that for frequencies around 5 Hz or higher, the influence of creep contributions is not as significant for specimen failure in PE, as it is for rather low frequencies (<0.1 Hz) [91, 97], as long as no significant hysteretic heating takes place. For PE-HD materials frequencies of up to 10 Hz at moderate loading were found to impose only minor influence in this regard [93, 97]. Similar trends were found for polycarbonate [98] and glass fibre-reinforced polyamide [95]. However, the contribution of creep is mainly addressed at either high R -ratios and/or rather low frequencies (mostly below 1 Hz), where the pronounced creep damage contribution leads to lower cycles to failure. Frank et al. [97] tested PE-HD under the conditions of $R = 0.1$ and frequencies between 5 and 20 Hz. In this study, only minor differences in total cycle number to failure was observed. Contrary to findings at very low frequencies, in this study higher frequencies (20 Hz) lead to a minor decrease in total cycle number, which may be attributed to some hysteretic heating in the specimen (ΔT around 7 °C).

Pegoretti et al. [96] showed in their work for glass fibre-reinforced PP, that if crack growth da/dN for a constant ΔK_I (at $R = 0.4$) is plotted as a function of different fatigue time period (=frequency⁻¹) the contribution of viscoelastic creep and amount of “true fatigue” can be estimated. For the examined material with 10 wt% glass fibre the contribution creep was about 140 times higher to failure than fatigue induced damage at 0.1 Hz. Contrary, at 10 Hz fatigue and creep were on par. Besides frequency, hysteretic heating, loading levels, etc. there have also been discussions about changes of fibrillary movement in crazes during fatigue tests due to different R -ratios. At higher R -ratios close to 1, fibrils in crazes are constantly loaded in a tensile mode for both σ_{\max} and σ_{\min} . For low R -ratios close to 0 a change to tensile mode at σ_{\max} and bending at σ_{\min} has been envisaged (compare [60, 90] for PE or [99] for polystyrene). As pointed out in [86] and described above, there are several processes running simultaneously during crack propagation in PE and establishing a generalised model which accounts for all factors is still challenging.

Nevertheless, for PE-HD at reasonable temperatures it was found, that the cyclic part was dominant during fatigue tests. The transition from fatigue dominated damage at low R -ratios to the purely creep crack growth dominated failure at $R = 1$ was found to be reflected in the micromorphology of the fracture surfaces. In Fig. 3.6 this transition is depicted for PE-HD tested at 60 °C and fatigue loads with R -ratios of 0.1, 0.3, 0.5 and the static case of $R = 1$ at $K_{I\max} = 0.45 \text{ MPa m}^{0.5}$ and equal crack growth rates. With increasing R -ratio appearances of fractographs under fatigue load are alike those of tests under constant loads [86].

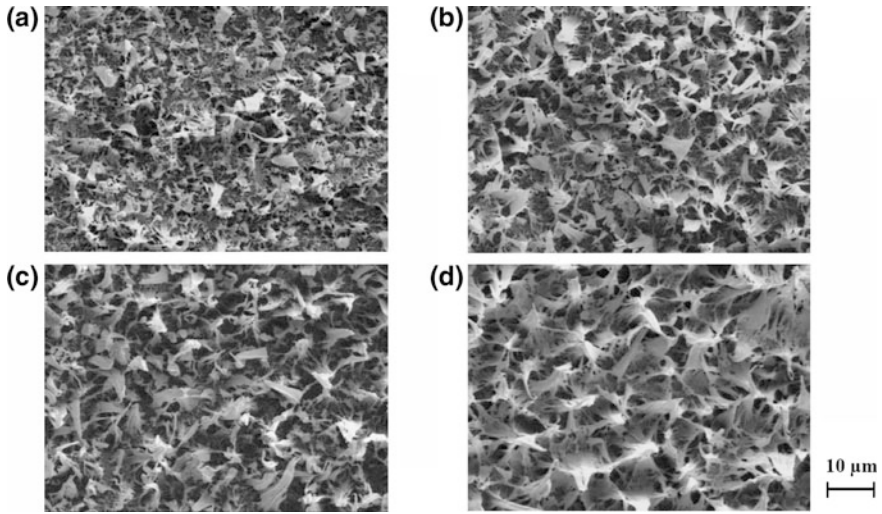


Fig. 3.6 Changes in micromorphology of fracture surfaces of PE-HD tested at $T = 60\text{ }^{\circ}\text{C}$ and R -ratios of 0.1 (a), 0.3 (b), 0.5 (c) and 1 (d) [86]

Therefore, it seems to be an acceptable hypothesis that the variation of R -ratio, taking into account that at a testing frequency of 10 Hz the influence of frequency itself is highly reduced, can be used to extrapolate to static loading of $R = 1$ from fatigue tests at lower R -ratios. This extrapolation procedure is depicted below in Fig. 3.7.

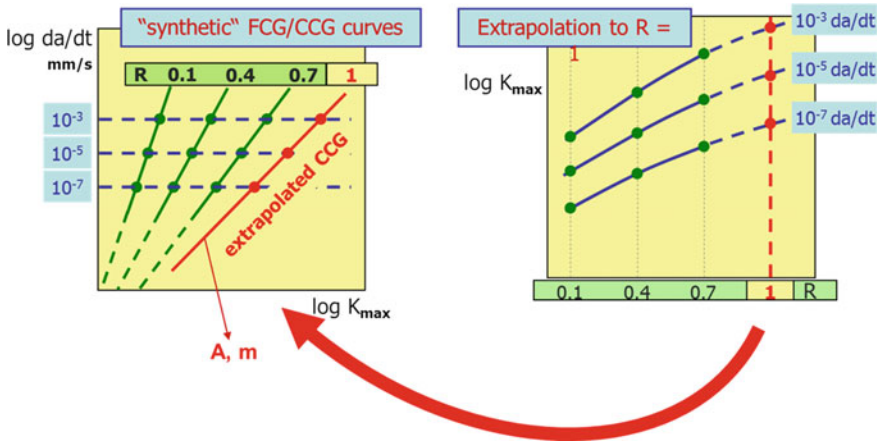


Fig. 3.7 Extrapolation procedure from fatigue tests at various R -ratios to the “synthetic” creep crack growth curve under static loading of $R = 1$ [40, 100–102]

3.5 Lifetime Calculation of PE Pipe Grades

Using the approach described in the sections above, it should be possible to calculate lifetimes for modern PE pipe systems using LEFM and fatigue tests. However, resin manufacturers have been diligently improving pipe grade materials as well. Compared to a few decades back, resistance of modern PE pipe grades has improved remarkably.

Due to the high resistance against crack growth, even with cyclic loading either long testing times have to be endured or higher loads have to be chosen. Unfortunately, due to the rather ductile behaviour of modern PE grades, plastic zones develop rather easy at higher loads [compare (3.6)]. This inevitably invalidates the limitations of LEFM, rendering the whole method unusable. Therefore, new specimen geometries compared to the classical compact tension (CT), wedged open loading (WOL), etc. specimens have to be used, where formation of plastic zone sizes is restricted. Since the size of a plastic zone is significantly influenced by the stress state [either plane stress or strain, see (3.6)] specimen geometry with significant amount of plane strain would be preferable. Plane stress mainly forms at free surfaces. Therefore, a round specimen with a circumferential notch without a free surface perpendicular to the notch seems promising (Fig. 3.8) [66].

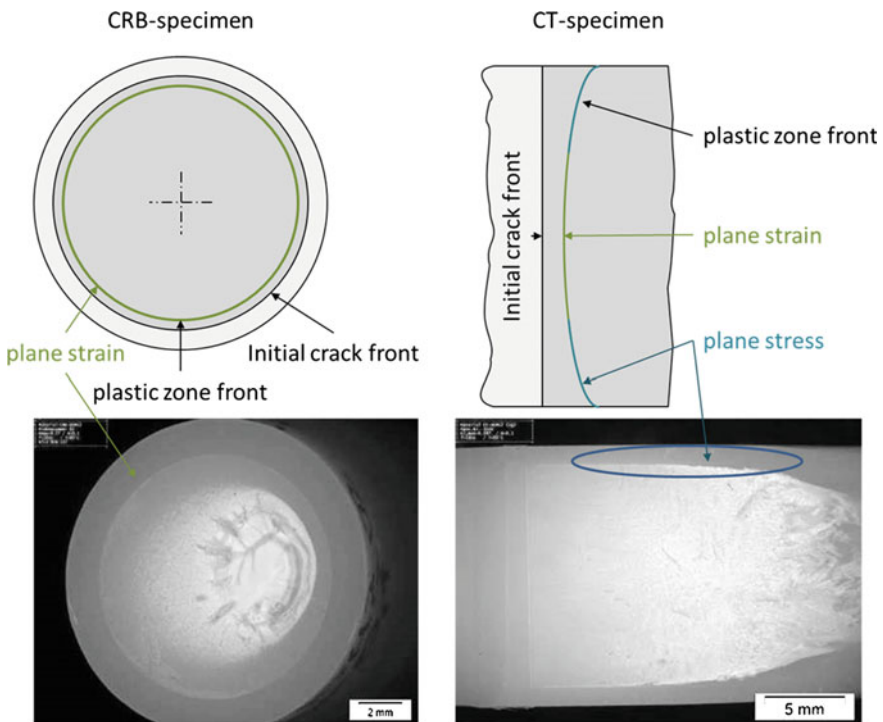


Fig. 3.8 Areas of different stress states and their impact on the fracture surface of compact tension and cracked round bar specimen [103]

$$r_p = \frac{1}{m \cdot \pi} \cdot \frac{K_I^2}{\sigma_{ys}^2} \quad \text{with } m = 1 \text{ for plane stress and } m = 3 \text{ for plane strain} \quad (3.6)$$

The impact of different stress states for crack kinetics of the same PE material tested at 80 °C is shown in [103]. In this work significantly different values for crack growth kinetics for CT and CRB specimens were measured for different R -ratios which are necessary for the extrapolation to the static case. This might be an indication that for this material and chosen load levels CT specimens are not usable within the limitations of LFM.

The downside of CRB specimens is that crack initiation and propagation cannot be monitored directly using optical methods. Therefore, a compliance calibration with pre-notched specimens and extensometers around the specimens is necessary to monitor crack kinetics. The exact procedure for this calibration is described in [89, 104]. Also crack initiation can be calculated with the approach described in [105]. However, since this approach is rather time-consuming an assessment of accuracy and feasibility has to be made individually. When neglecting crack initiation times in lifetime estimations of PE pipe systems they can be seen as an additional safety margin.

3.6 Lifetime Calculation of a PE Pipe Grade at 80 °C Using Cyclic CRB Tests

The following section will present PE pipe lifetime calculations as a matter of validation for the approach presented. Since failure time data of real PE pipe systems under application conditions are scarce and not broadly available, all measurements were carried out at 80 °C and compared to internal pipe pressure tests at 80 °C. Contrary to classical EN ISO 9080 [1] tests, the pipes subjected to internal pressure were provided with sharp axial razor blade notches ($a_{ini} = 0.8$ mm and a width of $2b = 10$ mm) on the inside pipe wall. This special preparation method was chosen to be able to calculate the exact K_I values at the position of CGI using FEA. Additionally, testing times are significantly shorter compared to classical EN ISO 9080 tests, while still producing quasi-brittle cracks.

The tested material was a commercially available PE-HD for pipe applications. As a first step, compliance calibration according to [89] was performed for CRB specimens. The data was fitted with a 2nd order polynomial for crack length calculation. The fit is shown in Fig. 3.9. Afterwards, cyclic CRB tests were performed at several different load levels to ensure failure in quasi-brittle failure mode and to measure crack kinetics for the loading cases of $R = 0.1$; 0.3 and 0.5 (compare Fig. 3.10). The data was extrapolated to the “synthetic” CCG curve of $R = 1$ according to [40] using a logarithmic fit.

For comparison, the same method was applied to CT specimens. The results for crack kinetics at $R = 1$ after extrapolation are shown in Table 3.1. The next step for

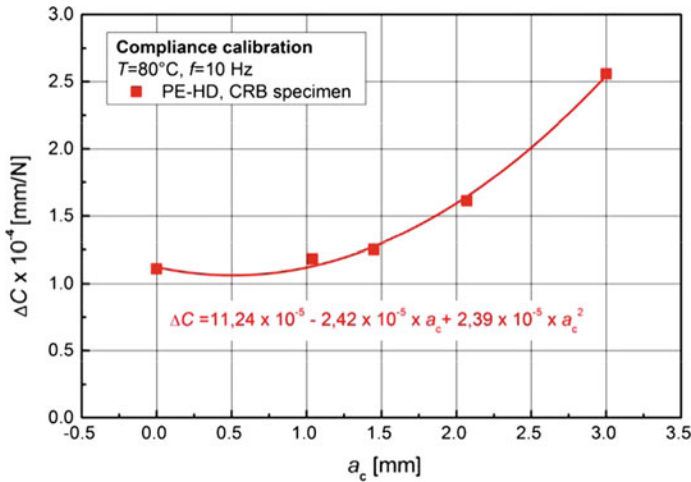


Fig. 3.9 Compliance calibration curve ΔC as a function of the crack length a_c for CRB specimens of the investigated PE-HD at a temperature of $T = 80^{\circ}\text{C}$ [103]

the lifetime estimation is the development of the stress intensity factor K_I of the component in question. As previously mentioned and shown in Fig. 3.3 FEA provides the necessary data for this step.

Values in Table 3.1 were taken from Fig. 3.10 [103]. In this diagram the big differences in crack kinetics due to different specimen configuration is shown. It is quite noticeable, that besides different slopes at K_I values the impact of the R -ratio is much less distinctive in CRB specimens compared to the classical CT specimen.

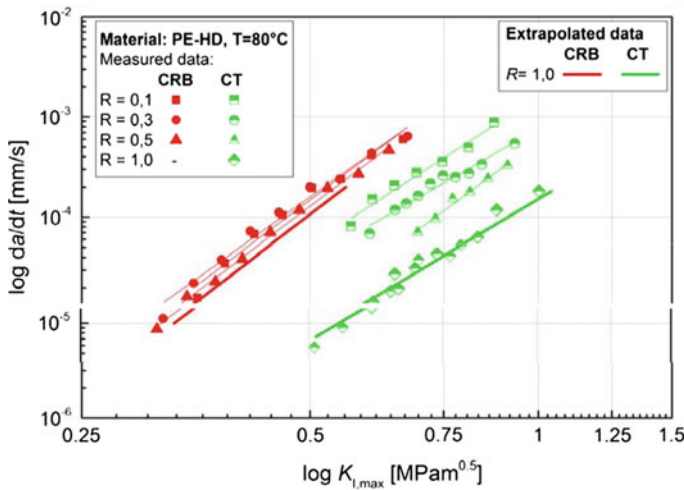


Fig. 3.10 Influence of specimen geometry on crack growth kinetics at different R -ratios [103]

Table 3.1 Fracture mechanics material parameter A and m for SCG at static loading in PE-HD at a temperature of $T = 80\text{ }^\circ\text{C}$ determined with CRB and CT specimens [103]

Specimen geometry	A	m
CRB	59.2×10^{-4}	5.8
CT	1.5×10^{-4}	4.5

The final step, after estimation of crack growth kinetics and K_I development is the integration according to (3.3). The overlap of the extrapolated data with measured crack kinetics at $R = 1.0$ for CT specimens generally confirmed the validity of the used extrapolation procedure [103].

From previous studies it is known, that in internal pipe pressure tests with un-notched pipes typical initial defect sizes are within the range of 100–400 μm [37]. As mentioned before, the broad range of initial defect sizes leads to high scatter in the results of internal pipe pressure tests. The precise pre-notching of the pipes to an initial defect size depth of $a_{ini} = 0.8\text{ mm}$ in this case resulted in a well-defined initial K_I . Due to the knowledge of the exact initial crack length a significant decrease of scatter and also a reproducible reduction of failure times was achieved [103].

Calculated lifetimes and measured lifetimes due to SCG of internal pressurised pre-notched pipes are shown in Fig. 3.11. In this figure the logarithmic failure time t_f is shown as a function of the applied hoop stress (σ_{hoop}). In the diagram a clear linear correlation between σ_{hoop} and t_f can be seen for the internally pre-notched pipes. All data points in the diagram from pipe pressure tests failed in quasi-brittle mode with cracks initiating at one of the internal pre-notches. In comparison to the

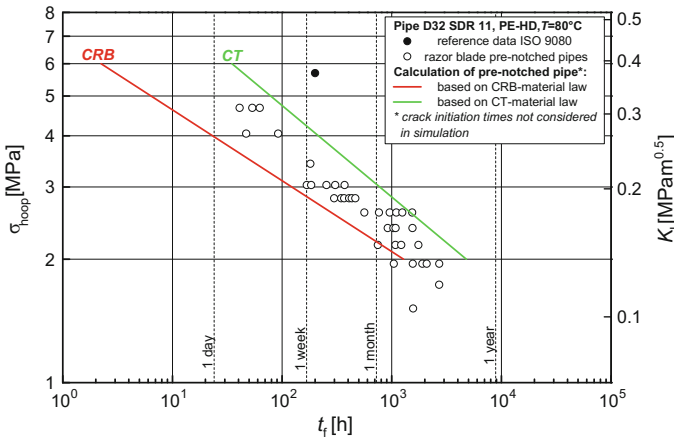


Fig. 3.11 Comparison of lifetimes according to calculated CCG of CT and CRB specimens with failure times from internal pipe pressure tests performed at $80\text{ }^\circ\text{C}$

included reference point from EN ISO 9080 it can be seen, that the lifetimes were about one decade shorter due to the internal pre-notching.

The parameters for crack growth kinetics determined via CRB specimen provide a very good correlation with real failure times. The agreement of predicted pipe lifetimes based on CRB extrapolation with experimental lifetimes was also confirmed in several previous studies [40, 106, 107]. Considering, that CGI was neglected in this study for both CRB and CT specimens which would shift the curves of total lifetime to the right, it can be seen, that crack kinetics taken from CT specimen tests tend to overestimate lifetimes of pipes. This can mainly be attributed to the formation of significant plastic zones during testing, which restrict crack growth and can undermine limits of LEFM.

3.7 Conclusion and Outlook

When performing lifetime estimations using extrapolation concepts, it is vital to estimate the uncertainties which always accompany accelerated testing methods. Uncertainties may arise from deviating parameters such as changes in environmental conditions, temperature, different loading ratios, chemicals such as stress cracking agents, etc. Only when these influences are known it is justifiable to go into lifetime calculations.

Recent studies of Pinter et al. [103] showed, that fracture mechanics extrapolation concepts for accelerated prediction of PE pressure pipes using short-time fatigue tests provide valid results when compared to pre-notched internal pipe pressure tests. The use of a CRB specimen for LEFM tests improves the results compared to classical CT specimens, which tend to overestimate lifetimes. This can mainly be attributed to bigger plastic zone sizes which restrict SCG in CT specimens. Another advantage is the similarity of constraint and K_I -development between a pipe and CRB specimens. Summarising, the extrapolation concept using short-term fatigue tests on CRB specimens provides a valuable and valid tool to perform lifetime estimations for pipe systems made from PE-HD pipe materials.

Further steps in the development of the approach using cyclic CRB Tests are currently under evaluation. For example, the implementation of influences due to media [108, 109] is an important addition, to be able to cover the area of media and crude oil transportation. The impact of CGI is also a topic which has yet to be addressed. So far it has often been neglected in lifetime estimations due to complex testing procedures [105]. Also the use of the cyclic CRB Test for different polymeric pipe materials [110] is currently examined. Seeing that only about a third of all thermoplastic pipes is produced from PE-HD material [111, 112] this is a logical next step.

Besides lifetime estimation, the use of the cyclic CRB Tests at $R = 0.1$ is also discussed for ISO-standardisation for material quality control [30, 110, 112, 113]. Good correlations with established methods support its claim as a precise and fast ranking tool for PE-HD pipe grades [114, 115].

References

1. EN ISO 9080 (2012): Plastics piping and ducting systems—Determination of the long-term hydrostatic strength of thermoplastics materials in pipe form by extrapolation
2. ASTM D 2837 (2013): Standard test method for obtaining hydrostatic design basis for thermoplastic pipe materials or pressure design basis for thermoplastic pipe products
3. Richard, K., Gaube, E., Diedrich, G.: Trinkwasserrohre aus Niederdruckpolyäthylen. *Kunststoffe* **49**, 516–525 (1959)
4. Gaube, E., Gebler, H., Müller, W., Gondro, C.: Zeitstandfestigkeit und Alterung von Rohren aus HDPE. *Kunststoffe* **75**, 412–415 (1985)
5. Lustiger, A.: Environmental stress cracking: the phenomenon and its utility. In: Browstow, W., Corneliusen, R.D. (eds.) *Failure of Plastics*, pp. 305–329. Carl Hanser, Munich (1986)
6. Kausch, H.H.: *Polymer Fracture*. Springer, Berlin (1987)
7. Ifwarson, M., Tränkner, T.: Gebrauchsdauer von Polyethylenrohren unter Temperatur und Druckbelastung. *Kunststoffe* **79** (198) 525–529
8. Lang, R.W.: Polymerphysikalische Ansätze zur Beschreibung des Deformations- und Versagensverhaltens von PE-Rohren. *3R Int.* **36**, 40–44 (1997)
9. Lang, R.W., Pinter, G., Balika, W.: Ein neues Konzept zur Nachweisführung für Nutzungsdauer und Sicherheit von PE-Druckrohren bei beliebiger Einbausituation. *3R Int.* **44**, 32–41 (2005)
10. Krishnaswamy, R.K.: Analysis of ductile and brittle failures from creep rupture testing of high-density polyethylene (HDPE) pipes. *Polymer* **46**, 11664–11672 (2005)
11. Barker, M.B., Bowman, J., Bevis, M.: The performance and causes of failure of polyethylene pipes subjected to constant and fluctuating internal pressure loadings. *J. Mater. Sci.* **18**, 1095–1118 (1983)
12. Stern, A.: *Fracture Mechanical Characterization of the Long-Term Behavior of Polymers Under Static Loads*. Ph.D. thesis, Montan University Leoben, Leoben (1995)
13. Pinter, G.: *Rißwachstumsverhalten von PE-HD unter statischer Belastung*. Ph.D. thesis, Montan University Leoben, Leoben (1999)
14. Böhm, L.L., Enderle, H.F., Fleissner, M.: High-density polyethylene pipe resins. *Adv. Mater.* **4**, 234–238 (1992)
15. Brown, N., Lu, X., Huang, Y.: The fundamental material parameters that govern slow crack growth in linear polyethylene. *Plast. Rubber Compos. Process. Appl.* **17**, 255–258 (1992)
16. Egan, B.J., Delatycki, O.: The morphology, chain structure and fracture behaviour of high-density polyethylene. Part I: Fracture at a constant rate of deflection. *J. Mater. Sci.* **30**, 3307–3318 (1995)
17. Egan, B.J., Delatycki, O.: The morphology, chain structure and fracture behaviour of high-density polyethylene. Part II: Static fatigue fracture testing. *J. Mater. Sci.* **30**, 3351–3357 (1995)
18. Pinter, G., Lang, R.W.: Creep crack growth in high density polyethylene. In: Moore, D. R. (ed.): *The Application of Fracture Mechanics to Polymers, Adhesives and Composites*. ESIS Publication 33, Elsevier Science, Oxford (2004), pp. 47–54
19. Dörner, G.F.: *Stabilisatoreinflüsse auf das Alterungs- und Zeitstandverhalten von Rohren aus PE-MD*. Ph.D. thesis, Montan University Leoben, Leoben (1994)
20. Choi, B., Chudnovsky, A., Paradkar, R., Michie, W., Zhou, Z., Cham, P.: Experimental and theoretical investigation of stress corrosion crack (SCC) growth of polyethylene pipes. *Polym. Degrad. Stab.* **94**, 859–867 (2009)
21. Dugdale, D.: Yielding of steel sheets containing slits. *J. Mech. Phys. Solids* **8**, 100–104 (1960)
22. Barenblatt, G.J.: The mathematical theory of equilibrium cracks in brittle fracture. *Adv. Appl. Mech.* **7**, 55–129 (1962)

23. Friedrich, K.: Crazes and shear bands in semi-crystalline thermoplastics. In: Kausch, H.H. (ed.) *Crazing in Polymers*. Advances in Polymer Science 52–53, pp. 225–274. Springer, Berlin (1983)
24. Lang, R.W.: Applicability of linear elastic fracture mechanics to fatigue in polymers and short-fiber composites. Ph.D. thesis, Lehigh University, Bethlehem (1984)
25. Kausch, H.H., Gensler, R., Grein, C., Plummer, C.J.G., Scaramuzzino, P.: Crazing in semicrystalline thermoplastics. *J. Macromol. Sci., Part B Phys.* **38**, 803–815 (1999)
26. Kausch, H.H. (ed.) *Crazing in Polymers*, vols. 1 and 2. Advances in Polymer Science 52/53 and 91/92. Springer, Berlin (1983, 1990)
27. Lustiger, A., Ishikawa, N.: An analytical technique for measuring relative tie-molecule concentration in polyethylene. *J. Polym. Sci., Part B: Polym. Phys.* **29**, 1047–1055 (1991)
28. Pinter, G., Lang, R.W.: Effect of stabilization on creep crack growth in high-density polyethylene. *J. Appl. Polym. Sci.* **90**, 3191–3207 (2003)
29. Haager, M., Pinter, G., Lang, R.W.: Estimation of slow crack growth behavior in polyethylene after stepwise isothermal crystallization. *Macromol. Symp.* **217**, 383–390 (2004)
30. Frank, A., Pinter, G.: Evaluation of the applicability of the cracked round bar test as standardized PE-pipe ranking tool. *Polym. Testing* **33**, 161–171 (2014)
31. van der Stok, E., Scholten, F.: Strain hardening tests on PE pipe materials. In: *Proceedings of Plastics Pipes XVI* (Barcelona, 24.–26.09.2012). Barcelona (2012), 10 p
32. Irwin, G.R.: Analysis of stresses and strains near the end of a crack traversing a plate. *J. Appl. Mech.* **24**, 361–364 (1957)
33. Paris, P., Erdogan, F.: A critical analysis of crack propagation laws. *J. Basic Eng.* **85**, 528–534 (1963)
34. Murakami, Y. (ed.): *Stress Intensity Factors Handbook*, 2nd edn. Pergamon Press, Oxford (1990)
35. Dixon, J.R., Pook, L.P.: Stress intensity factors calculated generally by the finite element technique. *Nature* **224**, 166–167 (1969)
36. Yamamoto, Y., Tokuda, N.: Determination of stress intensity factors in cracked plates by the finite element method. *Int. J. Numer. Meth. Eng.* **6**, 427–439 (1973)
37. Lang, R.W., Stern, A., Dörner, G.F.: Applicability and limitations of current lifetime prediction models for thermoplastics pipes under internal pressure. *Angew. Makromol. Chem.* **247**, 131–145 (1997)
38. Anderson, T.L.: *Fracture Mechanics: Fundamentals and Applications*, 3rd edn. CRC Press, Taylor & Francis, Boca Raton (2005)
39. Krishnamachari, S.I.: *Applied Stress Analysis of Plastics: A Mechanical Engineering Approach*. Van Nostrand Reinhold, New York (1993)
40. Frank, A.: Fracture mechanics based lifetime assessment and long-term failure behavior of polyethylene pressure pipes. Ph.D. thesis, Montan University Leoben, Leoben (2010)
41. Hutař, P., Ševčík, M., Náhlík, L., Mitev, I., Frank, A., Pinter, G.: Numerical simulation of the failure behavior of PE pressure pipes with additional loads. In: *Proceedings of 67th Annual Technical Conference of the Society of Plastics Engineers 2009 (ANTEC 2009, Chicago, 22.–24.06.2009)*. Society of Plastics Engineers, Brookfield (2009), 2163–2168
42. Ševčík, M., Hutař, P., Zouhar, M., Náhlík, L.: Numerical estimation of the fatigue crack front shape for a specimen with finite thickness. *Int. J. Fatigue* **39**, 75–80 (2012)
43. Portch, D.J.: An investigation into the change of shape of fatigue cracks initiated at surface flaws. Report RD/B/N4645, Central Electricity Generating Board, Research Division, Berkeley Nuclear Laboratories, Berkeley (1979)
44. Hutař, P., Ševčík, M., Zouhar, M., Náhlík, L., Kučera, J.: The effect of residual stresses on crack shape in polymer pipes. In: *Carpinteri, A. (ed.) Proceedings of the 4th International Conference on Crack Paths (CP 2012, Gaeta, 19.–21.09.2012)*. Gaeta (2012), pp. 489–496
45. Broek, D.: *Elementary Engineering Fracture Mechanics*, 3rd edn. Martinus Nijhoff, The Hague Boston London (1982)

46. Broek, D.: *The Practical Use of Fracture Mechanics*, 2nd edn. Kluwer, Dordrecht Boston London (1989)
47. Hertzberg, R.W.: *Deformation and Fracture Mechanics of Engineering Materials*, 4th edn. Wiley, New York (1996)
48. Parsons, M., Stepanov, E.V., Hiltner, A., Baer, E.: Correlation of fatigue and creep slow crack growth in a medium density polyethylene pipe material. *J. Mater. Sci.* **35**, 2659–2674 (2000)
49. Favier, V., Giroud, T., Strijko, E., Hiver, J., G'Sell, C., Hellinckx, S., Goldberg, A.: Slow crack propagation in polyethylene under fatigue at controlled stress intensity. *Polymer* **43**, 1375–1382 (2002)
50. Pinter, G., Haager, M., Balika, W., Lang, R.W.: Fatigue crack growth in PE-HD pipe grades. *Plast., Rubber Compos.* **34**, 25–33 (2005)
51. Balika, W., Pinter, G., Lang, R.W.: Systematic investigations of fatigue crack growth behavior of a PE-HD pipe grade in through-thickness direction. *J. Appl. Polym. Sci.* **103**, 1745–1758 (2007)
52. Majer, Z., Hutař, P., Frank, A., Ševčík, M., Zouhar, M., Pinter, G., Náhlík, L.: Point load effect on the buried polyolefin pipes lifetime. *Polym. Eng. Sci.* **56**, 79–86 (2016)
53. Bhattacharya, S.K., Brown, N.: Micromechanisms of crack initiation in thin films and thick sections of polyethylene. *J. Mater. Sci.* **19**, 2519–2532 (1984)
54. O'Connell, P.A., Bonner, M.J., Duckett, R.A., Ward, I.M.: The relationship between slow crack propagation and tensile creep behaviour in polyethylene. *Polymer* **36**, 2355–2362 (1995)
55. Kausch, H.H.: Energy considerations for crack growth in thermoplastics. *Kunststoffe* **66**, 538–544 (1976)
56. Balika, W.: *Rissausbreitung in Kunststoff-Rohrwerkstoffen unter statischer und zyklischer Belastung: Vergleich kommerzieller Rohrwerkstoffklassen und Einfluss der Werkstoffmikrostruktur*. Ph.D. thesis, Montan University Leoben, Leoben (2003)
57. Chan, M.K.V., Williams, J.G.: Slow stable crack growth in high density polyethylenes. *Polymer* **24**, 234–244 (1983)
58. Hamouda, H.B.H., Simoes-betbeder, M., Grillon, F., Blouet, P., Billon, N., Piques, R.: Creep damage mechanisms in polyethylene gas pipes. *Polymer* **54**, 25–37 (2001)
59. Choi, B., Balika, W., Chudnovsky, A., Pinter, G., Lang, R.W.: The use of crack layer theory to predict the lifetime of the fatigue crack growth of high density polyethylene. *Polym. Eng. Sci.* **49**, 1421–1428 (2009)
60. Parsons, M., Stepanov, E.V., Hiltner, A., Baer, E.: Correlation of stepwise fatigue and creep slow crack growth in high density polyethylene. *J. Mater. Sci.* **34**, 3315–3326 (1999)
61. Shah, A., Stepanov, E.V., Capaccio, G., Hiltner, A., Baer, E.: Stepwise fatigue crack propagation in polyethylene resins of different molecular structure. *J. Polym. Sci., Part B: Polym. Phys.* **36**, 2355–2369 (1998)
62. Parsons, M., Stepanov, E.V., Hiltner, A., Baer, E.: Effect of strain rate on stepwise fatigue and creep slow crack growth in high density polyethylene. *J. Mater. Sci.* **35**, 1857–1866 (2000)
63. Shah, A., Stepanov, E.V., Hiltner, A., Baer, E., Klein, M.: Correlation of fatigue crack propagation in polyethylene pipe specimens of different geometries. *Int. J. Fract.* **84**, 159–173 (1997)
64. Shah, A., Stepanov, E.V., Klein, M., Hiltner, A., Baer, E.: Study of polyethylene pipe resins by a fatigue test that simulates crack propagation in a real pipe. *J. Mater. Sci.* **33**, 3313–3319 (1998)
65. Hertzberg, R.W., Manson, J.A.: *Fatigue of Engineering Plastics*. Academic Press, New York (1980)
66. Irwin, G.R.: Plastic zone near a crack and fracture toughness. In: *Proceedings of 7th Sagamore Ordnance Materials Research Conference* (Raquette Lake, 16.–19.08.1960). Syracuse University, Syracuse (1960), IV-63

67. Brown, N.: A fundamental theory for slow crack growth in polyethylene. *Polymer* **36**, 543–548 (1995)
68. Braga, M., Rink, M., Pavan, A.: Variations in the fracture behaviour of polyethylene pipe materials induced by thermal treatments. *Polymer* **32**, 3152–3161 (1991)
69. Brown, N., Lu, X., Huang, Y., Qian, R.: Slow crack growth in polyethylene—a review. *Makromol. Chem. Macromol. Symp.* **41**, 55–67 (1991)
70. Haager, M., Zhou, W., Pinter, G., Chudnovsky, A.: Studies of creep and fatigue crack growth in HD-PE pipe materials. In: Proceedings of 64th Annual Technical Conference of the Society of Plastics Engineers (ANTEC 2005, Boston, 01.–05.05.2005). Society of Plastics Engineers, Bethel (2005), 3538–3542
71. Reynolds, P.T., Lawrence, C.C.: Mechanisms of deformation in the fatigue of polyethylene pipe. *J. Mater. Sci.* **28**, 2277–2282 (1993)
72. Haager, M.: Bruchmechanische Methoden zur beschleunigten Charakterisierung des langsamen Risswachstums von Polyethylen-Rohrwerkstoffen. Ph.D. thesis, Montan University Leoben, Leoben (2006)
73. Lang, R.W., Balika, W., Pinter, G.: Applicability of linear elastic fracture mechanics to fatigue in amorphous and semi-crystalline polymers. In: Moore, D.R. (ed.) *The Application of Fracture Mechanics to Polymers, Adhesives and Composites*. ESIS Publication 33, Elsevier, Amsterdam (2004), pp. 83–92
74. Pinter, G.: Slow Crack Growth in PE-HD under Static and Cyclic Loads. Habilitation thesis, Montan University Leoben, Leoben (2008)
75. Brown, N., Donofrio, J., Lu, X.: The transition between ductile and slow-crack-growth failure in polyethylene. *Polymer* **28**, 1326–1330 (1987)
76. Lu, X., Brown, N.: The transition from ductile to slow crack growth failure in a copolymer of polyethylene. *J. Mater. Sci.* **25**, 411–416 (1990)
77. Huang, Y., Brown, N.: The effect of molecular weight on slow crack growth in linear polyethylene homopolymers. *J. Mater. Sci.* **23**, 3648–3655 (1988)
78. Huang, Y., Brown, N.: The dependence of butyl branch density on slow crack growth in polyethylene: Kinetics. *J. Polym. Sci., Part B: Polym. Phys.* **28**, 2007–2021 (1990)
79. Huang, Y., Brown, N.: Dependence of slow crack growth in polyethylene on butyl branch density: morphology and theory. *J. Polym. Sci., Part B: Polym. Phys.* **29**, 129–137 (1991)
80. Lu, X., Qian, R., Brown, N.: Notchology—the effect of the notching method on the slow crack growth failure in a tough polyethylene. *J. Mater. Sci.* **26**, 881–888 (1991)
81. Ward, A.L., Lu, X., Huang, Y., Brown, N.: The mechanism of slow crack growth in polyethylene by an environmental stress cracking agent. *Polymer* **32**, 2172–2178 (1991)
82. Lu, X., Mcghe, A., Brown, N.: The dependence of slow crack growth in a polyethylene copolymer on test temperature and morphology. *J. Polym. Sci., Part B: Polym. Phys.* **30**, 1207–1214 (1992)
83. Expertise (Gutachten) No. K 14 450. Technologisches Gewerbemuseum (TGM), Vienna (1993)
84. Chudnovsky, A., Moet, A., Bankert, R.J., Takemori, M.T.: Effect of damage dissemination on crack propagation in polypropylene. *J. Appl. Phys.* **54**, 5562–5567 (1983)
85. Pinter, G., Haager, M., Balika, W., Lang, R.W.: Cyclic crack growth tests with CRB specimens for the evaluation of the long-term performance of PE pipe grades. *Polym. Testing* **26**, 180–188 (2007)
86. Pinter, G., Balika, W., Lang, R.W.: A correlation of creep and fatigue crack growth in high density poly(ethylene) at various temperatures. In: Remy, L., Petit, J. (eds.) *Temperature–Fatigue Interaction*. ESIS Publication 29, Elsevier, Amsterdam, pp. 267–275
87. Zhou, Z., Hiltner, A., Baer, E.: Predicting long-term creep failure of bimodal polyethylene pipe from short-term fatigue tests. *J. Mater. Sci.* **46**, 174–182 (2011)
88. Frank, A., Lang, R.W., Pinter, G.: Accelerated investigation of creep crack growth in polyethylene pipe grade materials by the use of fatigue tests on cracked round bar specimens. In: Proceedings of 66th Annual Technical Conference of the Society of Plastics Engineers

- (ANTEC 2008, Milwaukee, 04.–08.05.2008). Society of Plastics Engineers, Bethel (2008), pp. 2435–2439
89. Frank, A., Freimann, W., Pinter, G., Lang, R.W.: A fracture mechanics concept for the accelerated characterization of creep crack growth in PE-HD pipe grades. *Eng. Fract. Mech.* **76**, 2780–2787 (2009)
 90. Ayyer, R., Hiltner, A., Baer, E.: A fatigue-to-creep correlation in air for application to environmental stress cracking of polyethylene. *J. Mater. Sci.* **42**, 7004–7015 (2007)
 91. Nishimura, H., Narisawa, I.: Fatigue behavior of medium-density polyethylene pipes. *Polym. Eng. Sci.* **31**, 399–403 (1991)
 92. Zhou, Y., Brown, N.: The mechanism of fatigue failure in a polyethylene copolymer. *J. Polym. Sci., Part B: Polym. Phys.* **30**, 477–487 (1992)
 93. Janssen, R.P.M., Govaert, L.E., Meijer, H.E.H.: An analytical method to predict fatigue life of thermoplastics in uniaxial loading: sensitivity to wave type, frequency, and stress amplitude. *Macromolecules* **41**, 2531–2540 (2008)
 94. Hertzberg, R.W., Manson, J.A., Skibo, M.D.: Frequency sensitivity of fatigue processes in polymeric solids. *Polym. Eng. Sci.* **15**, 252–260 (1975)
 95. Wyzgoski, M.G., Novak, G.E., Simon, D.L.: Fatigue fracture of nylon polymers. *J. Mater. Sci.* **25**, 4501–4510 (1990)
 96. Pegoretti, A., Ricco, T.: Fatigue crack propagation in polypropylene reinforced with short glass fibres. *Compos. Sci. Technol.* **59**, 1055–1062 (1999)
 97. Frank, A., Redhead, A., Pinter, G.: The influence of test frequency and eccentric crack growth on cyclic CRB tests. In: *Proceedings of 70th Annual Technical Conference of the Society of Plastics Engineers (ANTEC 2012, Orlando, 02.–04.04.2012)*. Society of Plastics Engineers, Bethel (2012), 1899–1904
 98. Moskala, E.J.: Effects of mean stress and frequency on fatigue crack propagation in rubber-toughened polycarbonate/copolyester blends. *J. Appl. Polym. Sci.* **49**, 53–64 (1993)
 99. Brown, H.R., Kramer, E.J., Bubeck, R.A.: Studies of craze fibril deformation during fatigue in polystyrene. *J. Polym. Sci., Part B: Polym. Phys.* **25**, 1765–1778 (1987)
 100. Lang, R.W., Pinter, G., Balika, W., Haager, M.: A novel qualification concept for lifetime and safety assessment of PE pressure pipes for arbitrary installation conditions. In: *Proceedings of Plastic Pipes XIII (Washington, 02.–05.10.2006)*. Washington (2006), 12 pages
 101. Pinter, G., Lang, R.W., Haager, M.: A test concept for lifetime prediction of polyethylene pressure pipes. *Monatshefte für Chemie* **138**, 347–355 (2007)
 102. Pinter, G., Haager, M., Lang, R.W.: Lifetime and safety assessment of PE pressure pipes based on fracture mechanics fatigue tests. In: *Proceedings of 65th Annual Technical Conference of the Society of Plastics Engineers (ANTEC 2007, Cincinnati, 05.–10.05.2007)*. Society of Plastics Engineers, Bethel (2007), 2921–2925
 103. Pinter, G., Arbeiter, F., Berger, I., Frank, A.: Correlation of fracture mechanics based lifetime prediction and internal pipe pressure tests. In: *Proceedings of Plastic Pipes XVII (Chicago, 22.–24.09.2014)*. Chicago (2014), 10 pages
 104. Freimann, W.: Charakterisierung des Risswachstumsverhaltens von Cracked Round Bar (CRB) Prüfkörpern auf Basis der Materialnachgiebigkeit. Master thesis. Montan University Leoben, Leoben (2008)
 105. Redhead, A., Frank, A., Pinter, G.: Investigation of slow crack growth initiation in polyethylene pipe grades with accelerated cyclic tests. *Eng. Fract. Mech.* **101**, 2–9 (2013)
 106. Frank, A., Pinter, G., Lang, R.W.: Lifetime prediction of polyethylene pipes based on an accelerated extrapolation concept for creep crack growth with fatigue tests on cracked round bar specimens. In: *Proceedings of 67th Annual Technical Conference of the Society of Plastics Engineers (ANTEC 2009, Chicago, 22.–24.06.2009)*. Society of Plastics Engineers, Bethel (2009), 2169–2174
 107. Frank, A., Hartl, A.M., Pinter, G., Lang, R.W.: Validation of an accelerated fracture mechanics extrapolation tool for lifetime prediction of PE pressure pipes. In: *Proceedings of*

- 68th Annual Technical Conference of the Society of Plastics Engineers (ANTEC 2010, Orlando, 16.–20.05.2010). Society of Plastics Engineers, Bethel (2010), 1638–1643
108. Schoeffl, P.F., Bradler, P.R., Lang, R.W.: Yielding and crack growth testing of polymers under severe liquid media conditions. *Polym. Testing* **40**, 225–233 (2014)
 109. Schoeffl, P.F., Lang, R.W.: Effect of liquid oilfield-related media on slow crack growth behavior in polyethylene pipe grade materials. *Int. J. Fatigue* **72**, 90–101 (2015)
 110. Arbeiter, F., Pinter, G., Frank, A.: Characterisation of quasi-brittle fatigue crack growth in pipe grade polypropylene block copolymer. *Polym. Testing* **37**, 186–192 (2014)
 111. Market Study: Plastic Pipes—World. Ceresana Research, Constance (2011)
 112. Frank, A., Berger, I., Arbeiter, F., Pinter, G.: Characterization of crack initiation and slow crack growth resistance of PE 100 and PE 100 RC pipe grades with cyclic cracked round bar (CRB) tests. In: *Proceedings of Plastic Pipes XVII* (Chicago, 22.–24.09.2014). Chicago (2014), 10 pages
 113. ISO 18489 (2015): Polyethylene (PE) materials for piping systems—Determination of resistance to slow cracked growth under cyclic loading—Cracked Round Bar test method
 114. Kratochvilla, T.R., Frank, A., Pinter, G.: Determination of slow crack growth behaviour of polyethylene pressure pipes with cracked round bar test. *Polym. Testing* **40**, 299–303 (2014)
 115. Frank, A., Redhead, A., Kratochvilla, T., Dragaun, H., Pinter, G.: Accelerated material ranking with cyclic CRB tests. In: *Proceedings of Plastic Pipes XVI* (Barcelona, 24.–26.09.2012). Barcelona (2012), 10 pages

Chapter 4

Thermographic Characterisation of the Deformation and Fracture Behaviour of Polymers with High Time and Spatial Resolution

M. Stein and K. Schneider

Abstract The thermo-mechanical coupling of polymers describes the dissipative heating during plastic deformation, which again changes the local molecular mobility. It was investigated at the example of poly(ethylene terephthalate) (PET) and polycarbonate (PC). Depending on the sample geometry certain amount of stored elastic energy is available for neck initiation accompanied by local heating of the sample. In case of the semicrystalline PET temperature jumps until and above the glass transition temperature (T_g) can be observed, meanwhile the temperature increase at yield is significant below T_g for PC. At crack initiation and fracture a further increase of the temperature is detectable for both materials, for PET close to the melting temperature of the crystalline phase and for PC above T_g . The discussion of polymer yielding and fracture with respect to preceding temperature changes casts a new light on relevant molecular processes.

4.1 Introduction

The use of polymeric materials is still a driving force of innovation in various industries. Processed as composites they establish the basis of light weighting components especially for automotive or aerospace applications. The knowledge of the stiffness as well as the behaviour after yield and during fracture builds therefore characteristic information and the basis of dimensioning, e.g. to perform crash simulations. The dissipation of heat and thereby coupled self-heating of the material and whose influence on the mechanical behaviour is an already known phenomena and have been discussed primary on the background of large stretching ratios. Furthermore, it is understood that this effect influences the mechanical behaviour

M. Stein (✉)
Institute of Processing Machines and Mobile Machinery,
Dresden University of Technology, Dresden, Germany

K. Schneider
Leibniz Institute for Polymer Research Dresden e.V., Dresden, Germany

significantly at high strain rates [1–3]. In addition to the experimental investigations first thermomechanical coupled material models have been developed to include the self-heating effect in simulations [4–6].

One of the initial experimental works on the thermal reaction of plastics during mechanical load was performed by Cross and Haward and their colleagues using one of the first available thermographic cameras more than 50 years ago [7–9]. They found an instantaneous temperature jump of some 25 °C in the immediate area around the fracture of drawn poly(vinyl chloride) (PVC) samples. They supposed additional heating up to melting temperature on a very small size [7].

Yamauchi recorded the thermal reaction of 60 µm thin films of poly(ethylene terephthalate) (PET) [10]. He found a constant temperature rise at post-yield deformation up to 15 °C at 120% elongation. Moreover Bazhenov et al. found a significantly higher increase of temperature [11]. They used powder with various melting temperatures to detect the maximum surface temperature of samples of PET and other polymers. Therefore they prepared the samples by coating the surface with the different powders and analysed the samples after deforming until the first powder with decreasing melting temperature didn't melt. Using this method they proved a maximum temperature of about 140 °C during neck propagation in PET at a crosshead speed of 1000 mm/min. In summary the known publications describing the self-heating effect show significant temperature rise mainly at large strains, together with a clear distance to the yield point.

To the best of our knowledge there are no studies describing the local temperature distribution during yield and fracture with high local and time resolution. Typical lateral resolution using such infrared thermography is about 10 µm and recording frequency till 100 Hz [12]. Actual developments on the field of thermographic sensing and data processing permit recording under significantly higher dynamics [13].

The present work concentrates on the hypothesis that a strong coupling of the mechanic and thermal reaction can be found on the very local scale. Therefore the paper shows the first results of investigations focused on the thermomechanical behaviour of thermoplastics. The results show a dissipation of considerable amount of stored elastic energy during yielding and stretching as well as fracture depending on the morphology of the tested materials. The final temperature field inside the samples is strongly dependent on time and deformation history. These findings permit to extent the discussion of strain-dependent interaction between amorphous and crystalline phases and cast a new light on relevant molecular processes at yield and fracture.

4.2 Experimental

4.2.1 Materials

The present work concentrates on the specific behaviour of semi-crystalline polymers and their differences to amorphous polymers. Therefore PET and polycarbonate (PC) have been selected as representatives for semi-crystalline and

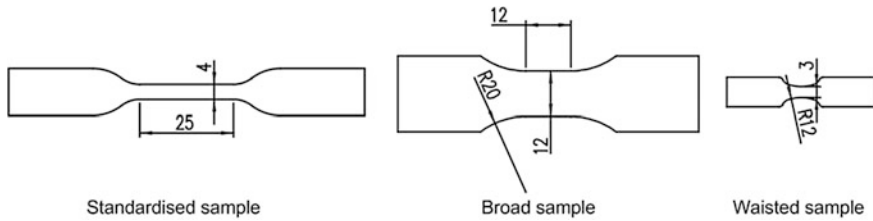


Fig. 4.1 Sample geometries used in the present work

amorphous material respectively. The PET has a glass transition temperature T_g of about 80 °C and a melting temperature T_m of 260 °C. The raw material in the form of extruded film has a mainly amorphous structure with a crystallinity below 10% determined by dynamic-mechanical analysis (DMA) and differential scanning calorimetry (DSC) tests. The dog-bone samples were cut out of an extruded film processed by Wipak (Walsrode, Germany) with a controlled thickness of about 400 μm .

The PC samples were milled out of an injection moulded plates with a thickness of about 1.3 mm. The plates were processed from granules of Lexan 121 from GE Plastics (Frankfurt, Germany) at the Leibniz-Institut für Polymerforschung Dresden. The characteristic glass transition of PC is about 150 °C.

The three different kinds of sample geometries according to Fig. 4.1 were used. It enables to analyse the influence of the specimen size and to adjust the test setup on the view area of the thermographic camera:

- Standardised sample (according to DIN ISO 527-5A): Standardised geometry provides correlation with standard material properties and previous results from the literature.
- Broad sample: High width allows analysing the propagation of the crack.
- Waisted sample: Non-constant cross section but nearly parallel length of about 5 mm allows a simple focusing on the zone of neck initialisation.

4.2.2 Methods

The samples were stretched with an electro-dynamic test rig with crosshead speeds between 1 and 3000 mm/min. The tests were performed under controlled climate condition at ambient temperature.

The temperature radiation was monitored by an infrared thermographic camera Image IR 8300 from InfraTec (Dresden, Germany) in the spectral range of 2–5 μm wave length. This camera permits measurements up to 850 pictures per second. However, at this high speed recording only the fourth part of the maximum pixel size of the sensor of 640×512 pixels is available. Recording with maximum view area could be performed with 100 Hz, half size with 350 Hz respectively.

Two different lenses were used in the present work. The telephoto lens can record with lateral resolution of $70 \times 70 \mu\text{m}^2$, which leads to a maximum view area of $45 \times 36 \text{mm}^2$. The macro lens allows us to measure with lateral resolution of $15 \times 15 \mu\text{m}^2$ but reduced maximum view area to $9.6 \times 7.7 \text{mm}^2$. On the other hand the lateral resolution plays an important role to measure the correct temperature distribution of a strong localised temperature field. The temperature of one pixel is determined as a kind of mean value of the observed area. This means that temperatures with a lower spread than the lateral resolution can't be determined correctly [13]. This leads to the considerable limitations of thermographic measurements concerning resolution of the time and the geometry and the size of the view area.

For a quantitative analysis the measuring system must be calibrated. Thus raw material and material of stretched samples of both investigated materials were heated up with the help of a controlled heated air stream with temperatures up to $150 \text{ }^\circ\text{C}$. The surface temperature was determined by the thermographic camera and a calibrated thermo-couple. At the end of the procedure nearly linear calibration curves $K(T)$ were available with material-dependent calibration coefficients.

The calibration of the recorded temperature distribution T_0 built the first step of the performed data analyses (Fig. 4.2).

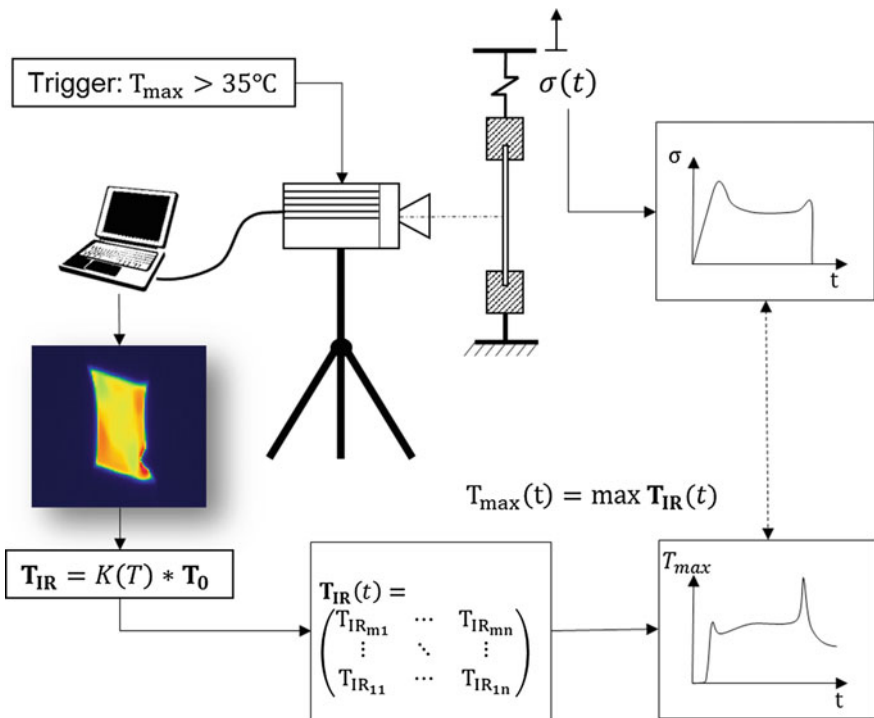


Fig. 4.2 Experimental setup and algorithm for data analysis

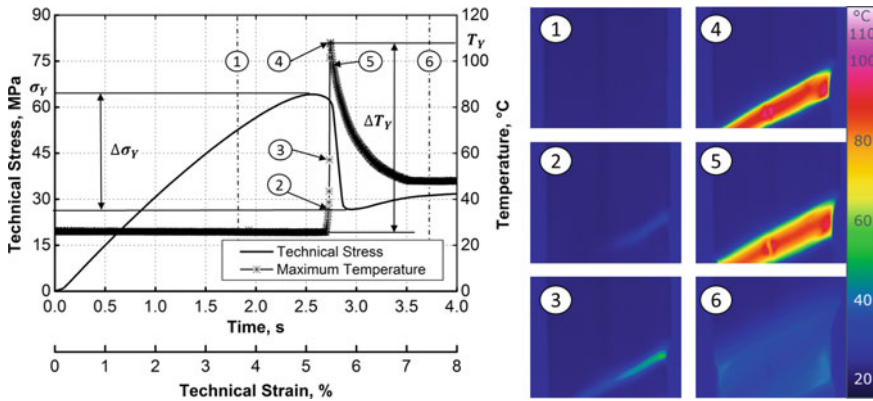


Fig. 4.3 Temperature jump of PET at the yield point: Thermographic images of the deformation process for 50 mm/min stretching velocity using 15 μm spatial and 3.125 ms time resolution (*right*) and correlation of the maximum temperature and stress curve (*left*)

The thermographic camera starts recording after reaching a trigger temperature. Additional saving of about 600 recordings before reaching the trigger allows analysing temperature rise from the start of the stretching process. The maximum temperature T_{max} was determined from the calibrated temperature data T_{IR} and compared with the technical stress. Due to the separately recorded data of temperature and strain resp. stress the two time axes had to be synchronised. According to the characteristic temperature–time and stress–strain curves of Fig. 4.3 the instant time-to-fracture of the sample can be found as complete stress decrease and as starting point of cooling down to room temperature. This characteristic point was used to shift the temperature curve. If the crack propagations happened outside the visual field the shifting was done manually synchronising the start of neck propagation and the yield point. This method enables to analyse the dependency between mechanical and thermal behaviour directly and allows the supposed correlation of temperature decrease on the one side and the stress increase simultaneously.

4.3 Results

4.3.1 Thermomechanical Characterisation of PET

The first result shows the thermomechanical behaviour for the investigated slightly crystalline PET. Starting with the standard samples the characterisation has been focused on the specific dependency at reaching the yield point. Afterwards the results have been concentrated on investigations using the broad sample to characterise the propagating crack. Finally the use of the waisted samples has been enabled to investigate the complete tensile stretching process. Thereby the investigation of the influence of the sample geometry was possible.

The first key result of the present study is: for PET, the dissipation of the elastically stored energy happens concentrated and in time with reaching the yield point (Fig. 4.3). The main reason for the stress decrease after the yield point is caused by the material softening due to the temperature dependent strength.

The typical stress–strain curve of semi-crystalline materials was measured with increase after yield and propagation of a constant plastic plateau. In the present example the standard sample was deformed with 50 mm/min crosshead speed. Before reaching the yield point the material showed homogeneous deformation with the strain rate of about 0.04 s^{-1} . The material temperature decreased moderately of about 1 K according to the elastic cooling effect (image 1 in Fig. 4.3). In the moment reaching σ_y the temperature starts to increase at the right side of the sample (2). The heated material zone propagates under shear deformation along a line and at a certain angle to the stretching direction until reaching the other side of the sample (3). Arriving the opposite border triggered an immediately following temperature jump to the yield temperature T_y of about $107 \text{ }^\circ\text{C}$ well above the glass transition temperature (T_g) (4). This process from the first energy dissipation until reaching the maximum temperature happened very dynamically within less than 13 ms. However, the used time resolution of about 3.1 ms could not resolve the temperature jump like the direct successive images 3 and 4 illustrate.

The dramatically temperature increase ΔT_y at the yield point caused a stress decrease $\Delta\sigma_y$ from about 64 MPa to below 27 MPa due to the softening of the heated material. The weak material at this small zone was stretched afterwards (5). Additionally the material started cooling by heat convection and marginal conduction. In time the temperature decreased below T_g , the decrease of stress stopped and initiated the propagation of a constant stress and temperature level. The typical neck was formed under further deformation. The green colour and within the maximum temperature of about $47 \text{ }^\circ\text{C}$ at the corner of the two fronts at image 6 indicates the expired shear deformation for propagating of the neck. However the used macro lens and within the lateral resolution of $15 \text{ }\mu\text{m}$ were probably not enough to resolve the true maximum temperature in this stage of stretching, which might be higher.

To study the dependency of the described thermomechanical behaviour at the yield point, tests were performed with various rates of loading. Like expected the mean values of at least three measurements indicated that the yield stress increases moderately with higher stretching rates. The yield temperature was determined well above T_g for rates greater than 5 mm/min. A constant level of about $120 \text{ }^\circ\text{C}$ could be observed above 20 mm/min (Fig. 4.4).

The influence of the limited resolution has to be kept in mind for evaluating the decrease of yield temperature below 5 mm/min. But the decrease $\Delta\sigma_y$ of stress after yield point was determined correspondingly and showed a nearly constant level for all rates of loading with yield temperatures above T_g (Table 4.1).

The significant influence of T_g was evidenced by the coefficient C_{therm} scaling the decrease of stress according (4.1).

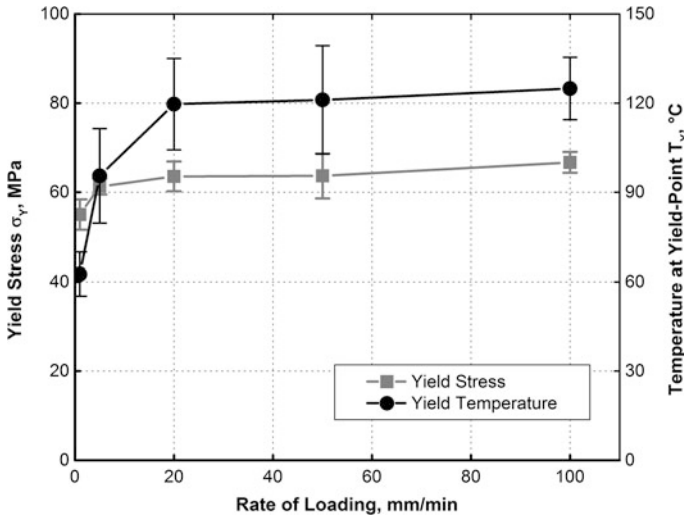


Fig. 4.4 Influence of the rate of loading on the thermomechanical behaviour of PET

Table 4.1 Coupling of the thermomechanical behaviour for standard sample made from PET

Rate of loading ν (mm/min)	Strain rate $\dot{\epsilon}$ (10^{-3} s^{-1})	Yield temperature T_y (°C)	Decrease of stress $\Delta\sigma_y$ (MPa)	Temperature increase at yield point ΔT_y (K)	Coefficient of thermal impact C_{therm} (MPa/K)
1	0.83	62.56	24.96	39.56	0.639
5	4.17	95.51	37.05	72.51	0.515
20	16.67	119.65	38.50	96.65	0.400
50	41.67	121.09	38.89	98.09	0.399
100	83.33	124.91	39.42	101.91	0.389

$$C_{\text{therm}} = \Delta\sigma_y / \Delta T_y \tag{4.1}$$

The coefficient decreased until 5 mm/min and showed a constant level of about 0.4 MPa/K for higher strain rate. That means that the thermal behaviour had the highest impact for temperature rise until exceeding the level of T_g . The amorphous phase loses the strength whereby the crystal structure stabilises the heated zone and prohibits a spontaneous dissolving. Thus the additional temperature change above T_g for the investigated crosshead speeds had only a small impact on the mechanical behaviour (stress decrease) due to the significantly distance to the melting temperature of the crystal phase. This relationship between stress–strain curve and molecular mobility at the yield point is one of the central findings of the present work.

However, the recording of the yield temperature was taking a high effort using the standard samples and needed a huge number of trails to capture the initial

heating zone. The neck could initialised randomly at the whole parallel length of the sample of about 25 mm. The used test setup had a view area of only 3.85 mm in stretching direction. Additionally the constant neck propagation led to the exceeding of the front out of the view area boundary under minor strain (image 6 in Fig. 4.3). For the investigation of the broad sample and to record the whole deformation process with the help of the waisted samples, the telephoto lens was used in the following thermographic measurements.

The found thermal behaviour of temperature jump above T_g and cooling down to a constant level for neck propagation could also be observed for the broad sample at equivalent strain rates (Fig. 4.5a). The curves of two different samples of the same rate of loading illustrates the variation of the measured yield temperature due to the

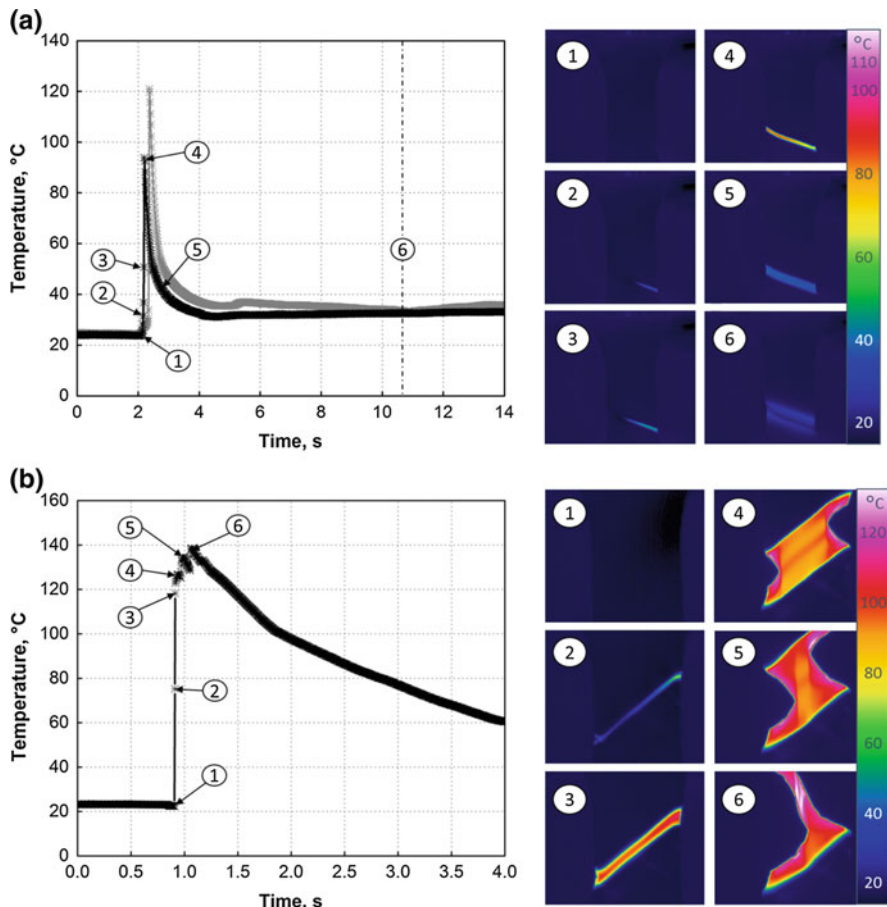


Fig. 4.5 Thermographic measurement of PET: temperature distribution of the broad sample until deformation (*right*) and curves of maximum temperature (*left*) for crosshead speeds of **a** 10 mm/min (0.014 s⁻¹) and **b** 3000 mm/min (4.17 s⁻¹)

limited lateral and time resolution at low rates and the smaller shear zones involved (dark vs. grey solid line in Fig. 4.5a).

The major width of the samples caused longer time for propagation of the linear heating zone until reaching the opposite side of the sample. Thus the propagation could also be re-recorded for the deformation with high speed (image 2 in Fig. 4.5b). The yield temperature was determined of about 120 °C (3) equivalent to the slow crosshead speeds. The material in the middle area of the shear zone was heated well above T_g . The fast deformation of the heated material prevented the decrease of the temperature, which would be necessary for increasing of the strength and transition to constant propagation of the neck. Thus excluding the heated material was spread under homogeneous temperature distribution (Fig. 4.6a) until it was split by the growing cracks.

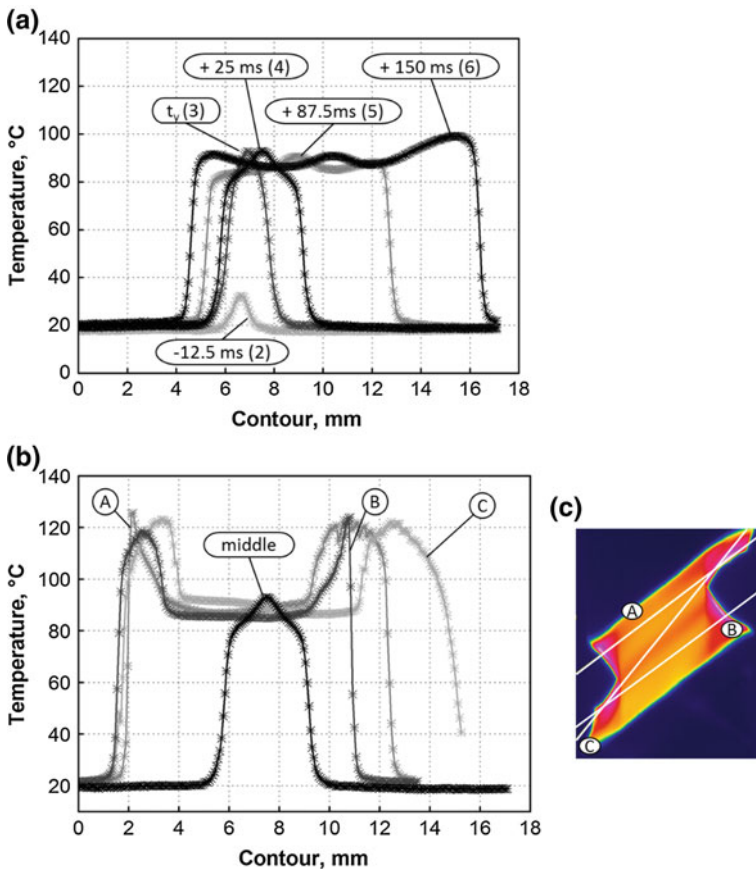


Fig. 4.6 Section of the temperature distribution until deformation in the middle of the sample made from PET **a** according to the images in Fig. 4.5b and along the indicated lines **c** at characteristic positions

The two cracks on both sides of the sample were initiated immediately after the shear zone was formed. Thereby the temperature increased due to the further dissipation at the flanks of the crack. The very strong transition on the left side of section A and on the right side of section B in Fig. 4.6b indicate that the temperature at the crack tip and at the flanks could be considerably higher due to the localised fracture zone and limited resolution.

Finally tests using the waisted sample were performed to record the thermo-mechanical behaviour of the whole deformation process (Fig. 4.7).

The measurements could be performed with 430 Hz for 100 mm/min and 850 Hz for 1000 mm/min due to defined localisation of the neck initialisation and small size of the sample. Both measurements showed the direct coupling of the thermal and mechanical behaviour and the already progresses at the yield point known from the standard sample. A stable neck propagation was observed at all

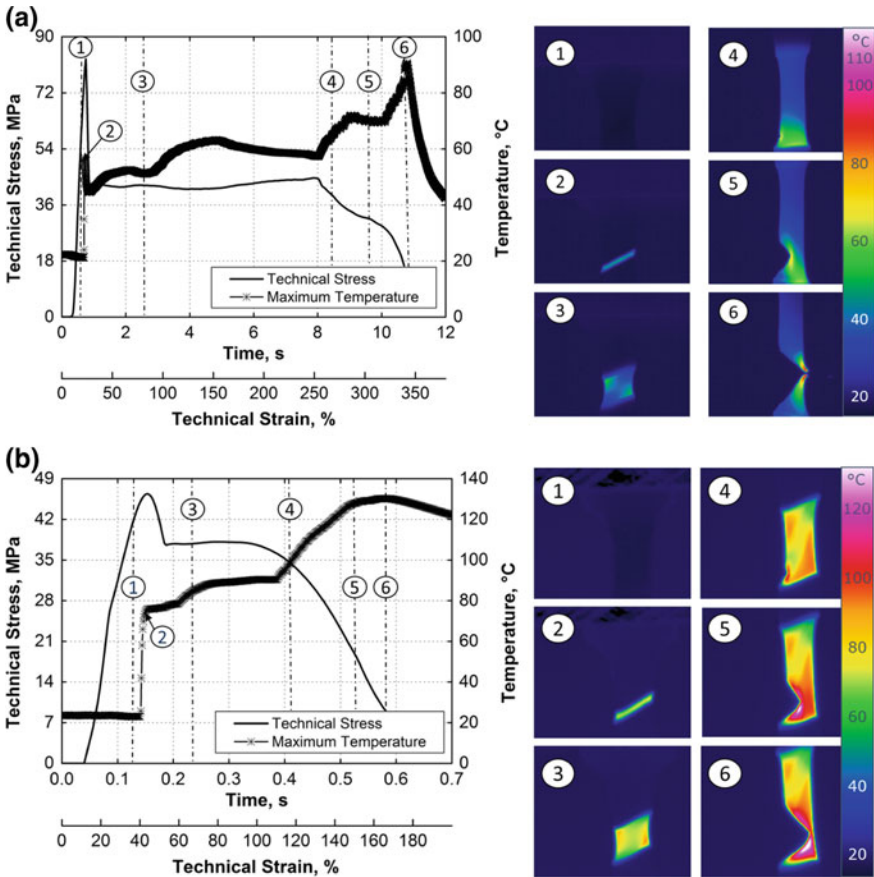


Fig. 4.7 Thermographic measurement of PET: temperature distribution of the waisted samples (right) and curves of maximum temperature and stress for crosshead speeds of **a** 100 mm/min (0.33 s^{-1}) and **b** 1000 mm/min (3.33 s^{-1})

investigated strain rates despite the waisted geometry and missing the parallel part with constant cross section.

Both fronts of the neck seemed to propagate homogeneously at the beginning of the post yield deformation because of an additional head dissipation at each front (image 3 in Fig. 4.7a). In the predominant number of investigated samples the neck propagation transferred to one of the sides was found with increasing strain (4). A switch of this active front to the other side of the neck could also be observed just before reaching the clamps of the sample.

The initial temperature jump was determined to lower values than for the tested standard samples at significantly lower strain rates (Table 4.1). One reason therefore could be the small width of the shear zone and so the limitation of the lateral resolution. The measured yield temperature at the fast deformation increased close to T_g , but didn't exceed it despite a larger shear zone. This finding indicates the significant influence of the sample size on the capacity to store elastic energy. A second effect was found with the fast deformation in this context. The crack wasn't initialised directly after yield point in contrast to the broad sample at the same strain rate. An initial situation of neck establishment was determined instead (images 3 and 4 in Fig. 4.7b). The part of the heated material in the middle of the sample cooled down below T_g and initiated the grow of the neck same as the behaviour described of the standard samples but with significantly less strain rates.

The characteristic temperature distribution gives an impression of a larger part of shear deformation, what could be realised by the waisted sample geometry. The initiation of the crack caused a further increase of the temperature to about 130 °C for 1000 mm/min and about 90 °C for 100 mm/min. The highly localised fracture and temperature gradients around the crack tip and the flanks could cause a considerably higher fracture temperature than determined again.

The small sample size and the use of the telephoto lens enabled the recording of the complete stretching process as expected and the comparison of both domains of the investigated material behaviour (diagrams in Fig. 4.7). The initial temperature jump was observed at the same time then the yield point in the stress-strain curve. More than this, these measurements indicated that the temperature jump was the release button and the yield point could be described as the logical consequence due to the temperature-dependent material behaviour. This proves the hypothesis of direct coupling of mechanical and temperature reaction.

4.3.2 Thermomechanical Characterisation of PC

In addition to the characterisation of the semi-crystalline PET, thermographic measurements of the fully amorphous PC were performed using the waisted sample geometry.

The lack of a distinct localised necking behaviour and the significantly lower strain at fracture enabled the observation of the complete deformation process of the

PC with the smallest view area of $11.2 \times 8.96 \text{ mm}^2$ and the maximum measuring frequency of about 850 Hz.

According to the observed elastic behaviour of PET a moderately cooling at the beginning of the stretching process was determined. In contrast to the semi-crystalline material no temperature jump at the yield point was observed, but local heating within the zone of plastic deformation. Thus the stress decreased after yield much less compared to PET due to the lower temperature rise. Further loading extends the plastic deformation region over the whole nearly parallel length. This happened under high stress level and moderately decreasing of the stress, which might be intensified by the decreasing cross section. The median temperature at the plastic level decreased with higher strain rates (32 K at 10 mm/min to more than 55 K at 3000 mm/min with 44 K at 100 mm/min and 48 K at 1000 mm/min, indicated in Fig. 4.8). The plastic

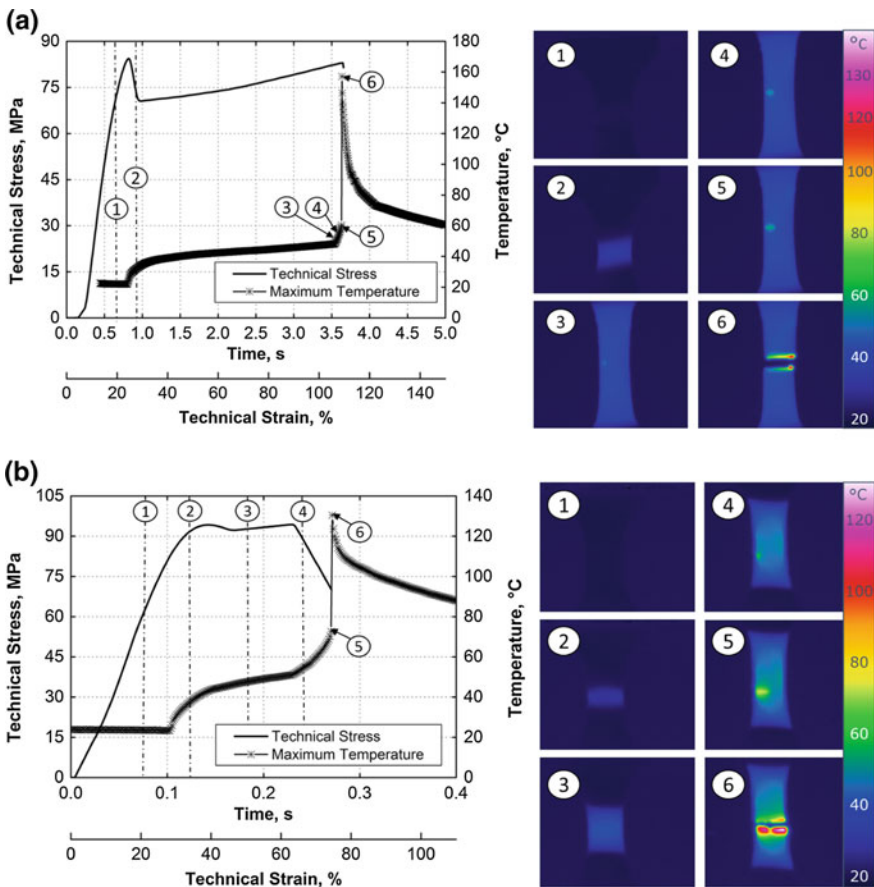


Fig. 4.8 Thermographic measurement of PC performed with $70 \mu\text{m}$ lateral and 1.17 ms time resolution: temperature distribution of the waisted sample (*right*) and curves of maximum temperature and stress (*left*) for crosshead speeds of **a** 100 mm/min and **b** 1000 mm/min

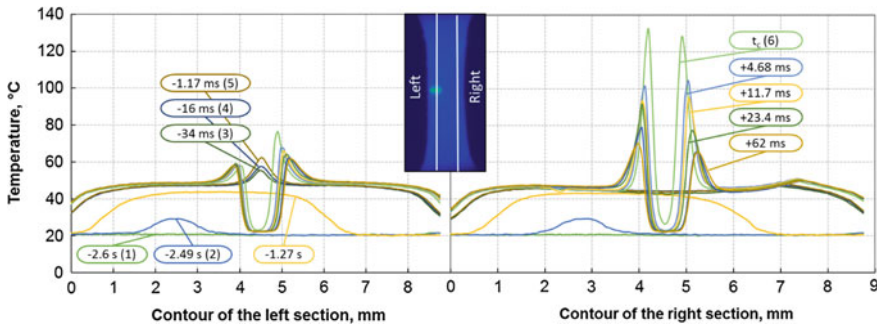


Fig. 4.9 Longitudinal section of the *left* and *right* position of the 100 mm/min tensile test according to Fig. 4.8a with appropriated build number and allegation of the lag to the moment of crack (t_c)

deformation shows an almost completely affine characteristic, non-component of shear deformation was detectable at the temperature distribution (image 3 of Fig. 4.8a, b). After the homogeneous plastic deformation an additional local heat dissipation could be observed at one side of the sample just before the spontaneous crack happened (see image 4 and 5 of Fig. 4.8a, b).

The local inhomogeneity had a point shape and grew over a few tenths of a second. In the centre a temperature increase of about 14 K was observed for the test with 100 mm/min (curves of the left section in Fig. 4.9) and 22 K for 1000 mm/min. The following fracture of the sample happened within less than 1.17 ms between two successive points of the measurement (curve 5, 6). Therefore the propagation of the crack wasn't recordable. Nonetheless the material at the fracture surface showed a temperature increase up to or above T_g which seemed to be independently of the strain rate. However an increase of the width of the heated zone was observed for decreasing strain rates.

The maximum temperature after fracture was located on the side of the sample opposite to crack initiation, what might indicate the propagating direction of the crack. The temperature distribution varied between nearly symmetric division at both fracture surfaces (Fig. 4.8a) and complete shearing off at one surface (Fig. 4.8b).

4.4 Discussion

One of the main goals of the present work was to prove the supposed direct coupling between thermal reaction and mechanical behaviour of thermoplastic materials. Furthermore the influence of a particular morphology on the thermal and thereby the mechanical behaviour during deformation should be investigated, therefore measurements were performed with PET and PC.

4.4.1 Polycarbonate—Affine Deformation with Uniform Energy Dissipation

The amorphous PC shows a nearly homogeneous temperature field starting at a local area of plastic deformation. During steady propagation of both the area of plastic deformation and the corresponding temperature field within the complete length of the sample, the temperature only moderately increases. The temperature level remains clearly below T_g , which is in good agreement with the determined values given by Koenen [14]. However, the stress–temperature curves in the present study show the initial point of the temperature rise at the significantly earlier stage of deformation even in the moment respectively before the yield point was reached. The low increase of the temperature corresponds to the moderately decrease of stress after the yield point.

It appears that the most part of the dissipated energy is caused by internal friction due to the movement of polymer chains in the amorphous polymer. Thereby the increasing degree of orientation of the molecules during plastic deformation causes a higher stress increase than the softening effect due to the heating of the material. The required mobility of the chains for initialising and propagating of plastic deformation seems to be lower than for semi-crystalline materials. On the other side a remarkable amount of elastic energy is stored until the first initialisation of a local instability.

For the initialisation of the crack and the fracture a significantly higher degree of mobility of the amorphous morphology is necessary. The nearly linear decrease of stress before fracture was also described in previous investigations, for example by Cao et al. [15]. This decrease seems to be the mechanical reaction of the described local heating. Consequently a constant reduction of the local strength can be observed. At this last stage of deformation the stored elastic energy is transformed to thermal energy and the crack is initialised and propagates.

The so-called brittle fracture is coupled with a previous temperature jump about or above T_g . That local temperature rise leads to a significantly increase of the mobility of the polymer chains in the area of the fracture. Abrupt sliding of the chains is the consequence, which explains the highly dynamic crack propagation, without additional plastic deformation at regions around the crack. The missing of a crystal structure causes a significant drop of strength after reaching T_g , which enables the fracture.

4.4.2 Poly(Ethylene Terephthalate)—Localised Deformation and Complex Influence of Two Phases

In the case of the investigated PET the stabilising influence of the crystalline phase of the semi-crystalline polymer above T_g was found. After an initial slight decrease of temperature due to the elastic cooling effect a strong localised, linear temperature increase was observed for all investigated sample geometries. Thus the stored

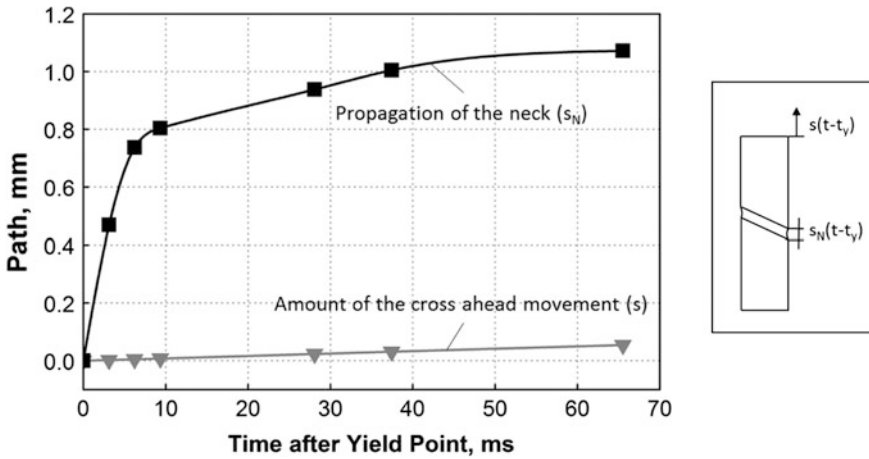


Fig. 4.10 Spread of the shear deformation zone: amount of the crosshead movement after yield $s(t-t_y)$ and of the initial propagation of the neck $s_N(t-t_y)$ for the tensile deformation of the standard geometry and 50 mm/min crosshead speed indicated in Fig. 4.3

elastic energy at the beginning of the deformation process is transformed to a high degree to heat energy already during the neck formation and as a consequent of the time-dependent behaviour also at the first stage of neck propagation.

From the mechanical point of view the initial temperature increase up to or above T_g over the complete cross section causes a significant and highly dynamic decrease of the stress. This causes the strong pronounced yield point in the stress–strain curve. Furthermore, the viscoelastic strain of the non-heated material decreases according to the lower stress level. This leads to an additional spread of the heated material (Fig. 4.10).

The magnitude of the spread is influenced by the stretching rate and length of the sample due to the viscoelastic part of the mechanical material behaviour. Higher strain rates cause a higher overstress in the material due to the less time for stress relaxation until yielding [16]. On the one hand more elastic respectively potential energy is stored and is available for transforming into heat, which influences the value of the temperature jump and the decrease of the stress after the yield point. On the other hand overstress is coupled with higher part of viscoelastic strain, what increases the spread of the heated material after yielding. These two amplifying effects appear to be the reason for the influence of the strain rate on the transition of the stress–strain behaviour after reaching the yield stress. The additional observed influence of the sample geometry is caused by the different storage capacity of elastic energy.

The focused stretching at the initial heated material in combination with temperature up to or above the level of T_g has a significant influence on the morphology and the propagation of the neck. With the described dependency on the rate of loading and the sample geometry the results show three different kinds of neck and crack propagation, which can be described as follows:

- *Stable neck propagation*: Initial heating generates an increase of the temperature above or slightly below T_g and stretching of the weak material. Temperature and stretching introduced crystallisation in combination with cooling of the amorphous phase below T_g causes transition to a stable neck propagation and following crack initialisation in the necked material.
- *Unstable neck propagation*: Initial heating generates a temperature increase above T_g and stretching of the weak material without remarkable load due to constant temperature of the necked area above T_g . Crack initialisation follows immediately after yield and causes further temperature increase. The crack propagates through the weak material.
- *Shearing off at neck initiation*: Initial heating generates temperature increase highly above T_g and probably up to melting point of the crystalline phase. The direct shearing off the weak material provokes spontaneous fracture.

The last case is a special case of the unstable neck propagation and would be called as brittle fracture. This kind wasn't shown explicit in the results but could also be observed for the standard geometry at fast deformation rates.

The question with respect to the necessary temperature at the crack tip of semi-crystalline materials can't be answered finally. But the results gave strong indications and it would be a logical consequence of the previous discussion that the melting temperature must be exceeded. The strongly focused temperature field and highly dynamic process prevent to be proved with the present test setup and probably also couldn't be determined by the method of Bazhenov et al. using the various melting powders [11]. However, first investigations using a microscope objective lens supported this hypothesis, which has to be verified in further work.

Beside the described softening and decrease of orientation of the amorphous phase, the crystalline structure together with crystallisation and cavitation processes influence the mechanical behaviour. Based on the presented results the influence of the crystal phase seems to be:

1. The amorphous phase needs higher mobility for plastic deformation which provokes significantly higher temperature increase at the yield point due to the interacting with the fixed crystal structure (e.g. entanglements).
2. The crystal structure stabilises the mobile amorphous zones and prohibits a spontaneous failure.
3. Strain-introduced and thermal crystallisation [17, 18] led to significant increase of the strength of the necked material in the active front. On the one side the higher strength than the raw material causes neck propagation through the sample, while it only dissipates heat in a very limited amount.

Although this comprehensive study of the thermomechanical behaviour with only one representative material for each group of thermoplastic materials, most of the given hypotheses in the beginning of this work could be proved by the presented results. The generalisation of the results has to be verified by investigation of further polymer systems. An additional study of the energy balance could lead to a deeper theoretical understanding and help to explain and model the behaviour of the polymer under investigation.

4.5 Conclusion

The energy dissipation and local heating of polymers under load determines the typical known mechanical behaviour. This was investigated with the help of thermographic measurements. The new experimental opportunities with high speed recording of temperature distributions on a very small scale enable to determine the highly dynamic and strongly focused energy dissipation under tensile deformation. The described method enables the characterisation of the field of the complex coupling and interdependency mechanism between mechanical strength, local energy dissipation and molecular mobility. At the yield point a first general local instability could be observed. Beyond the yield point a large region of stable deformation occurs depending on strain rate and sample geometry.

For PET as semi-crystalline polymer the behaviour is determined by the additional crystal phase: Additional to heat dissipation due to the glassy state of the PET as well as strain and thermal introduced crystallisation a stabilisation of the weak material at the yield point due to the semi-crystalline structure can be observed, which influences the crack propagation due to higher melting temperature of the crystallites.

For the amorphous structure of the PC a very local deformation and energy dissipation in the pre-cracking region can be observed before a crack is established. At brittle fracture the stored elastic energy is transferred to heat very locally and the temperature at this region increases above T_g , which can be described as softening and coupled spontaneous fracture of an amorphous material.

In the presented measurements the available lateral resolution enabled particularly only a rough estimation of maximum temperature. Using systematically a macro and microscope lens will improve the local resolution and enable a better estimation of the size of dissipative zones in further studies. In the case of fracture an estimation of the local temperatures at the crack edge would require frame rates in the sub-millisecond range.

The explanatory approach of mechanisms influencing the transition at the yield point and fracture will be investigated and verified for other polymers in future work. The analysis of the dissipated and supplied energy will establish the basis for a thermomechanical model of the investigated materials.

References

1. Rittel, D.: On the conversion of plastic work to heat during high strain rate deformation of glassy polymers. *Mech. Mater.* **31**, 131–139 (1999)
2. Regev, A., Rittel, D.: Simultaneous transient temperature sensing of impacted polymers using infrared detectors and thermocouples. *Exp. Mech.* **48**, 675–682 (2008)
3. Garg, M., Mulliken, A.D., Boyce, M.C.: Temperature rise in polymeric materials during high rate deformation. *J. Appl. Mech.* **75**, 1–8 (2008)
4. Ames, N.M., Srivastava, V., Chester, S.A., Anand, L.: A thermo-mechanically coupled theory for large deformations of amorphous polymers. Part II: Applications. *Int. J. Plast.* **25**, 1495–1539 (2009)

5. Maurel-Pantel, A., Baquet, E., Bikard, J., Bouvard, J.L., Billon, N.: A thermo-mechanical large deformation constitutive model for polymers based on material network description: Application to a semi-crystalline polyamide 66. *Int. J. Plast* **67**, 102–126 (2015)
6. Bouvard, J.L., Francis, D.K., Tschopp, M.A., Marin, E.B., Bammann, D.J., Horstemeyer, M. F.: An internal state variable material model for predicting the time, thermomechanical, and stress state dependence of amorphous glassy polymers under large deformation. *Int. J. Plast* **42**, 168–193 (2013)
7. Cross, A., Haward, R.N.: Thermal fracture of plastics. *J. Polym. Sci.: Polym. Phys. Ed.* **11**, 2423–2439 (1973)
8. Cross, A., Hall, M., Haward, R.N.: Thermal effects in the necking of thermoplastics. *Nature* **253**, 340–341 (1975)
9. Haward, R.N.: Heating effects in the deformation of thermoplastics. *Thermochim. Acta* **247**, 87–109 (1994)
10. Yamauchi, T.: Observation of polymer film drawing by use of thermography. An introductory investigation on the thermodynamics. *J. Appl. Polym. Sci.* **100**, 2895–2900 (2006)
11. Bazhenov, S.L., Keckeyan, A.S.: Heating of polymers during neck propagation. *Polym. Sci. Ser. A* **55**, 404–414 (2013)
12. Brites, C.D.S., Lima, P.P., Silva, N.J.O., Millan, A., Amaral, V.S., Palacio, F., Carlos, L.D.: Thermometry at the nanoscale. *Nanoscale* **4**, 4799–4829 (2012)
13. Vollmer, M., Möllmann, K.-P.: *Infrared Thermal Imaging: Fundamentals, Research and Applications*. Wiley, Berlin (2011)
14. Koenen, J.A.: Observation of the heat exchange during deformation using an infra-red camera. *Polymer* **33**, 4732–4736 (1992)
15. Cao, K., Wang, Y., Wang, Y.: Effects of strain rate and temperature on the tension behavior of polycarbonate. *Mater. Des.* **38**, 53–58 (2012)
16. Kästner, M., Obst, M., Brummund, J., Thielsch, K., Ulbricht, V.: Inelastic material behavior of polymers—Experimental characterization, formulation and implementation of a material model. *Mech. Mater.* **52**, 40–57 (2012)
17. Gorlier, E., Haudin, J.M., Billon, N.: Strain-induced crystallisation in bulk amorphous PET under uniaxial loading. *Polymer* **42**, 9541–9549 (2001)
18. Pawlak, A., Galeski, A., Rozanski, A.: Cavitation during deformation of semicrystalline polymers. *Prog. Polym. Sci.* **39**, 921–958 (2014)

Chapter 5

Mechanical and Fracture Mechanical Properties of Polymorphous Polypropylene

A. Monami, B. Langer, J. Sadilek, J. Kučera and W. Grellmann

Abstract Polypropylene (PP) is a widely used thermoplastic material and shows a polymorphic behavior. Results of three different types of PP, namely non-nucleated, α - and β -nucleated PP are presented. These materials were prepared under different cooling rates to influence the degree of crystallinity within the materials. The materials resistance against stable crack propagation was described by R-curves. The J_d - Δa curves were determined using the instrumented Charpy impact test to apply a higher loading velocity. The results show not only the influence of the cooling rate on the degree of crystallinity but also a correlation between the degree of crystallinity and the materials resistance against stable crack propagation.

5.1 Introduction

Mechanical properties and especially toughness of polymeric materials are strongly influenced by their structure and morphology [1–3]. Polypropylene (PP) is a widely used polymorphous material, which can crystallise in different crystal modifications, the α -, β - or γ -modification [4, 5]. All crystal modifications can exist at the same time and convert into each other [6]. The α -modification (α PP) is characterised by a helix in a monoclinic unit cell. It is the thermal most stable crystal modification of PP and occurs therefore most often within PP [5–7]. The β -modification (β PP) is slightly less ordered compared to the α -modification, hexagonal and has non-parallel, crossed lamellae [6, 8, 9]. The orthorhombic γ -modification (γ PP) can result from high pressure [6] or by using an nucleation agent [8, 9].

A. Monami (✉) · W. Grellmann
Polymer Service GmbH Merseburg, Merseburg, Germany

B. Langer
Department of Engineering and Natural Sciences, University of Applied
Sciences Merseburg, Merseburg, Germany

J. Sadilek · J. Kučera
Polymer Institute Brno, Brno, Czech Republic

Due to the different physical and mechanical properties of the crystal modifications, the mechanical properties of PP are influenced by them [8, 9]. PP with dominating β -modification shows a lower modulus of elasticity and a lower yield strength [10] at comparable deformation rates, but at the same time a higher impact strength [11], a higher strain at break [6, 11] and a higher crack resistance [12, 13] compared to PP with dominating α -modification. The better deformation ability of β PP is caused by the structure of radial lamellae within its spherulites, allowing the initiation and propagation of plastic glide more easily compared to α PP [14]. The higher toughness and ductility of β PP compared to α PP is well known [15]. Raab [12] showed, that structure, crystal modification and the content of β -modification influence the toughness of PP very strongly. An increase of the content of β -modification leads to an increase of the crack toughness [12]. Karger-Kocsis [10] also discussed the critical stress intensity factor K_{Ic} and the energy release rate G_{Ic} of β PP as function of morphology [10]. The lower spherulite size of β PP lead to a higher ductility of β PP compared to non-nucleated α PP. The linear elastic fracture mechanics (LEFM) concept is assumed as still valid, although the materials break in a ductile manner. Due to the similar maximum load F_{max} in the load–deflection curves of α PP and β PP, the critical stress intensity factor K_c is quite similar. But the critical energy release rate G_c at the point of unstable crack growth of β PP is two times higher than of α PP [10].

The crystal structure of polymers can be influenced by inserting reinforcements like fibres, filling with particles, using nucleation agents to change the crystallinity, by optimisation of the fibre–matrix interface by coupling agents or by varying the cooling rate of the melt to a solid polymer (see also Fig. 5.1).

An overview over some possibilities to change the properties of polymeric materials is shown in Table 5.1. Different technologies are used to insert additives to polymeric materials. This improves their properties and allows tailoring them. The aims of using additives are for example improvement of toughness, increase of strength and stiffness, achievement of the correct colour, a higher degree of crystallinity, better processability, improvement of the efficacy of other fillers and reinforcements and decrease of undesired effects or ageing.

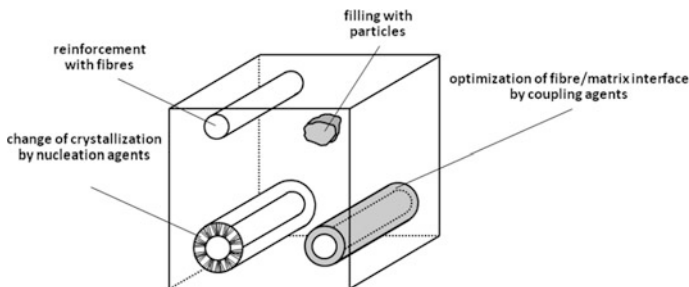


Fig. 5.1 Typical use of reinforcements and fillers to modify properties of polymers according to [16]

Table 5.1 Possibilities of changing properties of polymers by using additives according to [16]

Technology	Additive	Desired change of properties
Modifying, blending	Elastomeric materials, impact toughener	Improvement of toughness
Reinforcement	Long- and short-glass fibre	Increase of strength and stiffness
Filling	Mineralic or biologic substances	Economic aspects
Addition of auxiliary substances	Pigments	Colour
	Nucleation agent	Higher degree of crystallinity, better processability
	Coupling agent	Improvement of efficacy of fillers and reinforcements
	Stabilisers	Decrease of undesirably effects, ageing

The use of nucleation agents and the change of cooling rate of the polymer melt are applied here to characterise the influence of the different crystal modifications on the mechanical and fracture mechanical properties of PP. Therefore an α as well as a β -nucleation agent was used and plates of PP, α PP and β PP cooled with different velocities while pressing them. This simulates the variation of structure through the cross section of a technical part induced by cooling a thick, compact bulk PP.

5.2 Experimental Part

Nucleation agent was added to isotactic random copolymer containing 3.9 mol% ethylene (abbreviated with PP, Mosten EH 801 by Unipetrol), to induce crystal growth either in α -modification (α PP, ADK STAB[®]NA-21 von Adeka Palmarole) or in β -modification (β PP, NJSTAR-NU100 von New Japan Chemical Co., Ltd.). These three materials were used to press plates with different cooling rates v_c , which were 1 K/min (-1) and 15 K/min (-15). Quenching (-Q) of the plates led to a noticeable higher cooling rate. The pressed plates had a length $l = 170$ mm, a width $w = 100$ mm and a thickness $t = 4$ mm. Specimen with a smooth surface were prepared by sawing and milling.

For the determination of degree of crystallinity χ , a differential scanning calorimeter of the type Q100 of TA Instruments was used. The samples were heated with a rate of 10 K/min up to $T = 170$ °C and cooled with different rates v_c . The used cooling rates were 0.06, 0.1, 0.5, 1, 2, 5 and 20 K/min. The melt enthalpy of PP was determined of the thermogram of the second heating and the degree of crystallinity χ was calculated by dividing the measured melt enthalpy by the melt enthalpy of a completely crystalline PP ($\Delta H_m = 207$ J/g) [17]. The total crystalline content was determined without distinguishing between the α - or β -modification.

Using a microtome, samples of a thickness of 50 μm were prepared and applied on a sample holder, heated by a hot stage to $T = 180\text{ }^\circ\text{C}$ and investigated using the polarisation microscope Motic BA 410 in combination with the thermosystem Mettler Toledo FP900 at the technically highest possible cooling rate v_c of 10 K/min.

To characterise the materials resistance against stable crack initiation and crack growth, crack resistance (R-) curves were generated by determination of J -value J_d as a function of the stable crack growth Δa . Therefore, the Instrumented Charpy Impact Test (ICIT) combined with the stop block method was performed, using an impact velocity of 1 m/s [18–20].

During ICIT, the load(F)–deflection(f) curves of unnotched and notched specimens (SENB specimens with an initial crack length $a_0 = 4.5\text{ mm}$; SENB—single-edge-notched bending) are recorded and the characteristic values maximum load F_{max} , the characteristic load value corresponding to the transition from elastic to elastic–plastic material behaviour F_{gy} and the associated deflection values f_{max} and f_{gy} determined. Based on the F – f diagrams of the unnotched specimens, the dynamic flexural modulus E_d and the yield stress σ_d at dynamic load [see (5.1) and (5.2)] are determined. The support span is $s = 40\text{ mm}$, the thickness $B = 4\text{ mm}$ and the width $W = 10\text{ mm}$.

$$E_d = \frac{F_{\text{gy}} s^3}{4BW^3 f_{\text{gy}}} \quad (5.1)$$

$$\sigma_d = \frac{3F_{\text{gy}} s}{2BW^2} \quad (5.2)$$

Based on the recorded F – f diagrams of the notched specimens, the total energy can be split into an elastic (A_{el}) and a plastic (A_{pl}) part and J_d calculated according to (5.3), whereat η_{el} and η_{pl} are elastic and plastic factors considering the geometry of the specimens.

$$J_d = \eta_{\text{el}} \frac{A_{\text{el}}}{B(W-a)} + \eta_{\text{pl}} \frac{A_{\text{pl}}}{B(W-a)} \left[1 - \frac{(0.75\eta_{\text{el}} - 1)\Delta a}{W-a} \right] \quad (5.3)$$

The crack growth is interrupted at different deflections of the specimens by stopping the pendulum hammer by a stop block. Afterwards the specimens are cooled by liquid nitrogen and cracked at high speeds to enforce a brittle residual fracture. The length of stable crack growth Δa can be measured using a light microscope. Regarding the validity of the values, J_d – Δa diagrams are constructed and fitted according to (5.4). The tearing modulus T_J can be determined based on the slope of the curve and describes the resistance of the materials against stable crack growth [see (5.5)]. The determination of the tearing modulus $T_J^{0.5}$ is performed at a stable crack growth of 0.5 mm.

$$J_d = C_1 \Delta a^{C_2} \quad (5.4)$$

$$T_I = \frac{dJ}{d\Delta a} \frac{E}{\sigma_d^2} \quad (5.5)$$

The characterisation of the fracture surfaces using a scanning electron microscope (SEM) enables the determination of the deformation mechanisms.

5.3 Results and Discussion

5.3.1 Degree of Crystallinity

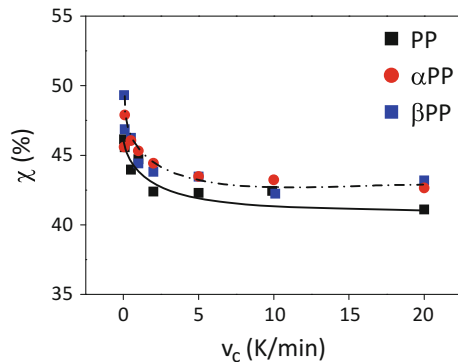
The degree of crystallinity of the different polymers depends on the cooling rate (see also Fig. 5.2).

At lower cooling rates like 0.06 K/min, the degree of crystallinity is comparable high and decreases with rising cooling rate as expected. With increasing cooling rate, the available time for formation and growth of crystallites is reduced. This leads to a reduction of degree of crystallinity.

The degree of crystallinity of PP, α PP and β PP is quite similar, by trend slightly higher for the polymers containing nucleating agent. At cooling rates higher than 2 K/min, the degree of crystallinity χ as a function of cooling rate v_c is nearly constant, at least within the analysed range of temperature. That means, the degree of crystallinity of the materials cooled between 1 and 15 K/min is independent of the cooling rate (see also [3]).

The influence of the nucleating agent on the size of the spherulites is shown exemplarily for β PP by POM pictures in Fig. 5.3. Due to the nucleating agent, many uniform spherulites are built, whose size is considerably reduced compared with the crystallites of non-nucleated PP. The reduction of spherulite size of β PP is attended by an increase of ductility [10].

Fig. 5.2 Degree of crystallinity χ as a function of cooling rate v_c



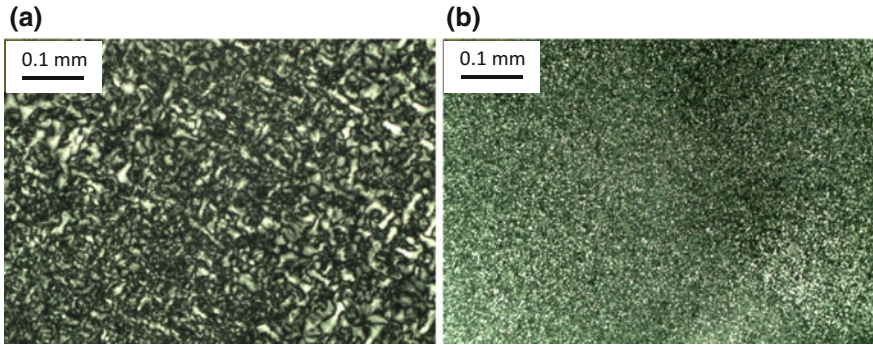


Fig. 5.3 Polarisation microscope pictures of PP (a) and β PP (b) at a cooling rate of 10 K/min

5.3.2 Influence of Cooling Rate on the Resistance Against Stable Crack Initiation and Crack Growth

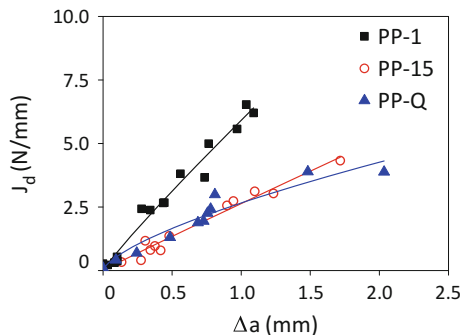
The $J_d-\Delta a$ curves of differently cooled non-nucleated PP is shown in Fig. 5.4. The resistance against stable crack growth is influenced by the cooling rate.

At higher cooling rates (PP-15 and PP-Q), the slope of the curve is lower compared to PP-1.

At an assimilable stable crack growth Δa , hence J_d of PP-1 is higher than J_d of PP-15 and PP-Q. That means the resistance against stable crack growth of PP-1 is higher than the resistance of PP-15 and PP-Q. The $J_d-\Delta a$ curves of PP-15 and PP-Q are quite similar, indicating the independence of the resistance against stable crack growth of PP at these cooling temperatures.

In Fig. 5.5 the crack surfaces of PP-1 and PP-15 are displayed. The amount of stable crack growth Δa of PP-1 is smaller than of PP-15. This zone is characterised by a smooth and even surface. The stable crack growth is generated during ICIT and interrupted by the stop block. It is clearly delimited by the neighbored area of residual crack growth, which is produced after ICIT and shows the typical signs of a brittle break.

Fig. 5.4 $J_d-\Delta a$ curves of non-nucleated PP at different cooling rates



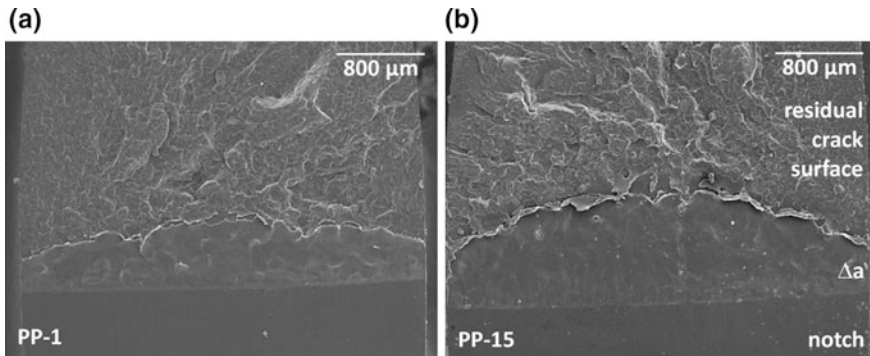
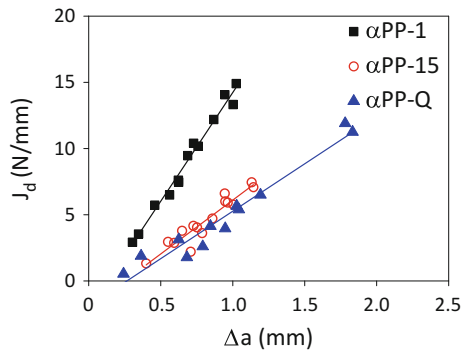


Fig. 5.5 Typical SEM pictures of PP-1 (a) and PP-15 (b)

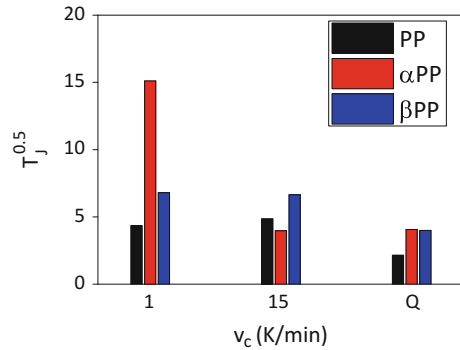
Fig. 5.6 $J_d-\Delta a$ curves of α PP cooled with different rates



In Fig. 5.6 the $J_d-\Delta a$ curves of nucleated and differently cooled α PP are displayed. The $J_d-\Delta a$ curves show the strong influence of the cooling rate on the materials resistance against stable crack growth. At a slow cooling rate of 1 K/min, J_d is higher than J_d of α PP-15 and α PP-Q at comparable Δa . On the other hand, $J_d-\Delta a$ curves of α PP-1 and α PP-Q show only very slight differences. The influence of the cooling rate on β PP is basically lower.

The tearing modulus $T_J^{0.5}$ at a stable crack length of $\Delta a = 0.5$ mm of the different materials depends on the cooling rate and the crystalline structure (see Fig. 5.7). The most noticeable difference exists between the tearing modulus of the polymers cooled with 1 K/min. With increasing cooling rate and decreasing degree of crystallinity, the tearing modulus of nucleated α PP decreases. This effect is strongest for α PP. For PP and β PP, the influence of the cooling rate and the degree of crystallinity is smaller. Hence, the influence of nucleating agent on the resistance against stable crack growth at a cooling rate of 1 K/min is the highest.

Fig. 5.7 Tearing modulus $T_J^{0.5}$ of the different polymers at a stable crack length $\Delta a = 0.5$ mm



5.4 Conclusion

The influence of a nucleating agent, either α or β , and the cooling rate on the resistance against stable crack initiation of polypropylene and stable crack growth is analysed. It is shown, that the resistance against stable crack growth of the materials PP and α PP correlates with the degree of crystallinity. The higher the degree of crystallinity, the higher is the materials resistance against stable crack growth. This correlation is not valid for β PP. The R-curves of β PP are marginally influenced by the degree of crystallinity.

Acknowledgements The authors thank Prof. H. Roggendorf and Dipl.-Ing. S. Borreck (†) of Martin Luther University Halle-Wittenberg for SEM investigations. We also thank Prof. R. Androsch of Martin Luther University Halle-Wittenberg for polarisation microscopy investigations.

References

1. Grellmann, W., Langer, B., Bierögel, C., Schoßig, M., Mecklenburg, T.: Bruchmechanische Zähigkeitsbewertung nukleierter glasfaserverstärkter Polyolefinwerkstoffe. In: Pohl, M. (eds.) Konstruktion, Qualitätssicherung und Schadensanalyse. Verlag Werkstoff-Informationsgesellschaft, Frankfurt (2004), pp. 327–332
2. Monami, A.: Struktur, Exfolierungszustand und Eigenschaften von PA6/OMMT-Verbundwerkstoffen. Mensch und Buch Verlag, Berlin (2013)
3. Monami, A., Langer, B., Sadilek, J., Kučera, J., Grellmann, W.: Fracture mechanics properties of polymorphic polypropylene. *Procedia Mater. Sci.* **3**, 276–281 (2014)
4. Phillips, R.A., Wolkowitz, M.D.: Structure and morphology. In: Moore, E.P. (ed.) Polypropylene Handbook, pp. 113–118. Carl Hanser, Munich Vienna New York (1996)
5. Chiu, F.-C., Lai, S.-M., Chen, J.-W., Chu, P.-H.: Combined effects of clay modifications and compatibilizers on the formation and physical properties of melt-mixed polypropylene/clay nanocomposites. *J. Polym. Sci., Part B: Polym. Phys.* **42**, 4139–4150 (2004)
6. Maier, C., Calafut, T.: Polypropylene—The Definitive User’s Guide and Databook. William Andrew Publishing/Plastics Design Library (1998)

7. Foresta, T., Piccarolo, S., Goldbeck-Wood, G.: Competition between α and γ phases in isotactic polypropylene: effects of ethylene content and nucleating agents at different cooling rates. *Polymer* **42**, 1167–1176 (2001)
8. Marigo, A., Causin, V., Marega, C., Ferrari, P.: Crystallization of the gamma form in random propylene–ethylene copolymers. *Polym. Int.* **53**, 2001–2008 (2004)
9. Marigo, A., Marega, C., Causin, V., Ferrari, P.: Influence of thermal treatments, molecular weight, and molecular weight distribution on the crystallization of beta-isotactic polypropylene. *J. Appl. Polym. Sci.* **91**, 1008–1012 (2004)
10. Karger-Kocsis, J., Varga, J., Ehrenstein, G.W.: Comparison of the fracture and failure behavior of injection-molded α - and β -polypropylene in high-speed three-point bending tests. *J. Appl. Polym. Sci.* **64**, 2057–2066 (1997)
11. Wang, C., Zhang, Z., Ding, Q., Jiang, J., Li, G., Mai, K.: β -crystallization of isotactic polypropylene in the presence of β -nucleating agent and different crystallinity poly(ethylene terephthalate). *Thermochimica Acta* **559**, 17–22 (2013)
12. Raab, M., Kotek, J., Baldrian, J., Grellmann, W.: Supermolecular structure and mechanical behaviour of polymers. In: Grellmann, W., Seidler, S. (eds.) *Deformation and Fracture Behaviour of Polymers*, pp. 153–160. Springer, Berlin (2001)
13. Kotek, J., Raab, M., Baldrian, J., Grellmann, W.: The effect of specific β -nucleation on morphology and mechanical behavior of isotactic polypropylene. *J. Appl. Polym. Sci.* **85**, 1174–1184 (2002)
14. Aboulfaraj, M., G'Sell, C., Ulrich, B., Dahoun, A.: In situ observation of the plastic deformation of polypropylene spherulites under uniaxial tension and simple shear in the scanning electron microscope. *Polymer* **36**, 731–742 (1995)
15. Karger-Kocsis, J.: How does “phase transformation toughening” work in semicrystalline polymers? *Polym. Eng. Sci.* **36**, 203–210 (1996)
16. Langer, B., Bierögel, C., Grellmann, W.: Eigenschaften von Polypropylen gezielt bewerten. *Kunststoffe* **5**, 87–97 (2008)
17. Ton-That, M.T., Leelapornpisit, W., Utracki, L., Perrin-Sarazin, F., Denault, J., Cole, K., Bureau, M.: Effect of crystallization on intercalation of clay-polyolefin nanocomposites and their performance. *Polym. Eng. Sci.* **46**, 1085–1093 (2006)
18. Grellmann, W., Seidler, S., Hesse, W.: Testing of plastics—Instrumented Charpy impact test; Procedure for determining the crack resistance behaviour using the instrumented Charpy impact test; Part I: Determination of characteristic fracture mechanics parameters for resistance against unstable crack propagation; Part II: Determination of characteristic fracture mechanics parameters for resistance against stable crack propagation (2014)
19. Grellmann, W., Seidler, S. (eds.): *Polymer Testing*. Carl Hanser, Munich (2013)
20. Grellmann, W., Bierögel, C., Reincke, K.: *Lexikon Kunststoffprüfung und Diagnostik*. Merseburg. see: <http://wiki.polymerservice-merseburg.de> (2014)

Chapter 6

Numerical Modelling of Damage Initiation and Failure of Long Fibre-Reinforced Thermoplastics

L. Schulenberg, D.-Z. Sun and T. Seelig

Abstract Characterising the mechanical properties of long fibre-reinforced thermoplastic (LFT) composites including failure is a challenging task. The macroscopic behaviour is generally associated with parameters like fibre orientation, volume fraction and length. A thorough understanding of the micromechanical mechanisms gets more and more important for describing macroscopic behaviour. Large aspect ratios (fibre length divided by fibre diameter) make it difficult to create numerical models of the random LFT microstructure since representative volume elements (RVE) that consider the microstructure in a cross section over the entire thickness lead to a large computational effort. Numerical explorations of selectively predetermined fibre constellations can reduce the model size. In addition, complex interface behaviour can be considered. Therefore a numerical study is performed to identify relevant parameters in micromechanical finite element models of a long fibre-reinforced thermoplastic composite. Different unit cell models of discontinuous fibres embedded in a polypropylene matrix are analysed numerically to identify major mechanisms related to damage and failure in relevant loading directions.

6.1 Introduction

Long fibre-reinforced thermoplastics (LFT) are a class of composite materials that have a high priority in industrial applications. The advantages of LFT arise from the combination of short fibre-reinforced thermoplastics and from those of infinitely long fibres that give the material excellent properties, e.g. high strength. Characterising the mechanical properties including failure is a challenging task. The macroscopic behaviour is generally associated with parameters like fibre orientation, fibre density and fibre length. A thorough understanding of the

L. Schulenberg (✉) · D.-Z. Sun
Fraunhofer Institute for Mechanics of Materials (IWM), Freiburg, Germany

T. Seelig
Karlsruhe Institute of Technology (KIT), Institute of Mechanics,
Karlsruhe, Germany

micromechanical mechanisms gets more and more important for describing macroscopic behaviour. Large aspect ratios (fibre length divided by fibre diameter) of LFTs make it difficult to create numerical models of the microstructure. Representative Volume Elements (RVE) for LFT that consider the microstructure in a cross section over the entire thickness lead to a large computational effort. Numerical explorations of selectively predetermined fibre constellations can reduce the model size. In addition, complex interface behaviour can be considered.

6.2 Problem Formulation

6.2.1 Experimental Observation

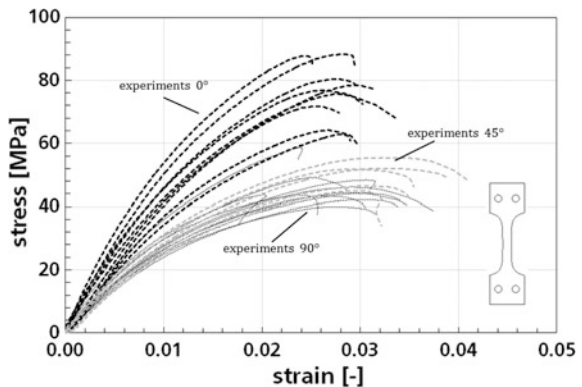
An injection moulded LFT of polypropylene and 30 wt% glass fibres has been examined. Uniaxial tension tests in three different extrusion directions (0° , 45° , 90°) have been performed and are shown in Fig. 6.3. Haul-off speed was 0.01 mm/s. For simplicity, in the present study strain rate effects are not considered. The material shows an anisotropic behaviour. In uniaxial tension the highest strength has been observed in 0° and the lowest strength in 90° towards the extrusion direction.

6.2.2 Microscopic Observation

As shown in Fig. 6.2 there are three regions of distinct fibre directions over the thickness coming from the flow direction during manufacturing. Apparently each layer has a fibre direction rotated through 90° to the next layer.

As the middle layer is very thin it is feasible that experimental results perpendicular to the flow direction have a lower strength than tension tests in 0° (Fig. 6.1).

Fig. 6.1 Experimental results of uniaxial tension tests in three different extrusion directions for LFT made of polypropylene and 30% glass fibres (weight fraction)



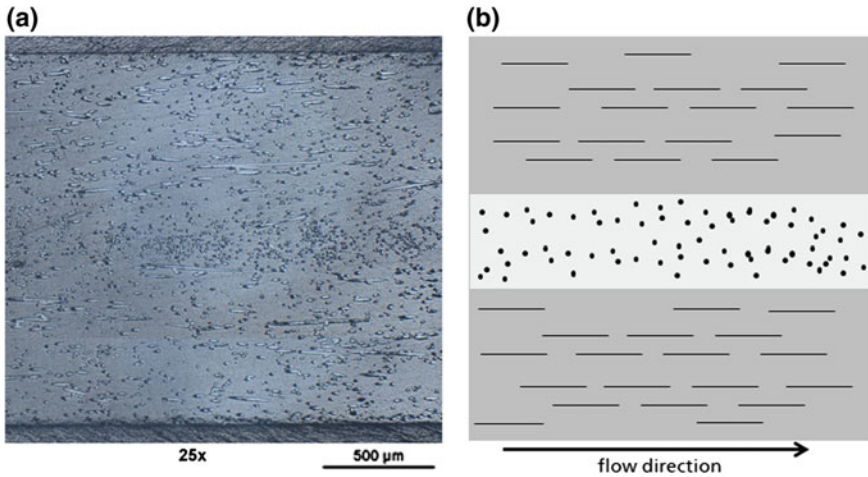
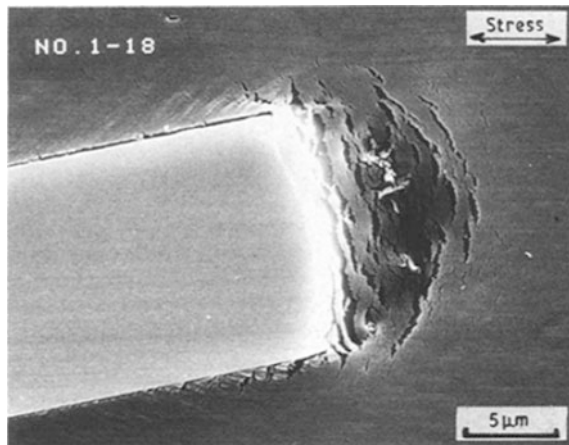


Fig. 6.2 Polished micrographic cross section of LFT parallel to injection moulded flow direction (a). Schematic drawing of the principle fibre orientation (b)

Considering the whole thickness of a cross-section like Fig. 6.2b in one RVE, the large aspect ratio of LFT would lead to a large computational effort. Therefore selectively predetermined fibre constellations can be used to reduce the model size. The significant advantages of those smaller models are by illustrating the complex interactions of fibre and matrix as well as the interface behaviour in much more detail.

Experimental studies of comparable classes of materials [1] show that primary damage initiation starts in the fibre–matrix interface and can be identified as the initial mechanism (Fig. 6.3). In a micro-mechanical simulation this fact is largely to take into account in order to gain useful results and deeper insights into the failure

Fig. 6.3 Microcracks occurring in the matrix around the fibre tip where interface debonding starts. Example of a short fibre-reinforced thermoplastic composite, which was obtained under about 50% of failure load [1]



process. There are many different ways to identify the interface behaviour experimentally. Common methods are for example the Micro-Bond Test and the Fibre-Pull-Out Test [2]. These tests have in common that interface debonding is analysed under uniaxial tension in fibre direction. Thinking about the plausible fact that loading parallel towards the fibre direction is giving the composite its highest strength then this mechanical mechanism of interface failure along the fibres should play a high role in the composite damage behaviour.

6.2.3 Numerical Microstructural Model

A three-dimensional unit cell model out of under-integrated solid elements has been generated for the numerical analysis using the explicit finite element solver LS-Dyna (Fig. 6.4).

The material model for the matrix of polypropylene is an elastic–plastic material model (MAT_024 in LS-Dyna) with isotropic hardening according to von Mises. Viscoelastic behaviour like strain rate dependency and time depended relaxation has been neglected. The matrix failure criterion is based on a Johnson-Cook failure curve plotting equivalent plastic strain against stress triaxiality. The material model for the glass fibres are based on a purely elastic model (MAT_ELASTIC in LS-Dyna) with a failure criterion based on maximum principal stress. Parameters were taken from literature and are based on experimental tests.

The interface behaviour is described by a cohesive zone model using a bilinear mixed-mode traction-separation law (Fig. 6.5). It is dependent on the parameters of fracture toughness for mode I (T), mode II (S) and critical energy release rates for both modes respectively described as area under each triangle shaped curve. Interface failure occurs when the crack opening reaches the critical value δ^F .

After interface failure fibre pull-out occurs. This is influenced by residual stresses and friction between fibre surface and matrix. A shear stress after interface failure at the fibre surface arising from friction is a result of normal stresses towards a rough debonded fibre surface (e.g. [3]). It is known that LFT implies residual stresses coming from curing in the manufacturing process where normal stresses on the fibre surface can be allocated too. Those induced residual stresses are modelled

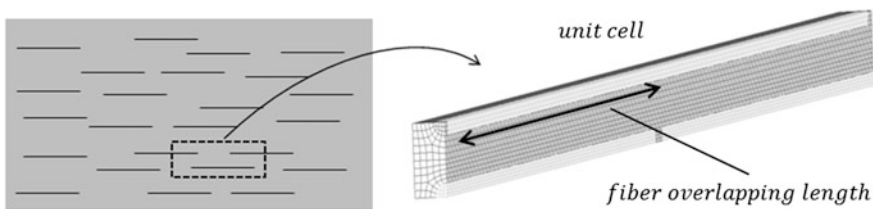


Fig. 6.4 Unit cell from one layer of LFT with a quasi-unidirectional fibre orientation and discontinuous staggered fibres

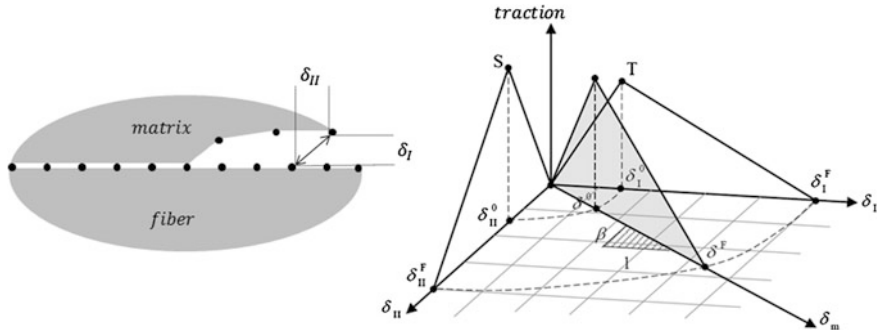


Fig. 6.5 Schematic drawing of crack opening at interface (*left*). Mixed-mode traction-separation law of the cohesive zone formulation for interface behaviour between fibre and matrix (*right*) [4]

by a homogeneous dynamic relaxation of the matrix depending on a thermal expansion coefficient and a temperature difference. The friction itself is modelled using a high friction coefficient in a surface-to-surface contact algorithm.

The interface parameters have been fitted numerically. The Micro-Bond Test has a repetitious accuracy. It is shown in [3] that analytical equations are giving a good approach for the experimental force–displacement curves of the Micro-Bond Test. For this study a numerical model of the Micro-Bond Test has been set up. The interface parameters for failure of the cohesive zone model and the frictional sliding behaviour after interface failure have been fitted by comparing the numerical force–displacement curves with the analytical solutions. This procedure is according to [2] where a numerical model of the Micro-Bond Test is modelled equally.

6.3 Numerical Results

6.3.1 Single-Fibre Unit Cell Under Uniaxial Tension

To elaborate the interface mechanisms between fibre and matrix a simple single-fibre unit cell model has been generated. Uniaxial tension loading under 0° towards the fibre direction (here z-direction in Fig. 6.6) causes the described interface failure mechanism. Crack propagation starts at fibre tips and proceeds from both sides.

The overall stress–strain curves are shown in Fig. 6.7. For elongation up to a strain of about 0.5% the response of the unit cell is elastic. For higher elongation interface failure starts and the crack between fibre and matrix grows along the fibre. The decreasing load is an indication of unstable crack growth. After the crack tips reach the middle of the fibre (strain between 0.25 and 0.3%) strain hardening of the matrix material sets in and in addition the influence of frictional sliding can be identified.

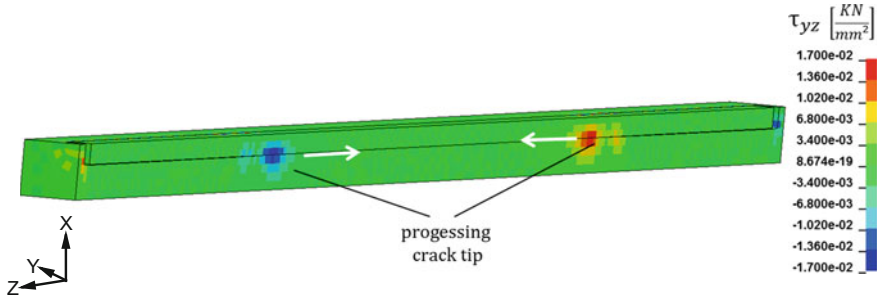


Fig. 6.6 Single-fibre unit cell model under uniaxial tension in 0° fibre direction. The highest shear stresses (*dark*) show where the crack tip of interface failure is located

It is shown in Fig. 6.7 that induced residual stresses increase the peak force and crack initiation starts at higher strains. This suggests a better adhesive strength when residual stresses exist. To understand the force transfer from matrix to fibre Fig. 6.8 shows the shear stresses along the interface over a normalised fibre length. Frictional sliding reduces the speed of unstable crack propagation identified from $\epsilon_{\text{true}} = 0.01$ of elongation. The significant lower stress–strain curve from Fig. 6.7 becomes clear by noticing that for higher strains a bigger force transfer through shear stresses exists (Fig. 6.8 with $\epsilon_{\text{true}} = 0.128$).

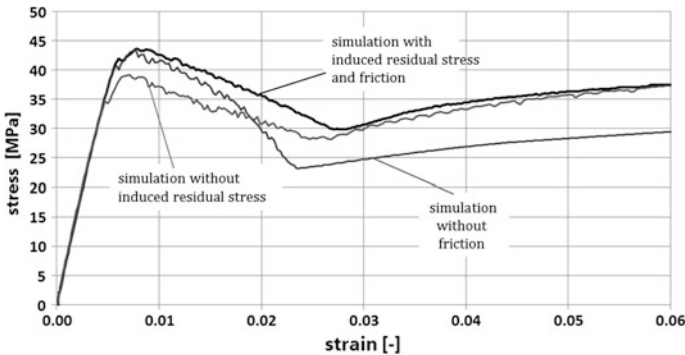


Fig. 6.7 Stress–strain curves from single-fibre unit cell model under uniaxial tension in 0° fibre direction illustrating the influence of interface friction and residual stresses

6.3.2 Unit Cells Containing Three Fibres

More complex stress states can be analysed by unit cell models containing staggered fibres (Fig. 6.9). Uniaxial tension loading in 0° fibre direction gives the stress–strain curves shown in Fig. 6.10.

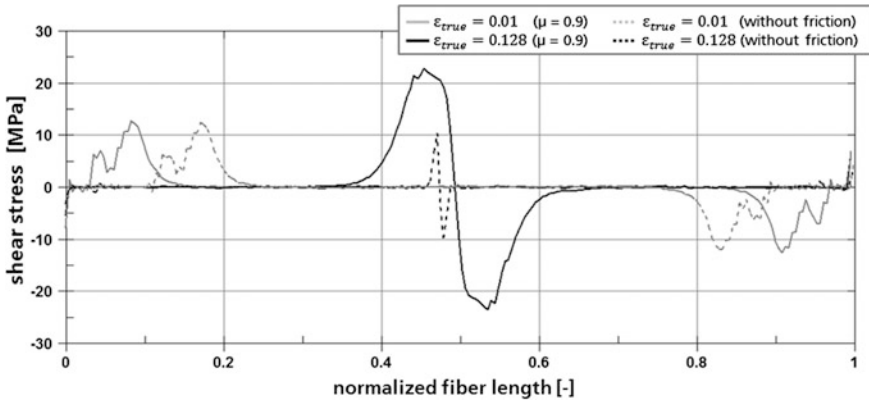


Fig. 6.8 Shear stresses along the fibre from FEM calculations in the matrix elements at the interface. Two different stages of elongation are shown to illustrate the effect of frictional sliding

Five different sections in the stress–strain curve can be identified. Section I again shows a pure elastic response. The kink at II is where crack initiation starts at fibre tips. Different from the single-fibre unit cell, crack propagation along fibres proceeds with an increasing load (section III) and can be identified as stable crack propagation. At section IV stable crack propagation turns into an unstable behaviour. This drop down of the force is related to a quick load rearrangement from fibres to the matrix. The crack tips of the staggered fibres grow in opposite directions (Fig. 6.9) until the cracks cross each other. Section V is according to the single-fibre unit cell where the load is basically carried by the matrix material and only transferred onto the fibres by frictional sliding at the debonded interface. After unstable crack propagation a strong oscillation in the numerical model can be identified and is related to the strong effect of quick load rearrangements in the explicit finite element simulation. In this unit cell model the influence of residual

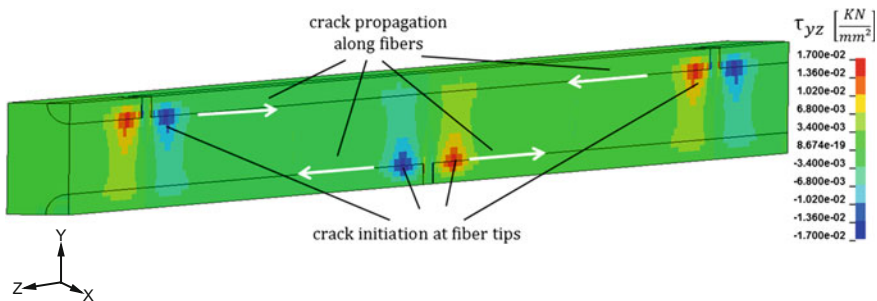


Fig. 6.9 Mechanism of interface failure for three-fibre unit cell. High shear stresses at each crack front (*dark*)

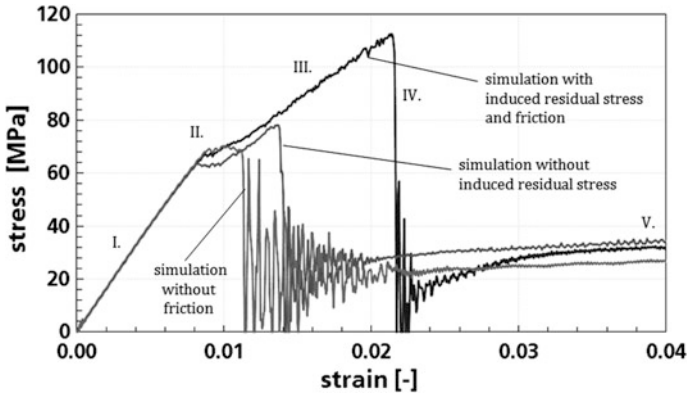


Fig. 6.10 Typical stress–strain curves of a unit cell element loaded under uniaxial tension in 0° fibre direction. Influence of induced residual stress and friction is shown

stresses and friction have a much higher effect on the peak force than in the single-fibre unit cell.

6.3.3 Variations of the Fibre Overlapping Length and Load Direction

When stable crack propagation proceeds load capacity increases until the crack tips of the neighbouring fibres cross each other. A logical consequence is that the fibre overlapping length (Fig. 6.4) is responsible for the maximum load capacity of a unit cell. Figure 6.11 shows the results of different unit cell calculations.

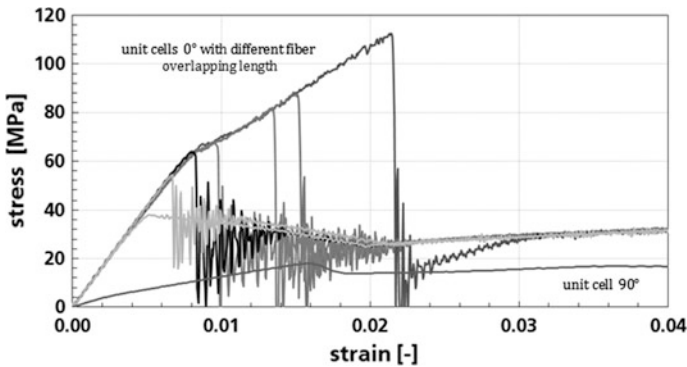


Fig. 6.11 Stress–strain curves of numerical unit cell calculations with different fibre overlapping length and two loading directions (0° and 90°)

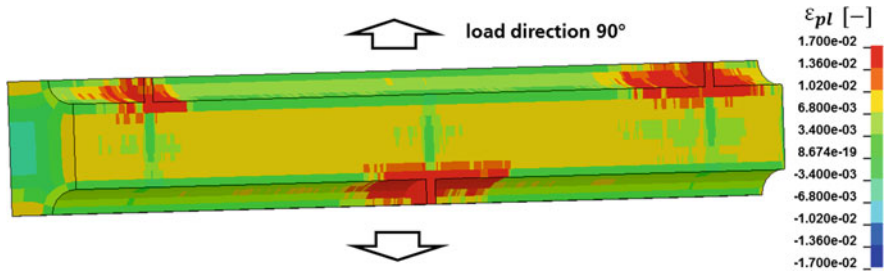


Fig. 6.12 Unit cell under tensional load 90° towards the fibre direction. The contour plot shows the equivalent plastic strain in the matrix material just before interface debonding starts ($\epsilon_{\text{true}} = 0.016$). High plastic strains (*dark*) occur around the fibre tips

The minimum fibre overlapping lengths is 0 mm which produces a stress–strain curve analogical to the single-fibre unit cell. The longest fibre overlapping length with 1.33 mm (half of the fibre length) shows the highest stress. The shorter the length of overlapping, the early unstable crack propagation occurs. The simulations cover a wide range of possible stress–strain curves for loading in 0° towards the fibre direction. A loading direction perpendicular (Fig. 6.12) towards the fibres is independent of the fibre overlapping length and therefore for all unit cells very similar in its stress–strain response.

6.4 Discussion

The numerical results of the unit cells with variations in fibre overlapping length and loading direction (Fig. 6.11) compared to the experiments (Fig. 6.1) show that the stress–strain curves of the numerical results cover the area of experiments. Reconsidering the microscopic observation (Fig. 6.2) that three different layers of main fibre orientations have been examined it appears to be logical that a combination of unit cells and load directions of 0° and 90° to the fibre orientation could be able to represent the macroscopic behaviour. Obviously this study builds only a foundation for further calculations where several other effects for example strain rate dependency or a more complex matrix failure criteria can be considered. The great relevance of induced residual stresses and the effects of friction towards damage and failure behaviour of LFT composite materials have been turned out.

6.5 Summary

The main subject of this numerical study is to identify relevant parameters in a micromechanical finite element model of a long fibre-reinforced thermoplastic (LFT) composite. Therefore different unit cell models of discontinuous fibres

embedded in a polypropylene matrix are analysed numerically to identify major mechanisms related to damage and failure in relevant loading directions.

References

1. Sato, C., Kurauchi, T., Sato, S., Kamigaito, O.: Microfailure behaviour of randomly dispersed short fibre reinforced thermoplastic composites obtained by direct SEM observation. *J. Mater. Sci.* **26**, 3891–3898 (1991)
2. Sockalingam, S., Moutushi, D., Gillespie Jr., J., Keefe, M.: Finite element analysis of the microdroplet test method using cohesive zone model of the fibre/matrix interface. *Compos. A* **56**, 239–247 (2014)
3. Zhandarov, S., Gorbatkina, Y., Mäder, E.: Adhesional pressure as a criterion for interfacial failure in fibrous microcomposites and its determination using a microbond test. *Compos. Sci. Technol.* **65**, 149–160 (2005)
4. LS-DYNA Keyword User's Manual, Version R7.0. Livermore Software Technology Corporation, Livermore (2007)

Part II
Advanced Structure-Sensitive Methods for
Analysing Cracks and Fracture Surfaces

Chapter 7

Characterisation of Polymers in the Scanning Electron Microscope— From Low-Voltage Surface Imaging to the 3D Reconstruction of Specimens

A. Zankel, M. Nachtnebel, C. Mayrhofer, K. Wewerka
and T. Müllner

Abstract The scanning electron microscope (SEM) is a versatile tool for the characterisation of polymers. The nowadays available broad variety like the conventional SEM (CSEM), the variable pressure SEM (VPSEM) and the environmental SEM (ESEM) enable different investigation techniques for analysis. In this article special modes of performance are discussed. These are the low-voltage mode of the CSEM for the characterisation of surfaces without preparation, the low-vacuum mode of the ESEM utilising an imaging gas for charge compensation at nonconductive samples and the ESEM mode enabling the investigation of wet samples. These modes not only facilitate appropriate characterisations of conventional polymer specimens e.g. for the purpose of fractography, but even open the field for new in situ investigations, where the change of the sample due to e.g. a mechanical influence can be imaged time-resolved.

7.1 Introduction

The scanning electron microscope (SEM) is a versatile tool for the characterisation of polymers [1–3]. Different technical improvements concerning electron optics, the quality of the electron beam or the performance of detectors have changed the demand on specimen preparation and the way of imaging over the last decades. The nowadays available broad variety of different types of SEMs like the conventional

A. Zankel (✉) · M. Nachtnebel · K. Wewerka
Institute for Electron Microscopy and Nanoanalysis,
Graz University of Technology, Graz, Austria

A. Zankel · C. Mayrhofer
Austrian Centre for Electron Microscopy and Nanoanalysis, Graz, Austria

T. Müllner
Department of Chemistry, Philipps University, Marburg, Germany

SEM (CSEM), the variable pressure SEM (VPSEM) and the environmental SEM (ESEM) enable different investigation techniques for analysis [4, 5]. Aside from common specimen preparation methods where an electrically conducting layer is deposited on the specimen's surface e.g. by vacuum evaporation coating of a carbon layer or by sputter coating with different metals like Au, Pd or Cr, in this article special modes of performance are discussed. These are the low-voltage mode of the CSEM for the characterisation of surfaces without preparation, the low-vacuum mode of the ESEM utilizing an imaging gas for charge compensation and the ESEM mode enabling the investigation of wet samples. These modes not only facilitate appropriate characterisations of conventional polymer specimens e.g. for the purpose of fractography, but even open the field for new in situ investigations, where the change of the sample due to e.g. a mechanical influence can be imaged time-resolved.

7.2 Low-Voltage Mode of the SEM

Investigations of electrically non-conducting specimens, like most polymers, performed in the conventional scanning electron microscope, where electron beam energies are in the range of 5–50 keV [6], commonly demand an electrically conducting layer to prevent charging on the surface. However, low-voltage scanning electron microscopy (LVSEM) permits imaging of the neat surface without an artificial layer by working at electron energies in the range of 0.5–5 keV [6]. Specimen charging can be minimised by operating at a special energy value, called the crossover energy E_2 , where the number of beam electrons equals the number of emitted secondary electrons (SE) and backscattered electrons (BSE) [1, 3]. This value is a material constant, which has to be varied with the investigation of different polymeric materials [1, 6, 7].

The main advantage of LVSEM is a lower electron penetration depth in the material, thus delivering information correlated to thin surface layers. Furthermore a reduced depth of specimen radiation damage can be achieved [6]. This technique was supported by the progress in the construction of field-emission guns (FEG) and sensitive SE inlens detectors. In [8] LVSEM was performed using the Everhart-Thornley detector (ETD) of the high resolution SEM Zeiss Ultra 55 for the characterisation of the surfaces of cellulose fibres and the formerly bonded area (FBA) of fibre–fibre joints after the determination of the breaking force. The applied method causes minimum beam damage of the specimen's surface. In Fig. 7.1a the FBA of a fibre was imaged with an electron energy of 650 eV, Fig. 7.1b shows a detail of the investigated surface. In order to illustrate the quality of low-voltage imaging, the same region of carbon coated cellulose fibres was imaged with beam energies of 1 keV (Fig. 7.1c) and 20 keV (Fig. 7.1d). It is obvious that in Fig. 7.1c more surface details can be observed compared to images at higher energies where the interaction volume of the electrons in the bulk of the specimen is much bigger.

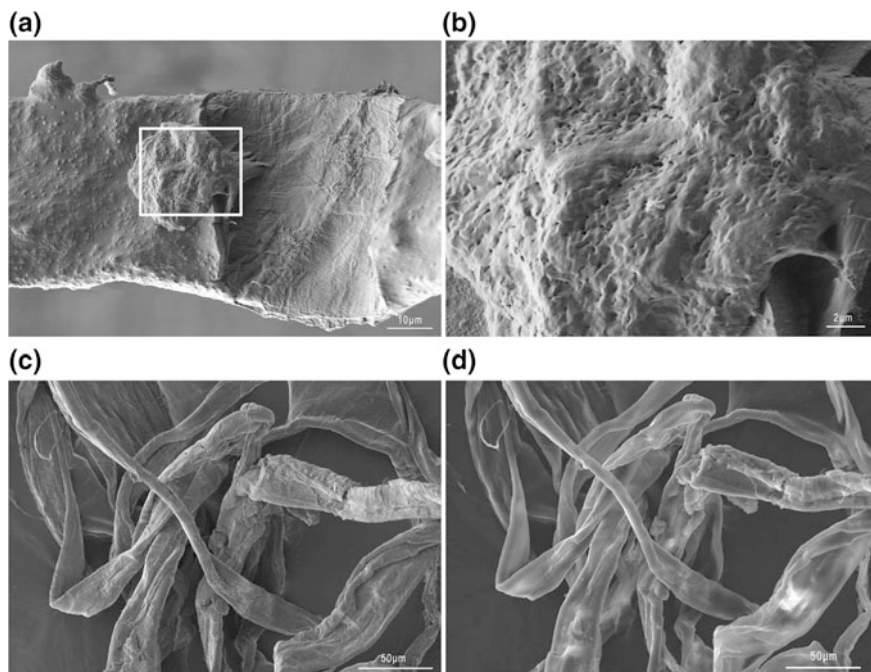


Fig. 7.1 Low-voltage characterisation of cellulose fibres: formerly bonded area (FBA) of a cellulose fibre imaged with LVSEM (electron energy: 650 eV) (a); detail of Fig. 7.1a (b); a quantity of carbon coated cellulose fibres imaged with a beam energy of 1 keV (c); the same position on the specimen as Fig. 7.1c imaged with 20 keV (SE images) (d)

In [7] the different values of E_2 are listed for common polymers like polypropylene, polyethylene and polyvinylchloride. A drawback of the method is the fact that it is only applicable to homogenous materials since inhomogeneity means different values of E_2 correlated to different material phases. However, even in situ investigations can be performed in the low-voltage mode like in situ tensile testing of electrically non-contacting materials, when the material is homogenous and the correlated energy value E_2 is known.

7.3 Low-Vacuum Mode of the ESEM

While the CSEM operates in high vacuum a recent generation of SEMs utilises a gas for signal amplification and simultaneously provides charge compensation for specimens which are electrically non-conducting. Different terms like “variable pressure scanning electron microscope” (VPSEM), “extended pressure SEM” or “environmental scanning electron microscope” (ESEM) can be found in the literature [5]. The mentioned results were gained using an ESEM Quanta 600 FEG

(FEI, Eindhoven, The Netherlands). This microscope provides the conventional high-vacuum mode as well as two modes for operation in the presence of an imaging gas, the low-vacuum mode and the ESEM mode (see Sect. 7.4). In both cases electrically non-conducting specimens can be imaged without coating since ionisation processes in the gas, which are primarily caused by electrons accelerated to the detector, produce positive ions, which can compensate negative charges on the surface stemming from the electron beam. The low-vacuum mode operates at pressures of about 10–200 Pa using typically water vapour, air or nitrogen as imaging gas. While for imaging with SE a special detector type has to be used contrary to operating in the high vacuum, the conventional high-vacuum BSE detector works even in the low-vacuum mode [4, 5].

This enables the characterisation of polymers and other types of electrically non-conducting specimens without specimen altering preparation steps. In Fig. 7.2 two SEM images of a glass fibre-reinforced thermoplastic specimen after a tensile test are shown, which were acquired simultaneously in the low-vacuum mode of the ESEM. Figure 7.2a was made using SE which deliver topographic contrast [1].

Hence morphological variations of the specimen can be characterised giving information about different effects resulting from the mechanical test like earing of the matrix material, crack propagation, void formation, pull-out or fracture of fibres etc. However, despite a good resolution of a specimen's topography it is not that easy to distinguish between polymer parts and glass fibres. In this case Fig. 7.2b may help, since imaging with BSE mainly delivers compositional contrast, which means that parts of a specimen with a higher mean atomic number appear brighter than the other parts [1]. This enables a distinction between glass and polymer. This example illustrates that in the low-vacuum mode of the ESEM an uncomplicated specimen characterisation is possible, by using different signals for different information without the need of specimen preparation aside from potential

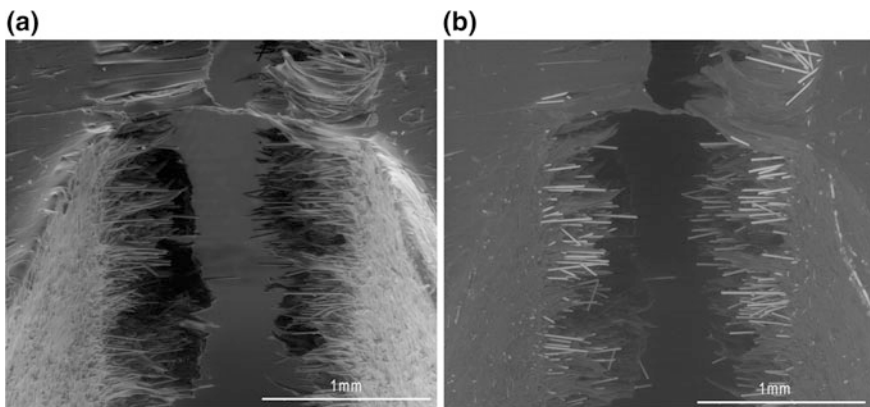


Fig. 7.2 Characterisation of a glass fibre-reinforced thermoplastic specimen after a tensile test using the low-vacuum mode of the ESEM: SE image delivering topographic contrast (a); BSE image showing compositional contrast (electron energy: 15 keV) (b)

mechanical pre-treatment like sawing, cutting, polishing or microtomy and mere mounting of the sample. Beside this comfort the low-vacuum mode is fundamental for the performance of several in situ investigations. So different alterations of specimens during an investigation can be imaged and even video films of the process can be made, since putting a layer on the surface of the specimen is not deserved any more, which restricts a specimen on mere static imaging.

In Fig. 7.3 the setup for the in situ investigation of micro-deformation processes of sealed peel films can be seen [9–11]. Figure 7.3a is a schematic of the investigation principle of this “T-peel test”. The letter “T” symbolises the “T”-like mounting geometry of the film, where the observation of the crack propagation is performed directly in the seal area, while the film is pulled symmetrically at a constant test speed. Fundamental for this investigation is a tensile stage (Fig. 7.3b) designed for in situ investigations in the specimen chamber of the ESEM. In Fig. 7.3b the load cell (1), the clamps (2), the peel film (3) and a special groove (4) for the stabilisation of the T-geometry are indicated. Figure 7.3c–e show the seal area before, during and at the end of the tensile test at different magnifications showing the evolution of crack features. In [9] series of micrographs were correlated to force–elongation curves (peel curves) of sealed low-density polyethylene/isotactic polybutene-1 (PE-LD/iPB-1) films with a content of 3–20 wt% (mass percentage) of iPB-1. In this experiment a correlation between the size of

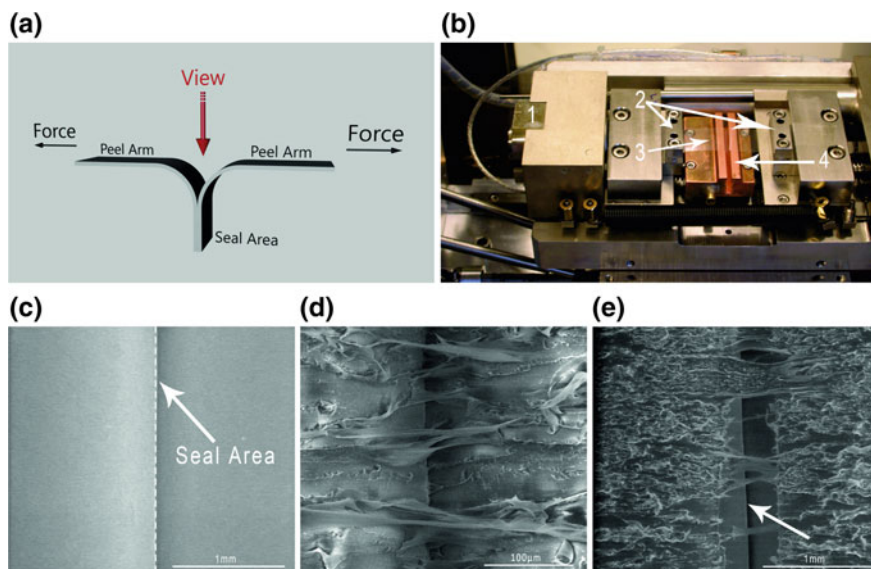


Fig. 7.3 In situ investigation of the peel behaviour of polyethylene/polybutene-1 peel films: schematic of the T-peel test indicating the optical axis of the electron microscope, the direction of the applied forces and the T-geometry of the film (a); tensile stage (b): 1 load cell, 2 clamps, 3 peel film, 4 groove for the stabilisation of the T-geometry; seal area before applying the forces (c); seal area during peel test (d); seal area at the end of the test, the arrow indicates the separation of the peel arms (SE images, electron energy: 10 keV) (e)

developing fibrils and the mass percentage was found. Additionally the influence of the peel angle was monitored leading to the in situ characterisation of two specific phenomena, the “interlaminar” and “translaminar” crack propagation [9].

This example illustrates that the low-vacuum mode of the ESEM facilitates the design of several new in situ investigation methods by combining well established material testing with electron microscopic imaging. Not only the topographic contrast can be used but also changes in material contrast of heterogeneous materials can be imaged in situ like e.g. at the tensile testing of glass fibre-reinforced polymers [12].

7.4 The ESEM Mode

Performing the third operation mode of the ESEM enables the investigation of wet samples (ESEM mode). Prerequisites for such investigations are water vapour as imaging gas and cooling of the sample with a cooling stage (e.g. Peltier cooling). According to the thermodynamic phase diagram of water, the choice of the appropriate values of the specimen temperature and the pressure of the water vapour (minimum pressure: 609 Pa) enables the maintenance of the wet phase of water during investigations [1, 4, 5].

Thus it is possible to perform condensation experiments, drying processes or investigating samples with a special amount of embodied water. In the diagram of Fig. 7.4 the parameters of an in situ investigation for wetting and drying of polyethersulfone (PES) membranes can be seen. The process is controlled by the temperature of the cooling clamps and the variation of the water vapour pressure. Additionally the temperatures of the two different membrane surfaces (air side, roll side) are simultaneously recorded to provide information about the interior membrane structure and the interaction between the water and the pore walls using micro thermocouples. The number of each arrow at the temperature curves, which show the temperature characteristics of the two membrane surfaces, is correlated to one of the micrographs below showing the development of the polymer membrane during wetting and drying. It has to be emphasised that for this work [13] a new Peltier investigation setup was developed, while for conventional “wet investigations” standard Peltier cooling stages are available.

This example shows the comfortable possibility of time-dependent monitoring of a specimen during wetting and drying, which may lead to new information about the material behaviour under a changing water environment. This can give rise to new ideas in the context of in situ mechanical testing. A combination of tensile testing and controlling the specimen’s environment could be established e.g. for the investigation of the fracture behaviour of foam-like polymer samples in wet environment.

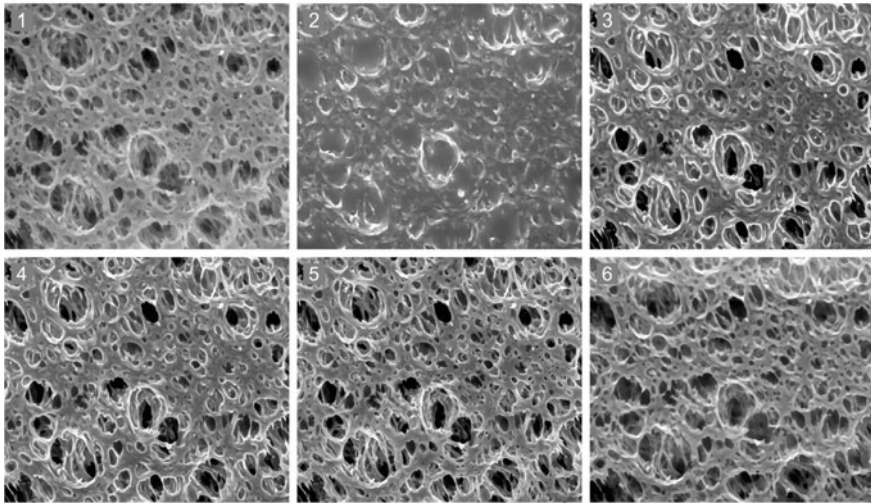
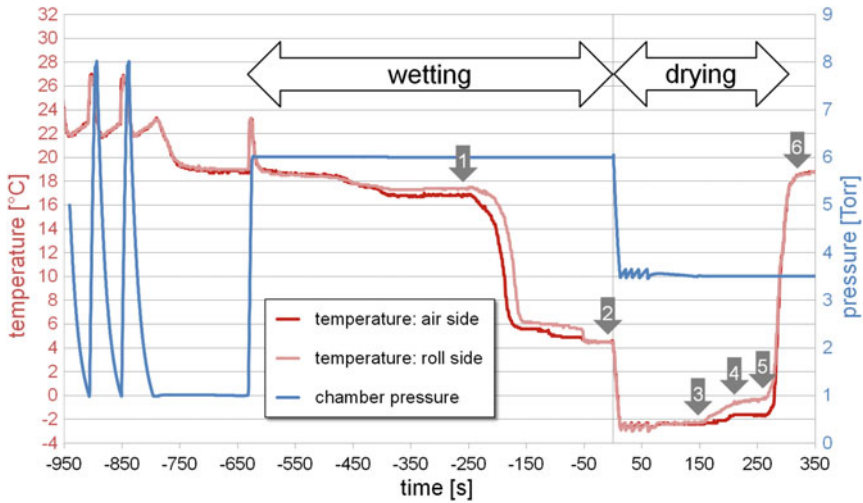


Fig. 7.4 In situ investigation of polyethersulfone membranes in the ESEM mode. *Top* Membrane surface temperature (red, light red) and pressure of the imaging gas (blue) as a function of time. The arrows are correlated to the micrograph numbers; *bottom 1–6*: micrographs of one position on the roll side of the membrane during wetting and drying (SE images; image width: 217 μm ; electron energy: 7 keV)

7.5 Artefacts and Beam Damage

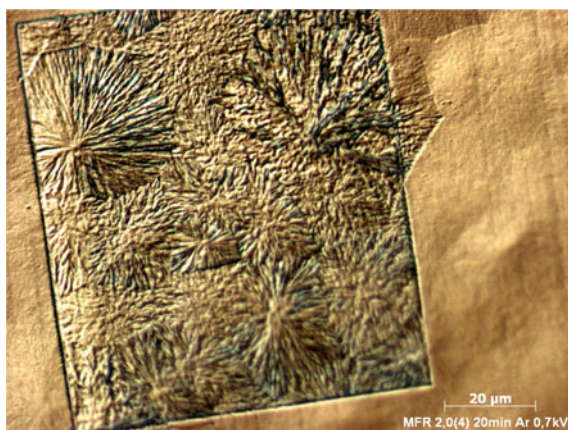
Imaging materials in the SEM represents a time-dependent influence on the specimen's surface. A well-known phenomenon is the contamination of a surface with carbon, which may deteriorate the image quality scan by scan [1] especially at lower electron energies.

Contrary to LVSEM where an uncoated surface can be imaged, for the investigation at higher electron energies in the CSEM polymers have to be coated with a conductive layer. During sputter coating potential artefacts can be induced e.g. by thermal damage of the specimen. However, a conducting metal layer on the surface will support stability against beam damage during imaging. Beam damage depends on electron energy, beam current, specimen temperature and the consistency of the material [1, 3, 14]. Additionally it strongly depends on the magnification, which limits the accessible resolution.

In some cases an investigation at a special magnification may only be realised by additional preparation steps. E.g. the embedded PES membrane of Fig. 7.6d shows sufficient compositional contrast, but at a special threshold of magnification further stable imaging can only be realised by additional staining with ruthenium tetroxide. Conventionally stained polymers are even less prone to beam damage, but when polymers are investigated in the low-vacuum mode with neither coating nor staining beam damage has to be estimated. This may be done by observing potential alterations of the surface by switching the magnification of the microscope or using e.g. Fourier transform infrared spectroscopy (FTIR) [11, 15]. Contrary to CSEM the type of imaging gas has additionally to be taken into account in the low-vacuum mode. The use of water vapour leads to the formation of free radicals, which can lead to rapid beam damage [5]. Since the use of water vapour is fundamental for the ESEM mode potential beam damage has to be considered during the investigation of wet specimens.

In some rare cases the beam influence on the surface has a positive impact on investigations. In [16, 17] it was mentioned that during cutting and imaging the influence of the beam on the material may stabilise the cutting quality even when the amount of staining agent is tremendously lowered. Another example of a beneficial effect of electron irradiation on a specimen's surface is shown in Fig. 7.5. The surface of an isotactic polypropylene specimen (MFR 2), cut with a microtome,

Fig. 7.5 Surface of a specimen of isotactic polypropylene (MFR 2) after microtomy and ion etching (light microscopic image). The interior *rectangle* was irradiated with electrons in the low-vacuum mode of the ESEM prior to ion etching



can be seen and the scan field, where the surface was irradiated in the low-vacuum mode of the ESEM, reveals the spherulites of the material in a more brilliant way compared to the residual surface after ion etching [18].

7.6 3D Information Using In Situ Ultramicrotomy

In 2004 the combination of ultramicrotomy and imaging in the low-vacuum mode of the ESEM was published in a landmark paper of Denk [16]. During the performance of this so-called serial block face scanning electron microscopy (SBEM) a sample is cut by a diamond knife and imaged with SEM resolution periodically. While each slice accumulates outside the field of investigation as debris, the block face is imaged after each cut. That is the reason why alignment is not necessary. This “slice and view” process delivers a stack of micrographs which offers the opportunity of 3D reconstructions of specimens. Prerequisite for this technique is a sliceable material, hard enough to avoid smearing and delivering sufficient contrast for imaging. Imaging is typically performed using BSE due to compositional contrast [1] since the surface of a cut sample is smooth and therefore shows no topographic contrast which may be exploited for imaging [17, 19].

This technique was invented for life science investigations, thus heavy metal-staining of tissues, performing techniques which are routine for transmission electron microscopy (TEM), is commonly used (see Fig. 7.6a) [20]. Since heavy metal-staining is also established in polymer microscopy [2, 3], this is the preparation of choice for polymer blends. Figure 7.6b shows a part of the blockface of an isotactic polypropylene (iPP) sample (modified with ethylene–propylene rubber, EPR) after a tensile test [17]. Nevertheless, some polymer specimens have an intrinsic compositional contrast like talcum-filled polypropylene (see Fig. 7.6c, [21]) also allowing the investigation without preparation aside from trimming, pre-cutting with a conventional microtome and glueing of the native material on the specimen holder.

Figure 7.6d shows an embedded polyethersulfone membrane which could be imaged without complicated chemical pre-treatment since the polymer has a higher mean atomic number compared to the resin leading to sufficient compositional contrast [22]. However, there are rare situations when the topographic contrast of SE can be used. In Fig. 7.6e the interface of wood and a homogenous polymer can be seen [17]. In [23] contrast enhancement by staining for BSE-imaging was not sufficient so the simultaneously stored stack of SE images of a resin-embedded hyper-cross-linked poly(styrene–divinylbenzene) monolith was used for 3D reconstruction. In Fig. 7.6f one of the SE images of the stack can be seen.

In the flow diagram of Fig. 7.7 the whole process of in situ ultramicrotomy is sketched. All steps from the embedding of the specimen to final data analysis coming from 3D reconstructions are outlined. The schematic shows a prototype in situ ultramicrotome 3View from Gatan (Pleasanton, CA) attached to an ESEM Quanta 600 FEG instrument (FEI, Eindhoven, The Netherlands). As a

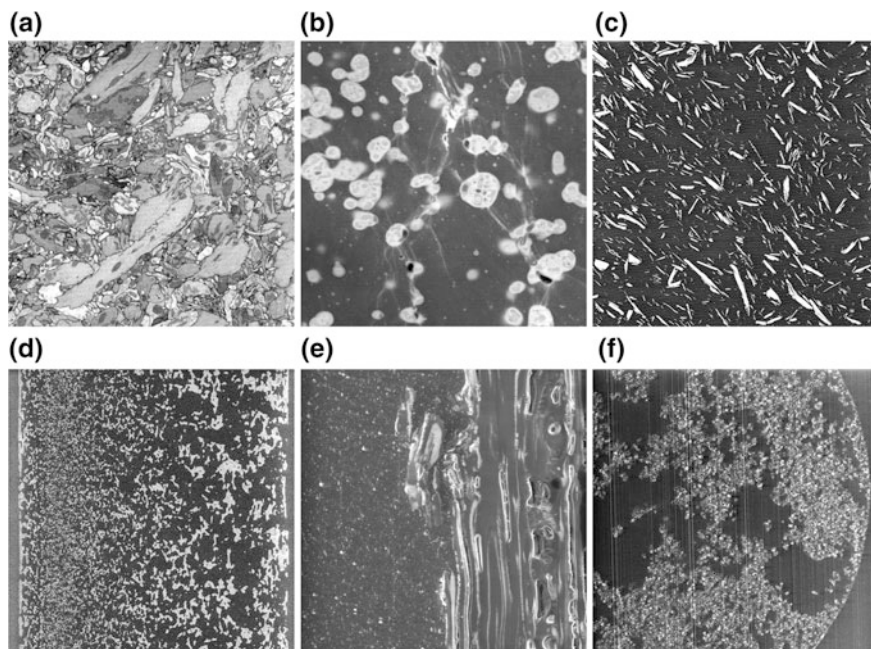


Fig. 7.6 Sample surfaces for SBEM: heavy metal-stained tissue of locust's retina (a); heavy metal-stained iPP/EPR blend (b); intrinsic compositional contrast of the blockface of talcum-filled polypropylene (c); embedded polyethersulfone membrane (d); interface of wood and ABS (e); resin-embedded hyper-cross-linked poly(styrene–divinylbenzene) monolith (f) (Fig. 7.6a–d; imaged with BSE, Fig. 7.6e, f imaged with SE; image widths 25 μm (a), 20.5 μm (b), 76 μm (c), 155 μm (d), 120 μm (e), 60.5 μm (f))

representative example the steps during the investigation of a hyper-crosslinked poly(styrene–divinylbenzene) (PS–DVB) monolith are sketched [24].

The photograph of step 1 shows the polyimide-coated capillary containing the monolith. The capillary has an outer diameter of about 365 μm and an inner diameter of about 100 μm . The inner tube contains the polymer (the diameter of the capillary is compared with the margin of a Euro coin) and the graphic shows the specimen being embedded in resin. Embedding is required for the stabilisation of the specimen and may be preceded or followed by chemical pre-treatment for contrast enhancement. Step 2 documents the application of conventional microtomy. The embedded specimen has to be trimmed to an appropriate geometry, typically a cuboid with a size of about $0.6 \times 0.6 \times 0.6 \text{ mm}^3$, which is then glued onto a rivet using superglue. The rivet is a single-use specimen holder made of aluminium. This rivet is then screwed into a specimen holder which can be aligned orthogonally to the axis of the rivet. Then pre-cutting of the specimen has to be performed with a conventional microtome equipped with a diamond knife. The specimen holder with rivet and glued specimen is mounted in the in situ ultramicrotome (step 3) where the alignment of the holder relative to the knife position and

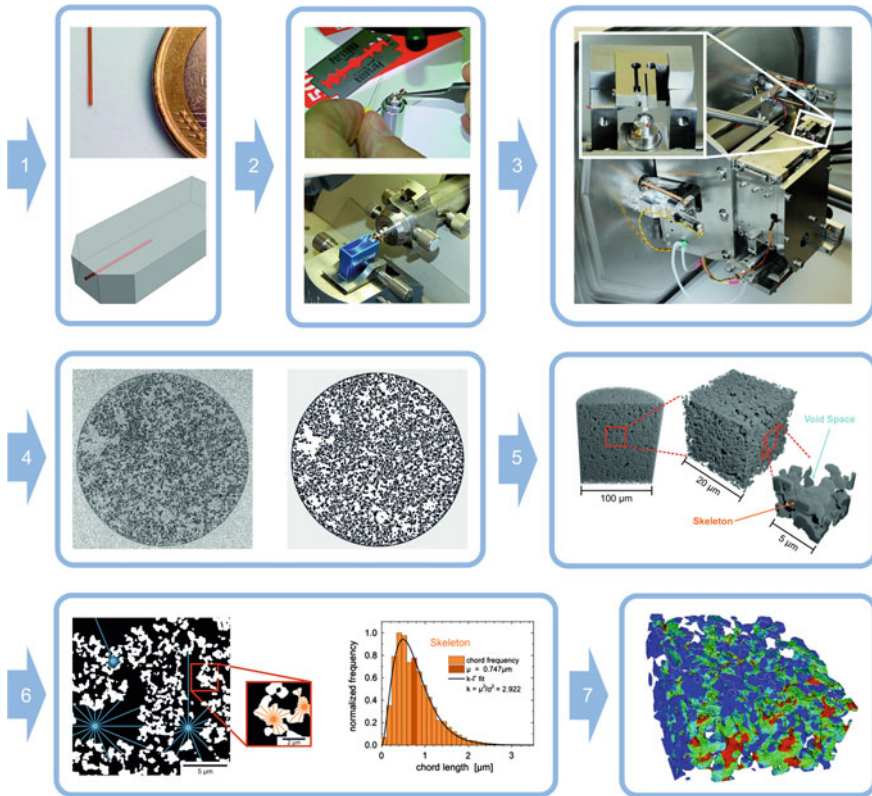


Fig. 7.7 Serial block face scanning electron microscopy (SBEM). *Step 1* polymer monolith sample (size compared with margin of coin), monolith embedded in resin; *step 2* glueing a trimmed sample on a rivet, pre-cutting with diamond knife of conventional microtomy; *step 3* mounting of the specimen holder in the in situ ultramicrotome; *step 4* acquisition of micrographs and image processing; *step 5* 3D reconstruction; *step 6* application of special mathematics (here CLD) on the data and resulting distribution of chord lengths; *step 7* simulation of the stress distribution in the material

the optical axis of the electron microscope has to be done. The photograph shows the built in holder and a small diamond knife coming from the side.

In step 4 the specimen is imaged by the electron microscope and further steps of image processing follow like filtering, digital alignment, binarisation etc. A stack of post processed images can be used for 3D reconstructions (step 5) leading to a better insight into a specimen, here resolving the skeleton structure of the material. Step 6 shows the ability of data analysis by applying special mathematical tools. A chord length distribution (CLD) was applied giving information about the skeleton and void space size and homogeneity in the material [24]. Furthermore step 7 symbolises the possibility of doing simulations using the 3D data gained from this technique. The picture shows the three-dimensional stress distribution in the material.

In situ ultramicrotomy was invented for life science investigations but recently some papers concerning applications in materials science were published [25–27]. This rather new technique enables the analysis of different properties. It reveals e.g. the steric distribution and orientation of filler particles in a matrix, the quality of an interface between several phases or paves the way to predictions of mechanical behaviour via computer simulations. In the context of fracture analysis it enables a 3D investigation of samples after mechanical treatment. In [17] this was demonstrated for the first time by investigating an EPR-modified PP specimen. The staining of the material revealed the heterogeneous material and additionally showed the location of cracks relative to different structures like the filler particles etc. So a new 3D fractography (compare the article “3D reconstruction of cracks in polymers—New insight into the fracture behaviour?” in this book) can be established, which can be enriched with mechanical simulations additionally resulting from this method.

7.7 Conclusions

The scanning electron microscope (SEM) is a highly versatile tool for the morphological characterisation of polymers, bridging the gap between light microscopy, where large dimensions are measured at a low resolution, and high-resolution techniques like AFM and TEM. Technical improvements, new preparation methods and new investigation approaches are still developed and will lead to a wealth of new information about polymeric materials especially in the field of fracture analysis.

The low-voltage mode of the conventional scanning electron microscope was discussed enabling surface characterisation of specimens without a preceding coating step delivering good surface resolution. Another mode for the characterisation of a surface without the need of preparation steps is the low-vacuum mode of the environmental scanning electron microscope where dual imaging with SE and BSE can be done offering topographic and compositional contrast. This enables uncomplicated fractography and specimen characterisation. As a recent application of this mode in situ investigations are discussed, where an alteration of a specimen (e.g. during tensile testing) can be performed and monitored simultaneously using SE and BSE for imaging. Fundamental for this mode is the different vacuum (i.e. low vacuum) compared to the high vacuum of conventional SEM. However there is a further mode, the ESEM mode, which enables the investigation of wet specimens. Here condensation processes and the wetting and drying behaviour of materials can be studied additionally combining this property with in situ mechanical testing. Finally in situ ultramicrotomy was discussed which can serve for the characterisation of materials and further delivers the starting point for computer simulations concerning different material properties and e.g. predicting its mechanical behaviour.

Acknowledgements The authors would like to thank Margit Wallner for graphical support and Manuel Paller for drawing the schematic of Fig. 7.3. We are grateful to G. Leitinger from the Medical University Graz, Austria, for image courtesy of Fig. 7.6a (tissue of the retina of an insect).

References

1. Goldstein, J.I., Newbury, D.E., Echlin, P., Joy, D.C., Lyman, C.E., Lifshin, E., Sawyer, L., Michael, J.R.: Scanning Electron Microscopy and X-Ray Microanalysis, 3rd edn. Kluwer Academic/Plenum Publishers, New York (2003)
2. Michler, G.H.: Electron Microscopy of Polymers. Springer, Berlin (2008)
3. Sawyer, L.C., Grubb, D.T., Meyers, G.F.: Polymer Microscopy, 3rd edn. Springer, New York (2008)
4. Danilatos, G.D.: Foundations of environmental scanning electron microscopy. *Advan. Electron. Electron Phys.* **71**, 109–250 (1988)
5. Stokes, D.J.: Principles and Practice of Variable Pressure/Environmental Scanning Electron Microscopy (VP-ESEM). Wiley, Chichester (2008)
6. Reimer, L.: Image Formation in Low-Voltage Scanning Electron Microscopy. SPIE-Press, Bellingham, Washington (1993)
7. Joy, D.C., Joy, C.S.: Low voltage scanning electron microscopy. *Micron* **27**, 247–263 (1996)
8. Fischer, W.J., Zankel, A., Ganser, C., Schmied, F., Schroettner, H., Hirn, U., Teichert, C., Bauer, W., Schennach, R.: Imaging of the formerly bonded area of individual fibre to fibre joints with SEM and AFM. *Cellulose* **21**, 251–260 (2014)
9. Nase, M., Zankel, A., Langer, B., Baumann, H.-J., Grellmann, W., Poelt, P.: Investigation of the peel behavior of polyethylene/polybutene-1 peel films using in situ peel tests with environmental scanning electron microscopy. *Polymer* **49**, 5458–5466 (2008)
10. Grellmann, W., Seidler, S. (eds.): Polymer Testing, 2nd edn. Carl Hanser, Munich (2013)
11. Zankel, A., Chernev, B.S., Brandl, C., Poelt, P., Wilhelm, P., Nase, M., Langer, B., Grellmann, W., Baumann, H.J.: Assessment of beam damage in polymers caused by in situ ESEM analysis using IR spectroscopy. *Macromol. Symp.* **265**, 156–165 (2008)
12. Schoßig, M., Zankel, A., Bierögel, C., Pölt, P., Grellmann, W.: ESEM investigations for assessment of damage kinetics of short glass fibre reinforced thermoplastics—Results of in situ tensile tests coupled with acoustic emission analysis. *Compos. Sci. Technol.* **71**, 257–265 (2011)
13. Reingruber, H., Zankel, A., Mayrhofer, C., Poelt, P.: A new in situ method for the characterization of membranes in a wet state in the environmental scanning electron microscope. *J. Membr. Sci.* **399**, 86–94 (2012)
14. Egerton, R.F., Li, P., Maláč, M.: Radiation damage in the TEM and SEM. *Micron* **35**, 399–409 (2004)
15. Kitching, S., Donald, A.M.: Beam damage of polypropylene in the environmental scanning electron microscope: an FTIR study. *J. Microsc.* **190**, 357–365 (1998)
16. Denk, W., Horstmann, H.: Serial block-face scanning electron microscopy to reconstruct three-dimensional tissue nanostructure. *PLoS Biol.* **2**, 1900–1909 (2004)
17. Zankel, A., Kraus, B., Poelt, P., Schaffer, M., Ingolic, E.: Ultramicrotomy in the ESEM, a versatile method for materials and life sciences. *J. Microsc.* **233**, 140–148 (2009)
18. Piller, M., Neubauer, C.: Entwicklung einer neuartigen Methode zur Oberflächenätzung von Polymeren unter der Verwendung des “beam-damage” eines Elektronenmikroskopes. Projektarbeit, Chemie-Ingenieurschule Graz, Graz (2010)
19. Zankel, A., Wagner, J., Poelt, P.: Serial sectioning methods for 3D investigations in materials science. *Micron* **62**, 66–78 (2014)

20. Wernitznig, S., Rind, F.C., Poelt, P., Zankel, A., Pritz, E., Kolb, D., Bock, E., Leitinger, G.: Synaptic connections of first-stage visual neurons in the locust *Schistocerca gregaria* extend evolution of tetrad synapses back 200 million years. *J. Comp. Neurol.* **523**, 298–312 (2015)
21. Koch, T., Salaberger, D., Zankel, A., Reingruber, H., Steiger-Thirsfeld, A., Voronko, Y., Seidler, S.: Methods for characterizing the 3-D morphology of polymer composites. *Macromol. Symp.* **315**, 115–124 (2012)
22. Reingruber, H., Zankel, A., Mayrhofer, C., Poelt, P.: Quantitative characterization of micro-filtration membranes by 3D reconstruction. *J. Membr. Sci.* **372**, 66–74 (2011)
23. Müllner, T., Zankel, A., Mayrhofer, C., Reingruber, H., Hoeltzel, A., Lv, Y., Svec, F., Tallarek, U.: Reconstruction and characterization of a polymer-based monolithic stationary phase using serial block-face scanning electron microscopy. *Langmuir* **28**, 16733–16737 (2012)
24. Müllner, T., Zankel, A., Svec, F., Tallarek, U.: Finite-size effects in the 3D reconstruction and morphological analysis of porous polymers. *Mater. Today* **17**, 404–411 (2014)
25. Hashimoto, T., Curioni, M., Zhou, X., Mancuso, J., Skeldon, P., Thompson, G.E.: Investigation of dealloying by ultra-high-resolution nanotomography. *Surf. Interface Anal.* **45**, 1548–1552 (2013)
26. Koku, H., Maier, R.S., Czymmek, K.J., Schure, M.R., Lenhoff, A.M.: Modeling of flow in a polymeric chromatographic monolith. *J. Chromatogr. A* **1218**, 3466–3475 (2011)
27. Trueman, A., Knight, S., Colwell, J., Hashimoto, T., Carr, J., Skeldon, P., Thompson, G.: 3-D tomography by automated in situ block face ultramicrotome imaging using an FEG-SEM to study complex corrosion protective paint coatings. *Corros. Sci.* **75**, 376–385 (2013)

Chapter 8

3D Reconstruction of Cracks in Polymers—New Insight into the Fracture Behaviour?

M. Nachtnebel, A. Zankel, C. Mayrhofer, M. Gahleitner and P. Pölt

Abstract The fracture behaviour of ethylene–propylene rubber (EPR) and linear low-density polyethylene (PE-LLD)-modified polypropylene was investigated. Most interpretations of the fracture behaviour of such polymers are based on results gained from completely fractured samples. To gain deeper insight into the fracture mechanisms the focus was put on the very early stages of the fracturing process. For this purpose tensile tests of the samples were stopped at predefined forces far below the yield. Subsequently 3D reconstructions of the already damaged regions were performed, using serial block-face scanning electron microscopy to get the image stacks. In a comprehensive discussion of the sample preparation the limitations of this method are disclosed. The EPR- and PE-LLD-modified samples showed completely different fracture behaviour, at least at the crack initiation and at low stresses. The results also seem to prove that the interparticle distance is a decisive parameter in the interpretation of the results.

8.1 Introduction

The fracture of polymers, especially of polypropylene (PP), is an already widely investigated topic. By far the majority of these investigations is however based upon parameters and characteristics resulting from mechanical tests, e.g. stress–strain diagrams from tensile tests. These bulk parameters necessarily yield only partly correct information in case of the mostly multi-phase PP materials [1] used in technical applications of this polymer family, i.e. the applications where fracture processes are of highest interest. Additional information can be gained from micrographs recorded from the fracture surfaces by light and electron microscopy. But all these experiments and results provide only limited insight into what is

M. Nachtnebel (✉) · A. Zankel · C. Mayrhofer · P. Pölt
Institute for Electron Microscopy and Nanoanalysis, Graz University of Technology,
Graz, Austria

M. Gahleitner
Borealis GmbH, Linz, Austria

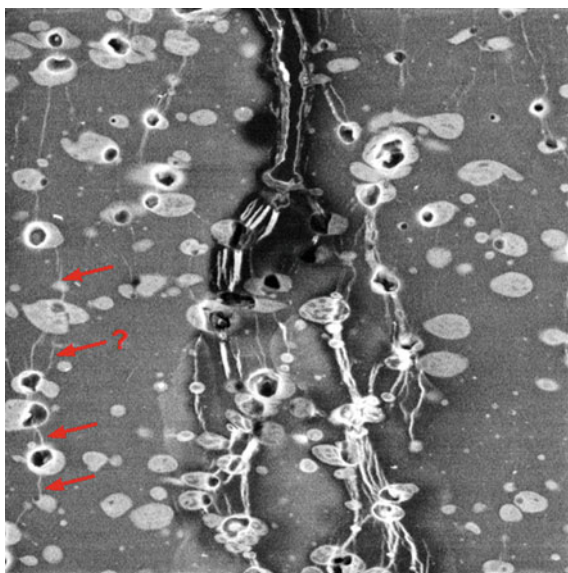
happening in the material during the tests themselves at a microscopic length scale. It was therefore of interest to study fracture processes “in vivo”, a task which has proven difficult in the past [2].

Performing such experiments in a microscope and observing the microstructures developing at the crack tip or at the surface of the specimen at high magnification might be one possibility to overcome this obstacle [3, 4]. Additionally the combination of mechanical tests with other methods like acoustic emission analysis can help to elucidate some of the micromechanical processes [5].

But even this does not give information about the structures forming in the bulk of the specimen during the tests. To this aim tensile tests were stopped at a pre-defined force. Subsequently the specimens were removed from the stage and sectioned by ultramicrotomy. Although some relaxation will take place in the material, the cracks already formed will not heal. In fact it will often be a matter of crazes, but at the magnifications used fibrillation, even if present, cannot be detected. Thus a clear-cut classification is not possible and therefore in what follows always the term crack is used.

However, from a single image a clear-cut determination of the length of the cracks is not possible. In the scanning electron microscopy (SEM) image of a cross-section of a sample that underwent a tensile test (Fig. 8.1) the cracks which are marked by arrows could either be individual disjointed cracks stopping at the EPR particles, or they could be parts of a single crack encompassing the particles. And, of course, from a single image the calculation of neither the area of the fracture face nor its texture and roughness is possible. Since these are vital parameters which can help to assess the energy necessary for the creation of the cracks and to gain knowledge about the fracture behaviour at the microscale, 3D reconstructions of the fracture region are imperative.

Fig. 8.1 SEM image of a cross-section of isotactic PP (MFR [melt flow rate] 10)/EPR (ethylene-propylene rubber (17 wt% rubber), MFR 4.8); tensile test stopped at around 25% yield (image width: 47 μm)



8.2 Preparation and Image Processing

Isotactic polypropylene (iPP) samples modified with either ethylene-propylene rubber (EPR) or linear low-density polyethylene (PE-LLD) particles of different sizes were subjected to a tensile test, with the test stopped at a predefined force, around 25% yield for the results presented here. Notched samples were used and immediately before the tensile test (test speed: 1 mm/min) they were additionally precracked with a razor blade (depth: 0.5 mm). After the removal of the samples from the tensile stage a part of the fracture region was extracted and stained in RuO₄. Thereafter automated slicing and imaging of the fracture region was performed by use of the in situ ultramicrotome 3View[®] (Gatan, Pleasanton, CA) mounted in an environmental scanning electron microscope (ESEM) Quanta FEG 600 (FEI, Eindhoven, NL). The slice thickness was 100 nm. As always the block face is imaged, all the images are already aligned. Finally the resulting stack of images was used for the 3D reconstructions of the fracture faces and particles

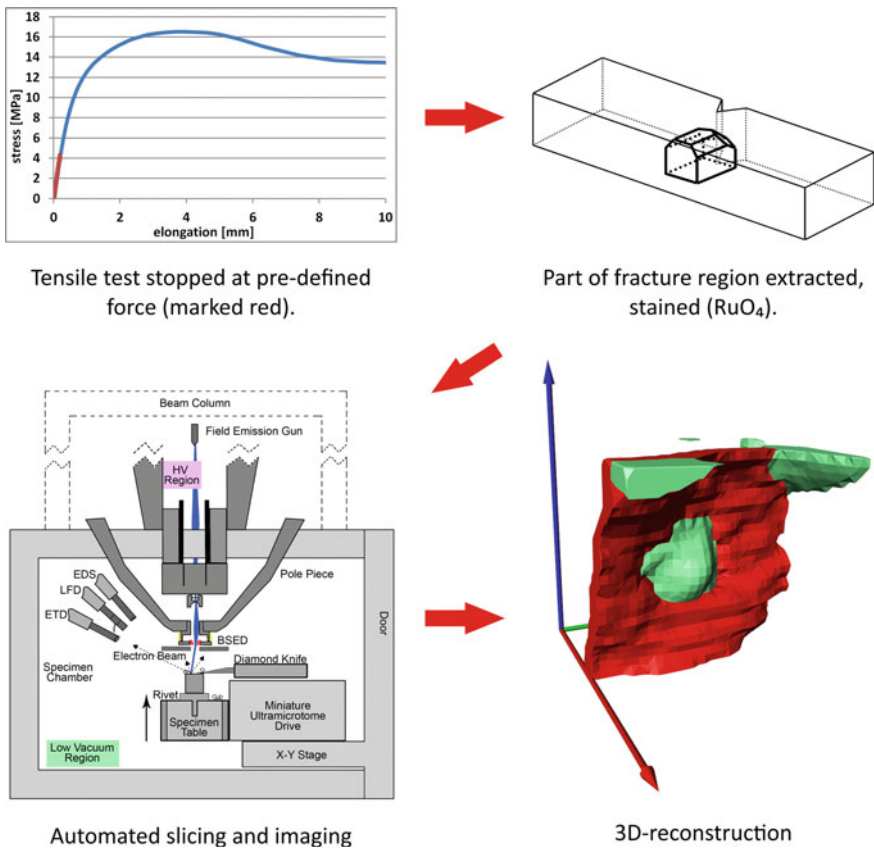


Fig. 8.2 Schematic representation of the steps leading to the 3D reconstruction

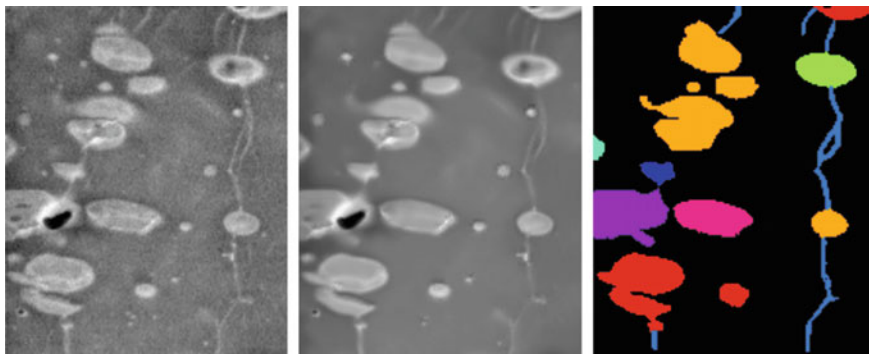


Fig. 8.3 SEM image of a cross-section of iPP (MFR 10)/EPR (17 wt% rubber), MFR 4.8; tensile test stopped at around 25% yield (image width: 13.6 μm) (*left*). The same image after application of a non-local mean (NLM) filter (*centre*). Binary image after thresholding and searching for connected regions in the whole image stack. Regions which are in immediate neighbourhood and bear the same colour belong in the 3D reconstruction to the same particle (*right*)

(Software: Avizo Fire 7.1, FEI, Eindhoven, NL). A schematic representation of the whole procedure can be found in Fig. 8.2.

Before the 3D reconstruction could take place noise filtering and image segmentation had to be performed, as is demonstrated in Fig. 8.3. For noise removal a non-local mean (NLM) filter was used. It is based on a non-local averaging of all pixels in the image [6]. Subsequently thresholding was carried out using the segmentation algorithm “Connected Components”. This routine searches for connected three dimensional regions in the grey level images of the whole image stack within predefined intensity ranges. Some of the features visible in the image in the centre of Fig. 8.3 were excluded because their 3D volume was below a predefined value. After the segmentation into different regions these regions had to be manually assigned to the corresponding components (particle, crack and polypropylene matrix). This finally enables the 3D reconstruction, even if it represents some simplification with respect to the internal structure of EPR particles [7]. All the necessary algorithms were provided by the software Avizo itself.

To be able to get a reliable 3D reconstruction without too much manual intervention, a sufficiently great difference in the brightness of the individual components is necessary. Figure 8.3 shows that this can pose a problem especially in the case of very fine cracks.

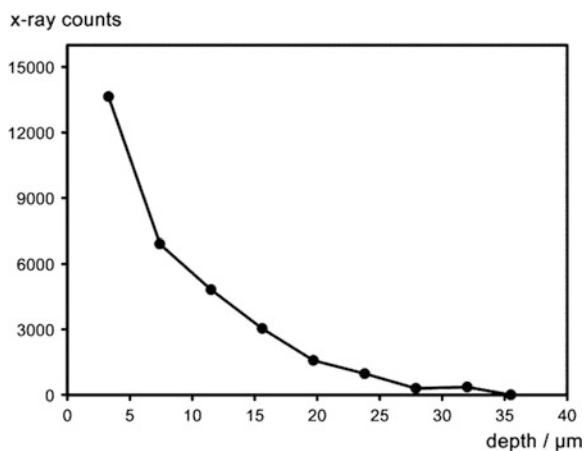
8.3 Results and Discussion

Without staining of the polymer sample it is impossible to differentiate in the SEM images between the EPR or PE-LLD particles and the polypropylene matrix. At least in case of polypropylene staining additionally causes a hardening of the

material. Thus the need for cooling the material below the glass transition temperature during slicing with the ultramicrotome can be avoided. Unfortunately, however, the staining medium penetrates the sample only to a limited depth, restricting the size of the volume which can be reconstructed. In case of polypropylene stained with RuO_4 this depth is around $30\ \mu\text{m}$. For estimating the staining depth samples were cross-sectioned after staining and subsequently the decrease of the ruthenium concentration as a function of depth was measured by Energy-Dispersive X-ray Spectrometry (EDS, see Fig. 8.4). With the decrease of the Ru concentration both the contrast between matrix and particles and the sample hardness decrease. This is at least partially compensated by the fact that electron irradiation of these materials causes crosslinking of the molecular chains and thus hardening of the material. It also seems to act differently on matrix and EPR particles [8].

But for some polymers, e.g. poly(ethylene terephthalate), the penetration depth of the stain is rather in the sub-micrometre range [9]. Another problem often met is the already mentioned damage soft materials generally experience when they are irradiated by electrons during imaging in the SEM, even at well-stained regions. This may be tackled by cooling of the specimens, but this is not yet implemented at the 3View[®] microtome. Both problems could be avoided by use of an atomic force microscope (AFM) coupled with a cryo-ultramicrotome [10–12]. Furthermore, if the second component of a blend contains an element of an atomic number higher than that of oxygen, staining would not be necessary. Also X-ray tomography might be an alternative, if the density differences between the polymer components are big enough to give sufficient contrast (see e.g. the work of Kosek et al. [13]). A limitation of X-ray tomography is the rather poor resolution of most laboratory size instruments. The best resolution attainable is around $50\ \text{nm}$. If better resolution or contrast is required the use of an instrument attached to a synchrotron might be necessary. But in case of high X-ray intensities also specimen damage may occur. However, for example for glass fibre-reinforced polymers, which cannot be cut by

Fig. 8.4 Sample of iPP, stained with RuO_4 . EDS measurements: X-ray counts of the RuL X-ray line as a function of the depth at the cross-section. Depth 0 corresponds to the surface of the sample



an ultramicrotome, this is the only possible choice. X-ray tomography may also be well suited for polymers with inorganic filler particles of an appropriate size [14]. Serial sectioning by focused ion beams (FIB) is not really advisable, because fine cracks could be closed due to both irradiation damage and redeposition of sputtered material.

In the images of both Figs. 8.1 and 8.3 many cracks are visible, although they were recorded from samples which were only tested to a maximum force of around 25% yield. Thus it was investigated, whether any steps during the preparation, for example the precracking with the razor blade or the cutting with the ultramicrotome, could have created these cracks or at least the majority of them. To this aim two samples were prepared in completely the same way and from the same region of the samples, but whereas the first sample did not undergo a tensile test, the second sample was subjected to a test, with the test stopped at a force of around 25% yield. In the image of the untested sample nearly no cracks are visible, whereas in the tested sample many cracks appear, with some of the cracks even lying beyond the boundaries of the image (Fig. 8.5). In each case several TEM lamellae (TEM—transmission electron microscopy) were cut and investigated. Occasionally even at lamellae from the untested sample a few cracks appeared, but concentrated close to

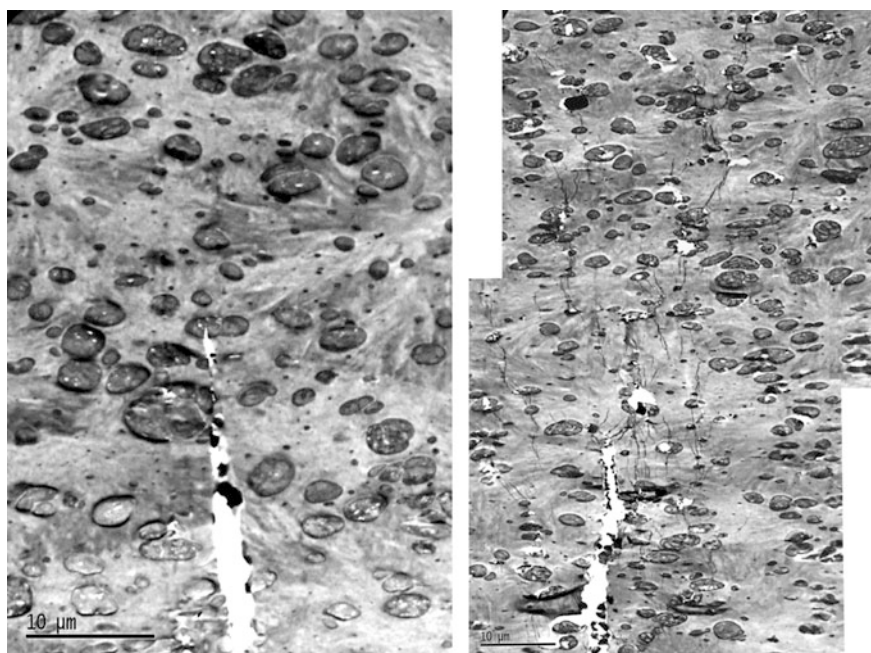


Fig. 8.5 TEM images of lamellae of iPP (MFR 10)/EPR (17 wt% rubber), MFR 4.8, precracked with a razor blade. No tensile test performed (image width: 34.7 μm) (*left*). Tensile test stopped at 25% yield (image width: 53.2 μm). The bright wedge-shaped structures visible in the lower region are the precracks (*right*)

the tip of the precrack at a much smaller area than even in case of a sample undergoing a tensile test which was stopped at a force of 7% yield. Thus, at least for various types of EPR-modified polypropylene, crack formation seems to start at rather small forces, far below the yield.

In Fig. 8.6 the force–elongation characteristics of two iPP samples, one of them modified with EPR and the other one with PE-LLD particles, can be found. The TEM images at the right should give a rough impression of the size and the distribution of the particles. The percentage of weight of the particles was in both cases around 20%.

In Fig. 8.7 the 3D reconstructions of both the fracture faces of an EPR-modified sample and of the same fracture faces with additionally the EPR particles are

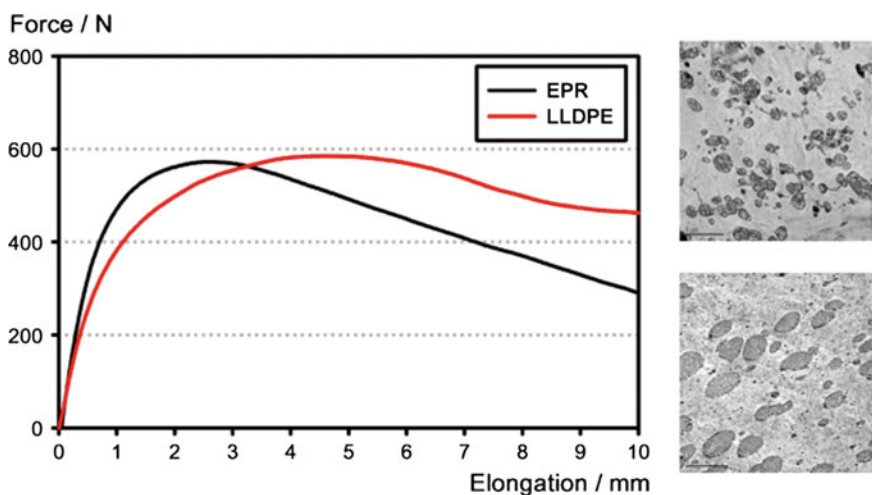


Fig. 8.6 Force–elongation characteristics of iPP samples (test speed: 1 mm/min). EPR: iPP (MFR 10)/EPR (20 wt%), MFR: 2.3; PE-LLD: iPP (MFI 8)/PE-LLD (20 wt%) (*left*). TEM images (image width: 24 μm) showing the size and distribution of the EPR (*top*) and the PE-LLD (*bottom*) particles in the matrix (*right*)

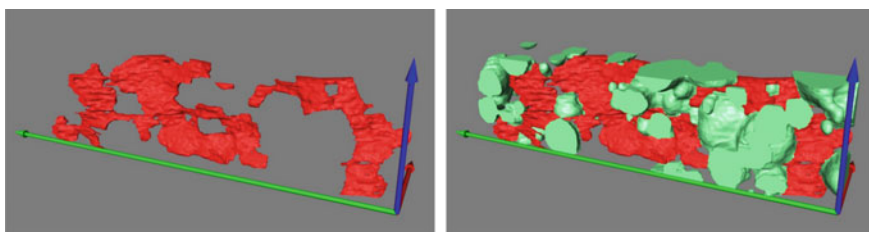
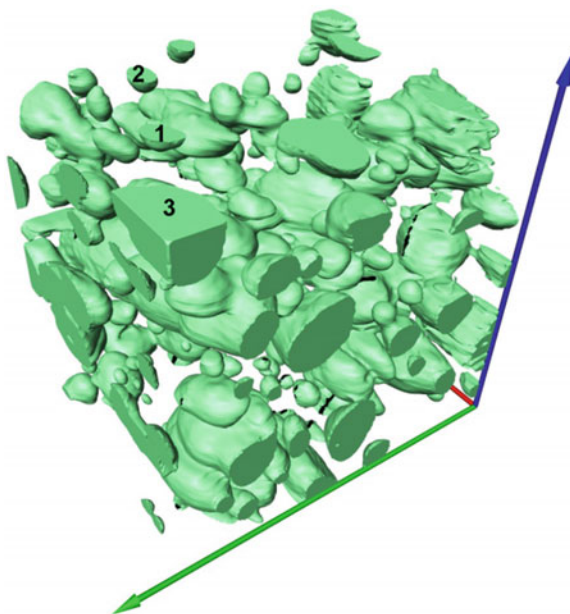


Fig. 8.7 3D reconstruction of cracks (*left*) and the same cracks including the EPR particles (*right*) of iPP (MFR 10)/EPR (17 wt% rubber), MFR 4.8, tensile test stopped at around 25% yield (reconstructed volume: $4 \times 21 \times 6 \mu\text{m}^3$, voxel size: $94 \times 94 \times 100 \text{ nm}^3$)

represented. It is clearly visible that some of the particles are encircled by cracks, whereas at other particles the cracks seem to stop. Very often one fracture surface seems to encompass several EPR particles. It is conspicuous that the distance between these particles is often smaller than the sum of their average diameters. At particles stress concentration occurs if the particle is softer than the matrix and if the ratio of the shear moduli of particle and matrix is smaller one [15, 16]. The stress concentration decreases rapidly with increasing distance from the particles and goes down to zero at approximately a distance of the particle diameter. Hence, if two particles are close together the strong stress concentration between them might initiate a crack, causes stress relaxation and thus prohibits further crack propagation. Thus a decisive parameter is the distribution of the nearest neighbour distances of the particles. But as Fig. 8.8 demonstrates, a reliable distribution can only be calculated from a 3D reconstruction. The nearest neighbour of particle 1 is not particle 2 or particle 3 from the same cross-section, but a particle below that area.

The samples modified with PE-LLD particles show, compared to the EPR-modified samples, a completely different behaviour concerning the formation of cracks. This can already be seen in the force–elongation curves of Fig. 8.6 (bulk parameters), but in more detail in Fig. 8.9. In both cases the tensile test was stopped at around the same force and at the same percentage of their yield. In the EPR-modified sample long cracks appear, with a large lateral spread. On the contrary only very fine cracks concentrated in a narrow region around the direction of crack propagation are visible in the cross-section of the sample with PE-LLD as impact modifier particles. However, in the two materials not only the type of the

Fig. 8.8 3D reconstruction of the EPR particles in the sample iPP (MFR 10)/EPR (17 wt% rubber), MFR 4.8 (reconstructed volume: $13 \times 17 \times 16 \mu\text{m}^3$)



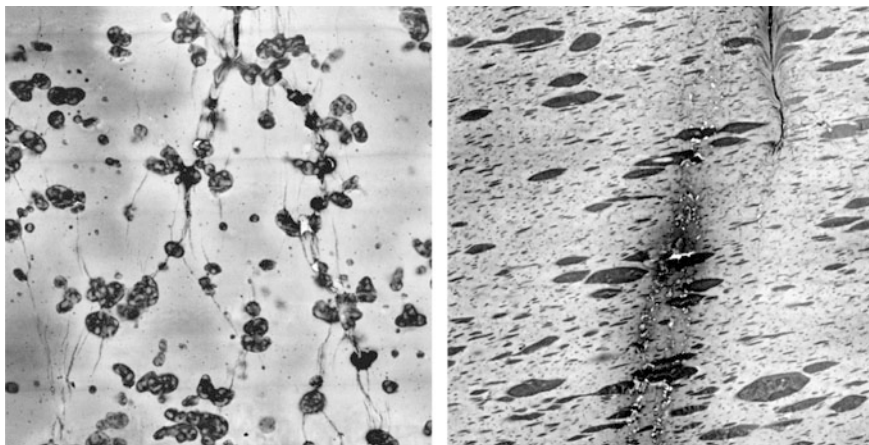


Fig. 8.9 SEM images (contrast inversion, image width: 32.2 μm) of cross-sections of 2 different samples after a tensile test. iPP (MFR 10)/EPR (17 wt% rubber), MFR 4.8, maximum force: 143 N (*left*); iPP (MFI 8)/PE-LLD (20 wt%), maximum force: 146 N. The tail of the precrack is visible at the upper boundary of the images (*right*)

particles, but also the particle size distribution is different. Thus it is difficult to figure out which of both is mainly responsible for the differences observed in the crack propagation.

Though, in addition to Fig. 8.7 also both images in Fig. 8.9 confirm that cracks propagate predominantly along paths with the shortest distances between the particles. Thus, for these materials not the average particle distance is a decisive parameter determining the crack propagation, but rather the half width of the particle distance distribution.

The reconstruction of large volume is necessary to enable better statistics concerning the determination of parameters like the area of the fracture faces, the number of EPR particles connected with individual cracks and the distribution of nearest neighbour distances. This can be very time-consuming, but new instruments optimised especially for the serial sectioning and imaging, which is the decisive step in creating the image stacks, will in future reduce the expenditure of time considerably [17, 18].

8.4 Conclusion

The current results demonstrate that 3D reconstructions of both the distribution of the filler particles and the fracture faces in polymers performed after mechanical testing might be a useful tool to gain deeper insight into the fracture mechanisms on a microscopic length scale. Especially if tensile tests are stopped at forces far below the yield it is possible to study crack formation, for example where the very first

cracks start, where they stop, how they propagate and how cracks and impact modifier resp. filler particles are connected to each other. Also the area and structure of the fracture faces can be determined. In case of polymer blends this method is restricted to materials which can be stained to a sufficient depth. No such limitations exist for materials consisting of inorganic particles in a homogeneous polymer matrix, which is brittle enough that it can be cut by an ultramicrotome at room temperature. Other problems often encountered are due to irradiation damage during image recording. As irradiation damage increases with increasing magnification, it limits mainly the size of the smallest structures that can be imaged.

References

1. Gahleitner, M., Doshev, P., Tranninger, C.: Heterophasic copolymers of polypropylene: development, design principles and future challenges. *J. Appl. Polym. Sci.* **130**, 3028–3037 (2013)
2. Kim, G.-M., Michler, G.H., Gahleitner, M., Mühlhaupt, R.: Influence of morphology on the toughening mechanisms of polypropylene modified with core–shell particles derived from thermoplastic elastomers. *Polym. Adv. Technol.* **9**, 709–715 (1998)
3. Poelt, P., Zankel, A., Gahleitner, M., Ingolic, E., Grein, C.: Tensile tests in the environmental scanning electron microscope (ESEM)—Part I: Polypropylene homopolymers. *Polymer* **51**, 3203–3212 (2010)
4. Zheng, Y., Shen, Z., Wang, M., Ma, S., Xing, Y.: In situ observation of plerosphere/polypropylene composites in the tensile test. *J. Appl. Polym. Sci.* **106**, 3736–3742 (2007)
5. Schofig, M., Zankel, A., Bierögel, C., Pölt, P., Grellmann, W.: ESEM investigations for assessment of damage kinetics of short glass fibre reinforced thermoplastics—Results of in situ tensile tests coupled with acoustic emission analysis. *Compos. Sci. Technol.* **71**, 257–265 (2011)
6. Buades, A., Coll, B., Morel, J.M.: A non-local algorithm for image denoising. In: Proceedings of the International Conference Computer Vision and Pattern Recognition. San Diego (20–26.06.2005). San Diego (2005), Vol. 2, pp. 60–65
7. Qiu, B., Chen, F., Lin, Y., Shangguan, Y., Zheng, Q.: Control of multilayered core–shell dispersed particles in HPP/EPR/EbP blends and its influences on crystallization and dynamic mechanical behaviour. *Polymer* **55**, 6176–6185 (2014)
8. Zankel, A., Kraus, B., Poelt, P., Schaffer, M., Ingolic, E.: Ultramicrotomy in the ESEM, a versatile method for materials and life sciences. *J. Microsc.* **233**, 140–148 (2009)
9. Haubruge, H.G., Jonas, A.M., Legras, R.: Staining of poly(ethylene terephthalate) by ruthenium tetroxide. *Polymer* **44**, 3229–3234 (2003)
10. Efimov, A.E., Gnaegi, H., Schaller, R., Grogger, W., Hofer, F., Matsko, N.: Analysis of native structures of soft materials by cryo scanning probe tomography. *Soft Matter* **8**, 9756–9760 (2012)
11. Alekseev, A., Efimov, A., Loos, J., Matsko, N., Syurik, J.: Three-dimensional imaging of polymer materials by scanning probe tomography. *Eur. Polym. J.* **52**, 154–165 (2014)
12. Zankel, A., Wagner, J., Poelt, P.: Serial sectioning methods for 3D investigations in materials science. *Micron* **62**, 66–78 (2014)
13. Zubov, A., Pechackova, L., Seda, L., Bobak, M., Kosek, J.: Transport and reaction in reconstructed porous polypropylene particles: model validation. *Chem. Eng. Sci.* **65**, 2361–2372 (2010)

14. Koch, T., Salaberger, D., Zankel, A., Reingruber, H., Steiger-Thirnsfeld, A., Voronko, Y., Seidler, S.: Methods for characterizing the 3-D morphology of polymer composites. *Macromol. Symp.* **315**, 115–124 (2012)
15. Michler, G.H., Baltá-Calleja, F.J.: *Nano- and Micromechanics of Polymers: Structure Modification and Improvement of Properties*, pp. 165–174. Munich, Carl Hanser (2012)
16. Liang, J.Z., Wang, L.: Particle interaction effects on interfacial stress in extension of rubber-toughened polypropylene. *Polym. Plast. Technol. Eng.* **48**, 1282–1286 (2009)
17. Marx, V.: Brain mapping in high resolution. *Nature* **503**, 147–152 (2013)
18. Keller, A.L., Zeidler, D., Kemen, T.: High throughput data acquisition with a multi-beam SEM. In: Postek, M.T., Newbury, D.E., Platek, S.F., Maugel, T.K. (eds.) *Proceedings of SPIE 9236: Scanning Microscopies 2014*. (2014), Paper. 92360B

Chapter 9

Determination of the Stable Crack Growth by Means of the Fluorescence Adsorption-Contrast Method (3D-FAC Method)

M. Kroll, B. Langer and W. Grellmann

Abstract The aim of this study was to develop new opportunities to measure crack resistance curves at conditions of high ductility of reinforced polyamide 6 (PA6) compounds with high glass fibre content. The addition of toughening modifiers in glass fibre-reinforced compounds, the hygroscopic behaviour of polyamides as well as raised temperatures limit the validity range of conventional toughness evaluation with the experimental methods of linear elastic fracture mechanics and the J -integral method. The determination of J -crack resistance (R)-curves is necessary for a complete toughness evaluation. The fluorescence dyeing technique showed to be an efficient, accurate and reliable method to enhance the measurement of stable crack growth portions on roughly structured fracture surfaces. Within the study a fractional factorial statistical design of experiments was used to prove the reliability and accuracy of the method. Fluorescence microscopy has its definite advantages compared to light microscopy or scanning electron microscopy (SEM) especially when it is applied by use of a 3D digital microscope with depth from defocus which was used for the study. Finally additional information about the toughness behaviour of highly reinforced PA6 compounds with different amounts of elastomeric modifier could be revealed by means of the newly developed fluorescence adsorption-contrast method (3D-FAC method).

M. Kroll (✉)
BASF Leuna GmbH, Leuna, Germany

B. Langer
Department of Engineering and Natural Sciences,
University of Applied Science Merseburg, Merseburg, Germany

W. Grellmann
Centre of Engineering, Martin Luther University Halle-Wittenberg,
Halle/Saale, Germany

9.1 Introduction

The deformation and fracture behaviour of PA6 materials was deeply analysed in case of unreinforced materials [1], glass fibre- and carbon fibre-reinforced materials [1–3], polymer blends with an elastomeric blend partner [1, 4–12] and so-called hybrid materials consisting of PA6, an elastomeric component and glass fibres [13–18]. There still is the necessity to investigate the fracture behaviour under conditions of stable crack propagation in compounds with high amounts of glass fibres. Different material properties and testing conditions make this essential. The most important ones are raised temperature and moisture content of the polyamide phase that alone or in combination promote ductile fracture behaviour with raising amounts of plastic deformation and stable crack growth even under conditions of impact loading [19]. On the basis of the J -integral approach of Rice [20], crack resistance (R) curves have been calculated in multi-specimen testing as well as with the help of well-established single specimen approximation approaches like the normalisation method, the load separation principle method or the elastic compliance method for many unreinforced and elastomer-modified polymers [3, 19, 21–24].

Even if a reliable and reproducible measurement of the J -value has been identified as potential scattering reason in a round robin for toughened polyamides [25], another problem of investigating stable crack propagation mechanisms in highly reinforced polyamide compounds is the difficulty of measurement of stable crack growth [3]. Several approaches have been used to characterise the fracture processes of polymers, if a conventional microscopic measurement of stable crack growth was not possible [2, 3, 26]. In previous studies concerning reinforced polyamides either the stable crack growth has been replaced through the indirect parameter of fracture time [2] or the measurement of the stable crack growth area was performed by use of the cut method [3]. These methods have proved to be effective to identify differences in the fracture behaviour of the compared materials in each case. But the objective still was to experimentally determine J -R-curves with the conventional method of relating the J -value of each specimen with the microscopically measured stable crack growth Δa after cryo-fracture. This multi-specimen approach is well-established and reliable and the measured values could be compared to many different polymers and composites that have been analysed in the past.

Therefore the aim of this study was to develop a reliable experimental procedure to directly measure the portion of stable crack growth on the fracture surface of highly reinforced polyamide 6 with inexpensive and easy-to-use laboratory equipment like this has been done before in case of unreinforced polymers by simply cryo-fracture the ligament and measure the portions of notch, stable crack growth, an eventual process zone and cryo-fracture area on the specimens fracture surface [19, 27].

As a promising technology fluorescence microscopy in combination with an emulsifiable penetration dye system was chosen to reach this objective. Despite excited emission fluorescence is a traditional but technological evolving technique in microscopic biotechnology [28, 29] and macroscopic failure observation [30], there are applications in the field of fracture process analysis e.g. an auspicious approach about the visualisation of crack-tip blunting by Samuel and Haque [31].

9.2 Experimental

9.2.1 Materials

The analysed materials were produced on a co-rotating twin screw extrusion machine. The matrix polymer PA6 is a commercial PA6 grade ULTRAMID[®] B27 from BASF [32]. The glass fibres that were incorporated within the reinforced materials are industrial E-glass fibres providing an optimised facing for the use in polyamides. The elastomeric polymer used was a commercial maleic anhydride grafted ethylene-propylene rubber (EPR-g-MA). All materials were coloured black by use of a carbon black masterbatch. The influence of carbon black on the fracture behaviour of glass fibre-reinforced PA6/PA66 blends was analysed before [2, 3]. After drying granulates at 80 °C for 24 h in a condensation dryer, the specimens were injection moulded. The compounds were conditioned at 62% relative humidity and 70 °C until the moisture equilibrium had established according to ISO 1110 [33]. The moisture content of the PA6 phase c_W^{PA6} can be calculated according to (9.1).

$$c_W^{PA6} = \frac{c_W^{Compound}}{\omega_{PA6}} \quad (9.1)$$

Here ω_{PA6} is the mass fraction of PA6 within the compound. The total moisture absorptions of the compounds $c_W^{Compound}$ were measured gravimetrically in relation to the dry specimens. The material composition is expressed by its nomenclature as follows. PA6/E \underline{x} GF40 \underline{m} is describing a PA6/elastomer blend with 40 wt% of glass fibres and a weight fraction of elastomer defined by \underline{x} and a moisture state \underline{m} which can be dry (d) or conditioned (c). The composition of each of the materials of this study together with the moisture absorption and some mechanical properties are shown in Table 9.1.

Tensile tests were performed according to ISO 527 [34] at 50 mm/min testing speed. Humidity in polyamides is decreasing the glass transition temperature T_g . Therefore T_g has been determined in dynamic-mechanical analysis as the maximum of the loss modulus according to ISO 6721-1 [35]. Glass transition temperatures in these compounds were $T_{g PA6} = 4$ °C and $T_{g EPR-g-MA} = -49$ °C.

Table 9.1 Analysed material system

PA6/Ex GF40 c			Moisture absorption		Tensile test ^a		
PA6 (wt%)	EPR-g-MA (wt%)	Blend ratio PA6/E	Compound (wt%)	PA6 phase (wt%)	E_t (MPa)	σ_m (MPa)	ε_B (%)
59	0	100/0	1.78	3.02	8,570	144	6.94
54	5	92/8	1.62	3.01	7,880	132	7.95
51.5	7.5	87/13	1.56	3.03	Not determined		
49	10	83/17	1.44	2.95	7,230	121	9.25

^a E_t tensile modulus, σ_m tensile strength, ε_B strain at break

9.2.2 J-R-Curve Determination

For a profound characterisation of the crack growth behaviour of the compounds, the stable crack propagation process was analysed using the second part of the procedure described in [27]. In a multi-specimen experiment, a stop block was used to realise different crack propagations and to record crack resistance curves (R-curves) as they are known in the literature [27, 36]. For each material, several SENB (single-edged-notched bending) specimens with an initial crack length of 4.5 mm consisting of a V-shape notch with a length of 3 mm and a sharp metal blade cut with a length of 1.5 mm. By deploying the stop block as a device for holding the pendulum, different deflections were realised and a load–deflection diagram for each specimen was recorded. Each deflection results in a different length of stable crack growth Δa , which has to be measured before building up the J-R-curve from the pairs of J-values of each diagram and the corresponding Δa .

To measure the portion of stable crack growth the precracked specimens were cooled in liquid nitrogen and instantaneously broken with a 15 J impact pendulum. As a new experimental approach fluorescent penetration technique was used to differentiate between stable crack propagation Δa and the remaining ligament that was broken by cryo-fracture. The fluorescent penetration colouring is described in Sect. 9.3.

By application of this technique J– Δa data points could be employed to generate a curve fit on base of a power law described in (9.2).

$$J = C_1 \Delta a^{C_2} \quad (9.2)$$

Here C_1 and C_2 are power law constants to adapt the curve function to the measured J– Δa pairs of values. Thereby it was possible to determine the J-value $J_{0.2}$ at a stable crack growth of $\Delta a = 0.2$ mm as technical crack initiation value and the tearing modulus T_J that corresponds to the slope of the J– Δa curve according to (9.3). Cause all J-R-curves were fitted by a power law with $C_2 \neq 1$, T_J is changing as a function of Δa . T_J was uniformly determined at the point $\Delta a = 0.2$ mm to characterise the material resistance against crack propagation directly after crack initiation.

$$T_J = \frac{dJ}{d(\Delta a)} \frac{E_d}{\sigma_d^2} \quad (9.3)$$

Here E_d is the dynamic flexural modulus and σ_d the dynamic yield stress, both values were determined in the ICIT (instrumented Charpy impact test) using unnotched specimens according to (9.4) and (9.5) [27]. Here F_{gy} and f_{gy} are the load and the deflection at the point of yield in the load (F)–deflection (f) diagram that marks the transition from elastic to elastic–plastic deformation [27]. Further in s is the support span, B is the specimen thickness and W is the specimen width.

$$E_d = \frac{F_{gy}s^3}{4BW^3f_{gy}} \quad (9.4)$$

$$\sigma_d = \frac{3F_{gy}s}{2BW^2} \quad (9.5)$$

9.3 Development of a Fluorescence Microscopy Procedure for Δa Measurement

9.3.1 Fluorescent Penetration Dye Colouring

For the purpose of generating crack resistance curves an accurate and valuable measurement of the stable crack growth Δa is necessary. With a raising amount of glass fibres the increasing roughness and unevenness of the specimen fracture surface avoid an accurate identification and measurement of the different fracture surface portions [2, 3].

In this approach a procedure for stable crack growth measurement was developed that combines the advantages of three different experimental techniques:

- conventional R-curve recording by use of the stop block method [27],
- fluorescent dye colouring of macroscopic cracks and surface defects [30, 37, 38],
- 3D digital microscopy with high depth of focus by depth from defocus [39–41].

A commercial fluorescent penetration system was used to develop the new experimental procedure. It consists of the medium-sensitive emulsifiable fluorescent penetrant ARDROX 985P12 and the appropriate emulsifier ARDROX 9PR12. That kind of fluorescent system is commonly used for non-destructive testing of metallic or ceramic parts and assemblies of different size scales and in several variations of the technical principle [37, 38].

The aim of this sort of material testing is the identification and localisation of near surface cracks, cavities or other defects that might lead to a critical material failure in use. The method's principle can be assumed as follows:

- wetting of the material surface with a penetration dye (visible or fluorescent),
- cleaning of the material surface after a certain residence time (by water or an emulsifier),
- drying of the material surface and eventual application of a powder developer,
- observation of material surface macroscopically or microscopically.

The contrast between defects and the undamaged material surface occurs because the dye is incorporating any kind of cavity or crack above a certain diameter which is mainly depending on the penetrant's viscosity and the wettability of the material. After surface cleaning only the defects still include penetrant that could not be rinsed. Therefore the defects can easily be localised afterwards by observation under visible light, UV light or blue light depending on the penetrant. The image quality is influenced by the use of a powder developer, different light sources or special optical filters to intensify the contrast [38].

For image generation a digital microscope Keyence VHX-500F was used. Fluorescent images were illuminated with a standard 2000 μW UV lamp. Images were recorded both using the built-in circular light of the microscope and the UV light source to document the differences of quality and contained information of both types of images. By use of the so-called depth-from-defocus method it is possible to generate complete in-focus images even if the observed microscopic object has got a very rough and structured surface that includes very different levels. Thereby this microscopic application is in fact ideal for the purposes of this study.

9.3.2 Optimisation of the Fluorescent Application Process

First of all the standard process of the ARDROX fluorescent system had to be adjusted to fit the special requirements of the task to permit accurate, reliable and reproducible optical measurements of the Δa portion on rough fracture surfaces of high reinforced polyamide composites. Therefore the influences of both the parameters of the fluorescent dyeing process and the specimens' properties on the accurateness and robustness of crack length measurements were identified with methods of statistic design of experiments (DOE).

In accordance to the standard procedure the first experimental strategy 1 was to first wet the precracked specimens with fluorescent dye, to rinse and to dry the specimens afterwards and to break the ligament in cryo-fracture mode at the end of the process. An alternative strategy 2 was taken into account where precracked specimens were first cryo-fractured and the fluorescent was used to wet the open fracture surface to eventually benefit from significant microstructural differences between the stable crack growth area and the cryo-fractured ligament.

To analyse effects of parameter variations SENB specimens of PA6/E7.5 GF40 d were notched by fresh razor blades in the experimental optimisation approach and the experimental strategy 1 was applied. In this initial experimentation step there were no loads applied on the specimen and no crack

growth part of the analysis. The fluorescent was dyed with a paint brush around the specimen on each of the three sides of the notch plane. The fluorescent dye application procedure is based on the regards of standard instructions of the ARDROX 985P12 system [42] and is illustrated in Table 9.2. In Fig. 9.1 fracture surfaces of 2 different specimens of this first experiment are illustrated both in UV mode and under visible light each.

Two different response variables y_1 and y_2 were defined. On the one hand the notch plane’s fluorescing fraction y_1 was determined as the ratio between the definitely dyed notch area under UV light and the total notch area measured with visible light. On the other hand y_2 was defined as the ratio between the area of the broken fracture surface that must have been dyed during or after specimen breakage and the total notch area. In this case y_2 should be 0% whereas y_1 is a response variable that ideally should converge 100%.

The first trial revealed the influence of the razor blade thickness and sharpness on the fluorescent penetration. Following the initial process of Table 9.2, the specimens were notched by two different razor blades resulting in 0.13 and 0.3 μm notch-tip radius. Table 9.3 illustrates the results of this analysis. The dyed notch fraction was significantly increased by using a thicker razor blade. The fluorescent could better penetrate the notch. A notch-tip radius of 0.13 μm was chosen to

Table 9.2 Fluorescent dye application procedure and varied experimental parameters

Process step	Procedure	Residence time/parameters ^a
1	Notch specimens	$a = 2 \text{ mm}$, varied r_N
2	Clean specimen surfaces with emulsifier dilution	10% aqueous dilution
3	Apply fluorescent on complete notch	$t_{RF} = 10 \text{ min}$
4	Rinse the specimen in emulsifier dilution	$t_{RE} = 120 \text{ s}$, 10% aqueous dilution
5	Dry the specimen in oven	$t_{RD} = 10 \text{ min}$, $T_D = 85 \text{ }^\circ\text{C}$
6	Break the ligament	
7	Observe the fracture surface under UV light	

^a a notch length, r_N notch-tip radius, t_{RF} , t_{RE} and t_{RD} times for applying fluorescent, rinsing in emulsifier dilution and drying, T_D temperature for drying

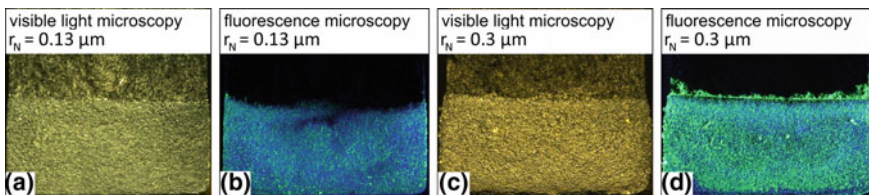


Fig. 9.1 Comparison of fluorescence dyeing efficiency

Table 9.3 Influence of razor blade choice on the response variables y_1 and y_2

Variables			Parameter variation	
			Narrow notch	Wide notch
Number of specimens	N	–	5	5
Notch-tip radius	r_N	μm	0.13	0.3
Notch length	a	mm	2	2
Dyed notch fraction ^a	\bar{y}_1	%	96.10	98.50
	s_1	%	0.81	1.14
Dyed after breakage ^a	\bar{y}_2	%	0.20	1.10
	s_2	%	0.40	2.43

^aMean values (\bar{y}_1 and \bar{y}_2) and standard deviations (s_1 and s_2)

optimise the dyeing process. Narrow notches afford a sensitive response variable y_1 and approximate the geometrical conditions of a crack better than wide notches.

To investigate the influence of notch depth and penetration process variables, an experimental design with six independent variables of two levels each in a fractional factorial 2^{6-1} plan was created and observed two times. In total 64 notched specimens were investigated. Table 9.4 contains an overview of independent variables and measured factor effects on response variable y_1 . There are three factors that are significantly influencing the response variable y_1 . An increasing notch length leads to less percentage of coloured notch area. Using the undiluted concentrate of the penetration dye results in a higher percentage of coloured notched area and increasing the oven drying time by 100% increases the coloured notch area.

The significant factors notch length a , fluorescent concentration c_f and drying time t_{RD} showed very small influence on the fluorescing fraction of notch plane y_2 . The only significant influence on y_2 arose from the factor c_f where an effect of 1.95 was determined. Even if the process parameters were adjusted according to these experimental results, very small variations in y_1 and y_2 together with the overall mean values of $y_1 = 99.07\%$ and $y_2 = 1.29\%$ proved that fluorescence penetration works very accurate, reproducible and even robust in the case of razor blade notches.

Table 9.4 Influence of dying process parameters^a

Independent factors				Factorial level		y_1		
				–	+	Effect	Coeff.	Sign.
Notch length	x_1	a	mm	1.5	2.0	–0.21	–0.11	Yes
Fluorescent concentration	x_2	c_f	%	50	100	1.19	0.60	Yes
Fluorescent application	x_3			Half	Full	–0.05	–0.02	No
Fluorescent residence time	x_4	t_{RF}	min	5	15	–0.02	–0.01	No
Emulsifier rinse time	x_5	t_{RE}	s	90	150	0.13	0.06	No
Oven drying time at 80 °C	x_6	t_{RD}	min	10	20	0.60	0.30	Yes

^aValues rounded on two decimals; coeff. = coefficient, sign. = significant factor

9.3.3 *Fluorescence Adsorption-Contrast Method (3D-FAC Method)*

To transfer this process on Δa measurements, the J - Δa curve of conditioned 40 wt% glass fibre-reinforced PA6 composite with 7.5 wt% EPR-g-MA (PA6/E 7.5 GF40 c) was determined according to the mentioned experimental procedure in ICIT at normal climate (23 °C, 50% r.h.). Notched specimens were loaded by different deflections through adjusting the stop block position. Each deflection was run with two different specimens. One was dyed with fluorescent before cryo-fracture according to strategy (1) The other one was first broken in frozen state and the fracture surface dyed afterwards following strategy (2) The complete process after parameter optimisation is illustrated for both strategies in Table 9.5 together with example pictures of stable crack growth referring to each strategy and a J -R-curve fit that has been calculated with each of the strategies.

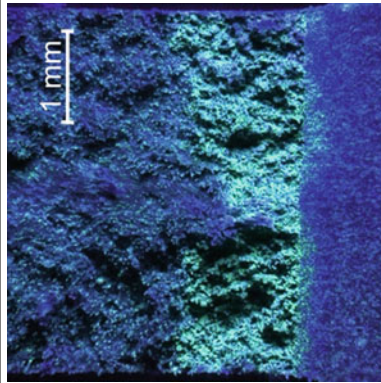
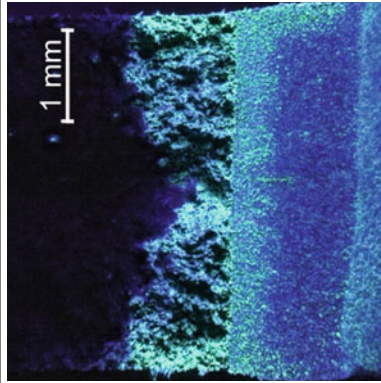
The UV pictures in Table 9.5 show the fracture surfaces of two specimens, which were loaded with the same stop block adjustment but different dyeing strategies. Both specimens showed a similar portion of bright areas directly after the notch. It is assumed that this area is the portion of stable crack growth. There are several facts that together prove this conclusion. First of all the identification of a bright fracture surface with strategy 1 means that there must be a significant crack growth and crack opening so that the fluorescent dye could easily penetrate the crack during fluorescent residence time before the specimen was completely broken. In this case it is of course not possible to decide whether the fluorescent really reached the end of the stable crack. Further on the picture of the specimen dyed by strategy 2 proves that there must be structural differences between the stable crack area and the cryo-fracture area that result in a difference of fluorescent penetration and a different picture brightness respectively.

These structural differences could be evidenced by scanning electron microscopy (SEM) and are illustrated in Fig. 9.2 for a specimen of PA6/EPR-g-MA GF40 with the lowest EPR-g-MA concentration of 5 wt%. In more detailed views of raised magnification in Fig. 9.2b (stable crack following the notch) and Fig. 9.2c (cryo-fracture) the structural differences become obvious.

The large amount of plastic deformation with cavitations at room temperature caused by the elastomer component and its influence on deformation [9, 43] enables the fluorescent to deeply penetrate the fracture surface and disturbs the emulsifier in rinsing it. The cryo-fractured surface is of course still rough in a macroscopic point of view. But the smoothness of the matrix and fibres lead to a lower amount of fluorescent penetration and of course the dyed fluorescent can more easily be rinsed by the emulsifier. Contrast is generated between stable crack propagation and cryo-fracture area in fluorescence microscopy respectively. Because of this fact the fluorescent dye colouring of fracture surfaces to measure structural differences in the deformation behaviour is called the 3D fluorescence adsorption-contrast method (3D-FAC method).

Table 9.5 Main steps of fluorescence dyeing process for $\Delta\alpha$ -measurements on precracked specimens—The 3D-FAC method in principle

Process step	Strategy 1		Strategy 2	
	Procedure	Parameter	Procedure	Parameter
1	Notch specimen	$a = 4.5$ mm $r_N = 0.3$ μm	Notch specimen	$a = 4.5$ mm $r_N = 0.3$ μm
2	Load specimen in stop block method	4 J pendulum, 1.5 m/s	Load specimen in stop block method	4 J pendulum, 1.5 m/s
3	Clean specimen surfaces with emulsifier dilution	10% aqueous dilution	Break the ligament	Cryo-fracture
4	Apply fluorescent on notch		Clean specimen surfaces with emulsifier dilution	10% aqueous dilution
5	Rinse the specimen in emulsifier dilution	$t_{RF} = 15$ min	Apply fluorescent on fracture surface	$t_{RF} = 15$ min
6	Oven dry the specimen	$t_{RE} = 150$ s $t_{RD} = 30$ min $T_D = 80$ °C	Rinse the specimen in emulsifier dilution	$t_{RE} = 150$ s 10% aqueous dilution
7	Break the ligament	Cryo-fracture	Oven dry the specimen	$t_{RD} = 30$ min $T_D = 80$ °C
8	UV fluorescent picture depth-fused 3D technique	Observe the fracture surface under UV light		



(continued)

Table 9.5 (continued)

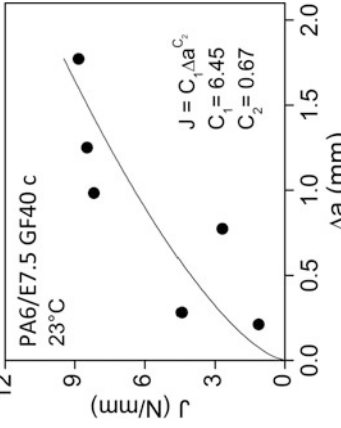
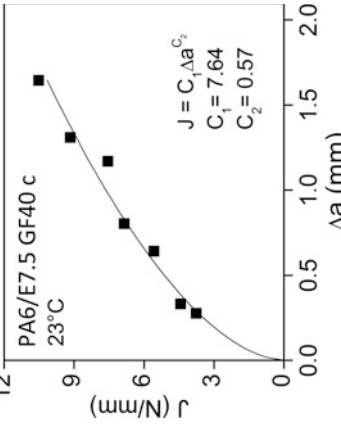
Process step	Strategy 1		Strategy 2	
	Procedure	Parameter	Procedure	Parameter
J-R-curve	 <p>PA6/E7.5 GF40 c 23°C</p> <p>$J = C_1 \Delta a^{C_2}$ $C_1 = 6.45$ $C_2 = 0.67$</p>		 <p>PA6/E7.5 GF40 c 23°C</p> <p>$J = C_1 \Delta a^{C_2}$ $C_1 = 7.64$ $C_2 = 0.57$</p>	

Fig. 9.2 Fracture surfaces of PA6/E 5 GF40 c: different portions of fracture surface (a); cryo-fractured ligament (b); stable crack propagation (c)

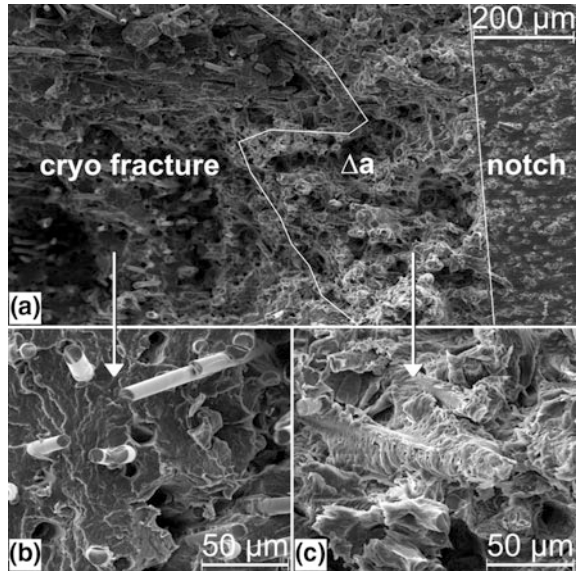
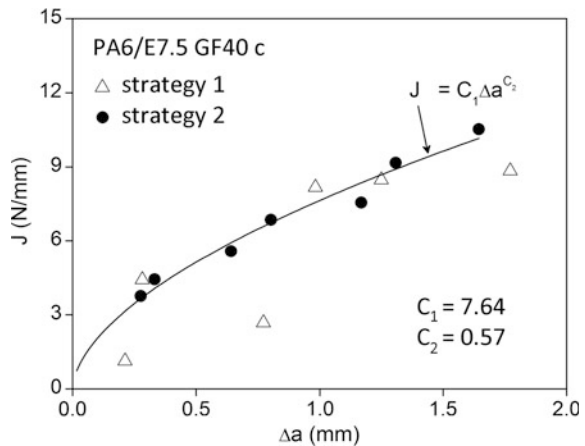


Fig. 9.3 J - Δa curve of PA6/E7.5 GF40 c, curve fit determined by points of strategy 2



As a result of experimentation development the fluorescent dyeing strategy 2 was chosen to determine J - Δa curves of reinforced PA6 composites with different elastomer contents of this study. Fluorescence images thereby afford an accurate measurement of Δa , additional information about structural differences between stable and unstable crack portion and the resulting crack resistance curves can exactly be fitted like this can be seen in Fig. 9.3, where the above points of both strategies are composed in the same diagram. Several points of strategy 1 dyeing also fit the curve that is determined by a power law following (9.2). Each of the three inaccurate points of strategy 1 is located below the curve. Presuming both a

reliable determination of J according to MacGillivray [25] and an accurate measurement of Δa by strategy 2 the Δa portion of these points has been determined as too long which is indicating a potential dye overflow error as it was observed in optimisation of the test procedure before.

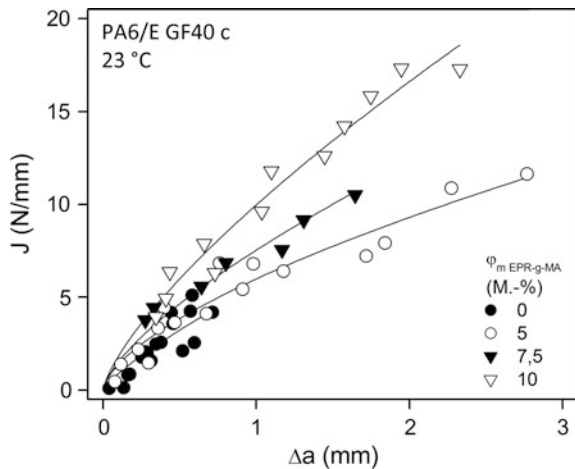
9.4 Results and Discussion

Crack resistance curves according to the procedure described in the experimentation part are illustrated in Fig. 9.4. The slope of the curve rises dramatically with increasing EPR-g-MA content. That can be ascribed to enhanced energy dissipation during crack propagation. To result in the same stable crack length much more energy is consumed when more elastomeric particles are dispersed in the matrix.

This was supported by the SEM images that can be viewed in Fig. 9.5. Figure 9.5a–c indicate the rising amounts of plastic deformation, yielding and cavitations in the stable crack growth area with increasing EPR-g-MA content.

Figures 9.6 and 9.7 reveal the dependence of the resistance against crack initiation and propagation in shape of $J_{0,2}$ and T_J as functions of PA6/EPR-g-MA blend ratio. Whereas $J_{0,2}$ is linearly increasing with rising $\varphi_{\text{EPR-g-MA}}$ (Fig. 9.6), the tearing modulus T_J stays relatively constant up to an elastomer content of 5 wt% (Fig. 9.7). Beyond this point T_J is exponentially increasing. The temperature is dramatically enhancing crack resistance. At 40 °C the complete amorphous fraction of PA6 is present in the entropy elastic state and thereby is enhancing large amounts of plastic deformation and yielding during crack propagation process. This can be ascribed to the existence of a ductile–brittle transition temperature which is increasing with higher elastomer content [44, 45].

Fig. 9.4 Crack resistance curves of PA6/E GF40 with different EPR-g-MA content



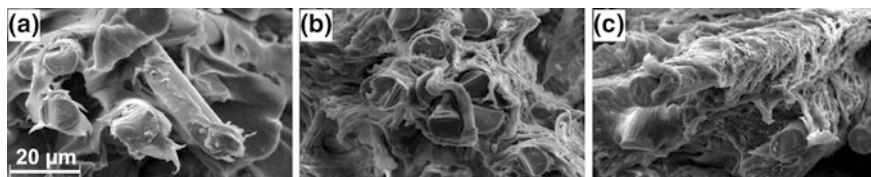


Fig. 9.5 Deformation in the stable crack area of unmodified and rubber-toughened PA6/E GF40 c: unmodified (a); 5 wt% EPR-g-MA (b); 10 wt% EPR-g-MA (c)

Fig. 9.6 Crack initiation parameter $J_{0.2}$ of PA6/E GF40 c as a function of EPR-g-MA content and temperature

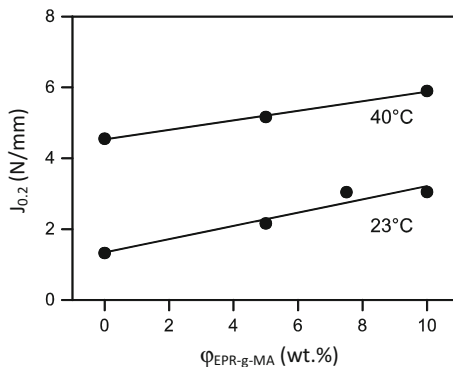
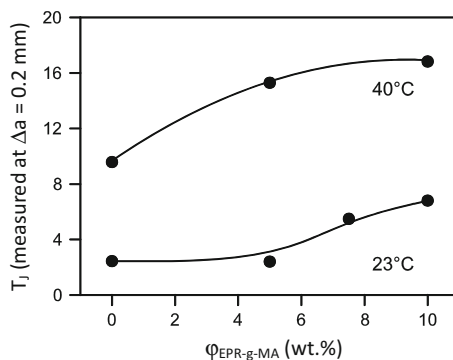
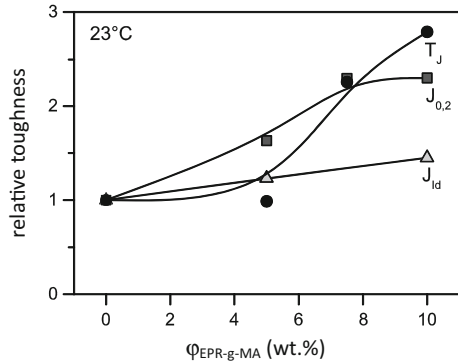


Fig. 9.7 Crack propagation parameter T_J of PA6/E GF40 c as a function of EPR-g-MA content and temperature



It is necessary to characterise both the resistance against unstable crack propagation and the resistance against stable crack initiation and propagation to get complete information about the toughness behaviour of these materials. Figure 9.8 supports this by comparing the toughness change caused by EPR-g-MA addition in relation to the unmodified composite for each fracture mechanical value at room temperature. While the material resistance against unstable crack propagation ($J_{I,d}$) as the $J_{I,d}$ -value only increases slightly in a linear way, the massive changes in matrix plasticity and deformation processes lead to an increase of the material

Fig. 9.8 Comparison of fracture mechanical values of unstable [44, 45] and stable crack propagation relative to the unmodified composite PA6GF40 as a function of EPR-g-MA content



resistance against stable crack initiation $J_{0.2}$ on a value twice as high in the material with 10 wt% EPR-g-MA. The ability of the material to dissipate energy during crack propagation and thereby the value of T_J is nearly tripling at the same time.

9.5 Conclusions

The aim of this study was to develop new opportunities to measure crack resistance curves at conditions of high ductility of reinforced PA6 compounds with high glass fibre content. The most important results are stated in the following list.

1. The addition of toughening modifiers in glass fibre-reinforced compounds, the hygroscopic behaviour of polyamides as well as raised temperatures limit the validity range of conventional toughness evaluation with the experimental methods of LEFM (linear elastic fracture mechanics) and the J -integral method. The determination of J -R-curves is necessary for a complete toughness evaluation.
2. The fluorescence dyeing technique is an efficient, accurate and reliable method to enhance the measurement of Δa portions on roughly structured fracture surfaces. Fluorescence microscopy has its definite advantages compared to light microscopy or SEM as follow:
 - The generated images are independent of specimen colour.
 - There are no reflections on plane areas on the fracture surface like in the case of bright field microscopy. The picture generating principle is UV-excited emission and not reflection. Therefore the optical properties of the specimen material like reflection, gloss or optical refraction do not affect the quality of the picture.
 - Picture contrast only is build up by the structure and the wettability of the fracture surface and thereby the picture provides additional structural information. The contrast between different fracture surface portions is very

high in case of modified compounds because of the surface differences between the unstable crack area and the stable crack propagation area with large amounts of microscopic cavities and plastic deformations.

- It is an easy, fast experimental technique and less expensive than SEM especially when several specimens have to be characterised as in case of multi-specimen R-curve determination.
3. The experimental results showed that EPR-g-MA significantly increased the materials resistance against stable crack initiation and propagation. The elastomer-induced change of the resistance against stable crack propagation was much higher than the measured change of the instability value J_{Id} . This additional information about the toughness behaviour of highly reinforced PA6 compounds with different amounts of elastomeric modifier could be revealed by means of the fluorescence adsorption-contrast method (3D-FAC method).

References

1. Langer, B.: Bruchmechanische Bewertung von Polyamid-Werkstoffen. Logos Verlag, Berlin (1998)
2. Kroll, M., Langer, B., Schumacher, S., Grellmann, W.: The influence of carbon black batches on the fracture behavior of glass fiber reinforced PA6/PA66 blends. *J. Appl. Polym. Sci.* **116**, 610–618 (2010)
3. Nase, M., Langer, B., Schumacher, S., Grellmann, W.: Toughness optimization of glass-fiber reinforced PA6/PA66-based composites: effect of matrix composition and colorants. *J. Appl. Polym. Sci.* **111**, 2245–2252 (2009)
4. Bethge, I., Reincke, K., Seidler, S., Grellmann, W.: Influence of modifier content and temperature on toughness behaviour of polyamide. In: Grellmann, W., Seidler, S. (eds.) *Deformation and Fracture Behaviour of Polymers*. Springer, Berlin (2001), pp. 242–256
5. Muratoglu, O.K., Argon, A.S., Cohen, R.E., Weinberg, M.: Microstructural processes of fracture of rubber-modified polyamides. *Polymer* **36**, 4771–4786 (1995)
6. Araújo Jr., E.M., Hage, E., Carvalho, A.J.F.: Effect of compatibilizer in acrylonitrile–butadiene–styrene toughened nylon 6 blends: Ductile–brittle transition temperature. *J. Appl. Polym. Sci.* **90**, 2643–2647 (2003)
7. Kayano, Y., Keskkula, H., Paul, D.R.: Fracture behaviour of some rubber-toughened nylon 6 blends. *Polymer* **39**, 2835–2845 (1998)
8. Kayano, Y., Keskkula, H., Paul, D.R.: Evaluation of the fracture behaviour of nylon 6/SEBS-g-MA blends. *Polymer* **38**, 1885–1902 (1997)
9. Burgisi, G., Paternoster, M., Peduto, N., Saraceno, A.: Toughness enhancement of polyamide 6 modified with different types of rubber: the influence of internal rubber cavitation. *J. Appl. Polym. Sci.* **66**, 777–787 (1997)
10. Oshinski, A.J., Keskkula, H., Paul, D.R.: The role of matrix molecular weight in rubber toughened nylon 6 blends: 1. Morphology. *Polymer* **37**, 4891–4907 (1996)
11. Oshinski, A.J., Keskkula, H., Paul, D.R.: The role of matrix molecular weight in rubber toughened nylon 6 blends: 2. Room temperature Izod impact toughness. *Polymer* **37**, 4909–4918 (1996)
12. Oshinski, A.J., Keskkula, H., Paul, D.R.: The role of matrix molecular weight in rubber toughened nylon 6 blends: 3. Ductile–brittle transition temperature. *Polymer* **37**, 4919–4928 (1996)

13. Laura, D.M., Keskkula, H., Barlow, J.W., Paul, D.R.: Effect of rubber particle size and rubber type on the mechanical properties of glass fiber reinforced, rubber-toughened nylon 6. *Polymer* **44**, 3347–3361 (2003)
14. Ching, E.C.Y., Li, R.K.Y., Tjong, S.C., Mai, Y.-W.: Essential work of fracture (EWF) analysis for short glass fiber reinforced and rubber toughened nylon-6. *Polym. Eng. Sci.* **43**, 558–569 (2003)
15. Laura, D.M., Keskkula, H., Barlow, J.W., Paul, D.R.: Effect of glass fiber surface chemistry on the mechanical properties of glass fiber reinforced, rubber-toughened nylon 6. *Polymer* **43**, 4673–4687 (2002)
16. Cho, J.W., Paul, D.R.: Glass fiber-reinforced polyamide composites toughened with ABS and EPR-g-MA. *J. Appl. Polym. Sci.* **80**, 484–497 (2001)
17. Laura, D.M., Keskkula, H., Barlow, J.W., Paul, D.R.: Effect of glass fiber and maleated ethylene–propylene rubber content on the impact fracture parameters of nylon 6. *Polymer* **42**, 6161–6172 (2001)
18. Laura, D.M., Keskkula, H., Barlow, J.W., Paul, D.R.: Effect of glass fiber and maleated ethylene–propylene rubber content on tensile and impact properties of nylon 6. *Polymer* **41**, 7165–7174 (2000)
19. Langer, B., Seidler, S., Grellmann, W.: Influence of temperature and moisture on toughness behaviour of polyamide. In: Grellmann, W., Seidler, S. (eds.) *Deformation and Fracture Behaviour of Polymers*. Springer, Berlin (2001), pp. 209–228
20. Rice, J.R.: A path independent integral and the approximate analysis of strain concentration by notches and cracks. *J. Appl. Mech.* **35**, 379–386 (1968)
21. Gomina, M., Pinot, L., Moreau, R., Nakache, E.: Fracture behaviour of short glass fibre-reinforced rubber-toughened nylon composites. In: Blackman, B.R.K., Pavan, A., Williams, J.G. (eds.) *Fracture of Polymers, Composites and Adhesives II*.ESIS Publication 32. Elsevier, Amsterdam (2003), pp. 399–418
22. Nair, S., Subramaniam, A., Goettler, L.: Fracture resistance of polyblends and polyblend matrix composites: Part II Role of the rubber phase in Nylon 6,6/ABS alloys. *J. Mater. Sci.* **32**, 5347–5354 (1997)
23. Zhu, X.-K.: *J*-integral resistance curve testing and evaluation. *J. Zhejiang Univ. Sci. A* **10**, 1541–1560 (2009)
24. Baldi, F., Riccò, T.: High-rate *J*-testing of toughened polyamide 6/6: applicability of the load separation criterion and the normalization method. *Eng. Fract. Mech.* **72**, 2218–2231 (2005)
25. MacGillivray, H.J.: *J*-fracture toughness of polymers at impact speed. In: Moore, D.R., Pavan, A., Williams, J.G. (eds.) *Fracture Mechanics Testing Methods for Polymers, Adhesives and Composites*.ESIS Publication 28. Elsevier, Amsterdam (2001), pp. 159–175
26. Hornsby, P., Premphet, K.: Fracture toughness of multiphase polypropylene composites containing rubbery and particulate inclusions. *J. Mater. Sci.* **32**, 4767–4775 (1997)
27. Grellmann, W., Seidler, S., Hesse, W.: Procedure for determining the crack resistance behaviour using the instrumented impact test. In: Grellmann, W., Seidler, S. (eds.) *Deformation and Fracture Behaviour of Polymers*, pp. 71–86. Springer, Berlin (2001)
28. Heilemann, M.: Fluorescence microscopy beyond the diffraction limit. *J. Biotechnol.* **149**, 243–251 (2010)
29. Blake, R.A.: Cellular screening assays using fluorescence microscopy. *Curr. Opin. Pharmacol.* **1**, 533–539 (2001)
30. Stadthaus, M.: Ja zur Anregung mit LED! Aber warum müssen es gerade 365 nm sein? – Anmerkungen zu zwei Artikeln über die Anwendung von LED in der *ZfP*-Zeitung Nr. 116. *ZfP-Zeitung* **117**, 21–22 (2009)
31. Samuel, B.A., Haque, M.A.: Visualization of crack blunting using secondary fluorescence in soft polymers. *Polym. Testing* **27**, 404–411 (2008)
32. PlasticsPortal Europe.: BASF, Ludwigshafen (2007), see: <http://www.plasticsportal.net>. 2 June 2017
33. ISO 1110 (1995): *Plastics—Polyamides—Accelerated conditioning of test specimens*
34. ISO 527-1 (2012): *Plastics—Determination of tensile properties—Part 1: General principles*

35. ISO 6721-1 (2011): Plastics—Determination of dynamic mechanical properties—Part 1: General principles
36. Grellmann, W., Seidler, S. (eds.): *Polymer Testing*, 2nd edn. Carl Hanser, Munich (2013)
37. Forster, G.A., Ellingson, W.A.: An investigation of penetrant techniques for detection of machining-induced surface-breaking cracks on monolithic ceramics. Argonne National Laboratory, Energy Technology Division, Argonne (1996)
38. Riess, N., Ivankov, A.: UV-Strahlung oder Blaulicht. *ZfP-Zeitung* **116**, 26–27 (2009)
39. Leroy, J.-V., Simon, T., Deschenes, F.: Real time monocular depth from defocus. In: Elmoataz, A., Lezoray, O., Nouboud, F., Mammass, D. (eds.) *Image and Signal Processing*. Springer, Berlin (2008), pp. 103–111
40. McCloskey, S., Langer, M., Siddiqi, K.: Evolving measurement regions for depth from defocus. In: Yagi, Y., Kang, S.B., Kweon, I.S., Zha, H. (eds.) *Computer Vision—ACCV 2007*, pp. 858–868. Springer, Berlin (2007)
41. Schechner, Y.Y., Kiryati, N.: Depth from defocus vs. stereo: How different really are they? *Int. J. Comput. Vision* **39**, 141–162 (2000)
42. Technical Datasheet Ardrex 985P11–985P14. Chemetall, Frankfurt (2003)
43. González-Montiel, A., Keskkula, H., Paul, D.R.: Impact-modified nylon 6/polypropylene blends: 3. Deformation mechanisms. *Polymer* **36**, 4621–4637 (1995)
44. Kroll, M.: *Hybride PA6-Werkstoffe – Methoden der bruchmechanischen Zähigkeitscharakterisierung und Eigenschaftsprofil in Abhängigkeit von den Verarbeitungsbedingungen und der Werkstoffzusammensetzung*. Berichte aus der Kunststofftechnik. Shaker Verlag, Aachen (2013)
45. Kroll, M., Langer, B., Grellmann, W.: Toughness optimization of elastomer-modified glass-fiber reinforced PA6 materials. *J. Appl. Polym. Sci.* **127**, 57–66 (2013)

Chapter 10

Acoustic Emission Analysis for Assessment of Damage Kinetics of Short-Glass Fibre-Reinforced Thermoplastics—ESEM Investigations and Instrumented Charpy Impact Test

M. Schoßig, A. Zankel, C. Bierögel, P. Pölt and W. Grellmann

Abstract The acoustic emission (AE) analysis is a structure-sensitive test method of plastic diagnostics, which enables the characterisation of the damage kinetics as well as damage mechanisms under specific conditions. The AE analysis is linked to release of stored elastic energy, which propagates as spherical volume wave in the material. In this work, short-glass fibre-reinforced thermoplastic materials were examined in the quasi-static tensile test in the environmental scanning electron microscope (ESEM) with simultaneously recording of the AE as well as under impact-loading conditions in the instrumented Charpy impact test (ICIT). Therefore, it was possible to couple the mechanical, the acoustic and the micromechanical results to describe the damage kinetic as well as the damage mechanisms. In dependence on the bonding conditions of the glass fibre in the polymer matrix, different mechanisms of damage to be related to typical frequency ranges can be detected: (i) fibre fracture, (ii) matrix deformation with slipping of fibres in the delamination area and friction processes of the fibres in the matrix, (iii) debonding and pull-out with/without matrix yielding. The coupling of the AE analysis with the ICIT allows the assessment of the damage kinetic and therefore, the determination of the damage initiation under impact-loading conditions. However, in dependence on various bonding conditions, different results could be found. For good bonding conditions, the damage initiation takes place before the material behaviour changes from elastic to elastic–plastic behaviour. This could be found for the short-glass fibre-reinforced high-density polyethylene materials. For

M. Schoßig (✉) · C. Bierögel · W. Grellmann
Polymer Service GmbH Merseburg, Merseburg, Germany

C. Bierögel · W. Grellmann
Centre of Engineering, Martin Luther University Halle-Wittenberg,
Halle/Saale, Germany

A. Zankel · P. Pölt
Institute for Electron Microscopy and Nanoanalysis, Graz University of Technology,
Graz, Austria

the fibre-reinforced polybutene materials, the first AE takes place at the point of elastic–plastic material behaviour. An energetic approach of the damage initiation by the parameter J_{Si} shows an independent behaviour from the polymer matrix as well as from the glass fibre content. For all investigated thermoplastics, a J_{Si} -value of 0.8 N/mm as resistance against stable crack propagation could be determined.

10.1 Introduction

Short-glass fibre-reinforced thermoplastics are versatile polymeric materials with many application areas. The reason for this, on the one hand, is the possibility to realise complex shapes by injection moulding, how it is typical for polymeric materials. On the other hand, with such reinforced materials, it is possible to obtain tailor-made mechanical properties, corresponding to the individual applications. Important properties are the stiffness, strength, ratio of stiffness and strength as well as the toughness. All these requirements can be fulfilled by short-glass fibre-reinforced thermoplastics [1].

The acoustic emission (AE) analysis is a test method which responds sensitively on damage mechanisms like interaction of glass fibres with the polymeric matrix (sliding friction, re-orientation of glass fibres next to the surface), debonding and pull-out of fibres as well as fibre fracture during the loading of materials. However, to correlate results of the AE with defined damage mechanisms, it is necessary to carry out further methods, e.g. in situ techniques, which allow a physical-based description of relevant properties. The use of in situ methods in combination with microscopy affords the possibility to observe damage mechanisms during loading of the material. To examine polymeric material, the environmental scanning electron microscope (ESEM) is a useful tool because it is not necessary to coat electrically non-conducting specimens with a thin conductive layer to avoid surface charging caused by electron irradiation. This is of particular importance if new surfaces such as new crack surfaces are generated during experimental investigation [2–4]. By the realisation of in situ tensile tests in the ESEM while simultaneously recording the damage-sensitive AE, both the assessment of the damage kinetics and correlations between characteristic frequencies ranges and damage mechanisms are possible.

In addition, by the chronological registration of the first detectable damages in the material, it is possible to characterise the damage initiation respectively the onset of damage. This is of particular interest by transient processes, such as impact loading.

This article deals in the first part with results from tensile tests in the ESEM with simultaneously recording of the AE of notched short-glass fibre-reinforced polyolefin materials. In the second part of this article, results from coupling of the AE measurements with the instrumented Charpy impact test (ICIT) were discussed. The aims of these investigations are the determination of correlations of AE characteristic with occurring damage mechanisms as well as the damage initiation under impact loading.

10.2 Theoretical Background

10.2.1 Acoustic Emission (AE) Analysis

In material science, the AE analysis is a quasi non-destructive test method, which is linked to load induced damage processes in the material. In principle the acoustic emission signals can be generated by mechanically, biologically, or chemically induced mechanical stress. The resulting mechanical stress waves propagate as a spherical volume wave from the AE source and can be recorded on the surface as Rayleigh wave with suitable piezo-electric transducers (Fig. 10.1).

A classification of the recorded analogue electrical signal into two principal types is done on the basis of the time domain. Non-separable signals are appointed as continuous emissions and events with a short period of time as burst emissions or transient signals [5]. Continuous acoustic emissions are obtained by homogeneous plastic deformations in metals, by leakage flows or yielding in metals. Discontinuous events like crack formation and crack propagation as well as fibre pull-out and fibre fracture in fibre-reinforced materials lead to burst emissions. The AE analysis can be applied in two fundamental fields. On the one hand, applications in a technical manner, for example in the field of component supervision or in the monitoring of bridges and dams, are possible [6, 7]. On the other hand, in the field of material science, the assessment of damage mechanisms and resultant correlations to material parameters are of substantial interest [5, 8]. The presentation of acoustic signals in a sum and rate form enables the characterisation of signal dynamics and thus damage growth and damage accumulation. The presentation of amplitude values, AE events per hit as well as results from the frequency analysis allows the determination of damage mechanisms and damage chronology or kinetics. The increase of significance is indicated in Fig. 10.2 by an arrow on the left side.

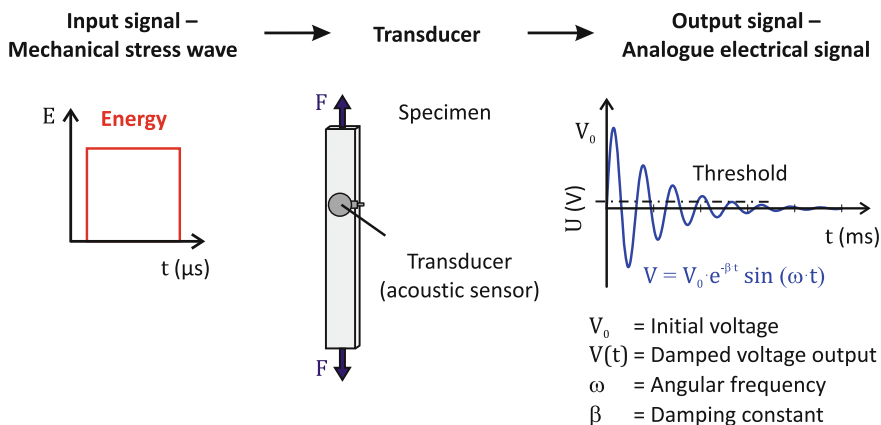


Fig. 10.1 Schematic presentation of the signal processing of acoustic emissions, according to [5]

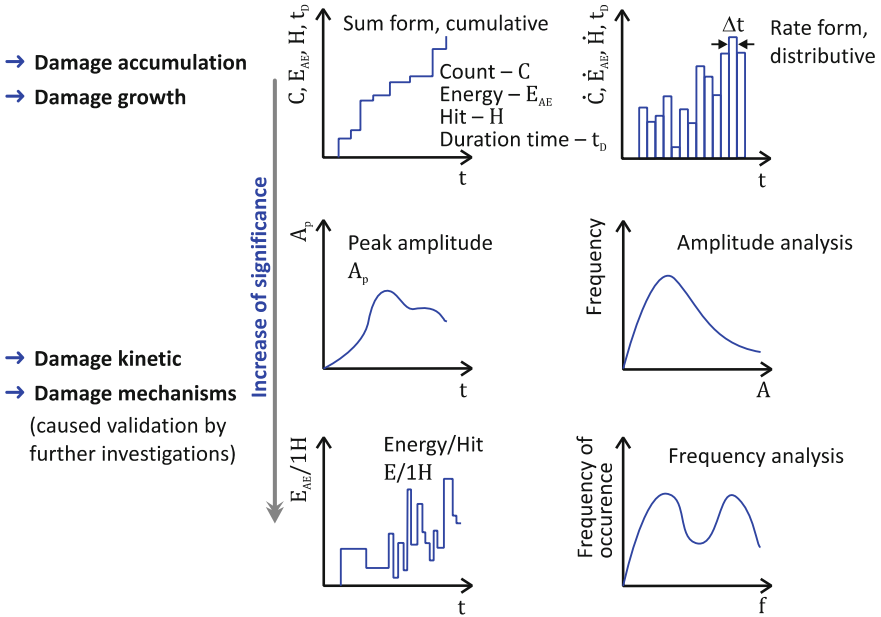


Fig. 10.2 Possible representations of AE analysis results; according to [5]

However, the use of amplitude values is only possible under limited conditions, such as the test sample has large transverse dimensions so that the sample edge reflections do not alter the signal peak amplitude, the sources have the same radiation pattern and the depth (in the thickness direction of the specimen) of the sources are nearly the same. A general problem is also the dependency of the attenuation of the mechanical stress wave on the distance between AE sensor and AE source. For this reason, Bohse and Ramirez-Jimenez indicated in [8, 9] that the correlation between amplitude values and damage mechanisms is valid only in combination with the results of frequency analyses and/or in situ methods. Extensive tests with the aim to propose correlations between amplitude values and damage mechanisms were performed in [10–12]. However, many authors deal with correlations between damage mechanisms and characteristic frequency ranges [8, 9, 13–18]. Figure 10.3 provides an overview of the literature results regarding the reported frequency ranges and deformation mechanisms for different specimen types (unidirectional—UD, single-fibre—SF) and material systems. For the mechanism “fibre failure”, a frequency range between 30 and 700 kHz was assumed. This can be attributed to complex influencing factors.

Apart from the orientation of the fibres in relation to the loading direction as well as to crack propagation direction, also the bonding of the fibres in the polymeric matrix, the fibre type, fibre content, fibre length, inherent loss mechanisms as well as the resulting wave modes from the external loading [8] are significant. In addition, the frequency f of the recorded AE signal depends on the resulting normal

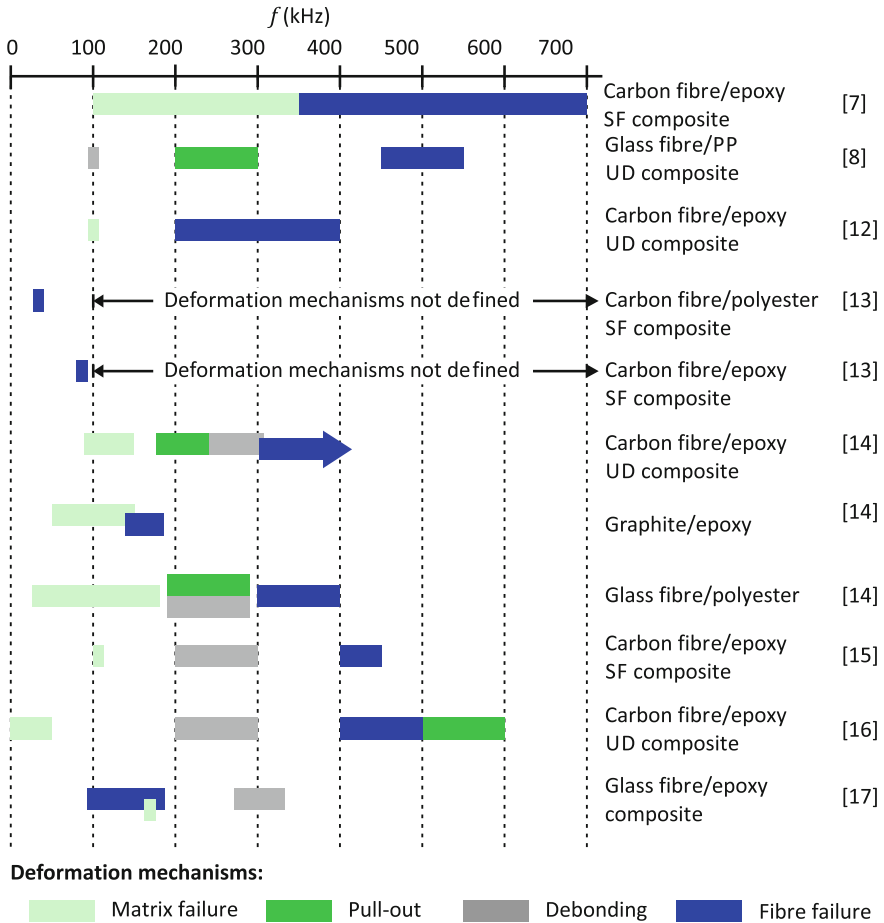


Fig. 10.3 Literature results, which indicate correlations between characteristic frequency ranges and deformation mechanisms (*SF* single-fibre, *UD* unidirectional)

stress σ_N in the fibres. Under good bonding conditions of the fibres in the polymeric matrix, the increase in load F results in an increasing normal stress σ_N within the fibres. The higher the stress in the fibre, the higher the stored elastic energy and thus the frequency ranges of the fibre fracture/failure process. This is indicated by F_1-F_3 and $\sigma_{N1}-\sigma_{N3}$ in Fig. 10.4. However, a generalisation of this assumption is not possible, because the external loading can also lead to other damage mechanisms such as pull-out of fibres resulting in a lower normal stress within the fibres (F_4 and σ_{N4} in Fig. 10.4).

Due to the crack propagation, fibre fracture occurs, if the crack has no possibility to propagate along the fibre–matrix interface or in the polymeric matrix. Reasons for this can be high-test speed (dynamic conditions), higher fibre contents and orientation of the fibres in relation to the crack propagation direction. It can be

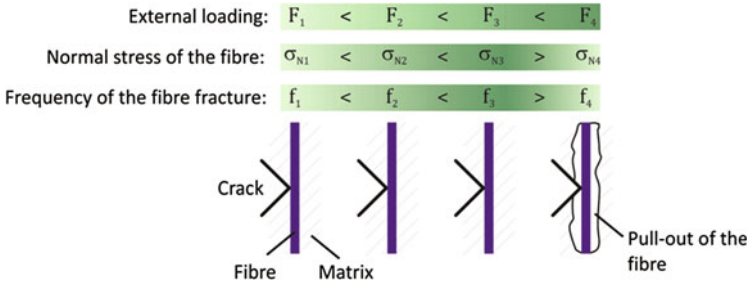


Fig. 10.4 Schematic presentation of the frequency f of the fibre fracture in dependence on the external load F and normal stress σ_N of the fibre [19]

concluded that bad bonding conditions of the fibres to the matrix as well as pre-damage of fibres lead to lower frequency ranges. Thus, for the mechanism “fibre fracture” different fracture modes are characteristic. The fibre can burst due to a tensile load or due to a flexural load caused by the crack propagation. The latter one can also occur if the fibres have no or only a partial bonding to the matrix.

10.2.2 Frequency Analysis—Wavelet Transform (WT)

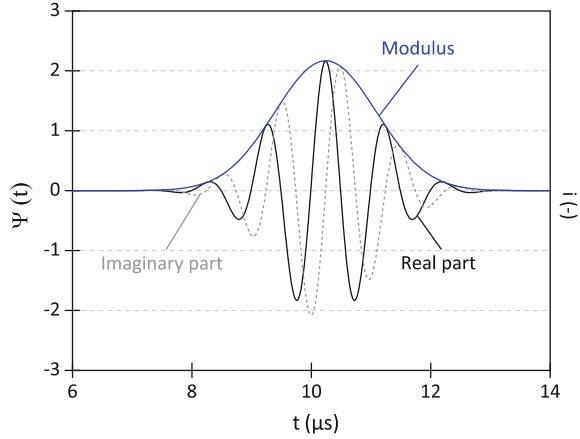
For the transformation of the recorded AE (transient signals) during the mechanical loading, the wavelet transform on the basis of a *Gabor wavelet* (mother wavelet) was used [20]. By means of the wavelet transform, the problem of the non-existent chronological correlation of the frequencies (Fourier transform) and the opposed time and frequency resolution (short-time Fourier transform) is avoided because parameters a and b are used to change the window width as well as the number of oscillations. Equation (10.1) shows the wavelet transform W of a time signal f_t , while (10.2) shows the Gabor wavelet Ψ [20, 21]. The real and imaginary parts as well as the modulus of the Gabor wavelet are shown in Fig. 10.5.

$$Wf_t(a, b) := \langle f_t, \Psi_{a,b} \rangle = \frac{1}{\sqrt{|a|}} \cdot \int_{-\infty}^{\infty} \int f_t(t) \overline{\Psi\left(\frac{t-b}{a}\right)} dt \quad (10.1)$$

$$\Psi(t) = \pi^{-0.25} \cdot \left(\frac{\omega_p}{\gamma}\right)^{0.5} \cdot \exp\left[-\frac{t^2}{2} \cdot \left(\frac{\omega_p}{\gamma}\right)^2 + i\omega_p \cdot t\right] \quad (10.2)$$

$$\gamma = \pi \cdot \left(\frac{2}{\ln 2}\right)^{0.5} = 5.336 \quad (10.3)$$

Fig. 10.5 Real and imaginary part as well as the modulus of the Gabor wavelet $\Psi(t)$; selected centre frequency ω_p of 450 kHz



$$\hat{\Psi}(\omega) = (2 \cdot \pi)^{0.5} \cdot \pi^{-0.25} \cdot \left(\frac{\omega_p}{\gamma}\right)^{0.5} \cdot \exp\left[-\frac{t^2}{2} \cdot \left(\frac{\omega_p}{\gamma}\right)^2 \cdot (\omega - \omega_p)^2\right] \quad (10.4)$$

By using parameters a and b , the wavelet function Ψ can be changed so that the time signal can be calculated. Parameters a and b describe the scaling and translation of the mother wavelet, which Morlet called wavelet [22]. In (10.2), ω_p is the centre frequency and the constant γ is needed to realise an orthogonal system (10.3). The half-life of $2\gamma/\omega_p$ for the Gabor wavelet as well as the half-value of frequency $0.5\omega_p/\gamma$ can be calculated from the Fourier transform $\hat{\Psi}$ (10.4).

As a result of the wavelet transform, a multiplicity of wavelet coefficients (WT coefficients) were obtained in which every coefficient is defined by parameters a and b and can thus be related to frequency and time. The presentation as contour plot (spectrogram or voiceprint) enables the interpretation of the signal intensity in dependence on time and the characteristic properties of the acoustic signals [20].

10.3 Experimental Details

10.3.1 *In Situ Tensile Tests in ESEM Coupled with AE Measurement*

To assess the damage mechanisms and then correlate the results with characteristic frequency ranges of the recorded AE, in situ tensile tests in the ESEM were performed. The low-vacuum mode of the ESEM [23, 24] enables the investigation of electrically nonconductive specimens without the necessity of a conductive layer such as gold or carbon which are typical for conventional scanning electron

microscopy (CSEM). Thus, even dynamic investigations like in situ mechanical testing can be performed [19, 25–27] with SEM resolution.

In this work short-reinforced PP and PB-1 materials were investigated. Both materials were reinforced with 20 wt% E-glass fibres with an average fibre diameter of 11 μm . For the PP system, an optimised maleic anhydride (MAH) was used as coupling agent to improve the bonding conditions between fibres and matrix. The same type of coupler was also used for the PB-1 material system. However, the bonding of the fibres in the PP matrix differs from that in the PB-1 matrix. While for PP good bonding of the glass fibres in the polymer occurs, the fibres in the PB-1 material system are not bonded to the matrix due to the non-optimised coupling agent. The in situ tensile tests with simultaneous recording of the damage-sensitive AEs were performed with a test speed of 0.2 mm/min. The specimens used for the in situ tensile tests had the dimensions $60 \times 10 \times 4 \text{ mm}^3$ and were obtained from the multi-purpose test specimens (type 1A) by saw off the shoulders. The strain rate, resulting from the grip-displacement-time curve, was 0.0027 min^{-1} . By polishing the injection-moulded specimens with silicon carbide sandpaper, the characteristic flash was removed. A notch with a tip radius of 0.1 mm and a depth of 2 mm was made to achieve stress concentration. Furthermore, this notch offered the possibility to observe some of the damage mechanisms directly during the loading of the specimen. The tensile loading was implemented by using the motorised MT5000 tensile device from Deben (Suffolk, UK), equipped with a load cell of 5 kN and mounted on the stage of the ESEM Quanta 600 FEG equipped with a Schottky emitter (FEI, Eindhoven, The Netherlands). The tensile stage was tilted at 30° to the tilt axis of the specimen stage of the ESEM to achieve a better monitoring of the damage mechanisms occurring during the tests. Figure 10.6 shows schematically

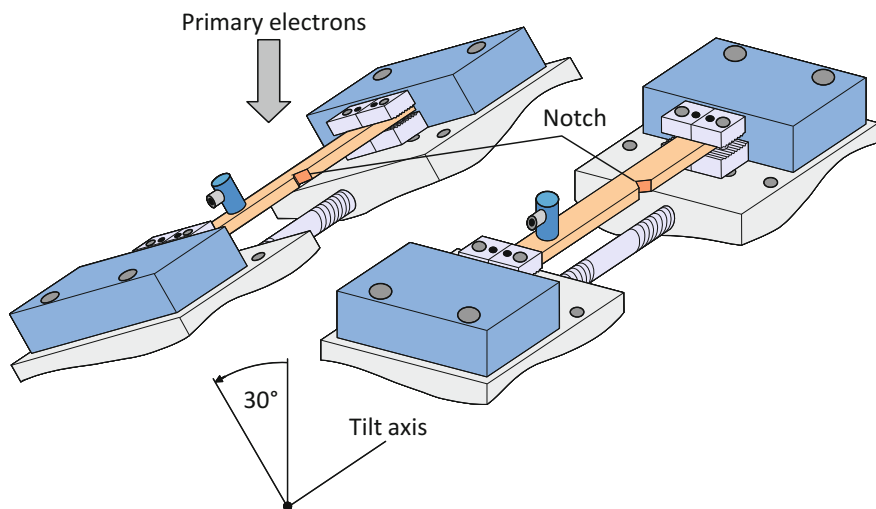


Fig. 10.6 Schematically representation of the tilted tensile stage [25]

the test set-up of the tensile test. For the clamping of the specimen, a torque of 1 Nm was used to realise a defined surface stress to the grip region of the specimens. Parallel to the load–time and AE data, audio video interleaved (avi) movies of the deformation and fracture process at the crack tip were recorded, using secondary electrons (SE) and backscattered electrons (BSE) simultaneously.

The AE measurements were realised with the 3-channel measuring system AMSY-4 (Vallen-Systeme, Icking, Germany) including the preamplifier AEP-3 and a broadband sensor AE204A with a cable length of 1.2 m. For the connection of the broadband sensor with the preamplifier a feed through in the sample chamber of the ESEM and a cable with a length of 1 m was used. The bandwidth of the preamplifier and the AE sensor were 95–1000 and 150–650 kHz (calibration certificate), respectively. For a suitable coupling of the broadband sensor to the specimen surface, beeswax was used and the distance between the AE sensor and the notch tip was 30 mm. Based on the given experimental setup it was not possible to use a specific clip to realise a fixing of the sensor. Therefore, only the coupling agent held the sensor in place.

As a result of pre-examinations, a good adhesion of the sensor on the specimen surface was found [19]. The values used for the AE analysis are the peak amplitude values A_p of all hits as well as energy E_{AE} in a distributive form. Direct observation of damage mechanisms at the notch tip allows a chronological correlation to AE values. It should be noted that only the surface of the specimen could be observed.

10.3.2 Coupling ICIT and AE Analysis

More than three decades ago, the assessment of toughness parameters for plastics by means of fracture mechanics concepts under impact-loading conditions was established [28, 29]. In particular, the fracture mechanics characterisation delivers parameters with increased information content, because a differentiated assessment of the deformation energy can be conducted. In comparison to the conventional test, where the integral deformation energy is measured, a fracture mechanics analysis can regard the elastic and the plastic deformation energy separately [30–35].

In these examinations, polyethylene high-density (PE-HD) and polybutene-1 (PB-1) materials provided by LyondellBasell Industries (Frankfurt, Germany) were investigated. All materials were reinforced with E-glass fibres (GF) in the content range of 10–50 wt% and added with maleic anhydride (MAH) as coupling agent to improve the bonding conditions between fibres and matrix. For both materials, an enhanced crystallinity was reached with the nucleating agent Echtblau (i.e. German for “true blue”) with an optimised content of 0.1 wt%. The influence of the glass fibre content on the mechanical properties like strength, stiffness, toughness, and hardness is shown for the PP and PB-1 materials in [36]. In this article, the results for the materials reinforced with 20 and 50 wt% glass fibre were discussed.

According to MPK-ICIT procedure [37], instrumented Charpy impact tests (ICIT) for the assessment of the toughness under impact loading were executed.

The test speed v was 1.0 ms^{-1} , which corresponds to a falling angle of 40° by the used pendulum impact tester with a maximum work capacity of 4 J [19]. Single-edge-notched bending (SENB) specimens ($80 \times 10 \times 4 \text{ mm}^3$) were prepared from multipurpose test specimens, and the notches were produced by means of a manual notching device with a razorblade with a blade tip radius r of approx. $0.3 \text{ }\mu\text{m}$. Initial crack length a was 2 mm , which corresponds to a ligament length of 8 mm and a crack length/width (a/W) ratio of 0.2 , respectively. Support span s was 40 mm , and to ensure comparable conditions for all specimens, they were stored in standard climate (16 h at $23 \text{ }^\circ\text{C}$ and 50% humidity).

For the assessment of the toughness, fracture toughness K_{Id} , critical crack-tip-opening displacement δ_{Id} , and critical J -value J_{Id} were used according to the evaluation method of Sumpter and Turner (ST). Detailed information about fracture mechanics concepts as well as on the geometry independence of the fracture mechanics parameters can be found in [29–31, 35, 38, 39].

Next to the assessment of the toughness with the help of fracture mechanics concepts, it is possible to detect the initial material damage by the evaluation of the quantity load at the beginning of damage F_s , the deflection at the beginning of damage f_s , and the corresponding energy A_s . The calculations of the fracture mechanics parameters at initiation of micro-mechanical damages were carried out according to (10.5)–(10.7).

$$K_{\text{Si}} = \frac{F_s \cdot s}{B \cdot W^{3/2}} \cdot f\left(\frac{a}{W}\right) \quad (10.5)$$

$$\delta_{\text{Si}} = \frac{1}{4} \cdot (W - a) \cdot \frac{4 \cdot f_s}{s} \quad (10.6)$$

$$J_{\text{Si}} = \eta_{\text{el}} \cdot \frac{A_s}{B \cdot (W - a)} \quad (10.7)$$

AE takes place during an external loading, which can induce specific damage mechanisms like debonding, pull-out with matrix yielding and/or fibre fracture. For the AE measurements, the identical equipment, which was discussed in the prior section, was used. For a suitable coupling of the broadband sensor to the specimen surface, beeswax was used. To prevent a one-sided clamping of the specimen, no specific clip for realising a fixing of the sensor was necessary. Based on the given experimental set-up with a support span s of 40 mm , the distance between the broadband sensor and the notch tip was 30 mm . The acoustic sensor was connected directly with a digital oscilloscope Yokogawa DL1620 (Yokogawa Deutschland GmbH). Therefore, a simultaneous recording of the load signal and the transient AE characteristic (HF signal) on the one hand, and a wavelet transform (WT) of the complete high-frequency signal on the other hand are possible. Figure 10.7 shows the test set-up with the AE sensor mounted on the specimen surface.

By means of a repeatable recording of an artificial transient signal, it was possible to verify the operability of the used AE sensors according to [40].

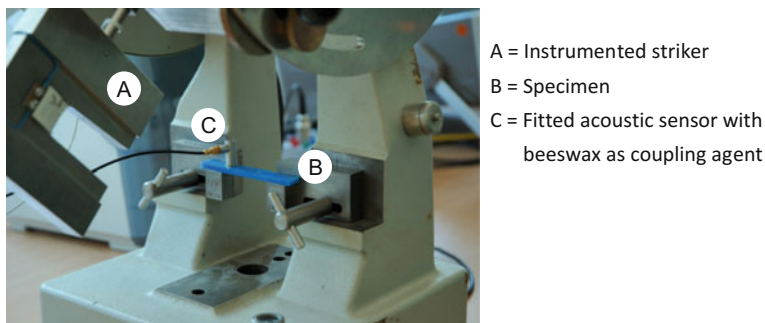


Fig. 10.7 Test set-up of the ICIT with simultaneously AE measuring

10.4 Results

10.4.1 ESEM Investigations—Coupling the In Situ Tensile Test with AE Analysis

ESEM micrographs of the occurring damage mechanisms in the *PP/20 material* at different times are shown in Fig. 10.8. In front of the notch tip, low forces lead to elastic deformation around the glass fibres as well as to elastic widening of the crack flanks. At the point of the transition from linear viscoelastic to non-linear viscoelastic behaviour, the loading leads to void formation at the end of the glass (fibres indicated by the letter i) as well as to a blunting of the sharp surface crack (ii), which is a result of the notching and the polishing of the specimen. The onset of the irreversible damage of the material at 81 s correlates with the increased hits and energy E_{AE} , respectively. A further increase in the loading results in a fibrillation of the matrix (iii) due to a further widening of the notch and in plastic deformations around the glass fibres (i), according to the loading direction. From the strong plastic deformations around the glass fibres, good bonding conditions of the fibres in the PP matrix can be derived. This is connected with possible load transmission between matrix and fibres and leads to a local ductility in the bordering matrix [41, 42]. At this time, the dissipation zone is of a larger volume and it causes a larger number of AE events. This is marked with the letter “A” in Fig. 10.8. The dissipation zone is, in accordance with the literature [41, 43, 44], the zone in front of the notch tip in which the deformation processes are extended to a certain area due to the stress field resulting from the external loading. The widening of the notch as well as the plastic deformation around the glass fibres in the dissipation zone increases with further loading. In addition, trough-shaped plastic deformations in front of the notch tip can be found (iv). Figure 10.8 shows that the glass fibre directly in front of the notch breaks as a consequence of the increasing size of the dissipation zone. The increasing widening of the notch leads, next to the fibrillation of the matrix, to debonding and afterwards to the pull-out of glass fibres. Based on the good bonding conditions, slip processes along the glass fibres can be recognised

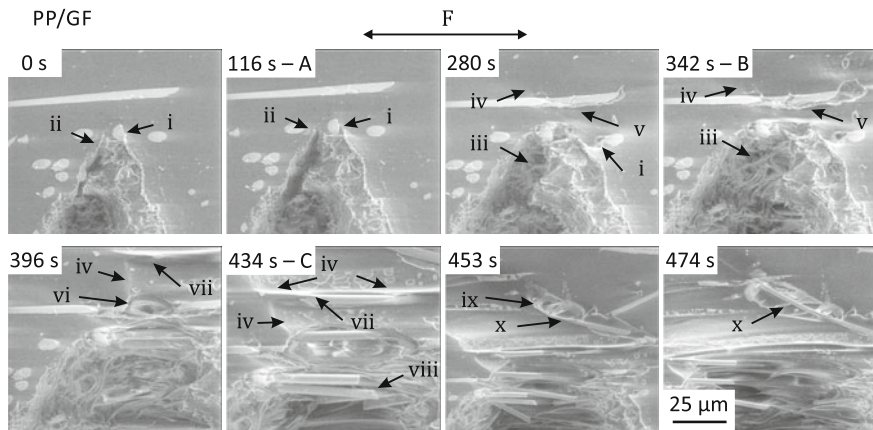


Fig. 10.8 ESEM micrographs at defined times for PP/20; explanation of the micromechanical deformation mechanisms (i–x) is given in the text; the scale in the last micrograph is valid for all ESEM micrographs

which result in an increase in AE energy (B), because of the identical distribution of the hits [19]. The damage in front of the notch tip is characterised by void formation and drawing out of matrix material into the voids (vi), which looks similar to a typical craze growth mechanism [41]. The pull-out of the glass fibres corresponds to friction processes due to the good bonding conditions (vii). The plastic deformations after a time of 434 s reach a magnitude at which the fibres are detached from one side of the matrix (viii), eventually leading to the load maximum (C). At this time, the recognised damage mechanisms are fibrillation of the crack flanks, visible surface damage in form of trough-shaped plastic deformations, and local impressions, as well as pull-out of fibres with strong plastic deformation of the covering matrix (viii). At the same time, the interface between fibre/matrix with fibrillation of the remaining matrix ligaments fails (Fig. 10.8-ix). The low deformation hindrance of fibres near the surface leads, in opposition to fibres in the centre of the specimen, to an orientation towards the loading direction (x).

The failure of the specimen is characterised by two different stages. On the basis of different ESEM micrographs, it can be assumed that at the point of maximum load stable crack propagation occurs. The further reduction of the ligament leads to the ultimate failure of the specimen in form of unstable crack propagation.

The functional interrelationship between the load–time curve, the energy E_{AE} and the peak amplitude values A_p for the PP/GF material is shown in Fig. 10.9a, b. For the frequency distribution of the energy, a period (bin size) of 5 s, which correlates to 100 sections at a test duration of approx. 500 s, was used. From the curve progression, a separation of the characteristic AE behaviour into three segments can be carried out. The separation of the different segments is highlighted by vertical dotted lines. Segment I is characterised by linear elastic and linear viscoelastic behaviour with minor AE activity. At the test duration of 81 s, the

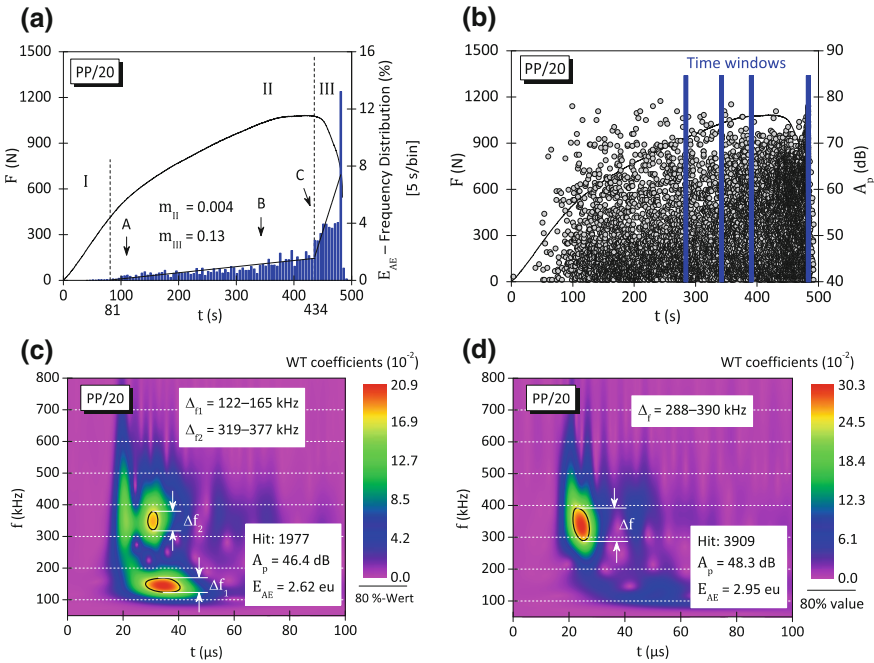


Fig. 10.9 Load (F)–time (t) diagrams and frequency distribution of the energy E_{AE} (a) as well as presentation of the considered time windows (blue lines) for the frequency analysis (b) and correlation of characteristic frequency ranges with the occurring damage mechanisms fibre fracture (c) and debonding and pull-out with matrix yielding as well as friction in the polymer matrix (d) for PP/20

transition from linear viscoelastic to non-linear viscoelastic behaviour in form of a continuous increase in AEs (segment II) occurs [19]. In the last section, an increase in AE activity is recognisable due to the stable crack propagation after the maximum load (434 s). The maximum energy release takes place at the point of unstable crack propagation at 484 s, which can be attributed to damage accumulation as a result of the fracture of the specimen (segment III).

A mathematical description of the functional interrelationship between the increase in the load and the cumulative energy presentation (Fig. 10.9a) can be deduced from a linear regression of segments II and III. The slope of the regression curves (m_{II} and m_{III}) is a measure of the increase in the energy due to increased AE activity. An increase in the slope in the range of 2 is recognisable. A separation into three segments was not possible for the A_p values because of the dependency of the attenuation of the mechanical stress wave on the distance between AE sensor and AE source and/or superposition of source signal and reflections. This leads to a non-specific distribution of the A_p values (Fig. 10.9b). Precondition for correlations between damage mechanisms and frequency ranges is the chronological validation of the damage mechanisms. On the basis of the results, suitable time windows can

be derived with a sufficient number of AEs (hits). The determination of time windows allows the analysis of the recorded hits in the defined time windows with the help of the wavelet transform. Figure 10.9a illustrates the considered time windows (highlighted in blue) for PP/20 with a width of 4 s for the first three and a width of 0.6 s for the last time window at the point of ultimate failure. The basis for the identification of frequency ranges is the functional relationship between frequency f , time t and wavelet coefficients (WT coefficients). Figure 10.9c, d shows the determination of the frequency ranges by means of selected transient signals. The main frequency range is identified by the 80% criterion; this means that only WT coefficients, which are higher or equal to the 80% value of the maximum, were considered. However, for the definition of the characteristic frequency ranges and the categorisation concerning the damage mechanisms for PP/20, all hits in the time windows were used. Thus, three frequency ranges could be determined. The range between 122 and 165 kHz can be attributed to the mechanism “fibre fracture”, whereas the first observed fibre fractures result from the polishing process (Fig. 10.9c). As mentioned above, the mechanism “fibre fracture” was described in the literature in a broad frequency spectrum of 30–700 kHz (see Fig. 10.3). It should be noted that the notch and the increased loading rate support the assumption of the occurring mechanism “fibre fracture”. Also, in consequence of the polishing process as well as of the notching of the specimen, the load-bearing capacity of damaged fibres is less than of non-damaged fibres, resulting in a lower stored elastic energy. On the other hand, these pre-damages lead to fibre fracture below the critical fibre length and to a lower frequency range because of the lower load-bearing capacity [19]. From the frequency analysis, a further frequency range of 319–377 kHz (Fig. 10.9c) could be determined, which may have been caused by friction processes of fractured fibres in the PP matrix. A further loading leads to void formation in front of the notch, followed by deformation of matrix material with slipping of material into the voids and friction of fibres in the delamination area (major volume area). Another characteristic frequency range is presented in Fig. 10.9d. On the basis of the results from the in situ tensile, it was possible to correlate the range of 288–390 kHz with the mechanism “pull-out with matrix yielding” as well as with friction processes in the PP matrix. In consideration of all hits (transient signals in the time windows), a frequency chart could be obtained (Fig. 10.10).

From the representation of the normalised frequency distribution in Fig. 10.10, it could be derived that the dominant damage mechanisms are debonding and pull-out with matrix yielding. It is noticeable that the fibre fracture, induced by the polishing process, occurred only at the beginning of the test and contributed only a minor proportion to the entire damage process. The results correlate with the qualitative assessment of the ESEM micrographs taken during the in situ tensile test and with the following fractography of the fracture surface. They are also in agreement with the literature [19, 45, 46].

In this part, the results for the *PB-1/20 material* are discussed. The deformation mechanisms should be illustrated with different ESEM micrographs at defined times (Fig. 10.11). With increasing loading, elastic widening of the crack flanks can be

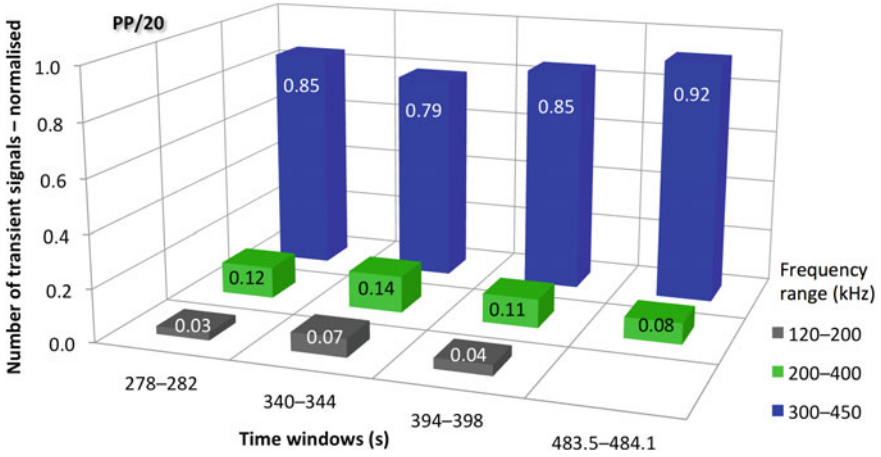


Fig. 10.10 Normalised number of transient signals (hits) with frequency ranges for PP/20

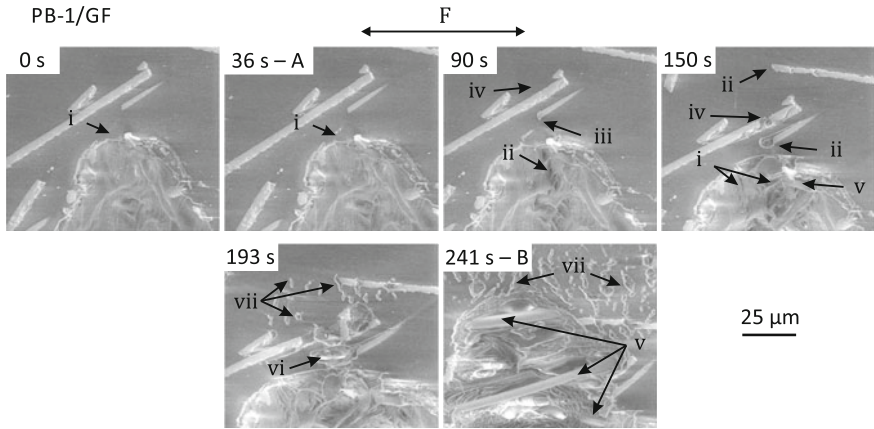


Fig. 10.11 ESEM micrographs at defined times for PB-1/20; explanation of the micromechanical deformation mechanisms (i–vii) given in the text; the scale is valid for all ESEM micrographs

observed. This is indicated in Fig. 10.11 by the letter i. A further increase in the load leads to fibrillation of the matrix (ii) and to void formation at the ends of the glass fibres (iii). In contrast to the interactions of the glass fibres with the PP matrix, due to the good bonding conditions (see Fig. 10.8), in PB-1/20 no fibrillation of matrix material at the end of the glass fibres is visible and therefore the load transmission between matrix and fibre is limited. By increasing loading, the glass fibre directly in front of the notch is broken (iv); the reason for this occurrence was given in the last section for PP/20 above. The strong widening of the notch leads to the pull-out of glass fibres, so that at one crack flank glass fibres become visible (v). The damage mechanisms after a time period of 191 s are characterised by the

Table 10.1 Correlation of frequency ranges and damage mechanisms of PP/20

Frequency range (kHz)	Damage mechanisms
110–210	Fibre fracture
200–440	Matrix deformation with slipping of fibres in the delamination area and friction processes of the fibres in the matrix
300–470	Debonding and pull-out with matrix yielding

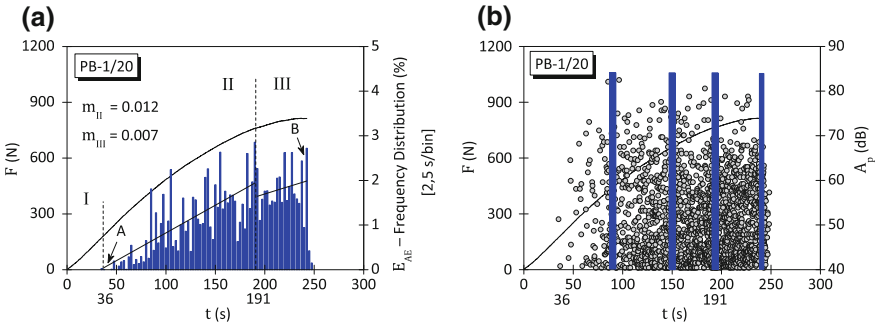


Fig. 10.12 Load–time diagrams and frequency distribution of the energy E_{AE} (a) as well as presentation of the considered time windows (blue lines) for the frequency analysis (b) for PB-1/20

formation of voids in front of the notch (vi) and the deformation of these voids with sliding of a certain volume of matrix material. At this time, surface cracks (vii) which grow through the increasing dissipation zone, are visible. This process also leads to coalescence of several surface cracks and hence finally to crack propagation.

By means of this frequency distribution and under consideration of the chronological damage mechanisms, correlations between time, damage mechanisms and frequency are possible (Table 10.1).

Figure 10.12a, b shows energy E_{AE} and peak amplitude values A_p for PB-1/20 in combination with the load–time curve. Similar to PP/20, for PB-1/20 E_{AE} is represented as frequency distribution with a bin size of 2.5 s. The bin size results from the shorter test time of 250 s and correlates to 100 sections. For this reason, it is possible to compare the results among each other. The separation of the AE results into three segments with different AE activity is possible for PB-1/20 too. The transition from linear to non-linear viscoelastic behaviour is characterised by a continuous increase in the AEs. This transition is indicated in Fig. 10.12a by the letter A (cf. Fig. 10.11). In segment III, before the maximal load is reached, saturation of energy E_{AE} and thus of the hits occurs. This means that an increase of the loading and therewith the increase of the dissipation zone leads to a constant quantity of AE events [19]. Analogous to the mathematical description of the energy release of PP/20, the slopes in segment II and III were determined.

The comparison of these values leads also to the conclusion that energy E_{AE} in segment II is insignificantly higher than in segment III due to the saturation of the hits in segment III. An explanation of this behaviour is mentioned below. The fracture of PB-1/20 at a time of 242 s (B) is characterised by unstable crack propagation (abrupt decrease in the load) with no significant energy release at the break of the specimen. This means that the fracture behaviour of PB-1/20 is different to that of PP/20.

Due to the bad bonding conditions and the formation of surface cracks after 191 s, a description of the mentioned saturation effect is possible. The formation of surface cracks shows only a low interaction between the glass fibres and therefore only limited energy dissipative processes like pull-out with matrix yielding as well as sliding of glass fibres. This is the reason for the saturated AE activity in segment III between 191 s and the ultimate failure of PB-1/20. A quantitative expression for this behaviour is provided by the comparison of the amount of energy E_{AE} at the point of fracture and the slope of the regression curves in segment III. The obtained values for energy E_{AE} and the slopes of PP/20 and PB-1/20 are 12 and 3% of the total energy and 0.13 and 0.007, respectively. However, the stress concentration at the surface cracks of PB-1/20 leads to a further increase in load until the specimen breaks.

The wavelet transform of the recorded AEs for PB-1/20 takes place in the same manner as for PP/20 under consideration of the chronological correlation of the damage mechanisms in front of the notch tip. Thus, also for these materials direct correlations with characteristic frequency ranges are possible. The classification of three frequency ranges like for PP/20 could be realised also for PB-1/20. To provide an example, Fig. 10.13a–c shows the results of the wavelet transform of selected hits (transient signals). The frequency distribution of the occurring frequency ranges in the selected time windows, normalised to the total number of hits, is illustrated in Fig. 10.14. The frequency range of 113–186 kHz could be correlated with the mechanism “fibre fracture” (Fig. 10.13a), although it could be observed that it contributed a larger proportion to the ultimate failure than PP/20 did. This can be traced back to the polishing process. Because the difference in hardness between PB-1 matrix and glass fibres is higher than that for the PP matrix and glass fibres, a higher increase in temperature during the polishing process occurs. This is visible on the specimen surface in form of striations. Therefore, the pre-damage in PB-1/20 is greater than in PP/20, which the frequency distribution in Fig. 10.14 clearly shows. Furthermore, the load-bearing capacity of the fibres is limited due to poor bonding of the fibres in the PB-1 matrix. This means that the stored elastic energy is also limited. This leads to a lower frequency range for the mechanism “glass fibre fracture”. The material failure is characterised by unstable crack propagation and the dominant damage mechanism is the pull-out of fibres connected with friction processes in the PB-1 matrix. At this time, almost no glass fibre fractures occurs, which can be reduced to the relation between the mean fibre length of 276 μm and the theoretically calculated critical fibre length of 1200 μm [19]. The plastic deformation leads to void formation in front of the notch, followed by deformation of the voids and thus a consideration of a larger volume area. The typical frequency

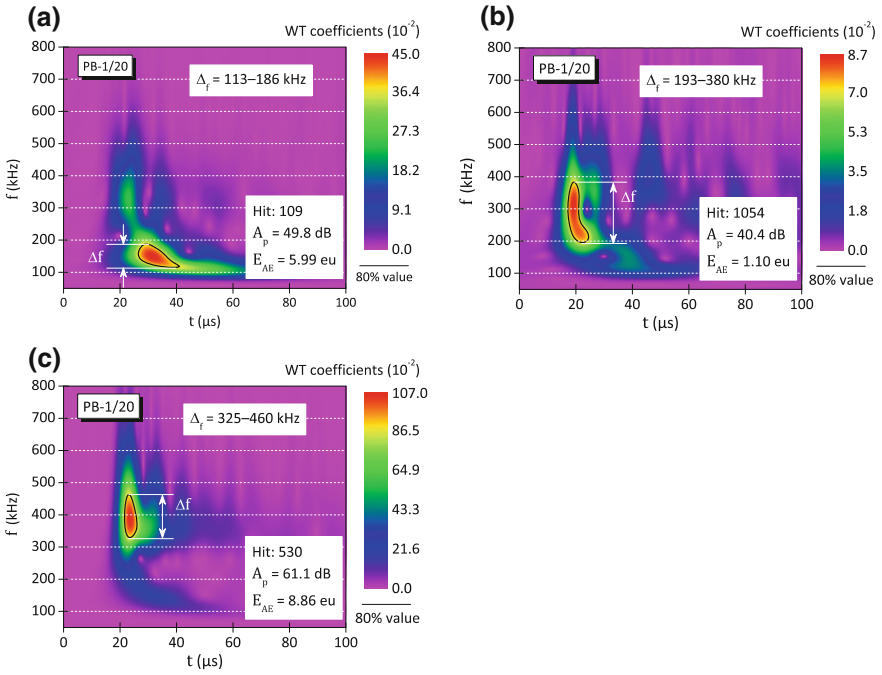


Fig. 10.13 Correlation of characteristic frequency ranges with the occurring damage mechanisms fibre fracture (a), plastic deformation of matrix material with slipping of material into the voids and friction processes (b) as well as pull-out of fibres without matrix yielding (c) for PB-1/20

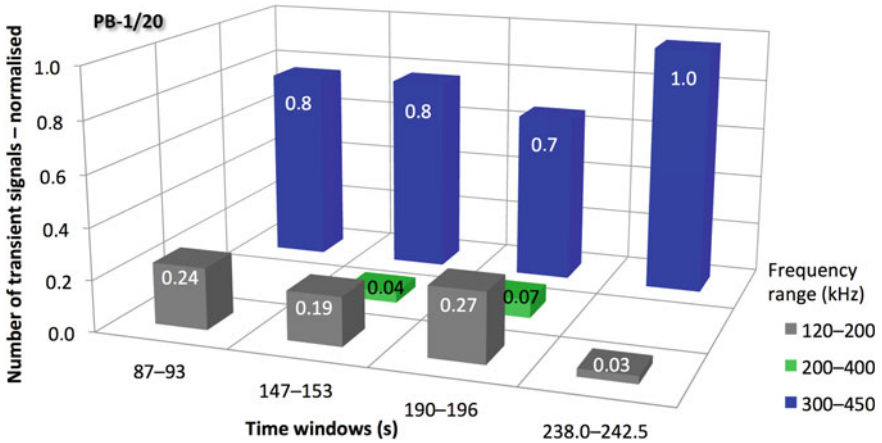


Fig. 10.14 Normalised number of transient signals (hits) with frequency ranges for PB-1/20

Table 10.2 Correlation of frequency ranges and damage mechanisms of PB-1/20

Frequency range (kHz)	Damage mechanisms
120–200	Fibre fracture
200–410	Matrix deformation with slipping of fibres in the delamination area and friction processes of fibres in the matrix
300–450	Pull-out of fibres without matrix yielding

pattern for these mechanisms ranges between 193 and 380 kHz (Fig. 10.13b). Due to the poor fibre/matrix bonding, the frequency range of 325–460 kHz (Fig. 10.13c) can be correlated with the dominant damage mechanisms “pull-out of fibres without matrix yielding” and “friction of fibre” in the PB-1 matrix.

Table 10.2 lists the characteristic frequency ranges determined in the observed time windows as well as the corresponding damage mechanisms.

10.4.2 AE Measurements During ICIT

Figures 10.15a–d and 10.16a–d show the electrical output voltages of the acoustic sensor U , as well as the results of the WT coefficients combined with the load–time diagram (F – t diagram) for PE-HD/20, PE-HD/50, PB-1/20, and PB-1/50 as examples.

The PE-HD/20 material is characterised by an elastic–plastic material behaviour with a part of crack propagation energy (Fig. 10.15a). The latter is indicated by a slight decrease of load F after reaching maximum load F_{\max} and occurs under energy consumption. The PB-1/20 shows an identical material behaviour, this means, it is also characterised by an elastic–plastic behaviour with a distinctive part of crack propagation energy. Further information about the fracture mechanical behaviour of the short-glass fibre-reinforced polyolefins can be found in [47].

The AEs were recorded at different times. At maximum load F_{\max} , this means at the beginning of the crack propagation, an increased number of AEs were recorded. However, the stored elastic energy in the specimen is transferred into mechanical and acoustic energy during the crack propagation. The temporary onset of the AE for PE-HD/20 and PE-HD/50 is clearly recognisable before the transition of elastic to elastic–plastic behaviour, indicated by F_{gy} , takes place. Thus, it is possible to determine the corresponding load at the point of the first AEs, which is indicated by F_s in Fig. 10.15a–d. In contrast to this typical behaviour of PE-HD/GF, the onset of the AEs for the PB-1/20 and PB-1/50 materials takes place directly at the transition of elastic to elastic–plastic behaviour (Fig. 10.16a–d). The first AEs can be correlated with the blunting process of the original crack tip due to the plastic deformation. This means that the first AEs represent the beginning of material damage. The plastic deformations are characterised especially for neat polymers as stretch zone height (SZH) and stretch zone width (SZW) at the fracture surface. Due

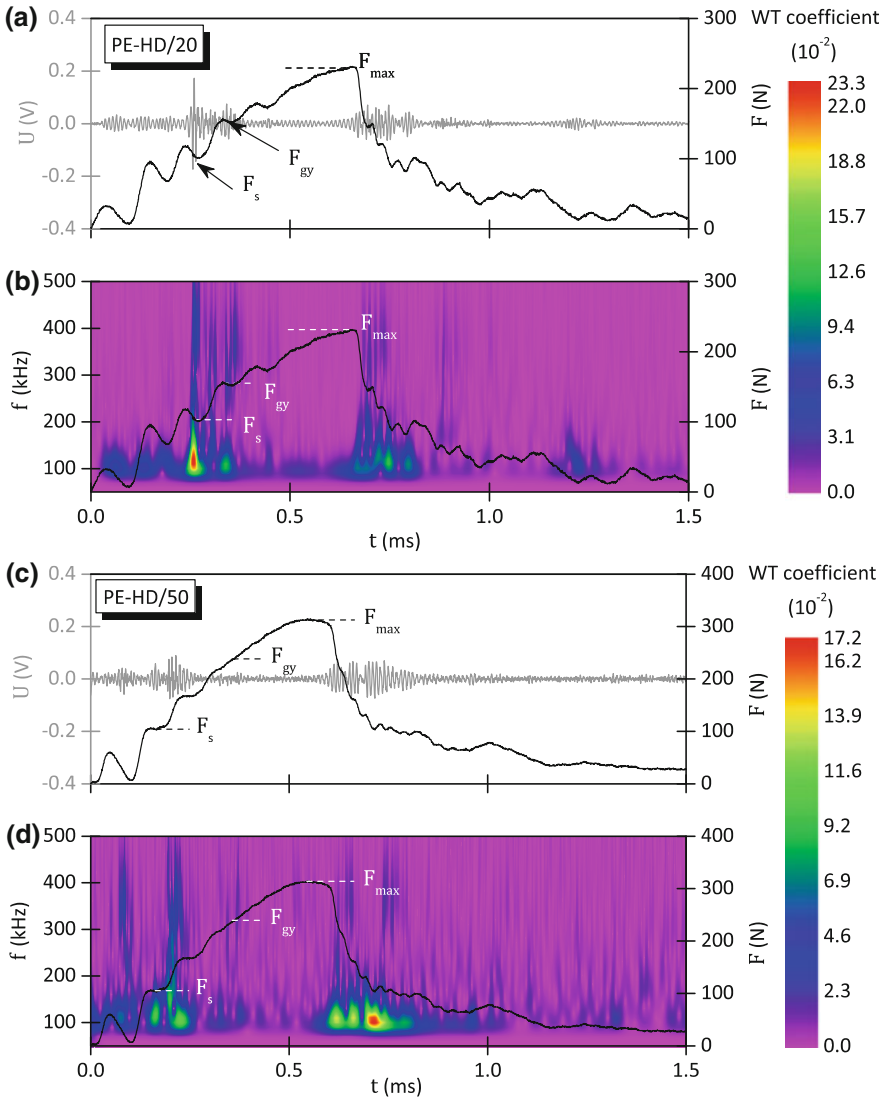


Fig. 10.15 Load (F)-time (t) diagrams as well as recorded electrical voltage signals of the acoustic sensor and the results of the wavelet transform for PE-HD/20 (a, b) and PE-HD/50 (c, d)

to the complexity of the glass fibres on the top of the fracture surfaces, the detection of SZH and SZW is strongly limited; therefore, the recording of the AEs can be used as an indirect detection method of the blunting process and the beginning of stable crack propagation. The good bonding between PE-HD matrix and glass fibres leads to AEs before the transition of elastic to elastic-plastic behaviour takes place. However, the first AEs of the PB-1 materials occur at F_{gy} . This behaviour can be

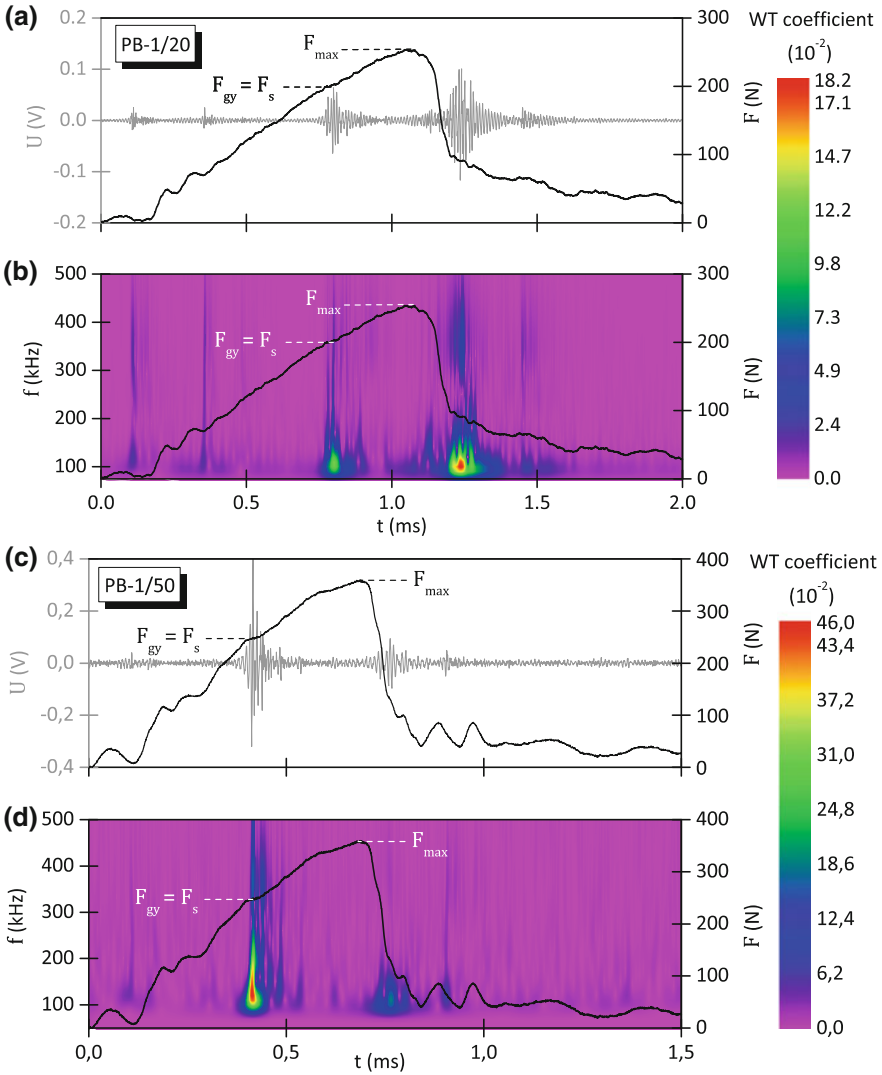


Fig. 10.16 Load (F)–time (t) diagrams as well as recorded electrical voltage signals of the acoustic sensor and the results of the wavelet transform for PB-1/20 (a, b) and PB-1/50 (c, d)

explained with the weak bonding of the glass fibres in the PB-1 matrix and therefore with the limited load-bearing capacity. For this reason, the blunting process does not release enough elastic energy to receive AEs. In addition, for PE-HD/20, PE-HD/50, PB-1/20, and PB-1/50, further AEs were only recorded at the point of unstable crack propagation. The input energy during the stable crack propagation is obviously dissipated and only at the point of unstable crack propagation, a release of the stored elastic energy occurs.

The WT of the recorded AEs show different frequency ranges at various times. A physical classification of the occurring damage mechanisms according to the frequency ranges is impractical without a validation, for example, through the coupling of the in situ tensile test in the environmental scanning electron microscope (ESEM) with AE analysis. Results of such investigations are discussed in the previous sections.

The damage in the notch base can be described with the AE analysis and quantified by the measured values F_s and f_s . Thus, an assessment of the material behaviour regarding the initiation of micro-mechanical damage mechanisms according to (10.5)–(10.7) is possible. A graphical representation of the fracture mechanics value versus damage initiation shows Fig. 10.17a–c.

The load-determined K_{Si} values increase continuously for both materials with higher glass fibre contents (Fig. 10.17a), whereas the higher fibre content leads to the reduction in the deformation ability and therefore to a decrease in the δ_{Si} -values (Fig. 10.17b). For this reason, the energy-determined J_{Si} -values are affected neither by the addition of glass fibres nor by the different matrix systems due to the superposition of the load and deformation part of the fracture. Thus, fracture parameter J_{Si} describes the energy part, which is needed for the blunting of the crack tip (Fig. 10.17c). However, at a critical energy, the stable crack propagation with constant energy consumption occurs. The determination of parameter J_{Si} based on the results of AE measurements is a quantitative assessment of the blunting of the crack tip and thus an assessment of the resistance against stable crack propagation [19]. The results of this work are consistent with the work of Seidler [48], who found, on the basis of crack resistance curves (R-curves) for different polymer systems, that the morphology of a polymer material has a stronger effect on the stable crack propagation behaviour than on the crack initiation behaviour.

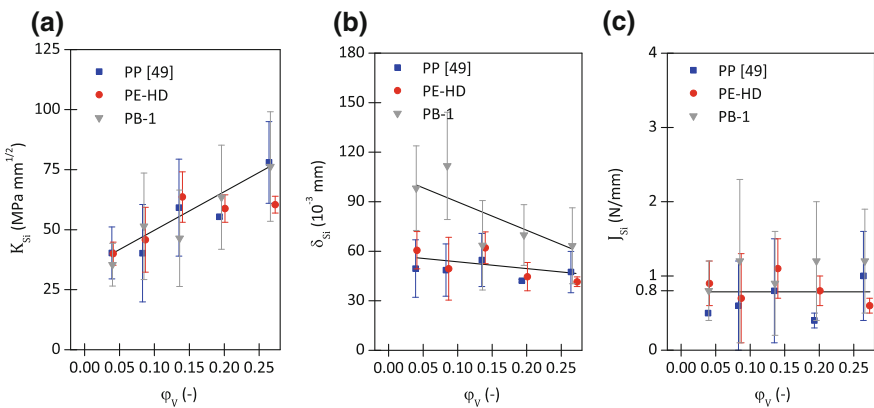


Fig. 10.17 Fracture mechanics values K_{Si} (a), δ_{Si} (b), and J_{Si} (c) at the damage initiation in dependence on the glass fibre content for PE-HD/GF and PB-1/GF composites; results for the PP/GF composites obtained from [47]

10.5 Summary

The AE analysis is a structure-sensitive test method of plastic diagnostics, which enables the characterisation of the damage kinetics as well as damage mechanisms under specific conditions. The AE analysis is linked to release of stored elastic energy, which propagates as spherical volume wave in the material.

In this work, short-glass fibre-reinforced thermoplastic materials were examined in the quasi-static tensile test in the ESEM with simultaneously recording of the AE as well as under impact-loading conditions in the ICIT. Therefore, it was possible to couple the mechanical, the acoustic and the micromechanical results to describe the damage kinetic as well as the damage mechanisms. In dependence on the bonding conditions of the glass fibre in the polymer matrix, the following correlations could be made (Table 10.3).

Table 10.3 Correlation of frequency ranges and damage mechanisms

Frequency range (kHz)	PP/20 Good bonding conditions	Frequency range (kHz)	PB-1/20 Poor bonding conditions
110–210	Fibre fracture	110–200	Fibre fracture
200–440	Matrix deformation with slipping of fibres in the delamination area and friction processes of the fibres in the matrix	200–410	Matrix deformation with slipping of fibres in the delamination area and friction processes of fibres in the matrix
300–470	Debonding and pull-out with matrix yielding	300–450	Pull-out of fibres without matrix yielding

Based on the results from the AE analysis for different phases in the tensile test, the debonding and pull-out with matrix yielding for PP/20 as well as debonding and pull-out without matrix yielding for PB-1/20 as dominant damage mechanisms could be defined.

The coupling of the AE analysis with the ICIT allows the assessment of the damage kinetic and therefore, the determination of the damage initiation under impact-loading conditions. However, in dependence on various bonding conditions, different results could be found. For good bonding conditions, the damage initiation takes place before the material behaviour changes from elastic to elastic–plastic behaviour. This could be found for the short-glass fibre-reinforced PE-HD materials. For the fibre-reinforced PB-1 materials, the first AE takes place at the point of elastic–plastic material behaviour. An energetic approach of the damage initiation by the parameter J_{Si} shows an independent behaviour from the polymer matrix as well as from the glass fibre content. For all investigated thermoplastics, a J_{Si} -value of 0.8 N/mm as resistance against stable crack propagation could be determined.

Acknowledgements The authors would like to thank LyondellBasell Industries, Frankfurt, Germany for providing the short-glass fibre-reinforced materials used in this study. Dr. T. Mecklenburg is acknowledged for his help and many fruitful discussions.

References

1. Grellmann, W., Seidler, S. (eds.): *Polymer Testing*, 2nd edn. Carl Hanser, Munich (2013)
2. Zankel, A., Pölt, P., Ingolic, E., Gahleitner, M., Grein, C.: The fracture behaviour of polymers—In situ investigations in the ESEM. *Imaging Microsc.* **7**, 16–18 (2005)
3. Zankel, A., Pölt, P., Gahleitner, M., Ingolic, E., Grein, C.: Tensile tests of polymers at low temperatures in the environmental scanning electron microscope: an improved cooling platform. *Scanning* **29**, 261–269 (2007)
4. Nase, M., Zankel, A., Langer, B., Baumann, H.J., Grellmann, W., Poelt, P.: Investigation of the peel behavior of polyethylene/polybutene-1 peel films using in situ peel tests with environmental scanning electron microscopy. *Polymer* **49**, 5458–5466 (2008)
5. Bardenheier, R.: Schallemissionsuntersuchungen an polymeren Verbundwerkstoffen – Teil I: Das Schallemissionsmeßverfahren als quasi-zerstörungsfreie Werkstoffprüfung. *Zeitschrift für Werkstofftechnik* **11**, 41–46 (1980)
6. Grosse, C.U., Ohtsu, M. (eds.): *Acoustic Emission Testing—Basics for Research—Applications in Civil Engineering*. Springer, Berlin (2008)
7. Bierögel, C.: Hybrid methods of polymer diagnostics. In: Grellmann, W., Seidler, S. (eds.) *Polymer Testing*, 2nd edn. Carl Hanser, Munich (2013), pp. 497–511
8. Bohse, J.: Acoustic emission characteristics of micro-failure processes in polymer blends and composites. *Compos. Sci. Technol.* **60**, 1213–1226 (2000)
9. Ramirez-Jimenez, C.R., Papadakis, N., Reynolds, N., Gan, T.H., Purnell, P., Pharaoh, M.: Identification of failure modes in glass/polypropylene composites by means of the primary frequency content of the acoustic emission event. *Compos. Sci. Technol.* **64**, 1819–1827 (2004)
10. Barré, S., Benzeggagh, M.L.: On the use of acoustic emission to investigate damage mechanisms in glass-fibre-reinforced polypropylene. *Compos. Sci. Technol.* **52**, 369–376 (1994)
11. Ségard, E., Benmedakhene, S., Laksimi, A., Laï, D.: Damage analysis and the fibre–matrix effect in polypropylene reinforced by short glass fibres above glass transition temperature. *Compos. Struct.* **60**, 67–72 (2003)
12. Kocsis, Z., Czigány, T.: Investigation of the debonding process in wood fiber reinforced polymer composites by acoustic emission. *Mater. Sci. Forum* **537–538**, 199–206 (2007)
13. Yu, Y.-H., Choi, J.-H., Kweon, J.-H., Kim, D.-H.: A study on the failure detection of composite materials using an acoustic emission. *Compos. Struct.* **75**, 163–169 (2006)
14. Giordano, M., Calabrò, A., Esposito, C., Salucci, C., Nicolais, L.: Analysis of acoustic emission signals resulting from fiber breakage in single fiber composites. *Polym. Compos.* **20**, 758–770 (1999)
15. de Groot, P.J., Wijnen, P.A.M., Janssen, R.B.F.: Real-time frequency determination of acoustic emission for different fracture mechanisms in carbon/epoxy composites. *Compos. Sci. Technol.* **55**, 405–412 (1995)
16. Ni, Q.-Q., Iwamoto, M.: Wavelet transform of acoustic emission signals in failure of model composites. *Eng. Fract. Mech.* **69**, 717–728 (2002)
17. Gutkin, R., Green, C.J., Vangrattanachai, S., Pinho, S.T., Robinson, P., Curtis, P.T.: On acoustic emission for failure investigation in CFRP: Pattern recognition and peak frequency analyses. *Mech. Syst. Signal Process.* **25**, 1393–1407 (2011)
18. Haselbach, W., Lauke, B.: Acoustic emission of debonding between fibre and matrix to evaluate local adhesion. *Compos. Sci. Technol.* **63**, 2155–2162 (2003)

19. Schoßig, M.: Schädigungsmechanismen in faserverstärkten Kunststoffen – Quasistatische und dynamische Untersuchungen. Vieweg+Teubner/Springer, Wiesbaden (2011)
20. Suzuki, H., Kinjo, T., Hayashi, Y., Takemoto, M., Ono, K.: Wavelet transform of acoustic emission signals. *J. Acoust. Emission* **14**, 69–84 (1996)
21. Blatter, C.: Wavelets—Eine Einführung. Advanced Lectures in Mathematics Series, 2nd edn. Friedrich Vieweg & Sohn, Braunschweig (2003)
22. Goupillaud, P., Grossmann, A., Morlet, J.: Cycle-octave and related transforms in seismic analysis. *Geoexploration* **23**, 85–102 (1984)
23. Stokes, D.J.: Principles and Practice of Variable Pressure/Environmental Scanning Electron Microscopy (VP-ESEM). John Wiley & Sons, Chichester (2008)
24. Dragnevski, K.I.: A brief overview of in-situ mechanical testing in the environmental scanning electron microscope. *Micro Nanosyst.* **4**, 92–96 (2012)
25. Schoßig, M., Zankel, A., Bierögel, C., Pölt, P., Grellmann, W.: ESEM investigations for assessment of damage kinetics of short glass fibre reinforced thermoplastics—Results of in situ tensile tests coupled with acoustic emission analysis. *Compos. Sci. Technol.* **71**, 257–265 (2011)
26. Michler, G.H., Lebek, W.: Ultramikrotomie in der Materialforschung. Carl Hanser, Munich (2004)
27. Zankel, A., Chernev, B., Brandl, C., Poelt, P., Wilhelm, P., Nase, M., Langer, B., Grellmann, W., Baumann, H.J.: Assessment of beam damage in polymers caused by in situ ESEM analysis using IR spectroscopy. *Macromol. Symp.* **265**, 156–165 (2008)
28. Jungbluth, M.: Untersuchungen zum Einfluß der Prüfkörperdicke und der Temperatur auf die Zähigkeitseigenschaften von PVCC und PVC bei stoßartiger Beanspruchung. Diploma thesis, Technische Hochschule Carl Schorlemmer Leuna-Merseburg, Merseburg (1982)
29. Grellmann, W.: Beurteilung der Zähigkeitseigenschaften von Polymerwerkstoffen durch bruchmechanische Kennwerte. Habilitation thesis, Technische Hochschule Carl Schorlemmer Leuna-Merseburg, Merseburg (1985)
30. Grellmann, W., Sommer, J.-P.: Beschreibung der Zähigkeitseigenschaften von Polymerwerkstoffen mit dem *J*-Integralkonzept. *Fracture Mechanics, Micromechanics and Coupled Fields (FMC) Series 17*, pp. 48–72 (1985)
31. Grellmann, W., Sommer, J.-P., Hoffmann, H., Michel, B.: Application of different *J*-integral evaluation methods for the description of toughness properties of polymers. In: Proceedings of the 1st Conference on Mechanics (29.06.–03.07.1987, Prague). Prague (1987), vol. 5, pp. 129–133
32. Grellmann, W., Seidler, S., Lauke, B.: Application of the *J*-integral concept for the description of toughness properties of fiber reinforced polyethylene composites. *Polym. Compos.* **12**, 320–326 (1991)
33. Grellmann, W., Seidler, S.: *J*-integral analysis of fibre-reinforced injection-moulded thermoplastics. *J. Polym. Eng.* **11**, 71–101 (1992)
34. Blumenauer, H.: 100 Jahre Kerbschlagbiegeversuch nach Charpy. *Materialwiss. Werkstofftech.* **32**, 506–513 (2001)
35. Grellmann, W.: Fracture toughness measurements in engineering plastics. In: Grellmann, W., Seidler, S. (eds.) *Polymer Testing*, 2nd edn. Carl Hanser, Munich (2013), pp. 233–286
36. Schoßig, M., Grellmann, W., Mecklenburg, T.: Characterization of the fracture behavior of glass-fiber reinforced thermoplastics based on PP, PE-HD and PB-1. *J. Appl. Polym. Sci.* **115**, 2093–2102 (2010)
37. Grellmann, W., Seidler, S., Hesse, W.: Testing of plastics—Instrumented Charpy impact test (ICIT)—procedure for determining the crack resistance behaviour using the instrumented impact test (MPK-ICIT): Part I: Determination of characteristic fracture mechanics parameters for resistance against unstable crack propagation; Part II: Determination of characteristic fracture mechanics parameters for resistance against stable crack propagation. Merseburg (2016). http://wiki.polymerservice-merseburg.de/index.php/MPK-Prozedur_MPK-IKBV_englisch

38. Anderson, T.L.: *Fracture Mechanics—Fundamentals and Applications*. Taylor & Francis, Boca Raton (2005)
39. Grellmann, W., Lach, R., Seidler, S.: Determination of geometry-independent fracture mechanics values of polymers. In: Francois, D., Pineau, A. (eds.) *From Charpy to Present Impact Testing*. Publication 30, Elsevier Science: Oxford (2002), pp. 145–154
40. Schoßig, M., Bierögel, C., Grellmann, W.: *Prüfung von Kunststoffen—Schallemissionsanalyse—Prozedur zur Validierung von AE-Sensoren (PSM-AE)*. Merseburg (2010)
41. Michler, G.H.: *Kunststoff-Mikromechanik: Morphologie, Deformations- und Bruchmechanismen*. Carl Hanser, Munich Vienna (1992)
42. Cantwell, W.J., Roulin-Moloney, A.C.: Fractography and failure mechanisms of unfilled and particulate filled epoxy resins. In: Roulin-Moloney, A.C. (ed.) *Fractography and Failure Mechanisms of Polymers and Composites*, pp. 233–290. Elsevier Applied Science, London (1989)
43. Grellmann, W., Seidler, S. (eds.): *Deformation and Fracture Behaviour of Polymers*. Springer, Berlin (2001)
44. Michler, G.H.: *Electron Microscopy of Polymers*. Springer, Berlin (2008)
45. Michler, G.H., Baltá-Calleja, F.J.: *Nano- and Micromechanics of Polymers—Structure Modification and Improvement of Properties*. Carl Hanser, Munich (2012)
46. Friedrich, K.: Fractographic analysis of polymer composites. In: Friedrich, K. (ed.) *Application of Fracture Mechanics to Composite Materials*, pp. 425–487. Elsevier Science, Amsterdam (1989)
47. Schoßig, M., Bierögel, C., Grellmann, W.: Assessment of fracture behavior under impact loading with simultaneous recording of acoustic emission. *Mater. Test.* 84–91 (2013)
48. Seidler, S.: Anwendung des Reißwiderstandskonzeptes zur Ermittlung strukturbezogener bruchmechanischer Werkstoffkenngrößen bei dynamischer Beanspruchung. *Fortschritts-Berichte VDI-Reihe 18: Mechanik/Bruchmechanik Nr. 231*, VDI-Verlag, Düsseldorf (1997)

Chapter 11

The Fractography as a Tool in Failure Analysis—Possibilities and Limits

I. Kotter and W. Grellmann

Abstract Damage to plastic products often results in a fracture. Therefore, the fracture surface examination (fractography) is particularly important when performing failure analysis. By application of standardized fracture surface structures, the location of crack initiation and the direction of crack growth can be determined. Furthermore, the influence of temperature, type of loading, loading speed or stress due to media on the plastic product can be detected. It is very important that fractography is applied in combination with other methods of polymer diagnostics and analytics as a tool for damage assessment. In particular at filled and reinforced polymeric materials, the applicability of fractography is limited because of the jagged fracture surface induced by fillers and reinforcement materials.

11.1 Introduction

Damage to plastic products often results in a fracture. Hereby, a fracture is a material separation of a whole component into at least two parts due to not proper application. It is the consequence and final stage of crack propagation. Therefore, the fracture surface examination (fractography) is particularly important when performing failure analysis.

Initial statements to type of load, foreign inclusions or material impurity can be taken by macroscopic fractography already [1, 2]. A further microscopic assessment of fracture surfaces can provide information about e.g. temperature effect, loading speed, ageing processes, stress due to media or faulty processing [3].

Different structures are formed on fracture surfaces in dependence on crack propagation processes. So, a conclusion from the fracture patterns on the fracture processes is possible. It can detect the location of crack initiation. Furthermore

I. Kotter (✉) · W. Grellmann
Polymer Service GmbH Merseburg, Merseburg, Germany

W. Grellmann
Centre of Engineering, Martin Luther University Halle-Wittenberg,
Halle/Saale, Germany

statements about the fracture pattern, the direction of crack propagation, the cracking speed and the type of fracture can be done [4]. A stable crack growth, in which the crack propagation takes place at a relatively low speed while consuming energy, can be detected, for example, through comparatively large plastic deformations on the fracture face. In cases where the crack propagation is unstable, i.e. takes place at high speed and with the release of energy, the plastic deformation on the fracture surface is far less pronounced.

Fractography is the fracture surface examination—details and structures on fracture surface are identified. For this purpose, the imaging methods of light microscopy, scanning electron microscopy, atomic force microscopy and confocal microscopy are used. The sole use of fractography is for damage assessment usually not effective. In dependence on the task, it should be applied analytical methods for material identification or detection of material changes (e.g. degradation). Particularly in the case of glass fibre-reinforced materials, or even if one occurred tribological stress on the fracture surfaces, the success of fractography is limited.

11.2 Fractography—Fracture Surface Structures

In the failure analysis, it is important to know the location of crack initiation and the direction of crack propagation. With this knowledge, conclusions on the circumstances of the loss, such as type of loading, loading direction and loading height can be derived.

The characteristic structures of plastic fracture surfaces were summarised and discussed in VDI guideline VDI 3822 Part 2.1.4 [5].

Some typical fracture surface characteristics provide information about the crack propagation direction, by means of which the position of crack initiation can be also determined.

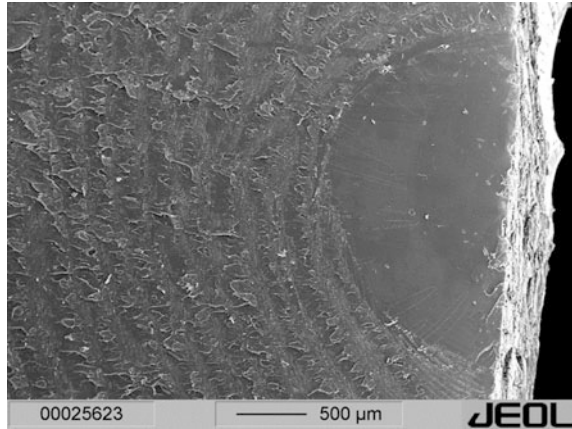
11.2.1 *Waves and Grid Lines*

Waves and grid lines are differences in elevation on the fracture surface in the shape of rings or lines. They usually emanating from the position of crack initiation. The main course of direction is perpendicular to the crack propagation direction.

Waves and grid lines occur as a result of change in the crack propagation rate up to crack arrest by reflection on steps, transitions surfaces or other structural heterogeneities. But waves and grid lines can also be the result of oscillating or cyclic stresses.

In Fig. 11.1 an example of fracture surface structure waves or grid lines is pictured. It shows the fracture surface of a notched specimen of PMMA (mill-cut notch), which was loaded in tension at room temperature by quasi-static loading conditions. The crack initiation occurred in the smooth crescent-shaped area on the

Fig. 11.1 Fracture surface structure *waves or grid lines* [5]

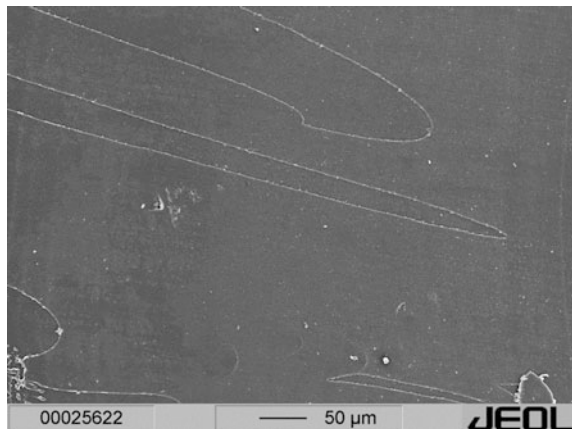


right side (mirror zone [6]). From here, the grid lines spread out in concentric rings around the position of crack initiation.

11.2.2 *Fracture Parabola Respectively U- or V-Shaped Ramps*

Fracture parabolas are named as U- or V-shaped ramps too. There are differences in height in the fracture plane. If the occurrence of fracture parabolas is isolated or separated and the height is relatively small, then it is an indication of low-deformation brittle material behaviour (see Fig. 11.2).

Fig. 11.2 Fracture surface structure *fracture parabola* at brittle material behaviour [5], PMMA



In the case of a more structured fracture surface and a lot of fracture parabolas, on a ductile material behaviour can be concluded (see Fig. 11.3).

The isolated fracture parabolas are open in the direction of crack propagation. This means that the vertex of the parabola points in the direction of crack initiation [5, 7, 8].

The amount or frequency of fracture parabolas increases by increasing ductility of material behaviour. So the individual parabolas cannot be considered separately.

The border of these fracture parabolas are usually deformed wavy due to the large plastic deformation in these areas before fracture occurs. Hereby, the vertex of each fracture parabolas cannot be clearly detected and the point of crack initiation is not clearly determined with only this fracture surface structure (Fig. 11.4). Here it is necessary to take other fracture structures into consideration. The crack propagates parallel to the border of the fracture parabolas.

Fig. 11.3 Fracture surface structure *fracture parabola* at ductile material behaviour, PA high impact: overview (a), higher magnification from Fig. 11.3a (b)

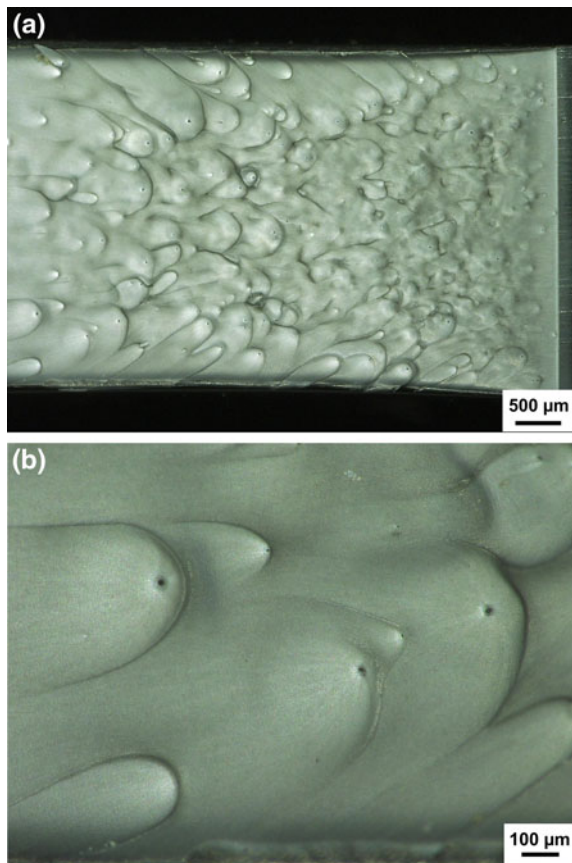
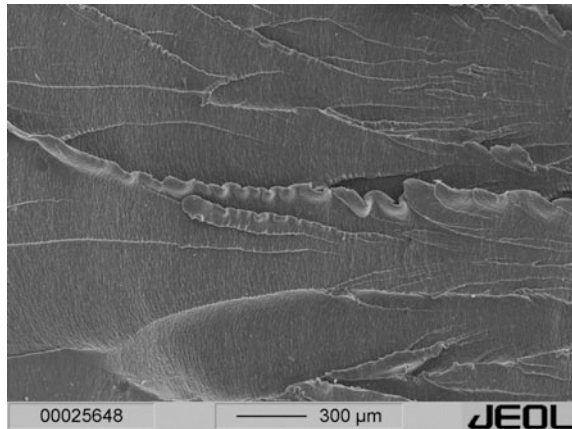


Fig. 11.4 Fracture surface structure *fracture parabola* respectively *U- or V-shaped ramps* in multiple occurrence at ductile material behaviour, PP (high molecular weight) [5]



11.2.3 Ramps, Bars or Steps

The terms ramps, bars or steps are used interchangeably in [5]. Ramps, bars or steps are differences in height of the fracture plane and are oriented parallel to the direction of the global crack propagation [9]. Just like the parabolas it can be distinguished here between brittle, low deformation behaviour of materials (Fig. 11.5a) and ductile material behaviour with plastic deformation of the ramps with earing (Fig. 11.5b). Hereby, ears are an additional fracture surface structure. An ear is a local plastic deformation. The end of the ears usually points in opposite direction to the main tensile stress. This has the following reason: During mechanical tensile loading, the material is stretched in tensile direction. The stresses occurring in the material consist of both plastic and elastic components of the deformations. In the region of ramps the plastic deformation is large before cracking occurs. In case of crack propagation, the elastic part of deformation is reversible. So the stretched material fold back because of the elastic deformation.

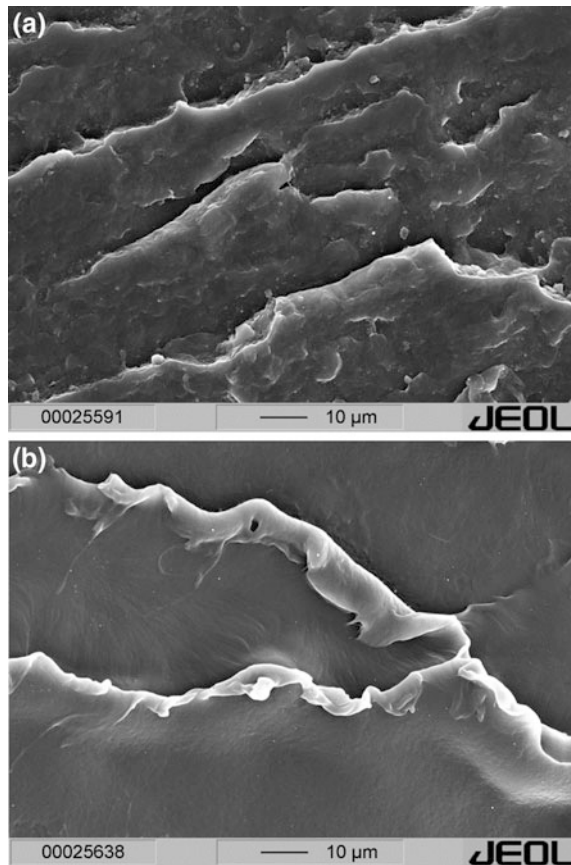
In the case of parallel occurring of the ramps, bars or steps, a direct conclusion on the location of crack initiation cannot be drawn with only this fracture surface structure.

But, in the case of radial occurring the crack propagates in the direction of the rays and the crack initiation is thus localised on the opposite side, nearby the (virtual) intersection of the rays.

11.2.4 Example: Fracture of a Multi-Layer Pipe

The fracture surface of a multi-layer pipe is shown in Fig. 11.6 in the area of crack initiation. Based on fracture surface structures, the location of crack initiation and the direction of crack propagation can be detected. The pipe was coextruded and consists of different types of polyamide.

Fig. 11.5 Fracture surface structure *ramps, bars, steps*: brittle material behaviour (PP, $T = -20\text{ }^{\circ}\text{C}$) (a), ductile material behaviour with *ears* (PP, $T = 23\text{ }^{\circ}\text{C}$) (b) [5]



In Fig. 11.6a, the fracture surface is shown without marking the several fracture surface structures. The intermediate layer is much more plastically deformed in comparison to the inner or outer layer. Here, stress whitening occurs because of the micro voiding after local exceeding of the yield stress. The stress whitening is based on light refraction at the inner surface of the micro voids.

The same fracture area section is shown in Fig. 11.6b. Hereby, the white arrows mark the local direction of crack propagation. The crack propagation starts on the lower edge. Ramps, bars or steps extend radially from this position over the entire fracture surface.

On the inner layer, waves or grid lines can be located on the left side.

Stress whitening occurs only after exceeding the yield point. Especially in the center of intermediate layer, the large plastic deformation is remarkable. In comparison to it, the fracture surface structures on the inner and outer layers are characteristic for brittle fracture. It can be concluded that the plastic deformation and thus the lower yield stress of the intermediate layer material is the cause for failure of this multi-layer pipe.

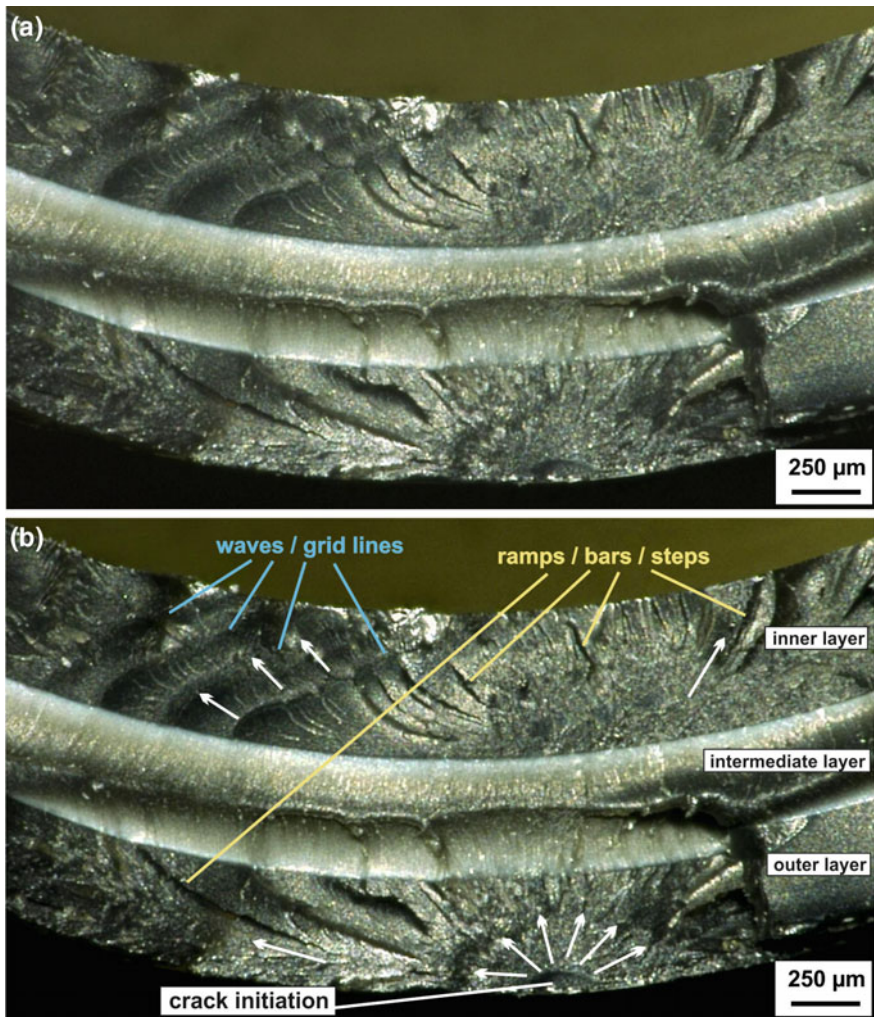


Fig. 11.6 Fracture surface structures on a multi-layer pipe of polyamide [7]

Furthermore it can be concluded that the yield point of the inner and outer layer has been not reached at the time of the break.

11.3 Limits of Validity of the Fractography for Filled and Reinforced Plastics

The fracture surface analysis is limited up to not suitable for polymeric materials which are filled or reinforced. Here, it cannot conclude to the point of crack initiation or direction of crack propagation.

The filler or reinforcement materials are barriers for crack propagation, where the crack is redirected or branched [10, 11]. The fracture surface is very jagged. So it is not possible to describe and interpret the fracture surface with the help of fracture surface structures as explained in Sect. 11.2.

The fracture surface of a PP–talc composite is shown in Fig. 11.7. Especially the lower magnification in Fig. 11.7a shows the brittle fractured surface with little deformation. The surface is unstructured and jagged. At higher magnification the orientation of the platelet-shaped talc is visible.

Further, on the basis of small balls it can be seen that the matrix material comprises a heterophasic structure, as is known, e.g., of elastomer-modified polypropylenes [12].

Figure 11.8 shows the fracture surface of a glass fibre-reinforced and mineral-filled polypropylene that has been stored in hot water for 500 h. After that it was notched by a razor blade and loaded at room temperature by the instrumented impact test.

Fig. 11.7 Scanning electron micrographs of brittle fracture surface of PP–talc composite according to impact loading at two different magnifications

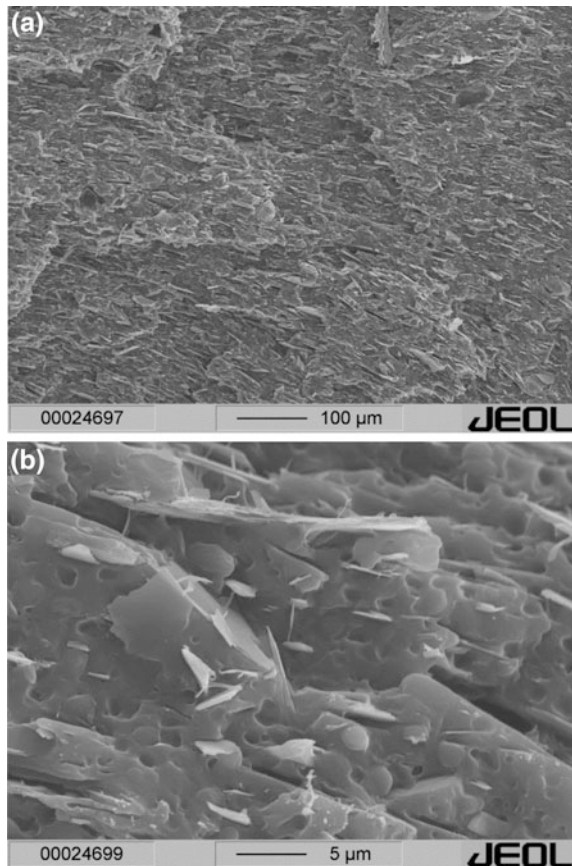
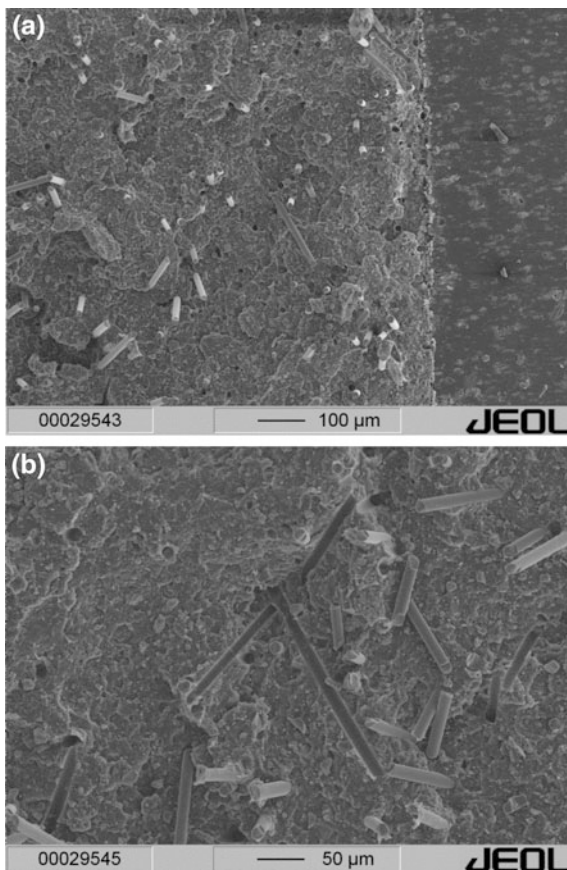


Fig. 11.8 Scanning electron micrographs of brittle fracture surface of a PP–GF–mineral composite after 500 h of storage in hot water (95 °C) and subsequent impact loading: overview with razor blade notch (a), detail with a little loss of the fibre–matrix adhesion (b)



Again, the direction of crack propagation based on the fracture surface features cannot be determined (see Fig. 11.8a).

Based on the smooth surface and the pulled-out fibres it is shown that the water storage has caused a little loss of the fibre–matrix adhesion (Fig. 11.8b).

11.4 Summary

Fractography is a very important tool for failure analysis of plastic products. By application of standardised fracture surface structures, the location of crack initiation and the direction of crack growth can be determined.

Furthermore, the influence of temperature, type of loading, loading speed or stress due to media on the plastic product can be detected. It is very important that fractography is applied in combination with other methods of polymer diagnostics and analytic as a tool for damage assessment.

In particular at filled and reinforced polymeric materials, the applicability of fractography is limited because of the jagged fracture surface induced by fillers and reinforcement materials.

References

1. Grellmann, W., Bierögel, C., Reincke, K. (eds.): Lexikon der Kunststoffprüfung und Diagnostik. Merseburg (2015). <http://wiki.polymerservice-merseburg.de>
2. Brostow, W.: Performance of Plastics. Carl Hanser, Munich (2001)
3. Brostow, W., Corneliusen, R.D.: Failure of Plastics. Carl Hanser, Munich (1986)
4. Ezrin, M.: Plastics Failure Guide—Cause and Prevention. Carl Hanser, Munich (1996)
5. VDI 3822 Part 2.1.4.: Failure analysis—Defects of thermoplastic products made of plastics caused by mechanical stress (2012)
6. Moalli, J.: Plastics Failure—Analysis and Prevention, Plastics Design Library. Elsevier, Norwich (2001)
7. Kotter, I.: Die Möglichkeiten der Fraktografie in der Schadensanalyse. In: Proceedings VDI-Technikforum 03FO006008—Fehler- und Schadensanalyse an Kunststoffprodukten (Aachen, 03.–04.12.2014). Aachen (2013), pp. 11.1–11.18
8. Kurr, F.: Praxishandbuch der Qualitäts- und Schadensanalyse für Kunststoffe. Carl Hanser, Munich (2011)
9. Ehrenstein, G., Engel, L., Klingele, H., Schaper, H.: SEM of Plastics Failure. Carl Hanser, Munich (2011)
10. Kotter, I., Grellmann, W.: Schadensanalyse an Kunststoffprodukten—Beispiele aus der Praxis. In: Borsutzki, M., Moginger, G. (eds.): Fortschritte in der Werkstoffprüfung für Forschung und Praxis (Proceedings Werkstoffprüfung 2012, Bad Neuenahr, 06.–07.12.2012). Stahleisen, Düsseldorf (2012), pp. 317–322
11. Kotter, I., Grellmann, W.: Schadensanalyse an Kunststoffprodukten—Die VDI-Richtlinie 3822 in der praktischen Anwendung. In: Proceedings Technomer 2013–23. Fachtagung über Verarbeitung und Anwendung von Polymeren (Chemnitz, 14.–15.11.2013). Chemnitz (2013), KP V 8.6, pp. 1–6
12. Kotter, I.: Morphologie-Zähigkeits-Korrelationen von EPR-modifizierten Polypropylenwerkstoffen. Mensch & Buch, Berlin (2003)

Part III
Fracture Mechanics and Related Methods
for Analysing the Fracture Safety
and Lifetime of Plastic Pipe Materials

Chapter 12

Slow Crack Growth of Polyethylene—Accelerated and Alternative Test Methods

B. Gerets, M. Wenzel, K. Engelsing and M. Bastian

Abstract Regarding lifetime of plastic products made of polyethylene (PE), resistance against slow crack growth failure is crucial. Therefore, in recent years material suppliers took a lot of effort into the improvement of PE materials leading to highly stress cracking resistant grades (e.g. PE 100-RC). This advantage in application unfortunately causes problems in material testing: As testing times become longer, highly resistant grades cannot be characterised quantitatively with standard test methods, like the Full-Notch Creep Test, anymore. Therefore, improved respectively new testing methods for the characterisation of slow crack growth resistance of PE have been developed. Results are presented and discussed for accelerated Full-Notch Creep Test (aFNCT), Strain Hardening Test (SHT) and Crack Round Bar (CRB) Test.

12.1 Introduction

Polyethylene (PE) is, with a share of about 30% of the European plastics demand [1], one of the most common plastics used today. Typical applications are packaging, bottles, containers, geosynthetics and pipes. As quality requirements raised for some applications continuously in recent years, lifetime requirements of 50 years up to 100 years are quite common, e.g. for building products. Therefore, design against failure and an exact forecast of the long-term behaviour is crucial in product development. In general three different failure mechanisms can be observed for PE products. At high mechanical loads ductile failure will appear after a short time caused by the local exceedance of yield stress. To avoid this, an adequate design is required as this failure mode results from mechanical overload. A second failure mechanism is slow crack growth. The resistance of PE grades against that failure mode is known as stress cracking resistance and mainly dominated by the molecular structure of the PE grades. For very long operating times a brittle failure nearly independent of the load applied can be observed, caused by thermo-oxidative

B. Gerets (✉) · M. Wenzel · K. Engelsing · M. Bastian
SKZ—German Plastics Center, Würzburg, Germany

degradation. Therefore, PE grades for long-term applications contain a suitable amount of stabilising additives, which prevent oxidation.

Since stress cracking failure is the most frequent cause for failure of plastic products [2], special effort was taken by material suppliers to improve PE grades and products. The ability to investigate and also to evaluate these highly stress cracking resistant PE qualities quantitatively is crucial for further material development as well as for product design regarding stress cracking resistance. As the established test methods are just about reaching their limit for those PE grades, an improvement of the existing and the development of alternative test methods are necessary [3].

12.2 Slow Crack Growth

The slow crack growth mechanism occurs for PE products exposed to small stresses, lower than the yield stress of the material, on the long-term scale. The underlying mechanism is a multi-step process. The initial step is the formation of micro-cavities due to a local increase in stress, predominantly at local defects respectively inhomogeneities. Under continuing mechanic loading the cavities will grow bigger and bigger, leading to the formation of fibrils by stretching the intervening material. As soon as these fibrils fail, a crack can be observed macroscopically. On the macroscopic scale failure appearance is brittle, but on the microscopic scale failure is ductile, dominated by yielding through the formation and growth of fibrils [4]. Resistance against stress cracking under operation conditions depends on two categories of factors. On the one hand internal factors like the molecular structure determine the entire material performance. On the other hand external factors, such as temperature, surrounding medium, notches and stress level, strongly affect the actual behaviour in application.

12.3 Test Methods to Determine Slow Crack Growth Behaviour of PE

12.3.1 *Conventional Test Methods*

To investigate the slow crack growth behaviour of PE grades and products several test methods exist. Most of them are creep or relaxation experiments. Basically it can be distinguished between methods for material testing and methods for product testing. Alternatively a classification of the test methods according to the load applied can be done: Methods using constant stresses and methods working with constant strains. Table 12.1 provides an overview of the most used test methods, established especially for PE products with high requirements regarding their stress cracking resistance, e.g. pipes.

Table 12.1 Conventional test methods to determine the stress cracking resistance of PE grades and products

Test methods	Standard	Applied load
Full notch creep test (FNCT)	ISO 16770	Constant stress
Double notch creep test (2NCT)	Analogous to ISO 16770	Constant stress
Accelerated creep test (ACT)	Analogous to ISO 16770 [5]	Constant stress
Notched constant tensile load (NCTL) test	ASTM D 5397	Constant stress
Pennsylvania edge notch tensile (PENT) test	ISO 16241	Constant stress
Notched pipe test (NPT)	ISO 13479	Constant stress
Point load test (PLT)	PAS 1075	Constant stress
Bent strip method	ISO 22088-3	Constant strain
Bell test	ASTM D 1693	Constant strain
Ball or pin impression method	ISO 22088-4	Constant strain
Cone test method	ISO 13480	Constant strain

All these test methods are designed to cause stress cracking faster than in field application, by the selected test conditions. As accelerating factors normally increased temperatures, initiating notches and detergents are used. Especially the Full Notch Creep Test (FNCT) according ISO 16770 is frequently used when it comes to material characterisation for pipe applications. In the past research was done on the reproducibility and comparability of FNCT, presented hereafter. Possibilities for further developments leading to an Accelerated Full Notch Creep Test (aFNCT) are shown.

With the Strain Hardening Test (SHT) and the Cracked Round Bar (CRB) Test alternative methods for the characterisation of highly stress cracking resistant PE grades have been developed in recent years. In contrast to test methods on the basis of creep or relaxation experiments, a special tensile test or dynamic-cyclic testing, respectively, are used herein. Both methods and their ability for material characterisation regarding stress cracking resistance are discussed in the following.

12.3.2 Accelerated Test Methods: (Accelerated) Full Notch Creep Test (FNCT and aFNCT)

FNCT measurements according to ISO 16770 are performed on circumferentially notched rods with a square or rectangular cross-section. Specimens are tested in an aqueous solution containing a neutral-type nonylphenoxy-(ethyleneoxy)-ethanol detergent with a concentration equivalent to 2% by mass. Test temperature T_{FNCT} and stress level σ_{FNCT} are constant during the measurement. It is important that the stress level applied leads to a mainly brittle failure, otherwise the ductile failure mode is measured instead of the slow crack growth failure mechanism. Typical conditions for the characterisation of PE grades are $T_{\text{FNCT}} = 80 \text{ }^\circ\text{C}$ and

$\sigma_{\text{FNCT}} = 4.0$ MPa (test condition B according to ISO 16770). The resulting time to failure t_{FNCT} characterises the stress cracking resistance of the material tested.

A round robin test was performed to evaluate and quantify potential differences between the FNCT results of different laboratories. The tests were done on three different PE qualities; samples were prepared from compression moulded and extruded sheets of 10 mm thickness $b_{\text{extr/comp}}$. To gain test conditions comparable as far as possible, the detergent used (Arkopal[®] N 100) was supplied by one laboratory. The solution was aged prior to testing for $t_{\text{FNCT,preaging}} = 250$ h at $T_{\text{FNCT}} = 80$ °C by all laboratories. Specimen geometry was chosen according to test condition B of ISO 16770, meaning a square diameter with a thickness b_{FNCT} and width w_{FNCT} of 10 mm and a length l_{FNCT} of 100 mm. All specimens under investigation were prepared by one lab, which also notched one half of the specimens. For the other half notching was done prior to testing by each laboratory itself. The tests on all three PE qualities were carried out sixfold at a test temperature T_{FNCT} of 80 °C and a stress σ_{FNCT} of 4.0 MPa. The results of two PE qualities are presented in Fig. 12.1. Since there is no difference between the blue and grey columns within the limits of measurement accuracy, no significant influence of notching on the FNCT results was found. Comparing the FNCT results for the low stress cracking resistant PE quality (Fig. 12.1, left side) and for the higher stress resistant PE quality (Fig. 12.1, right side), it becomes obvious that the longer the testing times, the larger absolute and relative scatter became. The resulting times to failure t_{FNCT} measured at seven European laboratories differed up to a factor of 3–4, although the test conditions were clearly defined and all other factors that can be directly influenced were identical. Thus the most likely explanation for the observed deviations seems to be the discrepancy in test bath design, leading to different flow conditions during FNCT measurement.

As a temporary approach to make results comparable, using a defined PE quality as reference material to control and rank the test baths might be ok. But for a long-term solution, assuring comparable FNCT results, the standardisation of test bath design respectively flow conditions and the use of another detergent is necessary. An alternative detergent should show a better ageing behaviour and lead to

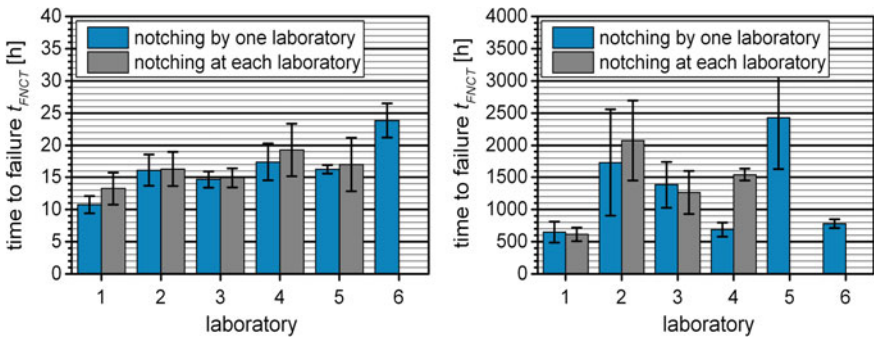


Fig. 12.1 Time to failure t_{FNCT} in FNCT of two PE qualities tested at different laboratories

shorter testing times. Especially regarding highly stress cracking resistant PE grades (e.g. PE 100-RC) shorter testing times are needed as the standard test conditions lead to test durations t_{FNCT} of 8760 h (=1 year) or even longer. In that case not only stress cracking, but also thermo-oxidation might lead to failure, preventing a quantitative characterisation of those PE grades.

Hence, the behaviour of potential alternative detergents was screened. The commonly used nonylphenolpolyglycoether (Arkopal[®] N 100, Clariant) served as reference. Tests were run on a media tensile creep tester from Institut für Prüftechnik Gerätebau GmbH & Co. KG (IPT), Todtenweis. The apparatus allows testing at six stations. As each station has the same design and contains only one sample, identical test conditions are assured for all samples at any time. The test temperature as well as the applied loads (either stress or strain) can be chosen individually at each testing station. For the screening measurements an Accelerated Full Notch Creep Test (aFNCT) procedure was performed. A test temperature T_{aFNCT} of 90 °C was chosen and a stress σ_{aFNCT} of 4.0 MPa was applied similar to the test conditions proposed by [5]. All specimens were cut of extruded plates with a thickness b_{extr} of 10 mm prepared from one PE grade, serving as reference material. Time to failure t_{aFNCT} and ageing behaviour of the tested detergents were analysed. The concentration of all solutions under investigation was chosen 2% by mass of the detergent used. Compared to the time to failure t_{aFNCT} measured with the reference detergent, significantly shorter testing times t_{aFNCT} were observed for sodium C14–17 secondary alkyl sulfonate (Hostapur[®] SAS 60, Clariant), lauramine oxide (Dehyton[®] PL, BASF) and sodium n-dodecyl benzene sulphonate (Maranil[®] A 55, BASF). Therefore, these three promising potential alternative detergents were examined in more detail. For that purpose ageing tests in an oven were run at $T_{\text{oven}} = 80$ °C with continuous monitoring. The reference detergent and two of the alternative detergents showed colour changes to brown, while no discolouring was observed for the solution prepared from lauramine oxide. Additional measurements of the molecular weight distribution showed a degradation of the reference detergent at long ageing times, whereas analogous investigations on the aqueous sodium n-dodecyl benzene sulphonate solution indicated only very small changes. As surface tension is normally assumed to provide a good first estimation regarding the compatibility of material and detergent, this was also measured. For all detergents under investigation the surface tension was about 30 mN/m, being in the same range as for PE (referred to with 33.2 mN/m in literature [6]) affirming the general suitability of the chosen detergents. Interestingly, only for the reference detergent (Arkopal[®] N 100) demixing was observed. So, especially for the reference detergent a very good mixing of the solution during creep testing is essential. Otherwise inhomogeneities in the test bath might appear, possibly effecting testing times. As it is well known that ageing of the commonly used detergent leads to an increase in time to failure in FNCT [7], for potential alternative detergents this has to be checked. Therefore, this was investigated in detail via testing the PE reference quality in detergent solutions of different age. When the sodium C14–17 secondary alkyl sulfonate is used, a behaviour similar to that of the reference detergent is observed, meaning acidification with increasing age of the solution accompanied by

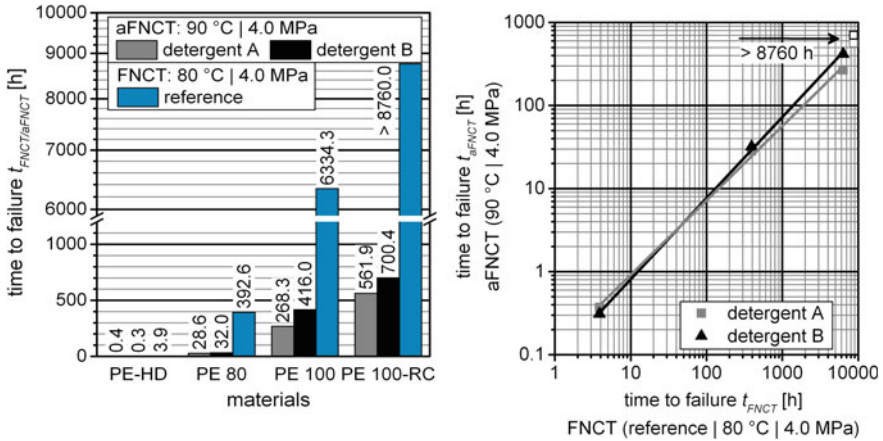


Fig. 12.2 Time to failure $t_{\text{FNCT}/\text{aFNCT}}$ in FNCT respectively aFNCT measurements (*left side*) and their correlation (*right side*) for different PE qualities

an increase in testing times t_{aFNCT} . The effect regarding time to failure t_{aFNCT} was nearly the same for the solution prepared from the sodium n-dodecyl benzene sulphonate, but the pH-value increases. Almost no increase in pH-value as well as in testing time t_{aFNCT} was detected for lauramine oxide.

As a result of the screening tests sodium n-dodecyl benzene sulphonate (detergent A) and lauramine oxide (detergent B) were chosen for further investigations. Different PE qualities were tested in standard FNCT (reference detergent/ $T_{\text{FNCT}} = 80 \text{ °C}/\sigma_{\text{FNCT}} = 4.0 \text{ MPa}$) and in an aFNCT setting (detergent A respectively B/ $T_{\text{aFNCT}} = 90 \text{ °C}/\sigma_{\text{aFNCT}} = 4.0 \text{ MPa}$). In Fig. 12.2 on the left side the resulting times to failure $t_{\text{FNCT}/\text{aFNCT}}$ of conventional FNCT and aFNCT measurements are presented. aFNCT leads to a distinct shortening in testing time corresponding to an acceleration factor of 10–15. This was reached by the combination of an alternative detergent and an increase in temperature to $T_{\text{aFNCT}} = 90 \text{ °C}$. If the times to failure $t_{\text{FNCT}/\text{aFNCT}}$ of FNCT and aFNCT are plotted against each other, a linear correlation is obtained in double logarithmic presentation (Fig. 12.2, right side) indicating the same failure mechanism under both testing conditions. The results of the highly stress cracking-resistant material (cf. Fig. 12.2, right side, open symbols) were not taken into account for the correlation, because in FNCT testing times become too long (>one year).

12.3.3 Alternative Test Methods: Strain Hardening Test (SHT)

Although the slow crack growth mechanism leads to a macroscopically brittle failure, it is ductile on the microscopic scale—dominated by the formation and

stretching of fibrils. On the basis of an analogy between the microscopic stretching process and the macroscopic stretching behaviour at high draw ratios in tensile tests, it was proposed to characterise the stress cracking resistance of PE grades through the investigation of the behaviour in the strain hardening regime [8]. The Strain Hardening Test (SHT) is carried out as a tensile test at constant temperature T_{SHT} and with a constant crosshead speed v_{SHT} . As a measure for the stress cracking resistance, the slope in the strain hardening region is used. For PE pipe grades the method was published as an international standard in 2015 [9]. The test is performed by the use of an universal testing machine equipped with a temperature chamber and an optical strain measurement system. Normally temperature T_{SHT} is set to 80 °C and a crosshead speed of $v_{\text{SHT}} = 20$ mm/min is chosen. The resulting stress–strain diagram (Fig. 12.3, left side) can be transferred into a plot of true stress $\sigma_{\text{true,SHT}}$ over draw ratio λ_{SHT} (Fig. 12.3, right side) by (1) and (2), if a constant volume is assumed.

$$\lambda_{\text{SHT}} = \frac{l}{l_0} = 1 + \frac{\Delta l}{l_0} = 1 + \varepsilon_{\text{tech,SHT}} \tag{1}$$

$$\sigma_{\text{true,SHT}} = \frac{F}{A} = \frac{F}{A_0} \cdot \frac{l}{l_0} = \sigma_{\text{tech,SHT}} \cdot \lambda_{\text{SHT}} = \sigma_{\text{tech,SHT}} \cdot (1 + \varepsilon_{\text{tech,SHT}}) \tag{2}$$

With draw ratio λ_{SHT} defined as the quotient of actual length l and the initial gauge length l_0 and technical strain $\varepsilon_{\text{tech,SHT}}$ being the relation of Δl (difference between l and l_0) and l_0 . In (2) is F the force measured and A the cross section respectively A_0 the initial cross section.

After fitting with a Neo-Hookean model the resulting curve is evaluated in the region between $\lambda_{\text{SHT}} = 8$ and $\lambda_{\text{SHT}} = 12$. The strain hardening modulus $\langle G_p \rangle$, characterising the stress cracking resistance, is defined as the slope in that region (exemplarily shown for PE-HD (light grey) in Fig. 12.3, right side). Generally the SHT allows a good distinction between different PE qualities. The higher the strain hardening modulus $\langle G_p \rangle$ the better is the stress cracking resistance of the PE grade

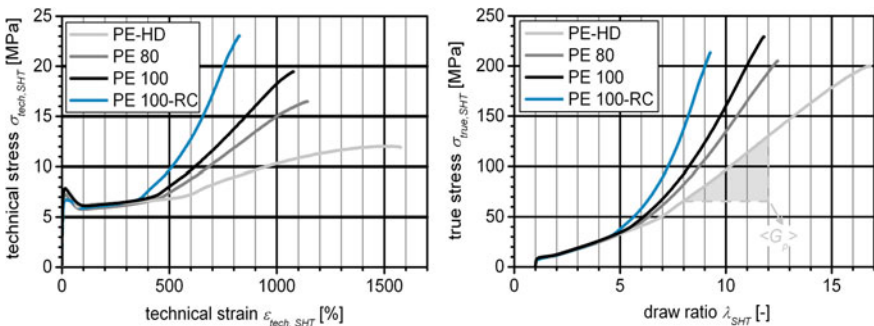
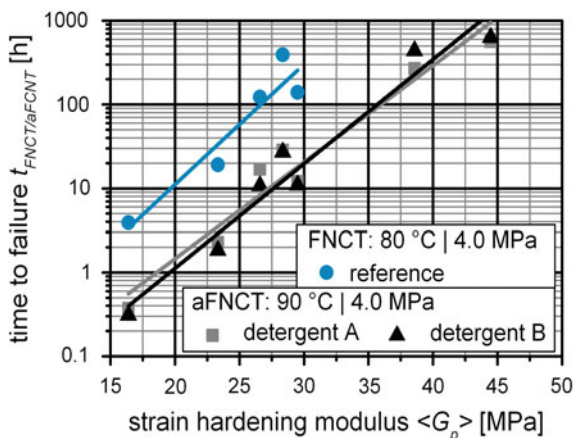


Fig. 12.3 Technical stress–strain diagram (left side) and true stress $\sigma_{\text{true,SHT}}$ plotted over draw ratio λ_{SHT} (right side) for different PE qualities

Fig. 12.4 Correlation between time to failure $t_{\text{FNCT/aFNCT}}$ in FNCT respectively aFNCT measurements and strain hardening modulus $\langle G_p \rangle$



tested. In contrast to the established test methods also highly stress cracking-resistant PE grades (e.g. PE 100-RC) can be characterised in very short times. If results of SHT and FNCT respectively aFNCT measurements are plotted against each other (Fig. 12.4) a linear correlation between the logarithm of time to failure $t_{\text{FNCT/aFNCT}}$ and strain hardening modulus $\langle G_p \rangle$ is gained. Thus the same underlying mechanism leading to failure in those fundamentally different test methods can be assumed. As the correlation holds for conventional FNCT as well as for aFNCT measurements, the change in test temperature and detergent for aFNCT provides the same results regarding the stress cracking resistance of the tested PE grades.

In order to investigate the influence of specimen geometry on the resulting strain hardening modulus $\langle G_p \rangle$ a series of different PE grades was tested with two different geometries fourfold (specimen according to [9] and modified type 5B DIN EN ISO 527-2). All specimens had a thickness h_{SHT} of 1 mm, punched from one compression moulded sheet. Test temperature T_{SHT} was chosen 80 °C and crosshead speed v_{SHT} was adjusted in a way that the resulting strain rate in the gauge length is the same for both specimens. As Fig. 12.5 (left side) shows, the resulting strain hardening modulus $\langle G_p \rangle$ is independent of the specimen geometry and reproducibility is high as the observed scatter is low. Using the modified specimen geometry is advantageous because the smaller dimension leads to less material consumption and significant reduction of the crosshead travel required. Additionally the influence of specimen thickness h_{SHT} on SHT results was investigated. For that purpose one specimen geometry was prepared from compression moulded PE sheets with thicknesses h_{SHT} of 0.3, 1.0 and 2.0 mm. SHT measurements were run with the standard test conditions $T_{\text{SHT}} = 80$ °C and $v_{\text{SHT}} = 20$ mm/min, each threefold. The resulting $\sigma_{\text{true,SHT}}-\lambda_{\text{SHT}}$ curves are shown in Fig. 12.5 (right side). Overlapping of the curves clearly illustrates that there is also no influence of specimen thickness, at least in the range tested.

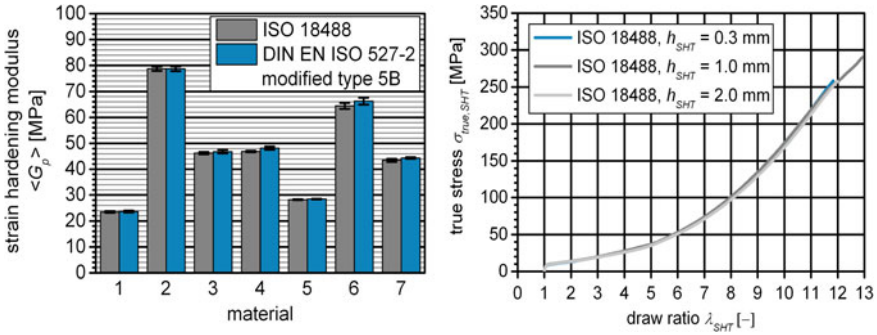


Fig. 12.5 Influence of specimen geometry (left side) and specimen thickness h_{SHT} (right side) on the strain hardening modulus $\langle G_p \rangle$

Table 12.2 Influence of specimen thickness h_{SHT} on the strain hardening modulus $\langle G_p \rangle$

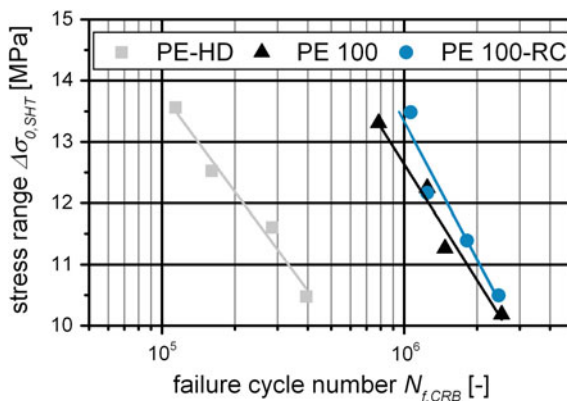
Specimen thickness h_{SHT} (mm)	Strain hardening modulus $\langle G_p \rangle$ (MPa)	Variation coefficient $Var(\langle G_p \rangle)$ (MPa)
0.3	40.2	4.27
1.0	40.8	0.74
2.0	40.9	1.83

The resulting strain hardening modulus $\langle G_p \rangle$ and the related variation coefficient $Var(\langle G_p \rangle)$ are summarised in Table 12.2. As deviation between the thickness dependent results is smaller than the measuring accuracy, the qualitative result of Fig. 12.5 (right side) is confirmed quantitatively thereby. As the absolute accuracy in compression moulding and thickness measurement is thickness independent, thicker specimen are rather beneficial due to a reduced relative measurement inaccuracy.

12.3.4 Alternative Test Methods: Cracked Round Bar Test—CRB Test

Besides the SHT another new test method called Cracked Round Bar (CRB) Test was developed to determine the stress cracking resistance of PE materials [10]. In CRB testing a circumferentially notched round bar is loaded sinusoidally with a frequency f_{CRB} of 10 Hz. Usually tests are run at $T_{CRB} = 23$ °C on a servo-hydraulic testing device. The failure cycle number $N_{f,CRB}$ as a function of the stress range $\Delta\sigma_{0,CRB}$ is analysed. To characterise the stress cracking resistance the number of cycles to failure $N_{f,CRB}$ respectively time to failures t_{CRB} is used. If results are measured on samples with differences in initial ligament diameter $D_{ini,CRB}^*$ or initial crack length $a_{ini,CRB}^*$, the stress intensity factor $\Delta K_{I,CRB}$ has to be used

Fig. 12.6 Stress range $\Delta\sigma_{0,CRB}$ over failure cycle number $N_{f,CRB}$ for different PE qualities



instead of the applied stress range $\Delta\sigma_{0,CRB}$. A standard for CRB testing of PE pipe grades was published in 2015 [11]. Plotting the applied stress range $\Delta\sigma_{0,CRB}$ respectively stress intensity factor $\Delta K_{I,CRB}$ over the failure cycle number $N_{f,CRB}$ or time to failure t_{CRB} allows for a quantitative comparison of different PE qualities (exemplarily shown in Fig. 12.6). Just like for the SHT [12] also for the CRB Test the reproducibility and comparability between different laboratories was examined and proved in a round robin test [13].

12.4 Conclusions

Test methods characterising the stress cracking resistance of modern PE materials reach their limits today. On the one hand the acceleration compared to the lifetimes in field application is not high enough to allow for an implementation of these methods for the purposes of further material development or quality control. On the other hand highly stress cracking resistant materials cannot be quantitatively characterised, due to the long testing times at elevated temperatures leading to thermo-oxidative failure before slow crack growth causes failure. Additionally testing times of about one year or even longer could not be tolerated under the aspect of economic efficiency. With the development of the accelerated FNCT shorter testing times and an improved reproducibility were reached. Alternative test methods like the SHT and CRB test allow a quantitative characterisation even of highly stress cracking resistant PE qualities. The main characteristics of the different test methods presented are summarised in Table 12.3.

Table 12.3 Test methods to characterise the stress cracking resistance of highly stress cracking resistant PE grades (e.g. PE 100-RC)

Test method	Testing time t	Temperature T (°C)	Acceleration through
FNCT	>1 year	80	Temperature, detergent, notches
Accelerated FNCT	<1000 h	90	Temperature, detergent, notches
SHT	ca. 3 h	80	Strain hardening in tensile testing
CRB test	ca. 100 h	23	Cyclic loading, notches

References

1. Plastics Europe: Plastics—The Facts 2014/2015: An analysis of European plastics production, demand and waste data. Information brochure, Brussels (2015)
2. Jansen, J.A.: Environmental stress cracking—The plastic killer. *Adv. Mater. Process.* issue June 50–53 (2004)
3. Wenzel, M., Gerets, B., Engelsing, K., Wüst, J., Heidemeyer, P., Bastian, M.: Neue Prüfmethode zum langsamen Risswachstum von Polyethylen. *3R No. 09* (2013) 60–62
4. Michler, G.H., Baltá-Calleja, F.J.: *Nano- and Micromechanics of Polymers*. Carl Hanser, Munich (2012)
5. ISO 16770 (2004): Plastics—Determination of environmental stress cracking (ESC) of polyethylene—Full notch creep test (FNCT)
6. McGoldrick, J., Bäckman, M., Haager, M., Hessel, J.: Prüfmethode zur Bestimmung der Beständigkeit von Druckrohrmaterialien PE 100-RC gegen langsame Rissfortpflanzung—Auf den Sprödbbruch kommt es an. *3R International* **48**, 2–5 (2009)
7. Menges, G., Haberstroh, E., Michaeli, W., Schmachtenberg, E.: *Werkstoffkunde Kunststoffe*, 5th edn. Carl Hanser, Munich Vienna (2005)
8. Kurelec, L., Teeuwen, M., Schoffeleers, H., Deblieck, R.: Strain hardening modulus as a measure of environmental stress crack resistance of high density polyethylene. *Polymer* **46**, 6369–6379 (2005)
9. ISO 18488 (2015): Polyethylene (PE) materials for piping systems—Determination of strain hardening modulus in relation to slow crack growth—Test method
10. Nishimura, H., Narisawa, I.: Fatigue behavior of medium-density polyethylene pipes. *Polym. Eng. Sci.* **31**, 399–403 (1991)
11. ISO 18489 (2015): Polyethylene (PE) materials for piping systems—Determination of resistance to slow crack growth under cyclic loading—Cracked round Bar test method
12. Van der Stok, E.J.W., Scholten, F.L.: Strain hardening tests on PE pipe materials. In: *Proceedings of Plastic Pipes XVI* (Barcelona, 24.–26.09.2012). Barcelona (2012)
13. Frank, A., Redhead, A., Kratochvilla, T., Dragaun, H., Pinter, G.: Accelerated material testing with cyclic CRB tests. In: *Proceedings of Plastic Pipes XVI* (Barcelona, 24.–26.09.2012). Barcelona (2012)

Chapter 13

Polypropylene for Pressure Pipes—From Polymer Design to Long-Term Performance

L. Boragno, H. Braun, A.M. Hartl and R.W. Lang

Abstract In order to create polypropylene materials that meet pipe applications requirements, good knowledge of the material's structure–property relationships is necessary, as well as the right analytical tools to assess the final properties. The effect of crystallisation conditions, polymorphism and processing on the impact resistance of some nucleated pipe grades was studied. A dependency between polymorphism, process conditions and final pipe properties is reported. A short-term method for measuring the slow crack growth was successfully developed and applied, and a crack has been observed via microscopy. It was observed that a large plastic zone is formed in the specimen before the crack initiation and also ahead of the crack tip.

13.1 Introduction PP Market Overview

Polypropylene (PP) has a global market of 50 million tons per year, divided into several main applications. Injection moulding is by far the main area, while pipe consists of about 3% of the overall polypropylene worldwide volume, as depicted in Fig. 13.1 [1].

The polypropylene pipes market is continuously expanding, requiring more volumes of materials with improved performance. Low specific weight, ease of installation, abrasion resistance, and excellent chemical resistance are among the main properties which make plastic pipe materials interesting and preferable against the main competing materials such as metal or concrete. In the area of pipe applications, key applications are industrial, hot-water and sewage pipes. In the area

L. Boragno (✉) · H. Braun
Borealis Polyolefine GmbH, Linz, Austria

A.M. Hartl · R.W. Lang
Institute of Polymeric Materials and Testing, Johannes Kepler University Linz,
Linz, Austria

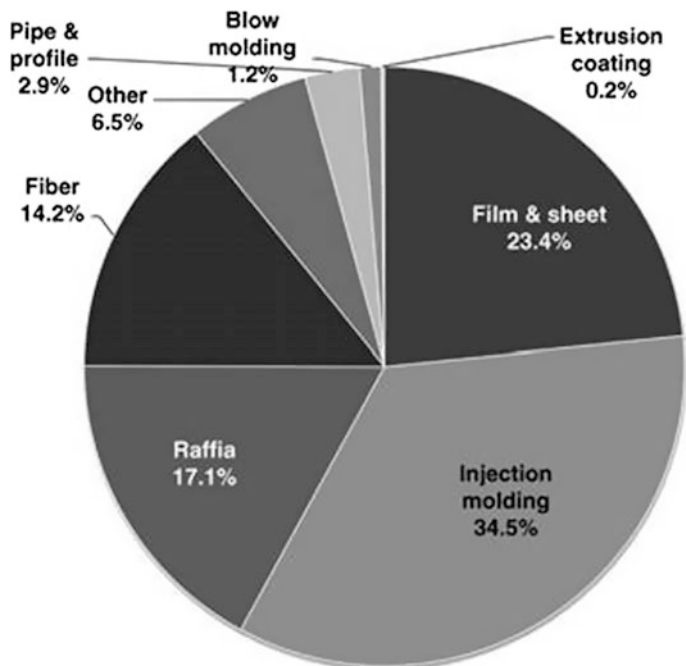


Fig. 13.1 Polypropylene applications as worldwide sales volumes [1]

of wastewater disposal, PP has become established alongside PVC as a standard material for pressureless pipes. Applications such as sewage, steel pipe coating, oil and gas transportation, require different materials having different and specific properties, in order to guarantee the best performances in each of them. For example, in sewage pipes, chemical resistance and high-load bearing properties are required, according to the in-use conditions and installation methods. For this reason, specific test methods need to be developed according to the application related needs, and modelling and simulation can also play an important role in the experimental design and result interpretation, as well as material behaviour prediction [2].

Pressure resistance, especially at high temperatures, is one of the most important properties which a pipe material should have when Hot and Cold water (H&C) applications are considered. Also good impact resistance is required to facilitate installation and endurance. In order to create materials fulfilling these application requirements, good knowledge of the material's structure–property relationships is necessary, as well as the right tools to measure such properties and to design the polymer architecture accordingly.

The main H&C related properties can be divided into two time-related categories, describing the material properties and the final application requirements. They can be summarised as follows:

- Short-term properties, intended as the material capability to resist external stresses of high intensity and short application time, which might lead to immediate failure.
- Long-term/final product properties; in this case the mechanical properties are more related to pressure resistance, thus lower stresses continuously applied for a long period of time.

For both categories proper evaluation methods and tests are necessary. Regarding the impact resistance of common H&C materials, it is interesting to study how to improve this property while keeping the balance with the other properties, since it is usually difficult to keep all properties at high level. Different possibilities will be illustrated here, covering polymer design, nucleation and optimised processing.

Pressure resistance is of course extremely important and the requirements are regulated by international standards. Nevertheless, for those who are involved in the material development for pipe applications, linking the short-term material behaviour to the long-term pressure resistance has always been of high interest. Predicting the behaviour of a pipe 50 years in advance is of course challenging, and would be a huge step forward for the design of new materials and the comprehension of certain aspects of PP mechanical behaviour. Thus, based on the experience reported on PE, an attempt has been done to close the gap between short- and long-term behaviour, for which some preliminary results will be reported.

13.2 Morphology and Polymorphism of PP

Isotactic polypropylene (iPP) has experienced a massive volume growth since its introduction in the mid-1950s and is nowadays present in an extremely wide range of applications. One of the essential reasons for this development is the flexibility of this polymer in terms of property design and processability. The polymorphism of iPP, i.e. its capability to solidify in the so far known five crystal modifications from α to ε [3–5] and in a mesomorphic state [6] is one key element of this flexibility. Since the early days of pressurised application the development of materials was centred around β -nucleation [7, 8]. The β -form can be obtained in industrial relevant environment mainly in particular crystallisation conditions or via specific nucleating agents. The morphology given to the material on a microscopic level is thought to be responsible for the good impact and pressure properties given to the so-called PP-RCT pipes.

In Fig. 13.2 the difference between α - and β -morphologies are evidenced. Several studies have been made to correlate the morphology of β - and α -forms to the different mechanical behaviour. α -form has a cross-hatched crystalline structure, which makes the structure more rigid and stiffer, while β has a “sheaf-like” structure formed by piles of lamellae connected by “tie chains” which gives more ductility to the material and favour stress transfer under load. This allows the dissipation of an

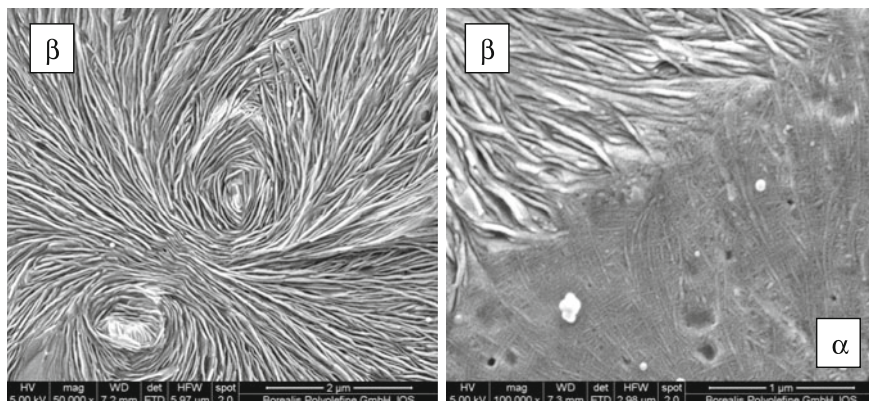


Fig. 13.2 SEM micrographs of samples crystallised in β -form (*left*) and mixed β - and α -form (*right*)

external stress on a larger volume, avoiding the concentration at the crack tip via deformation of the amorphous part of the material and formation of micro voids (crazes), which are an energy dissipation/absorption mechanism [9–11].

Also pressure resistance is influenced by the different crystalline morphology, according to the experimental evidences, but finding a link between microstructure and long-term properties is a complicated topic, which draws the attention of the scientific community since many years, but almost exclusively regarding polyethylene based materials. More details can be found in the section regarding the long-term properties (Sect. 13.6).

13.3 Short-Term Properties—Charpy and Pipe Falling Weight

Two PP base resins were compounded with different types and amounts of nucleating agent and under different conditions in order to obtain materials with varying content of the β -polymorph of iPP. The melt flow rate (MFR) of all the materials is around 0.2–0.5 g/10 min. The relative β -content has been measured via wide-angle X-ray scattering (WAXS) analysis, in order to have a direct and reliable evaluation of the crystalline structure of the polymers. Impact properties were measured on the compounded materials and on pipes prepared from the same polymer formulations. The effect of the β -content on the mechanical properties is discussed here, taking also other parameters into consideration, like the nucleating agent employed and the processing conditions.

The mechanical properties of the analysed materials have been correlated with the relative β -phase content.

In Fig. 13.3 the notched impact strength is reported as function of relative β -content in %, and compared for homo polypropylene and random copolymer. Despite the error in the measurement and the not so many data at intermediate β -content, a clear trend is visible with the impact resistance increasing on increasing the β -form amount in the specimen.

In Fig. 13.4 the same results as in the previous figure are reported but for the impact resistance at room temperature. Also here the same trend is seen, with NIS clearly increasing upon increasing β -content. From this plot it is also possible to notice that a certain threshold is needed in terms of β -content in order to gain good impact resistance. Up to 50% β -content the increase in impact is relatively small, but it grows much faster between 50 and 85% β -phase content.

Pipe falling weight test is a test conducted on pipe specimen cooled down to 0 °C, using a certain mass which falls onto the pipe. In a standard experimental procedure, the height at which the mass falls can be varied and is normally

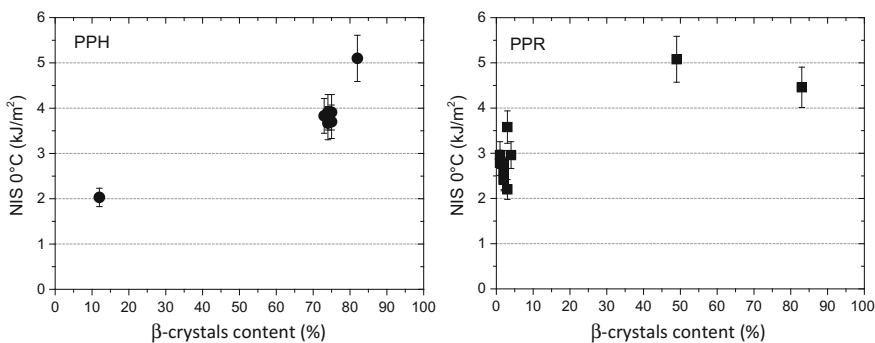


Fig. 13.3 Notched impact strength (NIS) measured at 0 °C for homopolymer (PPH, left) and random copolymer (PPR, right) of propylene, as function of relative β -content

Fig. 13.4 Notched impact strength (NIS) measured at 23 °C for random polypropylene copolymer (PPR) as function of β -content

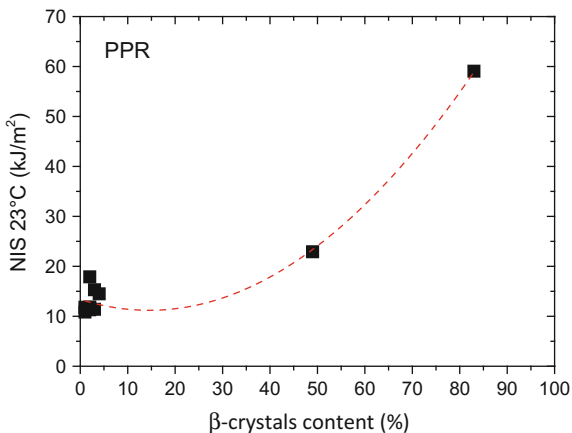
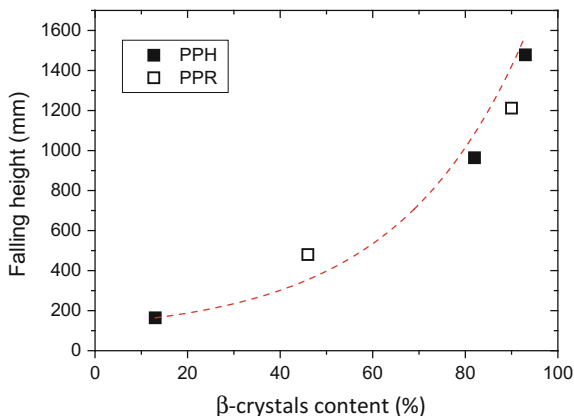


Fig. 13.5 Impact falling weight (FW) of pipe sample made from homo and random copolymers as function of β -content



increased when the pipe does not break, and decreased when the pipe breaks. A certain number of measurements are conducted during which failure of the pipe is recorded, and the result of the measurements (H50) indicates the falling height at which half of the specimens break.

Results from this test are reported in Fig. 13.5 together for homo and random polypropylene. From these results one can conclude that the amount of β -phase in the pipe is extremely important for the impact resistance, and that the crystalline form is possibly overruling the nature of the polymer (homo- or random-PP).

13.4 From Microstructure to Final Properties

The toughening effect of the β -phase has been widely studied and was explained mainly by means of the special lamellar morphology of the β -phase. Grein [7] extensively reviewed β -nucleated iPP behaviour, describing the influence of molecular features as well as processing conditions and fillers.

When considering the intrinsic features of random copolymers of polypropylene, mainly molecular weight and comonomer content are considered. Both at room and low temperature (23 and -20 °C), the effect of β -crystals on the impact is much stronger with decreasing MFR, i.e. the impact resistance is improved more for low molecular weight materials. The brittle-to-tough transition temperature is decreased by around 50 °C when the material is β -nucleated, irrespective of the MFR. Figure 13.6 shows this effect on β -nucleated and non-nucleated materials, having different MFR.

The effect of comonomer on the impact resistance of a β -nucleated iPP was also investigated. The efficiency of the β -nucleation as toughness enhancer is reduced with increasing amount of ethylene, up to an extent where the effect on impact resistance is practically negligible.

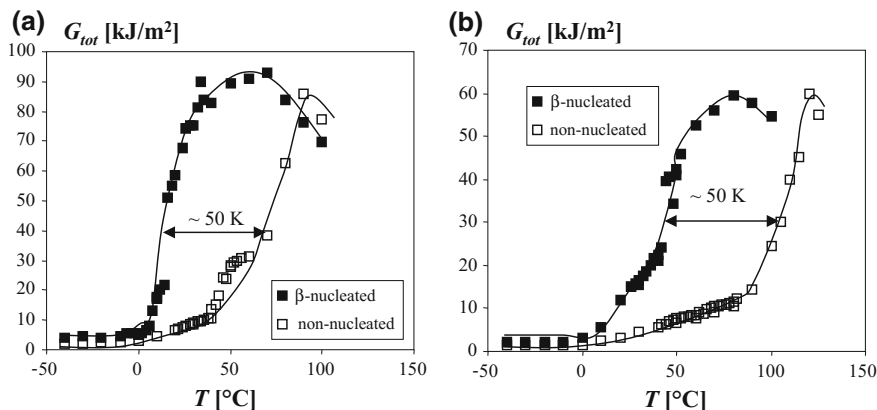


Fig. 13.6 Evolution of impact strength G_{tot} as function of temperature for β -nucleated and non-nucleated polypropylenes having MFR of 0.3 g/10 min (left) and 2 g/10 min (right); data taken from [7]

Another important aspect influencing mechanical behaviour of β -nucleated materials is the β -to- α transition. The transformation of β -crystals into α -crystals occurs in certain conditions, such as annealing at high temperatures [12] or when drawing specimen [13, 14]. Despite the efforts put by the scientific community in this topic, it is not clear yet if the $\alpha \rightarrow \beta$ transition is the reason of the toughening of the β -nucleated PP or the consequence. In other words, it is not clear if the transition occurs during the deformation, thus increasing the impact resistance of the material, or after the deformation as a “side effect”. The main arguments supporting the first hypothesis are about the microvoiding occurring in the material, which can be explained with the reduction in density due to the crystalline rearrangement. Moreover, the exothermic character of such transformation enhances plasticity. On the other hand, the arguments supporting the occurrence of the transition only after the deformation justify the microvoiding with the special lamellar morphology of the β -phase, and reports evidence that α -phase can be seen only after a certain strain. It is worth noticing that the $\alpha \rightarrow \beta$ transition can occur only with a rewinding of the PP chains and not just a short range spatial re-arrangement of chains [7].

The effect of lamellar architecture and cross hatching on the failure mechanism of β -nucleated PP materials has been already presented and discussed in Sect. 13.2, related to morphology and polymorphism. An aspect which was instead not discussed there was the influence of the amorphous phase. The different α - and β -crystalline morphology reflects on the amorphous topology and mobility. The amorphous phase is obviously involved in the stress transfer within the matrix during deformation and is thought to be the only part of the material subjected to deformation in the early stage of testing, before the strain is distributed also to the crystalline phase [7]. An higher continuity of the amorphous phase contributes to the general different properties of β -nucleated PP [15], and a more “mobile”

amorphous fraction, with less constrained tie molecules compared to what happens in a cross-hatched structure as in the α -crystals, definitely favours homogeneous stress transfer and thus toughness of the material [16].

13.5 Influence of Processing

One aspect that must be taken into consideration when linking polymer structure and material properties is the processing conditions. Cooling rate, shear, and pressure represent only an example of those and have all a big influence on the final properties. Polymorphism is strongly influenced by the cooling rate, which is usually only driven by production rate in industrial processes, and can completely change the crystallisation behaviour of a nucleated material, also depending on the presence of comonomer [17, 18]. An interesting example of that is reported in Fig. 13.7, where the evolution of the α - and β -phase amounts is reported as function of cooling rate, for a homopolymer and a random copolymer, both β -nucleated.

A cooling rate of 50 °C/s is sufficient to almost fully suppress the β -growth and favour the development of α -phase in a homopolymer, since the nucleating agent is effective only below such cooling speed [20]. For the random copolymer the situation is even less favourable, since they are intrinsically less prone to crystallise in the β -mesomorphic form due to the presence of chain defects [21]. At around 20 °C/s the amount of β -phase crystallising is basically already reduced to the minimum possible amount. Note that cooling rates in the range of 10–20 °C/s are among the slowest occurring in industrial processes, in the area of pipe extrusion.

The effect of temperature process parameters was studied varying the melt temperature during pipe extrusion of β -nucleated PPR, and measuring pipe falling weight on the specimen obtained at different conditions [22]. In Fig. 13.8 it is shown that increasing the melt temperature in the extruder leads to an improved impact resistance. Increasing the water temperature of the cooling bath, thus slowing down the overall cooling rate of the pipe, brings further improvement in the test results.

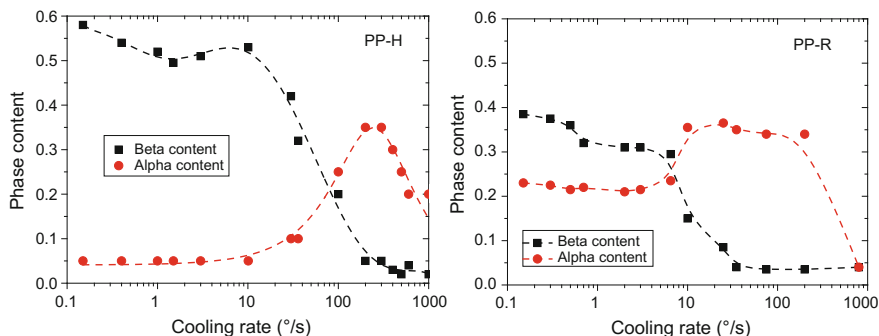


Fig. 13.7 α - and β -content for a polypropylene homopolymer (*left*) and a random copolymer (*right*) crystallised in a wide range of cooling rates; redrawn from [19]

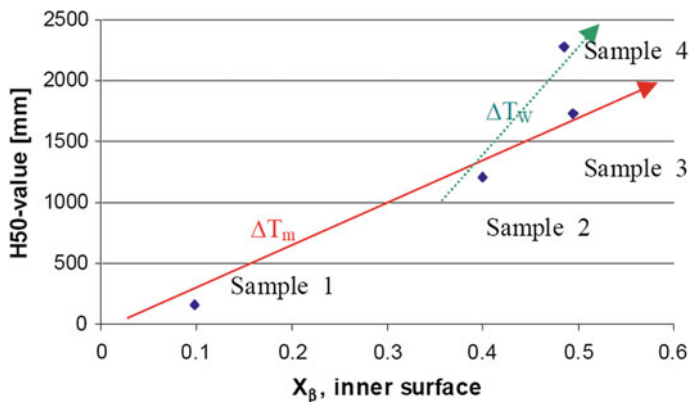


Fig. 13.8 β -content in pipes extruded applying different conditions, like increasing melt temperature (red arrow) and quenching water temperature (green arrow)

13.6 Long-Term Behaviour—Pressure Resistance and Slow Crack Growth in PP Materials

Typically, the failure of plastic pipes can be categorised in a ductile failure regime at high loads and short times, a brittle failure regime at lower stresses and longer times and a quasi-stress independent failure regime which can be attributed to large scale ageing of the material at very long times [23]. In PP pipes, however, a third regime between the ductile and brittle failure regime can sometimes be observed (see Fig. 13.9). In this “weeping” failure regime, the pressure in the pipe drops and leakage occurs without displaying any apparent crack or failure sites. The precise mechanisms of this type of failure are not yet known. Also the brittle pipe failure of PP has not yet been studied as extensively as for example for PE and care should thus be taken to differentiate between the details of the failure mechanisms of the respective materials.

A preliminary investigation of failed, un-nucleated random copolymer PP pipes from internal pressure tests also suggests that quite distinct behaviour to PE is observed for PP. All pipes investigated which failed without major ductile deformation displayed multiple apparent cracking sites. Further investigations revealed that some of these sites may be attributed to the formation of slender plastic deformation zones through the entire wall thickness of pipes. Whether superimposed interactions of local and/or global physical and chemical ageing take place and to what extent remains to be further investigated.

The common way to test long-term failure behaviour of pipe grade materials for pressure pipe application is to measure the failure times in internal pressure tests according to EN ISO 9080 (2013) and EN ISO 15874-2 (2013). However, improvements in the crack growth resistance in the pipe led to too long and impractical failure times. Hence in the last years, in the PE pipes field a method has been presented

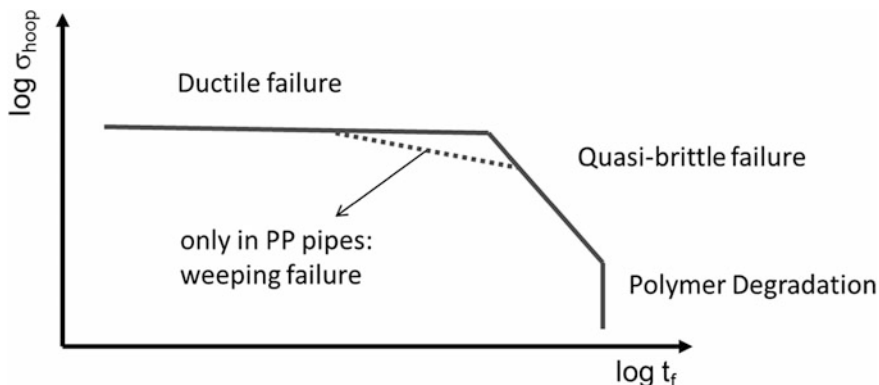


Fig. 13.9 Schematic pipe failure diagram of PP

and standardised [24] which applies cyclic fatigue loads and concepts of linear elastic fracture mechanics (LEFM) to cracked round bar (CRB) specimens resulting in a significant reduction in testing times (details on the test method are discussed elsewhere [25–28]). In this work a similar approach has been used to test PP pipe materials, with the aim of accelerating testing times and to gather a better understanding of the relevant failure mechanisms in the brittle failure regime. For CRB method implementation, a PP homopolymer was used as lower bound pipe material.

In Fig. 13.10, the cycles to failure and the cycles to crack initiation of ductile and brittle tests are plotted as a function of the initial, maximum stress intensity factor $K_{max,i}$. Contrary to tests with PE, major hysteretic heating was observed at 10 Hz and hence the frequency was reduced to 5 Hz. Thus, it was possible to initiate failure by slow crack growth at room temperature within one month of testing. The ratio of crack initiation to failure times was found to be approximately 70 and 90%. This ratio is much higher than in similar tests conducted on PE with

Fig. 13.10 Failure diagram of PP homopolymer tested at room temperature (RT), a ratio of minimum-to-maximum force (R -ratio) of 0.1 and at a frequency of 5 and 10 Hz, respectively (N_f —number of cycles)

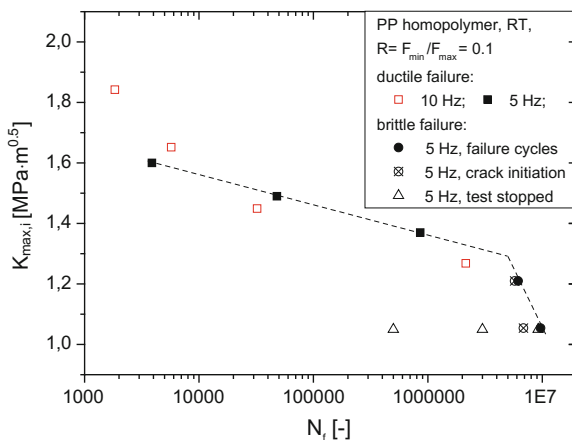
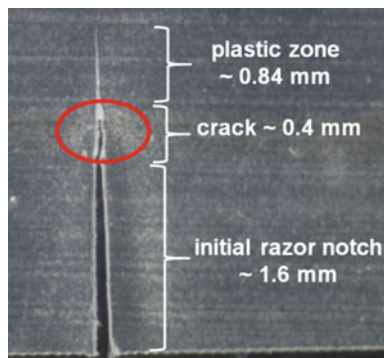


Fig. 13.11 Side view of crack (stopped after 9.2×10^6 cycles; test cycles beyond mechanically determined crack initiation cycles; diameter of CRB specimen: 13.8 mm)



values ranging from about 30 to 50%. In order to verify crack initiation, tests were repeated and interrupted shortly before and after the crack initiation as determined by extensometers. Consequently the specimens were microtomed and the length of the plastic zone and the crack determined (similar to [29]). Indeed, only after the crack initiation was determined with the extensometers a crack was detected also in microscopy. Again in comparison to PE, rather extensive plastic zone formation before crack initiation and also ahead of the crack tip was found (see Fig. 13.11). These observations regarding the longer crack initiation times and larger plastic zones also concur well with the extensive development of plastic zones observed in the failed pipes (see above).

13.7 Conclusions

Different properties of pipe materials were analysed, considering both short-term (impact behaviour) and long-term (pressure resistance) of the base resins.

The effect of crystallisation conditions on the impact resistance of the materials and of the final products (pipes) was studied. Influence of polymorphism and processing conditions is reported, showing that increasing the β -phase content in the base material leads to improved Charpy impact resistance, and increasing melt temperature and annealing temperature during pipe extrusion lead to an improvement in the pipe falling weight behaviour.

A short-term method for measuring the slow crack growth was successfully applied on one homopolymer PP material, and a crack has been observed via microscopy. The ratio of crack initiation to failure times was found to be approximately 70 and 90%, much longer than in PE. It was observed that a large plastic zone is formed in the specimen before the crack initiation and also ahead of the crack tip. This plastic deformation zone is much larger than what is normally observed for PE materials and slender plastic zones through the entire wall thickness have also been found in pipes with apparent brittle failure in internal to pressure tests.

References

1. Gahleitner, M., Kock, C., Pachner, E., Pham, T., Stubenrauch, K., Tranningner, M., Popp, P.: Polypropylene. *Kunststoffe Int.* **101**, 24–30 (2011)
2. Nestelberger, S., Herbst, H., Ek, C.-G.: Examining the long-term behaviour of deflected non-pressure plastic pipes. *3R Int.* **46**, 87–90 (2007)
3. Brückner, S., Meille, S.V., Petraccone, V., Pirozzi, B.: Polymorphism in isotactic polypropylene. *Prog. Polym. Sci.* **16**, 361–404 (1991)
4. De Rosa, C., Auriemma, F., Vollaro, P., Resconi, L., Guidotti, S., Camurati, I.: Crystallization behavior of propylene–butene copolymers: The trigonal form of isotactic polypropylene and form I of isotactic poly(1-butene). *Macromolecules* **44**, 540–549 (2011)
5. Lotz, B.: A new ϵ crystal modification found in stereodeficient isotactic polypropylene samples. *Macromolecules* **47**, 7612–7624 (2014)
6. Androsch, R., Di Lorenzo, M.L., Schick, C., Wunderlich, B.: Mesophases in polyethylene, polypropylene, and poly(1-butene). *Polymer* **51**, 4639–4662 (2010)
7. Grein, C.: Toughness of neat, rubber modified and filled β -nucleated polypropylene: From fundamentals to applications. *Adv. Polym. Sci.* **188**, 43–104 (2005)
8. Kathan, W.: Polypropylene, crystalline copolymers of propylene or compositions of polypropylene and other polyolefines having a high impact and stress crack resistance. European patent EP0177961 B1 (1988)
9. Norton, D.R., Keller, A.: The spherulitic and lamellar morphology of melt-crystallized isotactic polypropylene. *Polymer* **26**, 704–716 (1985)
10. Chen, H.B., Karger-Kocsis, J., Wu, J.S., Varga, J.: Fracture toughness of α - and β -phase polypropylene homopolymers and random- and block-copolymers. *Polymer* **43**, 6505–6514 (2002)
11. (a) Li, J.X., Cheung, W.L., Chan, C.M.: On the deformation mechanisms of β -poly-propylene: 1. Effect of necking on β -phase PP crystals. *Polymer* **39**, 6935–6940 (1998); (b) Li, J.X., Cheung, W.L.: On deformation mechanisms of β -polypropylene 2. Changes of lamellar structure caused by tensile load. *Polymer* **40**, 2089–2102 (1999); (c) Li, J.X., Cheung, W.L.: On deformation mechanisms of β -polypropylene 3. Lamella structures after necking and cold drawing. *Polymer* **40**, 3641–3656 (1999)
12. Rybnikar, F.: Transition of β to α phase in isotactic polypropylene. *J. Macromol. Sci. Part B Phys.* **30**, 201–223 (1991)
13. Guanyi, S., Feng, C., Guien, Z., Zhewen, H.: Plastic deformation and solid-phase transformation in β -phase polypropylene. *Makromol. Chem.* **190**, 907–913 (1989)
14. Krumova, M., Karger-Kocsis, J., Baltá Calleja, F.J., Fakirov, S.: Strain-induced β – α polymorphic transition in iPP as revealed by microhardness. *J. Mat. Sci.* **34**, 2371–2375 (1999)
15. Raab, M., Kotek, J., Baldrian, J., Grellmann, W.: Toughness profile in injection-molded polypropylene: the effect of the β -modification. *J. Appl. Polym. Sci.* **69**, 2255–2259 (1998)
16. Huy, T.A., Adhikari, R., Lüpke, T., Henning, S., Michler, G.H.: Molecular deformation mechanisms of isotactic polypropylene in α and β -crystal forms by FTIR spectroscopy. *J. Polym. Sci., Part B: Polym. Phys.* **42**, 4478–4488 (2004)
17. La Carrubba, V., Piccarolo, S., Brucato, V.: Crystallization kinetics of iPP: influence of operating conditions and molecular parameters. *J. Appl. Polym. Sci.* **104**, 1358–1367 (2007)
18. Cavallo, D., Gardella, L., Alfonso, G.C., Mileva, D., Androsch, R.: Effect of comonomer partitioning on the kinetics of mesophase formation in random copolymers of propene and higher α -olefins. *Polymer* **53**, 4429–4437 (2012)
19. Piccarolo, S.: Borealis cooperation report. Università di Palermo DICPM (2007)
20. Mollova, A., Androsch, R., Mileva, D., Gahleitner, M., Funari, S.S.: Crystallization of isotactic polypropylene containing beta-phase nucleating agent at rapid cooling. *Eur. Polymer J.* **49**, 1057–1065 (2013)

21. Van der Meer, D.W., Varga, J., Vancso, G.J.: The influence of chain defects on the crystallisation behaviour of isotactic polypropylene. *Express Polym. Lett.* **9**, 233–254 (2015)
22. Nestelberger, S., Gahleitner, M., Piccarolo, S., Kiflie, Z., Liedauer, S., Koch, T.: Polymorphic crystallization of β -nucleated polypropylene in pipe extrusion—Comparison between simulation and experiment. In: *Proceedings of the Polymer Processing Society 24th Annual Meeting (PPS-24; 15.–19.06.2008, Salerno)*. Salerno (2008)
23. Gedde, U.W., Viebke, J., Leijstrom, H., Ifwarson, M.: Long-term properties of hot-water polyolefin pipes—A review. *Polym. Eng. Sci.* **34**, 1773–1787 (1994)
24. ISO 18489 (2015): Polyethylene (PE) materials for piping systems—Determination of resistance to slow crack growth under cyclic loading—Cracked Round Bar test method
25. Favier, V., Giroud, T., Strijko, E., Hiver, J.M., G'Sell, C., Hellinckx, S., Goldberg, A.: Slow crack propagation in polyethylene under fatigue at controlled stress intensity. *Polymer* **43**, 1375–1382 (2002)
26. Lang, R.W., Pinter, G., Balika, W.: Konzept zur Nachweisführung für Nutzungsdauer und Sicherheit von PE-Druckrohren bei beliebiger Einbausituation. *3R Int.* **44**, 33–41 (2005)
27. Frank, A., Pinter, G., Kapur, M., Nezbedova, E.: Comparison of accelerated tests for PE grades lifetime assessment. In: *Proceedings of Plastic Pipes XVI (24.–26.09.2012, Barcelona)*. Barcelona (2012)
28. Pinter, G., Haager, M., Balika, W., Lang, R.W.: Cyclic crack growth tests with CRB specimens for the evaluation of the long-term performance of PE pipe grades. *Polym. Test.* **26**, 180–188 (2007)
29. Redhead, A., Frank, A., Pinter, G.: Investigation of slow crack growth initiation in polyethylene pipe grades with accelerated cyclic tests. *Eng. Fract. Mech.* **101**, 2–9 (2013)

Chapter 14

Lifetime of Polyethylene (PE) Pipe Material—Prediction Using Strain Hardening Test

E. Nezbedová, J. Hodan, J. Kotek, Z. Krulis,
P. Hutař and R. Lach

Abstract Pipe failure in long-term applications is characterised by creep crack initiation and creep crack growth. Both can be determined by fracture mechanics-based tests of the pipe materials. Nowadays, several accelerated tests are available: PENT (Pennsylvania Edge Notch Tensile Test), FNCT (Full Notch Creep Tensile Test), CRB (Cracked Round Bar Test) or SHT (Strain Hardening Test) and NCBT (Notched Cylindrical Bars Test). The PENT, CRB and SHT were applied to one unimodal polyethylene (PE 80), four bimodal polyethylene (three of PE 100 and one of PE 100-RC) and one PE-BF (for blow molding). The contribution is focused mainly on two topics: (i) difference in specimen's preparation and test conditions and (ii) comparison of the experimental results obtained using different accelerated tests.

14.1 Introduction

The traditional method to assess the lifetime of plastic pressure pipe materials is based on hydrostatic pressure testing. Due to time and cost expenses of this methodology, high effort of the researchers is dedicated to accelerated test development. Pipe failure for long-term applications is characterised by creep crack

E. Nezbedová (✉)

Polymer Institute Brno, Brno, Czech Republic

J. Hodan · J. Kotek · Z. Krulis

Academy of Sciences of the Czech Republic,
Institute of Macromolecular Chemistry, Prague, Czech Republic

P. Hutař

Academy of Sciences of the Czech Republic, Institute of Physics of Materials,
Brno, Czech Republic

R. Lach

Polymer Service GmbH Merseburg, Merseburg, Germany

© Springer International Publishing AG 2017

W. Grellmann and B. Langer (eds.), *Deformation and Fracture Behaviour of Polymer Materials*, Springer Series in Materials Science 247,
DOI 10.1007/978-3-319-41879-7_14

initiation and creep crack growth. Both can be determined by fracture mechanics based test methods of the pipe materials. Several accelerated tests were developed: Pennsylvania Edge Notch Tensile Test (PENT), Full Notch Creep Test (FNCT), Cracked Round Bar (CRB) Test or test using compact tension (CT) specimen. In 2008 at conference Plastic Pipes XIV there was presented a new test named SMART—Small Accelerated Reliable Test. The further developments of this test were continued and in 2012 the results of round robin test were presented at the conference Plastic Pipes XVI. The authors have got proposal to TC 138/SC 5 to admit this test as a “new work item” (NWI).

The contribution is focused mainly on the application of SMART to the high-density polyethylene (PE-HD) pipe grades and comparison of the experimental results obtained using different accelerated tests.

The failure mode called long-time brittle failure (due to slow crack growth—SCG) limits the lifetime of plastic pipes. Nowadays there are couple of accelerated tests (PENT, FNCT, CRB) that enable the estimation of the lifetime of PE-HD used in plastics pipes [1–3]. For unimodal grade the time to failure according these accelerated tests is about ten hours, for bimodal grade PE 100 it is roughly thousands hours and for the new PE 100-RC grade (RC—Resistant to Cracking) is often greater than 1 year. For the PE-HD pipes grade with higher resistance against SCG some modification or alternatively new tests should be developed that enable even for these materials to obtain the results in relatively short time. It is logical that the standard PENT and FNCT have to be modified. The other way is to introduce new tests. The authors [4, 5] suggested utilising tensile test as the possibility to judge the lifetime of plastic pipes. The development in this way went further. In 2008, SABIC company presented an elegant method to predict slow crack growth in materials. The resistance to slow crack growth is predicted from a simple tensile measurement at a temperature of 80 °C (for PE-HD). It was shown that the slope of the stress–strain curve above its natural draw ratio (i.e. strain hardening) correlates very well with results obtained by FNCT of the same material. The strain hardening method does not require notched specimen or detergents. This method dramatic decreases the test times from thousands of hours to only a few. It was confirmed that this method is very suitable in the development of new grades by researchers, but also very valuable as batch release test for both resin suppliers and pipe converters. The reasoning behind the relation between the strain hardening modulus and the craze–crack mechanism has been elaborated by Kurelec et al. [6, 7]. Van der Stock and Scholten applied Strain Hardening Test (SHT) to variety of PE pipe and resin materials [8]. The results were presented at Plastic Pipes XVI conference in 2012. Authors also presented the Round Robin Test on a PE 100-RC, PE 100 and PE 80 material. The results obtained by eight labs were reproducible and confirmed that SH test is very promising to assess the resistance to slow crack growth of a wide range of PE pipe materials. At present this method is elaborated in TC 138/SC 5 under the number ISO 18488: Polyethylene (PE) materials for piping systems—Determination of Strain Hardening Modulus in relation to slow crack growth—Test method.

14.2 Conventional Assessment of Long-Term Performance and Lifetime: The Pennsylvania Edge Notch Tensile Test and the Tensile Full Notch Creep Test

The Pennsylvania Edge Notch Tensile (PENT) Test [1, 9, 10] (Fig. 14.1) developed by N. Brown and his co-workers produces the same type of brittle fracture that occurs in pipes after long time in service. The geometry of the specimens corresponds to SENT (single-edge-notched tension) specimen, and can be taken either from compression-moulded plaques or from pipes. The notch is made by pressing a fresh razor blade into the specimen at a constant speed of 330 $\mu\text{m}/\text{min}$. The notch depth is chosen to minimise the failure time, but not to produce an excessive creep on the remaining ligament. The width, thickness and side grooves are chosen to ensure that the fracture is almost entirely plane strain. The kinetics of the failure process is observed under a constant nominal stress of 2.4 MPa and temperature of 80 °C. The crack opening displacement (COD) is measured with an optical microscope with resolution about 2 μm . The most important time that distinguishes the (PE-HD's with respect to their resistance to long-term failure is the time t_f to failure. The minimum slopes of the linear part on curve COD versus time represents the rate of stable crack growth and is further important parameter describing the kinetic of SCG.

Full Notch Creep Test (FNCT) [11] (Fig. 14.2) has for some time been widely used in Europe as one of the tests characterising slow crack growth (SCG) behaviour of particularly pipe and extrusion PE materials. Among other SCG tests used currently especially for PE pressure pipes, the FNCT was selected for ISO standardisation as relatively simple and still sensitive method to characterise PE materials. The method was standardised in ISO 16770 in 2004 as material property. However, the validity of FNCT data is still not satisfactory, exhibiting scatter of results. Since ISO 16770 publication, several sets of Round Robin Tests

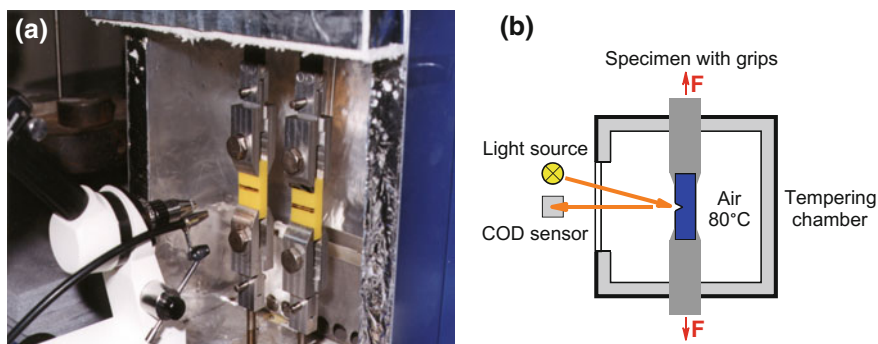
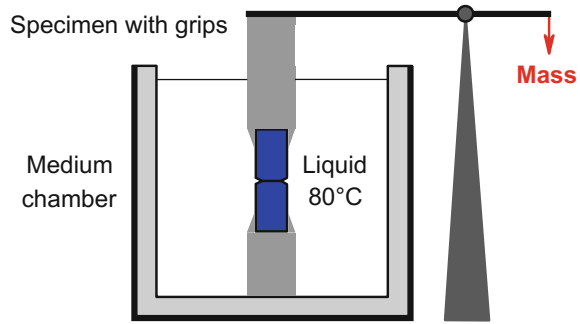


Fig. 14.1 Pennsylvania Edge Notch Tensile Test: experimental setup (a) and its schematic representation (b)

Fig. 14.2 Schematic representation of the Full Notch Creep Test



(RRT) have been performed with the aim to obtain precision data. In contrast to FNCT PENT Test enables to follow the kinetics of slow crack growth (SCG) and estimates some relevant parameters: time t_i for SCG initiation, rate of SCG (COD rate) and time t_f to failure.

14.3 Accelerated Assessment of Long-Term Performance and Lifetime: The Strain Hardening Test

The draft of the standard ISO 18488 [12] specified a method for the measurement of the strain hardening modulus. There are also given the details of required equipment, precision for generation of meaningful data. Test specimen geometry and dimensions are modified double bond specimen (0.30 mm thickness) punched from compression moulding sheet (ISO 1872-2). The specimen is clamped and pulled at 20 mm/min and at temperature 80 °C. During the test, the load sustained by the specimens and the elongation are measured. An optical or laser extensometer must be used, because the specimen is tested above its natural draw ratio, where the strain hardening occurs.

The draw ratio λ is calculated from the current length l and the initial specimen length l_0 between the gauge marks as shown by (14.1):

$$\lambda = 1 + \frac{\Delta l}{l_0}, \quad (14.1)$$

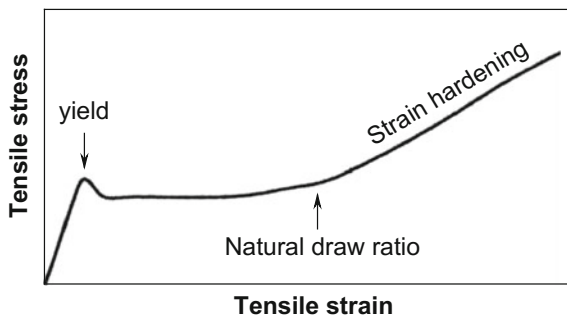
where $\Delta l = l_0 - l$ is the elongation of the specimen.

The true stress σ_{true} is calculated according to (14.2):

$$\sigma_{\text{true}} = \lambda \cdot \frac{F}{A}, \quad (14.2)$$

where F is the measured force, and A is the product of initial width and thickness.

Fig. 14.3 Typical stress–strain curve of PE-HD



The Neo-Hookean constitutive model (14.3) is used to fit and extrapolate the data from which the strain hardening (SH) modulus $\langle G_p \rangle$ for $8 < \lambda < 12$ is calculated (Fig. 14.3):

$$\sigma_{\text{true}} = \frac{\langle G_p \rangle}{20} \cdot \left(\lambda^2 - \frac{1}{\lambda} \right) + C \quad (14.3)$$

Here, C is a mathematical parameter of constitutive model describing the yield stress extrapolation to $\lambda = 0$.

14.4 Results

Test procedure that estimates values of SH modulus was applied to different generations of PE materials. Two types of PE 80 (PE-HD, PE-MD—medium-density polyethylene) were tested as well as three types of PE 100 and one type of PE 100-RC. The PE 100 types were from two manufactures. For each material five specimens were measured. Test specimens (modified type 3, ISO 37) were punched from the compressing moulding sheet of thickness 1 mm.

The measurement was carried out on the standard tensile test machine Instron 6025R5800 equipped with temperature chamber and video extensometer under the testing condition:

- Testing speed: 20 mm/min
- Temperature: 80 ± 1 °C

In Fig. 14.4 there are examples of true stress versus tensile strain diagrams for some (PE-HD pipe grades which have a somewhat other shape than the stress–strain curve for PE-HD schematically represented in Fig. 14.3. No more indications of geometrically induced drop-in after the yield point can be observed. The SH modulus was calculated from the curves in Fig. 14.4 according to (14.3). The results of SH modulus are summarised in Table 14.1. Both the slope of the true stress–strain diagrams and the SH modulus of PE-HD (are related to the resistance

Fig. 14.4 True stress versus tensile strain for PE-HD pipe grades

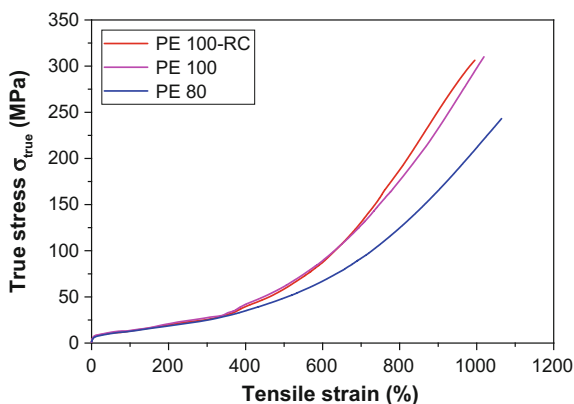


Table 14.1 The average values of SH modulus (incl. standard deviations)

Material	$\langle G_p \rangle$ (MPa)
PE 100-RC	67.2 ± 3.7
PE 100	63.3 ± 1.7
	58.7 ± 0.7
	48.4 ± 1.5
PE 80	40.9 ± 1.9
PE 80 MD	58.6 ± 2.1

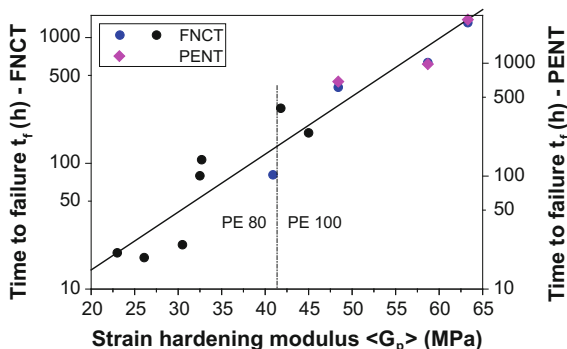
against SCG increasing in the order PE 80 \rightarrow PE 100 \rightarrow PE 100-RC which has been also found in [8]. This improvement of SCG resistance is the result of long-term intensive optimisation of the chemical architecture of the PE-HD pipe grades used in industry.

Some of the grades were tested also according to the PENT Test [9] (ISO 16241: Notch tensile test to measure the resistance to slow crack growth of polyethylene materials for pipe and fitting products (PENT)) under 2.4 MPa and the FNCT [11] (ISO 16770: Plastics—Determination of environmental stress cracking (ESC) of polyethylene—Full notch creep test (FNCT)) under the reference stress 4 MPa. In all tests the temperature was 80 °C. The results of this comparison are shown in Table 14.2. The general problem—that has been already stated in the “Introduction”—of all these conventional tests to assess the long-term performance and lifetime is that modern pipe grades consume enormous periods for testing (for example more than 100 days for the PENT Test in our case of PE 100-RC) which becomes more and more far away from requirements of both research and development and industrial practise. Therefore in Fig. 14.5, times to failure from FNCT and PENT Test are plotted versus strain hardening modulus from uniaxial tensile test using data in Table 14.2 and literature [8]. As it can be easily seen that a clear correlation ($R^2 = 0.89$) exists between $\langle G_p \rangle$ and t_f which, however, is highly non-linear and not linear as assumed in [8]. For the FNCT, this correlation can be empirically described by

Table 14.2 Comparison of SH modules with results of PENT test and FNCT

Material	$\langle G_p \rangle$ (MPa)	t_f FNCT (h)	t_f PENT (h)
PE 100	63.3	1312	2431
PE 100	58.7	632	982
PE 100	48.4	402	688
PE 80	40.9	81	

Fig. 14.5 Time to failure versus strain hardening modulus $\langle G_p \rangle$ (black symbols results from literature [8], coloured symbols own data from Table 14.2)



$$t_f = 1.7 \times 10^{0.046 \langle G_p \rangle} \tag{14.4}$$

($\langle G_p \rangle$ in MPa, t_f in h). Furthermore, the demarcation line in Fig. 14.5 at $\langle G_p \rangle = 41\text{--}42$ MPa splits the data of the SCG resistance of PE 80 from that of PE 100 (a similar demarcation has been also found in [8] to identify PE 100 and PE 100-RC).

14.5 Conclusions

- The results of measurements of the SH modulus are comparable with the results presented in [8] for different PE generations.
- The correlation between FNCT and PENT Test makes it possible to state that the strain hardening response is determined by the same molecular process that covers SCG resistance in PE-HD, assessed by another tests.
- Advantages of the strain hardening method are the very low measurement variation (absence of notches, surfactants) and, above all testing time of only few hours.
- Moreover, the use of universal test set up allows for an easy and cost effective implementation at all testing laboratories that are equipped with universal testing machine and relevant optical extensometer (video or laser) and with temperature chamber.

Acknowledgement This research was supported by the Czech Science Foundation by grant No. P108/12/1560.

References

1. Lu, X., Brown, N.: A test for slow crack growth failure in polyethylene under a constant load. *Polym. Test.* **11**, 309–319 (1992)
2. Nezbedová, E., Kučera, J., Zahradnickova, A.: Relation of slow crack growth failure time to structure of HDPE. *Mech. Time-Depend. Mater.* **5**, 67–78 (2001)
3. Hessel, J.: „PE 100-RC“—Ein PE 100 mit erweitertem Anwendungspotenzial. *3R Int.* **47**, 189–193 (2008)
4. Jivraj, N., Sehanobish, K., Dun, J.V., Damen, J., Wu, S.: Ductile failure and delayed necking in polyethylene. In: *Proceedings of Plastic Pipes XI (Munich, 03.–06.09.2001)*, pp. 697–704. Munich (2001)
5. Castagnetti, D., Dragoni, E., Simonazzi, C.: Quality assessment of HDPE pipes by mechanical testing. In: *Proceedings of Plastic Pipes XII (Milano, 19.–22.04.2004)*, Session 10b. Milano (2004)
6. Kurelec, L., Teeuwen, M., Schoffeleers, H., Deblieck, R.: Strain hardening modulus as a measure of environmental stress crack resistance of high density polyethylene. *Polymer* **46**, 6369–6379 (2005)
7. Deblieck, R., van Beek, D.J.M., Remerie, K., Ward, I.M.: Failure mechanism in polyolefines. The role of crazing, shear yielding and the entanglement network. *Polymer* **52**, 2979–2990 (2011)
8. Van der Stock, E., Scholten, F.: Strain hardening test on PE pipe materials. In: *Proceedings of Plastic Pipes XVI (Barcelona, 24.–26.09.2012)*, 10 p. Barcelona (2012)
9. ISO 16241 (2005): Notch tensile test to measure the resistance to slow crack growth of polyethylene materials for pipe and fitting products (PENT)
10. Nezbedová, E., Kučera, J.: Experimentelle Methoden zur Charakterisierung des Bruchverhalten von HDPE-Rohren. In: Grellmann, W., Seidler, S. (eds.) *Deformation und Bruchverhalten von Kunststoffen*. Springer, Berlin (1998), pp. 91–98
11. ISO 16770 (2004): *Plastics—Determination of environmental stress cracking (ESC) of polyethylene—Full-notch creep test (FNCT)*
12. ISO 18488 (2015): *Polyethylene (PE) Materials for piping systems—Determination of strain hardening modulus in relation to slow crack growth—Test method*

Chapter 15

Influence of Welding and Composition on the Short-Term Stable Crack Propagation Through Polyolefin Single- and Bilayered Structures

R. Lach, T. Krolopp, P. Hutař, E. Nezbedová and W. Grellmann

Abstract The overall stable crack initiation and propagation behaviour of fracture mechanics specimens cut from plastic pipes that were composed of different polyolefin materials were investigated using concepts of elastic–plastic fracture mechanics including the crack propagation kinetics. The effect of specimen shape, orientation, welding and lading rate on the crack resistance (R) behaviour of these materials has been thereby assessed. It was found in principle that specimen shape, orientation and welding have an influence indeed but only an unexpected small one on crack initiation behaviour and, particularly, on crack propagation behaviour. The crack initiation toughness is not sensitive to the orientation in most cases. In contrast, the crack propagation toughness is significantly affected by the orientation where the values for crack propagation in extrusion direction are larger than ones for crack propagation crosswise to that. This confirms that the morphology affects the stable crack propagation behaviour more than the stable crack initiation behaviour. In agreement with results of the microindentation test, fracture mechanics investigations also show that a lower welding pressure and a larger welding temperature, respectively, have no or a positive effect on the mechanical and fracture mechanics properties, whereas a larger pressure and a lower temperature, respectively, result in deterioration of the performance of the welded joint. Furthermore, the R-curve behaviour was investigated using specimens cut from bilayer pipe segments. It has been shown that an additional layer has a clear impact on the R-curve behaviour compared to the crack propagation in single-layer pipes, which

R. Lach (✉) · T. Krolopp · W. Grellmann
Polymer Service GmbH Merseburg, Merseburg, Germany

P. Hutař
Academy of Sciences of the Czech Republic, Institute of Physics of Materials,
Brno, Czech Republic

E. Nezbedová
Polymer Institute Brno, Brno, Czech Republic

W. Grellmann
Centre of Engineering, Martin Luther University Halle-Wittenberg,
Halle/Saale, Germany

can be explained thereby that the plastic constraint was affected by this additional layer. For clarification of the toughness-in- or -decreasing effect of an additional layer (with differing mechanical characteristics) on the layer where the crack was growing, R-curve ratios were introduced, that showed that the asymmetric mechanical properties of different layers were directly reflected in an asymmetric impact on the stable crack initiation and propagation behaviour.

15.1 Introduction

For some time, common pipe materials such as steel and cast iron for transportation of gaseous or liquid media were successfully exchanged with numerous polymers especially ones based on polyethylene, polypropylene, poly(vinyl chloride), poly(vinylidene fluoride) or polybutene. The large postulated lifetimes of these plastic pipes up to 100 years [1] can be achieved if and only if zero defect materials and parts are used (which is all but impossible) and the pipes are always loaded up to a maximum internal pressure specified in national standards (typically 10–16 bar) (SDR 11, DVGW standards).

To assess the lifetime of plastic pipe materials the Full Notch Creep Test (FNCT) according to ISO 16770, the Pennsylvania Edge Notch Tensile (PENT) Test according to ASTM F 1473 (both under static load), the Cracked Round Bar (CRB) Test according to ISO 18489 (under cyclic load) or the Strain Hardening Test according to ISO 18488 (under quasi-static load) are applied, for example. A method often used for testing butt welded joints is the Creep Rupture Test according to DVS 2203-4 (see [2]).

However, it should keep in mind that unlike metals only relatively small number of fracture mechanics investigations dealing with structure–property relationships of welded joints in plastic parts (including pipes) is available so far. Something near it applies for plastic multi-layer pipes and other multi-layer systems too. The present study is on assessing the stable crack propagation behaviour of different polyolefin pipe systems under short-term loading on the basis of concepts of elastic–plastic fracture mechanics.

15.2 Experimental

15.2.1 *Materials and Specimen Preparation*

On the one hand, as an object of investigation 1 m-long pipe segments were cut from commercial single-layer plastic pipes (outer diameter: 110 mm, wall thickness: 6.3 mm) being composed of PE 100, a specific high-density polyethylene (PE-HD) with bimodal molecular-weight distribution and used for gas

transportation. These were assembled from two 0.5 m-long pipe segments using heated-tool butt welding [3]. The welding parameters were either optimum parameters regarding to both welding temperature T and welding pressure p , or T or p , respectively, were slightly varied (little higher or lower values compared to optimum) at constant optimum values of pressure or temperature. All welded joints produced were from the same visually high quality. On the other hand, segments cut from bilayer plastic pipes with polyethylene (PE 80, a PE-HD type used for plastic pipes) as inner liner and polypropylene (PP) as outer liner were applied having near the same size than the single-layer PE 100 pipes. Furthermore, the investigations comprised also pipes segments (outer diameter: 500 mm) composed of PP materials (neat PP (IS), fibre-reinforced PP (AS), layered-particle reinforced PP (MS and MS-WB)), i.e. single-(IS, MS or MS-WB, respectively, and AS; wall thickness: 20 mm) and bilayer pipe segments (IS/MS and AS/MS, and IS/MS-WB and AS/MS-WB, respectively; wall thickness: 15–19 mm), for comparison. All pipes investigated were produced using the extrusion technique.

Specimens for fracture mechanics or other mechanical investigations were manufactured by machining (sawing, drilling, planing and grinding) or water jet cutting from pipe segments.

From PE 100 pipe segments, single-edge-notched specimens (single-edge-notched tension and single-edge-notched bending, SENT and SENB; with and without welded joint) oriented in extrusion direction (i.e., the crack propagates crosswise to extrusion direction) with the length of 80 mm as well as C, arc-shaped (length: 55 mm) and SENB specimens (length: 60 mm) oriented crosswise to extrusion direction (i.e., the crack propagates in extrusion direction) were machined. The thickness B of all these specimens was always 10 mm and the width W was equal to the wall thickness. Due to the curvature of the specimens and to simulate the worst case during the pipe being in use, notching was done from the inside of the pipe using a razor blade. Furthermore, small compact tension specimens (“mini” compact tension, mini-CT; size: 24–25 mm) were taken into account where crack propagation is crosswise to extrusion direction (specimens with and without welded joint) or crack propagation is in extrusion direction [4]. The thickness of the specimens is equal to the wall thickness of the pipes; to be required by geometry notching was done over the whole wall thickness. Thus, in summary, 10 different options were realised regarding the specimen shape (SENT, SENB, CT, arc-shaped and C specimens), the crack propagation (parallel or crosswise to extrusion direction, respectively) and the location of the crack (inside or outside of the welded joint). Thereby it has been investigated how the orientation, the plastic constraint and notching affect the stable crack propagation behaviour. The ratio of the notch depth a to the specimens width W was fixed to be $a/W = 0.5$ independently on the specimen shape. To guarantee state of plane strain (EDZ) and plain crack front for all specimens side grooving was additionally applied. For further information see [5].

Preparation and notching of specimens (SENB specimens oriented parallel or crosswise to extrusion direction as well as C specimens) cut from PE 80 pipe segments were done analogously to that cut from PE 100 pipe segments.

SENB specimens (thickness B : 10 mm, length: 80 mm, width: equal to wall thickness) made from PP materials were machined using single-layer pipes parallel or crosswise to extrusion direction and multi-layer pipes in extrusion direction. Like the PE pipes the specimens were generally notched from inside of the pipes, where the a/W ratio (if possible) was $a/W = 0.5$ too. Moreover, some of specimens cut from bilayer pipes were notched from the outside, to estimate experimentally the influence of a second layer on in- or decrease of crack propagation stability of the layer, where the crack was growing.

15.2.2 *Equipment and Data Analysis*

The quantitative assessment of the stable crack initiation and propagation behaviour depending on the basic pipe material (PE 100, PE 80, PP materials), the orientation (crack propagation direction parallel/crosswise to extrusion direction), welding and the welding conditions (optimum and non-optimum welding conditions; see above), the specimens shape (see above) as well as the loading conditions (such as loading speed) was based on investigations using the fracture mechanics crack resistance curve (R) concept (specimen preparation see above; some testing machines and equipment used: universal testing machine Zwick Z020, instrumented notch impact testing IKBV 4J, 3D reflected-light microscope VHX 500 D). For experimental determination of the R-curves at quasi-static (loading speed: 1–100 mm/min) and impact-like (loading speed: 1 m/s) conditions, the loading parameter J as a function the stable crack growth Δa was carried out using the multiple-specimen technique by analysing load–displacement diagrams of differently loaded, sharply-notched fracture mechanics specimens (SENT, SENB, CT, arc-shaped and C specimens) according to the description given in Chap. 2 of [6]. For this purpose light microscopic measurement of stable crack growth was required after exposing the Δa region by brittle fracture of the precracked specimens at low temperatures and high loading rates. Besides methodical and materials scientific problems, both the unloading compliance method generally applied to metallic materials as well as approximative and (quasi) single-specimen methods compiled in Chap. 3 of [6], for example, could not be used to determine R-curves, because they usually do not enable any information about the crack propagation and damage kinetics. Compared to [6] the limits of validity of R-curves, i.e. the exclusion of such J – Δa data not to be subject of J -controlled crack propagation from further analysis, are defined on the basis of examination of crack propagation kinetics (see below; details of the procedure are given in [5]). In the following, the J -value $J_{0.2}$ at stable crack growth of $\Delta a = 0.2$ mm and the slope $dJ/d\Delta a_{0.2}$ of the R-curves at $\Delta a = 0.2$ mm are calculated as resistance against stable crack initiation and propagation, respectively. The R-curves are characterised by a power law $J = C_1 \times \Delta a^{C_2}$ with the parameters C_1 and C_2 .

Different microscopic approaches were applied to assess damage mechanisms and to quantify fracture surface phenomena. Amongst others, a digital 3D reflected-light microscope (VHX 500 D, Keyence) was used for qualitative and quantitative microfractographic investigations, such as the measurement of the stable crack growth Δa on the fracture surfaces within the scope of fracture mechanics investigations.

15.3 Results and Discussion

15.3.1 Influence of Specimens Shape, Orientation, Welding and Loading Speed on Stable Crack Initiation and Propagation Behaviour in Single-Layer Pipes Made from PE 100, PE 80 and PP Materials

Influence of specimen shape, orientation and welding

Figure 15.1 summarises the influence of specimen shape (SENT, SENB, CT and arc-shaped specimens; data of C specimens are not shown), specimen orientation (SENB and CT specimens; crack propagation parallel or crosswise to the extrusion direction) as well as welding (SENT, SENB and CT specimens) on stable crack propagation behaviour of PE 100. Evidently, all influencing factors (specimens shape, orientation and welding) affect in principle the crack initiation and particularly the crack propagation behaviour indeed (resistance against stable crack initiation and propagation $J_{0.2}$ and $dJ/d\Delta a_{0.2}$). However, observed effects are unexpectedly small in each case but being advantageously for assessment of lifetime and fracture safety of PE 100 pipes otherwise. Against the background of increasing degree of crystallinity (analysed using DSC) by 6% compared to the basic material (degree of crystallinity: 50%)—besides changes of the crystalline structure—especially the only minor influence of welding (optimum welding parameters) on fracture mechanics performance (compared to the basic material) is remarkable (Fig. 15.2). On the other hand, the morphology significantly affects the mechanical basic properties, like Martens hardness and indentation modulus (determined applying depth-sensing microindentation test), as well as local strain (determined by means of laser extensometry using uniaxial tensile test) [4, 7].

Distinct systematic influence of specimen configuration on fracture mechanics behaviour within individual groups of R-curves (crack propagation parallel or crosswise to extrusion direction, or in the welded joint, respectively; Fig. 15.1a–c) was ascertained only for specimens loaded by tension (SENT specimens) and for the group of specimens loaded by bending (SENB, CT and arc-shaped specimens), but not for the individual bending specimens themselves. This observation is in contrast to results obtained by Hashemi and Williams [8], who have shown for PE-HD, that the R-curves based on SENB specimens are related to higher crack propagation resistance than that determined using CT specimens. However, it has

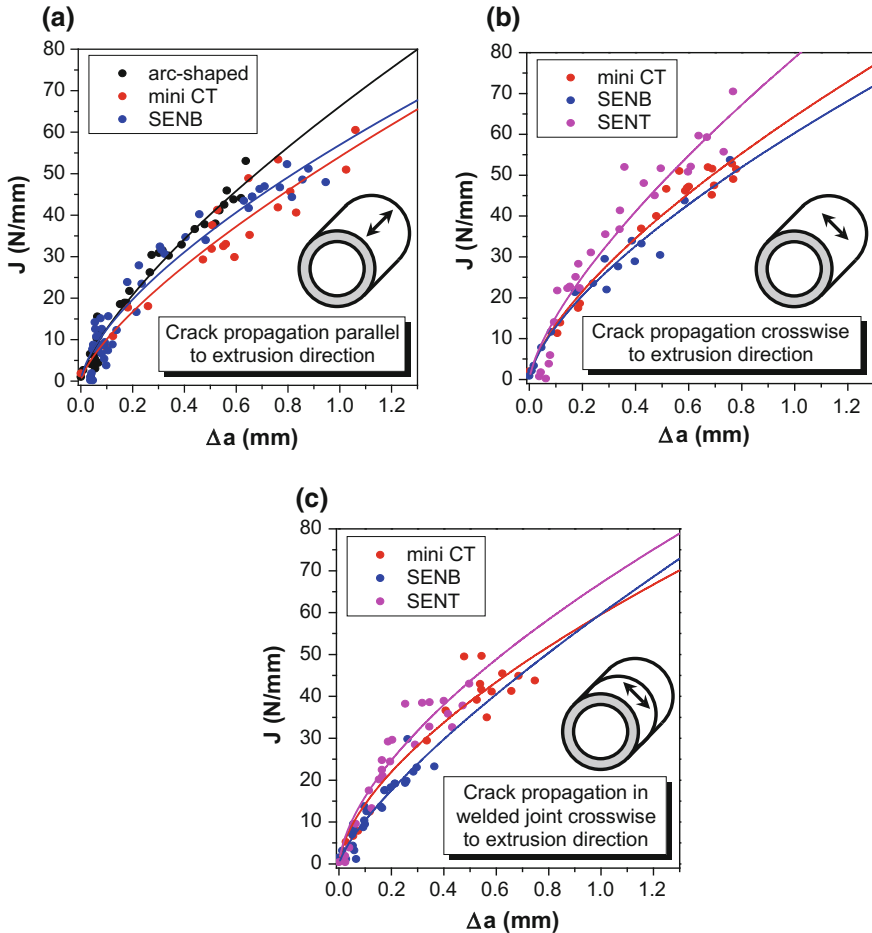


Fig. 15.1 Crack resistance (R) curves determined at room temperature and quasi-static loading conditions (loading speed: 10 mm/min) for specimens (SENB, SENT, mini CT and arc-shaped) cut from PE 100 plastic pipes: crack propagation inside the basic material parallel (a) or crosswise (b) to extrusion direction, or in welded joint, respectively (c); the relationship between the loading parameter J and stable crack growth Δa is characterised using a power law

been shown by the same authors for PE-LLD and PE-MD—similarly to the results found in the present study—that the specimen shape does not influence the crack propagation behaviour. The here found larger values for crack propagation of SENT specimens (Fig. 15.2b) are justified by lower plastic constraint due to only tensile loading, where the extent of plastic constraint is reflected in the amount of effective T -stresses. For a given basic material at the same loading conditions, the effective T -stresses (as non-singular stress portions of constant values acting parallel to the crack plane, that are superimposed of the stress singularity) are only

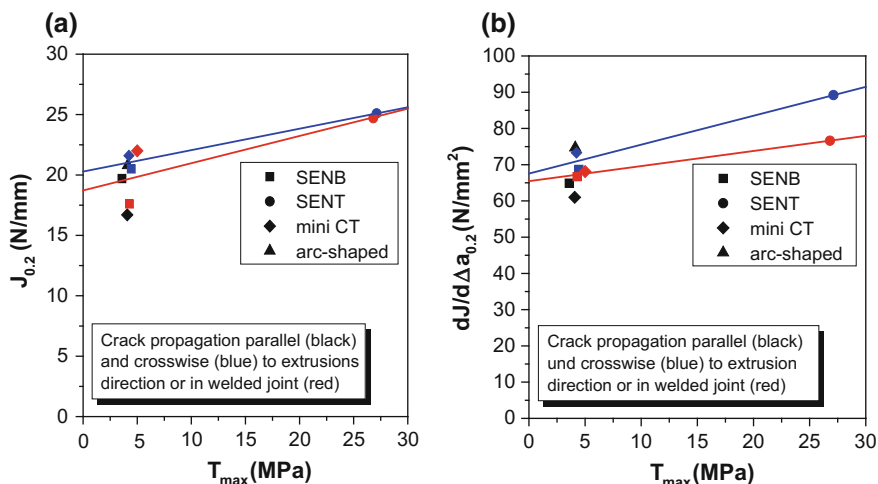


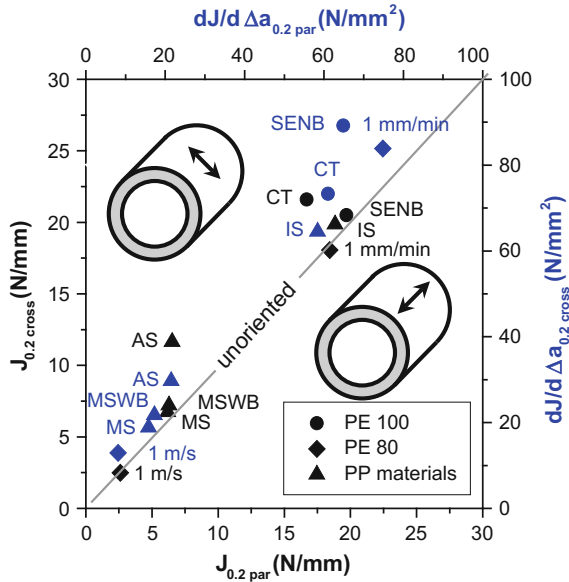
Fig. 15.2 Fracture mechanics parameters as resistance against stable crack initiation (a) and crack propagation (b) depending on the level of effective T -stresses (the *straight lines* are plotted to illustrate the general trend)

depending on specimen geometry, particularly the configuration of the specimens. In the present case, the effective T -stresses of C specimens (having the smallest crack propagation resistances of all specimens investigated) are about 1 MPa (not shown here), that of specimens loaded at bending (having medium crack propagation resistances) approximately 4 MPa and that of SENT specimens (having the largest crack propagation resistances) about 27 MPa. Within the scope of multi-parametric fracture mechanics (such as the J - T “locus”), diagrams like Fig. 15.2 also enable the determination of effective T -stresses of specific components, such as pipes, for example. For this reason, the estimation of their corresponding short-term fracture mechanics performance is closely related and thus the direct transfer of data obtained under laboratory conditions to components, which has been previously applied only rarely for plastics [9] or more general for materials with viscoelastic or viscoplastic behaviour [10].

Influence of orientation and loading speed

Shear forces acting during extrusion of the pipes across the wall thickness result in orientation of the material in extrusion direction, i.e. directional formation of crystalline structures as well as additional orientation of flaky and fibrous reinforcing particles in some of the PP materials (MS and MSWB as well as AS). If fracture mechanics values—determined parallel or crosswise to extrusion direction, respectively—are related to one another, it comes to mind that the crack initiation toughness is not sensitive to orientation, independently on whether PE 100, PE 80 or PP materials are considered (except CT specimens of PE 100 and the PP material AS) (Fig. 15.3). The crack propagation toughness, however, is significantly affected

Fig. 15.3 Influence of orientation (crack propagation parallel [par] and crosswise [cross] to extrusion direction) on stable crack initiation (black symbols) and propagation behaviour (blue symbols) of PE 100 (SENB and CT specimens, loading speed: 10 mm/min), PE 80 (SENB specimens; loading speed: 1 mm/min and 1 m/s) and PP materials (IS, AS, MS and MSWB; SENB specimens; loading speed: 10 mm/min)



by the orientation with larger values parallel than crosswise to extrusion direction. The long standing experiences of the authors are reconfirm thereby, that the morphology controls stable crack propagation behaviour much more than stable crack initiation behaviour (the orientation in our case). The last one is mainly influenced by the matrix.

Besides applying concepts of multi-parametric fracture mechanics, another approach to transfer data obtained under laboratory conditions to components is to consider the crack propagation kinetics. In the case of EDZ the stable crack propagation behaviour can be described as a three-stage process of crack-tip blunting/stable crack initiation (stage 1), non-steady state stable crack propagation (stage 2) and steady state stable crack propagation (stage 3; related to constant crack propagation rate \dot{a}_{lim}), as it has been found by Lach et al. [11, 12] to be universally valid for thermoplastic polymer materials. This behaviour was also observed for all materials investigated (for PP, for example, see Fig. 15.4; compare [4, 13] too). Thus, the ratio of \dot{a}_{lim} to external loading rate v_{extern} is a measure of the crack propagation stability being depending on the material, the specimen configuration and the loading rate (Fig. 15.5). For PE 80 and PP materials, straight lines result from plotting \dot{a}_{lim}/v_{extern} versus the crack propagation resistance in a double-logarithmic scale (i.e. $\dot{a}_{lim}/v_{extern} \sim (dJ/d\Delta a_{0.2})^n$ with $n = 0.6 \pm 0.1$), which enables an estimation of the crack propagation rate and thus the lower limit of the lifetime too (to a certain extent) if the crack propagation resistance of the component is known (by analysing effective T -stresses, for example, as shown in Fig. 15.2b).

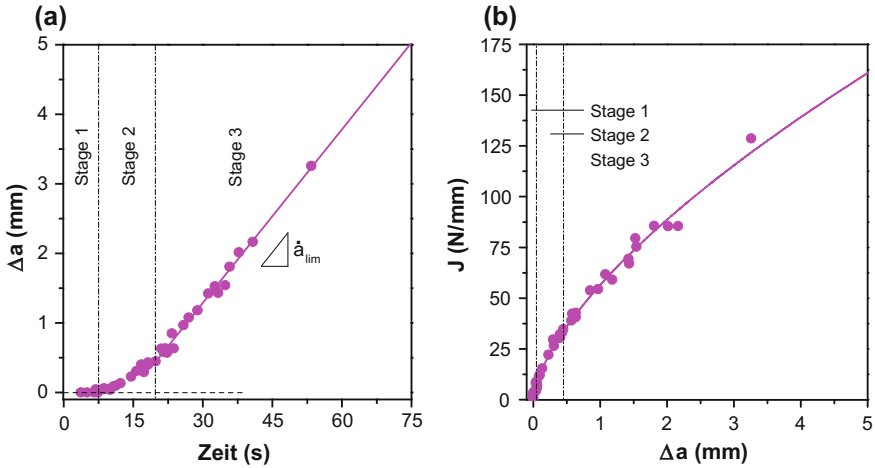
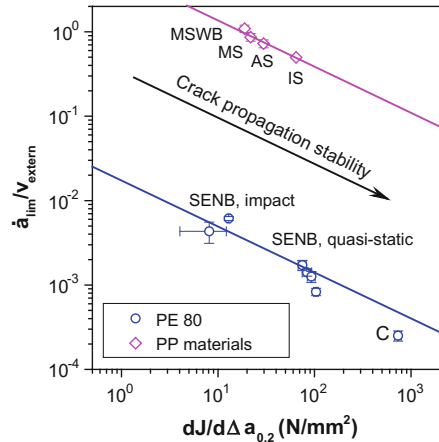


Fig. 15.4 Crack propagation kinetics (a) with the stages of crack propagation (stage 1: crack-tip blunting/stable crack initiation, stage 2 and 3: non-steady state and steady state stable crack propagation) and crack resistance (R)-curve (b) of the PP material IS (SENB specimens with crack propagation crosswise to extrusion direction, loading speed: 10 mm/min, room temperature)

Fig. 15.5 Relationship between relative crack propagation rate in stage 3 (for definition see Fig. 15.4) and resistance against stable crack propagation of PE 80 (as a function of loading speed (1–100 mm/min [quasi-static loading], 1 m/s [impact-like loading]) and PP materials (experimental details: see Fig. 15.4) depending on modification



Influence of welding parameters

Because heated-tool butt welding is one of the most common procedures for joining modern PE plastic pipes in infrastructure applications for transportation of water, gas and other media, the question comes to mind in practise to what extent small deviations from optimum welding conditions (particularly welding pressure and welding temperature or soaking time, respectively) are influencing the lifetime and fracture safety or generally the mechanical performance. Although currently long-term investigations of welded pipes are still essential despite their immense

expenditure of time, relatively less time-consuming investigations of the mechanical space-resolved basic properties and the short-term behaviour can already provide adequate information on the quality of welding, however.

The state of the material inside the welded joint and the surrounding heat-affected zones, defined by the welding procedure used, is different from that inside the unaffected basic material (regarding degree of crystallinity and crystalline mesostructure as well as orientation, for example). By way of example, this has been visualised by transmitted light-microscopic analysis of thin slices using polarised light [4, 7].

Data of Martens hardness and indentation modulus location-dependending determined using the depth-sensing microindentation test exhibit clear increase of the indentation modulus of about 80–125 MPa at optimum welding conditions, corresponding to a local constraint (laser extensometry), and less distinct increase of Martens hardness of about 0.6–1.8 N/mm² within the welded joints compared to the data of the basic material [4, 7]. The reason for it is the increase of the degree of crystallinity (56% inside the welded joint and 50% inside the basic material according to DSC measurements [4, 7]). Baltá-Calleja and Fakirov [14] showed that the microhardness of PE increases proportionally with increasing degree of crystallinity. Decrease of welding pressure or increase of welding temperature does not affect the stiffness gradient across the welded joint compared to optimum loading conditions, whereas larger pressure and lower temperature have a major impact. Larger pressure results in pressing more material, being melted during the welding process, out the welding zone into the welding beads, which causes lowering in the thickness of the welded joint and, thus, a less wide stiffness increment. Lower temperature results therein that the welded joint is not detectable by means of microindentation test anymore, although the joint is still well-visible by naked eyes.

By assessing R-curves (not shown here) of welded SENB specimens (loading rate: 10 mm/min, room temperature) with crack propagation inside the welded joint crosswise to extrusion direction the resistance against stable crack propagation $dJ/d\Delta a_{0.2}$ was quantified as a function of the welding conditions (Fig. 15.6). In agreement with results of the microindentation test (see above) it becomes apparent that a lower welding pressure or a larger welding temperature, respectively, have no or a positive influence on the mechanical and fracture mechanics performance (and may be possibly accepted thereby), whereas a larger pressure or a lower temperature, respectively, result in decline of performance of the welded joint and must be avoided, therefore.

15.3.2 Influence of Interlayers and Crack Propagation Direction on Stable Crack Initiation and Propagation Behaviour in Bilayer Pipes Made from PP Materials

In addition to single-layer plastic pipes, multi-layer plastic pipes are increasingly applied for different reasons (among others protection against outside damage,

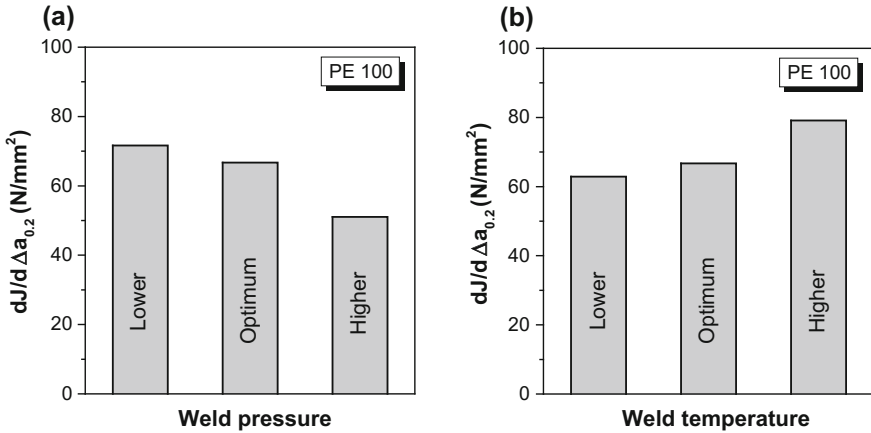


Fig. 15.6 Resistance against stable crack propagation $dJ/d\Delta a_{0.2}$ of welded-joined SENB specimens made from PE 100 depending on welding parameters such as welding pressure (a) and welding temperature (b)

improvement of stiffness, minimising of friction). Thereby the problem becomes currently more important, that the interlayer between the different layers as well as asymmetries in composition and mechanical properties of the layers are affecting the crack propagation behaviour and more general the fracture mechanics parameters.

In the following, determination of R-curves of SENB specimens composed of PP materials, which were cut from bilayer pipe segments (IS/MS and AS/MS or IS/MS-WB and AS/MS-WB, respectively; for further information see above), was taken into consideration. Here, the crack propagated from the inner (IS) or outer layer (AS) on the one hand or from the middle layer (MS or MS-WB, respectively) on the other hand towards the respective interlayer. As shown in Fig. 15.7, the additional layer has an influence on the R-curve behaviour compared to the crack propagation in single-layer plastic pipes, which is due to the interference of the additional layer with plastic constraint. In- or decreased plastic constraint is reflected in the slope of the R-curves and also related thereby to the R-curve parameter C_2 . In comparison to single-layer systems exhibiting C_2 values of $C_2 \sim 0.58$, C_2 decreases to $C_2 \sim 0.39$ for multi-layer systems with crack propagation from IS or AS, respectively (Fig. 15.7a; increased plastic constraint). For multi-layer systems with crack propagation from the middle layer (MS or MS-WB, respectively), however, C_2 increases to $C_2 \sim 1.02$ (Fig. 15.7b; decreased plastic constraint). The pictures shown in Fig. 15.7a, b for IS and MS, respectively, apply accordingly for AS and MS-WB, respectively. Correspondingly, the resistance against stable crack propagation $dJ/d\Delta a_{0.2}$ either decreases (Fig. 15.7c) or increases (Fig. 15.7d). This effect is distinctly pronounced in Fig. 15.7c for IS where $dJ/d\Delta a_{0.2}$ drops to less than the half of the initial value.

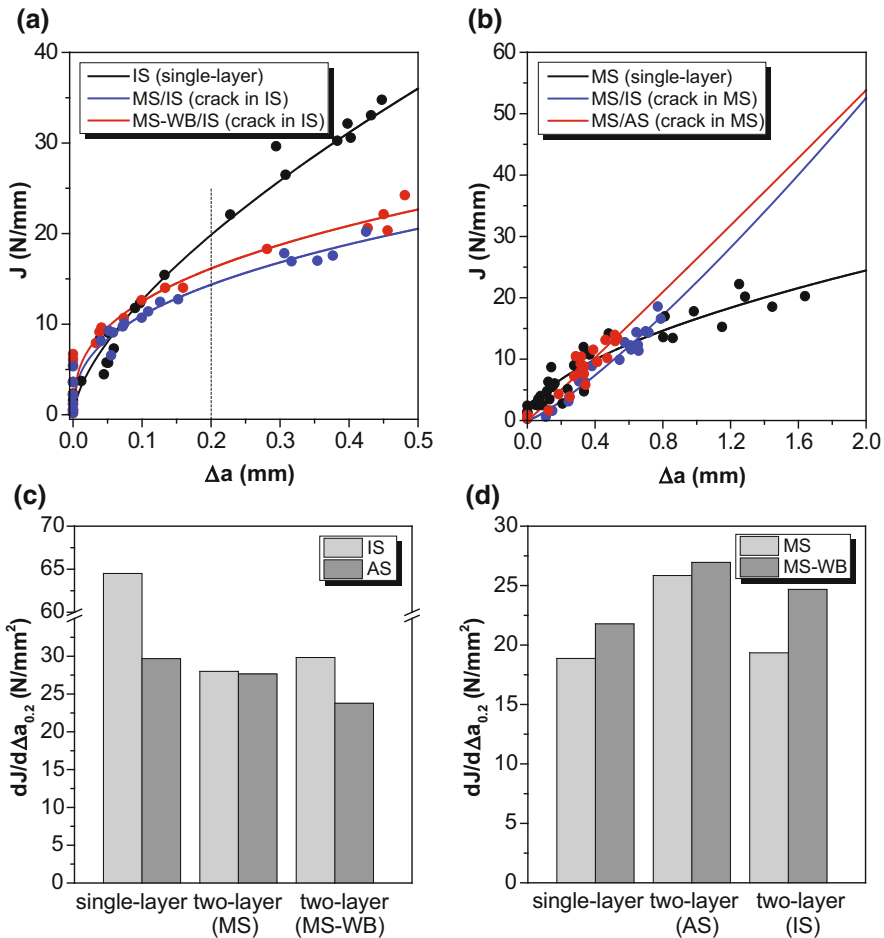


Fig. 15.7 R-curves depending on the material (single-layer pipes) or material combinations (multi-layer pipes), respectively, and the crack propagation direction (crack crosswise to extrusion direction growing from IS or AS, or MS, respectively) (a, b); comparison of the resistance against stable crack propagation $dJ/d\Delta a_{0.2}$ of single- and multi-layer systems (c, d); some of the results in Fig. 15.7c, d are derived by analysis of the R-curves shown in Fig. 15.7a, b

Whether the crack propagation stability in multi-layer increases (crack propagation from MS or MS-WB, respectively) or decreases (crack propagation from IS or AS, respectively) compared to single-layer systems depends on the ratio of the resistances against plastic deformation of both layers. As a measure of the resistances against plastic deformation, $E_t \varepsilon_y^2$ is here provided (E_t —modulus of elasticity and ε_y —yield strain measured using uniaxial tensile test), a parameter to be approximately proportional to the deformation energy dissipated up to the yield point at tensile loading (Table 15.1). The different crack propagation behaviour is also reflected

Table 15.1 Compilation of relative values of the resistance against elastic and plastic deformation (E_t and $E_t \varepsilon_y^2$) of PP materials determined using the uniaxial tensile test

Material	Resistance against	
	Elastic deformation	Plastic deformation
	E_t (relative values)	$E_t \varepsilon_y^2$ (relative values)
IS	0.321	1.000
AS	0.646	0.412
MS	0.963	0.212
MS-WB	1.000	0.178

E_t —modulus of elasticity, ε_y —yield strain

therein that size and shape of the plastic zone are affected by the plastic constraint factor [14]. Whether the cracks propagates from layer 1 to layer 2, de- or increases of the crack propagation stability in the cases of $E_t \varepsilon_y^2$ (layer 1) $>$ $E_t \varepsilon_y^2$ (layer 2) or $E_t \varepsilon_y^2$ (layer 1) $<$ $E_t \varepsilon_y^2$ (layer 2), respectively, were observed. Based on concepts of linear elastic fracture mechanics (LEFM) with the stress intensity factor K as parameter describing the crack field (in place of J as being used here) a similar result has been found by Hutař et al. [15] in principle by numerical simulations applying the finite element method (FEM). In that case however, K correlates with differences in stiffness of the layers (where E_t is used as a measure of the stiffness, for example). It means that K is increased (decreased) if the modulus of layer 1 is smaller than that of layer 2 (and vice versa). By introducing an effective stress intensity factor $K_{0.2}^{\text{eff}}$ with $K_{0.2}^{\text{eff}} = (J_{0.2} \cdot E_t / (1 - \nu^2))$ (where $\nu = 0.35$) this issue could be verified, since both $J_{0.2}$ and $K_{0.2}^{\text{eff}}$ as well as $E_t \varepsilon_y^2$ and E_t are inverse to each other in each case (compare Table 15.1). Hutař et al. [16] assumed good interfacial adhesion in his FEM calculations. This assumption forms the basis of the present investigations too (also due to consistent use of PP as matrix polymer in this study), because never interlaminar crack propagations alongside of interfaces between the layers but always only unhindered crack propagation from a layer to another one through the interface has been observed.

For clarification of the toughness-increasing or -decreasing effect of a second layer with a mechanical performance to be different from that of the layer where the crack propagates the R-curve ratios are summarised in Fig. 15.8. If the crack propagates from a layer with larger resistance against plastic deformation (IS or AS) to a layer with lower resistance against plastic deformation (MS or MS-WB, respectively), the decrease of toughness compared to the single-layer system (except Δa values smaller than 0.5 mm) is the larger the larger the mismatch of the $E_t \varepsilon_y^2$ values is (compare IS with AS on the left of the individual images of Fig. 15.8, and Table 15.1). In contrast, if the crack propagates from a layer with lower resistance against plastic deformation (MS or MS-WB, respectively) to a layer with larger resistance against plastic deformation (IS or AS) decrease of toughness was observed compared to the single-layer system for $\Delta a > 0.5$ mm (compare on the right the individual images of Fig. 15.8). That is that the asymmetry in mechanical properties of the different layers is directly reflected in asymmetric impact on stable crack initiation and propagation behaviour.

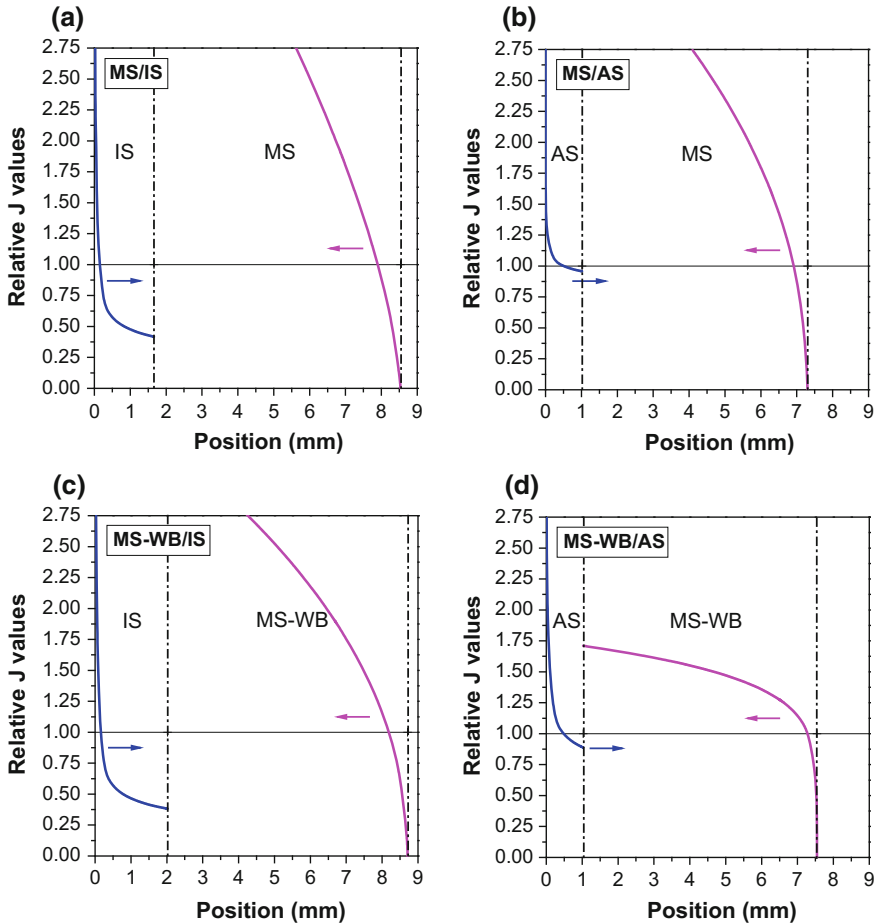


Fig. 15.8 Compilation of ratios of the R-curves of multi-layer systems to the R-curves of single-layer systems (for such R-curves see Fig. 15.7a, b for example); the *dashed lines* at a position of 1–2 mm represent the interfaces between the two layers; the *arrows* indicate the respective crack propagation direction

15.4 Summary

The overall stable crack initiation and propagation behaviour of fracture mechanics specimens cut from plastic pipes that were composed of different polyolefin materials (PE 100, PE 80 and PP materials) were investigated using concepts of elastic–plastic fracture mechanics including the crack propagation kinetics. The effect of specimen shape, orientation, welding and lading rate on the crack resistance (R) behaviour of these materials has been thereby assessed. It was found in principle that specimen shape, orientation and welding have an influence indeed but

only an unexpected small one on crack initiation behaviour and, particularly, on crack propagation behaviour. A distinct and systematic impact of specimen configuration on fracture mechanics behaviour within individual groups of R-curves was only observed among specimens loaded to tension (SENT specimens) and that group of specimens loaded to bending, but not among the individual bending specimens themselves, what is in contrast to results in literature. The larger crack propagation resistance found for SENT specimens can be justified by lower plastic constraint being reflected in the extent of the effective T -stresses. The statements given in this study within the scope of multi-parametric fracture mechanics (such as the J - T “locus”) enable via the determination of effective T -stresses for a concrete part the estimation of related values of short-term fracture toughness and thus the direct transfer from data obtained on the laboratory scale to data of components. This was done very rarely for plastics and comparable materials so far. Another approach to transfer parameters obtained using specimens on the laboratory scale to components in practise is to consider the crack propagation kinetics, whereby the crack propagation rate can be estimated and, thus, (to a certain extent) the minimum lifetime too. The crack initiation toughness is—independently on the material used—not sensitive to the orientation in most cases. In contrast, the crack propagation toughness is significantly affected by the orientation where the values for crack propagation in extrusion direction are larger than ones for crack propagation crosswise to that. This confirms that the morphology (the orientation in our case) affects the stable crack propagation behaviour more than the stable crack initiation behaviour.

In agreement with results of the microindentation test, fracture mechanics investigations (resistance against stable crack propagation) also show that a lower welding pressure and a larger welding temperature, respectively, have no or a positive effect on the mechanical and fracture mechanics properties, whereas a larger pressure and a lower temperature, respectively, result in deterioration of the performance of the welded joint.

Furthermore, the R-curve behaviour of PP materials was investigated using SENB specimens cut from bilayer pipe segments. The crack was growing from the inner or outer layer, respectively, or from the middle layer to the respective inter-layer. It has been shown that an additional layer has a clear impact on the R-curve behaviour compared to the crack propagation in single-layer pipes, which can be explained thereby that the plastic constraint was affected by this additional layer. The larger or lower plastic constraint is reflected in the slope of the R-curves and the related R-curve parameters too. Correspondingly, the resistance against stable crack propagation either decreased or increased. Whether an increase or decrease was observed compared to single-layer systems only depends on the ratio of the resistances against plastic deformation of both layers. On the basis of concepts of linear elastic fracture mechanics comparable results have been found in the literature by numerical simulations based on the finite element method. In that case, however, the in- or decrease of the stress intensity factor correlates with the ratio of the stiffness of both layers. For clarification of the toughness-in- or -decreasing effect of an additional layer (with differing mechanical characteristics) on the layer

where the crack was growing, R-curve ratios were introduced, that showed that the asymmetric mechanical properties of different layers were directly reflected in an asymmetric impact on the stable crack initiation and propagation behaviour.

Acknowledgements W. Grellmann and R. Lach wish to thank the German Research Foundation (projects GR 1141/30-1, 31-1 and 32-1) and the German Academic Exchange Service (DAAD) (PPP 2004/2005) for financial support. Furthermore, they would like to acknowledge the Austrian Research Promotion Agency (FFG) for financial support of the project 832113 as part of the BRIDGE 1 program. P. Hutař wishes to thank the Czech Science Foundation (GACR) for supporting this study through the projects 101/09/J027 and P108/12/1560.

References

1. Hessel, J.: 100 Jahre Nutzungsdauer von Rohren aus Polyethylen. Rückblick und Perspektive. 3R Int. **46**, 242–246 (2007); Hessel, J.: 50 Jahre Rohre aus Polyethylen—Eine ingenieurtechnische Betrachtung. 3R Int. **45**, 128–133 (2006)
2. DVS-Taschenbuch.: Fachbuchreihe Schweißtechnik, vol. 68/IV, 15th edn. Verlag für Schweißen und verwandte Verfahren (DVS-Verlag), Düsseldorf (2014)
3. Neumann, J.A., Bockhoff, F.J.: Welding of Plastics. Literary Licensing LLC, Whitefish (2013)
4. Lach, R., Grellmann, W., Knesl, Z., Hutař, P., Nezbedová, E., Bierögel, C.: Verfahren zur Bewertung der lokalen mechanischen Kurzzeiteigenschaften von Schweißnähten in PE 100-Rohren. Joining Plastics—Fügen von Kunststoffen **6**, pp. 126–133 (2012)
5. Krollop, T.: Einfluss der Prüfkörperform, der Orientierung und der Schweißung auf das stabile Rissausbreitungsverhalten des Rohrwerkstoffs PE 100 unter quasistatischen Beanspruchungsbedingungen. Diploma thesis, Martin Luther University Halle-Wittenberg, Halle/Saale (2011)
6. Grellmann, W., Seidler, S. (eds.): Deformation and Fracture Behaviour of Polymers. Springer, Berlin (2001)
7. Lach, R., Hutař, P., Vesely, P., Nezbedová, E., Knesl, Z., Koch, T., Bierögel, C., Grellmann, W.: Assessment with indentation techniques of the local mechanical behavior of joints in polymer parts. Polimery **58**, 900–905 (2013)
8. Hashemi, S., Williams, J.G.: The effects of specimen configuration and notch tip radius on the fracture-toughness of polymers using J_C . Plast. Rubber Process. Appl. **6**, 363–375 (1986)
9. Jayadevan, K.R., Narasimhan, R., Ramamurthy, T.S., Dattaguru, B.: Effect of T -stress and loading rate on crack initiation in rate sensitive plastic materials. Int. J. Solids Struct. **39**, 1757–1775 (2002)
10. Hallstrom, S., Grenestedt, J.L.: Mixed mode fracture of cracks and wedge shaped notches in expanded PVC foam. Int. J. Fract. **88**, 343–358 (1998)
11. Lach, R., Seidler, S., Grellmann, W.: Resistance against the intrinsic rate of fracture mechanics parameters for polymeric materials under moderate impact loading. Mech. Time-Depend. Mat. **9**, 103–119 (2005)
12. Lach, R., Grellmann, W.: Time- and temperature-dependent fracture mechanics of polymers: general aspects at monotonic quasi-static and impact loading conditions. Macromol. Mater. Eng. **273**, 555–567 (2008)
13. Lach, R., Krollop, T., Hutař, P., Grellmann, W.: Influence of the interface and the additional layer on the stable crack propagation through polyolefin bilayered structures. Procedia Mat. Sci. 867–872 (2014)

14. Baltá-Calleja, F.J., Fakirov, S.: *Microhardness of Polymers*. Cambridge Solid State Science Series. University Press, Cambridge (2000)
15. Šestáková, L., Náhlik, L., Hutař, P., Knesl, Z.: Fracture mechanics parameters of multilayer pipes. *Appl. Comput. Mech.* **1**, 299–306 (2007)
16. Han, Y., Lach, R., Grellmann, W.: The Charpy impact fracture behaviour in ABS materials. *Angew. Makromol. Chem.* **270**, 13–21 (1999)

Chapter 16

Influence of Different Welding Conditions of Polyolefin Pipes on Creep Crack Growth

J. Mikula, P. Hutař, M. Ševčík, E. Nezbedová, R. Lach,
W. Grellmann and L. Náhlik

Abstract The main aim of the paper is to study the influence of both material inhomogeneity and weld bead geometry on crack propagation in welded polyolefin pipes. Lifetime of three pipes welded by different welding procedures is numerically estimated. Experimentally observed shapes of weld bead and change of material properties inside the welded region (the change of Young's modulus) is implemented into the numerical model of welded pipes. Circumferential crack is of interest during the crack propagation through the pipe wall and the stress intensity factor is evaluated. It is shown that the deformation of welded region plays an important role whatever it is caused by, either the inhomogeneous distribution of Young's modulus or the amount of material in that region. The change of weld bead notch radius is not proved to be important for slow crack growth. It is shown that non-optimal welds can significantly decrease lifetime of pipe systems. The results of this research can be used for lifetime estimation and prediction of creep crack growth and further optimisation of welding conditions and butt weld technology.

J. Mikula (✉) · P. Hutař · M. Ševčík · L. Náhlik
Institute of Physics of Materials, Academy of Sciences of the Czech Republic,
Brno, Czech Republic

J. Mikula
Brno University of Technology, Brno, Czech Republic

E. Nezbedová
Polymer Institute Brno, Brno, Czech Republic

R. Lach · W. Grellmann
Polymer Service GmbH Merseburg, Merseburg, Germany

W. Grellmann
Centre of Engineering, Martin Luther University Halle-Wittenberg,
Halle/Saale, Germany

16.1 Introduction

Polyolefin pipes are widely used for water and gas transportation in pipeline industry [1]. This material combines many advantages which prefer it to be used instead of steel or other common materials. For many pipeline applications the high-density polyethylene (PE-HD) is being used. The material is highly resistant to corrosion, chemicals or vibrations, is very flexible, lightweight and able to be welded.

A demand on lifetime of polyolefin pipes is generally increasing and a new generation of pipes is required to sustain the operating conditions up to 100 years. The most common failure of polyolefin pipes is related to slow (creep) crack growth (SCG) [2, 3]. The creep crack growth could theoretically take over 100 years but the process is accelerated by many intrinsic or extrinsic factors.

This paper is focused on the influence of the welding joint on pipe lifetime. The welded region has different material properties in compare to the basic pipe material as well as the stress–strain field near the weld bead is much more complex in comparison to internally pressured pipes only. The welded connection is examined here, and different welding conditions are compared. The linear elastic fracture mechanics concept (proposed in [3–5]) is used to study the slow crack propagation in the weld-affected area and a subsequent lifetime prediction of the welded structure is shown.

16.2 Welding of Polyolefin Pipes

Polyolefin pipes are usually butt-welded. This welding technology is based on heat and pressure action creating a weld bead. Welding of polyolefin pipes is standardised e.g. by ISO 21307 [6]. Time versus pressure diagram of the welding process according to this standard is shown in Fig. 16.1. For the presented study, the polyethylene pipe from production of Pipe Life was chosen (PE-100, 110×6.3 SDR 17.6). The welding was performed by the ROWELD P160B welding equipment. The welding regime was chosen depending on type of polymer material and the dimensions of welded pipe.

The specific times for each step of the welding process are: alignment of the joining surfaces $t_1 = 15$ s, time for preheating of the joining surface $t_2 = 63$ s, time of the removal of the heating plate $t_3 = 6$ s, time to achieve joining pressure $t_4 = 6$ s and cooling time of the weld at joining pressure $t_5 = 9$ min (see Fig. 16.1). After this procedure (optimal welding conditions for given pipe) the experimental specimens from the welded pipes were prepared and used for laboratory tests.

Change of material properties and weld bead geometry depend on welding conditions. Usually the correct welding procedure leads to the so-called optimal weld bead shape. This case is shown in Fig. 16.2a. If the welding is not performed

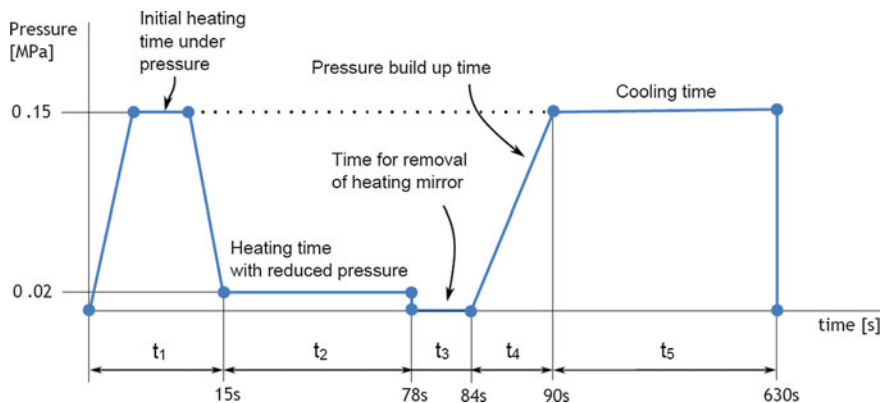


Fig. 16.1 Time versus pressure diagram of the welding process according to ISO 21307

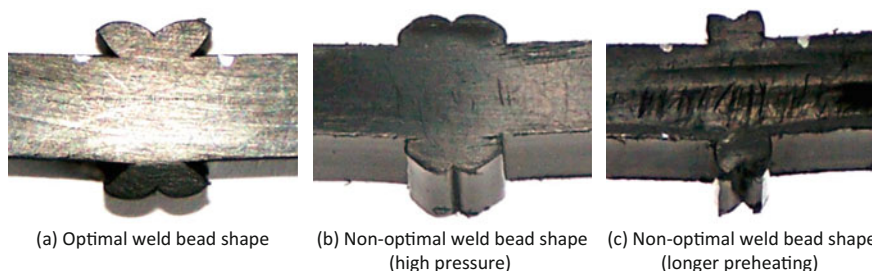


Fig. 16.2 Weld bead shapes in a pipe wall

correctly a non-typical weld bead shape is created. Two additional welding conditions are compared in the paper:

- high joining pressure (p higher)—joining pressure was increased from 0.15 MPa (optimum welding conditions) up to 0.75 MPa, see Fig. 16.2b,
- long time for preheating (t_2 longer)—preheating of the joining surfaces was increased from $t_2 = 63$ s to $t_2 = 126$ s, see Fig. 16.2c.

16.3 Material Properties of the Welded Region

Figure 16.3 shows well-visible changes in the microstructure of the welded connection [7]. The degree of crystallinity is highest inside the heat affected zone and decreases approaching the basic material. This statement is in a good agreement with the microhardness tests [8]. The inhomogeneous distribution of the material properties in the welded connection can be described by the change of Young’s modulus over the weld. It was shown that the ratio E_{max}/E_{min} of the maximum and the minimum Young’s modulus is important [9]. For different welding conditions

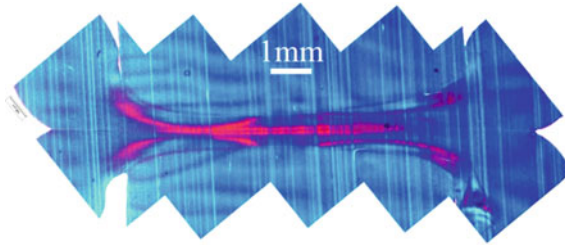


Fig. 16.3 Optical micrograph of the welded connection in polarised light [7]

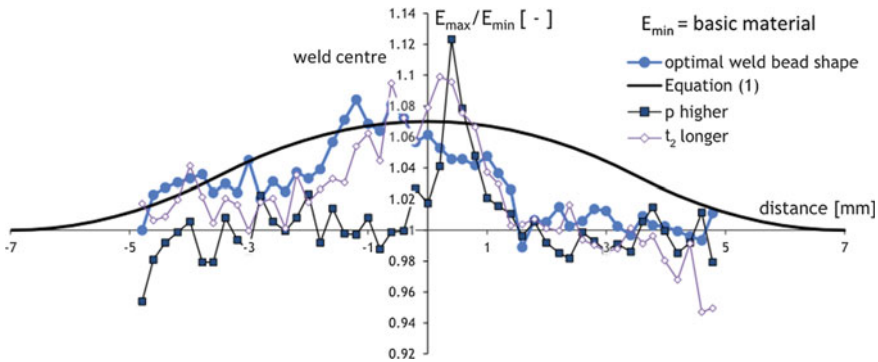


Fig. 16.4 Normalised Young’s modulus from microindentation tests for different welding conditions

the experimentally obtained data of the inhomogeneity based on microhardness tests are shown in Fig. 16.4 [8]. The data are divided with respect to weld bead shapes (see Fig. 16.2). The basic pipe material is homogeneous, where the ratio $E_{max}/E_{min} = 1$. The maximum ratio (the highest inhomogeneity) is situated roughly in the middle of the weld. Ratio E_{max}/E_{min} for different welding conditions and for polyethylene varies only in a small range (1.09–1.12), therefore in all the cases the distribution of Young’s modulus was fitted by the same function corresponding to the optimal welding conditions (16.1).

For the optimal welding conditions the distribution of Young’s modulus can be extrapolated by the following power-law function [9]:

$$\begin{aligned}
 E(z) &= h_1(z) \cdot E_{max} + (1 - h_1(z)) \cdot E_{min} & \text{for } 0 \leq z \leq w/2, \\
 E(z) &= h_2(z) \cdot E_{max} + (1 - h_2(z)) \cdot E_{min} & \text{for } w/2 \leq z \leq w,
 \end{aligned}
 \tag{16.1a}$$

where the functions $h_{1,2}(z)$. are:

$$\begin{aligned}
 h_1(z) &= \frac{1}{2} \left(\frac{z}{w/2} \right)^p & \text{for } 0 \leq z \leq w/2, \\
 h_2(z) &= 1 - \frac{1}{2} \left(\frac{w-z}{w/2} \right)^p & \text{for } w/2 \leq z \leq w.
 \end{aligned}
 \tag{16.1b}$$

This function was used in the numerical model to simulate the inhomogeneity. Figure 16.4 shows this function as the black bold line. The ratio E_{\max}/E_{\min} was chosen to 1.07, the exponent p was 2 and the half-width of the welded region w was 7 mm.

To properly describe the long-term properties the fatigue tests using the cracked round bar (CRB) specimens directly lathed from the pipe wall were performed as documented in the paper [10]. The testing conditions (frequency of 10 Hz, R -ratio of 0.1 and temperature of 23 °C) were applied. It was found, that the pipe material itself shows significantly better resistance against the fatigue loading than the welded area itself [10]. The results of the CRB tests were confirmed by our own Pennsylvania Edge Notch Tensile (PENT) Tests using the same material. Therefore the resistance against slow crack growth is significantly weaker in the centre of the polymer weld than in the basic pipe material. On one side the material properties are weakened in the welded region on the other side the connection is strengthened by more of the material in the form of weld bead.

16.4 Numerical Model Description

Geometry of the welded pipe is schematically presented in Fig. 16.5. Dimensions of the pipe are: outer diameter $d = 110$ mm and pipe wall thickness $s = 6.3$ mm. Geometry of the weld bead is based on the real experimentally obtained geometries as

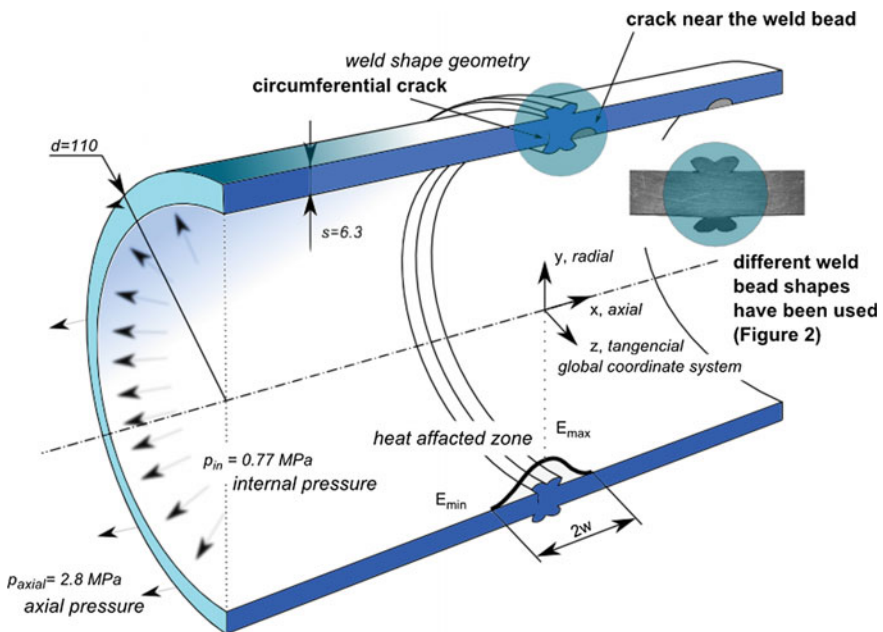


Fig. 16.5 Basic geometry description of welded PE pipes with a weld bead

shown in Fig. 16.2. The double power-law function (16.1) was implemented into the model simulating the inhomogeneity inside the welded area. This function was discretised into 42 values and was prescribed directly to the elements without any necessity of creating special volumes or areas.

For the pipe with a circumferential crack an axisymmetry could be used to develop a two dimensional numerical model. The initial crack length in the numerical model was considered as 0.05 mm. The stress intensity factor (SIF) values were estimated based on the nodal displacements near the crack tip [11] and further crack propagation was predicted by the maximum tangential stress (MTS) criterion [12] with the crack increment of 0.05 mm.

For all the numerical models the pipe was assumed to stay at the room temperature for which the Young's modulus of polyethylene is $E = 950$ MPa and the Poisson's ratio $\mu = 0.35$. The inner pipe pressure was calculated as $p_{in} = 0.77$ MPa, which creates the desirable hoop stress $\sigma_{hoop} \approx 6$ MPa. For a closed pipe system additional stress p_{axial} acting in axial direction has to be accounted for. It is calculated directly from equilibrium of forces in that direction from the internal pressure with $p_{axial} = 2.8$ MPa.

16.5 Location of Crack Initiation

The crack initiates near the stress concentrations which are situated close to the weld bead notches. Depending on further crack propagation it can be distinguished between axial and circumferential cracks. These two cases are shown in Figs. 16.6 and 16.7, where the optimal weld bead geometry is present. The plotted stress fields represent the stress component which is responsible for crack opening. For the axial crack the tangential stress is critical, whereas for the circumferential crack it is the axial stress.

For the non-optimal weld bead shapes the situation is similar, just the geometry of the bead is slightly changed (see Fig. 16.2). From the previous studies it has been

Fig. 16.6 Axial crack initiation (tangential stress) in a closed pressurised pipe

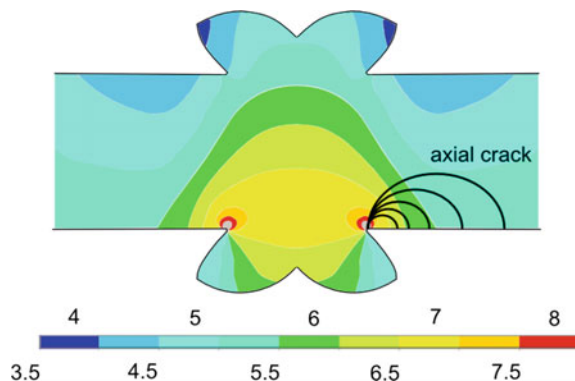
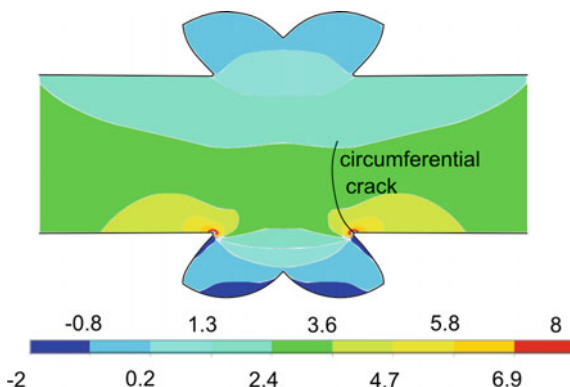


Fig. 16.7 Circumferential crack initiation (axial stress) in a closed pressurised pipe



shown that removing of the weld bead after the welding process might have a negative influence on lifetime of the pipe [9]. This negative influence is related to the axial crack propagation in the area of low resistance against slow crack growth. The existence of the weld bead shields the area of low crack resistant material and forces the crack to propagate in the weld affected zone with comparable material properties as the basic material. For this configuration the circumferential crack starting from the stress concentration in the weld bead notch is more dangerous, (see Fig. 16.7). Therefore the following numerical calculations were focused on the influence of material inhomogeneity, weld bead radius and weld bead shape having a circumferential crack. For the failure analyses the SIF will be used.

16.6 Stress Intensity Factors for Different Configurations

16.6.1 Influence of Material Inhomogeneity

The influence of inhomogeneous distribution of Young's modulus in case of the circumferential crack was studied for the case of optimal weld bead geometry and a closed pipe system. The normalised results of the SIFs for this case are shown in Fig. 16.8. The figure shows that increasing the inhomogeneity (the ratio E_{\max}/E_{\min}) leads to an increase of the stress intensity factor. This effect is relatively small especially in the range of possible ratio E_{\max}/E_{\min} for polyethylene pipe materials (1–1.2).

The black bold line represents the values of the SIFs for the axial crack in a homogeneous area of pipe. The significant increase of the stress intensity factor especially for small circumferential cracks ($a/s < 0.1$) in comparison to homogeneous pipe decreases lifetime of the welded area. It can be concluded, that the effect of the weld bead notch is more important than material inhomogeneity inside the polymer weld.

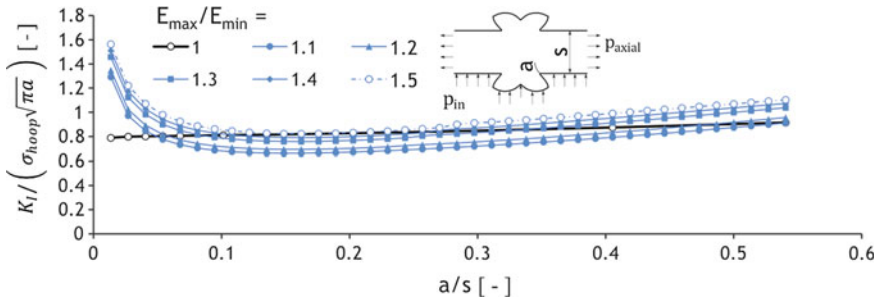


Fig. 16.8 Normalised stress intensity factor values for different ratio of inhomogeneity

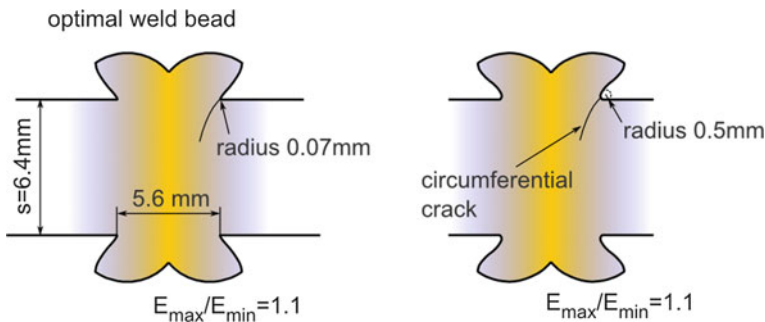


Fig. 16.9 Weld bead radius geometry

16.6.2 Influence of the Weld Bead Radius

The weld bead radius was studied on the optimal weld bead shape. Changing the radius brought insignificant change to the values of the stress intensity factor (see Fig. 16.10).

Geometry of the weld bead radius is given in Fig. 16.9. Various radii were considered from 0.07 to 0.5 mm. Smaller radius may influence crack initiation time to shorter times but in overall it doesn't influence the further crack propagation since the change in the stress concentration is just local and very small. The creep crack growth is influenced much more by the inhomogeneity of the welded region or by the weld bead shape as shown in the following section.

16.6.3 Influence of Different Weld Bead Shape

Different geometries of the weld bead shapes are shown in Fig. 16.2. Comparing the values of the stress intensity factors for different geometries (see Fig. 16.11) it

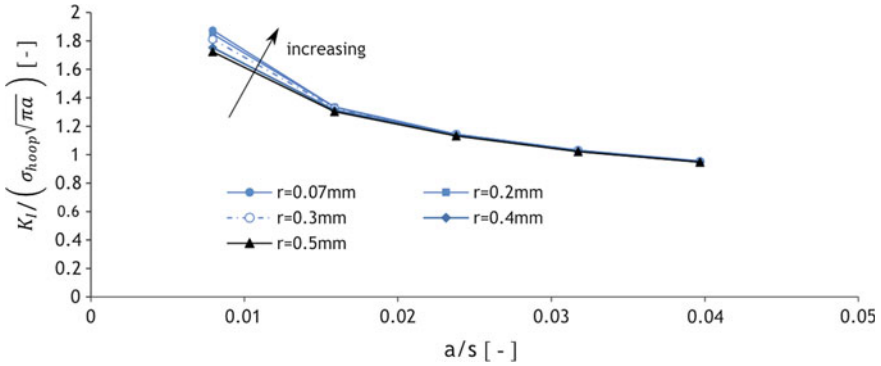


Fig. 16.10 Normalised stress intensity factor values for different weld bead notch radius

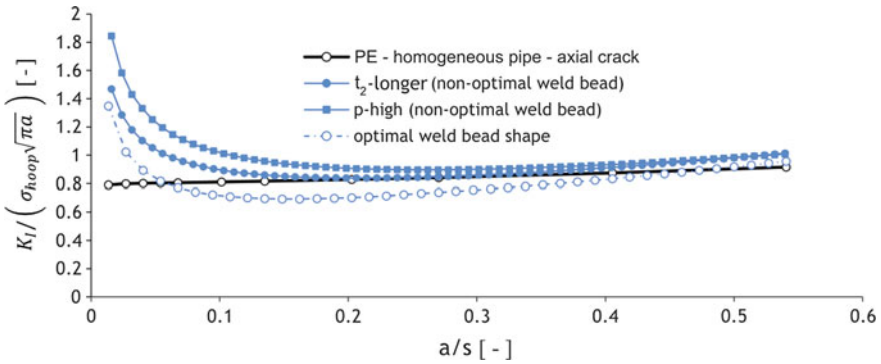


Fig. 16.11 Normalised stress intensity factors for different weld bead shapes

can be shown that the non-optimal shape caused by high pressure represents the worst case.

Why the SIFs are higher for this configuration can be explained looking at the deformation of the pipe in Fig. 16.12. The pipe is closed and pressurised. The stiffer the welded area is the higher the deformation near the weld bead appears. This deformation adds bending stresses to the axial stresses induced by the inner pressure in a closed pipe system. The bending is caused by the inhomogeneous distribution of Young's modulus and by the amount of material in the welded region. Deformed shapes for different weld bead shapes are scaled with a factor of 100 and compared in Fig. 16.12.

The crack initiates usually very close to the stiff area of the weld bead and that is the reason for having higher values of the SIFs. It can be concluded that having more material in the welded area leads to higher stress intensity factor values. From all of the three studied weld bead shapes the optimal one is the best case in terms of service lifetime.

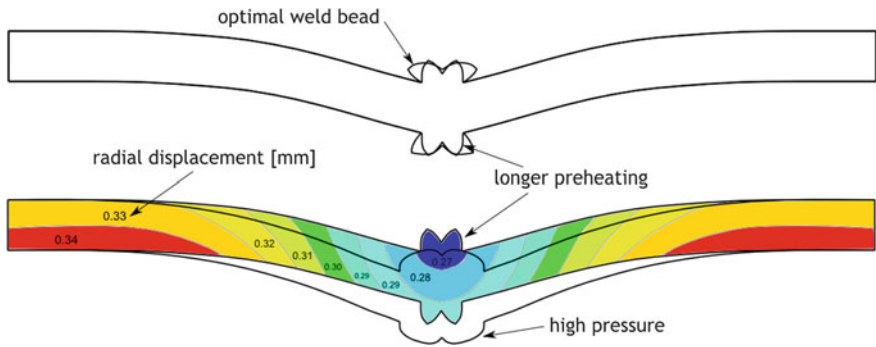


Fig. 16.12 Deformation of the pipe wall for different weld bead shapes

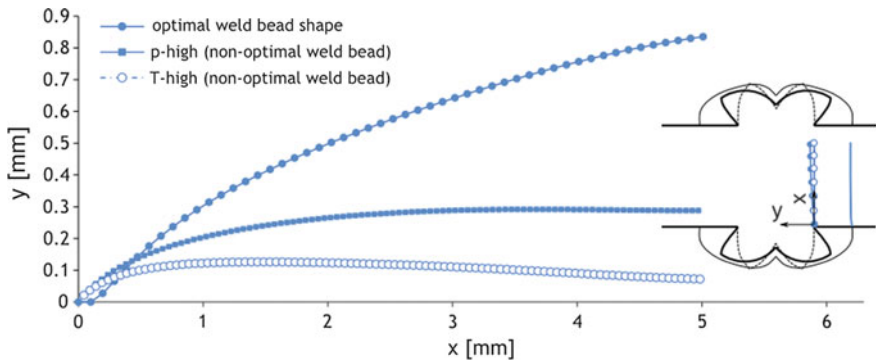


Fig. 16.13 Crack trajectories for different weld bead shapes

16.7 Crack Trajectories for Different Welds

Crack initiates near the weld bead notches and continues to propagate through the pipe wall. From the crack trajectories it can be seen that the crack is influenced by stress concentrations of the weld bead notch and later the trajectory is curved back attracted by the stress concentration of the opposite weld bead notch. Trajectories for different weld bead shapes are given in Fig. 16.13, where the y-axis is scaled to see the curvature of the crack path. The curvature is highest for the optimal weld bead shape but as seen in the small figure in the graph this change is hardly recognisable using true scale. All results correspond to PE-HD pipe with the ratio of Young’s modulus in welded area about $E_{max}/E_{min} = 1.1$.

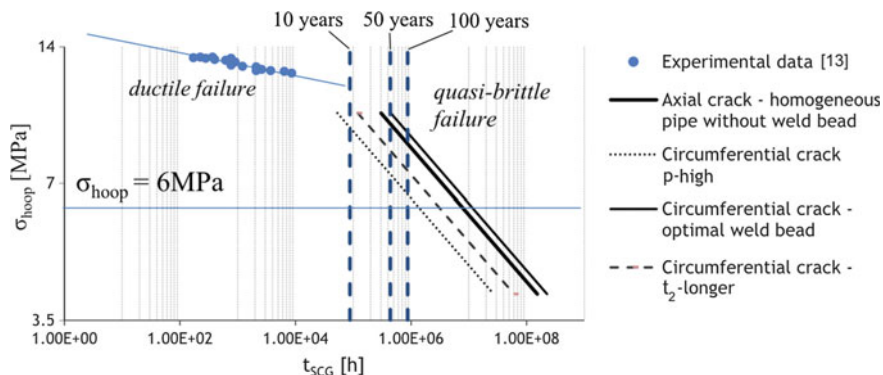


Fig. 16.14 Hoop stress versus time-to-failure diagram for different welding conditions considering the initial crack length of 0.4 mm

16.8 Lifetime Prediction

Based on the results described in previous chapters, time of slow crack growth (SCG) through the pipe wall can be evaluated. The methodology is described in [5]. The equation similar to the Paris-Erdogan law can be written as:

$$\frac{da}{dt} = C \cdot K^m \tag{16.2}$$

where the constants $C = 8.5^{-7}$ and $m = 6.8$ were experimentally found for polyethylene (PE 100) at the room temperature [13]. Integrating the equation, residual lifetime can be estimated for crack propagation from initial defect to final failure. Lifetime of polyolefin pipes is usually plot in “hoop stress versus time-to-failure” diagrams. For different weld bead shapes the diagram is shown in Fig. 16.14.

As it was previously shown the optimal weld bead shape has the best resistivity against the slow crack growth. The reason was explained on the deformed shapes, see Fig. 16.12. Due to smaller values of the stress intensity factor in case of optimal weld, see Fig. 16.11, the lifetime is comparable with lifetime of the non-welded pipe. In case of non-welded pipe the failure is given by the axial crack propagation in pipe wall [5]. In case of non-optimal welding conditions a significant decrease of lifetime is visible.

16.9 Conclusion

Lifetime predictions of three pipes welded by different welding procedures were numerically estimated. Experimentally observed shapes of weld bead and change of material properties inside the welded region (the change of Young’s modulus) was

implemented into the numerical model of welded pipes. Circumferential crack was of interest during the crack propagation through the pipe wall and the stress intensity factor was evaluated. It was shown that the deformation of welded region plays an important role whatever it is caused by, either the inhomogeneous distribution of Young's modulus or the amount of material in that region. The change of weld bead notch radius was not proved to be important for slow crack growth but it might influence the initiation time. Numerical calculations proved that lifetime of optimal closed welded pipes is comparable with a non-welded pipe failed by the axial crack propagation. It means that this type of welding technology is relatively safe without deteriorative effect on lifetime. However, non-optimal welds can significantly decrease lifetime of pipe systems. The results of this research can be used for lifetime estimation and prediction of creep crack growth and further optimisation of welding conditions and butt weld technology.

Acknowledgements This research was supported by German Research Foundation (DFG) by grant No. GR 1141/30-1, 31-1 and 32-1. Research team was also supported by the Ministry of Education, Youth and Sports of the Czech Republic throughout the project No. CZ.1.07/2.3.00/30.0063 "Talented postdocs for scientific excellence in physics of materials" and by CEITEC—Central European Institute of Technology with research infrastructure supported by the project CZ.1.05/1.1.00/02.0068 financed from European Regional Development Fund.

References

1. Janson, L.-E.: Plastic Pipes for Water Supply and Sewage Disposal. MagneStams Reklam/Christensons Grafika AB, Stockholm (1989)
2. Lu, X., Brown, N.: A test for slow crack growth failure in polyethylene under a constant load. *Polym. Test.* **11**, 309–319 (1992)
3. Lang, R. W., Pinter, G., Balika, W., Haager, M.: A Novel qualification concept for lifetime and safety assessment of PE pressure pipes for arbitrary installation conditions. In: Proceedings of Plastics Pipes XIII (Washington, 02.–05.10.2006). Washington (2006), pp. 1–10
4. Frank, A., Freimann, W., Pinter, G., Lang, R.W.: A fracture mechanics concept for the accelerated characterization of creep crack growth in PE-HD pipe grades. *Eng. Fract. Mech.* **76**, 2780–2787 (2009)
5. Hutař, P., Ševčík, M., Náhlík, L., Pinter, G., Frank, A., Mitev, I.: A numerical methodology for lifetime estimation of HDPE pressure pipes. *Eng. Fract. Mech.* **78**, 3049–3058 (2011)
6. ISO 21307 (2011): Plastics pipes and fittings—Butt fusion jointing procedures for polyethylene (PE) pipes and fittings used in the construction of gas and water distribution systems
7. Veselý, P., Kotter, I., Lach, R., Nezbedová, E., Kněsl, Z., Hutař, P., Grellmann, W.: Prüfmethoden zur Analyse des lokalen mechanischen Verhaltens von Schweißnähten in Polyethylen-Kunststoffrohren. In: Borsutzki, M., Geisler, S. (Eds.): Fortschritte der Kennwertermittlung für Forschung und Praxis (Proceedings Werkstoffprüfung 2009, Bad Neuenahr, 03.–04.12.2009). Verlag Stahleisen, Düsseldorf (2009), pp. 371–376
8. Lach, R., Hutař, P., Veselý, P., Nezbedová, E., Kněsl, Z., Grellmann, W.: Structural changes, evolution of damage parameters and crack propagation behaviour in welded plastic pipes. *Key Eng. Mater.* **465**, 427–430 (2011)

9. Mikula, J., Ševčík, M., Hutař, P., Náhlik, L.: Fracture mechanics assessment of cracked welded polyolefin pipes. In: Proceedings of Engineering Mechanics 2014 (Svratka, 12.–15.05.2014). Svratka (2014), pp. 396–399
10. Florian, A., Pinter, G., Frank, A.: Impact of single and dual pressure butt-welding procedures on the reliability of PE 100 pipe welds. In: Proceedings of EUROTEC 2013 (Lyon, 04.–05.07. 2013). Lyon (2013), pp. 136–141
11. Chan, S., Tuba, S., Wilson, W.: On the finite element method in linear fracture mechanics. *Eng. Fract. Mech.* **2**, 1–17 (1970)
12. Anderson, T.L.: *Fracture Mechanics: Fundamentals and Application*. CRC Press, Boca Raton (1991)
13. Frank, A., Hutař, P., Pinter, G.: Numerical assessment of PE 80 and PE 100 pipe lifetime based on Paris-Erdogan equation. *Macromol. Symp.* **311**, 112–121 (2012)

Chapter 17

Epoxy Modifications—A Novel Sealing Material for Rehabilitation of Pipe Joints

C. Schoberleitner, T. Koch and V.-M. Archodoulaki

Abstract The main reason for the flexibilisation of this epoxy sealing material is the necessity of the materials ability to compensate relative movements between the pipe segments. Epoxy (EP) modified with ethylene–propylene–diene rubber (EPDM) powder, reactive liquid polymer (ATBN—amine-terminated butadiene–acrylonitrile), and epoxidised modifiers as well as two customised epoxies were analysed. Concerning the dynamic-mechanical analysis, the formulations with reactive liquid polymer (ATBN) or EPDM showed nearly constant mechanical properties in the application temperature range (7–17 °C). The formulations with epoxidised modifier and the customised proprietary epoxy showed a slope in this temperature range. Generally the glass transition temperature decreased and thus a change of the materials operating temperature range occurred. Thermogravimetric analysis showed that all epoxy modifications absorb water after immersion. Due to the water absorption a plasticisation effect was observed. Further changes in the materials operating temperature ranges have to be considered. A comparison with neat epoxy shows for all formulations a reduction of the mechanical properties like tensile strength and modulus of elasticity. However, no enhancement of strain at break could be achieved by modifying with EPDM powder. The modified epoxy EP/ATBN 2 as well as the customised epoxy C-EP 1 fulfilled the requirement of pressure resistance up to 1 MPa. The measured major strain was negligible. Results of the pressure and inclination test at the fibre concrete test rig show, that the tightness as well as the flexibility (inclination) of the repaired socket can be guaranteed up to a pressure of 1.3 MPa. Finally, a pressure test in a first field application confirmed the suitability of the epoxy based material C-EP 1 for use as a robot processed sealing material.

C. Schoberleitner (✉) · T. Koch · V.-M. Archodoulaki
Institute of Materials Science and Technology, Vienna University
of Technology, Vienna, Austria

17.1 Introduction

The project Developing Water Loss Prevention (DeWaLoP, led by Vienna Water) includes a comprehensive concept for repairing leaky lead joint sockets. Sockets of 150 years old grey cast iron pipes were caulked up to the 1920s with a hemp pack and a lead ring [1] and are to be replaced.

The water tightness of the pipe connection was secured by a swollen hemp pack and a lead ring was stabilising the hemp in the socket. Biological degradation of the hemp pack and possible displacement of the lead ring can cause leakage [2]. However, the static and metallurgical integrity of these pipes are not critical. Described by Burn and Rajani in [3, 4], leakage leads to erosion of pipe bedding and, furthermore, imposes stress to the pipe. The likelihood of pipe breaks increases as a result of this process. Also an economic loss in terms of damages to foundation of roads and buildings and to the water supply systems arises [3, 5].

The designed DeWaLoP in-pipe robot crawls into water pipes (diameter 800–1000 mm), inspects, cleans and applies the sealing material in one step. The recent study covers a sealing material modification for pressure operating grey cast iron pipes for drinking water service. Such a special environment demands, that numerous boundary conditions and requirements have to be met. The material has to fulfill the requirements of the national standard ÖNORM B 5014-1 (2012) in order to eliminate a deterioration of the water quality. The operating pressure in supply systems ranges from 0.4 to 0.6 MPa. It depends on the difference in altitude. In the event of closing a gate valve in transport pipes, the pressure can increase up to 1 MPa [6]. Inexact alignment during the assembly can cause rehabilitation problems because of a varying socket gap clearance. For a successful rehabilitation a feasible socket gap is necessary. Thus, a gap clearance of 5 to 30 mm was set as boundary condition for a successful rehabilitation. Considering the above, the mechanical properties like strength and stiffness of the sealing material have to be sufficient. To compensate elongation due to minimal pipe movements also appropriate elasticity has to be ensured.

Based on the previous investigations [7], epoxy materials have proved advantageous for this application. The thermoset materials form a rigid network having in large part proper material properties like pressure resistance, high stiffness and adhesion. Adversely, the high stiffness prevents the material capability to absorb relative movements between pipe segments. Hence, the task is to develop a matched material formulation which combines a toughness enhancement and the good performance of the epoxy material. Therefore, in the recent work epoxy resin is modified by the addition of different components to improve the flexibility.

17.2 Experimental Section

The used base epoxy system is commonly used for pipe rehabilitation with an inliner. It is a proprietary material but commercial available. The liquid resin and hardener used in this work for all modifications were (the acronym for the virgin, cured epoxy is EP):

- A diglycidylether bisphenol-A (DGEBA) resin with the diluent 1,6-hexandiglycidyl-ether. The epoxy equivalent is 200 (g/eq),
- A customised proprietary amine curing agent.

The modifiers used are:

- EPDM rubber powder, grain size of 63–100 μm and a hardness of 40 Shore A,
- Reactive liquid polymer (RLP); an amine-terminated butadiene–acrylonitrile (ATBN) copolymer, 1300×16 , 16% acrylonitrile and an amine equivalent weight of 900 g/eq,
- Epoxidised modifier 1, (EM 1): glycidyl ether of castor oil (three epoxy end-groups), epoxy equivalent 656 is g/eq,
- Epoxidised modifier 2, (EM 2): triglycidyl ether of propoxylated glycerol (three epoxy end-groups), epoxy equivalent is 644 g/eq.

For reason of comparability two customised proprietary epoxies (primarily applied in the field for sewer rehabilitation) were also investigated (acronyms: C-EP 1, C-EP 2).

For preparing the formulations the components were stirred by hand in a bleaker to a homogenous mixture. The acronyms of the tested samples and their compositions are shown in Table 17.1. Producing the characteristic samples for the mentioned methods, silicon moulds were used. If needed the surface was grinded (polished) to remove irregularities.

To assess the glass transition temperature T_g and the storage modulus E' dynamic-mechanical analyses (DMA) were performed. Measurement parameters: oscillatory frequency of 1 Hz, heating rate of 3 K/min, amplitude of 70 μm , 3 point

Table 17.1 Acronyms for the epoxies and their composition

Acronym	Resin (g)	Modifier	Modifier content (g)	Silica (ml)
EP/EPDM 1	100	EPDM	10	60
EP/EPDM 2	100	EPDM	40	–
EP/ATBN 1	100	ATBN	20	60
EP/ATBN 2	100	ATBN	40	60
EP-EM 1	90	EM1	10	60
EP-EM 2	90	EM2	10	60
C-EP 1	Customised epoxy 1			
C-EP 2	Customised epoxy 2			
EP	Neat epoxy, used for modification			

bending mode (50 mm support span). The glass transition temperature was determined at the maximum of the loss modulus E'' . The measurements were arranged with a DMA 2980 (TA Instruments). Sample dimensions are 10 mm × 3 mm × 60 mm (width × height × length).

The mass change of a specimen as a function of time and/or temperature was determined by thermogravimetric analysis (TGA) with a TGA 2050 (TA Instruments). Cured material (initial condition) was investigated first, and then the material after exposure to water for 28 days at 40 °C was tested. The mass loss up to 200 °C was considered for determining the water content. The TGA experiments were carried out using a heating rate of 20 K/min, air atmosphere as purge gas a sample mass of app. 50 mg and an alumina pan. These tests were performed from ambient temperature to 600 °C.

By common tensile tests strain at break and tensile strength were determined. Each testing series consisted of 6 specimens of shape 5 A. For determining the modulus of elasticity the elongation was measured with an extensometer. Followed by cross head detection and 50 mm/min for measuring the tensile strength and strain at break.

To gather information about the materials adhesion properties at the grinded grey cast iron surface, adhesion tensile tests were arranged. The dimensions and the design of the samples are shown Fig. 17.1 (left). Test speed was 5 mm/min and the adhesion tensile strength was registered and a 2D image correlation analysis was applied (GOM, Aramis). The recording frequency was 4 Hz. As strain at break, the major strain at crack initiation was analysed as the medium of three sections through the measurement area (Fig. 17.1 (right)).

For the testing of the materials pressure resistance first an in-house developed pressure chamber (Fig. 17.2a) was built. During pretesting of the material in the testing plate (Fig. 17.2b) the influence of the gap size on the materials pressure resistance was analysed with a 3D image correlation system. Pictures are taken second by second by two inclined cameras. The maximum obtainable pressure is 1 MPa. The 3D image correlation analysis was arranged with Aramis (GOM) and

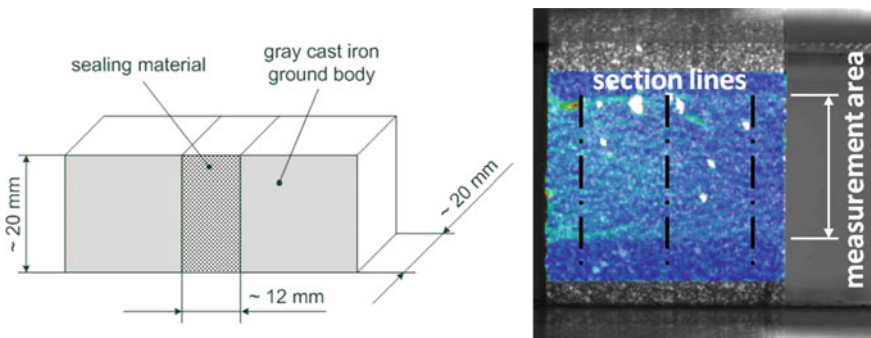


Fig. 17.1 Built up of the adhesion tensile test samples (left); scheme for determining the major strain at crack initiation from 2D image correlation analysis (right)

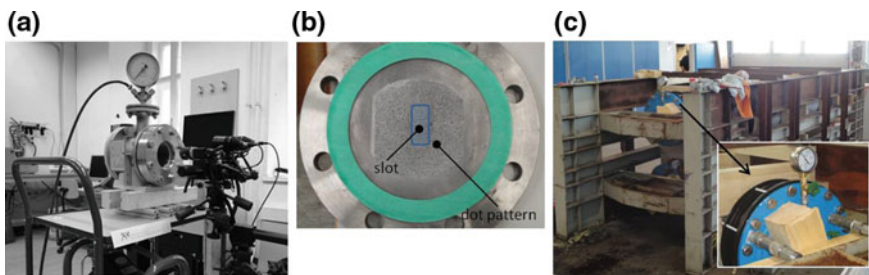


Fig. 17.2 In-house developed pressure chamber and optical system for the 3D image correlation system (a); testing plate with 30 mm slot and dot pattern (b); fibre concrete pipe pressure test rig (c)

the major strain is shown. As a next step forward a pipe test setup consisting of four fibre concrete pipes, each with a socket (Fig. 17.2c) was built. The sockets were repaired with a KA-TE[®] robot using the sealing material C-EP 1. In this test setup the performance of the repaired sockets were checked under pressure as well as inclination test were performed (1.5, 3 and 5 mm displacement was set perpendicular of a 1 m long pipe segment). Finally, as the last step in the material testing history a field pressure test of a 150 m long rehabilitated pipe was performed at a construction site near Eisenstadt, Austria (27 sockets repaired by a KA-TE[®] robot using the sealing material C-EP 1).

17.3 Results and Discussion

The modulus of elasticity measured by dynamic-mechanical analysis (DMA) is exemplarily depicted in Fig. 17.3 (left). Modifications with reactive liquid polymer (EP/ATBN 1) or rubber powder (EP/EPDM 1) form a two phase system. The

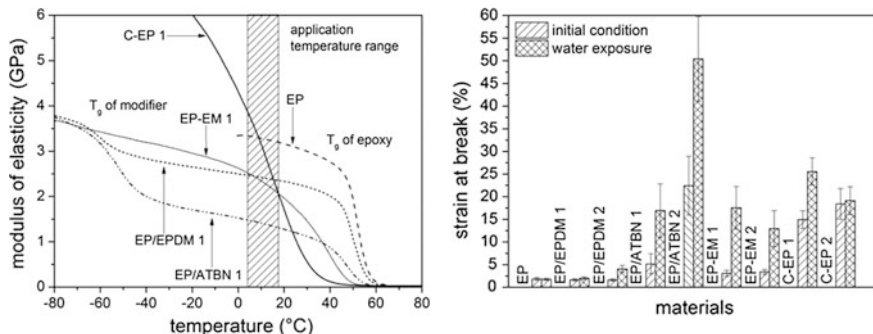


Fig. 17.3 Results determined by DMA, storage modulus E' , examples of characteristic curves (left); results of the tensile test, strain at break of the initial condition (fully cured) and of samples after water exposure for 28 days, at 40 °C (right)

reactive liquid polymer (ATBN) is miscible with epoxy resin. The functionalised amine chain ends of the RLP react with the epoxy phase and bond covalently to the epoxy resin. During curing, the rubber phase becomes less miscible with the resin, separates and forms dispersed rubber particles in the matrix [8]. It shows two glass transition temperatures (T_g) corresponding one to the modifier and one to the epoxy. Almost constant mechanical properties in the application temperature range and a decrease in the modulus of elasticity—in comparison to neat epoxy—can be observed. The modification with epoxidised modifier (EP-EM 1) belongs to the group of internal plasticised epoxies. They are added and dissolved as a second resin component and react with the curing agent. The modifying component is incorporated in the epoxy matrix. In the recent study trifunctional modifiers are used. The slope of the modulus of elasticity of this modification in the application temperature range is quite flat. The customised proprietary epoxy (C-EP 1) seems to be a copolymer of epoxy and flexibiliser. A strong slope of the modulus of elasticity in the application temperature range can be observed. Also undesired strong differences in the mechanical properties—between minimum and maximum application temperature—arise.

In order to avoid this, the T_g of the materials should not be in the same range as the application temperature. As reported in [9–11] modification of epoxy is linked to a decrease of the T_g . The dissolved rubber within the matrix of the formulations—with the RLP—as well as the reduced crosslink density of the formulations—with epoxidised modifiers—cause a shift of the T_g . This is discussed in [12] for all formulations and different modifier contents of the recent study. In addition, in any case the immersion to water of epoxy results in a further shift of the T_g to lower temperatures which is also explained by [13, 14]. Consequently the application temperature range is changed for each analysed material.

Mechanical properties like modulus of elasticity and strength of the epoxy will change after modification which is also reported in [9, 15, 16]. The strain at break of the material modification is depicted in Fig. 17.3 (right) and the influence on the tensile strength is shown in [12]. The main reason for the modification is the necessity of the materials ability to compensate relative movements between the pipe segments. These can be caused by temperature variations or subsidence in the pipe bedding. According to the results in Fig. 17.3 (right), the most successful method seems to be the addition of epoxidised modifiers or reactive liquid polymer. Chikhi explained the changes of the mechanical properties in [9] as follows: rubber affects the tensile properties. They depend on the intrinsic strength of the rubber, on the rubber content and on the compatibility of the rubber with the matrix. A consequence of ATBN addition is a decrease of the tensile strength, specifically might due to the effect of the softy structure in the matrix. As described in [15], rubber particles are known to enhance the strain at break because of an interaction of the crack-tip stress field with the rubber particles. The rubber particles cavitate and they initiate or assist yielding in the epoxy matrix. The chemical reaction between the epoxy and the ATBN is a precondition for the explanation above is. As described in literature, infrared spectroscopy is a valuable method to investigate the occurrence of chemical reactions between the epoxy resin and ATBN. But it should

be noted that ATBN hide the effect of the curing agent because both containing amine groups which react with the epoxy. Furthermore Chikhi described in [9] that an increase of strain at break as well as a decrease of glass transition temperature of the epoxy can be an indication for chemical reactions between the epoxy and the ATBN. Both could be observed in the recent study.

A strong influence of water absorption on the tensile properties can be seen in Fig. 17.3 (right) and further described in [12]. Epoxy absorbs water in dependence on crosslink density, exposure temperature and time. Water absorption increases the chain mobility because the inter-chain van der Waals forces are disrupted. So it acts like a plasticiser [17, 18]. Generally the tensile strength decreases and the strain at break increases. According to results of strain at break, the materials blended with rubber powder (EP/EPDM) are not suitable for this purpose.

In relation to the neat epoxy a change of the modulus of elasticity can be observed at all formulations. Due to the presence of the rubbery phase the modulus of elasticity of the cured epoxy polymer decreases, probably due to lowering the crosslink density [12]. After a water exposure for 28 days at 40 °C (Fig. 17.4 (left)) a further change of the modulus of elasticity can be observed for all materials. The modulus of elasticity of material C-EP 2 is on a very low level and additionally decreased by water exposure. Hence, the material is not suitable for application. The material C-EP 1 is highly influenced by water as well but can further consider for application. This influence of water absorption correlates well with the strong decrease of the strength, enhancement of strain at break as well as the shift of the T_g . The material properties gathered from tensile test differs significantly from the properties of the sealant applied on the grey cast iron. Therefore, adhesion tensile tests for the given purpose of the application are necessary. The results are shown in Fig. 17.4 (right). Adhesion tensile strength of neat epoxy is in on the same level than those of epoxy modified with ATBN and the customised epoxy C-EP 1. All remaining materials show a reduction of their adhesion tensile strength.

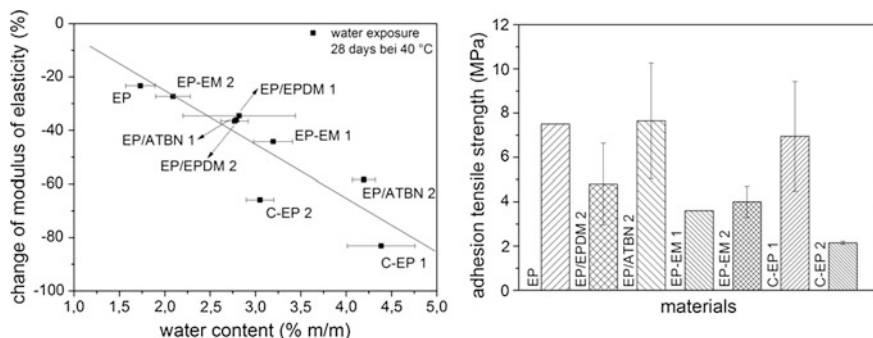


Fig. 17.4 Ordinate: change of the modulus of elasticity after water exposure for 28 day at 40 °C in relation to the initial condition (*fully cured*), abscissa: water content of the materials after 28 days at 40 °C (*left*); adhesion tensile strength of the materials, initial condition (*right*)

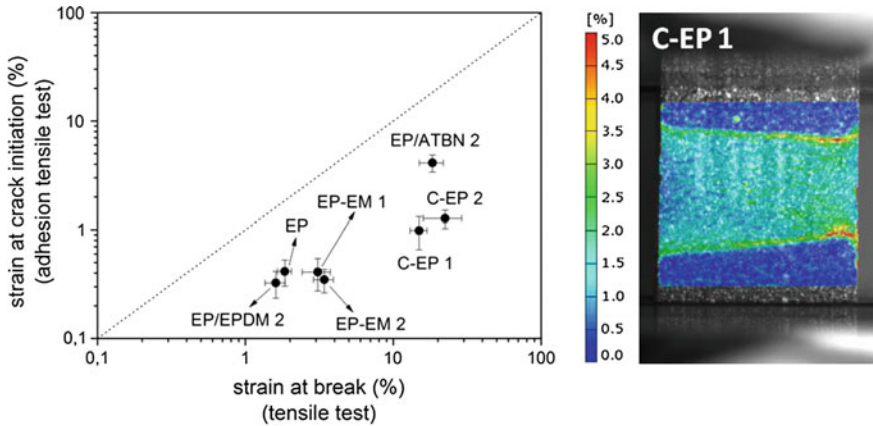


Fig. 17.5 Correlation of strain at break measured by common tensile test and strain at crack initiation from adhesion tensile test (*left*); 2D image correlation: major strain at crack initiation of an adhesion tensile test sample, E-CP 1 (*right*)

The correlation between the strain at break (tensile test) and major strain at crack initiation of the grey cast iron–epoxy compound is depicted in Fig. 17.5 (left). Processed as compound, no material could reach the strain at break measured by common tensile test. In this context the differences in the cross-section of the samples (tensile test, adhesion tensile test) have to be noted. In a common tensile test after an increase of sample cross-section a decrease of strain at break can be observed. Nevertheless, the differences were not as high as in the adhesion tensile test. As shown in Fig. 17.5 (right), it becomes clear that the strain distribution in the epoxy layer is inhomogeneous. Especially in the interphase near the adhesion surface the strain is much higher than in the bulk. It results in crack initiation and failure at lower loads. The best results could be achieved by the materials C-EP 1, C-EP 2 and EP/ATBN 2.

Also the ability to compensate the pressure due to water in the pipe is of great interest. Concerning the appropriate results of the materials EP/ATBN 2 and the customised epoxy C-EP 1 in the adhesion tensile test, the pressure resistance of these materials was investigated. At both, 10 and 30 mm slot this two materials fulfill the criterion of pressure resistance up to 1 MPa. The major strain is at both samples on a negligible level as can be seen in Fig. 17.6.

For the tests in the pipe test setup (Fig. 17.7 left) four sockets of fibre concrete pipes were repaired by a robot using the material C-EP 1. Water tightness of the sockets can be still guaranteed at a pressure of 1.3 MPa as well as up to 3 mm displacement (perpendicular to the 1 m long pipe segments). A displacement of 5 mm was leading to leakage at one of the four tested pipes. Here it should be mentioned, that 3 mm displacement of the pipe in the test rig has to be up-scaled to the real pipe length of 5 m. So during the operation of a repaired water pipe a displacement of 15 mm can occur and should not have any influence on the water

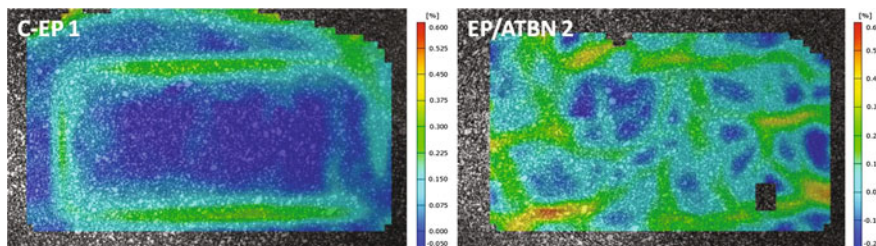


Fig. 17.6 Major strain distribution, testing plate with 30 mm slot at a pressure of 1 MPa: material C-EP 1 (left); material EP/ATBN 2 (right)

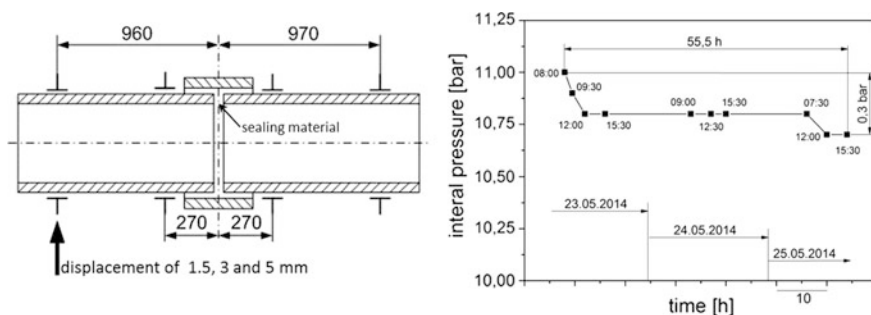


Fig. 17.7 Scheme of the fibre concrete pipe test rig (left); pressure depletion during the field test of 27 repaired sockets (right)

tightness of the system. Concerning the repaired pipe (27 sockets) at a construction site the pressure depletion during the performed pressure test for 55.5 h does not exceed the limit of 0.2 bar/h according to the ÖVGW specification W101 (Fig. 17.7 right). Comprehensively the tested material C-EP 1 showed not only the best results in the common material testing, also the application orientated pressure and inclination tests as well as the field test were passed.

17.4 Conclusion

The main reason for the flexibilisation of this epoxy sealing material is the necessity of the materials ability to compensate relative movements between the pipe segments. Epoxy modified with EPDM rubber powder, reactive liquid polymer (ATBN), and epoxidised modifiers as well as two customised epoxies were analysed. The results show a comparison of the different methods to enhance the flexibility: Concerning the DMA results, at the formulations with reactive liquid polymer (ATBN) or EPDM nearly constant mechanical properties in the application temperature range (7–17 °C) could be observed. The formulations with epoxidised

modifier and the customised proprietary epoxy showed a slope in this temperature range. Generally the glass transition temperature decreased and thus a change of the materials operating temperature range occurred. At all formulations a reduction of the mechanical properties like tensile strength and modulus of elasticity were observed. No enhancement of strain at break could be achieved by modifying with EPDM rubber powder. TGA measurements showed that all epoxy modification absorb water after immersion. Due to the water absorption a plasticisation effect was observed. Further changes in the materials operating temperature ranges have to be considered. The evaluated tensile properties could not be reached in the adhesion tensile test. Inhomogeneous strain distribution in these adhesive compounds and a maximum of stress near the interphase were leading to failure at lower loads. The modified epoxy EP/ATBN 2 as well as the customised epoxy C-EP 1 fulfilled the requirement of pressure resistance up to 1 MPa. The measured major strain was negligible. Results of the pressure and inclination test at the fibre concrete test rig show, that the tightness as well as the flexibility (inclination) of the repaired socket can be guaranteed up to a pressure of 1.3 MPa. Finally, a pressure test in a first field application confirmed the suitability of the epoxy based material C-EP 1 for use as a robot processed sealing material.

Acknowledgements This work is part-financed by the Project DeWaLoP from the European Regional Development Fund, Cross-Border Cooperation Program Slovakia-Austria 2007–2013 “Creating the Future” and Vienna Water.

References

1. Werderitsch, M.: Personal communication, 25th Aug. 2010
2. Kottmann, A.: *Rohre und Rohrwerkstoffe in der Gas- und Wasserversorgung*. Vulkan-Verlag, Essen (1997)
3. Burn, S., DeSilva, D., Eiswirth, M., Hunaidi, O., Speers, A., Thornton, J.: Pipe leakage—Future challenges and solutions. In: *Pipes Wagga Wagga (Wagga Wagga, 12.–14.10.1999)*. Wagga Wagga (1999), p. 18
4. Rajani, B., Zhan, C., Kuraoka, S.: Pipe-soil interaction analysis of jointed water mains. *Can. Geotech. J.* **33**, 393–404 (1996)
5. Hunaidi, O., Chu, W., Wang, A., Guan, W.: Detecting leaks in plastic pipes. *J. Am. Water Works Assoc.* **92**, 82–94 (2000)
6. Werderitsch, M.: Personal communication, 17th Oct. 2012
7. Schoberleitner, C., Archodoulaki, V.-M., Koch, T., Lüftl, S., Mateos, L.A., Vincze, M., Werderitsch, M., Kuschnig, G.: Development of a sealing material and robot for automatic socket rehabilitation of grey cast iron pipes in drinking water supply systems. *Water Sci. Technol. Water Supply* **13**, 924–931 (2013)
8. Jansen, B.J.P., Tamminga, K.Y., Meijer, H.E.H., Lemstra, P.J.: Preparation of thermoset rubbery epoxy particles as novel toughening modifiers for glassy epoxy resins. *Polymer* **40**, 5601–5607 (1999)
9. Chikhi, N., Fellahi, S., Bakar, M.: Modification of epoxy resin using reactive liquid (ATBN) rubber. *Eur. Polym. J.* **38**, 251–264 (2002)
10. Ikram, S., Munir, A.: Mechanical and thermal properties of chemically modified epoxy resin. *Open J. Synth. Theor. Appl.* **1**, 36–43 (2012)

11. Park, S.J., Jin, F.L., Lee, J.R.: Thermal and mechanical properties of tetrafunctional epoxy resin toughened with epoxidized soybean oil. *Mater. Sci. Eng., A* **374**, 109–114 (2004)
12. Schoberleitner, C., Archodoulaki, V.-M., Koch, T., Lüftl, S., Werderitsch, M., Kuschnig, G.: Developing a sealing material: Effect of epoxy modification on specific physical and mechanical properties. *Materials* **6**, 5490–5501 (2013)
13. de Nève, B., Shanahan, M.E.R.: Effects of humidity on an epoxy adhesive. *Int. J. Adhes. Adhes.* **12**, 191–196 (1992)
14. Zhou, J., Lucas, J.P.: Hygrothermal effects of epoxy resin. Part II: Variations of glass transition temperature. *Polymer* **40**, 5513–5522 (1999)
15. Balakrishnan, S., Start, P.R., Raghavan, D., Hudson, S.D.: The influence of clay and elastomer concentration on the morphology and fracture energy of preformed acrylic rubber dispersed clay filled epoxy nanocomposites. *Polymer* **46**, 11255–11262 (2005)
16. Miwa, M., Takeno, A., Hara, K., Watanabe, A.: Volume fraction and temperature dependence of mechanical properties of silicone rubber particulate/epoxy blends. *Composites* **26**, 371–377 (1995)
17. Moy, P., Karasz, F.E.: Epoxy–water interactions. *Polym. Eng. Sci.* **20**, 315–319 (1978)
18. Zhou, J., Lucas, J.P.: Hygrothermal effects of epoxy resin. Part I: The nature of water in epoxy. *Polymer* **40**, 5505–5512 (1999)

Part IV
Deformation Behaviour and Fracture
Mechanics Characteristics of Polymer
Films and Adhesive Systems

Chapter 18

Approaches to Characterise the Mechanical Properties of Films and Elastomers

K. Reincke and W. Grellmann

Abstract Modern elastomer and film testing involves the interaction of methods of mechanical and fracture-mechanical testing on the one hand and methods for the investigation of material composition (analytics), the structural composition and the physical and chemical properties on the other hand. A comprehensive description of the deformation and fracture behaviour of elastomers and films is only possible if a number of parameters are used. New test methods based on scientific findings are better suited for the evaluation and optimisation of the properties of these materials than technological methods that are based on empirical findings. One example shown here is supplementing the tear test with the conventional and instrumented notched tensile-impact tests, which provide further insights into the deformation and fracture behaviour.

18.1 Introduction

For research and development or quality control purposes, it is customary to conduct a diverse range of analyses in order to evaluate the mechanical properties of materials [1]. For elastomers, one of the most frequently used methods of mechanical testing is the hardness test (e.g. Shore A, Shore D, IRHD) because these tests can be performed easily and quickly. To characterise the strength and deformation properties of all kinds of polymers, tensile tests are performed. The viscoelastic behaviour of these materials can be described by means of dynamic-mechanical analysis (DMA). Depending on the use of the material, further tests to determine, for example, the tear propagation behaviour, the abrasion properties (e.g. tyres) or the compression or tension set (e.g. for sealing materials)

K. Reincke (✉) · W. Grellmann
Polymer Service GmbH Merseburg, Merseburg, Germany

K. Reincke · W. Grellmann
Centre of Engineering, Martin Luther University Halle-Wittenberg, Halle, Germany

are performed. The different methods of toughness testing, however, are not widely used for analysing films and elastomers. In the following, these methods of polymer testing and diagnostics are introduced and their informational value and limits of application are shown by means of examples.

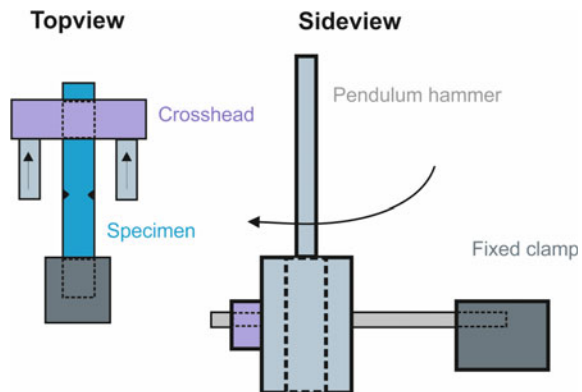
18.2 Experimental Opportunities of Mechanical Films and Elastomers Testing

18.2.1 Conventional Tensile and Notched Impact Test After ISO 8256

The conventional tensile impact test after ISO 8256 “Plastics—Determination of tensile-impact strength” [2] aims to investigate the behaviour of specimens under specified impact velocities and evaluate the brittleness or the toughness of plastics. In general, the tensile impact test (use of unnotched specimens) and notched impact test (use of notched specimens) are particularly suitable for the analysis of such materials for which the Charpy impact test is unsuitable because of the specimens’ properties regarding thickness or flexibility. This means that specimens made of films or flexible elastomer specimens can also be subjected to impact loading, thus investigating their toughness properties under impact-loading conditions.

Such tests are performed with commercially available pendulum impact testing machines that have special specimen mounts and pendulum hammers. The schematic representation of the test setup is shown in Fig. 18.1. The maximum test speed is 2.9 m/s when using pendulum hammers with a potential energy of 4 J at maximum angle of fall and 3.7 m/s with pendulum hammers with a potential energy of 50 J. For some commercially available pendulum impact testing machines, additional accessories are available which allow for the defined change of the angle of fall and hence of the test speed. For the determination of the tensile and notched

Fig. 18.1 Schematic representation of the experimental set-up for the (notched) tensile impact test with bifurcated pendulum hammer



impact toughness, specimens of Type 3 or Type 1 are used according to the applicable standard, although it is recommended to use the latter type. These double-edge-notched specimens have the following dimensions: length $l = 80$ mm, width between the notches $b_N = 6$ mm, notch depth a of the double-sided V-notches 2 mm each. The notch radius is 1 mm and the opening angle of the notch is 45° . For the determination of the tensile toughness, shouldered test bars with a length $l = 80$ mm, a gauge length $l_0 = 10$ mm, bar width $x = 10$ mm and shoulder width $b = 15$ mm are used. To perform the test, the specimen is put into the testing device and fasten by means of a fixed clamp on the one side and crossbar fixture on the other side (see Fig. 18.1). After releasing the pendulum hammer, the specimens are impacted longitudinally until they break. As a result of the test, the absorbed energy E_c is determined, which yields the conventional notched tensile impact strength a_{tN} or tensile impact strength a_{tU} .

18.2.2 Instrumented Notched Tensile Impact Test

The instrumented notched tensile impact test [3, 4] aims to determine fracture mechanical properties of plastics after the accredited MPK method “Testing of plastics—Instrumented notched tensile impact test” [5]. It is used for testing all kinds of materials ranging from thermoplastic polymers to films and elastomers. Compared to the conventional tensile impact test, the instrumentation of the pendulum machines can help in gaining further insights into the evaluation of toughness properties. The instrumentation is the addition of strain gauges or piezoelectric transducers so that the load–time signal can be recorded during the test.

To perform the instrumented notched-tensile impact test, specially fitted pendulum impact testing machines are used, similar to the conventional tensile impact test. The tests are performed on double-edge metal-blade-notched specimens (DENT specimens) which usually have the following dimensions: length $L = 64$ mm, width $W = 10$ mm and total notch depth $a = 2$ mm. In contrast to conventional tests, the load–time signal ($F-t$ signal) of the specimen is registered and converted into a load–deformation diagram ($F-l$ diagram) through double integration. This makes it possible to define and evaluate different proportions of energy involved in the total deformation. The evaluation is done according to [5] with the aim of determining the crack resistance values J_d and/or fracture toughness K_d according to (18.1) and (18.2). These parameters are regarded as measure of the material’s resistance against unstable crack propagation

$$J_d = \frac{\eta A_{\max}}{B(W - a)} \quad (18.1)$$

with the geometry function η

$$\eta = -0.06 + 5.99\left(\frac{a}{W}\right) - 7.42\left(\frac{a}{W}\right)^2 + 3.29\left(\frac{a}{W}\right)^3$$

and

$$K_d = \frac{F_{\max}}{B \cdot W^{1/2}} f(a/W) \quad (18.2)$$

with the geometry function

$$f(a/W) = \frac{\sqrt{\frac{\pi a}{2W}}}{\sqrt{1 - \frac{a}{W}}} \left[1.122 - 0.561 \left(\frac{a}{W}\right) - 0.205 \left(\frac{a}{W}\right)^2 + 0.471 \left(\frac{a}{W}\right)^3 + 0.190 \left(\frac{a}{W}\right)^4 \right]$$

with A_{\max} —energy up to the maximum load F_{\max} , B —specimen thickness, W —specimen width, a —initial crack length.

When comparing or optimising materials, the maximum load F_{\max} and deformation at a maximum force l_{\max} provide further important information for the interpretation of the crack resistance values and for the evaluation of the deformation and fracture behaviour.

18.2.3 Instrumented Puncture Impact Test

To determine the multiaxial impact behaviour of rigid polymers or films, the instrumented puncture impact test (also referred to as “instrumented free falling dart test”) according to ISO 6603-2 [6] is used. The performance of such tests is based on the use of drop impact testers with electronic data logging. The instrumentation of the dart enables the recording of load–time diagrams and the calculation of load–deformation diagrams which are required for a comprehensive and meaningful characterisation of materials. During the test according to the standard [6], the plate-shaped specimens or films (square 60 mm × 60 mm or round, diameter minimum 60 mm) are punctured with a falling weight vertically to the surface at a nearly constant speed of 4.4 m/s while recording the load–deformation diagram (see Fig. 18.2) at the same time. The tip of the falling weight is shaped like a spherical cap with a diameter of 20 mm. On the basis of the diagram and characteristic signs of damage, brittle, tough or very tough fractures can be distinguished from each other. Details of the classification of the diagrams are regulated in the standard [6]. Comparisons between individual materials can be made with this test if the specimen production, specimen dimensions, surface properties and experimental conditions are comparable. The thickness of the films or specimens plays a particularly important role in such tests. The puncture impact test can yield important results for the means of, for example, the maximum load F_M , maximum

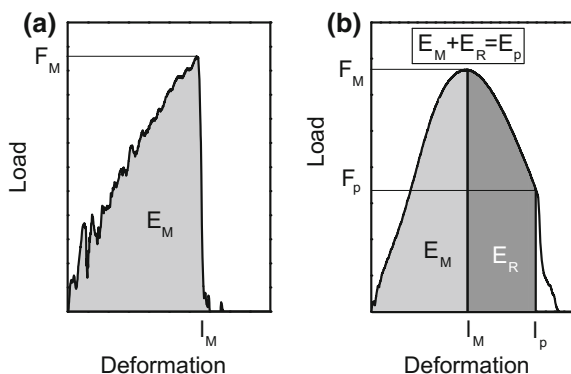


Fig. 18.2 Different types of load–deformation diagrams from the instrumented free falling weight test: **a** material with nearly linear elastic deformation behaviour and unstable crack growth and **b** material with elastic–plastic material behaviour and stable crack growth during puncture; characteristics values: F_M —maximum load, l_M —deformation at maximum load, E_M —energy up to maximum load, E_R —energy from maximum load up to l_p , E_p —puncture energy with $F_p = F_M/2$ and l_p —deformation at F_p

deformation l_M or the energy reached at maximum load E_M . Recent investigations [7] have shown that the instrumented puncture impact test can also provide important information about the deformation behaviour of elastomers at high speeds.

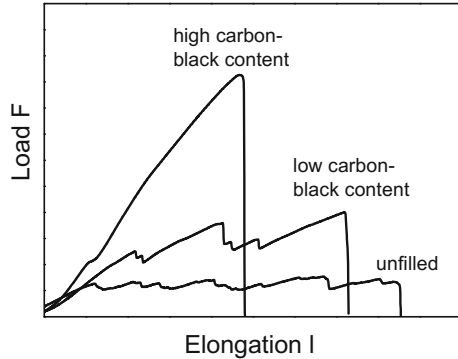
18.2.4 Tear Test

A reliable method for the characterisation of the tear behaviour of films and elastomers is the determination of the tear resistance T_S , for example, according to DIN 53363 [8] or ISO 34-1 [9]. The tests are usually performed under quasi-static loading conditions by means of universal testing machines. To determine the tear resistance of films according to DIN 53363, trapezoidal specimens are used. These specimens have a notch in the middle from where the tear process is initiated because of the stress concentration and the deformation state of the specimen due to the clamping. For the determination of the tear resistance of elastomers after ISO 34-1, trouser specimens (strip specimen with a cut parallel to the longitudinal axis) are frequently used. During loading of the specimen, the load–elongation diagram is recorded. Examples are provided in Fig. 18.3.

The tear resistance T_S is calculated using the following equation:

$$T_S = \frac{F_{\max/\text{med}}}{B} \quad (18.3)$$

Fig. 18.3 Typical load–elongation diagrams from tear tests of styrene–butadiene rubber vulcanisates (SBR) without and with carbon black as filler



with B being the specimen thickness and $F_{\max/\text{med}}$ the maximum or the median of the load. Depending on the behaviour of the material, the maximum load or the median of the load from the load–elongation diagram is used for F . However, the value yielded by means of this test method does not take into consideration the share of the deformation component in the total energy absorbed also or particularly regarding the tear resistance of the material. This should, however, be taken into consideration when choosing mechanical tests for quality control, material development and optimisation purposes.

18.2.5 Peel Tests

For the characterisation of the peel behaviour of films made of plastic or metal and metal–plastic bonds, the T-peel test according to ASTM D 1876 [10] and the fixed-arm peel test according to a ESIS-TC4 protocol [11] can be used. These peel tests are methods that can be performed relatively quickly and easily for the determination of the peel behaviour of two- or multi-layered polymer films (e.g. adhesive, cohesive) or metal–plastic bonds and can be used successfully both in research and development and in product and quality control.

The aim of the most commonly used T-peel tests (see Fig. 18.4a) is to characterise the peel

behaviour under symmetric peel conditions and with an ideal peel angle of 90° . In practice, this ideal configuration is not reached, especially when the sealing partners have different thickness and/or stiffness. In contrast to the T-peel test, the fixed-arm peel test (see Fig. 18.4b) is used to characterise the peel behaviour under a defined peel angle. One of the peel arms of the specimen is fixed onto a brass plate, where the adhesive strength has to be greater than the expected peel strength. After preparing the specimen, the brass plate is placed into the fixed-arm peel tester with which the defined peel angle can be regulated. The loose peel arm of the

specimen is clamped and then the peeling takes place similar to the T-peel test by moving the crosshead of the universal testing machine.

The load–traverse path diagram (peel curves) can be evaluated by means of the schema given in Fig. 18.5 and by using the characteristic plateau of the peel curve between 20 and 80% of the traverse path for the determination of the peel force. Furthermore, a fracture mechanical analysis of the peel process can be done by calculating the energy release rate G_{Ic} according to (18.4)

$$G_{Ic} = \frac{F_{peel}}{W} (1 - \cos \theta) \tag{18.4}$$

with F_{peel} —peel load, W —width of the sealing area, θ —peel angle.

Difficulties in conducting peel tests may arise from, for example, very small peel forces during testing very thin films, which requires the use of load cells with very small measuring ranges. Furthermore, the specimens need to have minimum dimensions so that one or both peel arms can be clamped into the upper and/or lower clamp. Also sometimes the analysis of the gained load–traverse path diagrams is difficult e.g. due to variation of the load in the peel area.

Fig. 18.4 Schematic representation of the T-peel test (a) and the fixed-arm peel test (b) for the investigation of the peel behaviour with θ —peel angle

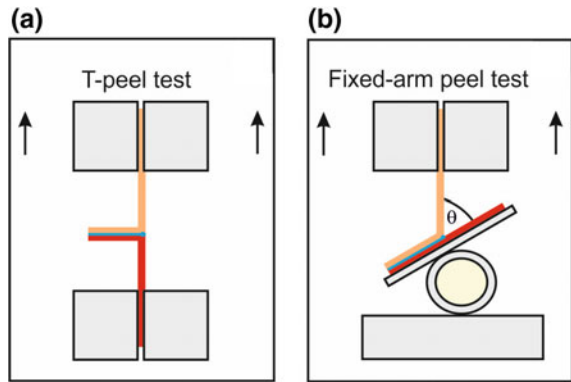
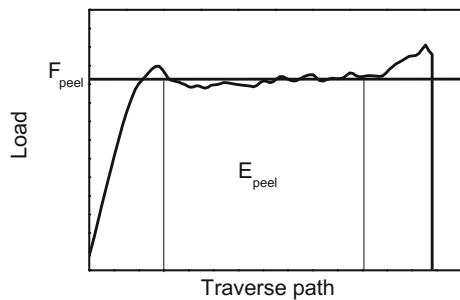


Fig. 18.5 Example of a load–traverse path (peel curve); F_{peel} —peel load and E_{peel} —peel energy



18.3 Examples of Use

18.3.1 Assessment of the Toughness Properties of Elastomers

The physical and chemical properties of elastomer materials are defined by the composition

of the mixture (polymer, filler, crosslinking system, plasticiser, etc.). In general, active fillers are added in order to improve the mechanical properties, resulting in an increase in, for example, the tensile strength σ_{max} , the storage modulus E' , the Shore hardness or the abrasion resistance. The mainly used active fillers are carbon black and precipitated silica. In recent years, many studies [4, 12, 13] have investigated the influence of the choice of the rubber matrix, the filler or the share of the filler on the crack resistance of elastomers. These studies have often found that the fracture mechanical values especially reflect the influence of structural parameter.

Figure 18.6, for example, shows some results of the instrumented notched-tensile impact test and the tear propagation test for solution-SBR vulcanisates reinforced by carbon black and silica in dependence on the share of the filler. It can be seen that both the toughness and the tear propagation resistance are strongly influenced by the share of the filler, while there are differences depending on the filler used. The J_d values that characterise the resistance against unstable crack growth are similar for both fillers, whereas the tear propagation resistance is higher for silica compounds if the filler level is higher.

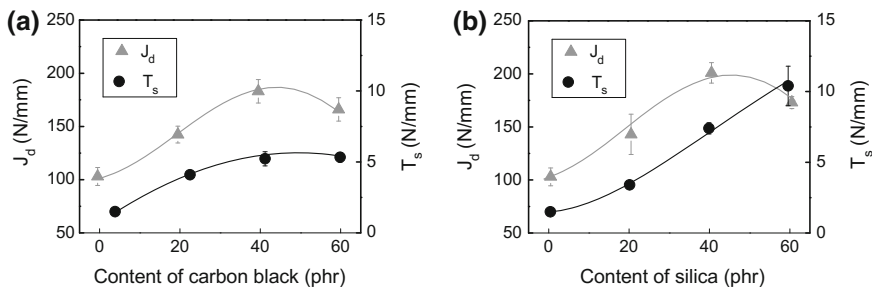


Fig. 18.6 Crack toughness values J_d determined within the instrumented tensile impact test as well as the tear strength T_s from the tear test for SBR vulcanisates reinforced with the active carbon black N339 (a) and the highly dispersive precipitated silica Ultrasil® 7000 GR (b) as a function of the filler content

18.3.2 *Influence of Chemical Loading on the Mechanical Properties of a Thermoplastic Film*

The subject of investigation was a tough PVC film with a thickness of ca. 0.8 mm, which is commercially available and used, for example, for swimming pool supplies. One aim of the investigation was to capture quantitatively the potential effects of the storage of the film in a chemical solution on the mechanical properties. For this purpose, specimens for mechanical tests were taken from the film and stored in an ammonium sulphate solution for a defined period (chemical loading). The solution contained an additional substance, which acts as a solvent for PVC. To characterise the influence of this possibly damaging substance, its concentration was varied between 25 and 500 mg/l. Another aim of the investigation was to compile a test catalogue for such investigations and to identify those test methods that can clearly show a potential deterioration of the properties. The investigation included the following tests:

- tensile test
- tear test
- conventional notched tensile impact test
- instrumented notched-tensile impact test
- instrumented puncture impact test

The starting point was the quantification of the level of the properties of the film in the chemically unloaded, initial state and the representation of possible anisotropy of the properties. It was found that the film exhibits a very good quality, which is associated with high strength and toughness level. Only very little anisotropy of the properties could be found, which, however, could only be proven for the crack resistance J_d by means of an instrumented notched-tensile impact test. Table 18.1 summarises the results (in percentage) for changes in the properties. The middle column of Table 18.1 shows that overall the storage in the solution with 25 mg/l compared with the chemically unloaded reference sample results in only slight changes in the properties. Essentially, the chemical loading leads to a slight improvement in strength, deformability and the E -modulus as a measure of stiffness, while the toughness is reduced. Significant changes, however, could be found only for the strain at tensile strength ε_M , the tensile impact strength a_{tN} and the deformation at the maximum load l_M during the instrumented puncture impact test. This is marked within Table 18.1 with (s).

Much more significant and in part greater changes in the material's properties are triggered by an increase in the substance concentration from 25 to 500 mg/l (see right column of Table 18.1). Essentially, the characteristics of the material's properties are reduced in terms of strength, stiffness and toughness, except for the tensile impact strength a_{tN} . However, while the strength (σ_{max}), the E -modulus E_t and the deformability (ε_M and l_M) change only slightly or insignificantly, a considerable decrease in the crack resistance J_d and energies E_M and particularly E_P can be found. This shows that the crack propagation behaviour, compared to the other

Table 18.1 Percentage change of the material parameters due to the exposure of the PVC specimens in the solution with 25 mg substance per litre (middle column) and increase in substance concentration from 25 to 500 mg/l; significant changes are marked with (s)

Parameter	Change in parameter (%) 0 → 25 mg/l	Change in parameter (%) 25 → 500 mg/l
σ_M^a	+1.1	-3.3 (s)
ε_M^a	+2.1 (s)	+0.3
E_t^a	+6.0	-8.6
T_s	-1.8	-1.7 (s)
a_{tN}	-4.0 (s)	+3.5 (s)
J_d	-2.3	-9.0 (s)
F_M	+2.1	-5.7 (s)
l_M	+8.0 (s)	-1.8
E_M	+2.8	-9.6 (s)
E_P	+5.5	-15.0 (s)

^aResults of the tensile testing: σ_M —tensile strength, ε_M —strain at tensile strength, E_t —elastic modulus in tension

properties such as strength, deformability, etc. is influenced strongly by the chemical loading. At the same time, the test reveals the importance of a comprehensive material description including the use of, for example, fracture-mechanical methods for the characterisation of toughness.

18.3.3 Influence of Chemical Loading on the Toughness Properties of Elastomers

With the help of this example, we aim to illustrate how the influence of chemical loading can be described quantitatively through mechanical and fracture-mechanical material characteristics and which methods of mechanical testing of polymers and technical fracture mechanics are suitable to verify this influence. For this purpose, specimens of two elastomer materials were subjected to chemical loading for a maximum period of 2000 h. After the chemical's exposure, the following experimental methods were used:

- tensile test
- tear test
- hardness test
- conventional notched tensile impact test
- instrumented notched tensile impact test

Results of the investigations are summarised in form of the changes in selected characteristics (in percentage) in Table 18.2. First, it can be seen that the properties of both materials are in part strongly influenced by the removal. The characteristic

Table 18.2 Percentage change of the material parameters after an exposure time of 1000 and 2000 h, respectively, in comparison to the initial state

Parameter	Elastomer 1 Change in parameter (%)		Elastomer 2 Change in parameter (%)	
	1000 h	2000 h	1000 h	2000 h
σ_{\max}	-21	-37	-4	-18
ε_R	-15	-18	-11	-14
T_S	-26	-37	-18	-28
Shore A hardness	+1	+1	-3	-3
a_{tN}	-27	-28	-16	-24
J_d	-30	-46	-24	-41

that is influenced the least by the removal is the Shore A hardness. Compared to the reference sample, the biggest changes—with a decrease of 46 and 41%—were found for the crack resistance J_d , that is, this characteristic is particularly sensitive in terms of structure. However, a decrease can also be found for the tensile impact strength a_{tN} , the tear resistance T_S and the tensile strength σ_{\max} , with differences between both elastomers being apparent.

Furthermore, it was found during the investigations that the values yielded can be divided into two categories: those values that reach a constant or nearly constant level after a specific removal period and those values that keep changing up to the maximum removal period of 2000 h. The first category includes the elongation at break ε_R and the Shore A hardness, which exhibit no more or very slight changes from a period of 1000 h onwards. The strength level, characterised by the tensile strength σ_{\max} , as well as the tear resistance T_S and the crack resistance J_d decrease throughout the entire exposure period.

In summary, it can be ascertained that for such investigations a careful selection of the test methods to be performed and the parameters to be determined needs to be done. This selection needs to include the consideration of the different sensitivities of the parameters in respect of a change of the properties through, for example, chemical loading and the informational value of the parameters with regard to the quantitative evaluation of the material properties strength, hardness, toughness and stiffness.

18.3.4 Evaluation of a PE/PB-1 Peel System

Following, selected results of tests on a cohesive peel-film system are shown. The peel film is a blend of two polymeric components: polyethylene (PE) and polybutene-1 (PB-1). To assess the influence of the PB-1 content on the peel behaviour, films with 3, 6, 10, 15 and 20 wt% PB-1 were produced and investigated [14, 15]. The films had a uniform thickness d_F of 0.05 mm. PE and PB-1 are thermodynamically incompatible. Therefore, when the mass ratio is in favour of PE,

a matrix–particle structure develops in which the PB-1 phase exists as separated particles. During mechanical loading like during a peel test, the PB-1 particles act as impurities that lower the peel resistance. This means that as the number of PB-1 particles increases the peel strength decreases, which is of high importance for the packaging industry. As a consequence, the industry has a great interest in optimising the PB-1 content in such peel systems since the costs for PB-1 are much higher as those for PE. The peel behaviour of the films investigated strongly depends on the peel angle, as demonstrated in Fig. 18.7 by means of selected results of fixed arm peel tests.

Figure 18.7a shows examples of peel curves at different peel angles for the peel system with 10 wt% PB-1; Fig. 18.7b shows the peel strength for 3 peel films with different PB-1 content depending on the peel angle. It can be seen that the characteristics of the peel curves are very strongly influenced by the peel angle. While a distinct plateau of the peel strength is reached from ca. 2 mm traverse path for the peel angles of 90° and 130°, for larger angles (from 160°) such a plateau as the basis for a steady peel process cannot be found. Furthermore, it becomes apparent that there is a stronger deformation of the specimen for the larger peel angle, which is the result of the much greater maximum value of the traverse path at the peel angle of 180° (see Fig. 18.7a). The peel strength yielded from the peel curves depending on the peel angle (see Fig. 18.7b) exhibits a clear dependence on the angle. It shows a minimum at peel angles ranging from 120° to 130° and increases steadily from a peel angle of 130° with larger and smaller angles. Moreover, it can be seen that the content of PB-1 has a great influence on the peel strength. The less PB-1 the greater the peel strength.

The investigations have shown that by conducting such systematic tests using in particular the fixed arm peel test, it is possible to take steps for optimising materials, for example, with regard to producing consumer-friendly, easy-open packaging.

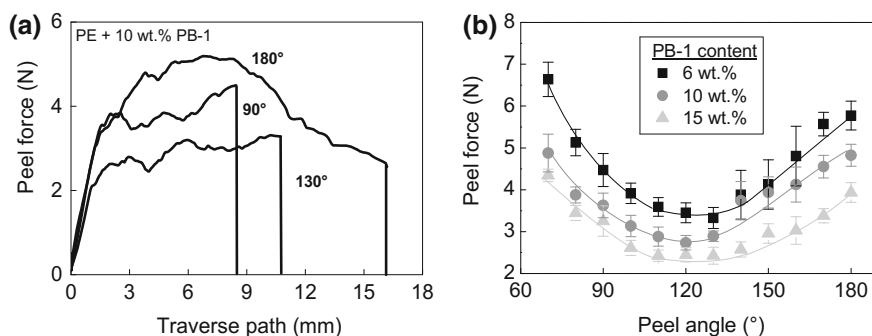


Fig. 18.7 Typical peel curves of PE/PB-1/PE-PB-1 sealed films (self-sealing) from the fixed-arm peel test at different peel angles (a) and dependence of the peel force on the peel angle for self-sealed PE/PB-1 films with 6, 10 and 15 wt% PB-1 (b) [14, 15]

18.4 Conclusions

Modern elastomer and film testing involves the interaction of methods of mechanical and fracture-mechanical testing on the one hand and methods for the investigation of material composition (analytics), the structural composition and the physical and chemical properties on the other hand. A comprehensive description of the deformation and fracture behaviour of elastomers and films is only possible if a number of parameters are used. New test methods based on scientific findings are better suited for the evaluation and optimisation of the properties of these materials than technological methods that are based on empirical findings. One example shown here is supplementing the tear test with the conventional and instrumented notched tensile-impact tests, which provide further insights into the deformation and fracture behaviour.

References

1. Grellmann, W., Seidler, S. (eds.): *Polymer Testing*, 2nd edn. Carl Hanser, Munich Vienna (2013)
2. ISO 8256 (2004): *Plastics—Determination of tensile-impact strength*
3. Grellmann, W., Reincke, R.: Quality improvement of elastomers. Use of instrumented notched tensile-impact testing for assessment of toughness. *Materialprüfung* **46**, 168–175 (2004)
4. Reincke, K., Klüppel, M., Grellmann, W.: Investigation of fracture mechanical properties of filler-reinforced styrene–butadiene elastomers. *Kautsch. Gummi Kunstst.* **62**, 246–251 (2009)
5. Grellmann, W., Reincke, K.: Testing of plastics—Instrumented tensile impact test (ITIT). Procedure for determining the crack resistance behaviour using the instrumented tensile-impact test (MPK-ITIT). Merseburg (2012). http://wiki.polymerservice-merseburg.de/index.php/MPK-Prozedur_MPK-IKZV_englisch
6. ISO 6603-2 (2000): *Plastics—Determination of puncture impact behaviour of rigid plastics—Part 1: Non-instrumented impact testing*
7. Söver, A., Frommann, L., Kipscholl, R.: High impact-testing machine for elastomers investigation under impact loads. *Polym. Test.* **28**, 871–874 (2009)
8. DIN 53363 (2003): *Prüfung von Kunststoff-Folien—Weiterreißversuch an trapezförmigen Proben mit Einschnitt*
9. ISO 34-1 (2015): *Rubber, vulcanized or thermoplastic—Determination of tear strength—Part 1: Trouser, angle and crescent test pieces*
10. ASTM D 1876 (2015): *Standard test method for peel resistance of adhesives (T-peel test)*
11. ESIS-TC4: *A protocol for determination of the adhesive fracture toughness of flexible laminates by peel testing: Fixed arm and T-peel methods* (2007). [http://www.imperial.ac.uk/media/imperial-college/research-centres-and-groups/adhesion-and-adhesives-group/ESIS-peel-protocol-\(June-07\)-revised-Nov-2010.pdf](http://www.imperial.ac.uk/media/imperial-college/research-centres-and-groups/adhesion-and-adhesives-group/ESIS-peel-protocol-(June-07)-revised-Nov-2010.pdf)
12. Reincke, K.: *Bruchmechanische Bewertung ungefüllter und gefüllter Elastomerwerkstoffe*. Mensch & Buch Verlag, Berlin (2005)
13. Reincke, K., Friedel, J., Grellmann, W.: Influence of process oils on the mechanical properties of elastomers. *Kautsch. Gummi Kunstst.* **62**, 506–514 (2009)

14. Grellmann W., Langer, B., Nase, M., Baumann, H.-J.: Fixed-Arm Peeltest—Bewertung von Grenzflächen in Polyethylen/Polybuten-1 Peelsystemen. In: Borsutzki, M., Geisler, S. (eds.): Fortschritte der Kennwertermittlung für Forschung und Praxis (Proceedings Werkstoffprüfung 2006, Bad Neuenahr, 07./08.12.2006). Verlag Stahleisen, Düsseldorf (2006), pp. 439–444
15. Nase, M., Langer, H.-J., Grellmann, W.: Fracture mechanics on polyethylene/polybutene-1 peel films. *Polym. Test.* **27**, 1017–1025 (2008)

Chapter 19

Fracture Mechanics Characterisation of Peelfilms

M. Nase, M. Rennert, S. Henning, A. Zankel, K. Naumenko and W. Grellmann

Abstract The present article gives a comparison of the peel behaviour of the adhesive peel system ethylene vinyl acetate copolymer/polyethylene (EVA/PE) and the cohesive peel system low-density polyethylene/isotactic polybutene-1 (LDPE/iPB-1) using the fracture mechanics values energy release rate G_{Ic} and adhesive energy release rate G_{alc} . The influence of the content of the peel component and the influence of the peel angle on the peel behaviour was investigated. In case of the adhesive peel system, an independence of the adhesive energy release rate on the peel angle was found. In case of the cohesive peel system, two zones of G_{alc} could be identified, (1) G_{alc} is independent of the peel angle and (2) G_{alc} depends linearly on the peel angle. This difference in G_{alc} could be strongly addressed to the type of crack propagation. In general the results revealed that fracture mechanics values like G_{Ic} and G_{alc} can be used to get further and deeper structure-sensitive information of the investigated material system.

M. Nase (✉) · M. Rennert
University of Applied Sciences, Hof, Germany

M. Rennert
Polifilm Extrusion GmbH, Südliches Anhalt, Germany

S. Henning
Fraunhofer Institute for Microstructure of Materials and Systems (IMWS), Halle/Saale, Germany

A. Zankel
Institute for Electron Microscopy and Nanoanalysis, Graz University of Technology, Graz, Austria

K. Naumenko
Institute of Mechanics, Otto Von Guericke University Magdeburg, Magdeburg, Germany

W. Grellmann
Centre of Engineering, Martin Luther University Halle-Wittenberg, Halle/Saale, Germany

19.1 Introduction

Packages with integrated peel systems are a growing field in the food packaging industry. Such packages are convenient and can be opened by hand applying defined low peel forces [1, 2]. Peel systems are also used in the medical sector to guarantee a comfortable and sterile handling during an operation.

In general, peel systems consist of a peel film and a seal film. Both partners have to be sealed together using a sealing process (see Fig. 19.1). Sometimes the seal film could also be another peel film. This means, that the peel film can also be sealed against itself.

The connection between peel film and seal film is called seal area. In practice, there are two main sealing processes, i.e., the heat conductive sealing and the ultrasonic sealing process, which can be used to realise such a seal area. The seal area is realised applying heat, time and pressure (seal temperature, seal time, seal pressure) using the heat conductive sealing process [3, 4]. The heat conductive sealing process is a thermal sealing process. In the other case, the seal area is realised applying seal force, seal time and a defined oscillation amplitude using the ultrasonic sealing process [5, 6]. The ultrasonic sealing process is a mechanical sealing process.

The peel film, in turn, mostly exhibits a three-layered structure, including a backbone layer, a middle layer and a functional peel layer (see Fig. 19.1). The composition/structure of the peel layer and of the associated seal film causes the type of the peel system.

In general, we differentiate between three main types of peel systems, (1) the cohesive peel system, (2) the adhesive peel system and (3) the hybrid peel system (see Fig. 19.2).

Cohesive peel systems are characterised by a cohesive failure within the seal area during the peel process. In other words, the crack propagation follows a zigzag-course through the seal area at microscopic scale. This specific crack propagation causes micro-deformations on and within the peeled seal area. The micro-deformations, in turn, scatter the incoming light. Thus, the peeled seal area looks white. In industrial practice, this phenomenon is called “whitening” of the

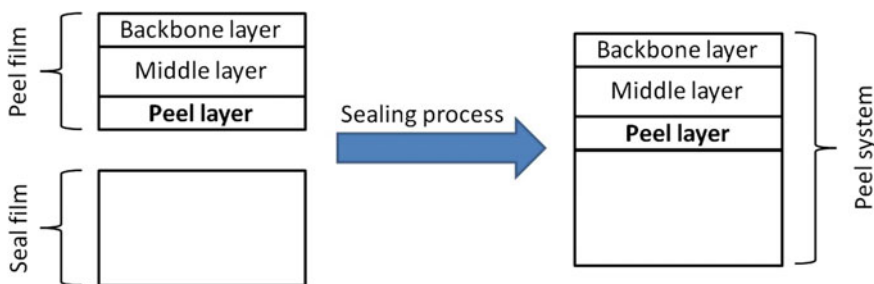


Fig. 19.1 Schematic of the peel system and the way how to create it

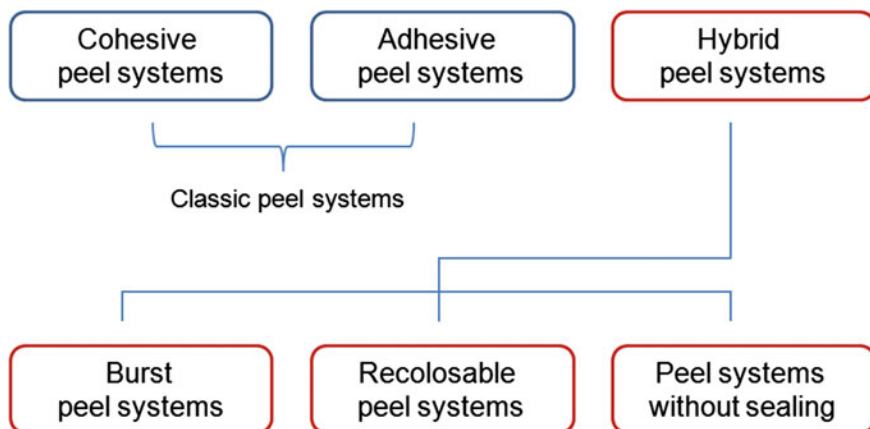


Fig. 19.2 Overview about the peel systems

peeled seal area. A very common cohesive peel system is the low-density polyethylene/isotactic polybutene-1 (PE-LD/iPB-1) peel system, which consists of low-density polyethylene as matrix and isotactic polybutene-1 as peel component [1, 7–10]. Thus, in this case, the peel layer of the peel film consists of a physical mixture of PE-LD and a variable content of iPB-1. The peel film can be sealed, e.g., against itself or against a polyethylene seal film. The peel system works well because of the incompatibility between the matrix and the peel component. This incompatibility leads to a matrix–particle structure of the PE-LD/iPB-1 mixture. So, the higher the content of iPB-1, the lower the peel force of the peel system has to be.

Adhesive peel systems are characterised by an adhesive failure within the seal area during the peel process. The connection between peel film and seal film is of adhesive character [11–13]. Therefore, the peel film can be peeled-off from seal film without any residues. Thus, the crack propagation during the peel process occurs exactly along the interface between peel film and seal film. This interface can be visualised by microscopy even the seal area was realised using heat and pressure. A very common adhesive peel system is the ethylene vinyl acetate copolymer/polyethylene (EVA/PE) peel system [13], which consists of ethylene vinyl acetate copolymer as matrix and linear low-density polyethylene (PE-LLD) as peel component. However, this system does work with and without existence of the peel component. Thus, in this case, the peel layer of the peel film consists of ethylene vinyl acetate copolymer with a variable content of vinyl acetate or a physical mixture of EVA and a variable content of PE-LLD. The peel film can be sealed, e.g., against a poly(ethylene terephthalate) (PET) seal film. Thus, the peel force can be adjusted by varying the vinyl acetate content or by varying the PE-LLD content.

Hybrid peel systems are characterised by a mixture of cohesive and adhesive failure within the seal area during the peel process. Burst peel systems, reclosable peel systems and peel systems without sealing belong to the group of hybrid peel

systems. All of these systems are mainly used in the packaging industry. The current article does not focus on hybrid peel systems.

In industrial practice, the measured value peel force is often used to characterise the peel behaviour of peel systems. The peel force is the average value of the forces, which occur during the peel process. From scientific point of view the peel force is not sufficient to evaluate the peel behaviour in full detail, because the peel force depends strongly on the shape of the specimen and the shape of the seal area and so on. Furthermore, the peel force does not consider the deformations, which occur during the peel process. To overcome these disadvantages, a fracture mechanics approach should be chosen. There are different experimental fracture mechanics and numerical fracture mechanics methods for an energy-determined characterisation of the peel behaviour. In [10] a way is described how to use the variables energy release rate G_{lc} and adhesive energy release rate G_{alc} . The energy release rate considers the total energy input during the peel process. In contrast, the adhesive energy release rate considers only the energy part, which is actually responsible for the separation of the peel system.

The present article gives a comparison of the peel behaviour of an adhesive and a cohesive peel system using fracture mechanics values. The influence of the content of the peel component and the influence of the peel angle on the peel behaviour was investigated.

19.2 Experimental

An adhesive and a cohesive peel system were investigated (see Fig. 19.3). The peel systems low-density polyethylene/isotactic polybutene-1 (PE-LD/iPB-1) and ethylene vinyl acetate copolymer/polyethylene (EVA/PE) were investigated. The peel

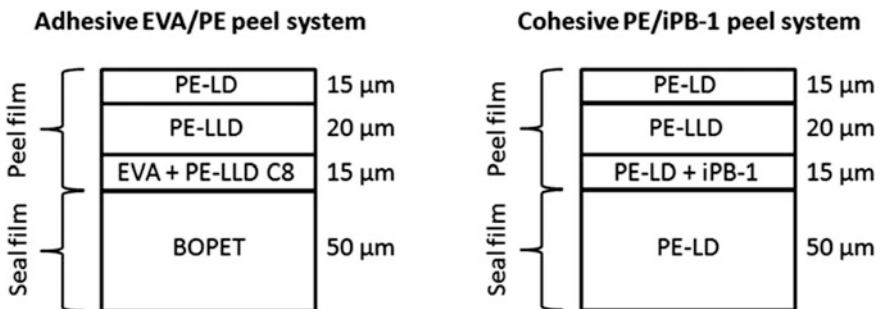


Fig. 19.3 Structure of the investigated adhesive and cohesive peel systems

component – iPB-1 in case of the cohesive and PE-LLD with octene comonomer types (PE-LLD C8) in case of the adhesive peel system – was varied between 0 and/or nearly 0 and 100 wt%.

The peel film and also the seal film have a thickness of 50 μm . The raw-materials, which were used for the recipes shown in Fig. 19.3, are listed in Table 19.1. The EVA used has a vinyl-acetate content of 18%.

The films were produced using the blown-film process and a set of standard processing parameters (see Table 19.2).

The final peel systems were created using the heat conductive sealing process (see Fig. 19.4). The seal temperature was 140 $^{\circ}\text{C}$, the seal time was 2.0 s and the seal pressure was 0.2 MPa.

To characterise the peel behaviour, the measured value peel force F_{peel} and the variables energy release rate G_{Ic} and adhesive energy release rate G_{aIc} were used. To estimate these variables, the T-peel test in accordance to [14] and the fixed-arm peel test in accordance to [15] was applied (see Fig. 19.5). The test speed was

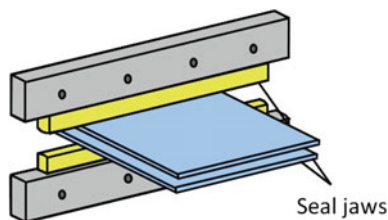
Table 19.1 Data of the used raw-materials

Description	Trade name	Density (g/cm^3)	MFI ($\text{g}/10 \text{ min}$)
PE-LD	Lupolen 2420F	0.923	0.73
PE-LLD	SABIC LLDPE 118 NE	0.918	1.0
PE-LLD C8	Dowlex SC 2107 G	0.917	2.3
iPB-1	PB 8640 M	0.906	1.0
EVA	Elvax 3170	0.940	2.5
BOPET	D-K Kunststoffolien	1.39	-

Table 19.2 Processing parameters of the blown-film process

	Parameters
Extruder parameters	Maddock mix and shear elements Screw speed: 100 rpm Temperature profile: 140–160–180–180–180 $^{\circ}\text{C}$
Die head parameters	Temperature profile: 180–180–180–180 $^{\circ}\text{C}$ Die gap size: 0.8 mm
Tube formation	Time of solidification: 1.8 s Blow-up ratio: 1:2 Draw-down ratio: 1:7.85

Fig. 19.4 Schematic of the heat conductive sealing (hcs) process



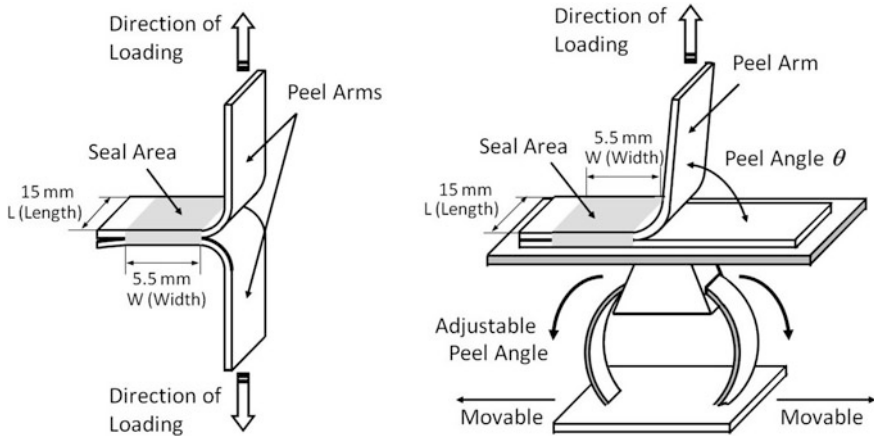


Fig. 19.5 Schematic of the T-peel test (*left image*) and of the fixed-arm peel test (*right image*)

100 mm/min. The clamping distance was 50 mm in case of the T-peel test and 25 mm in case of the fixed-arm peel test.

The variables energy release rate G_{Ic} and adhesive energy release rate G_{alc} were calculated following (1) and (2) (a more detailed version is described in [10]):

$$G_{Ic} = \frac{E_{tot}}{W \cdot L}, \quad (1)$$

Where E_{tot} —total energy input, W —width of the seal area and L —length of the seal area;

$$G_{alc} = \frac{E_{tot} - E_{d,P} - (l_B - l_{d,P} - W + W \cdot \cos \theta) \cdot F_{peel}}{W \cdot L}, \quad (2)$$

where $E_{d,P}$ —deformation energy of the peel arms, l_B —elongation at break, $l_{d,P}$ —actually start of the peel process, θ —peel angle and F_{peel} —peel force.

19.3 Results and Discussion

To characterise the peel behaviour of the investigated peel systems the practice oriented measured value peel force F_{peel} and the fracture mechanics variables energy release rate G_{Ic} and adhesive energy release rate G_{alc} were estimated.

At first, the influence of the content of the peel component on the peel behaviour was investigated. Figure 19.6 shows the dependence of the peel component on the peel force F_{peel} for the adhesive EVA/PE peel system (*left image*) and the cohesive PE/iPB-1 peel system (*right image*). For the adhesive peel system a constant level

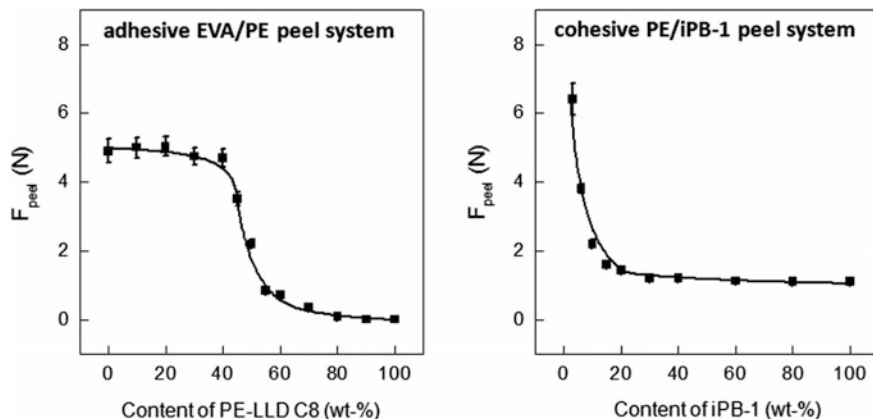


Fig. 19.6 Peel force F_{peel} in dependence on the content of PE-LLD C8 for the adhesive EVA/PE peel system (*left image*) and on the content of iPB-1 for the cohesive PE/iPB-1 peel system (*right image*)

of the peel force up to a content of the peel component of 40 wt% can be observed. Between 40 and 60 wt% PE-LLD C8 a distinct decrease of the peel force occurred. For PE-LLD C8 contents larger than 60 wt%, the peel force is again on a constantly low level. The connection of the adhesive peel system is due to the adhesive forces of the two sealing partners. The polarity of EVA supports the adhesion to PET. Unexpectedly, the adhesion between EVA and PET does not decrease with increasing content of PE-LLD following the “normal” rule of mixture. However, a top-down-behaviour of the peel force as a function of the peel component content was measured. In contrast to this, the peel force decreases continuously with increasing content of the peel component for the cohesive PE/iPB-1 peel system. In this case, the dependence of the peel force on the content of iPB-1 is of exponential character. For both peel systems, the established knowledge can be used to adjust the peel force according to customers wishes.

Furthermore, the peel tests reveal existence of deformation parts during the peel process. However, the measured value peel force does not consider these deformation parts. Thus, the peel behaviour in dependence on the content of the peel component for the adhesive and the cohesive peel system was evaluated using the fracture mechanics energy release rate. Figure 19.7 shows the dependence of the energy release rate G_{Ic} on the content of the peel component for the adhesive EVA/PE peel system (*left image*) and the cohesive PE/iPB-1 peel system (*right image*). In principle, the plots of the energy release rate (see Fig. 19.7) and of the peel force (see Fig. 19.6) in dependence on the content of the peel component are similar. However, the deformation parts during the peel process seem to be higher for the cohesive peel system in comparison to the adhesive peel system, especially for low contents of the peel component. This conclusion can be drawn, because the peel force data of Fig. 19.6 is nearly at the same level for the investigated adhesive and cohesive peel systems. In contrast to that, the energy release rate data of

Fig. 19.7 show larger values for the cohesive peel system (right image), especially for small contents of iPB-1. Thus, the higher values in comparison to the parallel investigated adhesive peel system must be due to larger deformations during the peel process. This finding could only be done using a fracture mechanics approach to characterise the peel behaviour of the peel systems.

From scientific point of view, the type of the connection between peel film and seal film is, among the mechanical and fracture mechanical analysis, of great interest. In case of the adhesive EVA/PE peel system, an adhesive connection between the EVA layer of the peel film and the PET seal film was expected. Among classical adhesive bonding like van der Waals forces and adhesion due to polarity, a mechanical connection probably due to molecular entanglement could be found (see Fig. 19.8). The enlarged detailed view of the transmission electron microscopic

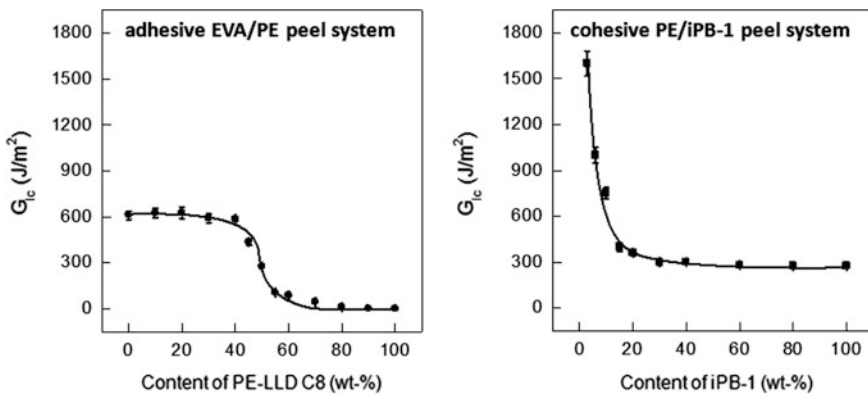


Fig. 19.7 Energy release rate G_{Ic} in dependence on the content of PE-LLD C8 for the adhesive EVA/PE peel system (*left image*) and on the content of iPB-1 for the cohesive PE/iPB-1 peel system (*right image*)

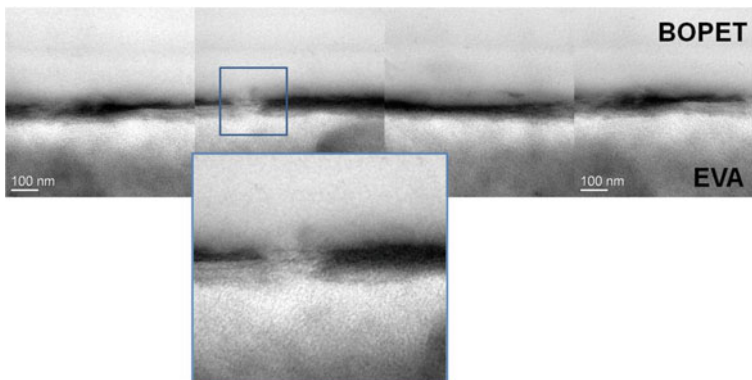


Fig. 19.8 TEM images of the seal area between BOPET and EVA of the adhesive EVA/PE peel system

(TEM) images reveals a so-called “cupping vessel structure”. Obviously, the molten EVA flows into vacancies of the PET during the sealing process. In case of the cohesive PE/iPB-1 peel system, there is a connection between the PE/iPB-1 layer of the peel film and the PE seal film due to interdiffusion of PE molecules at the border of the two films during the sealing process. The actual peel process occurs by zigzag crack growth through the seal area. The crack grows along the iPB-1 particles as revealed by Fig. 19.9. Because of the fact that the crack growth between the iPB-1 particles occurs through the PE matrix which, in turn, deforms/elongates, the crack growth course is of a zigzag shape and the already peeled seal area looks white.

In a second investigation step, the influence of the peel angle on the peel behaviour was analysed. For that reason the fracture mechanics adhesive energy release rate was calculated. The adhesive energy release rate considers only that energy part, which is actually responsible for the separation of the peel system. Thus, an independency of the adhesive energy release rate on the peel angle was expected.

The dependence of the adhesive energy release rate G_{alc} on the peel angle is shown in Fig. 19.10 for the adhesive peel system (left image) and the cohesive peel system (right image). In case of the adhesive peel system, the expected independence of the adhesive energy release rate on the peel angle was found. The average level of the adhesive energy release rate is at about 150 J/m^2 . In case of the cohesive peel system, also a constant level of the adhesive energy release rate can be observed up to 120° peel angle. However, the level of the adhesive energy release rate in this range is about 200 J/m^2 for the cohesive peel system. Thus, the energy which is necessary to separate the peel system is higher in case of the cohesive system compared with that one of the adhesive system. This difference can

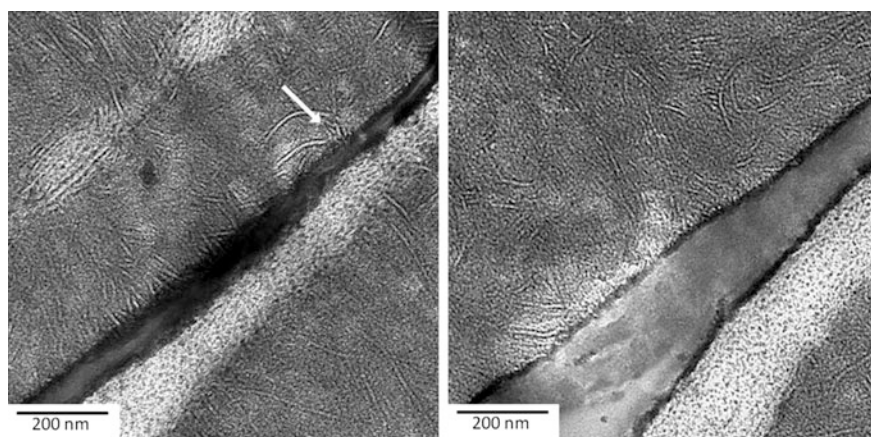


Fig. 19.9 TEM images of the peeled seal area of the PE-LD/iPB-1 peel system at an early progress of the peel process (*left image*; the beginning is marked by a *white arrow*) and a further progress of the peel process (*right image*)

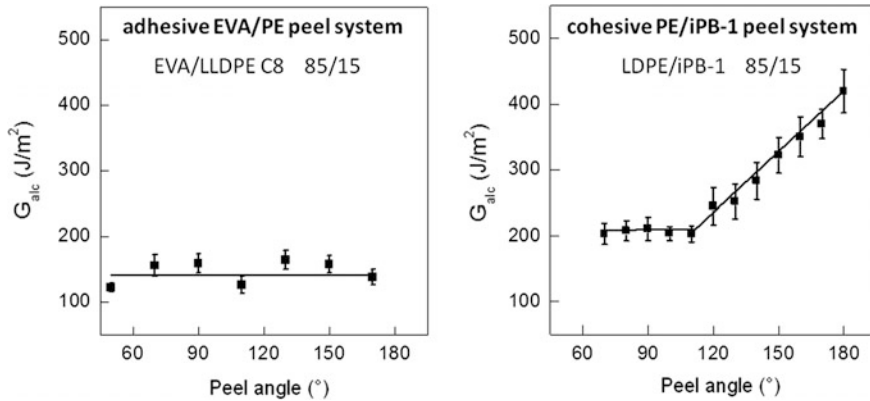


Fig. 19.10 Adhesive energy release rate G_{alc} in dependence on the peel angle for the adhesive EVA/PE peel system (*left image*) and for the cohesive PE/iPB-1 peel system (*right image*)

be addressed to the different connection types for cohesive and adhesive peel systems. For larger peel angles, the adhesive energy release rate shows an unexpected linear increase. Thus, there are two zones/areas:

- (1) G_{alc} is independent of the peel angle and
- (2) G_{alc} depends on the peel angle.

Zone (1) could be identified as “interlaminar”, i.e., the crack grows nearly along the centre of the seal area. Zone (2) could be identified as “translaminar”, i.e., the crack growth deviates from the centre of the seal area, the crack grows through the peel arm [7]. So, the adhesive energy release rate can be used to identify structural changes. It is a structure-sensitive fracture mechanics value.

Summarising the current research, it can be stated that fracture mechanics values like energy release rate G_{lc} and adhesive energy release rate G_{alc} can be used to get further and deeper structure-sensitive information of the investigated material system.

References

1. Hwo, C.C.: Polybutylene blends as easy open seal coats for flexible packaging and lidding. *J. Plast. Film Sheeting* **3**, 245–260 (1987)
2. Liebmann, A., Schreib, I., Schlözer, R.E., Majschak, J.P.: Practical case studies: Easy opening for consumer-friendly, peelable packaging. *J. Adhes. Sci. Technol.* **26**, 2437–2448 (2012)
3. Wool, R.P., Yuan, B.L., McGarel, O.J.: Welding of polymer interfaces. *Polym. Eng. Sci.* **29**, 1340–1367 (1989)
4. Stehling, F.C., Meka, P.: Heat sealing of semicrystalline polymer films. II. Effect of melting distribution on heat-sealing behaviour of polyolefins. *J. Appl. Polym. Sci.* **51**, 105–119 (1994)

5. Nase, M., Bach, S., Zankel, A., Majschak, J.-P., Grellmann, W.: Ultrasonic sealing versus heat conductive sealing of polyethylene/polybutene-1 peel films. *J. Appl. Polym. Sci.* **130**, 383–393 (2013)
6. Bach, S., Thürling, K., Majschak, J.-P.: Ultrasonic sealing of flexible packaging films—Principle and characteristics of an alternative sealing method. *Packag. Technol. Sci.* **25**, 233–248 (2012)
7. Nase, M., Zankel, A., Langer, B., Baumann, H.J., Grellmann, W., Poelt, P.: Investigation of the peel behaviour of polyethylene/polybutene-1 peel films using in-situ peel tests with environmental scanning electron microscopy. *Polymer* **49**, 5458–5466 (2008)
8. Nase, M., Langer, B., Grellmann, W.: Influence of processing conditions on the peel behavior of polyethylene/polybutene-1 peel systems. *J. Plast. Film Sheeting* **25**, 61–80 (2009)
9. Nase, M., Androsch, R., Langer, B., Baumann, H.J., Grellmann, W.: Effect of polymorphism of isotactic polybutene-1 on peel behaviour of polyethylene/polybutene-1 peel systems. *J. Appl. Polym. Sci.* **107**, 3111–3118 (2008)
10. Nase, M., Langer, B., Baumann, H.J., Grellmann, W.: Fracture mechanics on polyethylene/polybutene-1 peel films. *Polym. Test.* **27**, 1017–1025 (2008)
11. Mendoza-Navarro, L.E., Diaz-Diaz, A., Castañeda-Balderas, R., Hunkeler, S., Noret, R.: Interfacial failure in adhesive joints: experiments and predictions. *Int. J. Adhes. Adhes.* **44**, 36–47 (2013)
12. Santos, J.M., Ribeiro, M.R., Portela, M.F., Bordado, J.M.: Improved adhesion of polyethylene by copolymerization of ethylene with polar monomers. *Chem. Eng. Sci.* **56**, 4191–4196 (2001)
13. Nase, M., Großmann, L., Rennert, M., Langer, B., Grellmann, W.: Adhesive properties of heat sealed EVAc/PE films in dependence on recipe, processing and sealing parameters. *J. Adhes. Sci. Technol.* **28**, 1149–1166 (2013)
14. ASTM D 1876 (2015): Standard test method for peel resistance of adhesives (T-Peel test)
15. Moore, D.R., Williams, J.G.: Peel testing of flexible laminates. In: Moore, D.R., Pavan, A., Williams, J.G. (eds.) *Fracture Mechanics Testing Methods for Polymers Adhesives and Composites*,ESIS Publication 28. Elsevier, Amsterdam (2001), pp. 203–223

Chapter 20

Fracture Mechanics Characterisation of Low-Adhesive Stretch Films

M. Rennert, M. Nase, K. Reincke, R. Lach and W. Grellmann

Abstract Polymeric stretch films are wrapped around a packaging unit to keep it bundled and safe for transportation and storage. To maintain the generated retention forces and prevent a peel-off of the film, adhesive interactions between the film layers are required. Fracture mechanics investigations have been done in order to characterise the autohesive (cling) properties of the linear low density polyethylene/ α -olefin copolymer based stretch wrap films. Resistance against initiation and stable peel front propagation across the interface of the cold-welded peel films are supposed to indicate detailed adhesive interactions. Next to the energy release rate G_{IC} that considers all kind of deformations during the peel process, the adhesive energy release rate G_{aIC} was determined using the standard peel cling test for polymeric stretch films according to ASTM D 5458. As a function of the peeling angle, an independence of G_{aIC} between 10° and 90° could be observed for the investigated stretch films. The crack resistance curve concept was applied and crack initiation values could be determined next to stable crack propagation. The results might indicate multiple adhesive interactions due to the surface morphology and viscoelastic behaviour of the investigated films. In accordance to the calculated crack initiation, a physical crack initiation could be observed.

M. Rennert (✉) · M. Nase
University of Applied Sciences, Hof, Germany

M. Rennert
Polifilm Extrusion GmbH, Südliches Anhalt, Germany

K. Reincke · R. Lach · W. Grellmann
Polymer Service GmbH Merseburg, Merseburg, Germany

K. Reincke · W. Grellmann
Centre of Engineering, Martin Luther University Halle-Wittenberg, Halle/Saale, Germany

20.1 Introduction

Billion tons of goods, whether food or non-food products, are shipped around every year with an increasing tendency [1]. The majority of these unit loads are usually palletised and stabilised with polymeric stretch films, keeping the goods free of any damage and contamination during transportation and storage. Stretch films can be classified as primary packages, e.g. agricultural stretch films for silage bales (Fig. 20.1b) or as tertiary packages, e.g. stretch films for unit load stability (Fig. 20.1a). When transporting goods, the stretch film has to compensate forces arising from accelerations of 0.8 G in driving direction (brake manoeuvre and driveway) and transverse 0.5 G next to the vibration level, which makes it more than just a commodity product [1, 2].

Most of the today's used stretch films are high-technological thin co-extruded polyethylene (PE)-based multilayer film, blended with various largely branched polyolefin copolymer or low-molecular weight tacky additives that can migrate to the film surface. Basic requirements are

- sufficient mechanical properties,
- strain-independent adhesion,
- user-friendly application and low unwinding noise.

The most important polymer for stretch film applications is linear low-density polyethylene PE-LLD. The required mechanical properties mainly depend on type of monomer and comonomer, molecular weight, chain branching and morphology. The last one is highly depending on the extrusion parameters, since higher grades of crystallinity need to be avoided. The stretch film needs to be elongated up the range of strain hardening far below the elongation at break. Depending on recipe and process parameter the elongation can reach between 50% stretching (wrapping by hand) and 300% (automated stretch wrapping machines). The strain hardening causes the required high holding forces due to the immediate increase of the stress with each additional increase of the strain. The holding forces are necessary to keep the bundled good tight and avoid any kind of shifts or dissociation. Once applied,

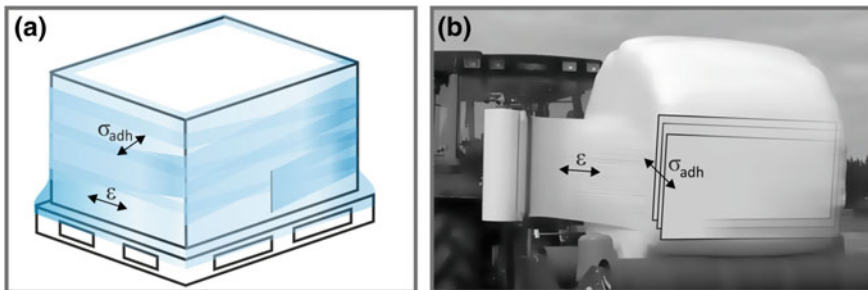


Fig. 20.1 Pre-stretched film applications for unit load stability as tertiary packaging (a) and for agriculture silage bale wrap (b)

the condition is supposed to keep stable over the whole duration of transport and storage. To avoid relaxation of the stored elastic energy fraction and to keep the holding forces the stretch film has to adhere to itself. This phenomenon of autoadhesion can be traced back to various adhesion mechanisms between the interlayer in the moment of wrap and the following interactions of both surface layers [3, 4]. Polymeric stretch films can be classified as low-adhesive peelable film systems. The bond strengths are much lower than e.g. for easy peelable films for food packages. Sealing and peel forces are mostly assessed by the $2 \times 90^\circ$ T-peel test according to the ASTM D 1876 and DIN 55529 [5, 6]. Common bond strengths for easy peelable film are between 2 and 5 N/75 mm², fixed sealed laminating films above 15 N/75 mm² [7]. Though it can be used to determine the adhesion between two stretch films, the registered forces are in the range of mN [8, 9]. Therefore, inhomogeneities and measurement uncertainties can adulterate the test result (Fig. 20.2).

To classify bonded systems it is very important to understand the underlying cohesive or adhesive mechanism or the crack initiation and propagation mechanism, respectively. Basically, cohesive peel systems are characterised by failure through or in the seal/peel arm, i.e. with residues on both peeled film surfaces. In adhesive peel systems the crack is running strictly among the surfaces of the interlayer. Cohesive-peelable systems are usually based on polyethylene (PE) matrices that can interdiffuse during heating and recrystallise. To reduce the resistance of crack propagation, the PE contains incompatible phases that can act as weak points to reduce the seal strength [10]. A very common system is low-density polyethylene blended with isotactic polybutene-1 (PE-LD/iPB-1). Adhesive-peelable systems are much more complex due to the diversity of adhesive interactions. For practical use, the cling performance of stretch films is usually characterised with the help of the cling force [11]. The cling force is the maximum force

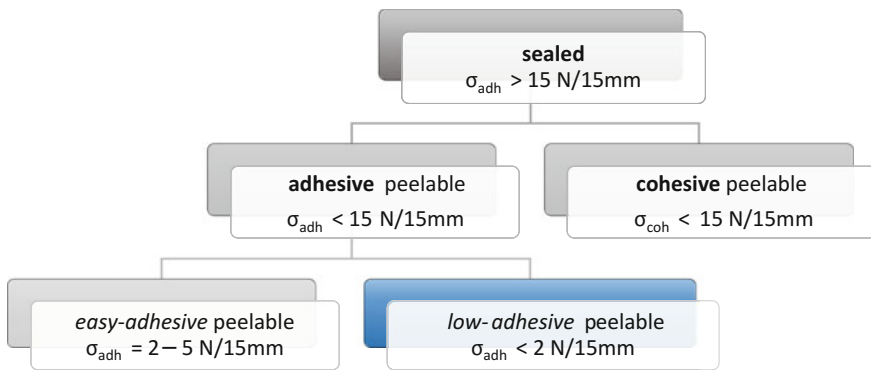


Fig. 20.2 Classification of bonded systems for packaging applications with the dimension of the seal/peel strength acc. to DIN 55529

that occurs during the peeling of both stretch films. The standard test method for peel cling of stretch wrap film, ASTM D 5458-95 as used in this study, is based on a peel angle (angle between peel arm and slope) of 20° and considers the pre-stretching of the films [12]. Thus lower angles cause higher cling forces due to shear deformation and the closer distance of both interacting films in the vicinity of the crack tip and therefore size of the zone of adhesive interactions. Assuming that the adhesive material behaviour occurs uniformly and isotropic across the peeled area, the peel angle and further testing parameters keep unchanged for the whole peel process according to e.g. ASTM D 1876, a peel force plateau appears after crack initiation. The average force level is called the peeled force. According to ASTM D 5458-95 the initial angle becomes more acute-angled and the cling force is continuously rising without reaching a plateau. Here the peel cling force equates to the force value at the cling line, where the peel process is stopped and which is mostly analogue to the maximum force. The cling force highly depends on the testing parameter, shape and size of the specimen and does not consider any kind of deformation that occurs during the peel cling process.

Fracture mechanics investigations can help to overcome these disadvantages and might give deeper insights into the behaviour on very small scales and help to quantify adhesive interactions. An approach is to extract the adhesive energy release rate that is free of any additional elastic–plastic deformation of the peeled film and bonded area or bending energy fraction [13]. Due to the residue-based peeling of adhesive film systems it might be assumed that the crack extension Δa is equal to the real peeled distance if deformations of the surface topography are negligible. Next to the energy balance study the fracture mechanic approach of the R-curve was applied to reveal the energy that is necessary to initiate and propagate the crack. Additionally, hysteresis curve with loading and reloading around the crack initiation have been done to examine a physical crack initiation and the associated energy release rate.

20.2 Experimental

20.2.1 *Material and Composition of the Films*

The polymeric stretch films that have been used for this study were produced on a Cast extrusion lab machine by Dr. Collin GmbH with a four layer ABCD feed block (schematically shown in Fig. 20.3). For both core and the outer skin layer 100% PE-LLD (ExxonMobil 1004 YB) was used. The inner skin layer represented the cling-modified layer. The matrix of the inner skin layer was PE-LLD (ExxonMobil LL 1004 VB). It was blended with two types of PE-LLD α -olefin copolymer with comonomers of 1-butene and 1-hexene and one polypropylene-based thermoplastic elastomer with comonomers of ethylene. An overview of all materials used in this study can be taken from Table 20.1.

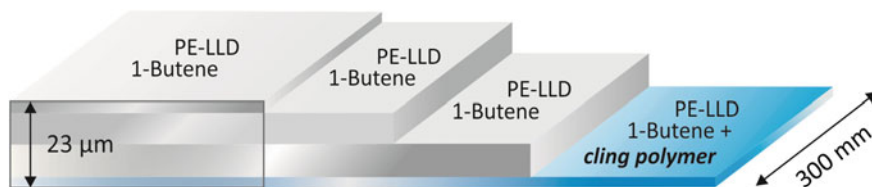


Fig. 20.3 Coextruded 4-layer film structure with cling component in skin layer

Table 20.1 List of the used matrix PE-LLD and cling material

Polymer	Trade name	Comonomer	Melt flow index (g/10 min)	Density (g/cm ³)
1 PE-LLD	ExxonMobil™ 1004 YB	1-butene	2.8	0.918
2 PE-LLD	DOW ATTANE™ 4607GC	1-hexene	4.0	0.904
3 PE-LLD	Versalis Clearflex® CL D0	1-hutene	3.0	0.900
4 SEBS	Kraton® MD 6700 GO	ethylen	4.9	0.900
5 TPE	ExxonMobil™ Vistamaxx 6202	ethylen	7.4	0.861

The core layer(s) is/are responsible for the required mechanical properties like adequate tensile strength in machine (MD) with less shrinkage in cross direction. The matrix PE-LLD ExxonMobil™ LL 1004 YB has a tensile strength of 50 MPa in MD and an elongation at break of 530% (based on a 21 μm single-layer cast extruded film). The thickness of each core layer was 9 μm. The skin layer thicknesses were 2.5 μm. The screw speed of the B and C extruder was 93 min⁻¹, extruder A and C (skin layer) was 25 min⁻¹. The temperature of the die was 230 °C. The chill roll had a draw down ratio of 25 m/min and was cooled to 20 °C. The outer skin layer was extruded directly on the chill roll and blended at the following ratio of ExxonMobil™ 1004 YB/cling additive (in wt%/wt%):

- DOW ATTANE™ 4607GC: 20/80
- Versalis Clearflex® CL D0: 80/20
- ExxonMobil™ Vistamaxx 6202: 93/7

20.2.2 Cling Test According to ASTM D 5458

The fracture mechanics investigations have been done by using the “Standard test method for peel cling of stretch wrap film” according to ASTM D 5458-95 (2007). Figure 20.4a shows schematically the construction of the instrumented peel cling

test. The base plate can be connected to each universal tensile testing machine. For this study a Zwicky Z2.5 by Zwick GmbH & Co. KG with the analysing software testXpertII V3.5 was used. Via the pulley the tie bar was connected to a 50 N load cell. The 20° slope was covered with a 5 × 7 inch² film sheet in machine direction (MD) with the back (non-cling side) to the top and wrinkle-free fixed with the help of a knob and a clamp. 1 × 5 inch² wide specimens were cut of the roll in machine direction and fixed with brush and constant pressure of 0.5 Pa in the centre of the covered slope in MD with the cling site to the bottom without air pockets and wrinkles. Behind the cling line and in front of the crack tip a non-adhesive paper was fixed to finish the peel process automatically and to avoid energy dissipation. The size of peel area was 1 × 2 inch², which deviates from the standard and made it possible to allocate the crack extension at each point of time. The tail of the specimen was connected to the tie bar and preloaded with $F_0 = 0.02$ N. The testing speed of the traverse was 100 mm/min. The schematic load–displacement curve can be seen in Fig. 20.4b. The shape of the curve can be divided into three segments. After the crack initiation a progressive run of the curve has been observed. Most of the peel process is dominated by a linear increase of the load or cling force, respectively. At the end of the peel process at declining run of the curve could be observed. The maximum force (point II in Fig. 20.4) represents the cling force F_{cling} . For each investigation ten specimens have been used [14].

To characterise the cling behaviour the total energy input E_G was calculated according to

$$E_G = \int F dL. \quad (1)$$

The energy release rate G_{IC} and the adhesive energy release rate G_{alC} have been calculated using the following equations

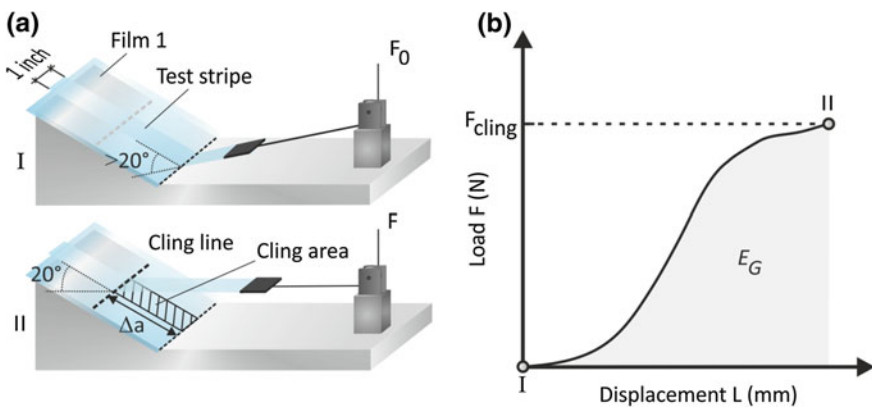


Fig. 20.4 Schematic testing procedure of cling peel test according to ASTM D 5458 (a) with measured load–displacement curve (b)

$$G_{IC} = \frac{E_G}{a \cdot B} \quad \text{and} \quad (2)$$

$$G_{alC} = \frac{E_G - E_{d,p} - (l_b - l_{d,p} - B - B \cdot \cos \theta) \cdot F_{cling}}{a \cdot B}, \quad (3)$$

where E_G —total energy input, a —length of the peeled area, B —width of the peeled area, $E_{d,p}$ —deformation energy of the peel arm, l_b —elongation at break, $l_{d,p}$ —actually start of the peel process, θ —peel angle and F_{cling} —cling force.

To investigate the influence of the peel angle on the adhesive energy release rate, the cling test according to ASTM D 5458 was modified using different acute angles $\theta = 0^\circ, 10^\circ, 45^\circ$ and 90° (Fig. 20.5a). It has been observed that the closer the angle comes to 90° the more distinctive is the required peel plateau, but the less load and therefore total energy is necessary to peel-off the cling film (Fig. 20.5b, c). Figure 20.5c shows the total energy E_G as a function of the peeled angle for different contents of the cling additive styrene–ethylene–butylene–styrene copolymer (SEBS) as thermoplastic elastomer (TPE).

Additionally, the R-curve concept was applied to investigate its practicality and to assess the fracture (peeling) process, i.e. the crack initiation values and crack resistance curves characterising the crack propagating behaviour [14]. The fracture

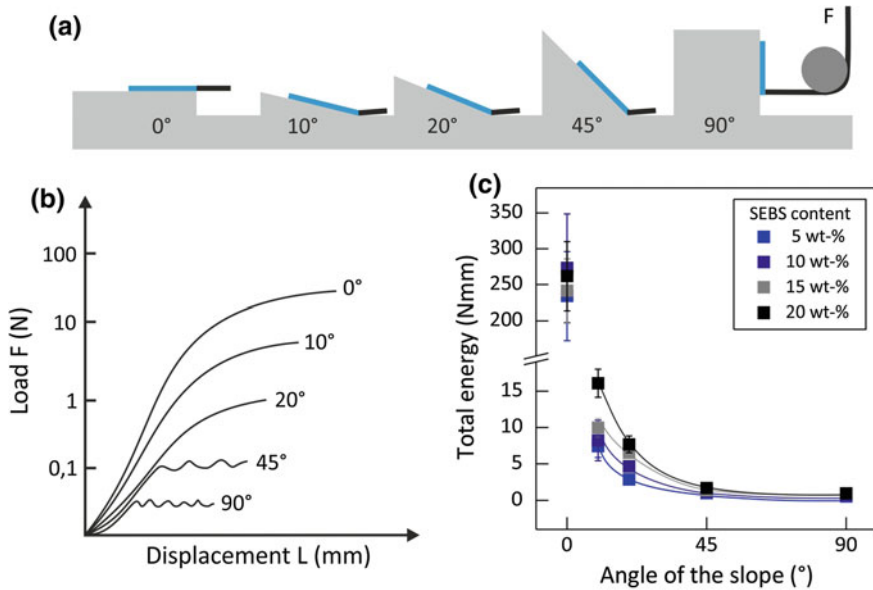


Fig. 20.5 Modified cling test according ASTM D 5854 with different acute peel angles (a) and corresponding load–displacement curves (b) and the relationship of total energy and angle of the slope for different mass fractions of SEBS cling component (c)

mechanics approach of the R-curve is part of the elastic–plastic fracture mechanics and represents the functional correlation between fracture toughness parameters (e.g. J or G) and stable crack growth Δa . The shape of the R-curve describes characteristic fracture behaviour. A rising R-curve describes stable crack propagation where an increasing driving (external) force is necessary to maintain the crack growth [15].

For this study the single-specimen method was applied, i.e. each R-curve represents one specimen or peel process, respectively. The peel process with the force–displacement measurement was recorded in situ by a high-speed camera with 1000 images/s (Fig. 20.6). Via indicator scale the truth Δa could be calculated afterwards.

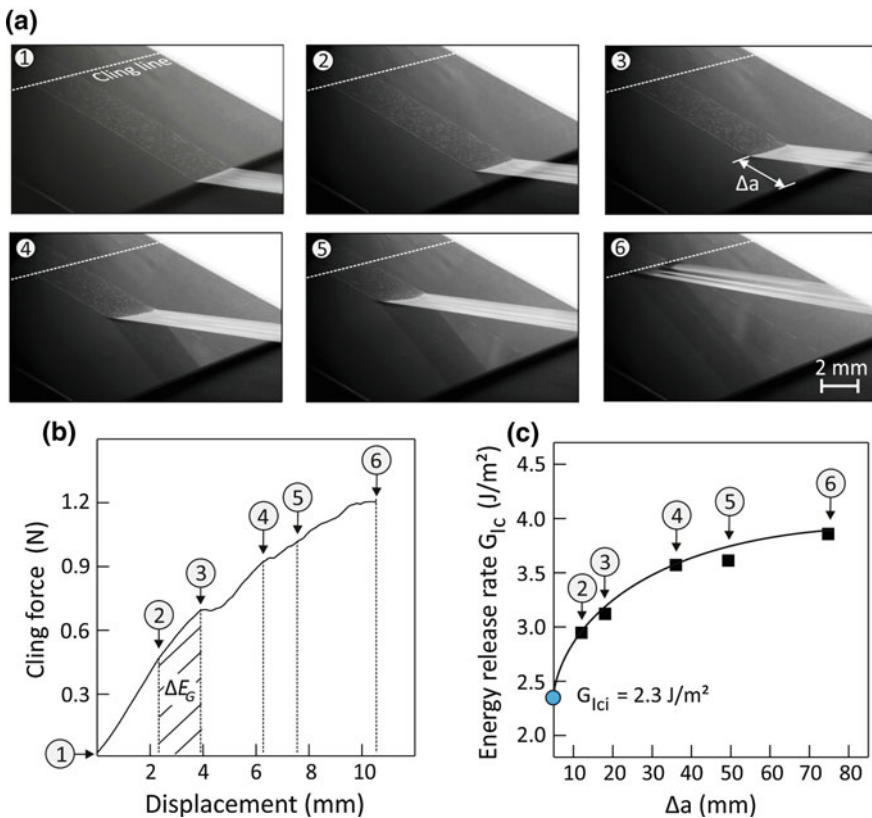


Fig. 20.6 Peel cling test according to ASTM D 5458 with crack extension Δa (a), the recorded cling force–displacement curve with the dedicated points of the pictures (b) and the resulting R-curve (c)

The energy release rate G_{IC} as a function of the crack extension Δa was calculated according to

$$G_{IC} = \frac{\Delta E_G}{\Delta a \cdot B} = f(a) \quad \text{with} \quad (4)$$

$$\Delta a = a_2 - a_1. \quad (5)$$

Additionally, the derivative of the crack extension Δa with respect to the peeling time, i.e. the crack speed \dot{a} , which can be used as an indication of the crack propagation kinetics is described by the following relation:

$$\dot{a} \sim \frac{dG_{IC}}{d\Delta a}. \quad (6)$$

Furthermore, the hysteresis of cling force–displacement curves with loading and reloading was investigated. Starting from a preloading of 0.01 N, the load within each loading cycle was stepwise increased by 0.03 N. Again a high-speed camera was used to detect crack propagation.

20.3 Results and Discussion

To characterise the cling behaviour of the investigated stretch films the fracture mechanics parameters energy release rate G_{IC} that comprises any energy dissipation of the peel process and the adhesive energy release rate G_{alC} have been identified next to common a cling force F_{cling} used in practise. At first, the influence of the peel angle was investigated.

Figure 20.7 shows the fracture mechanics parameters G_{IC} and G_{alC} , respectively, as a function of the slope or peel angle θ . The energy release rate G_{IC} showed an exponential decrease until approximately 45° to smaller values at larger angles. The higher values for small angles can be explained with the existence of additional energy dissipation during the peel process. Especially elastic–plastic deformations of the free peel arm due to the low cross section and therefore low mechanical strength as well as shearing within the cling area could be observed. Ethene/propene copolymer-based stretch films showed higher values for G_{IC} than the 1-hexene copolymer-based stretch films which corresponds to cling forces double of that what have been measured (see also Table 20.2). The higher standard deviation at low angles might be explained with partial inhomogeneous peeling of the film caused by slight measurement uncertainties on small scales. Due to higher deformations at lower angles the plane stress and plane strain conditions near the crack tip might change due to a slight necking of the free peel arm. Image N° 5 in Fig. 20.6 already indicates a slight curvature of the peel front with decreasing angle.

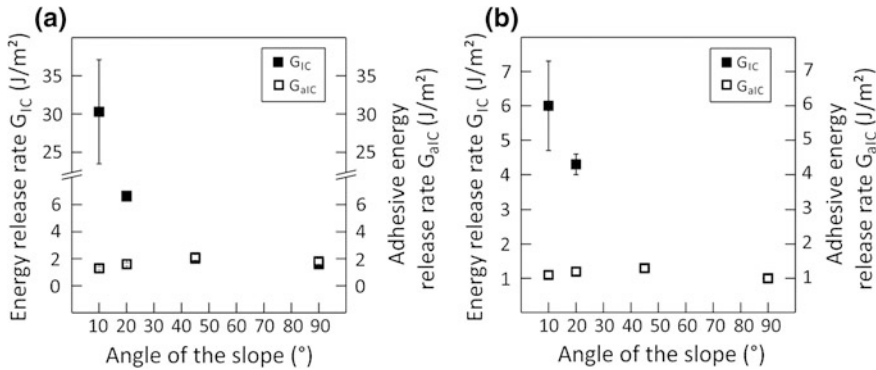


Fig. 20.7 Influence of the peel angle θ on the energy release rate G_{IC} and adhesive energy release rate G_{alC} for the ethene/propene copolymer modified cling layer (a) and the PE-LLD with 1-hexene comonomer as cling additive (b)

Table 20.2 Overview of cling force values F_{cling} and fracture mechanics parameters G_{IC} , G_{alC} , G_{ICi} and \dot{a} for the different cling additives according to ASTM D 5458 with a slope of 20°

Cling polymer	F_{cling} (N)	G_{IC} (J/m ²)	G_{ICi} (J/m ²)	G_{alC} (J/m ²)	\dot{a} (-)
Ethene/propene	2.1 ± 0.10	5.0	3.5	1.9	13.95
1-butene	0.9 ± 0.05	3.0	1.8	–	18.30
1-hexene	1.1 ± 0.05	2.8	1.7	1.2	18.50

For the adhesive energy release rate according to (3) an independence of the peeling angle between 10° and 90° was found. Angles less than 10° are hard to realise since the uncertainties described above increased drastically. For angles with $\theta > 90^\circ$ too weak signals were detected. For any further investigations in the field of very low-adhesive systems the measurement uncertainties need to be avoided. Nevertheless, it might be concluded that within the range of investigated angles the delamination or peeling occurs homogeneous and just depends on the adhesion level. The average level is approximately 1.9 J/m² for the ethene/propene copolymer and 1.2 J/m² for the 1-hexene copolymer and therefore 100 times lower than that of investigated cohesive peel films for packaging applications, where an independence of the peel angle could be observed until 120° [10]. The difference in the absolute value of the G_{alC} might help to provide deeper insight into how adhesive mechanisms are acting, which could result in quantification of adhesive processes.

Figures 20.8 and 20.9 show the calculated R-curves of the investigated cling systems. At first reproducibility was investigated due to the single-specimen method and the mentioned measurement uncertainties. A good correlation between the G_{IC} and the crack extension (Fig. 20.8b) could be found as well as a reliable reproducibility (Fig. 20.9a). The shape of the R-curve is raising and gets flat at the end of the peel process. This underlines the fact that an increasing external force is

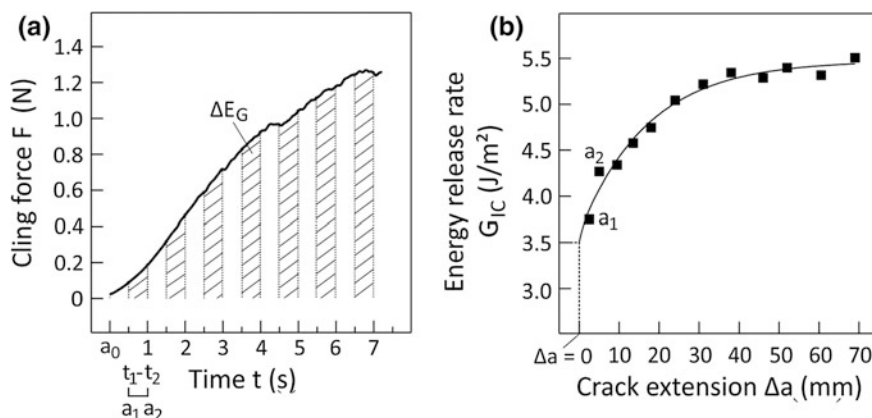


Fig. 20.8 Cling force as a function of time (a) and the resulting R-curve for the ethene/propene copolymer-based stretch film (b)

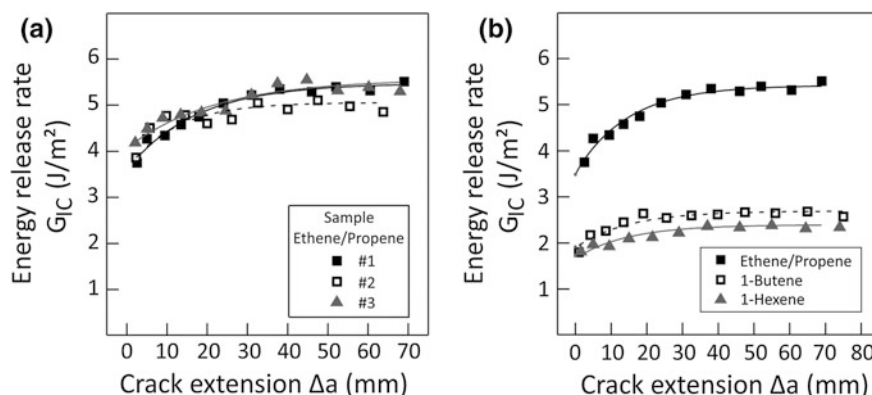


Fig. 20.9 Results of single-specimen fracture mechanics test (R-curves) for three samples (a) and a comparison of the R-curves for ethene/propene copolymer, 1-butene and 1-hexene copolymer-based stretch films (b)

necessary to maintain the crack growth. If the fitting curve is extended to the y-axis that is equal to a crack extension $\Delta a = 0$, the point of intersection indicates an initial energy release rate G_{ICi} , i.e. the energy value that is necessary to initiate the crack and start crack propagation. Figure 20.8b shows a comparison of R-curves acc. to the single-specimen method for ethene/propene, 1-butene and 1-hexene copolymer-based stretch films. The ethene/propene copolymer shows the highest value of G_{ICi} and also the strongest R-curve slope of all three copolymers (Fig. 20.9b). This indicates the highest resistance against crack initiation and propagation which is in accordance with the values of cling force. The 1-butene-based cling component showed slightly higher values of G_{ICi} than the

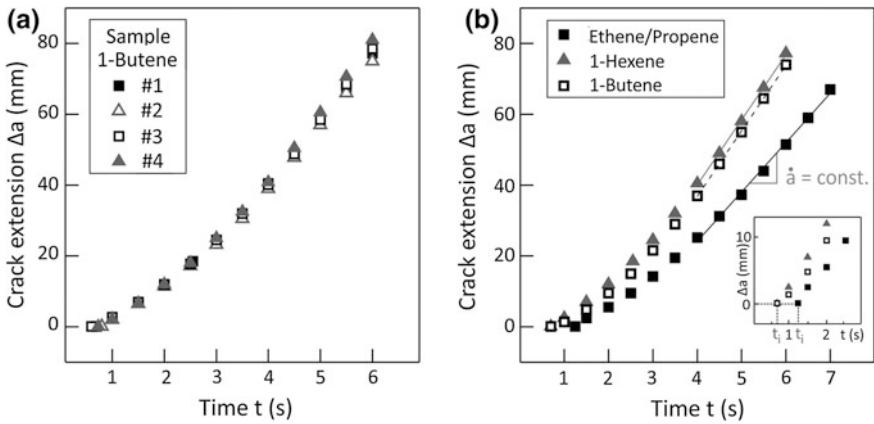


Fig. 20.10 Crack extension Δa as a function of peeling time for four samples in the one-specimen method (a) and with \dot{a} that characterises the crack propagation kinetics for all three cling additives (b)

1-hexene copolymer, which is not in accordance to the pure cling force measurement that is slightly higher for the 1-hexene copolymer. The R-curve slope and therefore the stable crack growth behaviour of both systems are approximately in the same range. The reason for that might be additional deformation portions during the peel process.

Figure 20.10 shows the crack extension as a function of the peel time. The slope \dot{a} of the linear function is a measure of the crack propagation kinetics (Fig. 20.10b and Table 20.2) and is proportional to $dG/d\Delta a$ [see (6)]. The parameter t_i is the time indicating the point of physical crack initiation and again a few ms larger for the ethene/propene copolymer than for both α -olefine copolymers.

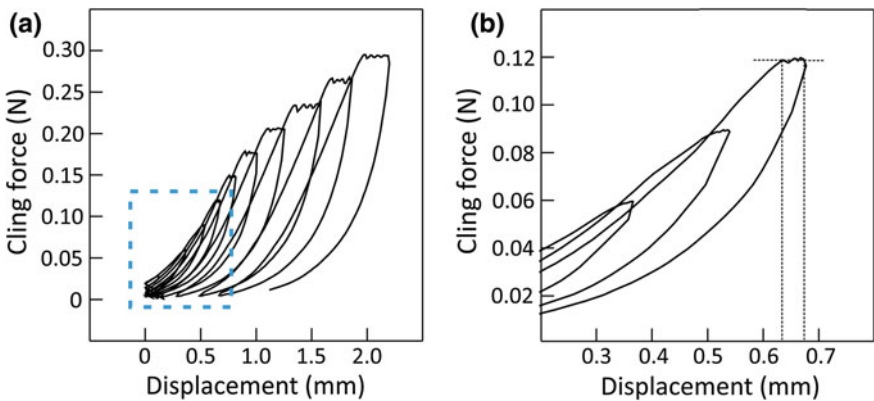


Fig. 20.11 Hysteresis of cling force–displacement curves of 10 loading cycles for the ethene/propene copolymer-based stretch film

A cyclic loading of the ethene/propene copolymer-based stretch film have been done to indicate the point of physical crack initiation. Therefore the high-speed camera was used to monitor the front of the crack tip. After 10 loading cycles the hysteresis was analysed and the high resolution of the load cell indicated a slight peel plateau from the 3rd loading cycle which was in common with a monitored crack opening at the crack tip. The calculated physical energy release was 2.6 J/m^2 , which is in accordance with the calculated G_{ICi} from the R-curve of ethene/propene copolymers (Fig. 20.11).

20.4 Conclusion

Fracture mechanics investigations have been done for low-adhesive polymer film systems in order to characterise the autoadhesive properties (cling) of stretch films or energy that is necessary to separate two bonded films, respectively. Next to the energy release rate G_{IC} that considers all kind of deformations during the peel process, the adhesive energy release rate G_{aIC} was determined using the standard peel cling test for polymeric stretch films according to ASTM D 5458. As a function of the peeling angle an independence of G_{aIC} between 10° and 90° could be observed for the investigated stretch films. The R-curve concept was applied and crack initiation values could be determined next to stable crack propagation. In accordance to the calculated crack initiation a physical crack initiation could be observed.

References

1. Wainer, M.V.: Stretch film properties—Effects of equipment and process variables. *J. Plast. Film Sheeting* **18**, 279–286 (2002)
2. Jarimopas, B., Singh, S.P., Saengnil, W.: Measurement and analysis of truck transport vibration levels and damage to packaged tangerines during transit. *Packag. Technol. Sci.* **18**, 179–188 (2005)
3. Bazskin, A., Ter-Minassian-Saraga, L.: Effect of surface polarity on self-adhesion of polymers. *Polymer* **19**, 1083–1088 (1978)
4. Del Rio, F.W., de Boer, M.P., Knapp, J.A., Reedy, D., Clews, P.J., Dunn, M.L.: The role of van der Waals forces in adhesion of micromachined surfaces. *Nat. Mater.* **4**, 629–634 (2005)
5. ASTM D 1876 (2015): Standard test method for peel resistance of adhesives (T-Peel test)
6. DIN 55529 (2012): Verpackung—Bestimmung der Siegelnahtfestigkeit von Siegelungen aus flexiblen Packstoffen
7. Dickmann, R.: Verpacken—Heißsiegelnähte—Untersuchung und Optimierung. *LVT Lebensmittel Industrie* ed. **5**(6), 54–55 (2004)
8. McNally, G.M., Small, C.M., Murphy, W.R., Garrett, G.: The effect of polymer properties on the mechanical behavior and morphological characteristics of cast polyethylene film for stretch and cling film applications. *J. Plast. Film Sheeting* **21**, 39–54 (2005)

9. Small, C.M., McNally, G.M., Marks, A., Murphy, W.R.: The effect of extrusion processing conditions and polyisobutylene concentration on the properties of polyethylene for stretch and cling film applications. *J. Plast. Film Sheeting* **18**, 245–258 (2002)
10. Nase, M., Zankel, A., Langer, B., Baumann, B., Grellmann, W., Poelt, P.: Investigation of the peel behavior of polyethylene/polybutene-1 peel films using in situ peel tests with environmental scanning electron microscopy. *Polymer* **49**, 5458–5466 (2008)
11. Rennert, M., Fiedler, S., Nase, M., Menzel, M., Günther, S., Kressler, J., Grellmann, W.: Investigation of the migration behavior of polyisobutylene with various molecular weights in ethylene/ α -olefin copolymer blown stretch films for improved cling properties. *J. Appl. Polym. Sci.* **131**, 4861–4874 (2014)
12. ASTM D 5458 (2012): Standard test method for peel cling of stretch wrap film
13. Kinloch, A.J., Lau, C.C., Williams, J.G.: The peeling of flexible laminates. *Int. J. Fract.* **66**, 45–70 (1994)
14. Grellmann, W., Bierögel, C., Reincke, K. (eds.) *Lexikon der Kunststoffprüfung und Diagnostik*. Merseburg (2015). see: <http://wiki.polymerservice-merseburg.de>
15. Anderson, T.L.: *Fracture Mechanics: Fundamentals and Applications*, 3rd edn. CRC Press, Boca Raton (2005)

Chapter 21

Thermal Stability and Lifetime Prediction of an Epoxide Adhesive System

R. Tiefenthaller, R. Fluch, B. Strauß and S. Hild

Abstract Epoxide systems, with diglycidyl ether of bisphenol A as the most popular representative, are known for their outstanding thermal stability. Nevertheless, lifetime predictions are indispensable for many applications. Therefore, the change of mechanical properties of an epoxide adhesive system was analysed. The observed embrittlement of the system could be explained and shown by chemical degradation reactions. To determine the long-term stability accelerated testing methods had to be applied: Steel panels were bonded with a thin layer of the adhesive system and aged at elevated temperatures. Lifetime predictions were based on the adhesive strength, which can be evaluated by different methods like peeling or shearing tests. The lifetime was strongly depending on the chosen parameter for the adhesive strength. However, if only the time at the high temperature was calculated, cyclic thermal loads came to the same results as constant high temperature regimes.

21.1 Introduction

Due to their remarkable properties epoxy resins are found today in many different fields of application. Industries for adhesives, coatings or electronics make use of these thermosetting materials [1–4]. They are commonly applied as matrices in polymer composites as well [2, 5–7]. Epoxide systems show outstanding adherence to a variety of substrates and have a good chemical and radiochemical resistance as well as a low degree of shrinkage at curing. Their excellent insulating properties in combination with a good thermal stability are beneficial for electrical applications. Still every application has its own requirements concerning processing or special properties in end-use. Since one system cannot fit all demands, there exists a range of different epoxy-based formulations. The mechanical properties can be tailored by

R. Tiefenthaller (✉) · S. Hild
Institute of Polymer Science, Johannes Kepler University Linz, Linz, Austria

R. Tiefenthaller · R. Fluch · B. Strauß
voestalpine Stahl GmbH, Linz, Austria

varying resin and hardener composition. These parameters can influence crosslinking kinetics as well [1–4, 8–11]. As binder diglycidyl ether of bisphenol-A (DGEBA) has gained greatest importance due to its low cost, easy processability and good stability caused by its aromatic structure [5, 12, 13]. In combination with dicyandiamide (DICY), which is an amine hardener with high latency, 1-K adhesive systems can be formulated [14, 15].

Although there is no doubt about the good thermal stability of epoxy systems compared to many other polymers, for many applications it is essential to determine the long-term stability of the material at increased temperatures. Testing at service temperatures (typically below 180 °C), however, is very time consuming; hence there is a need for accelerated testing methods which can estimate the lifetime of a material. Maybe the simplest approach for accelerated testing is an increase in ageing temperature, which is only applicable, if degradation mechanisms do not change while raising the temperature. Therefore, it is necessary to get a deeper insight into degradation mechanisms. A lot of research has already been done in the last years trying to understand the degradation of DGEBA-based systems [3, 4, 8, 15–20]. Spectroscopic techniques like infrared (IR) and Raman spectroscopy are capable of measuring the degradation on a molecular level. Thermogravimetric analysis (TGA) can register changes of the thermal stability of the polymer over ageing time. Finally, thermomechanical analysis (TMA) helps to better understand changes in the network structure upon ageing. With the help of this method some authors [3, 4] observed the formation of a second glass transition at lower temperatures emerging with increasing ageing time; others [21, 22] noticed a decrease of the glass transition temperature (T_g), which they interpreted in terms of bond scissions. A third possible phenomenon is characterised by an increase in T_g , which is often related to post-cure reactions [8, 13, 17].

Beyond the valuable information about possible degradation mechanisms and products, still the durability of the adhesive joint in its application is often questioned. To determine the lifetime of a material or compound ageing experiments are an opportunity. They are usually based on observations of a selected mechanical property such as impact strength, weight, adhesion, tensile strength or elongation over time. Since ageing experiments under real conditions may be very time consuming, in many cases accelerated testing procedures are necessary. One possibility for acceleration is to increase the temperature. In this approach the performance of the material over time is monitored at several temperatures. From the obtained degradation trends a quantitative relationship between temperature and selected property can be established applying an Arrhenius approach [21]. Since the result of the lifetime estimation is strongly depending on the evaluated property, it should be chosen carefully. Considering tests on the adhesive strength, the T-peel test is a very harsh test, which is very sensitive to typical ageing phenomena like embrittlement. On the contrary, the tensile lap-shear test is rather mild and registers changes in the system by far later. Completely different lifetimes for the same material will therefore be obtained, depending on the testing parameter chosen. For a comparison with service life, one has to take care that the selected testing parameter is indicative of the stress in real applications.

The aim of this study was to evaluate the stability of bonded steel adhered with less than 10 μm of an epoxide adhesive. For this purpose the chemical degradation and mechanical changing of the adhesive in combination with the durability of the composite material should be examined.

21.2 Materials and Methods

21.2.1 *Material and Samples*

The investigated adhesive system was based on a DGEBA resin and DICY as a hardener. For spectroscopic techniques, mechanical and gravimetric analysis free films of about 20 μm thickness were prepared by coating the adhesive on a Teflon foil. The adhesive films were cured for 30 min at 200 $^{\circ}\text{C}$. Thermal ageing of the adhesive films was realised with a drying cabinet, run at 200 $^{\circ}\text{C}$. Samples were taken out of the oven in irregular intervals and analysed.

For lifetime predictions the T-peel test and the tensile lap-shear test were chosen. Samples for tests on the adhesive strength were prepared by coating carbon steel with a smooth surface (arithmetic mean roughness $R_a < 0.4 \mu\text{m}$, offset yield point $R_{p0.2} = 275 \text{ MPa}$, ultimate tensile strength $R_m = 432 \text{ MPa}$, thickness = 0.5 mm) with 5 μm of the adhesive. For the T-peel test the coated steel sheets were cut into pieces of $25 \times 200 \text{ mm}^2$, two strips were stacked in a way that the coated sides faced each other and were then adhered under a pressure of 1 MPa for 2 h at 200 $^{\circ}\text{C}$. For the tensile lap-shear test the coated steel sheets were cut into $25 \times 100 \text{ mm}^2$ strips. On each strip a support plate of $25 \times 90 \text{ mm}^2$ was fixed so that the free ends of two samples could be adhered with an overlap area of 250 mm^2 . Curing conditions were the same as for the T-peel samples. The consecutive ageing experiments were performed in a drying cabinet at different temperatures (180, 190, 200, 220, 230, 250 $^{\circ}\text{C}$). Samples were taken out of the oven in irregular intervals depending on the ageing temperature.

21.2.2 *Spectroscopic Techniques and Mechanical Analyses*

Dynamic-thermomechanical analysis (DTMA) was performed on a Q400EM (TA Instruments). The glass transition temperature was determined in penetration as well as in tensile mode. For both modes a heating rate of 5 $^{\circ}\text{C}/\text{min}$ was chosen and an initial force of 0.02 N was modulated to 0.01 N at 0.10 Hz. T_g -values were determined as onset-values in the penetration mode and as maximum values of the tan δ -peak in the tensile mode. For infrared spectroscopy the ATR technique was used and was performed with a Bruker, Tensor 27. Raman spectroscopy was carried out with a Horiba Jobin Yvon spectroscope (Labram 010, Horiba Scientific),

equipped with a HeNe laser (633 nm). STA 409 PC Luxx from Netzsch was used for thermogravimetric analysis. All samples were measured in dynamic mode with a heating rate of 5 °C/min under nitrogen.

21.2.3 T-Peel Test and Tensile Lap-Shear Test

Tests on the adhesive strength were carried out in ambient conditions. Each sample consisted of 5 replicate specimens. For the T-peel test the initial 5 cm of the adhered sample were opened mechanically to form a T before testing the adhesive strength according to ISO 11339 [23] on a Zwick Roell Z020 testing machine. Samples for the tensile lap-shear test could be taken without further preparation and the tensile lap-shear strength was measured according to DIN EN 1465 [24] on the same device.

21.3 Results and Discussion

21.3.1 Thermomechanical Analysis

The tensile mode of DTMA was only applicable to films aged less than 170 h at 200 °C, because films became too brittle beyond these conditions. The evaluation of the glass transition revealed a constant increase of T_g with ageing time, starting at 100 °C with the non-aged, cured film and ending at 220 °C after ageing for 170 h at 200 °C (Fig. 21.1). As the embrittlement of the films does not limit the measurability in penetration mode, the trend of a T_g increase could be followed until

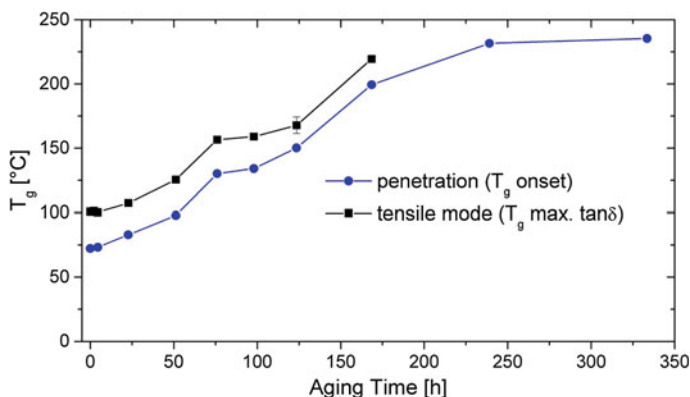


Fig. 21.1 T_g -evolution of free-standing adhesive films with increasing ageing time at 200 °C under atmospheric conditions in two DTMA testing modes

330 h of ageing. Since the determination of T_g is different, T_g onset values found for measurements in the penetration mode are about 25 °C lower than those evaluated in extension mode, where the maximum of $\tan \delta$ was evaluated. To an extent of about 15 °C the difference can be attributed to the fact that the maximum $\tan \delta$ values are characteristic of the midpoint of the glass transition, while the onset values are the starting of the transition to the rubber-like state. The remaining 10 °C difference can be explained by the different measurement modes. Measurements in penetration mode showed the same trend as those in extension mode. However, after longer ageing times of more than 200 h, the increase of T_g seems to slow down. Post-cure reactions are often named to be responsible for an increase in T_g during ageing [3, 4, 8]. Generally, it is explained by an immobilisation of the network segments and can be correlated to the network density [10–12]. Degradation processes associated with post-cure reactions are expected to produce a denser network with higher rigidity by e.g. eliminating freely rotatable elements.

21.3.2 ATR-IR Spectroscopy

The degradation process of the aged adhesive films was followed by IR spectroscopy. Several spectra obtained are displayed in Fig. 21.2. While spectra aged for less than 100 h had a good signal-to-noise ratio, in spectra aged for more than 150 h a growing background noise level was observed, which made quantification more difficult.

After attribution of the registered bands, as listed in Table 21.1, the course of the intensities over ageing time was normalised. This showed that all bands characteristic of the same functional group followed the same trend. For each functional

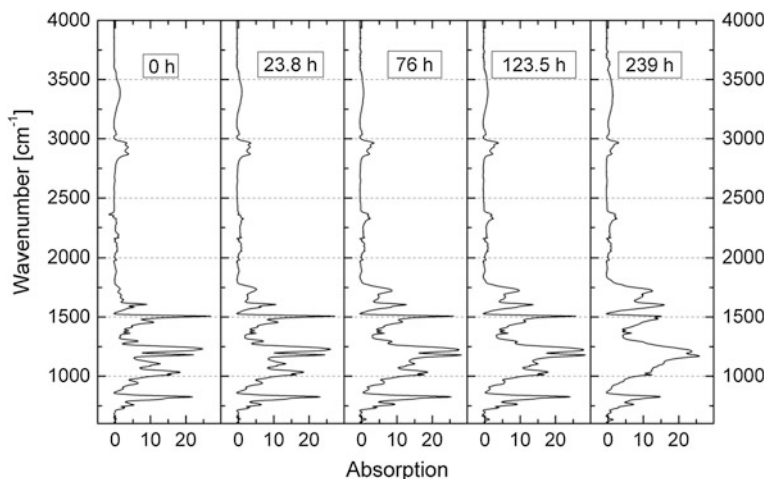


Fig. 21.2 IR spectra of adhesive films aged at 200 °C for different times

Table 21.1 Attribution of IR bands

Carbonyl (C=O), double bonds		
1725	$\nu(\text{C}=\text{O})$ in aldehyde, ketone, acid	[3, 4, 20]
1650–1700	$\nu(\text{C}=\text{C})$	
1650	$\nu(\text{C}=\text{O})$ in amide	[3, 4, 8, 9, 18, 25]
Ether (C–O)		
1231	$\nu_{\text{as}}(\text{C}-\text{O}-\varphi)$	[3, 18, 19]
1086	$\nu_{\text{s}}(\text{C}-\text{O}-\varphi)$	[3]
1034	$\nu_{\text{s}}(\text{C}-\text{O}-\text{C})$	[1, 2, 15, 18, 20]
1011	$\nu(\text{C}-\text{O}-\text{C})$	[20]
Methylene (CH₂)		
2929	$\nu_{\text{as}}(\text{C}-\text{H})$ from methylene	[1, 4, 17–20, 25]
2871	$\nu_{\text{s}}(\text{C}-\text{H})$ from methylene	[1, 4, 17, 18, 20, 25]
1456	$\delta(\text{CH}_2)$	[1, 18, 19, 25]
1293	$\delta(\text{CH}_2)$ twisting + wagging	[20]
Methyl (CH₃)		
2967	$\nu_{\text{as}}(\text{C}-\text{H})$ from methyl	[1, 19, 20]
1384	$\delta_{\text{sym}}(\text{CH}_3) + \delta(\text{C}-(\text{CH}_3)_2)$	[20]
1362	$\delta(\text{CH}_3) + \delta(\text{C}-(\text{CH}_3)_2)$	[1, 2, 20]
1180	$\nu(\varphi-\text{C}-(\text{CH}_3)-\varphi)$	[20, 26]
Para substituted aromatics		
1507	$\nu(\text{C}-\text{C})$ para-substituted aromatics	[2, 3, 15, 19, 20]
1415	semicircle stretching, para-substituted aromatics	[18, 20]
824	1,4-substituted aromatics: out-of-plane hydrogen wagging	[1, 18–20, 25, 27]
Unspecific aromatics		
1603	$\nu_{\text{s}}(\text{C}=\text{C})$ aromatics	[1–3, 19, 20]
1581	$\nu_{\text{s}}(\text{C}=\text{C}-\text{H})$ aromatics	[1, 20]
Other functionality		
1480	3-fold substituted aromatics: semicircle stretching	[20]

group a generalised trend over the ageing time could be calculated, which allowed an easier interpretation of the chemical degradation process (Fig. 21.3a). It can be concluded that methylene groups are least resistant to oxidation. Bands characteristic of the CH₂ group start decreasing first, while the intensities for bands of carbonyl or amide groups and C=C bonds, which can hardly be differentiated in the spectra, increase simultaneously. Mechanisms for thermo-oxidative degradation resulting in chain scission with carbonyl and C=C double bonds formation can be expected and are suggested in literature [4]. Typical deformation bands for para substituted aromatic compounds from the bisphenol-A moieties stay initially constant. After approximately 50 h these bands start degrading in two steps. In the first step a little decrease of the ether bands can be observed as well. Moreover, shifts of ether bands, which are increasing with ageing time, can be observed in the spectra.

Since both functional groups are vicinal, these phenomena can be explained by rearrangements of the polymer chains. In literature many different routes of rearrangements including bond breakage and new bond formations are proposed [3, 9, 20, 28–30]. During the second degradation step, characterised by a more pronounced decrease, a simultaneous strong degradation of the methyl and ether groups can be observed. Additionally, new bands characteristic of trisubstituted aromatic compounds come into existence. They can be formed by mechanisms like a Claisen rearrangement [20]. Since the methyl group related bands start degrading last, the isopropylidene group was assessed to be the most resistant group of the polymer network of the DICY-hardened DGEBA-based system, which is in contrast to the findings of Lin et al. [20]. Some possible degradation mechanisms of the different functional groups are proposed in Fig. 21.3b.

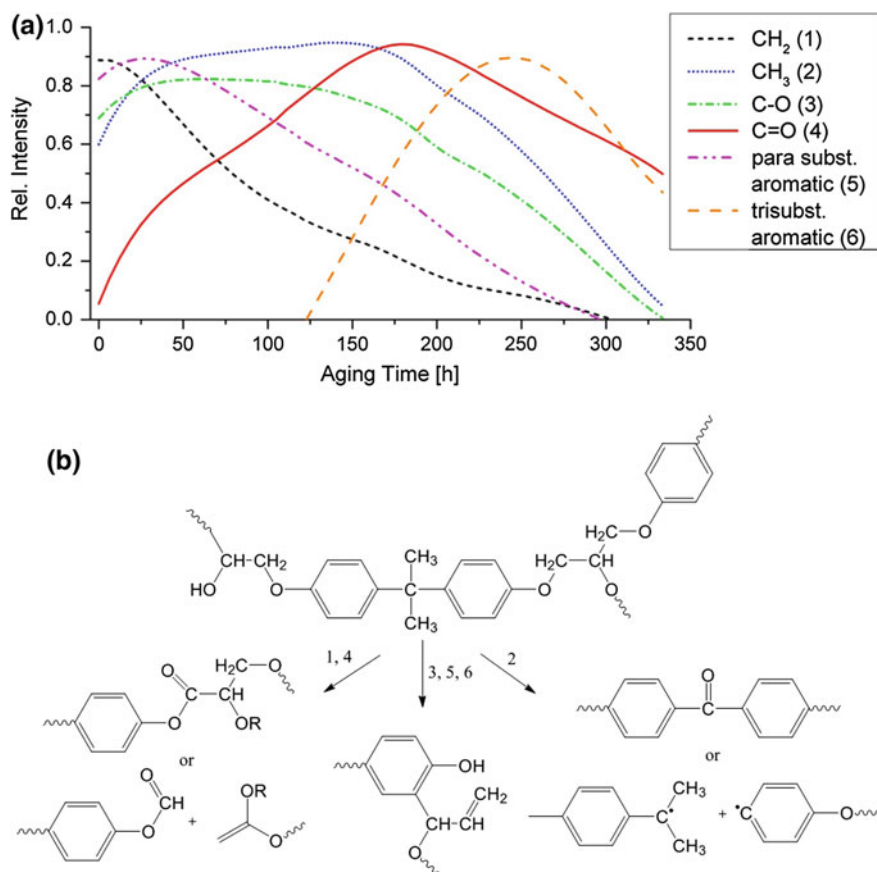


Fig. 21.3 Generalised trends of the absorption of functional groups over ageing time at 200 °C, derived from the IR spectra (a). Some possible degradation routes entailing the degradation or formation of the functional groups in Fig. 21.3a (b)

21.3.3 Raman Spectroscopy and Thermogravimetric Analysis

Due to the high fluorescence of the samples, which turned from transparent to brownish upon thermal treatment, only the non-aged sample and samples aged for more than 200 h could be measured. The obtained spectra clearly evidenced char formation (Fig. 21.4). In the spectrum of the non-aged sample typical bands for DGEBA could be found. For samples aged longer than 200 h at 200 °C these bands disappeared; instead strong signals typical of amorphous carbon (comparison to databases and [31]) could be detected in this frequency range.

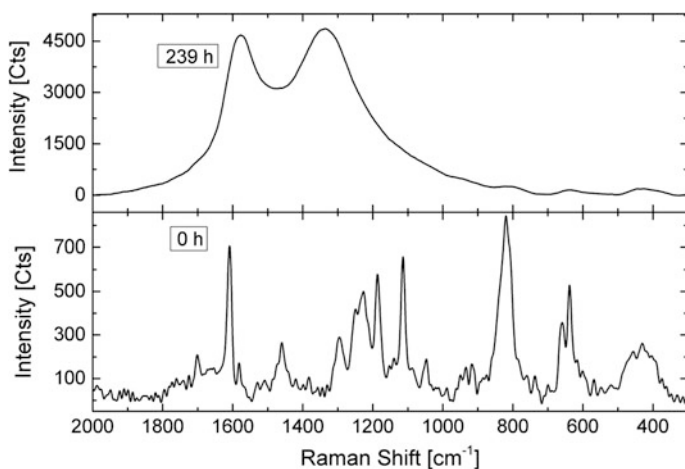


Fig. 21.4 Raman spectra of adhesive films; non-aged (0 h) and aged at 200 °C for 239 h

The low quality of the spectra did not allow quantitative analysis. A semi-quantitative analysis, however, could be performed with TGA. The residue at 500 °C in N₂ is a sign for char formation, as char does not decompose in nitrogen below 500 °C. It can be observed that the residue increases the longer the adhesive film was aged (Fig. 21.5). This indicates that the char formation process already starts at early ageing times, maybe first by increasing the network density through a combination of bond scission and post-curing reactions. The denser network either results in a higher char formation during measurement or it is already formed during ageing.

21.3.4 Lifetime Prediction: T-Peel Test and Tensile Lap-Shear Test

Lifetime predictions for the adhesive strength of the studied DGEBA- and DICY-based adhesive system are founded on the observation of the T-peel strength

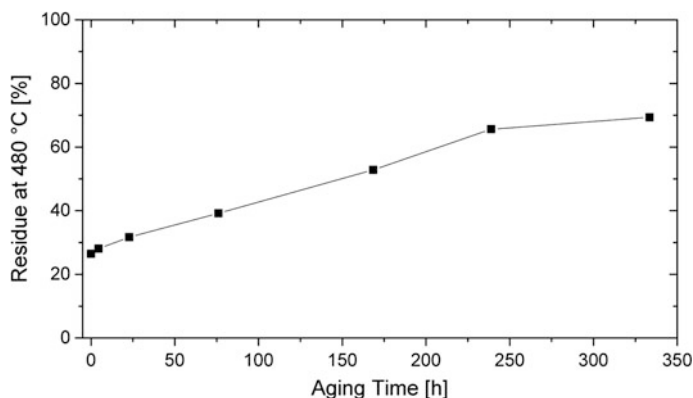


Fig. 21.5 Thermogravimetric analysis of adhesive films pre-aged at 200 °C for different times, performed in nitrogen at a heating rate of 5 °C/min: evaluation of the residue at 480 °C

and the tensile lap-shear strength under consideration of several different temperatures. Analysing the degradation trend on the basis of the T-peel strength (Fig. 21.6a), 4 different regimes which are independent from the ageing temperature can be observed. In an initial phase covering the first 5% of the total ageing time, a minor decrease in T-peel strength of about 1 N/mm is registered. This minor decrease is followed by a rather constant plateau, denominated regime 2, before the adhesive force exhibits a pronounced breakdown. After this third regime a kind of fade-out can be monitored (regime 4), where the adhesive strength slowly approaches zero. Comparable behaviour was found with lap-shear testing (Fig. 21.6b) with the exception of regime 1, which is missing in this case. Moreover, the timescales are significantly longer compared to T-peel results. The different regimes are marked by a grey background for the ageing trend at 230 °C in Fig. 21.6.

The first regime may be explained by post-cure reactions prevailing over degradation phenomena. Consequently, the polymer network becomes more rigid, which does not influence the tensile lap-shear strength negatively. For a good peeling strength, however, a certain elasticity of the polymer is necessary. Therefore the decrease in the first regime can be explained by an embrittlement of the polymer network. In the second regime post-cure and degradation reactions seem to be balanced. The third regime describes the breakdown of the polymer network, where decomposition reactions are predominant. In the fourth regime—the last period—other effects additionally influence the results from measuring the adhesive strength. In this period adhesive strengths are very low and close to the detection limit of the device, which also makes effects from sample preparation more important. Looking at the time needed until samples are fully degraded at 180 °C, the importance of accelerated testing becomes obvious. In case of the T-peel strength the ageing time was reduced from nearly 5000 h at 180 °C to 10 h at 250 °C. Considering the

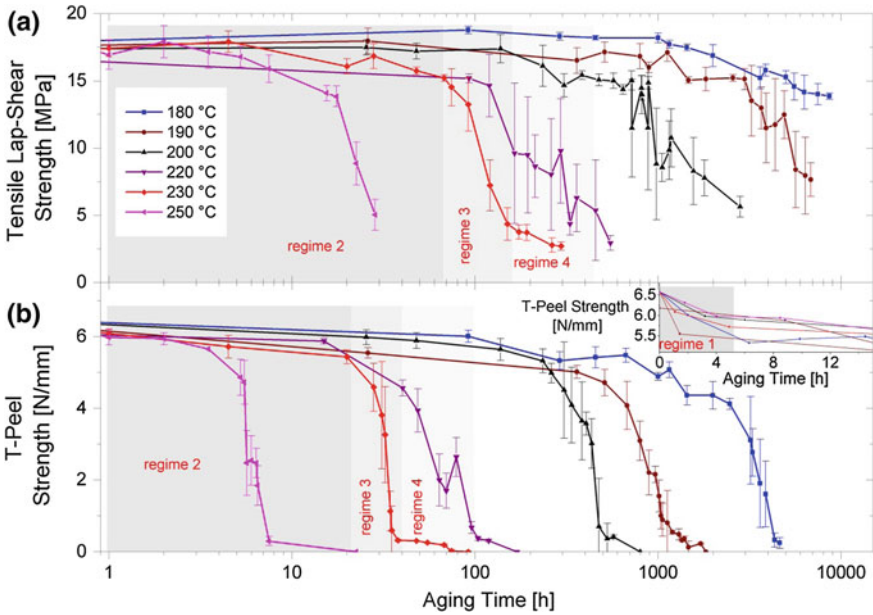


Fig. 21.6 Results for ageing investigations based on the tensile lap-shear test (a) and the T-peel test (b). The different regimes are indicated by a grey background for an ageing time of 230 °C

tensile lap-shear strength, the degradation trend monitored at 180 °C even could not be evaluated at all, because after 10,000 h the adhesive strength still was in regime 2, nevertheless, the steel panels were already strongly affected by the heat, so that further ageing would not display the adhesive strength of the adhesive system anymore.

Lifetime predictions were performed following the procedure described in DIN EN 60216 [32, 33]. First, the adhesive strength was normalised for every degradation process. In a second step an ageing time could be calculated, at which the adhesive strength had decreased to a defined percentage of its initial value. In accordance with an Arrhenius relationship as described in (21.1), a plot with the logarithm of the ageing time of a given adhesive strength level on the ordinate and the inverse absolute temperature on the abscissa can be established.

$$r_d \propto k_d(T) = k_{0,d} \cdot e^{-\frac{E_A}{RT}}, \tag{21.1}$$

with r_d —rate of degradation, $k_d(T)$ —degradation rate constant, $k_{0,d}$ —degradation pre-exponential factor, E_A —activation energy, R —gas constant and T —absolute temperature.

If all requirements are fulfilled and the degradation mechanisms do not change upon an increase of the ageing temperature, a linear fit will be obtained.

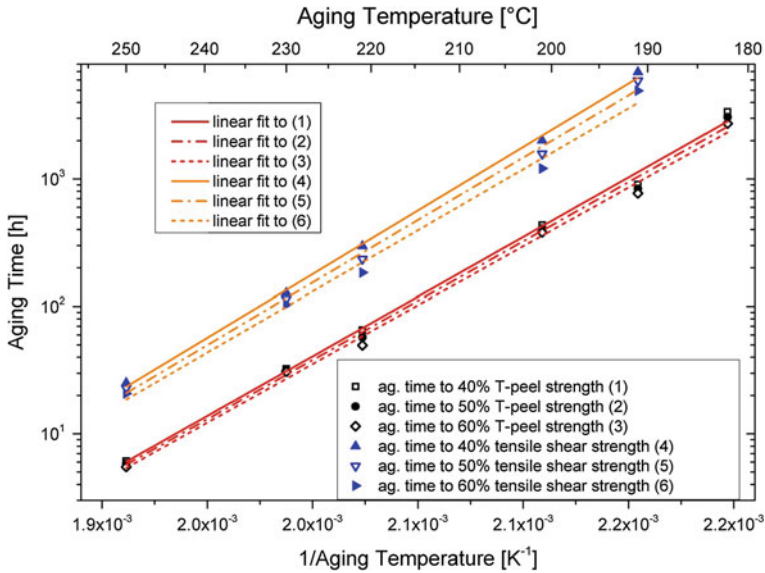


Fig. 21.7 Comparison of lifetime extrapolations obtained with the T-peel test and the tensile lap-shear test

Table 21.2 Calculated parameters for the lifetime predictions based on the T-peel strength

Adhesive strength level (%)	T-peel strength				
	30	40	50	60	70
Slope	9409	9354	9295	9221	9116
Intercept	-17.18	-17.10	-17.01	-16.89	-16.72
R ²	0.9961	0.9961	0.9957	0.9947	0.9929

Regime 3 turned out to be best suitable for lifetime predictions because of its steep decline, which allows making the least mistake in determining the ageing time. Figure 21.7 shows the plots for both the T-peel strength and the tensile lap-shear strength at 40, 50 and 60% of the adhesive strength. Tables 21.2 and 21.3 lists the obtained values for the linear fits. Tables 21.2 and 21.3 illustrates that very good correlations were obtained, when the extrapolations are performed in the range from 30–70% adhesive strength. Linearity is given over the whole chosen temperature range from 180 to 250 °C, which shows that accelerated testing for this system is applicable. Comparing the lifetimes obtained by the 2 different observables, the importance to predefine the needed testing value becomes clear. Choosing the T-peel test as observable for the investigated material a lifetime of 3180 h can

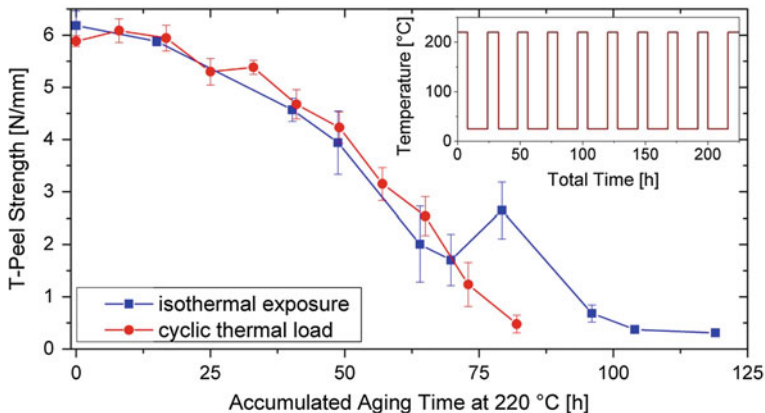


Fig. 21.8 Comparison of a constant temperature exposure at 220 °C and a cyclic thermal load alternating room temperature with 220 °C (see *inset*). The ageing time refers only to the accumulated exposure at 220 °C

Table 21.3 Calculated parameters for the lifetime predictions based on the tensile lap-shear strength

Adhesive strength level (%)	Tensile lap-shear strength				
	30	40	50	60	70
Slope	10,137	9979	9796	9581	9311
Intercept	-17.95	-17.95	-17.70	-17.40	-17.04
R ²	0.9988	0.9988	0.9981	0.9953	0.9905

be calculated for a decrease of the adhesive strength to 50% of its initial value at a constant ageing temperature of 180 °C. Doing the calculation for the same ageing conditions and the same material on the basis of the tensile lap-shear test, a lifetime of 16,350 h is computed. This example visualises the strong dependence of lifetime predictions on the testing mode.

Since in reality constant conditions at high temperatures will hardly ever be obtained, a cyclic test was applied, where the T-peel strength was used as observable. The cyclic thermal load was performed by exposing the samples alternately to 220 °C and room temperature for some time. If only the time at 220 °C is counted, the degradation trends will be about the same for the cyclic test and the constant temperature test (Fig. 21.8). This experiment showed that (accelerated) ageing at constant higher temperatures could simulate very well realistic cyclic thermal loads.

21.4 Conclusions

Thermal ageing of an DGEBA–DICY epoxide system under atmospheric conditions resulted in a stiffening of the polymer network, which is characterised by a continuous increase in T_g . Methylene groups have been found to be the least resistant functional groups of the polymer network to oxidation. At longer ageing times, all functional parts of the polymer were affected by rearrangement reactions. The isopropylidene group with its characteristic methyl groups turned out to be most resistant to temperature treatment. Char formation could be observed as a result of degradation. Lifetime predictions by accelerated ageing using an Arrhenius approach turned out to be possible in a temperature range from 180 to 250 °C, which means an acceleration factor of about 500. Both T-peel and tensile lap-shear tests are possible methods to investigate the stability of the adhesive strength; however, the results for the lifetime predictions strongly depend on the chosen test or tested property. The cohesive failure mode did not change over ageing time and did not depend on the ageing temperature. Results from a cyclic test evidenced that temperature changes do not additionally harm the system; only the time at high temperatures is relevant for degradation phenomena. Consequently, accelerated testing at constant temperature regimes is also predictive for cyclic thermal loads.

References

1. Nikolic, G., Zlatkovic, S., Cacic, M., Cacic, S., Lacnjevac, C., Rajic, Z.: Fast fourier transform IR characterization of epoxy GY systems crosslinked with aliphatic and cycloaliphatic EH polyamine adducts. *Sensors* **10**, 684–696 (2010)
2. González, M., Cabanelas, J., Baselg, J.: Applications of FTIR on epoxy resins—Identification, monitoring the curing process, phase separation and water uptake. In: Theophanides, T. (ed.): *Infrared Spectroscopy—Materials Science, Engineering and Technology*. InTech, pp. 261–284 (2012)
3. Pei, Y.M., Wang, K., Zhan, M.-S., Xu, W., Ding, X.J.: Thermal-oxidative aging of DGEBA/EPN/LMPA epoxy system: Chemical structure and thermal–mechanical properties. *Polym. Degrad. Stab.* **96**, 1179–1186 (2011)
4. Li, K., Wang, K., Zhan, M.-S., Xu, W.: The change of thermal–mechanical properties and chemical structure of ambient cured DGEBA/TEPA under accelerated thermo-oxidative aging. *Polym. Degrad. Stab.* **98**, 2340–2346 (2013)
5. Pascault, J.P., Williams, R.J.: *Epoxy Polymers: New Materials and Innovations*. Wiley-VCH, Weinheim (2010)
6. Siddiqui, N., Khan, S., Kim, J.K.: Experimental torsional shear properties of carbon fiber reinforced epoxy composites containing carbon nanotubes. *Compos. Struct.* **104**, 230–238 (2013)
7. Rahmanian, S., Suraya, A., Shazed, M., Zahari, R., Zainudin, E.: Mechanical characterization of epoxy composite with multiscale reinforcements: Carbon nanotubes and short carbon fibers. *Mater. Des.* **60**, 34–40 (2014)

8. Zahra, Y., Djouani, F., Fayolle, B., Kuntz, M., Verdu, J.: Thermo-oxidative aging of epoxy coating systems. *Prog. Org. Coat.* **77**, 380–387 (2014)
9. Damian, C., Espuche, E., Escoubes, M.: Influence of three ageing types (thermal oxidation, radiochemical and hydrolytic ageing) on the structure and gas transport properties of epoxy-amine networks. *Polym. Degrad. Stab.* **72**, 447–458 (2001)
10. Chen, J.S., Ober, C., Poliks, M., Zhang, Y., Wiesner, U., Cohen, C.: Controlled degradation of epoxy networks: Analysis of crosslink density and glass transition temperature changes in thermally reworkable thermosets. *Polymer* **45**, 1939–1950 (2004)
11. Chen, J.S., Ober, C., Poliks, M.: Characterization of thermally reworkable thermosets: Materials for environmentally friendly processing and reuse. *Polymer* **43**, 131–139 (2002)
12. Stoye, D., Freitag, W.: *Lackharze: Chemie. Eigenschaften und Anwendungen.* Hanser, Munich Vienna (1996)
13. Dyakonov, T., Chen, Y., Holland, K., Drbohlav, J., Burns, D., Velde, D., Seib, L., Soloski, E., Kuhn, J., Mann, P.; Stevenson, William T. K.: Thermal analysis of some aromatic amine cured model epoxy resin systems—I: Materials synthesis and characterization, cure and post-cure. *Polym. Degrad. Stab.* **53**, 217–242 (1996)
14. Fata, D.: *Epoxidsysteme im Verbund mit rostfreien Stählen—Vernetzung und Alterung.* Shaker, Aachen (2007)
15. Gaukler, J.: *Lagerungsstabilität Vernetzung und Eigenschaften von Epoxid-Dicyanidamid-Systemen für Nanoverbundwerkstoffe.* Shaker, Aachen (2012)
16. Dao, B., Hodgkin, J., Krstina, J., Mardel, J., Tian, W.: Accelerated aging versus realistic aging in aerospace composite materials. II. Chemistry of thermal aging in a structural composite. *J. Appl. Polym. Sci.* **102**, 3221–3232 (2006)
17. Lévêque, D., Schieffer, A., Mavel, A., Maire, J.-F.: Analysis of how thermal aging affects the long-term mechanical behavior and strength of polymer–matrix composites. *Compos. Sci. Technol.* **65**, 395–401 (2005)
18. Hong, S.G.: The thermal-oxidative degradation of an epoxy adhesive on metal substrates: XPS and RAIR analyses. *Polym. Degrad. Stab.* **48**, 211–218 (1995)
19. Monney, L., Belali, R., Vebrel, J., Dubois, C., Chambaudet, A.: Photochemical degradation study of an epoxy material by IR-ATR spectroscopy. *Polym. Degrad. Stab.* **62**, 353–359 (1998)
20. Lin, S., Bulkin, B., Pearce, E.: Epoxy resins. III. application of fourier transform IR to degradation studies of epoxy systems. *J. Polym. Sci.: Polym. Chem. Ed.* **17**, 3121–3148 (1979)
21. Anderson, B.: Thermal stability and lifetime estimates of a high temperature epoxy by T_g reduction. *Polym. Degrad. Stab.* **98**, 2375–2382 (2013)
22. Rasoldier, N., Colin, X., Verdu, J., Bocquet, M., Olivier, L., Chocinski-Arnault, L., Lafarie-Frenot, M.: Model systems for thermo-oxidised epoxy composite matrices. *Compos. A Appl. Sci. Manuf.* **39**, 1522–1529 (2008)
23. ISO 11339 (2010): Adhesives—T-peel test for flexible-to-flexible bonded assemblies
24. DIN EN 1465 (2009): Adhesives—Determination of tensile lap-shear strength of bonded assemblies
25. Sacher, E.: Kinetics of epoxy cure: 3. The systems bisphenol-A epoxides/dicy. *Polymer* **14**, 91–95 (1973)
26. Mailhot, B., Morlat-Thérias, S., Ouahioune, M., Gardette, J.-L.: Study of the degradation of an epoxy/amine resin, 1. *Macromol. Chem. Phys.* **206**, 575–584 (2005)
27. Hong, S.G., Wu, C.S.: DSC and FTIR analysis of the curing behaviors of epoxy/DICY/solvent open systems. *Thermochim. Acta* **316**, 167–175 (1998)
28. Grassie, N., Guy, M., Tennent, N.: Degradation of epoxy polymers: Part 1—Products of thermal degradation of bisphenol-A diglycidyl ether. *Polym. Degrad. Stab.* **12**, 65–91 (1985)
29. Grassie, N., Guy, M., Tennent, N.: Degradation of epoxy polymers: 2—Mechanism of thermal degradation of bisphenol-A diglycidyl ether. *Polym. Degrad. Stab.* **13**, 11–20 (1985)

30. Zhang, G., Pitt, W.G., Goates, S.R., Owen, N.L.: Studies on oxidative photodegradation of epoxy resins by IR-ATR spectroscopy. *J. Appl. Polym. Sci.* **54**, 419–427 (1994)
31. Debus, J.: Raman studies on amorphous carbon layers—Raman-Untersuchungen von amorphen Kohlenstoffschichten. ArXiv e-prints (2012) 1203.0035
32. DIN EN 60216-1 (2014): Electrical insulating materials—Thermal endurance properties—Part 1: Ageing procedures and evaluation of test results
33. DIN EN 60216-3 (2007): Electrical insulating materials—Thermal endurance properties—Part 3: Instructions for calculating thermal endurance characteristics

Part V
Fatigue Crack Propagation, Lifetime
and Long-Term Mechanical Behaviour
of Thermoplastics and Elastomers

Chapter 22

Morphology and Fatigue Behaviour of Short-Glass Fibre-Reinforced Polypropylene

M. Palmstingl, D. Salaberger and T. Koch

Abstract The fatigue behaviour of short-glass fibre-reinforced polypropylene was investigated in dependence on the fibre orientation. For that, a special plate geometry was developed which allows to exclude the effect of machining and leads to original injection surfaces at least in the region of the main (slightly concentrated) load. This “original” surface matches the surface situation of the injection moulded consumer parts. Furthermore, the plates consist of a notch region and a knit line. Morphology analysis can be done by sectioning and stereological principles or by X-ray computed tomography. The fatigue strength shows a strong correlation to fibre orientation, but the samples taken from the knit line and the notch region do not follow this correlation. In these regions the situations are more complex. The application of different methods for the characterization of the evolution of damage (development of dissipated energy, strain, normalized modulus, temperature) does not give a clear indication of damage; there are no clear signs of damage until shortly before the fracture. High-speed camera in combination with digital image correlation can give information on local strain and therefore on the localized occurrence of damage at a relatively early stage of fatigue life.

22.1 Introduction

The wide use and growing of industrial applications of short fibre-reinforced polymers (SFRP) has different reasons: low manufacturing costs, high production rate, good weight to stiffness and strength ratio and the possibility to mould it into complex shapes. In practice plastic components and constructions are often subject of cyclic loading which is one major reason of mechanical failures. Cyclic loading can lead to fatigue failure at essentially lower stresses or deformations than under

M. Palmstingl (✉) · T. Koch
Institute of Materials Science and Technology,
Vienna University of Technology, Vienna, Austria

D. Salaberger
University of Applied Sciences of Upper Austria, Wels, Austria

quasi-static loading conditions. Damages arise already in the region of linear-viscoelastic materials behaviour. The loading conditions are often very complex. Orientations, agglomerations, notches, weld lines, environmental conditions are factors influencing the fatigue failure. So, it is important to consider these parameters in fatigue testing. Also, all these things mean that a comprehensive description of mechanical materials or component behaviour requires—besides quasi-static, impact and creep testing—also fatigue testing.

A good overview about results on fatigue behaviour of polymeric materials is given in [1], a literature review on short fibre-reinforced polymers can be found in [2]. The most investigations were done on short fibre-reinforced polyamides [3–10] reflecting the fact that these thermoplastic materials are the most widely used matrix polymers of SFRPs in industrial applications. Investigations on SFR polypropylene are presented in [11–14].

It is well known that the orientations of the fibres have a large impact on the fatigue behaviour and all the test results cannot be assessed without the knowledge of the morphology of the composites. The morphology can be described by microscopy or X-ray tomography. Both methods need some efforts to receive adequate results.

To model the damage accumulation and predict the fatigue life different mechanical parameters are used in literature. They are mostly based on the dissipative response, for example on the progression of hysteresis loop, strain energy, non-linear viscoelasticity or hysteretic energy [2].

22.2 Analysis of Morphology of SFRP

Morphological characterisation provides fundamental information about the properties and behaviour of polymer composites. Since the microstructure of such composite materials highly affects bulk material properties, the prediction of morphological structures by simulation is of considerable interest for the designing of industrial applications. For the validation of moulding simulation models commonly morphological investigation methods like microscopic or tomographic techniques are used [15].

X-ray Computed Tomography (X-CT) (Fig. 22.1) is currently the most appropriate method to describe the morphology of short fibre-reinforced polymers, which is reflected by an increasing number of works in the literature. Fibre content, fibre orientation, fibre length distribution and the local 3-dimensional distribution of the three parameters can be obtained. Applying suitable segmentation methods is an essential requirement to extract correct quantitative morphology parameters from X-CT [16]. Especially agglomerates of fibres could influence the results, namely the calculated length distribution. With the onward development of equipment and software X-CT will become the standard for the investigation of polymer composites. At the moment the limiting factor are mainly the high costs of the devices or of contract measurements.

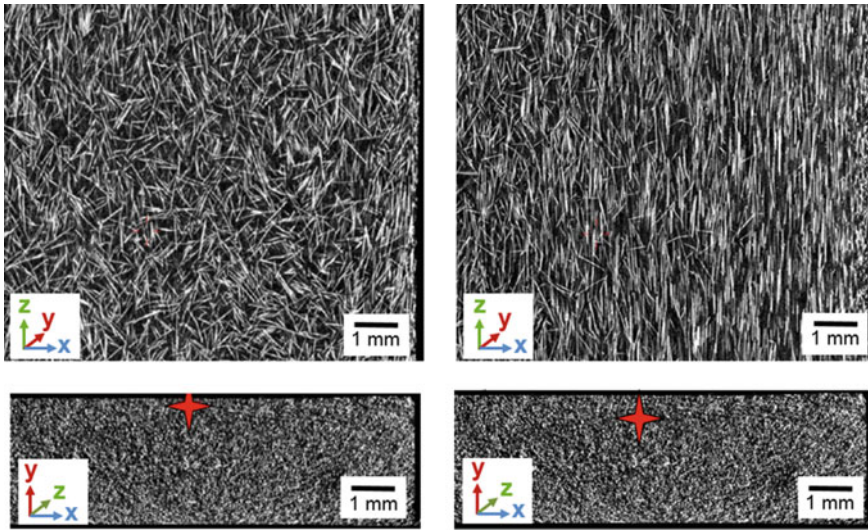


Fig. 22.1 Example of X-CT results on SFRP. Visualisation of fibre arrangement in different planes. Z injection direction, Y thickness direction. The stars indicate the position of the above shown X-Z-plane

Stereological principles are basic considerations for the analysis of microstructures with microscopic investigations of polished cut surfaces [17]. Although other methods were used frequently [18–22], the sectioning of fibre-reinforced polymers followed by light microscopic investigations and digital image analysis is still the most commonly used technique for the determination of the distribution of fibre orientation [23–28]. The relative simplicity of the required measurement setup, particularly compared with non-destructive techniques like tomographic ones, let this method be preferred even though it must be considered, that there are inaccuracies in the model [29, 30].

The theory bases on the optical observation of elliptical marks occurring by the intersection of cylindrical reinforcement materials like fibres. Polishing sections from a sample leads to such elliptical fibre marks due to the cutting of the cylindrical fibres. The two polar angles ϕ and θ , that define the orientation of the fibre, can be determined from the footprint of each fibre. The angle θ thereby defines the angle between the fibres longitudinal axis and the sectioned surface normal (22.1), whereby b is defined as the ellipses minor half axis and a as the ellipses major half axis. The second polar angle ϕ defines the angle between the major axis of the elliptical fibre mark and one of the in-plane axes (see Fig. 22.2).

$$\theta = \cos^{-1}\left(\frac{b}{a}\right) \tag{22.1}$$

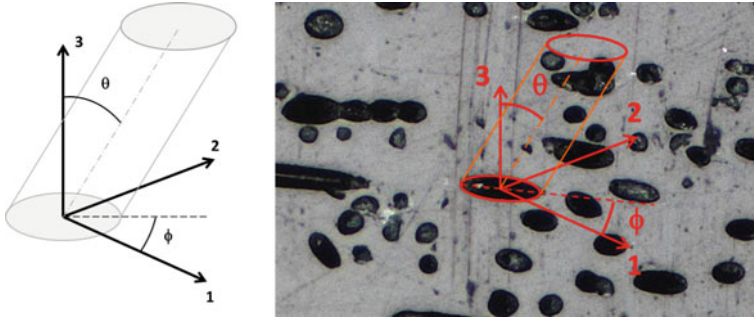


Fig. 22.2 The fibre orientation defined by means of the two polar angles ϕ and θ theoretically (*left*) and applied on a sample (*right*)

An example for the investigation of one of the observed plate positions is shown in Fig. 22.3. The location on the plate is called 0° -position. In Fig. 22.3b a high amount of fibres with a polar angle ϕ around 90° (parallel to axis 2) is already obvious and can also be confirmed through the analysis, shown in Fig. 22.3d. Regarding polar angle θ , fibres at this plate position are orientated either 0° or in the range of 70° – 90° . These calculated results (Fig. 22.3e) are again evident by interpreting the visible fibres in Fig. 22.3b. The almost circular appearing fibre marks represent an angle of 0° whereas the partially quite long ellipses illustrate the angles of 70° – 90° for θ .

Subsequently, the results of the so-called 90° -position on the plate (Fig. 22.4) can be concluded logically. The angle ϕ shows a quite equal distribution (Fig. 22.4d). There is no predominant “in plane”-orientation, which can also be recognised in the surface cuts of the different planes presented in Fig. 22.4b. The results of the polar angle θ (Fig. 22.4e) are very similar to the ones of the 0° -position.

The calculation of the two polar angles enables the determination of the orientation of a single fibre by expressing it as a second order orientation tensor a_{ij} . The calculation and a detailed discussion about the formation and application about orientation tensors can be found elsewhere [32]. The orientation of an individual fibre is defined by the main diagonal components of the tensor that are given in the following equations (22.2) [32].

$$\begin{aligned} a_{11} &= \sin^2 \theta \cdot \cos^2 \phi \\ a_{22} &= \sin^2 \theta \cdot \sin^2 \phi \\ a_{33} &= \cos^2 \theta \end{aligned} \quad (22.2)$$

The fibre orientation of an investigated sample is then given by the average of the single fibre orientation. For an unbiased estimation of the orientation tensor, the tensor components must be weighted for each fibre. Therefore the inverse of the probability of intersecting each fibre must be included. This weighted orientation tensor is described in earlier publications [26, 29].

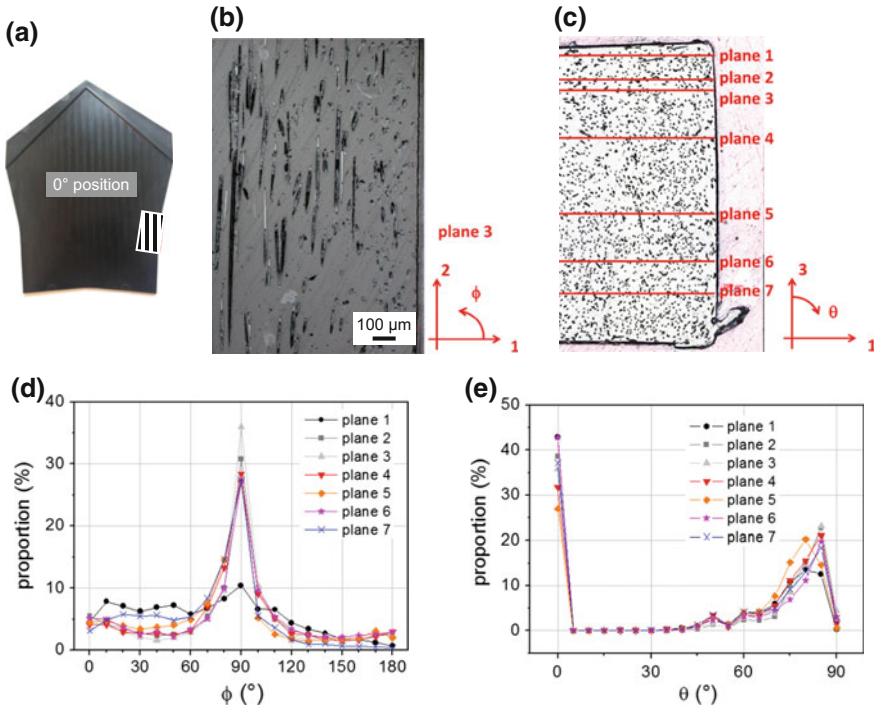


Fig. 22.3 The plate form and the labelled position (a), polished cut surface from 0°-position on plane 3 (b), plate cross section with marking of all investigated plane positions (c), distribution of polar angle ϕ in dependency of the sample planes (d), distribution of polar angle θ in dependency of the sample planes (e) [31]

For the presented examples of the 0°- and 90°-position (Figs. 22.3 and 22.4), Table 22.1 gives the calculated main diagonal components of the weighted orientation tensor. The polar angles distributions are reflected suitable through the calculated results of the microscopic analysis.

The contrast between glass fibres and the matrix material is usually inadequate for an automatic data analysis following a reflecting light microscopic investigation. Because of the poor contrast of glass fibres as well as the contrast dependence on different sample preparation parameters like the polishing procedure or the polishing time, there has to be a contrast enhancement prior to the optical image generation. Commonly used are etching approaches, where glass fibres were dissolved and the remaining holes, representing the originally existing fibres, will be analysed instead. For the etching procedure oxygen ions can be used [33, 34]. Figure 22.5 shows the difference between etched and untreated samples, whereby hydrofluoric acid was used as etching agent in this case.

Another major morphological characteristic of fibre-reinforced polymers is the average fibre length. There are approaches to determine an average fibre length from cross-sectional data by an indirect calculation, where the number of

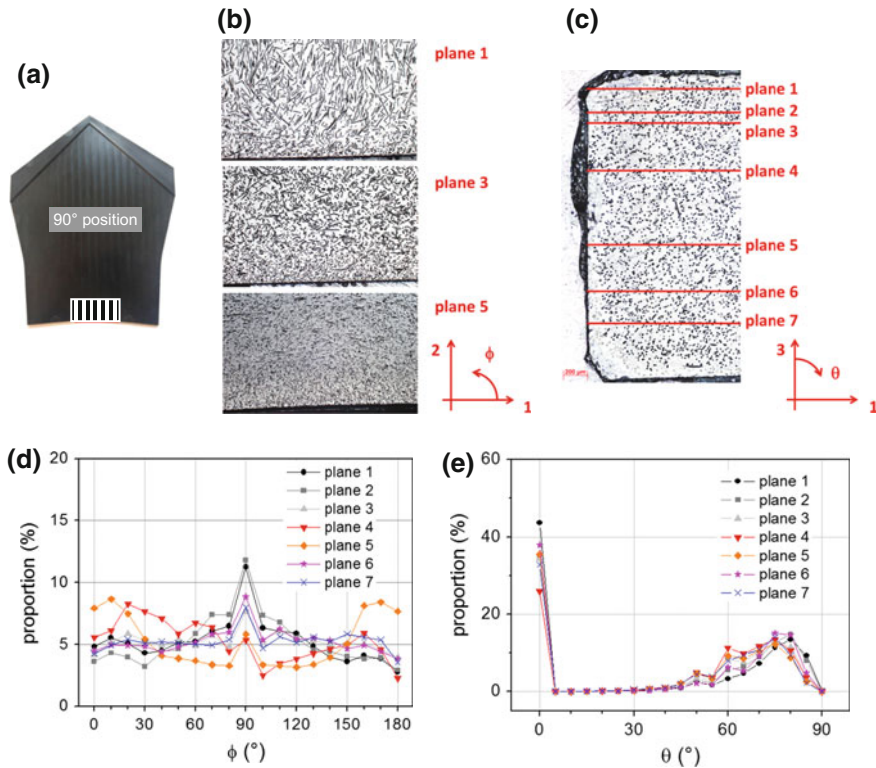


Fig. 22.4 The plate form and the labelled position (a), polished cut surface from 90°-position on planes 1, 3 and 5 (b), plate cross section with marking of all investigated plane positions (c), distribution of polar angle ϕ in dependency of the sample planes (d), distribution of polar angle θ in dependency of the sample planes (e) [31]

Table 22.1 Main diagonal components of the weighted orientation tensor calculated from the surface cuts after the microscopic analysis

Tensor component	0°-position	90°-position
a_{11}	0.053	0.191
a_{22}	0.304	0.162
a_{33}	0.643	0.647

intersected fibre ends on a cross-section image provides information for the estimation of the average fibre length [35]. Inaccuracies in the estimations lead to the two-section method, an approach, where two consecutive closely-spaced parallel cross-sections of a specimen provide a more precise estimation of the average fibre length directly from microscopic images after sectioning [36]. These images have to be transformed into a black and white image before a software tool can identify the related fibre ellipses in the two images of the same area but different closely-spaced planes. Figure 22.6 demonstrates the transformation of microscopic images into black and white images of the different planes and a superposition of both sections.

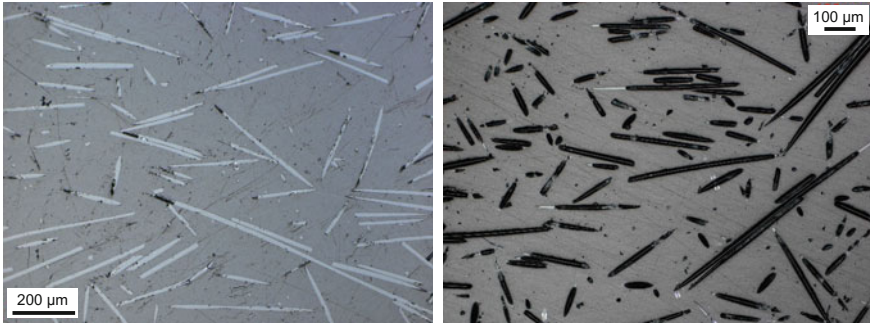


Fig. 22.5 Polished cut surfaces without etching (*left*) and etched (*right*)

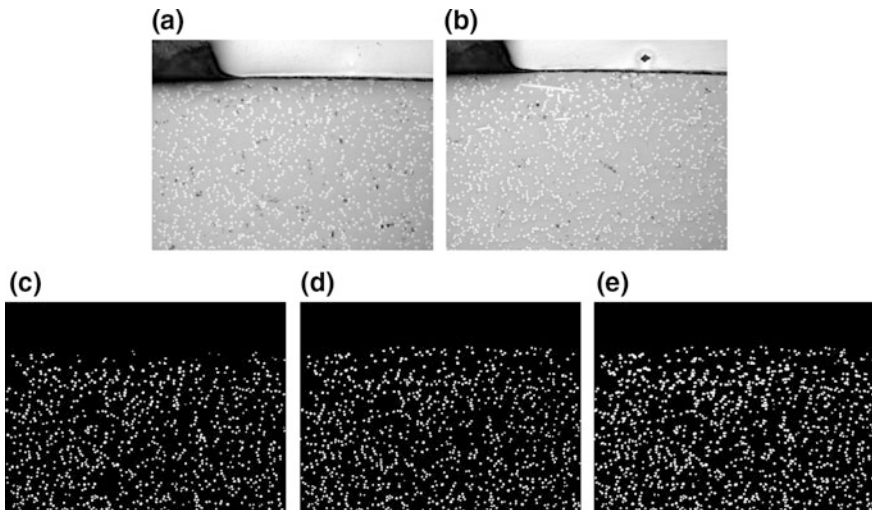


Fig. 22.6 Images generated for the two-section method: microscopic image of the upper plane (a), microscopic image of the lower plane (b), transformed black and white image of the upper plane (c), transformed black and white image of the lower plane (d), superposition of the black and white images of the two sections (e) [31]

A single fibre can be seen in either one or both planes. The superposition connects the two sections so that the fibres can be identified in both planes as the same fibre. The average fibre length can be estimated by using statistical analysis under the consideration of the distance between the planes and the probability that a fibre with a certain length has to cross both sections.

Another attempt to correct the estimated average fibre length as well as a method to determine the real fibre length distribution from measured lengths of the fibres from cross-section images is proposed elsewhere [30].

Besides the analysis of cross-sectional images, actually there are other destructive and non-destructive methods to measure the fibre length. Commonly used are methods, where the fibre length can be directly measured after the burnout or dissolution of the polymer [36, 37]. Hereby the remaining fibres after an ashing procedure at high temperatures are measured by means of image analysis and optical microscopy.

Figure 22.7 shows such a microscopic image. After the burnout of the polypropylene matrix at a temperature of 530 °C and a dwell time of 1.5 h, the remaining glass fibres were floated with ethanol. Then, random samples were drawn from the population and investigated with reflected light microscopy. The length of each single fibre is determined easily by directly measuring the observable length.

The fibre length as well as the fibre orientation distribution furthermore can be determined by Computed Tomography (CT) [16, 38, 39]. Thereby, a series of radiographic projections are taken at different angles. The internal structure of a sample is then reconstructed using an algorithm for combining the generated projections information. With an appropriate resolution and specific data evaluation concepts, the starting and end points of single fibres can be extracted and thus fibre characteristics like the fibre length and orientation determined [16].

Even though there are correction approaches for most of the methods, the summary of the determined fibre lengths, obtained with different investigation methods, in Table 22.2 shows an analogy of the CT and ashing result. The two-section method produced unsatisfactorily and unequal results.

Fig. 22.7 Drawn sample of fibres after burnout

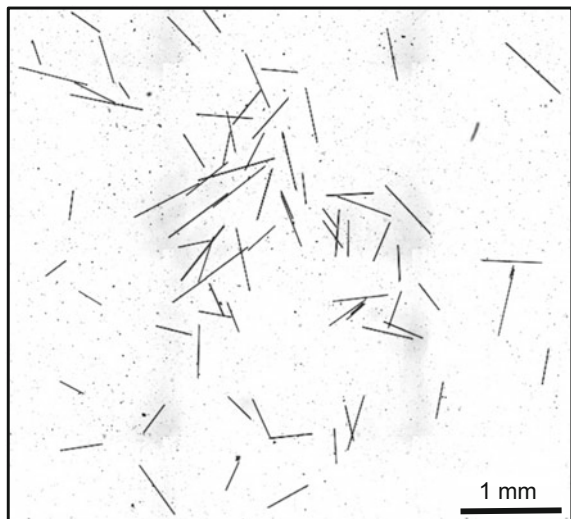


Table 22.2 Determined fibre lengths obtained with different investigation methods

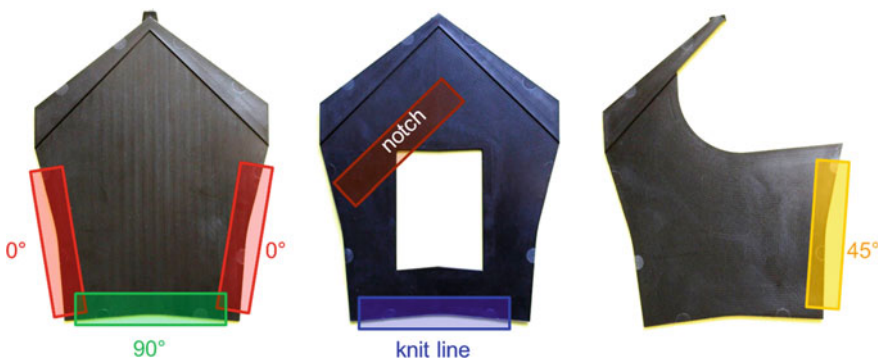
Method	No. of investigated fibres	Mean fibre length (μm)	Standard deviation (μm)
Two-section method	8101	233.7	68
Ashing	1541	293.4	6
CT	31,368	309.8	3

22.3 Determination of Fatigue Behaviour

The knowledge of the real existing fibre orientation is essential for the rating of investigation results for mechanical parameter like tensile strength or fatigue behaviour. Also the general known effect of a reduction in fibre length during processing [40] particularly of short fibre-reinforced polymers, which is not included in usual simulations, justifies the experimental investigation of morphological characteristics. The results of tensile tests, fatigue testing and durability analysis are then correlated with morphological characteristics and both are the basis for later executed simulations for fatigue behaviour and crack initiation.

Typically, specimens with different fibre orientations were machined from injection moulded plates with different angles of the specimen main axis to the injection direction. That means that the machined surfaces can influence the results obtained by fatigue testing. To exclude this possible effect it makes sense to produce specimens with original injection surfaces at least in the region of the main (concentrated) load. This “original” surface matches the surface situation of the injection moulded consumer parts.

For all subsequent investigations, the prepared specimens were taken from the three different injection moulded plate forms in two different types. The “standard” specimens were sampled from the positions of the plates, shown in Fig. 22.8.

**Fig. 22.8** Positions of the “standard” specimens prepared from the different plates

Only the 45°-specimen of the plate form with the eccentric inset was not considered satisfactory of its morphological properties and was not investigated henceforth. Figure 22.9 shows the dimensions of some of the other specimen positions. The special feature of this kind of preparation is the realisation of a little stress concentration as a consequence of the concave rounding of the specimen. Thus a defined area to locate the loading could be achieved for a targeted observation.

During the testing, it figured out, that the intended orientation of the “standard” specimen did not coincide with the analysed orientations from the morphological analysis in a satisfactory manner for some of the positions (Table 22.3). Though, a high degree of fibre orientation in combination with the belonging mechanical characteristics is required for satisfying simulation results. Therefore the “mini” specimens, the second types of prepared specimens, were intended. Due to the smaller area of the “mini” specimen a higher degree of orientation is reachable.

It turned out, that the highest degree of orientation could be achieved through the preparation of “mini” specimen from the testing plate with the centric inset. It is also the only plate form, where all for the simulation relevant kind of fibre orientations appear. Figure 22.10 shows the locations and positions of the places of sampling, the dimensions and also how these specimen types could be mounted in the testing machine.

The higher degree of orientation is clearly visible in Fig. 22.11. The 0°-position and the 90°-position obviously mirror them and show evidently a higher degree of orientation compared to the “standard” specimen. Due to the elaborated selection of the preparation positions no distinct layer constructions appeared. Table 22.4 shows

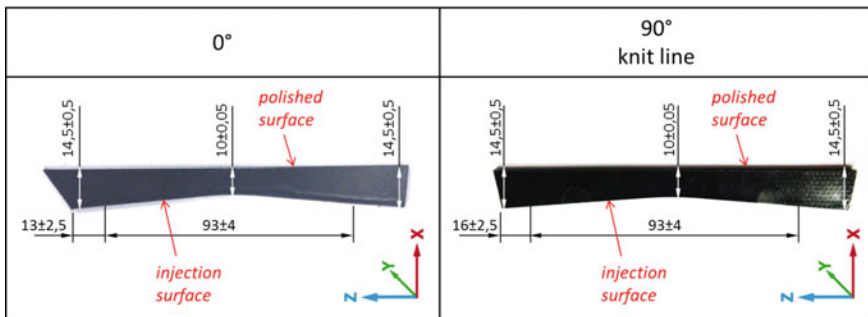


Fig. 22.9 Prepared “standard” specimen for 0°, 90° and knit line

Table 22.3 Main diagonal components of the orientation tensor considering the direction of the coordinates as defined in Fig. 22.9 for “standard” specimen determined by CT

Tensor component	0°-position	90°-position	Knit line	Notch
X	0.200	0.406	0.468	0.373
Y	0.086	0.136	0.141	0.102
Z	0.714	0.458	0.391	0.524

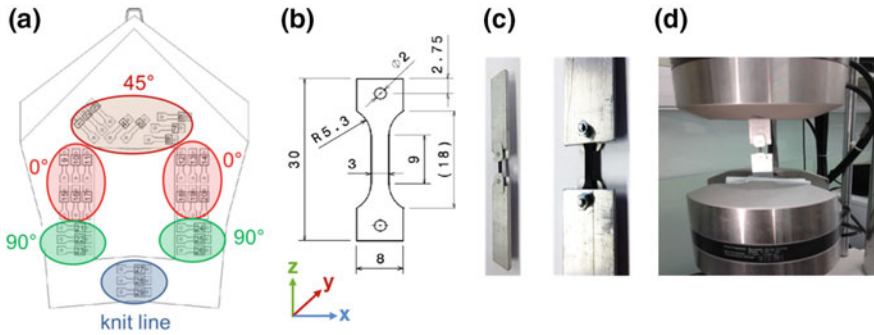


Fig. 22.10 Places of sampling of the “mini” specimen (a), dimensions of all “mini” specimen (b), fixing device for these specimen types (c), mounted “mini” specimen between the testing machine grips (d)

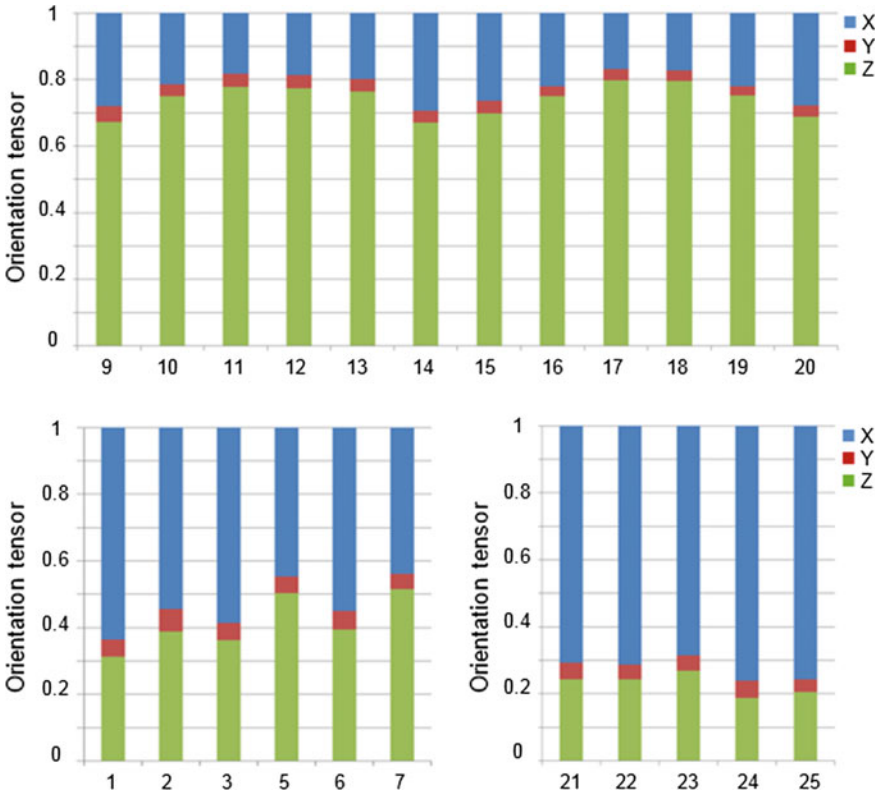


Fig. 22.11 Main diagonal components of the orientation tensor considering the direction of the coordinates as defined in Fig. 22.1 for the 0° (top), 45° (lower left) and 90° (lower right) “mini” specimen determined by CT

the tensor components for three layers (top, middle, bottom layer) of a 0° “mini” specimen.

The cyclic behaviour of glass fibre-reinforced thermoplastics is influenced by a number of different parameters [41, 42]. Main parameters are certainly the morphology of the material and the shape of the prepared specimen [14]. Also material anomalies like notches or knit lines have an impact on the fatigue behaviour. The other main parameters are loading factors like load type (tensile, compression, bending) [43], load profile (sine, rectangle, triangle), testing frequency [44, 45], thermal influence [46, 47] and other environmental effects.

Since fatigue strength is directly proportional to the tensile strength, tensile tests have been executed in advance of fatigue tests for a basic mechanical characterisation. Figure 22.12 shows load–elongation curves for the different specimen positions of the “standard” specimen. These results generated the basis for the following fatigue tests.

To characterise the fatigue behaviour a sinusoidal pulsating tensile loading was used for the load controlled testing. All results were obtained by a testing frequency of 10 Hz with $R = 0.1$ under room temperature. Only for the recording of high-speed images a cold-light source stressed the samples, though the light impulse lasted less than one second at each shot, there was no significant impact on the fatigue behaviour. The setup for the fatigue testing is shown in Fig. 22.13.

For the specification of materials fatigue behaviour commonly Wöhler curves were used, where strain is plotted against the number of cycles at fracture. Theoretical concepts for different loading types, the experimental planning and implementation of generating such curves are well known [41, 42, 48].

The generated Wöhler curves on the left side of Fig. 22.14 shows actually an expectable behaviour of the tested “standard” specimen. With the determined orientation tensors of the specimen positions, it was obvious that the 0° -position with a preferred fibre orientation parallel to the loading direction must perform best. Very similar results to these Wöhler curves have been made for other fibre-reinforced polymers [3–5]. The standardised Wöhler curves on the right side of Fig. 22.14 certify the proportionality of tensile and fatigue strength. It fits very well for the 0° - and notch-position. Only for the knit line a significant higher level and therefore a better fatigue behaviour related to the tensile behaviour compared with the usual characteristics of this polymer could be observed.

Table 22.4 Main diagonal components of the orientation tensor considering the direction of the coordinates as defined in Fig. 22.10b for a 0° “mini” specimen for three different layers determined by CT

Tensor component	Top	Middle	Bottom	Mean
X	0.22	0.18	0.21	0.20
Y	0.06	0.11	0.06	0.08
Z	0.72	0.71	0.73	0.72

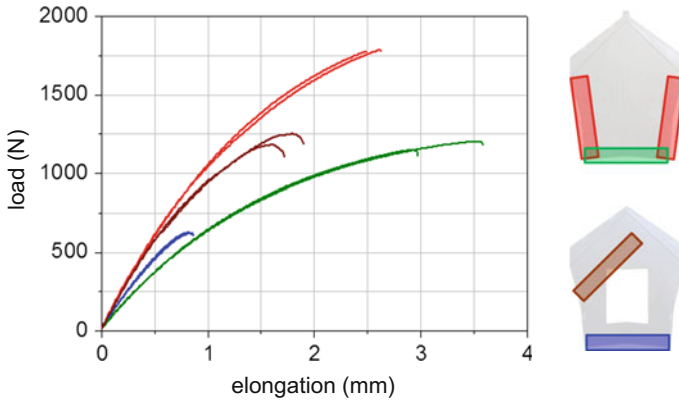


Fig. 22.12 Load–elongation curves for the different specimen positions

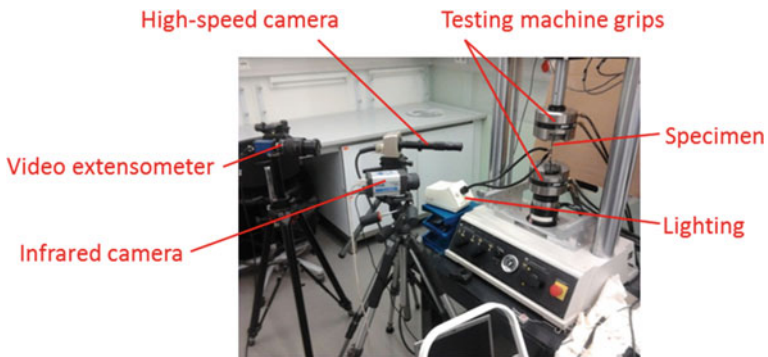


Fig. 22.13 Setup for fatigue testing with the different measurement systems

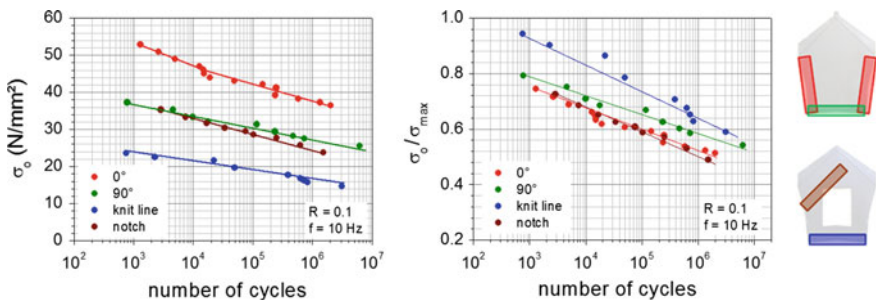


Fig. 22.14 Wöhler curves of the different positions of the “standard”-specimen (left) and normalised Wöhler curves of the same positions (right)

Plotting fatigue strength versus fibre orientation, represented by the main component of the orientation tensor parallel to loading direction shows a strong correlation (Fig. 22.15). The samples taken from the knit line and the notch region do not follow this correlation. In these regions the situations are more complex. For example in the notch region there is a strong stress concentration, which will lead to smaller values of fatigue strength.

For the durability analysis and the intended lifetime prediction several approaches were applied. Some of the used measurement equipment is illustrated in Fig. 22.13. Strain measurements are a main indication for the assessment of the fatigue status. Therefore strain was measured on different scales. By analysing the displacement of the testing machine grips a mean fatigue status over the entire specimen could be achieved. With the application of a video extensometer a more localised area near the place of the fracture was observable. For local strain measurements the installation of a high-speed camera in combination with digital image correlation was applied. Figure 22.16 shows strain measurement results of a knit-line specimen. The strain progression is quite continuous and shows equable fatigue behaviour also for different loadings.

By using the strain measurement results, a conventional analysis method is the investigation of energy dissipation and its changes with cumulative progress of the fatigue testing [11, 12]. The energy dissipation is determinable by calculating the area of the loading-based appearing hysteresis loops. Changes of size and shape or slope of the loops characterises the fatigue progress.

Results of a 0°-“standard” specimen show Fig. 22.17. The decrease of energy dissipation in the very beginning of the testing might be reasoned by an initial transient effect. Thereafter no significant change of size or slope could be obtained until shortly before break.

Another common approach is the analysis of the modulus [6, 7]. The development of the normalised modulus (E_N/E_0) shows Fig. 22.18. Compared to the

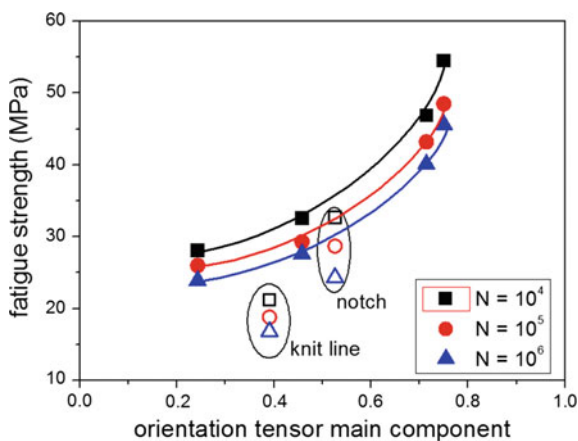


Fig. 22.15 Fatigue strength versus fibre orientation

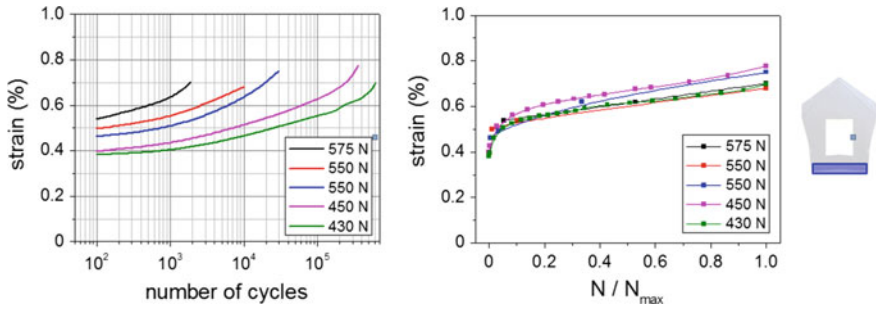


Fig. 22.16 Standardised strain against number of cycles (*left*) and lifetime progress (*right*) for a knit-line “standard” specimen measured with grip displacement method

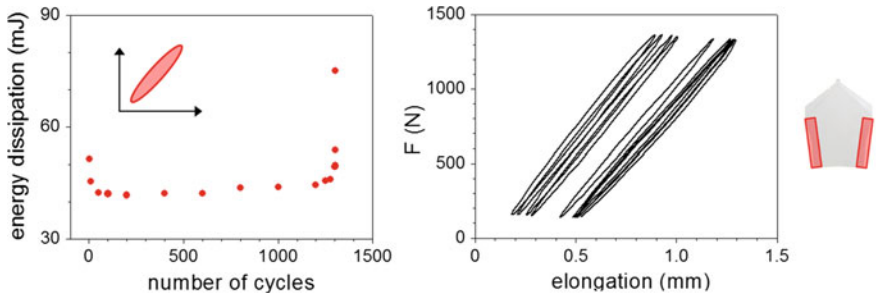


Fig. 22.17 Energy dissipation at different stages of cyclic loading (*left*) and the related hysteresis loops (*right*) for a 0°-“standard” specimen test

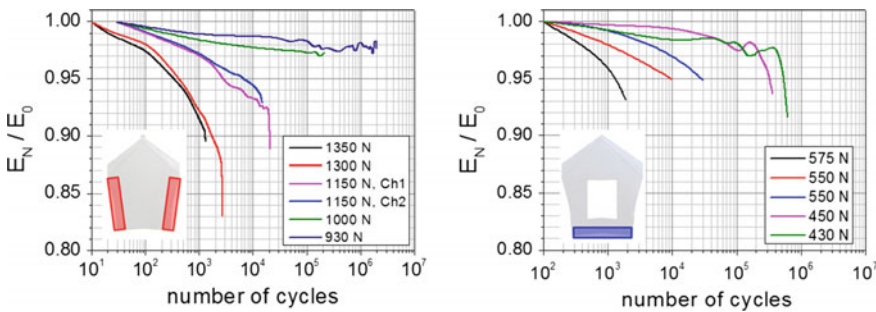


Fig. 22.18 Development of the normalised modulus (E_N/E_0) for a 0° (*left*) and a knit-line (*right*) “standard” specimen for different loadings

0°-position the specimen from the knit-line showed only a slight decline of the modulus, though occasionally there is an intermediate increase observable especially at higher loadings.

Besides the mechanical also temperature analysis methods were applied. An established approach is the measurement of the surface temperature with infrared cameras [7, 8]. The measured temperature development (see Fig. 22.19) corresponds quite well with the characteristic parameters of the mechanical analysis most notably with the energy dissipation. It seems that there are three stages in the progression of the surface temperature during the loading. After a rapid increase in the very beginning, a stage of constant temperature respectively continuous increase of the temperature (depending on the loading) lasting almost to the end of fatigue life appears. Also in the temperature progression a steep rise is observable not until the last cycles of the fatigue loading.

In general the achieved results with all that different analysis approaches gives no possibilities for a reliable lifetime prediction or the ability of an estimation of the actual fatigue status. There are no clear signs of damage until shortly before the fracture. For this reason the determination of local strain by digital image correlation was applied. Therefore the specimens are observed with a high-speed camera. Thus the maximum elongations at different progress of fatigue life could be determined even with unchanged testing frequency. A dot pattern is sprayed on the specimen. By analysing the local changes of this pattern, the local deformations could be visualised.

The progression of the local strain illustrated in Fig. 22.20 shows the advantage of this method. Very often there is an indication of the position of the later crack initiation visible in early stages of the fatigue testing. Sometimes these positions can be correlated to fibre clusters or slight surface imperfections. However an estimation of the actual fatigue life status is so far also with this method impossible. For this purpose the application of acoustic emission equipment appears promising.

One important task of evaluating the fatigue behaviour of SFRP parts is the modelling of fatigue damage accumulation and the prediction of lifetime under cyclic loading conditions. An overview on different approaches is given in [2].

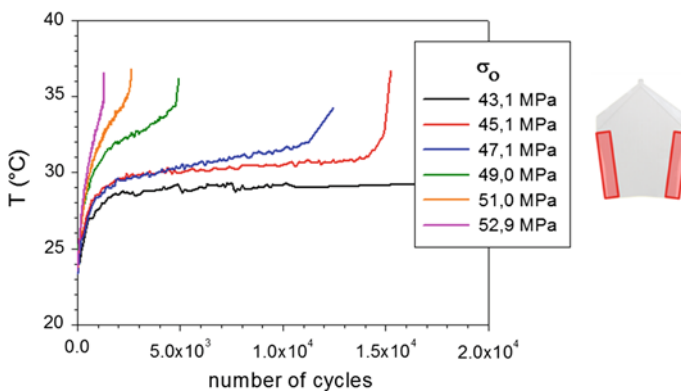


Fig. 22.19 Surface temperature as a function of the number of fatigue cycles of a 0°-“standard” specimen measured with IR-cameras for different loadings

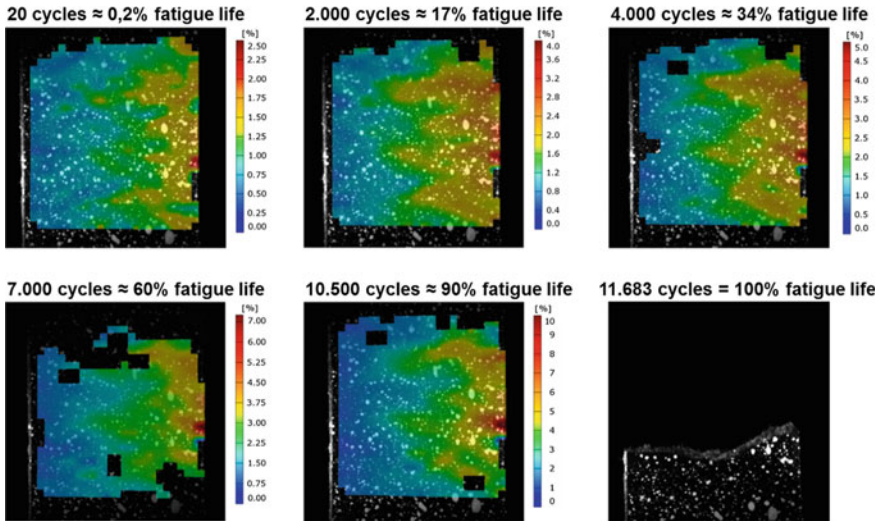


Fig. 22.20 Development of local strain fields obtained by digital image correlation for 90°-“standard” specimen loaded with $\sigma_O = 32$ MPa

Evolutions of size or slope of the hysteretic loop, the non-linear viscoelastic part, the strain energy density and energy dissipation are suitable methods to describe the effects of cyclic loading on the lifetime [2]. To predict the lifetime of injection moulded industrial parts the knowledge of fibre orientations and of local load distribution during application is required. The combination of injection moulding simulation, morphology analysis, cyclic testing and numerical analysis can help to understand, forecast and optimise the fatigue resistance of complex parts. In principle there are two possibilities for numerical analysis: single-fibre approach and continuums mechanics approach. In [49] a micromechanical model for the fibre–matrix interface damages and matrix degradation due to fatigue loading is presented. It consists of a fracture mechanics-based description of fibre debonding, a crack growth rate based approach of the composites fatigue behaviour and a Wöhler valuation for quantification of the matrix damage.

References

1. Bierögel, C., Grellmann, W.: Fatigue loading. In: Grellmann, W., Seidler, S. (eds.) Landolt-Börnstein, New Series Volume VIII/6A3 Mechanical and Thermomechanical Properties of Polymers. Springer, Berlin (2014), Chapter 4.5, pp. 241–285
2. Mortazavian, S., Fatemi, A.: Fatigue behavior and modeling of short fiber reinforced polymer composites: A literature review. *Int. J. Fatigue* **70**, 297–321 (2015)

3. Zhou, Y., Mallick, P.K.: Fatigue performance of an injection-molded short E-glass fiber-reinforced polyamide 6.6. I. Effects of orientation, holes, and weld line. *Polym. Compos.* **27**, 230–237 (2006)
4. Cosmi, F., Bernasconi, A.: Fatigue Behaviour of Short Fibre Reinforced Polyamide: Morphological and Numerical Analysis of Fibre Orientation Effects. *Forni di Sopra* (2010), pp. 239–242
5. Bernasconi, A., Davoli, P., Basile, A., Filippi, A.: Effect of fibre orientation on the fatigue behaviour of a short glass fibre reinforced polyamide-6. *Int. J. Fatigue* **29**, 199–208 (2007)
6. Arif, M.F., Saintier, N., Meraghni, F., Fitoussi, J., Chemisky, Y., Robert, G.: Multiscale fatigue damage characterization in short glass fiber reinforced polyamide-66. *Compos. B* **61**, 55–65 (2014)
7. Esmaeillou, B., Fitoussi, J., Lucas, A., Tcharkhtchi, A.: Multi-scale experimental analysis of the tension-tension fatigue behavior of a short glass fiber reinforced polyamide composite. *Procedia Eng.* **10**, 2117–2122 (2011)
8. Bernasconi, A., Cosmi, F., Taylor, D.: Analysis of the fatigue properties of different specimens of a 10% by weight short glass fibre reinforced polyamide 6.6. *Polym. Test.* **40**, 149–155 (2014)
9. Bernasconi, A., Conrado, E., Hine, P.: An experimental investigation of the combined influence of notch size and fibre orientation on the fatigue strength of a short glass fibre reinforced polyamide 6. *Polym. Test.* **47**, 12–21 (2015)
10. Launay, A., Marco, Y., Maitournam, M.H., Raoult, I., Szmytka, F.: Cyclic behavior of short glass fiber reinforced polyamide for fatigue life prediction of automotive components. *Procedia Eng.* **2**, 901–910 (2010)
11. Pegoretti, A., Riccò, T.: Fatigue crack propagation in polypropylene reinforced with short glass fibres. *Compos. Sci. Technol.* **59**, 1055–1062 (1999)
12. Meneghetti, G., Ricotta, M., Lucchetta, G., Carmignato, S.: An hysteresis energy-based synthesis of fully reversed axial fatigue behaviour of different polypropylene composites. *Compos. B* **65**, 17–25 (2014)
13. Pegoretti, A., Ricco, T.: Crack growth in discontinuous glass fibre reinforced polypropylene under dynamic and static loading conditions. *Compos. A* **33**, 1539–1547 (2002)
14. Palmstingl, M., Koch, T., Salaberger, D., Paier, T.: Morphological impact on the fatigue behaviour of short fibre reinforced polypropylene. *Mater. Sci. Forum* **825–826**, 830–837 (2015)
15. Guild, F.J., Summerscales, J.: Microstructural image analysis applied to fibre composite materials: a review. *Composites* **24**, 383–393 (1993)
16. Salaberger, D., Kannappan, K.A., Kastner, J., Reussner, J., Auinger, T.: Evaluation of computed tomography data from fibre reinforced polymers to determine fibre length distribution. *Int. Polym. Proc.* **26**, 283–291 (2011)
17. Bay, R.S., Tucker III, C.L.: Stereological measurement and error estimates for three-dimensional fiber orientation. *Polym. Eng. Sci.* **32**, 240–253 (1992)
18. Bechtold, G., Gaffney, K.M., Botsis, J., Friedrich, K.: Fibre orientation in an injection moulded specimen by ultrasonic backscattering. *Compos. Part A: Appl. Sci. Manuf.* **29A**, 743–748 (1998)
19. Clarke, A.R., Archenhold, G., Davidson, N.C.: A novel technique for determining the 3D spatial distribution of glass fibres in polymer composites. *Compos. Sci. Technol.* **55**, 75–91 (1995)
20. Eberhardt, C., Clarke, A.: Fibre-orientation measurements in short-glass-fibre composites. Part I: automated, high-angular-resolution measurement by confocal microscopy. *Compos. Sci. Technol.* **61**, 1389–1400 (2001)
21. Yaguchi, H., Hojo, H., Lee, D.G., Kim, E.G.: Measurement of planar orientation of fibers for reinforced thermoplastics using image processing. *Int. Polym. Proc.* **10**, 262–269 (1995)
22. Kim, E.G., Park, J.K., Job, S.H.: A study on fiber orientation during the injection molding of fiber-reinforced polymeric composites (comparison between image processing results and numerical simulation). *J. Mater. Process. Technol.* **111**, 225–232 (2001)

23. Fakirov, S., Fakirova, C.: Direct determination of the orientation of short glass fibers in an injection-molded poly(ethylene terephthalate) system. *Polym. Compos.* **6**, 41–46 (1985)
24. Fisher, G., Eyerer, P.: Measuring spatial orientation of short fiber reinforced thermoplastics by image analysis. *Polym. Compos.* **9**, 297–304 (1988)
25. O’Connell, P.A., Duckett, R.A.: Measurements of fibre orientation in short-fibre-reinforced thermoplastics. *Compos. Sci. Technol.* **42**, 329–347 (1991)
26. Vincent, M., Giroud, T., Clarke, A., Eberhardt, C.: Description and modeling of fiber orientation in injection molding of fiber reinforced thermoplastics. *Polymer* **46**, 6719–6725 (2005)
27. Mönnich, S., Glöckner, R., Becker, F.: Analysis of fibre orientation using μ CT data. In: *Proceedings of 8th European LS-DYNA Conference (Strasbourg, 23/24.05.2011)*. Strasbourg (2011), 15 pages
28. Bernasconi, A., Cosmi, F., Hine, P.J.: Analysis of fibre orientation distribution in short fiber reinforced polymers: a comparison between optical and tomographic methods. *Compos. Sci. Technol.* **72**, 2002–2008 (2012)
29. Eberhardt, C., Clarke, A., Vincent, M., Giroud, T., Flouret, S.: Fibre-orientation measurements in short-glass-fibre composites—II: A quantitative error estimate of the 2D image analysis technique. *Compos. Sci. Technol.* **61**, 1961–1974 (2001)
30. Fu, S.-Y., Mai, Y.-W., Ching, E.C.-Y., Li, R.K.Y.: Correction of the measurement of fiber length of short fiber reinforced thermoplastics. *Compos. A* **33**, 1549–1555 (2002)
31. Pesendorfer, H.: *Morphologische Analyse von Faserverbunden mittels Schliiffverfahren*. Master thesis, TU Wien, Vienna (2015)
32. Advani, S.G., Tucker III, C.L.: The use of tensors to describe and predict fiber orientation in short fiber composites. *J. Rheol.* **31**, 751–784 (1987)
33. Mlekusch, B., Lehner, E.A., Geymayer, W.: Fibre orientation in short-fibre-reinforced thermoplastics I. Contrast enhancement for image analysis. *Compos. Sci. Technol.* **59**, 543–545 (1999)
34. Vélez-García, G.M., Wapperom, P., Kunc, V., Baird, D.G., Zink-Sharp, A.: Sample preparation and image acquisition using optical-reflective microscopy in the measurement of fiber orientation in thermoplastic composites. *J. Microsc.* **248**, 23–33 (2012)
35. Zhu, Y.T., Blumenthal, W.R., Lowe, T.C.: Determination of non-symmetric 3-D fiber-orientation distribution and average fiber length in short-fiber composites. *J. Compos. Mater.* **31**, 1287–1302 (1997)
36. Zak, G., Haberer, M., Park, C.B., Benhabib, B.: Estimation of average fibre length in short-fibre composites by a two-section method. *Compos. Sci. Technol.* **60**, 1763–1772 (2000)
37. Thomason, J.L.: The influence of fibre length and concentration on the properties of glass fibre reinforced polypropylene: 5. Injection moulded long and short fibre PP. *Compos. A Appl. Sci. Manuf.* **33**, 1641–1652 (2002)
38. Bernasconi, A., Cosmi, F., Dreossi, D.: Local anisotropy analysis of injection moulded fibre reinforced polymer composites. *Compos. Sci. Technol.* **68**, 2574–2581 (2008)
39. Köpplmayr, T., Milosavljevic, I., Aigner, M., Hasslacher, R., Plank, B., Salaberger, D., Miethlinger, J.: Influence of fiber orientation and length distribution on the rheological characterization of glass-fiber-filled polypropylene. *Polym. Test.* **32**, 535–544 (2013)
40. Gupta, V.B., Mittal, R.K., Sharma, P.K., Menning, G., Wolters, J.: Some studies on glass fiber-reinforced polypropylene. Part I: Reduction in fiber length during processing. *Polym. Compos.* **10**, 8–15 (1989)
41. Oberbach, K.: Untersuchung des Dauerschwingverhaltens. In: Carlowitz, B. (Ed.): Band 1. *Die Kunststoffe. Chemie, Physik, Technologie*. In: Becker, G. W., Braun D. (Eds.): *Kunststoff-Handbuch*. Carl Hanser, Munich (1990), Chapter 5.3.3, pp. 659–686
42. Höniger, H.: Fatigue behavior. In: Grellmann, W., Seidler, S. (eds.): *Polymer Testing*, 2nd edn. Carl Hanser, Munich (2013), Chapter 4.5, pp. 161–170
43. Domininghaus, H.: *Plastics for Engineers. Materials, Properties, Applications*. Carl Hanser, Munich (1993)

44. Hertzberg, R.W., Manson, J.A., Skibo, M.: Frequency sensitivity of fatigue processes in polymeric solids. *Polym. Eng. Sci.* **15**, 252–260 (1975)
45. Pegoretti, A., Ricco, T.: Crack growth in discontinuous glass fibre reinforced polypropylene under dynamic and static loading conditions. *Compos. A* **33**, 1539–1547 (2002)
46. Kurashiki, K., Ni, Q.-Q., Maesaka, T., Iwamoto, M.: A study on evaluation of fatigue damage of GFRP by infrared thermography. 1st report. Fatigue temperature rise curves of GFRP. *Trans. Jpn. Soc. Mech. Eng. A* **66**, 960–965 (2000)
47. Katunin, A.: Thermal fatigue of polymeric composites under repeated loading. *J. Reinf. Plast. Compos.* **31**, 1037–1044 (2012)
48. Ehrenstein, G.W.: *Faserverbund-Kunststoffe. Werkstoffe, Verarbeitung, Eigenschaften*. Carl Hanser, Munich (2006)
49. Brighenti, R., Carpinteri, A., Scorza, D.: Micromechanical crack growth-based fatigue damage in fibrous composites. *Int. J. Fatigue* **82**, 98–109 (2016)

Chapter 23

Characterisation of the Deformation and Fracture Behaviour of Elastomers Under Biaxial Deformation

K. Schneider, R. Calabrò, R. Lombardi, C. Kipscholl, T. Horst,
A. Schulze, S. Dedova and G. Heinrich

Abstract A new biaxial testing machine from COESFELD is presented, which enables essential new and more comprehensive opportunities for non-destructive and fracture mechanical testing of elastomers, mainly under dynamical load. Some possible applications are described in detail.

23.1 Introduction

Elastomers are a widely used group of materials, which are used under very different loading conditions. For an appropriate use of these materials it is necessary to model devices under application oriented conditions. Therefore besides the straightforward quasi-static and dynamic unidirectional tensile, compression and

K. Schneider (✉) · R. Lombardi · A. Schulze · S. Dedova · G. Heinrich
Leibniz Institute for Polymer Research Dresden e.V., Dresden, Germany

R. Calabrò
Department of Chemistry, Materials and Chemical Engineering,
Polytechnic University of Milan, Milan, Italy

R. Lombardi
University of Naples Federico II, Naples, Italy

C. Kipscholl
Coesfeld GmbH & Co. KG, Dortmund, Germany

S. Dedova · G. Heinrich
Dresden University of Technology, Dresden, Germany

T. Horst
Faculty of Automobile and Mechanical Engineering, University of Applied Sciences
Zwickau, Zwickau, Germany

A. Schulze
Chemnitz University of Technology, Chemnitz, Germany

R. Lombardi
Bridgestone Technical Center Europe, Rome, Italy

shear tests with the material also tests under well-defined biaxial load are essential. As well for the characterisation of the failure behaviour of elastomers besides the classical uniaxial Tear Fatigue Test also investigations under complex application-related load are preferable. In cooperation between Coesfeld GmbH & Co. KG Dortmund and the Leibniz-Institut für Polymerforschung Dresden (IPF) a Biax Tester was designed, built and checked [1–3]. This new biaxial testing machine enables essential new and more comprehensive opportunities for non-destructive and fracture mechanical testing of elastomers, mainly under dynamical load. The device and some first results shall be presented here in detail.

23.2 Concept of the Biaxial Test Stand

An outline of the Biax Tester for Elastomer Materials is shown in Fig. 23.1. It consists mainly of four separately driven electro-mechanical linear motors, each with load cell and displacement sensor as well as a clamping system, which are arranged paired on opposite sites and have each a displacement range of initially 30 mm. By certain enhancement of the clamping system in the meantime the displacement of each axis could be increased to 120 mm.

The motors are controlled separately; they can transfer different deformation (overall load configurations) to the sample. The loads were defined via displacement profiles and are freely configurable (e.g. sine wave, pulse, rectangle, triangle

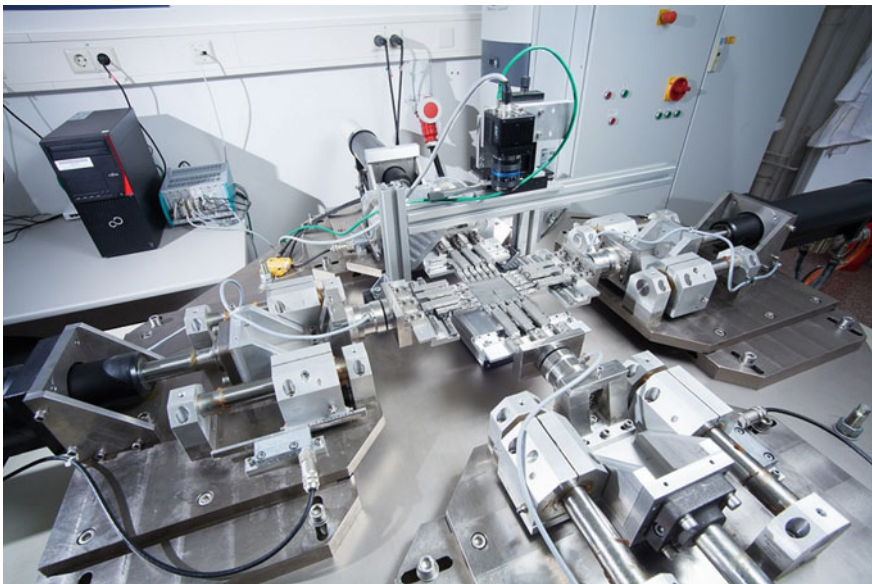


Fig. 23.1 Biax Test Stand of Coesfeld GmbH & Co. KG

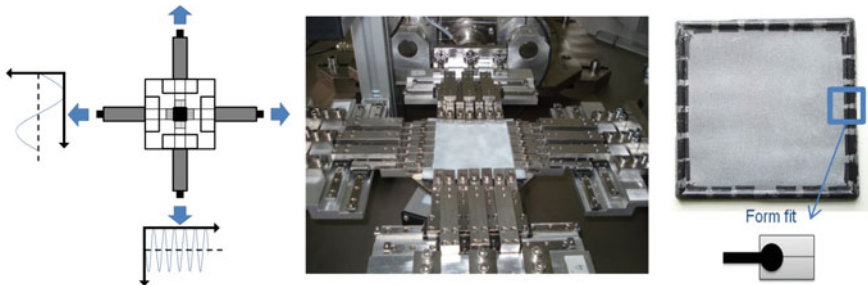


Fig. 23.2 Sketch of the test stand with individually configurable displacement profiles for each axis (*left*); clamping system of the Biax Tester, here with 7 individual clamps per axis (*middle*), principle of clamping by form fit (*right*)

or also free definable as external file). The real clamp displacement is always monitored by a displacement sensor. For the preferable dynamic tests each motor has an adaptive controller which realises the desired deformation profile. After a few cycles an optimal target performance is realised. Each linear motor is equipped with a load cell which is insensitive with respect to transversal load. The load cells carry directly the clamping system.

Each clamping system consists of a rail with up to 10 individual clamps with a width of each 10 mm, which can slide by a wheel bearing transversal to the loading axis, see Fig. 23.2.

In the case of clamps with traction the local load of the clamps causes irreproducible deformations. Therefore here preferable clamps with form fit are used and the rectangular (or squared) samples of 1–2 mm thickness should have a cylindrical edge with a diameter of 4 mm, which fits the clamp, see Fig. 23.2, right side. To prevent undefined displacements at the vertices the external clamps of each rail can be connected with each other.

A good adjustment of the motors is necessary to prevent friction and transversal load at the clamps. During measurement with frequencies above 10 Hz it is necessary to have the inertia of the clamps in mind to correct the monitored load (Table 23.1).

Mainly for the investigation of heterogeneous stress stages, like e.g. in samples with a crack, it is necessary to capture the 2D strain stage of the sample by image processing techniques. This is possible following the deformation of a random pattern at the sample surface and evaluation e.g. by ARAMIS (Digital Image Correlation (DIC), Fa. GOM, Braunschweig, Germany), or by recording of the crack contour at homogeneous illumination of the sample of the bottom side (Digital Image Elaboration (DIE)). For these tasks an infrared (IR) camera is used, which can be mounted feely on the ground plate by magnetic bases. The illumination of the sample is realised from top or bottom side, see Fig. 23.3.

The camera can be adapted for the different tasks, especially recording the whole sample as well as of individual details of the sample each with optimal resolution.

Table 23.1 Specifications of the Biax Test Stand

Excitation	Each axis separately or also pair-wise parallel feed
Displacement profiles	Sine wave, Gauss pulse, triangle, rectangle, free defined by the user
Load speed	Maximum 50 Hz, practically 10 Hz, maximum displacement each up to 30 mm (meanwhile improved to 60 mm)
Load range	2000 N
Data acquisition	Whole cycles, individual cycles or individual parameters of the cycles
Image acquisition	Continuous or triggered by individual events
Sample size	Rectangular or squared with up to $100 \times 100 \text{ mm}^2$, preferable $85 \times 85 \text{ mm}^2$ with circumferential cylindrical bulge with a diameter of 4 mm

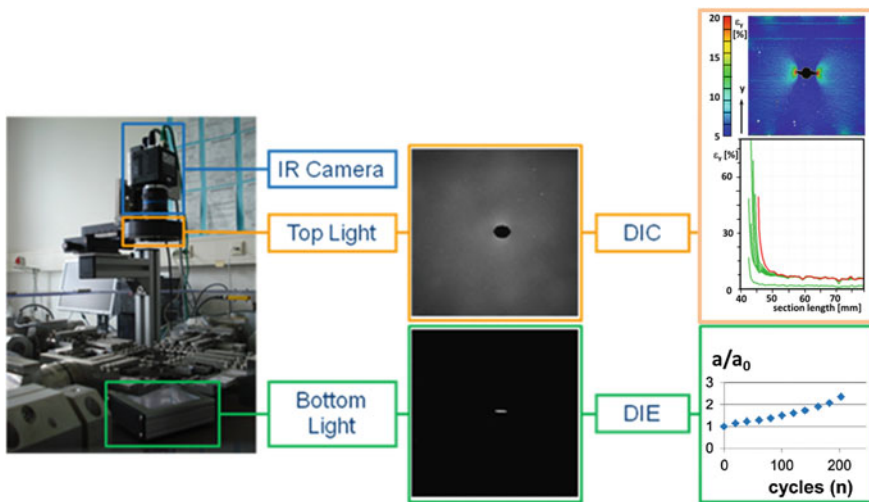


Fig. 23.3 Concept of the image acquisition system at the Biax Test Stand: experimental arrangement (*left*), captured images (*middle*), estimated diagrams: strain transversal to the crack direction versus the distance to the crack tip and 2D strain field (*right side, top*), increase of the crack length versus the number of loading cycles (*right side, bottom*)

23.3 Upgrading of a Biaxial Testing Method

The initial clamping system has some limits for the performance of experiments. These are mainly the restriction of the maximum length of stroke for each side (60 mm or 77% deformation for each axis) and the weight of the moving parts. The last one allows working with high deformation only with relative low frequencies due to the high inertial force.

For this reason the new clamping system was designed and built. The important points were:

- Increase of biaxial deformation range up to 150%,
- Possibility to test materials at higher frequencies,
- Possibility of making the crack propagation tests (relatively large specimen),
- Provide the homogeneous deformation field (for the error-free local deformation field analysis).

23.3.1 New Clamping System for High Biaxial Deformation

The new clamping system is shown on the Fig. 23.4. The new design of the clamp rails allows the measurement up to 150% biaxial deformation. This possibility is really important for such experiments like the parameterisation of constitutive models.

The new concept includes the weight reduction. New system is made of a carbon fibre composite and reaches much lower weight while retaining the same stiffness of the system.

The new system was tested under harmonic loading and compared with the old one. For this reason the layout parameters of Biaxial Test Stand were used. Due to the constructing changes and weight reduction the new design enables a much higher amplitude–frequency working range, compared with the old system (see Fig. 23.4 left).

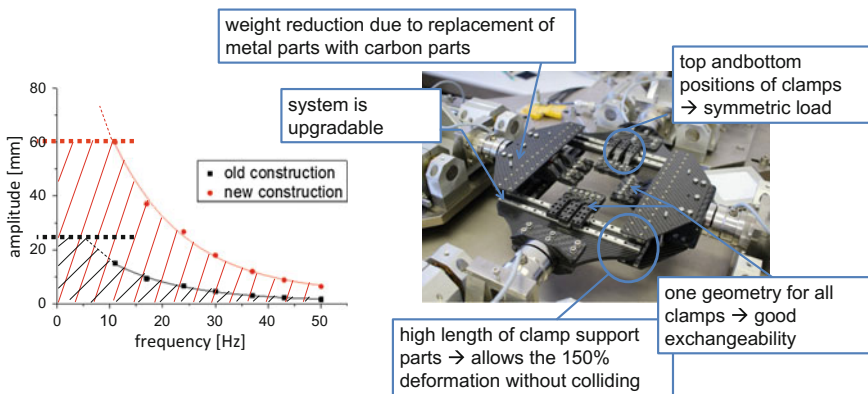


Fig. 23.4 New clamping system (*right*) and the possible amplitude–frequency working range (*left*)

23.3.2 Specimen Geometry

During the previous experiments some inhomogeneities in the deformation field, especially in the near-clamps area, were detected. This effect rises with a growing strain. It leads to errors in the strain field analysis which is necessary for example for the J -integral. Before the improvement of the new specimen geometry, the different concepts, used for different materials, were analysed.

Some biaxial specimens for rubber are known from the literature [4, 5]. The both concepts provide biaxial conditions in the middle of the specimen. It allows measuring the stress–strain behaviour, but cannot be used for the crack propagation experiments. For another materials (for example metals) some another geometries are used [6–12]. Using some of such concepts the crack grow experiments are possible. However, the specimen geometries in these cases cannot be used for the high strains. Some of the concept shows the increase of homogeneity by reduction of the middle thickness of the specimen. This idea was adopted and analysed for the current specimen geometry of Biax Test Stand.

The new geometry consists of two thicknesses of the plate—the middle area has a thickness of 1.5 mm and the border area with a thickness of 3 mm and width of 7 mm. At the edge there is again the cylindrical bulge for the form-fit. Figure 23.5 shows the FEM simulation of the deformation field of the two specimen geometries—currently used geometry and a new concept. The simulation was made using ANSYS software and Ogden model 3th order for a rubber material from [13]. For the simulation one quarter of the specimen was used.

The same state of applied residual strain leads to a different distribution of local strain over the sample. The deformed area of the previous sample shows a higher inhomogeneity compared with the new one. The inhomogeneous range has a width of about 20 mm from each specimen edge. With a stretched size of 158 mm this is equivalent to about 25% of the length (for each axis). In the middle area of the specimen there are no such distinct strain differences.

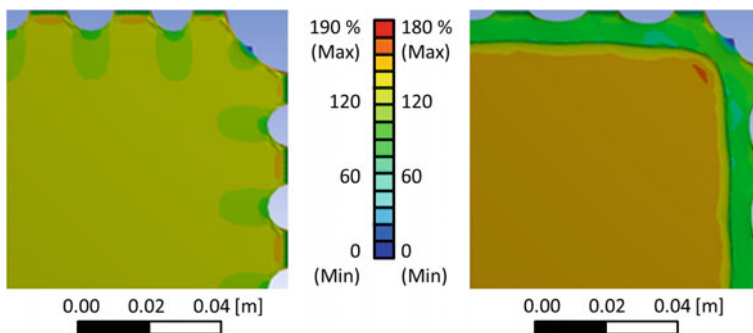


Fig. 23.5 FE analysis of elastic equivalent strain for the current specimen geometry (*left*) and new specimen geometry (*right*) ($\Delta\varepsilon = 100\%$)

The new specimen geometry ensures a high homogeneity of the biaxial strain in the middle area. The effect of local clamp inhomogeneities becomes compensated in the thicker edge area. This area corresponds to about 9% of the stretched specimen length.

23.3.3 Crack Propagation with the New Specimen

The improvements of the new geometry for the crack propagation experiments was analysed by FEM simulation and compared with the measured results. For this reason a notched sample (notch length of 30 mm) was used and stretched up to 48 mm in the y-direction. After that the strain field was analysed with the ARAMIS system (Fig. 23.6a).

The same experiment was repeated for the current and new geometry using FE simulation (Fig. 23.6b, c).

The measured and simulated current geometry shows a good agreement of results (Fig. 23.6a, b). The thick edge region of a new specimen remains inviolated and has no effect on the crack tip. That means that the new specimen can be used for the crack propagation experiments in the same way like a current geometry.

23.4 Material

Some representative tests were performed using natural rubber (NR), solution styrene–butadiene rubber (SBR) and hydrated acrylonitrile–butadiene rubber (HNBR) with carbon black (CB) as filler. Composition and labeling are shown in Table 23.2. Squared samples with a lateral length of 85 mm and a circumferential bulge of 4 mm were vulcanised in the IPF.

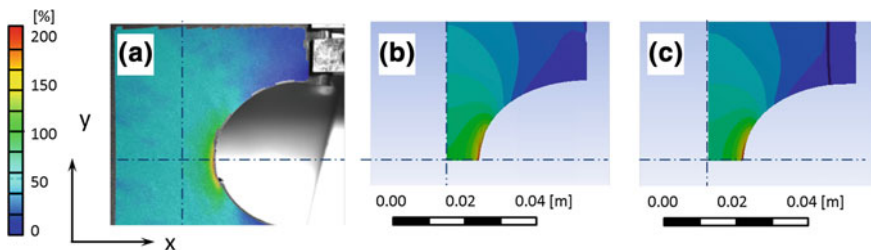


Fig. 23.6 FE analysis of equivalent strain for current and new geometry ($\varepsilon_x = 0$; $\varepsilon_y = 62\%$): **a** measured specimen, **b** current geometry (simulation), **c** new geometry (simulation)

Table 23.2 Materials

Labeling	Matrix	Filler
NR/50phrCB	Natural rubber	50 phr CB N550
SBR/50phrCB	Solution styrene–butadiene rubber	50 phr CB N550
HNBR/30phrCB	Hydrated acrylonitrile–butadiene rubber	30 phr CB N339

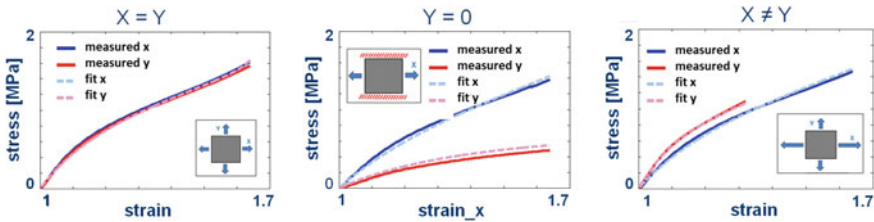


Fig. 23.7 Stress–strain behaviour under different load, measured values and values fitted by the extended tube model

23.5 Results

23.5.1 Material Behaviour Under Biaxial Load

The Biax Tester enables the estimation of stress–strain behaviour under complex load, e.g. the ratio of the x- and y-strain can be chosen free. Afterwards the different tests can be fitted by a suitable model, e.g. the extended tube model, see Fig. 23.7.

Like in the uniaxial case the characterisation of the stress–strain behaviour under biaxial load shows differences in loading and unloading curves (Fig. 23.8). Comparing both curves it is possible to split the total energy W_t into elastically stored and dissipated energy resp. W_e and W_d according to

$$W_d = W_t - W_e = \int_{\epsilon_r(\text{loading})}^{\epsilon_{\max}} \sigma_{\text{loading}} d\epsilon - \int_{\epsilon_r(\text{unloading})}^{\epsilon_{\max}} \sigma_{\text{unloading}} d\epsilon. \quad (23.1)$$

Here ϵ_r is the strain in the unloaded state during loading and unloading step, ϵ_{\max} the maximal strain; σ_{loading} resp. $\sigma_{\text{unloading}}$ are the stresses during the loading and unloading step.

As example a set of biaxial tests was performed with CB-filled natural rubber NR/50phrCB and strains ϵ_1 and ϵ_2 resp. in the range of 0–35% at 1 Hz. Pre-conditioning was performed by 500 cycles at maximum displacement. The measurement of the force–displacement diagrams was performed always after 100 cycles at the nominal strain, see Fig. 23.9.

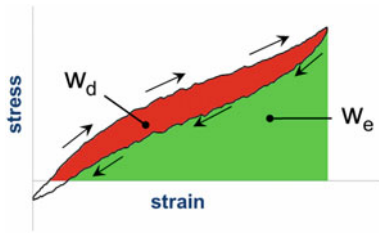
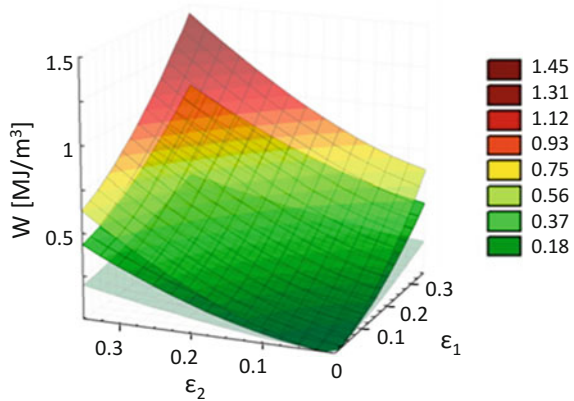


Fig. 23.8 Separation of the performed work to elastically stored and dissipated energy

Fig. 23.9 Total energy (upper surface), elastically stored energy (median surface) and dissipated energy (bottom surface) via strain at biaxial load of NR/50phrCB



In the range under investigation the elastically stored energy compared with the total applied energy is in the range of $W_e/W_t = 0.6-0.7$, while the dissipated amount is at $W_d/W_t = 0.3-0.4$. Thereby the amount of dissipated energy decreases slightly with increasing strain. The investigations will be continued within a larger strain range to check the parameterisation of material laws for bulk modelling.

23.5.2 Strain Amplification at the Crack Tip of a SENT Sample

By digital image correlation it is possible to estimate strain fields of 2D sample. So it is also possible to get strain amplification in the ligament of a SENT specimen (single-edge-notched tensile sample). In Fig. 23.10a certain strain step of a filled natural rubber sample NR/50phrCB is shown. Because the strain amplification is dependent on the sharpness of the pre-notch, the tip of the initial crack of 6 mm was sharpened by a razor blade.

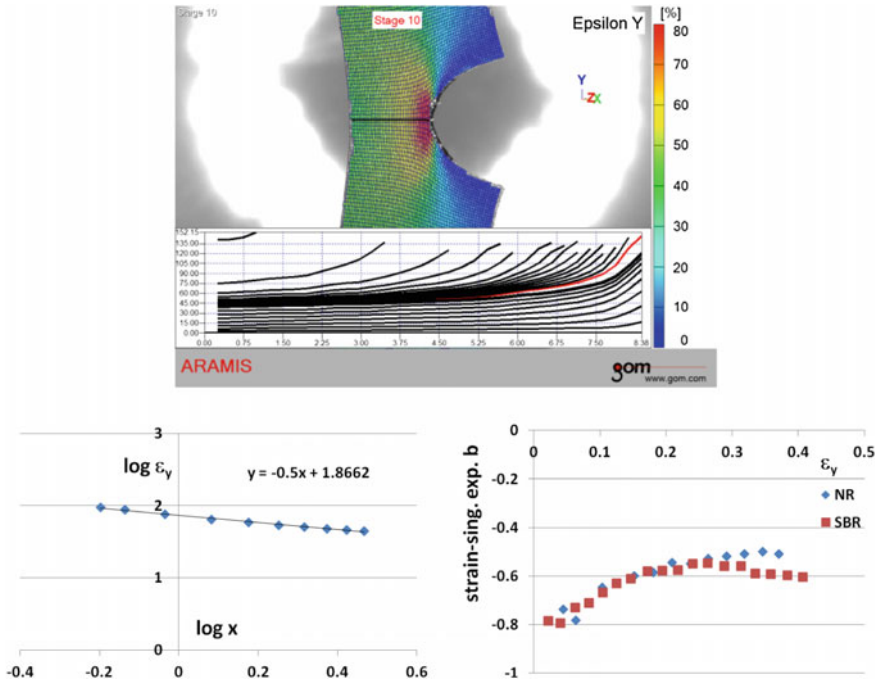


Fig. 23.10 Strain field around the crack tip of a SENT sample (*top*), estimation of the exponent of the strain singularity by linear regression of the strain versus the distance to the crack tip on a log-scale for NR/50phrCB (*bottom left*) as well as dependence of the exponent of strain singularity from the external applied strain for NR/50phrCB and SBR/50phrCB (*bottom right*)

The strain transversal to the crack propagation ϵ_y can be approximated by a power law as

$$\epsilon_y = kx^b. \tag{23.2}$$

Here b is the exponent of the strain singularity, k a pre-exponential factor. It should have the value of -0.5 [14]. In Fig. 23.10 the procedure for the estimation of b is illustrated and the exponents of two different materials are shown.

23.5.3 Crack Propagation Under Biaxial Load

Figure 23.11 shows an example of stable crack propagation. A centered pre-crack in the sample (Griffith crack, initial length 6 mm, crack tips sharpened by a razor blade) propagates under cyclic loading with amplitudes of $\epsilon_y = 25\%$ transversal to the crack and $\epsilon_x = 45\%$ in crack direction initially stable before spontaneous failure happens.

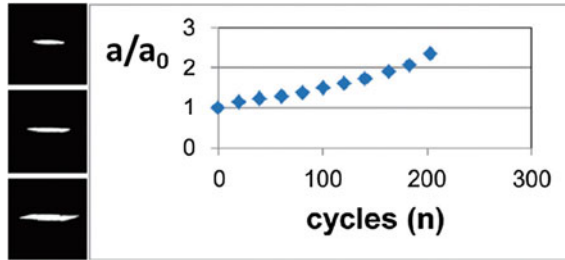


Fig. 23.11 Propagating crack after 0, 80 and 160 cycles respectively (*left side*) and change in the crack length a with the number of cycles, divided by the initial crack length a_0 ; harmonic loading of filled natural rubber NR/50phrCB during stable crack propagation at 1 Hz and strain amplitude $\varepsilon_y = 25\%$ in transversal direction (*crack opening*), $\varepsilon_x = 45\%$ in crack direction (*horizontally*)

23.5.4 Crack Propagation and Estimation of the Tearing Energy

Fracture mechanical characterisation of elastomers is possible by the concept of tearing energy, introduced by Rivlin and Thomas [15]. The tearing energy is the energy, which is necessary to increase the fracture surface by an infinitesimal amount. It can be estimated via the loss of elastically stored energy during infinitesimal crack propagation as

$$T = - \left. \frac{dW}{h_0 da} \right|_{l=\text{const.}} \quad (23.3)$$

Here W is the strain energy, h_0 the sample thickness and da the increment of the crack length. The differentiation dW/da has to be performed with constant displacement l of the boundaries. The work of external forces is zero.

For practical applications the tear fatigue test for rubber is established. Here a narrow specimen with a lateral pre-crack is loaded cyclically and the crack propagation is monitored. This test recently was modified in that way, that also pure-shear specimens with pre-crack can be used. Those specimen allow a more reliable estimation of the tearing energy [16, 17].

The evaluation of the measurements will be performed in analogy to the classical pure-shear test. The propagation of the crack on both sides of the homogeneous stretched resp. failed sample is monitored; the ratio of both values is estimated. Both evaluations were performed on the basis of the expressions for the estimation of the tearing energy in the case of self-similar crack propagation [15]. Numerous tests showed that the initial crack under biaxial load often becomes deflected yet in the first stage of crack propagation. Therefore the classical evaluation is not possible in these cases.

An alternative fracture mechanical characterisation can be performed using a hybrid method. The mean idea is that the hyper-elastic behaviour of the elastomers

can be characterised by certain parameters of an appropriate material model, which is parameterised by a set of different homogeneous deformation states. In the present case the Ogden model [18] as well as the extended tube model of rubber elasticity [19, 20] were used successfully. After the estimation of the deformation fields of the notched sample, using the material model, the elastic energy density is estimated and by this the related stress fields within the sample.

Generally there are two opportunities to estimate the tearing energy: On the one hand the direct evaluation of the elastically stored energy in the sample and its difference between two subsequent states with a small difference in the crack length, on the other hand the estimation of the J -integral [21], performing a line integral around the crack tip. Both methods are not restricted to self-similar crack propagation but also valid in the case of crack deflection. Therefore they are especially suitable for the use at the Biax Tester.

In the following the utilization of the J -integral shall be demonstrated. Here it is advantageous to use an integration path far away from the crack tip. This avoids experimental uncertainties in the estimation of the strain in regions of high displacement gradients in the direct vicinity of the crack. A vectorial form of the J -integral for large deformations will be evaluated [22–24] as

$$J = \int_{\Gamma} [\mathbf{W}^* \mathbf{I} - \mathbf{F}^T \mathbf{P}] \mathbf{n} \, d\Gamma. \quad (23.4)$$

Here \mathbf{W}^* is the elastic energy density, \mathbf{I} the unit vector, \mathbf{F} the deformation gradient, \mathbf{P} the 1st Piola-Kirchhoff stress tensor and \mathbf{n} the normal vector during the integration along a path Γ around the crack tip. In the case of hyperelasticity the stress \mathbf{P} can be written as

$$\mathbf{P} = \frac{\partial \mathbf{W}^*}{\partial \mathbf{F}} \quad (23.5)$$

(\mathbf{W}^* —elastic energy density, \mathbf{F} —deformation).

The components of the J -integral vector parallel to the tangent of the crack contour at the crack tip can be interpreted fracture mechanically as tearing energy [25, 26].

The applicability of this method was shown in the case of a pre-cracked squared sample under pure shear load (strain in crack direction was prevented). The values of the J -integral were compared with the values, estimated by the formula of Rivlin and Thomas for the estimation of the tearing energy for such a specimen

$$T = W^* h_0, \quad (23.6)$$

with the thickness h_0 of the specimen.

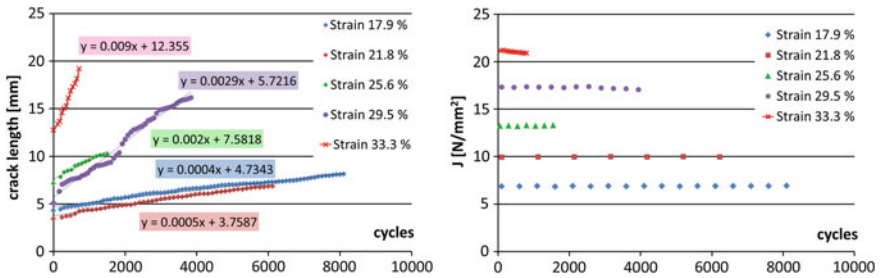


Fig. 23.12 Crack length versus the number of cycles, estimated at a hydrated acrylonitrile–butadiene rubber HNBR/30phrCB, with a sample under pure shear load (*left*) as well as tearing energy, estimated by the *J*-integral concept at different external load (*right*)

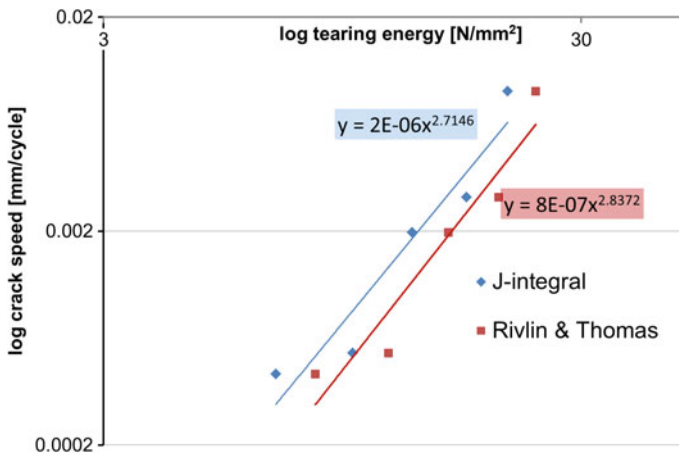


Fig. 23.13 Paris plot for a hydrated acrylonitrile–butadiene rubber (HNBR/30phrCB), estimated by the *J*-integral method as well as the method of Rivlin and Thomas, based on measurements of the Biax Tester

The measurements were performed at a hydrated acrylonitrile–butadiene rubber HNBR/30phrCB at squared samples by fixing the sample in crack direction and uniaxial load in transversal direction. Like in the case of the classical pure-shear specimen a constant crack propagation speed can be found, see Fig. 23.12.

In the Paris plot the tearing energies are shown, estimated with respect to the Rivlin-and-Thomas-method as well as the *J*-integral concept which allow conclusions about crack resistance of the samples. The small systematic differences are caused by dissipative processes within the bulk material, because the condition of hyperelasticity is not fulfilled sufficiently; see Fig. 23.13.

23.6 Conclusion

The new Biax Test Stand of Coesfeld strongly extends the static as well as dynamic characterisation techniques of elastomers. It delivers parameters for constitutive materials modelling under complex load, but also enables to trail the crack propagation under static as well as dynamic load, like it was shown at several examples. For a practice-oriented modelling of elastomer components also a quite complex characterisation is inevitable.

References

1. Biax Tester for Elastomer Material: Information brochure of Coesfeld GmbH & Co. KG., http://products.coesfeld.com/WebRoot/WAZ/Shops/44402782/5238/4E9A/BB18/5A3B/993E/D472/521A/76A8/61-490_Biastester_engl.pdf (01.06.2017)
2. Schneider, K., Calabrò, R., Lombardi, R., Kipscholl, C., Horst, T., Schulze, A., Heinrich, G.: Charakterisierung und Versagensverhalten von Elastomeren bei dynamischer biaxialer Belastung. *KGK–Kautsch. Gummi Kunstst.* **67**, 48–52 (2014)
3. Heinrich, G., Schneider, K., Calabrò, R., Lombardi, R., Kipscholl, C., Horst, T., Schulze, A., Gorelova, S.: Fracture behaviour of elastomers under dynamic biaxial loading conditions. *Tire Technol. Int.* 35–37 (2014)
4. Duncan, B.C.: Test Methods for Determining Hyperelastic Properties of Flexible Adhesives. NPL Report CMMT(MN)054, National Physical Laboratory, Teddington (1999)
5. Physical Testing Service: Information brochure of Axel Products Inc., <http://www.axelproducts.com> (01.06.2017)
6. Müller, W., Pöhlant, K.: New experiments for determining yield loci of sheet metal. *J. Mater. Process. Technol.* **60**, 643–648 (1996)
7. Kuwabara, T., Kuroda, K., Tvergaard, V., Nomura, K.: Use of abrupt strain path change for determining subsequent yield surface: Experimental study with metal sheets. *Acta Materialia*, 2071–2079 (2000)
8. Gozzi, J., Olsson, A., Lagerqvist, O.: Experimental investigation of the behavior of extra high strength steel. *Soc. Exp. Mech.* **45**, 533–540 (2005)
9. Yu, Y., Wan, M., Wu, X., Zhou, X.: Design of a cruciform biaxial tensile specimen for limit strain analysis by FEM. *J. Mater. Process. Technol.* **123**, 67–70 (2002)
10. Kelly, D.: Problems in creep testing under biaxial stress systems. *J. Strain Anal. Eng. Des.* **11**, 1–6 (1976)
11. Demmerle, S., Boehler, J.: Optimal design of biaxial tensile cruciform specimens. *J. Mech. Phys. Solids* **41**, 143–181 (1993)
12. Quak, G.: Biaxial testing of sheet metal: an experimental–numerical analysis. Master thesis, Eindhoven University of Technology, Eindhoven (2008)
13. Treloar, L.R.G.: Stress strain data for vulcanized rubber under various types of deformation. *Trans. Faraday Soc.* **40**, 59–70 (1944)
14. Broek, D.: *Elementary Engineering Fracture Mechanics*. Martinus Nijhoff Publishers, Dordrecht (1986)
15. Rivlin, R.S., Thomas, A.G.: Rupture of rubber. I. Characteristic energy of tearing. *J. Polym. Sci.* **10**, 291–318 (1953)
16. Stoček, R., Heinrich, G., Gehde, M., Kipscholl, R.: Analysis of dynamic crack propagation in elastomers by simultaneous tensile- and pure-shear-mode testing. In: Grellmann, W., Heinrich, G., Kaliske, M., Klüppel, M., Schneider, K., Vilgis, T.A. (eds.) *Fracture Mechanics*

- and Statistical Mechanics of Reinforced Elastomeric Blends. Springer, Berlin (2013), pp. 269–301
17. Stoček, R.: Dynamische Rissausbreitung in Elastomerwerkstoffen. PhD thesis, Technische Universität Chemnitz, Chemnitz (2012)
 18. Ogden, R.W.: Non-linear Elastic Deformation. Dover Publications, Mineola New York (1984)
 19. Kaliske, M., Heinrich, G.: An extended tube-model for rubber elasticity: Statistical-mechanical theory and finite element implementation. *Rubber Chem. Technol.* **72**, 602–632 (1999)
 20. Klüppel, M., Schramm, J.A.: Generalized tube model of rubber elasticity and stress softening of filler reinforced elastomer systems. *Macromol. Theory Simul.* **9**, 742–754 (2000)
 21. Rice, J.R., Rosengren, G.F.: Plane strain deformation near a crack in a power law hardening material. *J. Mech. Phys. Solids* **16**, 1–12 (1968)
 22. Maugin, G.A.: Material Inhomogeneities in Elasticity. Applied Mathematics and Mathematical Computation, Vol. 3. Chapman & Hall/CRC, Boca Raton (1993)
 23. Maugin, G.A., Muschik, W.: Thermodynamics with internal variables. Part I. General concepts; Part II. Applications. *J. Non-Equilib. Thermodyn.* **19**, 217–249, 250–289 (1994)
 24. Maugin, G.: Material forces: concepts and applications. *Appl. Mech. Rev.* **48**, 213–245 (1995)
 25. Behnke, R., Dal, H., Geißler, G., Näser, B., Netzker, C., Kaliske, M.: Macroscopical modeling and numerical simulation for the characterization of crack and durability properties of particle-reinforced elastomers. In: Grellmann, W., Heinrich, G., Kaliske, M., Klüppel, M., Schneider, K., Vilgis, T.A. (eds.) *Fracture Mechanics and Statistical Mechanics of Reinforced Elastomeric Blends*, pp. 167–226. Springer, Berlin (2013)
 26. Schulze, A.: Analyse der Verzerrungsfelder gekerbter Elastomerproben unter ein- und zweiachsiger äußerer Belastung. Diploma thesis, Technische Universität Chemnitz, Chemnitz (2012), 269–301

Chapter 24

Influence of Thermal Ageing Process on the Crack Propagation of Rubber Used for Tire Application

R. Stoček, O. Kratina, P. Ghosh, J. Maláč and R. Mukhopadhyay

Abstract The present work studies the influence of thermal aging behaviour of rubber compounds based on natural rubber (NR), styrene–butadiene rubber (SBR) and their blend NR/SBR 60/40 on dynamic-mechanical and fatigue crack growth properties. The thermal ageing at the temperatures 70 and 110 °C has been applied, which closely simulates the real service conditions of tires. Dynamic mechanical analysis (DMA) and fatigue crack growth (FCG) properties were characterised for the aged samples. The loss compliance J'' has been determined as a parameter, which effectively is detecting the embrittlement or softening/hardening behaviour of the aged rubber. Finally, the FCG studies revealed that increase in aging temperature has deleterious effect on crack growth resistance as was reflected in all the aged materials.

24.1 Introduction

Tire is a key component in a car and performs multiple functions. These include carrying vehicle weight, transmitting tractive and braking forces, cushioning against terrain as well as road surface irregularities and many more. In service, tires are subjected to highly dynamic loading, varying road asperities as well as are exposed to physical processes caused due temperature fluctuation, ozone concentration, solar radiation, fluid medium, etc. These extreme requirements have a significant effect on the fatigue and failure of tire material and lead to the degradation of the

R. Stoček
PRL Polymer Research Lab s.r.o, Zlín, Czech Republic

R. Stoček (✉) · O. Kratina · J. Maláč
Centre of Polymer Systems, Tomas Bata University in Zlín, Zlín, Czech Republic

O. Kratina · J. Maláč
Faculty of Technology, Department of Polymer Engineering, Tomas Bata University in Zlín,
Zlín, Czech Republic

P. Ghosh · R. Mukhopadhyay
Hari Shankar Singhanian Elastomer & Tyre Research Institute, Kankroli, Rajasthan, India

mechanical properties of rubber matrix. The initiation of local instability in tire due to fatigue is particularly caused by the nucleation of micro-crack. Its propagation may cause dangerous consequences because of the catastrophic failure of tires leading to fatal accidents due to loss of vehicle control. Hence the understanding of the crack initiation and its propagation in rubber with respect to the applied varied physical processes as well as loading conditions is a subject of high scientific interest. The better understanding of the subject will improve the safety, higher durability and life service of the tire as well. Tires generally are made of rubber compounded with various additives and filled with different types of reinforcing fillers (primarily carbon black and silica). It is now a very common practice to use blends of two rubbers and sometimes three to achieve desired performance of the product. The combination of natural rubber (NR), butadiene rubber (BR) or styrene-butadiene rubber (SBR) finds vast application in various tire components. Therefore the present work was focused on the study of NR/SBR blend, which is commonly used as tread and sidewall component in tire.

It is well known that the mechanical properties, especially fracture behaviour depend on the structure of rubber matrix. Particularly the characteristic behaviour are based on the filler network build with the nanoparticles, size of filler cluster, interaction of filler-filler and polymer-filler bonds and the specific surface of filler under the identical compounding conditions [1, 2]. The effect of rubber reinforcement caused due to rubber modification with various fillers on crack or fatigue resistance has been studied by several researchers [1, 3, 4] and are well described. Lake and Lindley [5] investigated the effect of carbon black on the fatigue behaviour of rubbers. They found that the addition of carbon black considerably reduces the temperature dependence of fatigue behaviour of SBR, but no such effect was observed in NR. In NR, hysteresis occurs mainly from crystallisation at high strain and is relatively unaffected by changes in temperature or frequency while the hysteresis of SBR is due to internal viscosity which is continually varying. Further, the addition of carbon black into NR compounds reduces the crack growth because of crystallisation occurring in regions of high constraint due to the filler particles and thus in the vicinity of the crack tip, where high strain locally occurs [6].

Tire rubber components are very much subjected to thermal ageing due to internal heat generation because of viscoelastic losses during rolling. For instance, as reported in [7], tread and sidewall experience temperatures of about 100 and 60 °C, respectively. Several researchers [8–10] have studied the thermal ageing characteristics of rubber. Studies of ageing behaviour using dynamic-mechanical analysis can also be found in earlier publications [1, 11–13]. However, the investigation on the relationship between dynamic properties of aged rubber and fatigue crack growth is rarely done.

The main factors influencing the rubber ageing behaviour are thermal processes with the simultaneous oxidative attack. In vulcanisates, the bond energy between sulfur crosslink atoms and the polymer backbone has highest influence on resistance against thermal effects. If the rubber is subjected to thermal ageing, it is necessary to observe the influence of oxidation and diffusion of oxygen. In the case of relatively low temperature, it has been observed that for cured rubber diffusion

predominates and therefore there is slow oxidation throughout the rubber material. On the contrary, as the thermal activity increases, the rate of oxidation increases significantly than the rate of diffusion. Thus a substantial oxidation occurs on the surface at higher temperature and a brittle oxidised surface is formed. The critical stress of polymer chains in an oxidised rubber surface occurs in a lower strain compared to the non-oxidised material which indicates the degradation of mechanical properties of rubber. The mechanical property degradation is reflected in important dynamic properties like complex modulus, E^* and loss factor, $\tan \delta$. The increase or decrease of E^* with ageing indicates hardening or softening of the rubber. The variation of loss factor reflects in terms of ductility and embrittlement of the rubber surface as well as matrix.

Generally the ageing is interconnected to loss of mechanical properties over the whole lifetime of rubber matrix or tire components [14]. Most of the efforts in this field of research were mainly concentrated to the observation of crack propagation or rupture of rubber test specimens under quasi-static loading conditions with no relationship to the fatigue behaviour of rubber matrix. Huang et al. [8] studied the phenomenon of cyclic ageing on NR. They found that for NR, ageing at lower temperatures leads to a decrease in modulus, while at higher temperatures it leads to an increase in modulus. Bauer et al. [15] studied the mechanical properties of skim tire based on butadiene rubber (BR) under the oxidative ageing in the environment of 50/50 blend of N_2/O_2 at various temperatures in the range of 50–70 °C. They have observed a decrease in elongation at break and increase of modulus with time in the whole range of temperature. This degradation of mechanical behaviour is caused due to micro-crack initiation. The micro-cracks in tire component are caused due to natural physical ageing in the tire steady-state condition, while in rolling, the high stress concentration under dynamic loading condition has a predominant effect.

Thus the aim of this study is to determine the influence of thermal ageing processes in air environment and in the temperature range of 70–110 °C which closely resembles the tire application environment in the field. In the present study, fracture crack growth (FCG) behaviour of NR and SBR blends suitable for tire applications have been investigated. A new parameter based on loss compliance factor has been identified for describing the embrittlement or softening/hardening of aged rubber matrix by using of dynamic-mechanical analysis (DMA). These evaluated data have been compared with the fracture crack growth parameters observed by the use of using of a dynamic testing machine, Tear Analyzer. The correlation between loss compliance parameter and fracture crack growth data has been evaluated.

24.2 Theoretical Background

24.2.1 Dynamic-Mechanical Analysis (DMA)

The dynamic-mechanical behaviour of rubber vulcanisates at small dynamic strain depends on temperature and frequency. When a linear viscoelastic rubber material is exposed to a sinusoidal tensile stress σ , the strain ε will also alternate sinusoidally but will be out of phase, the strain lagging the stress [16]. Then the ratio (stress/strain) defines the complex tensile modulus:

$$E^* = \frac{\sigma(t)}{\varepsilon(t)} = \frac{\sigma_0}{\varepsilon_0} e^{i\delta}. \quad (24.1)$$

The complex modulus E^* can be divided into real E' (storage modulus) and imaginary E'' (loss modulus) components:

$$E^* = E' + iE'', \quad (24.2)$$

while the loss factor $\tan \delta$ is defined as follow:

$$\tan \delta = \frac{E''}{E'}. \quad (24.3)$$

Heinrich and Klüppel [16] showed that the loss factor $\tan \delta$ is also a measure of the ratio of energy lost to energy stored in a cyclic deformation. They defined the energy loss density ΔE during one cycle of strain as follow:

$$\Delta E = \pi \cdot \sigma_0^2 \cdot \frac{E''}{|E^*|^2} = \pi \cdot \sigma_0^2 \cdot J'', \quad (24.4)$$

where J'' is the loss compliance which is defined as $E''/|E^*|^2$.

Because of the relatively small value of phase shift δ , it could be numerically taken into the account the following presumption: $E'' \ll E'$. Thus (24.2) can from the numerical point of view be modified as follow:

$$i^2 = -1 \rightarrow E^* = E' + iE'' \rightarrow |E^*|^2 = E'^2 + E''^2 \approx E'^2 \rightarrow |E^*| \approx E'. \quad (24.5)$$

The loss compliance J'' can be substituted due to using of (24.5) and thus it can be written:

$$J'' = \frac{E''}{|E^*|^2} = \frac{E''}{|E^*| \cdot |E^*|} \approx \frac{E''}{E'} \cdot \frac{1}{|E^*|} \rightarrow J'' \approx \frac{\tan \delta}{|E^*|}. \quad (24.6)$$

The loss compliance, J'' which is a function of $\tan \delta$ and E^* , can be used to represent the dependence of dynamic properties of rubber with respect to influence of ageing temperatures, cure variation and antioxidants. The variation of J'' over a wide temperature range can detect the embrittlement or softening/hardening of rubber materials.

24.2.2 Fracture Crack Growth (FCG)

An important quantity for fracture mechanical investigations is the tearing energy T , i.e. the energy released per unit area of crack surface growth. It was first introduced by Griffith [17] for metallic materials and later Rivlin and Thomas [18] formulated the tearing energy for elastomers. It proposes that the strain energy release rate is the controlling parameter for crack growth and it is mathematically defined as

$$T = -(\partial W / \partial A), \quad (24.7)$$

where T is the tearing energy, W is the elastic strain energy, A is the interfacial area of crack and partial derivative denotes that no external work is done on the system.

The commonly used FCG specimens are single-edge-notched tension (SENT) and pure-shear (PS) test specimens. The tearing energy for these specimens can be computed using separate mathematical expressions. For PS test specimen geometry, which is used in this study, the tearing energy T is considered by Rivlin and Thomas [18] to be independent of the crack length:

$$T = w \cdot L_0, \quad (24.8)$$

where w is the strain energy density stored in the unnotched test specimen and L_0 is the sample length at not-strained state.

Because of the dynamic fatigue loading conditions which is applied on tire tread, Gent et al. [19] determined experimentally the crack growth rate da/dn in dependence on the tearing energy T for rubber materials. Whereas the most important state for the dynamic fracture behaviour is the stable crack propagation, which is defined as follows:

$$\frac{da}{dn} = B \cdot \Delta T^m, \quad (24.9)$$

where B and m are material constants.

24.3 Experimental Details

24.3.1 Material Preparation

The detailed compositions of the blends studied are given in Table 24.1. The rubber compounds were prepared using a laboratory Banbury mixture of 1.5 L capacity in three stages. In the first stage, rubbers and all chemicals except curatives were mixed at 60 rpm for 4 min at 140 °C. The mixed compound was then re-milled at 30 rpm for 3 min at about 120 °C. The final batch containing curatives was mixed at 30 rpm for 3 min at about 100 °C. The rheometric properties were measured using a moving die rheometer (Monsanto MDR 2000E) at 141 °C for 1 h. The test specimens used for all the measurements were prepared by curing rubber compounds for 60 min at 141 °C in a compression mould.

Table 24.1 Composition of analysed rubber materials

Ingredients	A1 (phr)	B4 (phr)	B5 (phr)
Natural rubber	100	60	0
Styrene–butadiene rubber	0	40	100
Carbon black ^a	50	50	50
Zinc oxide	2.50	2.50	2.50
Stearic acid	2.50	2.50	2.50
Antioxidant ^b	2.25	2.25	2.25
Sulfur	2	2	2
Accelerator ^c	0.50	0.50	0.50

^aCarbon black type was N339

^b*N*-(1,3-dimethylbutyl), *N'*-phenyl-*p*-phenylenediamine (6 PPD)

^c*N*-oxydiethylene, 2-benzothiazole sulfenamide

phr—parts per hundred rubber

24.3.2 Ageing

To evaluate the effects of ageing on the dynamic-mechanical properties as well as fatigue crack growth of rubber matrix, the samples were aged for 72 h at varied temperatures of 30, 70, and 110 °C under aerobic conditions in a thermal chamber. The test specimens were placed on a thin aluminium sheet, and therefore the opposite surfaces of the test specimens were intentionally covered by identical aluminium sheets. Thus identical ageing conditions were accomplished for all of the test specimens. The test specimens are denoted according to the ageing temperature and provided in Table 24.2.

Table 24.2 Test specimen denotation according to the ageing temperature

Ageing temperature (°C)	Rubber compound		
	A1	B4	B5
30	A1-30T	B4-30T	B5-30T
70	A1-70T	B4-70T	B5-70T
110	A1-110T	B4-110T	B5-110T

24.3.3 DMA

The complex modulus E^* and loss factor $\tan \delta$ in the temperature range 30–200 °C were measured using a dynamic-mechanical analyser (TMA/SDTA840, Mettler-Toledo) in tensile mode at 0.33% strain and 1 Hz frequency. The heating temperature gradient was set on 2 K/min. The test specimens with the geometry $2 \times 10 \times 50 \text{ mm}^3$ (thickness \times width \times length) based on all of rubber compounds aged in accordance with the Table 24.2 analysed.

24.3.4 FCG

FCG measurements were carried out using a Tear Analyzer (Coesfeld GmbH) under sinusoidal loading conditions. The details of testing equipment used are given in previous publications by the authors [20–22]. In this study, two double-notched and one unnotched PS test specimens were simultaneously analysed, whereas the unnotched test specimen was used for determination of tearing energy [18]. The standard PS test specimen with the geometry ratio L_0 (length)/ Q (width) = 1:8 was used [20]. Two of the PS test specimen were notched with notch length $a_0 = 21 \text{ mm}$ on both sides of test specimen. The value a_0 was calculated from the definition of minimal notch length $a_{0\text{min}}$ in dependence on geometry ratio L_0/Q [20].

Table 24.3 lists the detailed test conditions used in the FCG investigation. The loading frequency was set at 10 Hz. The strain was varied between 13 and 25%. The influence of thermal ageing on FCG was observed for all of the mentioned rubber materials aged at 30 and 70 °C. The temperature of testing conditions was 30 °C.

Table 24.3 Test condition details

Denotation	Type of loading condition	Frequency (Hz)	Strain (%)	Ageing temperature (°C)	Ageing duration (h)	Testing temperature (°C)
x-30T	Sinusoidal	10	13–25	30	72	30
x-30T-70T				30		70
x-70T				70		30

x—denotes the varied type of rubber material

Additionally, FCG measurement of B4 compound was also done at 70 °C to see the influence of test temperature which directly affected the surface due to fatigue condition.

24.4 Results and Discussion

24.4.1 DMA

The variation in E^* (complex modulus) and $\tan \delta$ (loss factor) with temperature of ageing can be seen for the rubber material A1 based on pure NR in Fig. 24.1 (left). It has been observed that with an increase of ageing temperature the complex modulus E^* decreases over the complete range of temperature. It can also be observed that there is a convergence of E^* curves of all ageing conditions (A1-30T, A1-70T and A1-110T) near to 150 °C which could be purely attributed to thermal degradation at this high temperature. However, in the case of $\tan \delta$ variation, it shows an increasing trend up to a certain temperature, passing through a maxima and then reflects a decreasing trend for all ageing conditions. It is interesting note that $\tan \delta$ of samples aged at 70 °C is lower than those aged at 30 °C, indicating softening. Whereas, for 110 °C, it reported higher value than 30 °C which implies that material becomes more brittle.

The variation of loss compliances J'' of aged materials with temperature is shown in Fig. 24.1 (right). It is observed that J'' increases with increase in ageing temperature which clearly demonstrates softening of the material. It is also observed that there is a transition point (temperature) above which softening occurs and appearance of this point is shifted to lower temperature as the ageing temperature increases. This transition point can be termed as softening point.

From Fig. 24.2 (left), it was seen that the complex modulus E^* and loss factor $\tan \delta$ for the material B5 based on pure SBR exhibited different behaviour in

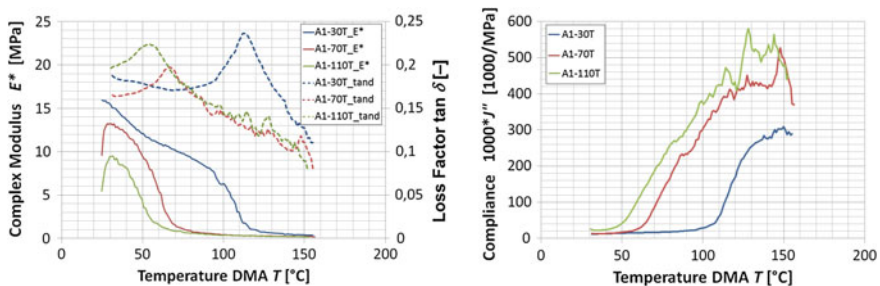


Fig. 24.1 Dynamic-mechanical properties of rubber based on A1 compound in dependence on varied ageing temperature, where the complex modulus E^* and loss factor $\tan \delta$ as a function of temperature are visualised in the *left diagram* and the loss compliance J'' as a function of temperature are shown in the *right diagram*

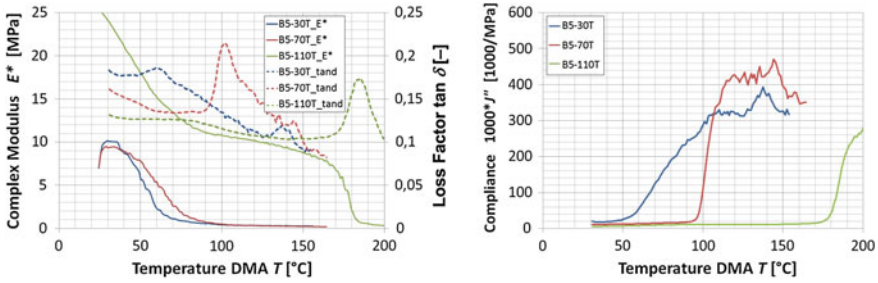


Fig. 24.2 Dynamic-mechanical properties of rubber based on B5 compound in dependence on varied ageing temperature, where the complex modulus E^* and loss factor $\tan \delta$ as a function of temperature are visualised in the *left diagram* and the loss compliance J'' as a function of temperature are shown in the *right diagram*

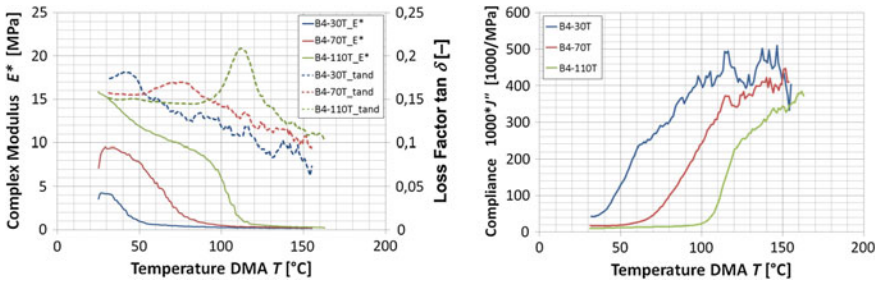


Fig. 24.3 Dynamic-mechanical properties of rubber based on B4 compound in dependence on varied ageing temperature, where the complex modulus E^* and loss factor $\tan \delta$ as a function of temperature are visualised in the *left diagram* and the loss compliance J'' as a function of temperature are shown in the *right diagram*

comparison to the material A1. The complex modulus E^* behaves identically for the ageing temperature 30 as well as 70 °C, whereas E^* significantly increases at 110 °C ageing condition. Thus the material become harder. The functions $\tan \delta$ in dependence on temperature shown in the Fig. 24.2 (right) demonstrate, that the increase of ageing temperature induces an embrittlement of rubber material B5 in the range up to the 90 °C of temperature, where the behaviours differs from their previous state.

The diagram of loss compliances J'' in dependence on thermal ageing process shown in Fig. 24.2 (right). It demonstrates the embrittlement of the rubber material B5 with increase in ageing temperature. On the contrary to the observation made for A1 material, the softening point for B5 material shifted towards higher temperature with increase in ageing temperature.

Data obtained from DMA over the given temperature for the material B4 based on NR/SBR blend in the dependence on ageing temperature demonstrate the total inverse behaviour in comparison to the material A1 [see Fig. 24.3 (left)]. The

complex modulus E^* increases in accordance with the rise of ageing temperature. Thus the rubber blend comes through the hardening phase with respect to the increased ageing temperature. The function $\tan \delta$ in dependence on temperature has demonstrated the more or less identical values over the complete analysed temperature range.

The diagram of loss compliances J'' in dependence on thermal ageing process shown in the Fig. 24.3 (right) demonstrates the embrittlement of the rubber material B4 in dependence on increased ageing temperature, whereas the increase of ageing temperature causes the higher point of temperature, where the softening of rubber material starts as observed in the case B5 material. The similarity in dynamic properties of B4 and B5 material can be attributed to the presence of SBR in these rubber compounds.

24.4.2 FCG

Figure 24.4 represents the double logarithmic plot of tearing energy versus crack growth rate (da/dn) of the materials in dependence of thermal oxidative ageing. The figure is divided into 3 separate diagrams according to the analysed rubber material, where (a) represent rubber material A1, (b) shows the results for rubber material B5 and in the diagram (c) the results are visualised for the rubber material B4. These plots clearly show that crack growth behaviour is entirely dependent on tearing energy and Power law dependency is observed. FCG parameters, B and m for all the materials under investigation are reported in Table 24.4.

In accordance with the general observation for rubber materials aged with low thermal influence (30 °C), it was found that rubber A1 based on pure NR has a higher resistance against fatigue crack growth rate in comparison to the rubber material B5 based on pure SBR. It is evident from the higher crack growth exponent, m for B5 material compared to A1 as reported in Table 24.4. It was found that the crack growth exponent m in the case of rubber blend B4 (60–40 NR/SBR) slightly increases in comparison to the A1 and B5 compound which are made of pure NR and SBR respectively. It was also observed that the FCG dependence trend is shifted to the range of higher tearing energies. Thus the material B4 based on NR/SBR compound can be denoted as a material with improved resistance against crack initiation but with reduced resistance against crack propagation in comparison to the basis rubber materials.

It is clearly shown that the increased thermal ageing condition has a significant influence on the crack growth behaviour. For all the rubber materials under investigation, the higher crack growth rate has been observed in test specimens aged at 70 °C in comparison to the rubber materials aged at low temperature of 30 °C. From Table 24.4 it is visible that identical crack growth exponent m was exhibited by both rubber materials A1 and B5 aged under varied thermal condition. However, the rubber blend B4 showed a slightly lower crack growth exponent m in dependence on increased ageing temperature, which is more or less identical with

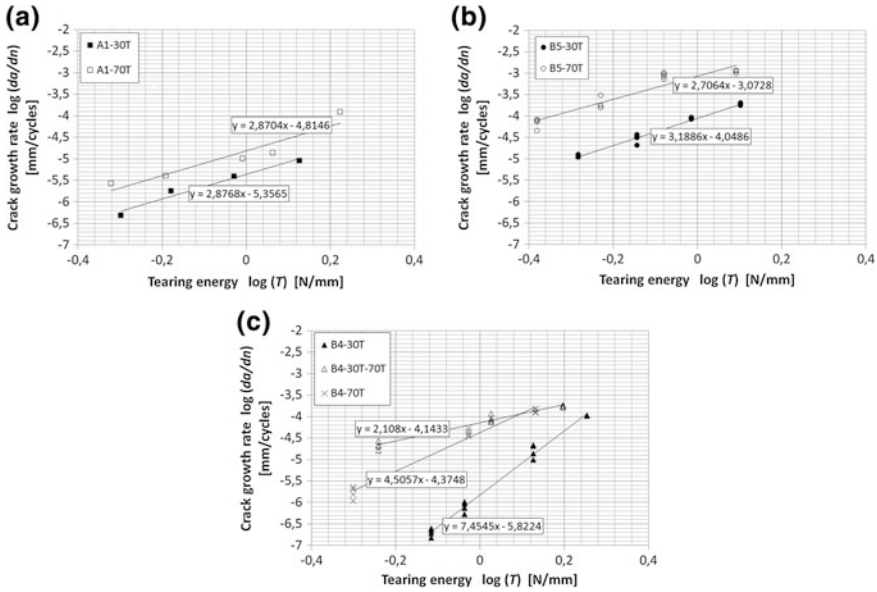


Fig. 24.4 Variation of crack growth rate with tearing energy (log-log plot) with respect to the different rubber material and the ageing temperature, where: diagram describing the FCG behaviour of rubber A1 (a), diagram describing the FCG behaviour of rubber B5 (b) and diagram describing the FCG behaviour of rubber B4 (c)

Table 24.4 The list of evaluated parameters of material constant B and m , which define the stable crack growth rate given by (24.9)

Parameters	Type of rubber material used for FCG analysis						
	A1-30T	A1-70T	B4-30T	B4-30-70T	B4-70T	B5-30T	B5-70T
B	-5.36	-4.81	-5.82	-4.14	-4.37	-4.05	-3.07
m	2.88	2.87	7.45	2.11	4.50	3.19	2.71

the crack growth exponent m observed in materials A1 and B5. The next observation shows that the values of tearing energies at given strain decreases in dependence on increased thermal ageing condition.

Finally the fracture investigation of rubber material B4 based on blend NR/SBR shows the significant influence of direct thermal influence of the rubber test specimens during the FCG analysis. However the rubber material tested at higher temperature (70 °C) shows a significantly lower crack growth exponent m (see Table 24.4). Thus it can be concluded, that the material B4 based on NR/SBR compound in dependence on direct thermal effect during the analysis has a lower resistance against crack initiation but behaves more or less stable in fatigue crack propagation process.

Generally it can be concluded that the point of temperature, which defines the start of rubber softening, is found to be around 50 °C or higher. Therefore the ageing process which could firstly be taken into account is in the range over the mentioned temperature, which generally tires experiences in service.

While the rubber material A1 behaves more soft with increased ageing temperature, the increase of FCG parameters was observed. The increase of FCG parameters is caused due to high strain which is the reason for inducing of crystallisation in the vicinity of the crack tip. However, the divergence of FCG in dependence on thermal ageing for material A1 could be considered as fractional. Secondly, it can be assumed, that the slight softening of the rubber material A1 during the thermal ageing correlates with the slight change in a tearing energy for identical loading amplitudes.

The results for the material B5 shows an embrittlement of the rubber matrix with increased ageing temperature. Hence, significantly higher FCG parameters were observed. Because of the embrittlement of the rubber matrix, the micro-cracks were initiated in rubber material and thus the tearing energy rapidly decreased at given strains for the material aged with higher temperature.

Similar dominating effect of rubber matrix embrittlement and micro-crack initiation have an influence on FCG behaviour in rubber material B4 based on NR/SBR blend. Therefore, the significantly higher FCG parameters were found for the rubber material aged under the higher temperature.

24.5 Conclusion

The present work discussed the influence of thermal ageing behaviour of rubber compounds made of NR (A1), SBR (B5) and their blend of 60–40 proportion (B4) on dynamic-mechanical and fatigue crack growth properties. The samples were thermally aged in the temperature range from 70 to 110 °C which closely simulates the real service conditions of tires. DMA and FCG properties were characterised for the aged samples. It was demonstrated that the loss compliance J'' can be effectively used to detect the embrittlement or softening/hardening point of the aged rubber material. It was also observed that the softening point appears near about 50 °C and was of interest for considering the ageing temperature for studying FCG characteristics. It was observed that dynamic properties of B4 and B5 were quite different from A1, which could be attributed to the presence of SBR in the former compounds. The FCG studies revealed that increase in ageing temperature has deleterious effect on crack growth resistance as was reflected in all the aged materials.

Acknowledgements This paper was written with the support of the Education for Competitiveness Operational Program co-funded by the European Social Fund (ESF) and the government of the Czech Republic, in the project entitled ‘Advanced Theoretical and Experimental Studies of Polymer Systems’ (reg. number: CZ.1.07/2.3.00/20.0104), and with the support of the Research and Development for Innovations Operational Program, co-funded by European Regional Development Fund (ERDF) and the government of the Czech Republic, in the project entitled ‘Centre of Polymer Systems’ (reg. number: CZ.1.05/2.1.00/03.0111).

References

1. Heinrich, G., Klüppel, M., Vilgis, T.A.: Reinforcement of elastomers. *Curr. Opin. Solid State Mater. Sci.* **6**, 195–203 (2002)
2. Klüppel, M.: The role of disorder in filler reinforcement of elastomers on various length scales. In: *Filler-Reinforced Elastomers/Scanning Force Microscopy. Advances in Polymer Science*, Vol. 164, pp. 1–86 (2003)
3. Dannenberg, E.M.: The effect of surface chemical interactions on the properties of filler reinforced rubbers. *Rubber Chem. Technol.* **44**, 440–478 (1975)
4. Klüppel, M., Schramm, J.: An advanced micro-mechanical model of hyperelasticity and stress softening of reinforced rubbers. In: Dorfmann, A., Muhr, A. (eds.) *Constitutive Models for Rubber*. A.A. Balkema, Rotterdam (1999), pp. 211–220
5. Lake, G.J., Lindley, P.B.: Ozone cracking, flex cracking and fatigue of rubber. Part 2: Technological aspects. *Rubber J.* **164**, 30–39 (1964)
6. Stacer, R.G., Yanyo, L.C., Kelly, F.N.: Observations on the tearing of elastomers. *Rubber Chem. Technol.* **58**, 421–435 (1985)
7. Schuring, D.J., Hall, G.L.: Ambient temperature effects on tire rolling loss. *Rubber Chem. Technol.* **54**, 1113–1123 (1981)
8. Huang, D., LaCount, B.J., Castro, J.M., Ignatz-Hoover, F.: Development of a service-simulating, accelerated aging test method for exterior tire rubber compounds I. Cyclic aging. *Polym. Degrad. Stab.* **74**, 353–362 (2001)
9. Celina, M., Wise, J., Ottesen, D.K., Gillen, K.T., Clough, R.L.: Correlation of chemical and mechanical property changes during oxidative degradation of neoprene. *Polym. Degrad. Stab.* **68**, 171–184 (2000)
10. Drozdov, A.D.: A model for the nonlinear viscoelastic response in polymers at finite strain. *Int. J. Solids Struct.* **35**, 2315–2347 (1998)
11. Payne, A.R.: The dynamic properties of carbon black-loaded natural rubber vulcanizates. Part I. *J. Appl. Polym. Sci.* **6**, 57–63 (1962)
12. Payne, A.R.: Strainwork dependence of filler-loaded vulcanizates. *J. Appl. Polym. Sci.* **8**, 2661–2686 (1965)
13. Lion, A.: Strain-dependent dynamic properties of filled rubber: a nonlinear viscoelastic approach based on structural variables. *Rubber Chem. Technol.* **72**, 410–429 (1999)
14. Baldwin, J.M., Bauer, D.R., Ellwood, K.R.: Rubber aging in tires. Part 1: Field results. *Polym. Degrad. Stab.* **92**, 103–109 (2007)
15. Bauer, D.R., Baldwin, J.M., Ellwood, K.R.: Rubber aging in tires. Part 2: Accelerated oven aging tests. *Polym. Degrad. Stab.* **92**, 110–117 (2007)
16. Heinrich, G., Klüppel, M.: Recent advances in the theory of filler networking in elastomers. *Adv. Polym. Sci.* **160**, 1–44 (2002)
17. Griffith, A.A.: The phenomena of rupture and flow in solids. *Philos. Trans. R. Soc. A* **221**, 163–198 (1920)
18. Rivlin, R.S., Thomas, A.G.: Rupture of rubber. I. Characteristic energy for tearing. *J. Polym. Sci.* **10**, 291–318 (1953)
19. Gent, A.N., Lindley, P.B., Thomas, A.G.: Cut growth and fatigue of rubbers. I. The relationship between cut growth and fatigue. *J. Appl. Polym. Sci.* **8**, 455–466 (1964)
20. Stoček, R., Heinrich, G., Gehde, M., Kipscholl, R.: A new testing concept for determination of dynamic crack propagation in rubber materials. *KGK—Kautsch. Gummi Kunstst.* **65**, 49–53 (2012)

21. Stoček, R., Heinrich, G., Gehde, M., Rauschenbach, A.: Investigations about notch length in pure-shear test specimen for exact analysis of crack propagation in elastomers. *J. Plast. Technol. Issue 1*, 2–22 (2012)
22. Ghosh, P., Stoček, R., Gehde, M., Mukhopadhyay, R., Krishnakumar, R.: Investigation of fatigue crack growth characteristics of NR/BR blend based tyre tread compounds. *Int. J. Fract.* **188**, 9–21 (2014)

Chapter 25

Development of Magnetorheological Elastomers (MREs) for Strength and Fatigue Resistance

J. McIntyre and S. Jerrams

Abstract Natural rubber (NR)-based magnetorheological elastomers (MREs) exhibiting a reasonable switching effect were fabricated and tested. They were strong enough for use in automotive applications but still needed protection against ageing. Ethylene–propylene–diene rubber (EPDM) is a cost-effective material that is frequently used in the automotive industry because of its advantageous range of properties. With these applications in mind, it was a logical progression to the development of EPDM-based MREs. Unlike strain-crystallising NR, EPDM requires reinforcement to render its tensile and fatigue strength suitable for use in most applications. While small amounts of carbon black were sufficient for the NR-based MREs, a trade-off between non-reinforcing carbonyl iron powder (CIP) and reinforcing carbon black fillers was necessary to imbue the EPDM-based MREs with reasonably good mechanical properties. With a limit on the quantities of fillers that could be added, attention was turned to the matrix material itself and the blend of polymers employed in EPDM2 and EPDM3 were chosen in order to strengthen the EPDM-based MREs by enhancing polymer molecular weight and reinforcement. However, an unwanted effect of the stronger polymer network was the high-viscosity matrix in these compounds which hindered the alignment of magnetic particles early in the vulcanisation process. This led to poorer magnetic particle orientation, resulting in a more homogenous dispersion of the CIP and consequently produced MRE specimens that were more isotropic than anisotropic. Subsequently the switching effect of these materials was lower than would be obtained in MREs with a low viscosity (say, 40 MU) matrix. It was not feasible to sacrifice reinforcing carbon black in these compounds, but there are other possibilities open to the rubber compounder. An alternative means of reducing the viscosity of EPDM3 is simply to double the content of softening oil. This would have a slight but minimal negative effect on the tensile properties of the material. The addition of a small amount of retardant to delay vulcanisation and extend the time available for orientation of the magnetic particles into chains would also be

J. McIntyre (✉)

DKI – The German Institute of Rubber Technology, Hanover, Germany

S. Jerrams

Centre for Elastomer Research, Dublin Institute of Technology, Dublin, Ireland

© Springer International Publishing AG 2017

W. Grellmann and B. Langer (eds.), *Deformation and Fracture Behaviour of Polymer Materials*, Springer Series in Materials Science 247,
DOI 10.1007/978-3-319-41879-7_25

365

beneficial. This would also reduce the modulus of the compound, but the reduction would again be negligible. As in all material design, there is a trade-off to be made in choosing the right combination of properties, but both of these changes would result in the development of an effective magnetorheological compound.

25.1 Introduction

The future of material technology is likely not to lie in the passive conventional materials that have been used to date but in smart materials that adapt to changes in their environments. Elastomeric materials are also becoming “smart”; shape-memory polymers, self-healing polymers, elastomers that change colour in response to stress, are PH-sensitive or temperature responsive, are all examples of new materials that are “intelligent”.

A magnetorheological elastomer (MRE), possessing a stiffness that can be tuned to suit specific operating conditions encountered in service could prove useful in many situations. Many interesting ideas have been presented for MREs including seals [1] and valves [2–4], base isolation systems for buildings in earthquake zones [5]. Simpler ideas, but perhaps easier to reach fruition, might include using them as dampers or vibration absorbers in laboratories. Sensitive equipment needing protection from vibrations or background noise in their working environment might benefit greatly from the technology.

In spite of a myriad of possibilities, manufacturers have so far been reluctant to utilise MREs in products. This is surprising because their magnetorheological (MR) fluid analogues are commercially available and have been used in seat suspension systems for trucks [6, 7] and high-end braking systems [8]. It has been suggested that MRE materials are not strong enough for real world applications and will be useful only in very limited situations. Researchers have reported poor tensile properties [9] and short fatigue lives [10]. It has been reasonably questioned whether the change in stiffness when a magnetic field is applied, the MR effect or switching effect, is sufficient to justify the complexity and cost of production. Much of the published literature describes MRE materials of low zero-field modulus (the initial modulus of the material, before a change is induced by the application of a magnetic field) and thus low stiffness, which can exhibit very significant switching effects (up to several hundred per cent). While such materials might be useful in applications where loading is minimal, potential applications, particularly where the MRE is subjected to higher dynamic loading are limited. This text examines some of these issues and how they might be solved.

MREs respond to increases in magnetic flux density, resulting from the application of an external magnetic field, by stiffening. Many of the most significant changes have been in elastomers of low zero-field modulus. If the matrix material is of low stiffness to begin with, the movement of magnetic particles when a magnetic field is applied may deform the matrix and initiate a dimensional change [11–13], resulting in a magnetostrictive material.

An MRE consists of an elastomer matrix filled with magnetic particles or powder. On applying a magnetic field to the composite MRE material, magnetic interactions between the particles cause them to pull together and to attempt to align along the magnetic field lines. This leads to an increase in modulus of the material (which is observed as a switching effect when the field is switched on and off). The magnitude of this effect depends on the magnetic flux density of the field so as the flux density increases the modulus also increases and hence a component fabricated from an MRE material becomes stiffer. If the magnetic filler is magnetically soft, as in a material in which the magnetic field can be easily reversed, exhibiting little or no remanence, the increase in modulus is instantaneously reversible. Ferromagnetic powders are most commonly used as fillers in MR materials, with carbonyl iron powder (CIP) being the most widely adopted MRE filler. CIP exhibits a very high magnetic saturation and thus has the potential to contribute a larger switching effect than less magnetic materials [13, 14].

Research has found that the switching effect can be significantly enhanced if the dispersion of the particles throughout the rubber matrix is anisotropic [15]. While a homogenous dispersion of particles does result in a material that shows a switching effect, Boczkowska and Awietjan [16] have found that anisotropic materials exhibit higher switching effects. They described a correlation between switching effect and “anisotropy coefficient”. This anisotropy, in the form of chains of magnetic particles running through the specimen or component, can be achieved by the application of a magnetic field during the curing process which directionalises the particles so that they are oriented along the lines of flux density [9, 17].

Much research has been conducted on MREs with a natural rubber (NR) matrix. The reasons for choosing NR as a starting point when selecting a matrix material were its high tensile and elevated fatigue properties. Even without reinforcement, NR exhibits a high tensile strength compared to most rubber materials, a benefit generally attributed to its ability to strain-crystallise. This increase in tensile strength, caused by the high orientation of the crosslinked macromolecules of the network [18], renders vulcanised NR very useful in automotive applications such as engine mounts and suspension bushings.

Unfortunately NR has very poor ageing properties and the use of CIP in an NR matrix accentuates this problem because large quantities of iron particles in a natural rubber matrix can accelerate ageing [19]. These iron particles tend to have iron oxides on their surfaces. This can lead to increased levels of oxygen being incorporated into the rubber matrix, quickening the rate of oxidative ageing [19–21]. An attempt to solve this problem by modifying the surface of the CIP particles with silane was made. Two grades of CIP which contained silicon dioxide (SiO_2) on the surface were chosen for silanisation with silane coupling agent Si 69. In theory, the silane reaction would form covalent bonds with the OH groups on the surface of the particles and improve dispersion of the particles throughout the rubber matrix, while acting as a coupling device to enhance the bond between particle and rubber matrix. This would require that each particle be completely coated in silica so that a silica shell was formed around individual particles. Unfortunately the silanisation was not successful and on further investigation of the

particle surfaces it was discovered that the number of OH sites available for bonding was too few. There was simply not enough organic material on the particle surfaces. While the development of a suitable method to modify the CIP particles to compatibilise them with natural rubber would be a significant step in bringing MREs into applications, this would open another sphere of study in the field of chemistry which goes beyond the scope of this work. In consequence, an alternative polymer must be sought.

Synthetic ethylene–propylene–diene (EPDM) is easy to process and is quite resistant to oxidation and ageing. EPDM is ideally suited to resist the temperatures experienced by automotive components. At the time of writing, it is also an economical choice, providing favourable properties while being cheaper than many other types of rubber. This makes it a very popular alternative to NR in sealing applications in the automotive and construction industries. However, EPDM has its own limitations: unfilled EPDM gum has a tensile strength of approximately 4 MPa; much lower than that of NR gum (16 MPa). Unlike NR, it does not possess the ability to strain-crystallise when deformed, necessitating reinforcement with substantial amounts of reinforcing fillers such as silica or carbon black (CB), leaving less room for non-reinforcing fillers such as CIP. EPDM shows inferior resistance to crack initiation and propagation and has lower fatigue resistance by comparison with NR [18]. These limitations must be taken into account when developing an EPDM compound.

A material that combined the advantages of temperature and ageing resistance offered by EPDM with the tensile and fatigue properties of natural rubber would be very useful to manufacturers and end users. If such a material could be employed as a matrix for MRE composites it would overcome concerns in respect of low zero-field modulus observed in most switchable MREs, the short fatigue lives observed by Zhou et al. [22] and the threat of accelerated ageing that is usually present in composites filled with iron particles.

25.2 Preparation of Materials

The NR series of sample compounds, consisted of specimens containing 400 phr (approximate 25 vol%) of micron-sized carbonyl iron powder (CIP) (BASF Grade SM). Of these compounds, two contained a low concentration of carbon black (5 phr) while the other two had the carbon black content increased to 30 phr to further reinforce the material. Softener was also added to a batch of each of these two recipes so that a significant difference between each of the compounds was their viscosities. These materials were compared to identify the factors that would most readily maximise the magnetorheological (MR) or switching effect.

Thereafter, in order to obtain MRE materials with improved resistance to ageing, the focus shifted to EPDM-based MREs. The knowledge gained in the research using the NR materials was employed in designing an initial base compound, EPDM1. Rather than comparing a series of similar recipes with each other, this base

Table 25.1 Composition of compounds

Sample	CIP (vol.%)	CB (vol.%)	Softener (vol.%)	Mooney viscosity (MU)	Zero-field shear storage modulus, G'_0 (MPa)
NR1	28	0.5	–	43	3.28
NR2	22	0.5	3.6	28	1.10
NR3	25	2.8	3.5	29	3.41
EPDM1	22	1.3	2.7	38	1.80
EPDM2	15	4.3	3.1	70	1.40
EPDM3	18	2.9	4.7	70	1.72

recipe, EPDM1 was tested and further refined in two successive iterations in materials EPDM2 and EPDM3. EPDM1 contained a polymer blend of low molecular weight as a matrix filled with 400 phr CIP (22 vol%). The EPDMs required larger amounts of reinforcing carbon black than the NR MREs for the reasons discussed in Sect. 25.1. However, the amount of filler that can be added to a rubber matrix is limited. Large quantities of filler make the mixture powdery and difficult to mix. Temperature can climb very rapidly in the mixer and it must be controlled so that vulcanisation does not begin during mixing. For the first EPDM sample, 15 vol.% carbon black was chosen. EPDM1 had a Mooney viscosity of 38 MU.

A polymer of a higher molecular weight was employed in EPDM2. The amount of CIP in EPDM2 was reduced to 200 phr (15 vol%) so that the amount of carbon black could be increased to 40 vol.% to improve tensile strength. Unlike carbon black or silica, CIP is a non-reinforcing filler; although it can increase the hardness and viscosity of the rubber compound, it does not contribute to an improvement in the strength of the compound. Due to the high molecular weight of the polymer and the increased amount of carbon black, the viscosity of EPDM2 was increased to 68 MU.

The same high molecular weight polymer was employed in EPDM3 but a lower quantity of a more active carbon black was used. The reduction in the amount of carbon black permitted an increase of the CIP content to 350 phr (18 vol%), while the higher activity of the carbon black compensated for its lower volume fraction (30 vol%). As these changes would also increase the viscosity of the mixture, the amount of softener was also increased from 15 vol% in EPDM1 and EPDM2 to 30 vol.% in EPDM3 in order to aid processing. This kept the viscosity of EPDM3 at a similar level to EPDM2 at 70 MU. The compositions of the materials investigated are given in Table 25.1.

25.3 Experimental Methodology

The switching effect of magnetorheological materials is often evaluated by observing the increase in the shear storage modulus of a sample material when an external magnetic field is applied. Such tests can be conducted using double-lap-shear specimens subjected to uniaxial loading or by torsional shear in a

rheometer using disc specimens of 20 mm diameter. For the latter, the evaluations were carried out using an Anton Paar Physica MCR 501 plate–plate rheometer, which contained a magnetic cell beneath the lower plate. As the specimens were subjected to a torsional shear strain of 0.5%, a magnetic field was switched on and off at intervals and the magnetic flux density increased each time the field was switched on. The response of each of the materials (the increase in shear storage modulus, G') was observed as the magnetic field was applied (G'_1) and strength successively increased. The increase $\Delta G'$ in G' at the highest magnetic flux density obtained, 1 T, was compared with the zero-field modulus G'_0 of the specimen (in the absence of a field) and recorded as both absolute values and as a percentage of the zero-field modulus. All of the rheometric tests were conducted on anisotropic MREs, specimens that had been vulcanised in the presence of a magnetic field of 0.6 T.

The strength and fatigue properties of each material were characterised by static and dynamic tensile and dynamic uniaxial cyclic testing. Tensile testing was carried out on a Zwick universal test machine 1445 in accordance with DIN 53504 using S2 (dog-bone) specimens. Fatigue behaviour was investigated by subjecting dumbbell specimens such as those shown diagrammatically in Fig. 25.1 to displacement controlled cyclic uniaxial deformation in an MTS 831.50 high frequency elastomer test system. This allowed the Wöhler curves shown in Fig. 25.2 to be plotted. The specimens were strained in tension to 60, 80, 120 and 160% until rupture and the number of cycles to failure recorded. In all cases, these tensile and fatigue tests were conducted on isotropic MRE samples which had been vulcanised in the absence of a magnetic field. This was simply because the apparatus used to vulcanise anisotropic specimens in the presence of a magnetic field was not large enough to accommodate the moulds used to fabricate dumbbell specimens. An investigation using dumbbells vulcanised in a magnetic field would be highly informative and is recommended for future research.

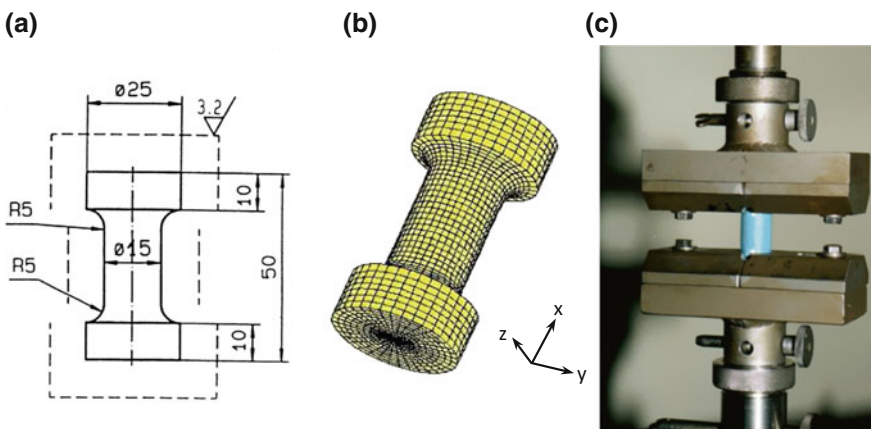


Fig. 25.1 Dimensions of a dumbbell specimen (a), a 3D computer model of the specimen (b) and a specimen in situ during fatigue testing (c)

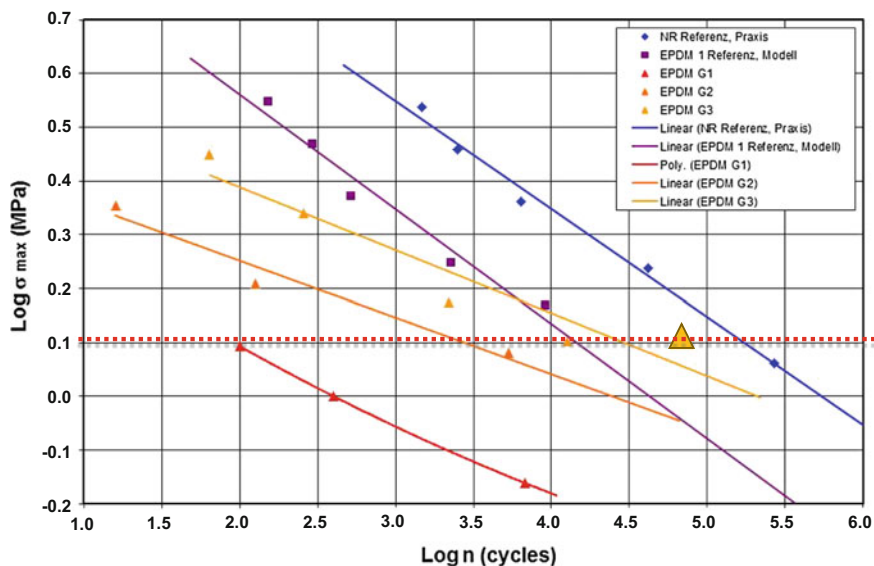


Fig. 25.2 Log stress (σ_{\max}) versus log cycles (n) to failure for EPDM specimens (linear curve fit)

25.4 Results and Discussion

The effect of the slight variations in the recipes was evident in the zero-field moduli of the NR-based MREs. A clear correlation between switching effect and Mooney viscosity of the materials can be seen in the rheometric results summarised in Table 25.2. EPDM1, with its lower Mooney viscosity, exhibited a greater increase in the relative switching effect ($\Delta G'/G_0$) than the more viscous compounds. This confirms the benefit of a low-viscosity matrix in assisting particle orientation during vulcanisation. The viscosity of the matrix can hinder the alignment of magnetic particles into chains early in the vulcanisation stage, leading to poorer magnetic particle orientation with them adopting a more homogenous dispersion of the CIP. This results in MRE specimens that tend more to isotropy than anisotropy. While a homogenous dispersion of particles results in a material that shows a switching effect, it has been shown that anisotropic materials exhibit superior switching effects [15–17]. Research described in much of the published work used matrix materials of low viscosity containing large quantities of softening oils to reduce rigidity in order to maximise switching effect. Another option to further improve magnetic particle alignment is to add small amounts of retardant to the compound recipes to delay the onset of vulcanisation. Using a retardant in this way increases the incubation time allowing the ideal period for particle alignment to occur [23] while simultaneously slightly reducing the viscosity of the melt. In order to obtain an indication of the tensile strength that might be expected from these materials, tensile testing was conducted on five specimens of the material that exhibited the

Table 25.2 Test results of compounds

Sample	G'_0 (MPa)	G'_1 (MPa)	$\Delta G'$ (MPa)	$\Delta G'/G'_0$ (%)	Tensile strength (MPa)	Elongation at break (%)	Fatigue (cycles)
NR1	3.28	3.88	0.60	18.10	–	–	–
NR2	1.10	1.78	0.68	61.82	14.2	530	–
NR3	3.41	4.06	0.65	19.09	–	–	–
EPDM1	1.80	2.20	0.40	22.00	5.9	560	100
EPDM2	1.40	1.47	0.07	5.00	11.8	525	3000
EPDM3	1.72	1.78	0.06	3.48	15.6	529	30,000

highest switching effect of the NR2 series. The tensile stress was found to be 14.2 MPa for an elongation at break of 530%.

The EPDM MREs were subjected to the same rheometric testing as the NR materials. The switching effect of EPDM1 was comparable to that of NR1 and NR3 at approximately 20%. The tensile strength however, was disappointingly low at 6 MPa. This was deemed insufficient for the applications referred to in the introduction. Rubber materials tend to be chosen because of their ability to be subjected to large deformations without breaking and to recover their original shapes.

All of the EPDM compounds showed similar values for elongation at break but the variations in their recipes led to differences in ultimate tensile strength. The changes led to a doubling of the tensile strength to 12 MPa in EPDM2. At this level, the tensile strength is sufficient for use in the automotive industry. The tensile strength was further improved in EPDM3, reaching almost 16 MPa, which is a significant improvement over what has been reported for MREs in literature to date.

The maximum stresses σ_{\max} experienced by the EPDM dumbbells during fatigue testing were plotted against the number n of cycles to failure on logarithmic scales to obtain Wöhler curves as shown in Fig. 25.2. Linear trend lines were fitted to the experimental curves. Two extra curves are included for reference: the blue curve is that of an NR material from experimental results. The purple curve is that of an EPDM material from a finite element (FE) simulation.

The remaining three curves are those of EPDM 1 (red), EPDM2 (orange) and EPDM3 (yellow). Generally, they exhibited shorter lifetimes than the other two reference materials. At a maximum stress of 1.28 MPa (log 0.1 on the y-axis of the graph in Fig. 25.2, indicated by the red line), the EPDM1 dumbbell had a life of merely 100 cycles. EPDM2 had superior fatigue characteristics reaching approximately 3000 cycles. At a maximum stress of 1.28 MPa the curve for the material EPDM3 surpassed the EPDM reference model reaching 30,000 cycles and approached that of the reference NR material that is currently being used in engine mounts. Indeed one specimen, denoted by a point located to the right of the linear fit, exhibited a life of 63,000 cycles (log 4.8 on the x-axis). The tensile and fatigue properties reported here are significantly higher than anything that has been reported in the literature to date.

However, this increase in tensile strength and fatigue life of EPDM2 and EPDM3 comes at the cost of a reduction in switching effect to only a few per cent. This was attributed to the higher matrix viscosity of the blend containing the high-molecular weight polymer and the higher quantities of carbon black required to reinforce the EPDM materials. The Mooney viscosities of these optimised EPDM compounds were almost twice those of the MREs which exhibited the higher switching effects. This returns the focus of the research to the initial question of how to improve the switching effect.

A solution is offered here: by improving the alignment of the magnetic filler particles to enhance the anisotropy of the MREs. Recall the influence of Boczkowska's anisotropy coefficient; the results of the background study proved that the matrix viscosity hinders the formation of particle chains during vulcanisation, leading to a more homogenous dispersion which exhibits a limited switching effect. In these two EPDM recipes, there is ample scope to reduce the viscosity of the material with the addition of softening oil. Retardant can also be added in small quantities to delay the onset of crosslinking. This will maximise the window of time allowed for magnetic particle orientation to occur before mobility is hindered by increasing viscosity as the elastomer cures.

25.5 Summary and Conclusions

NR-based MREs exhibiting a reasonable switching effect were fabricated and tested. They were strong enough for use in automotive applications but still needed protection against ageing. EPDM is a cost-effective material that is frequently used in the automotive industry because of its advantageous range of properties. With these applications in mind, it was a logical progression to the development of EPDM-based MREs. Unlike strain-crystallising NR, EPDM requires reinforcement to render its tensile and fatigue strength suitable for use in most applications. While small amounts of carbon black were sufficient for the NR-based MREs, a trade-off between non-reinforcing CIP and reinforcing carbon black fillers was necessary to imbue the EPDM-based MREs with reasonably good mechanical properties. With a limit on the quantities of fillers that could be added, attention was turned to the matrix material itself and the blend of polymers employed in EPDM2 and EPDM3 were chosen in order to strengthen the EPDM-based MREs by enhancing polymer molecular weight and reinforcement.

However, an unwanted effect of the stronger polymer network was the high-viscosity matrix in these compounds which hindered the alignment of magnetic particles early in the vulcanisation process. This led to poorer magnetic particle orientation, resulting in a more homogenous dispersion of the CIP and consequently produced MRE specimens that were more isotropic than anisotropic. Subsequently the switching effect of these materials was lower than would be obtained in MREs with a low viscosity (say, 40 MU) matrix.

It was not feasible to sacrifice reinforcing carbon black in these compounds, but there are other possibilities open to the rubber compounder. An alternative means of reducing the viscosity of EPDM3 is simply to double the content of softening oil. This would have a slight but minimal negative effect on the tensile properties of the material. The addition of a small amount of retardant to delay vulcanisation and extend the time available for orientation of the magnetic particles into chains would also be beneficial. This would also reduce the modulus of the compound, but the reduction would again be negligible. As in all material design, there is a trade-off to be made in choosing the right combination of properties, but both of these changes would result in the development of an effective magnetorheological compound.

Acknowledgements The support of the German Federal Ministry for Education and Research (BMBF, Grant no. 16SV3757) is gratefully acknowledged.

References

1. Magnetorheological elastomers with continually adjustable hardness. Information brochure, Fraunhofer-Institut für Silicatforschung ISC, Würzburg. http://www.cesma.de/content/dam/isc/cesma/de/documents/3_MR_Elastomers_2013_.pdf. 1 June 2017
2. Nguyen, Q., Choi, S., Wereley, N.M.: Optimal design of magnetorheological valves via a finite element method considering control energy and a time constant. *Smart Mater. Struct.* **17**, 1–12 (2008)
3. Rosenfeld, N., Wereley, N.M.: Volume-constrained optimization of magnetorheological and electrorheological valves and dampers. *Smart Mater. Struct.* **13**, 1303–1313 (2004)
4. Hu, W., Robinson, R., Wereley, N.M.: A design strategy for magnetorheological dampers using porous valves. In: 11th Conference on Electrorheological Fluids and Magnetorheological Suspensions, (Dresden, 25.–29.08.2008), *Journal of Physics: Conference Series* 149, 4 p. (2009)
5. Li, Y., Li, J., Tian, T., Li, W.: A highly adjustable magnetorheological elastomer base isolator for applications of real-time adaptive control. *Smart Mater. Struct.* **22**, 095020 (2013). (18 pages)
6. Reichert Jr., B.A.: Application of Magnetorheological Dampers for Vehicle Seat Suspensions. Master thesis, Virginia Polytechnic Institute and State University, Blacksburg (1997)
7. Marcu, F.: Semiactive Cab Suspension Control for Semitruck Applications. PhD thesis, Virginia Polytechnic Institute and State University, Blacksburg (2009)
8. Carlson, D.J., Leroy, D.F., Holzheimer, J.C., Prindle, D.R., Marjoram, R.H.: Magnetorheological Fluid Brake. US Patent 5460585 A (1998)
9. Chen, L., Gong, X., Jiang, W., Yao, J., Deng, H., Li, W.: Investigation on magnetorheological elastomers based on natural rubber. *J. Mater. Sci.* **42**, 5483–5489 (2007)
10. Zhang, W., Gong, X., Sun, T., Fan, Y., Jiang, W.: Effect of cyclic deformation on magnetorheological elastomers. *Chin. J. Chem. Phys.* **23**, 226–230 (2010)
11. Stepanov, G., Abramchuk, S., Grishin, D., Nikitin, L., Kramarenko, E.: Khokhlov, A: Effect of a homogenous magnetic field on the viscoelastic behaviour of magnetic elastomers. *Polymer* **48**, 488–495 (2007)
12. Guan, X., Dong, X., Ou, J.: Magnetostrictive effect of magnetorheological elastomer. *J. Magn. Magn. Mater.* **320**, 158–163 (2007)

13. Carbonyl Iron Powder: Information brochure, BASF SE, Ludwigshafen. https://www.dispersion-pigments.basf.com/portal/load/fid827906/CIP_General_PO_e.pdf. 18 Nov 2015
14. Jolly, M.R., Carlson, J.D., Munoz, B.C., Bullions, T.A.: The magnetoviscoelastic response of elastomer composites consisting of ferrous particles embedded in a polymer matrix. *J. Intell. Mater. Syst. Struct.* **7**, 613–622 (1996)
15. Boczkowska, A., Awietjan, S.F., Wejrzanowski, T., Kurzydowski, K.J.: Image analysis of the microstructure of a magnetorheological elastomers. *J. Mater. Sci.* **44**, 3135–3140 (2009)
16. Boczkowska, A., Awietjan, S.F.: Smart composites of urethane elastomers with carbonyl iron. *J. Mater. Sci.* **44**, 4104–4111 (2009)
17. McIntyre, J., Jerrams, S., Steinke, E., Maslak, A., Wagner, P., Möwes, M., Alshuth, T., Schuster, R.: Optimisation and characterisation of magnetorheological elastomer. In: Jerrams, S., Murphy, N. (eds.) *Constitutive Models for Rubber VII*. CRC Press/Balkema, Leiden (2011), pp. 313–317
18. Abraham, F.: *The Influence of Minimum Stress on the Fatigue Life of Non Strain-Crystallising Elastomers*. PhD thesis, Coventry University, Coventry (2002)
19. Lokander, M., Reitberger, T., Stenberg, B.: Oxidation of natural rubber-based magnetorheological elastomers. *Polym. Degrad. Stab.* **86**, 467–471 (2004)
20. Keller, R.W.: Oxidation and ozonation of rubber. *Rubber Chem. Technol.* **58**, 637–652 (1985)
21. Lee, L.-H.: Mechanisms of oxidative degradation I. Oxidation of synthetic rubbers catalyzed by metallic ions. *J. Appl. Polym. Sci.* **10**, 1699–1715 (1966)
22. Zhou, Y., Jerrams, S., Chen, L.: The effect of microstructure on the dynamic equi-biaxial fatigue behaviour of magnetorheological elastomers. In: Gil-Negrete, N., Alonso, A. (eds.) *Constitutive Models for Rubber VIII*. CRC Press, Boca Raton (2013), pp. 683–688
23. McIntyre, J., Alshuth, T.: Crack propagation in magnetorheological elastomers (MREs). *KGK Kautsch. Gummi Kunstst.* **66**, 29–35 (2013)

Chapter 26

Fibre-Reinforced Polyamides and the Influence of Water Absorption on the Mechanical and Thermomechanical Behaviour

P. Guttman and G. Pilz

Abstract Polyamides tend to absorb water from environment especially due to their polar structure. Aliphatic polyamides absorb water faster and to a higher extent than polyamides, aromatic parts within their backbone. The absorbed water causes a weakening of the hydrogen bonds between adjacent polyamide backbones. For both, aliphatic and semi-aromatic polyamides, a significant shift of the glass transition was found using dynamic mechanical analysis. In tensile tests the water absorption and increase of testing temperature show a decrease of the tensile modulus and tensile strength for the aliphatic polyamide 66 (PA66) and the semi-aromatic polyamide (PPA) types. Whereas PA66-GF30 and PA66-GF50 also show an increase of elongation at break with water absorption and higher testing temperature, no such effect can be found for PPA-GF35. An efficient creep test methodology using the Stepped Isothermal Method (SIM) and the principle of time–temperature superposition show differences in the long-term creep behaviour of the investigated polyamides in wet materials condition. It can be shown, that, if the testing or reference temperature of creep tests is chosen at the beginning of the glass transition range, the short-term mechanical properties remain at a high level, but the creep tendency is significantly increased. With testing temperatures distinctly above glass transition, PA66-GF30 and PA66-GF50 show a lower creep tendency compared to PPA-GF35 which was tested at a temperature close to the glass transition range. Physical or chemical ageing effects induced by water absorption of polyamides, which may occur after long-term exposure, are not considered within the present test program. Further specific materials characterisation methods after long-term immersion are recommended for the investigation of possible ageing effects.

P. Guttman (✉) · G. Pilz

Department Polymer Engineering and Science, Montan University Leoben,
Leoben, Austria

© Springer International Publishing AG 2017

W. Grellmann and B. Langer (eds.), *Deformation and Fracture Behaviour
of Polymer Materials*, Springer Series in Materials Science 247,

DOI 10.1007/978-3-319-41879-7_26

26.1 Introduction and Objectives

Thermoplastic polymers, especially fibre-reinforced types are increasingly used in fields of applications, which so far were dominated by metallic materials. Weight reduction and limitation of installation space require innovative and integrative components and subsequent development of polymers suitable for applications at elevated temperatures and humid environments. Polyamides, aliphatic or semi-aromatic types, exhibit comparatively high strength and stiffness combined with high toughness and are commercially available in high diversity and are therefore increasingly used for highly loaded structural parts.

Generally, the high mechanical property profiles of polyamides are strongly dependent on the strength of hydrogen bonds between carbonamide groups (CO–NH) and the methyl groups (CH₂) of adjacent backbones [1, 2]. Moreover, the polar structure of polyamides enables them to absorb water. Due to the ability of the absorbed water to form hydrogen bonds, too, some hydrogen bonds within the polyamide structure are opened and are saturated with water molecules [1–4]. The absorbed water in polyamide and subsequently weakened hydrogen bonds in the molecular network have a large influence on many properties of polyamides such as a shift of the glass transition range to lower temperatures, lowered modulus and yield stress levels and on the other hand an increase of elongation at break and toughness [1, 2, 5].

The present work focuses on the influence of end-use relevant conditions like water absorption, elevated temperatures and long loading times on the mechanical property profile of glass fibre-reinforced aliphatic and semi-aromatic polyamides—PA66-GF30, PA66-GF50 and PPA-GF35. For first evaluation immersion tests and subsequent dynamic-mechanical analysis (DMA) is used to investigate the impact of absorbed water on the temperature-dependent modulus $E(T)$. In further tensile tests the influence of water absorption on the tensile properties like short-term modulus E_t , tensile strength σ_M and elongation at break ε_B was analysed. Tensile creep tests in water were used to investigate the long-term creep behaviour at elevated temperatures of polyamides in wet materials condition.

26.2 Experimental

26.2.1 Materials

The materials investigated in this study are two aliphatic polyamide 66 types—a 30% and a 50% glass fibre-reinforced (PA66-GF30 and PA66-GF50)—and a semi-aromatic polyamide, 35% glass fibre-reinforced (PPA-GF35). All materials

are equipped with temperature and hydrolysis stabilisers and show a well-balanced mechanical behaviour for the use in highly loaded components at elevated temperatures in humid environments. Semi-aromatic polyamides are known for lower water absorption and higher glass transition temperatures compared to aliphatic polyamides like the present PA66 types.

26.2.2 *Experimental Procedure*

For all tests in this study multipurpose tensile test specimens type A, according to ISO 3167 [6], or parts of it (according to the relevant testing standards) are used. In a first step immersion tests at 60 °C in deionised water are performed to investigate the water absorption behaviour of the present polyamides, using the whole specimens (→ “wet” materials state). The relative water content was calculated based on the amount of matrix material (PA66 or PPA), the glass fibre content was supposed to not absorb any water. As a reference condition a dry materials state is provided by drying the specimens in a vacuum oven for at least 3 days at 60 °C until no further, significant moisture release is detected (→ “dry” materials state). Subsequently performed tensile tests according to ISO 527-2 [7] at 23 and 60 °C compare the short-term mechanical behaviour of dry and wet materials state. In dynamic-mechanical analysis (DMA) the temperature and frequency dependent thermomechanical behaviour and as a main comparative value the glass transition temperature T_g is investigated in 3-point bending mode for both materials conditions. The DMA tests are performed in a wide temperature range (−60 to 180 °C). As an evaluation test for the long-term performance of wet polyamides tensile creep tests at a constant creep stress of 20 MPa are used. To ensure a stable wet materials state the creep test are performed immersed in water, using a specially designed media cell (Fig. 26.1) [8, 9].

The creep tests are carried out at 60, 70 and 80 °C using the Stepped Isothermal Method (SIM) following ASTM D 6992-03 [10], an accelerated creep methodology. The decisive difference of the SIM method compared to classical creep methods is that the creep tests for multiple temperature-steps are tested within a single creep test at a single specimen and a continuously applied creep load [10, 11]. Based on these short-term creep tests (24 h for each temperature step) and time (t)–temperature (T) superposition creep modulus master curves $E_C(t)$ for a reference temperature of 60 °C can be created up to long extrapolation times. Additionally normalised creep modulus master curves (normalised to a creep modulus at $t = 0.01$ h, i.e. $E_{CN}(t)$) are used for evaluation of the relative creep tendency.

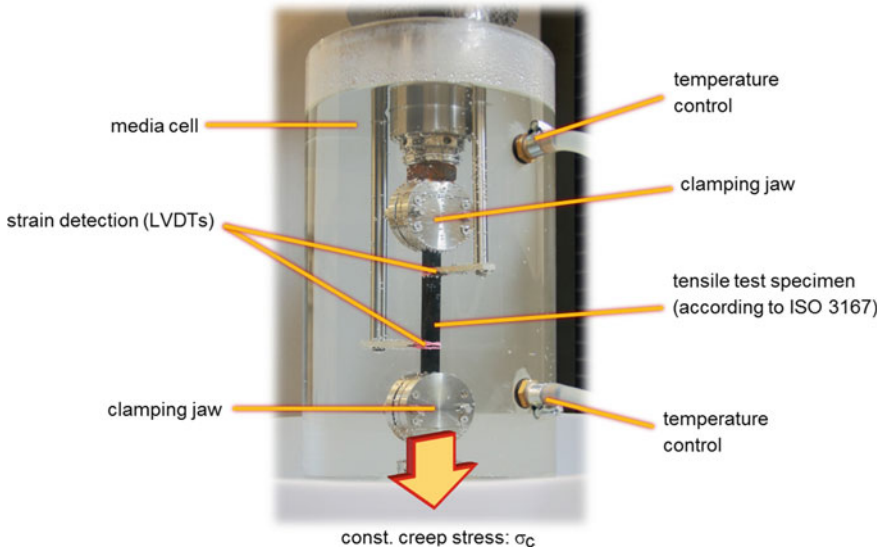


Fig. 26.1 Creep test setup with media cell for the creep behaviour at elevated temperatures in water [8, 9]

26.3 Results and Discussion

26.3.1 Water Absorption

Due to their chemical structure all polyamides have in common to absorb water from humid or water environments. Especially the polar nature of polyamides and the capability of carbon amide groups (CO–NH) to form hydrogen bonds enable distinct water absorption of polyamides, when immersed in water [4, 5]. Figure 26.2 shows the water absorption curves of the present polyamides immersed in water at 60 °C.

After 14 days a saturated state is assumed for the PA66 types, the saturation content of the semi-aromatic polyamide (PPA) is not reached after 14 days. The water content of the PA66-GF30 (calculated on the amount of matrix material) after 14 days of immersion can be found at about 7.5 wt%, whilst PA66-GF50 absorbs about 6.8 wt% water. The slight lower water content may be explained by the higher glass fibre-reinforcement and the associated obstruction of water diffusion. PPA-GF35 shows a significant lower absorption speed and lower water content of about 2.3 wt% after 14 days of immersion in water. The diffusion of water molecules between the polyamide molecules causes a weakening of or opens the hydrogen bonds between adjacent polyamide molecules. These open bonds between –CO and –NH groups can be saturated with water molecules. Further on the molecular mobility of the polyamide chains is increased and more space for water diffusion is created. This mechanism continues as long as free carbon amide

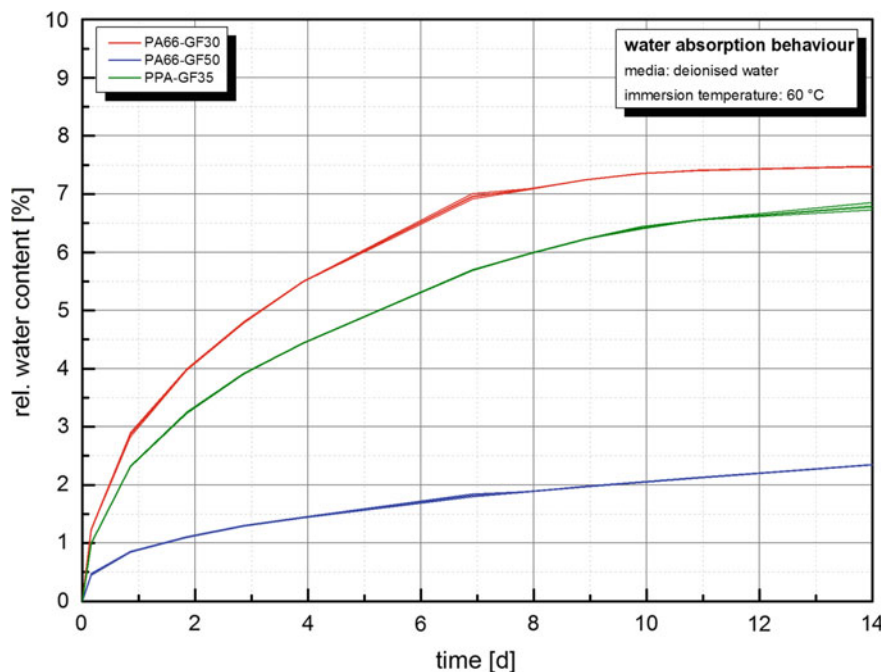


Fig. 26.2 Water absorption at 60 °C of the studied polyamide materials calculated on the amount of matrix material

groups are available. The aromatic parts in PPA reduce the available amount of carbon amide groups, which can explain the reduced water absorption speed and lower equilibrium water content of the semi-aromatic polyamide [1, 4, 5, 12]. The following result sections show some influences of water absorption on the mechanical behaviour of polyamides.

26.3.2 Dynamic-Mechanical Analysis (DMA)

A major effect of absorbed water on the behaviour of polyamides is a shift of the glass transition temperature to lower temperatures. The hydrogen bonds between the polyamide backbones are strongly contributing to the mechanical behaviour of polyamides. Due to the ability of the absorbed water to form hydrogen bonds, too, some hydrogen bonds within the polyamide structure are opened and are saturated with water molecules. Hence the higher molecular mobility of the polyamide molecules results in a distinct shift of the glass transition range to lower temperatures [1, 2, 4, 5]. Figure 26.3a–c shows the temperature dependent dynamic flexural modulus $E'(T)$ of the polyamides in dry and wet condition. Within the examined temperature range from -60 to 180 °C the characteristic decrease of the

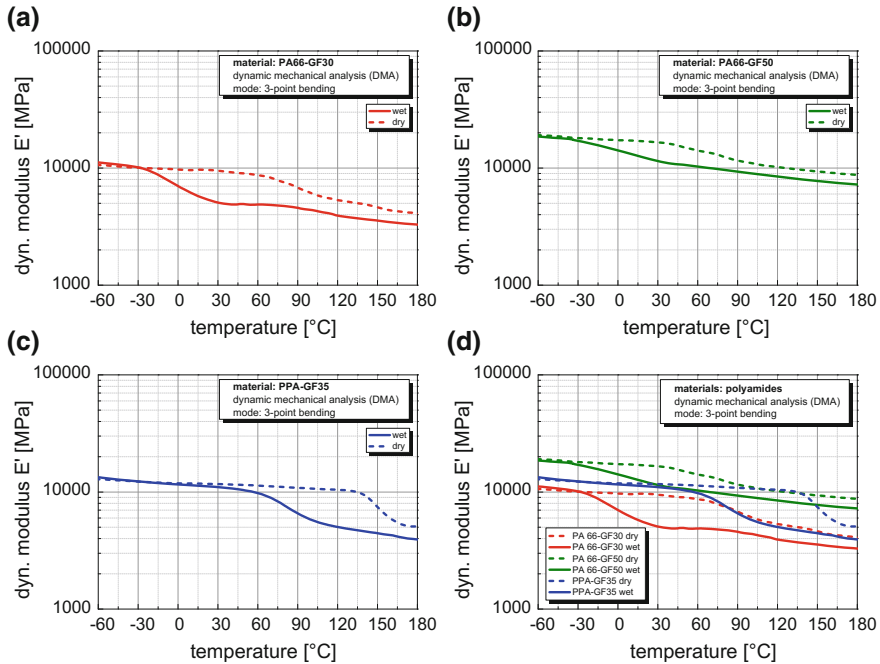


Fig. 26.3 Temperature dependency of the dynamic flexural modulus $E'(T)$ (a) and glass transition areas T_g (b) of the examined PA materials in dry and wet materials state

flexural modulus at the glass transition temperature T_g can be determined. In dry condition the glass fibre-reinforced aliphatic PA66 types show a glass transition temperature at about 50 °C, compared to the semi-aromatic polyamide PPA-GF35, which shows, caused by aromatic parts in the polyamide backbone, an explicit higher glass transition temperature at about 130 °C. The glass transition region for the PA66 types after water immersion and absorption can be found at about -35 °C. The semi-aromatic nature of PPA also means that aliphatic polyamide parts remain in the backbone and therefore can also be influenced by water absorption. Consequential the glass transition region of PPA is just as well shifted to significant lower temperatures and can be found at about 60 °C. Compared to each other (Fig. 26.3d) the glass fibre content of the investigated polyamides moves the flexural modulus level, but the glass transition and its strong dependence on the water absorption is clearly defined by the matrix polyamide.

26.3.3 Monotonous Tensile Tests

The monotonous tensile tests in this study show a combined influence of water absorption and testing temperature on the short-term mechanical behaviour. In

Fig. 26.4a–c representative technical stress–strain curves from monotonous tensile tests are shown for the investigated PA66 and PPA types at room temperature and 60 °C as typically found in end-use conditions for dry and wet materials condition. Caused by a weakening of the hydrogen bonds due to water absorption in the polyamide backbones as well as to increasing temperature the molecular mobility is increased and results in severe changes of the short-term mechanical behaviour. In general significant changes in tensile modulus E_t , tensile strength σ_M and elongation at break ϵ_B dependent on testing temperature and water absorption can be detected.

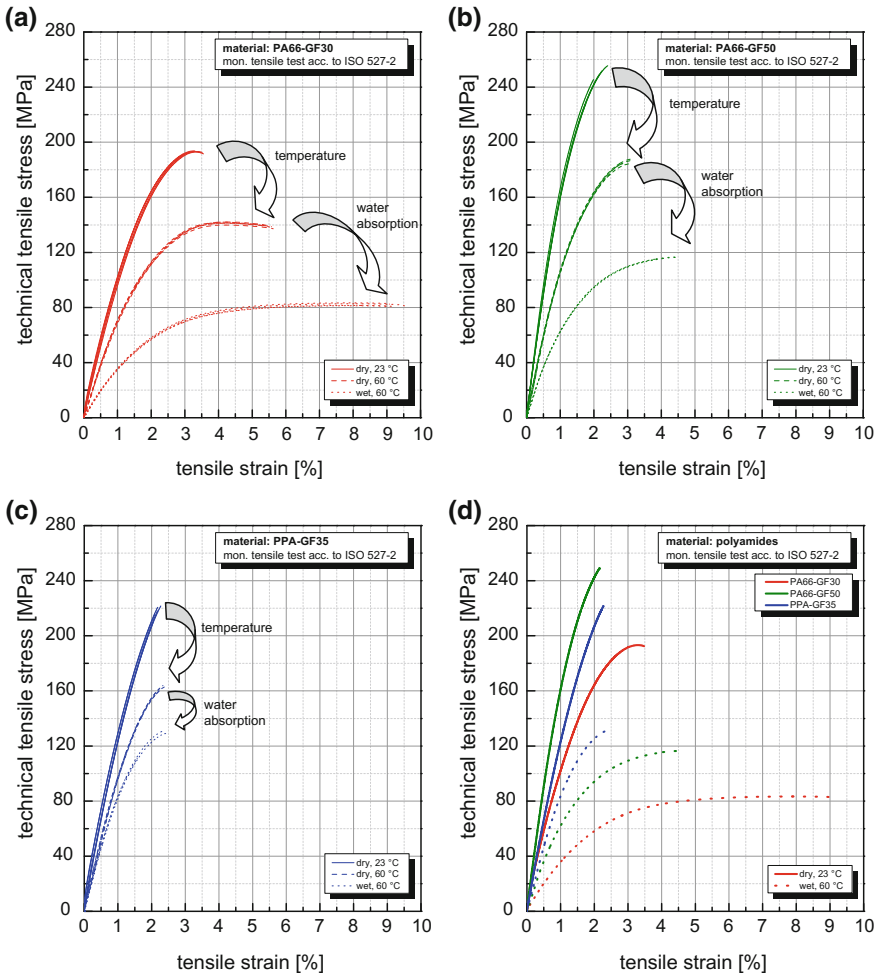


Fig. 26.4 Technical tensile stress–strain curves from monotonous tensile tests for dry and wet materials condition and testing temperatures of 23 and 60 °C for PA66-GF30 (a), PA66-GF50 (b), PPA-GF35 (c) and a comparative graph (d) for all investigated polyamides showing the impact of temperature increase and water absorption on the deformation behaviour

Table 26.1 Modulus E_t , tensile strength σ_M and elongation at break ε_B (respectively standard deviations in each case) of the investigated polyamides in dry and wet materials condition at 23 and 60 °C

Tensile modulus E_t (MPa)			
Material	23 °C/dry	60 °C/dry	60 °C/wet
PA66-GF30	11,000 ± 700	7400 ± 260	4000 ± 120
PA66-GF50	18,400 ± 780	11,500 ± 275	7700 ± 190
PPA-GF35	13,800 ± 330	10,000 ± 260	9300 ± 650
Tensile strength σ_M (MPa)			
PA66-GF30	193 ± 0.3	141 ± 0.8	82 ± 1.0
PA66-GF50	246 ± 10.5	184 ± 4.3	116 ± 0.8
PPA-GF35	217 ± 5.1	163 ± 1.3	124 ± 11.0
Elongation at break ε_B (%)			
PA66-GF30	3.5 ± 0.1	5.5 ± 0.1	9.2 ± 0.2
PA66-GF50	2.1 ± 0.2	2.9 ± 0.2	4.3 ± 0.2
PPA-GF35	2.2 ± 0.1	2.2 ± 0.1	2.2 ± 0.4

A comparison of all tensile properties determined for dry and wet state at 23 and 60 °C are shown in Table 26.1. In detail the tensile modulus E_t of PA66-GF30 in dry state at 23 °C can be found at 11,000 MPa and is decreased by increasing testing temperature to 7400 MPa. A further significant decrease caused by water absorption leads to a tensile modulus E_t of 4000 MPa. A similar trend can be found for tensile strength σ_M . A dry tensile strength at 23 °C of 193 MPa is decreased by temperature increase to 60 °C to a value of 141 MPa. Water absorption causes an additional decline of tensile strength to 82 MPa. The plasticising effect of increasing temperature and water absorption can also be seen in the final deformation behaviour as elongation at break ε_B . An increase of temperature causes an increase from 3.5% (in dry state at 23 °C) to 5.5% for dry condition at 60 °C and a further significant increase in wet state to 9.2%. PA66-GF50 shows dependent on the higher glass fibre-reinforcement a higher tensile modulus E_t , a higher tensile strength σ_M and lower elongation at break ε_B but due to the similar aliphatic polyamide matrix equal trends for the impact of temperature increase and water absorption and can be seen in detail in Table 26.1. Considering a glass transition temperature of 50 °C for both PA66 types in dry condition, therefore the tensile tests at 23 °C were performed below the glass transition region and show a high modulus, a high tensile strength and a low elongation at break. At a testing temperature of 60 °C PA66 is tested at the beginning of the glass transition temperature range. Therefore the beginning increase of the molecular mobility causes a decrease of the tensile modulus and tensile strength but an increase of elongation at break. In wet state at a testing temperature of 60 °C PA66 is analysed considerably above the glass transition region, resulting in an additional significant decrease of tensile modulus and tensile strength and a higher elongation at break. PPA-GF35 shows a glass transition temperature of about 135 °C in dry and 60 °C in wet materials condition. Hence tensile tests at 23 and 60 °C are performed considerably below the glass transition range in dry condition, which leads to a temperature-dependent decrease in dry condition of the tensile modulus from 13,800 to 10,000 MPa and a

decrease of tensile strength from 217 to 163 MPa. The beginning glass transition region at 60 °C in wet materials condition causes a slight decrease of the modulus and tensile strength, but compared to PA66 the impact of water absorption is less pronounced. A significant influence of temperature and water absorption on the final deformation behaviour of PPA-GF35, described by elongation at break ϵ_B , cannot be found.

26.3.4 Media Creep Tests

The creep behaviour of the investigated PA materials in saturated wet conditions for a reference temperature of 60 °C is depicted in Fig. 26.5. Determined from 24 h tensile creep tests according to Stepped Isothermal Method (SIM) [10, 11] at 60, 70 and 80 °C and subsequent application of the time–temperature superposition principle creep modulus master curves $E_C(t)$ for a reference temperature of 60 °C in wet materials state can be estimated for a wide time range up to a creep time of 10 years. The short-term value of creep modulus at the beginning of creep loading can be found for PA66-GF30 at low values of about 4100 MPa and decreases over an extrapolated creep time of 10 years to 3000 MPa. By comparison PA66-GF50 exhibits a higher creep modulus level caused by the higher glass fibre content.

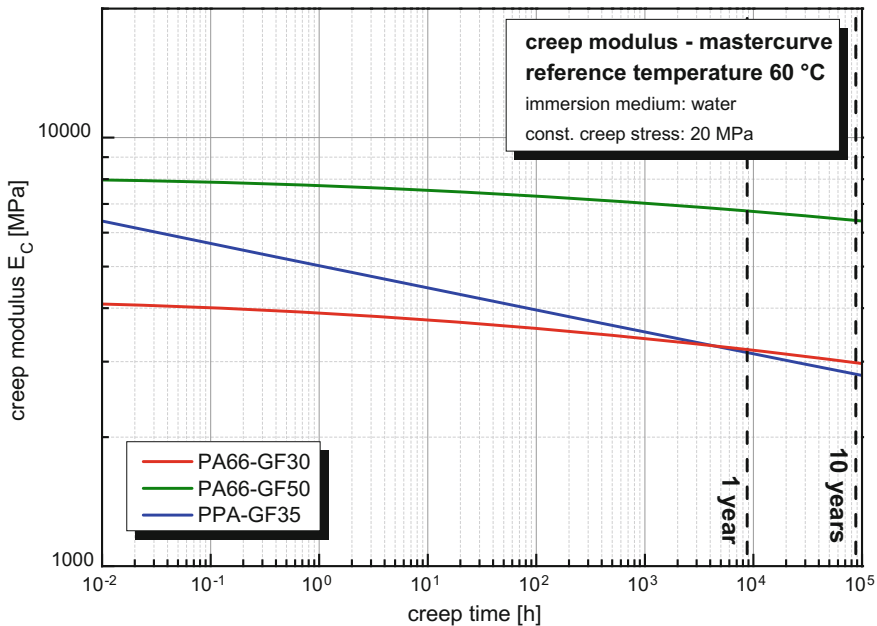


Fig. 26.5 Creep modulus master curves $E_C(t)$ for the various polyamides investigated for a reference temperature of 60 °C in wet materials state

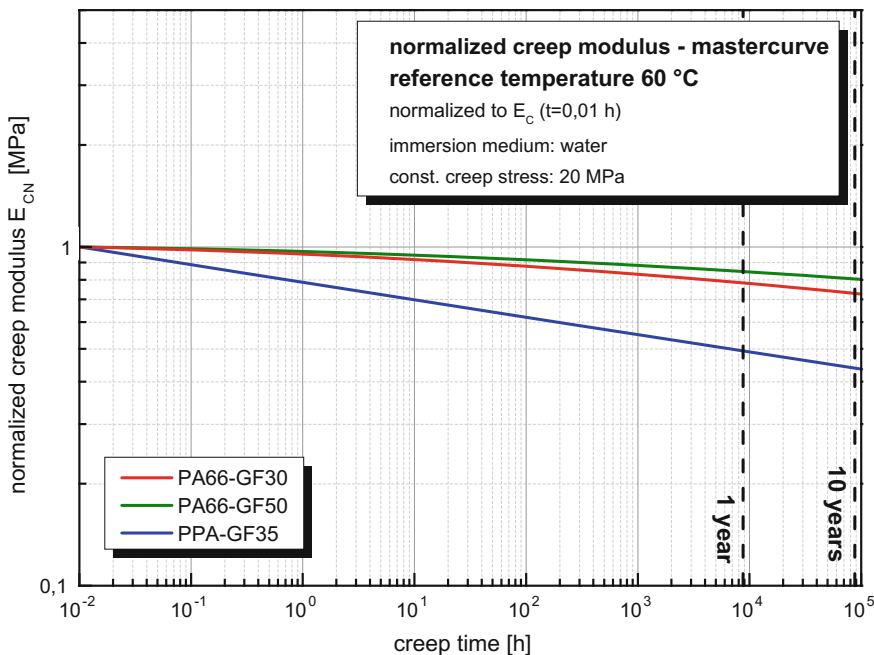


Fig. 26.6 Normalised creep modulus master curves $E_{CN}(t)$ for the various polyamides investigated for a reference temperature of 60 °C in wet materials state

Starting at 8000 MPa for short creep times at 0.01 h ($E_{CN}(t)$) the creep modulus is lowered to 6400 MPa for a predicted creep loading times of 10 years. The creep modulus of the semi-aromatic polyamide PPA-GF35 shows a distinctly stronger time dependency in water immersion at 60 °C compared to the aliphatic PA66 materials. A short time value of 6300 MPa after 0.01 h is reduced to 2900 MPa after extrapolation to a creep period of 10 years. A normalisation of the creep modulus to short-term values at 0.01 h [calculated by (26.1)] allows to compare the creep tendency of the different polyamides equalising the different initial creep modulus levels (Fig. 26.6).

$$E_{CN} = \frac{E_C}{E_C(t = 0.01 \text{ h})} \tag{26.1}$$

The lowest creep tendency can be found for PA66-GF50, showing a decline of about 20% over an extrapolated creep time of 10 years. Due to the lower glass fibre content the creep modulus level of PA66-GF30 is significantly lower, the creep tendency as normalised modulus trend is compared to PA66-GF50 only slightly increased to a decline of about 27% over an extrapolated creep time of 10 years. In comparison amongst the investigated polyamides the semi-aromatic PPA-GF35 shows the highest creep tendency. The short-term creep modulus at 0.01 h can be

found at a significantly higher value compared to PA66-GF30 at 6300 MPa, also due to the higher glass fibre content. The decline of the creep modulus of about 56% to value of 2900 MPa after 10 years of extrapolated creep time shows a significantly higher creep tendency than both aliphatic PA66 materials.

Reconsidering the dynamic-mechanical behaviour of PPA-GF35 in wet materials state shown in Sect. 26.3.2 it can be seen, that the reference temperature of 60 °C for the creep master curves is located at the beginning of the glass transition range. The molecular mobility of the amorphous phase of PPA-GF35 is significantly increased at the glass transition, leading to an increasing creep tendency. The use of an accelerated creep methodology and time–temperature superposition principle allows a time-efficient description of the long-term behaviour over a wide range of time. Additional physical or chemical ageing effects, which may occur under end-use conditions and long application times, exceeding the total experimental immersion and testing time, are not considered in the present creep testing method. Hence, the corresponding materials property changes by environmental ageing effects have to be estimated in further investigations.

26.4 Summary and Outlook

The polar structure of polyamides enables them to absorb water. Aliphatic polyamides absorb water faster and to a higher extend than semi-aromatic polyamides, due to the aromatic parts within the semi-aromatic polyamide structure. The absorbed water causes a weakening of the hydrogen bonds between adjacent polyamide backbones. For both, aliphatic and semi-aromatic polyamides, a significant shift of the glass transition was found. In tensile testing the water absorption and increase of testing temperature show a decrease of the tensile modulus E_t and tensile strength σ_M for the PA66 and the PPA types. Whereas PA66-GF30 and PA66-GF50 also show an increase of elongation at break with water absorption and higher testing temperature, no such effect can be found for PPA-GF35. An efficient creep test methodology using the Stepped Isothermal Method (SIM) and the principle of time–temperature superposition show differences in the long-term creep behaviour of the investigated polyamides in wet materials condition. It can be shown, that, if the testing or reference temperature of creep tests is chosen at the beginning of the glass transition range, the short-term mechanical properties remain at a high level, but the creep tendency is significantly increased. With testing temperatures distinctly above glass transition, PA66-GF30 and PA66-GF50 show a lower creep tendency compared to PPA-GF35 which was tested at a temperature close to the glass transition range. Physical or chemical ageing effects induced by water absorption of polyamides, which may occur after long-term exposure, are not considered within the present test program. Further specific materials characterisation methods after long-term immersion are recommended for the investigation of possible ageing effects.

References

1. Kohan, M.I. (ed.): *Nylon Plastics Handbook*. Carl Hanser, Munich (1995)
2. Greiner, R.: Technische Eigenschaften. In: Bottenbruch, L., Binsack, R. (eds.) *Technische Thermoplaste*. Carl Hanser, Munich (1998), pp. 193–269
3. Elsner, P.: Polyamide (PA). In: Domininghaus, H., Elsner, P., Eyerer, P., Hirth, T. (eds.) *Kunststoffe: Eigenschaften und Anwendungen*, 8th edn. Springer, Berlin (2012), pp. 638–731
4. Williams, J.C.L.: Moisture absorption, dimensional stability and density. In: Kohan, M.I. (ed.) *Nylon Plastics Handbook*. Carl Hanser, Munich (1995), pp. 324–333
5. El Sayed, A.: Modifizierung der Polyamide. In: Bottenbruch, L., Binsack, R. (eds.) *Technische Thermoplaste*, pp. 75–101. Carl Hanser, Munich (1998)
6. ISO 3167 (2014): *Plastics—Multipurpose test specimens*
7. ISO 527-2 (2012): *Plastics—Determination of tensile properties—Part 2: Test conditions for moulding and extrusion plastics*
8. Guttman, P., Röper, F., Pilz, G.: Polymer selection and testing methodology for high demand applications under environmental conditions. In: *Proceedings of the International Conference Polymeric Materials*, 12–14 Sept 2012, Halle (2012), pp. 58–59
9. Guttman, P., Röper, F., Pilz, G.: The impact of time, temperature and media on polymer selection for high demand applications. In: *Proceedings of the 3rd Austrian–Slovenian Polymer Meeting 2013*, 03–05 Apr 2013, Bled (2013), pp. 60–63
10. ASTM D 6992 (2016): *Standard test method for accelerated tensile creep and creep-rupture of geosynthetic materials based on time–temperature superposition using the stepped isothermal method*
11. Achereiner, F., Engelsing, K., Bastian, M., Heidemeyer, P.: Accelerated creep testing of polymers using the stepped isothermal method. *Polym. Test.* **32**, 447–454 (2013)
12. Goetz, W., Roerdink, E.: Teilaromatische, teilkristalline Polyamide. In: Bottenbruch, L., Binsack, R. (eds.) *Technische Thermoplaste*. Carl Hanser, Munich (1998), pp. 803–809

Chapter 27

Accelerated Measurement of the Long-Term Creep Behaviour of Plastics

F. Achereiner, K. Engelsing and M. Bastian

Abstract Plastic parts are increasingly used in engineering applications with high demands on long-term mechanical behaviour. Therefore, suitable accelerated test methods are strongly required. The Stepped Isothermal Method (SIM), a short-term creep experiment during which the temperature is elevated stepwise, was originally developed for product testing of geosynthetics. This method was successfully applied to characterise the long-term creep behaviour of polypropylene tensile specimens. The measured strain can be rescaled and subsequently shifted according to the time–temperature superposition principle (TTSP) to build a master curve out of a single experiment. SIM master curves matched the results of the classical TTSP procedure while reducing the experimental effort to a minimum. This offers a useful tool, e.g. for a quick screening of material formulations during the early development stages or the at-line assessment of resins as part of quality assurance. Furthermore, SIM experiments can be performed until creep failure and, thus, accelerate the determination of the creep strength and the construction of creep rupture curves.

27.1 Introduction

Plastic parts are increasingly used in engineering applications with high demands on long-term mechanical behaviour. Therefore, this behaviour needs to be considered in the early stages of product development in order to meet the requirements, particularly for products relevant to security or difficult to replace where the minimum guaranteed service life is often significantly longer than 10 years and may reach up to 50 or 100 years (e.g. for pipes and geomembranes for landfills).

The service life of products permanently exposed to mechanical load is mostly limited by failure or excessive deformation. Plastic pipes laid in the ground must be for example designed against the increasing deformation of the cross section to ensure full functionality. However, polymers are viscoelastic materials and their

F. Achereiner (✉) · K. Engelsing · M. Bastian
SKZ – German Plastics Center, Würzburg, Germany

mechanical behaviour strongly depends on time. A straightforward extrapolation of short-term creep experiments over more than one decade (log scale) is mostly impossible. Estimating the long-term deformation under static load would thus require conventional creep experiments over a long period of 5–10 years in order to account for product lifetimes of 50–100 years. Therefore, tight product development schedules necessitate a way to accelerate the strongly time-dependent creep response with adequate accelerated testing methods.

Increasing the temperature is a common way to accelerate the time-dependent creep response [1]. Based on the time–temperature superposition principle (TTSP) [2, 3], short-term creep experiments at various temperatures are sufficient to generate a master curve, which describes the long-term deformation at a reference temperature [4]. This method involves shifting the timescale with a temperature dependent factor a_T , so that the measured creep curves match the creep behaviour at a reference temperature, as described by Williams, Landel and Ferry (WLF) [5]:

$$\varepsilon_0(T_0, t) = \varepsilon\left(T, \frac{t}{a_T}\right), \quad (27.1)$$

where ε_0 is the strain at reference temperature, T_0 the reference temperature, t the time, ε the strain at the elevated temperature T . The shift factor a_T can usually be described with the WLF equation or an Arrhenius equation. The WLF equation, where C_1 and C_2 are empirical constants, is mostly employed for polymers above the glass transition temperature T_g :

$$\log a_T = \frac{-C_1 \cdot (T - T_0)}{C_2 + T - T_0}. \quad (27.2)$$

However, this equation is not valid for semi-crystalline polymers well below their melting points. Seitz and Balazs [4] showed that in this case the description of the shift factor a_T follows an Arrhenius equation:

$$\log a_T = \frac{\Delta H}{2.303 R} \cdot \left(\frac{1}{T} - \frac{1}{T_0}\right), \quad (27.3)$$

where ΔH is the activation energy and R the universal gas constant.

Despite these equations, the determination of the shift factors may be in practice somewhat difficult. Particularly when testing complete components, measurements scatter may be significant and the construction of a single master curve for one load level thus requires many short-term creep experiments at various temperatures implying long testing times and high costs. Therefore, Thornton et al. [6, 7] proposed a new experimental procedure called Stepped Isothermal Method (SIM) to measure all the creep information necessary for building the master curve while minimising both scattering effects and total testing time.

27.2 Principle of the Stepped Isothermal Method

The Stepped Isothermal Method (SIM) was originally introduced to predict the long-term creep behaviour of geogrids in soil reinforcement applications. This method makes use of the high surface-to-thickness ratio of the product, which is a specificity of most geosynthetics. The very fast heating of the sample allows elevating the temperature stepwise while maintaining the sample under constant load and so gather information about the creep behaviour of the material for various temperatures within a single creep experiment, i.e. for the same sample.

SIM master curves involve shifting creep curves using the temperature-dependent shift factor a_T based on TTSP. Some additional analysis steps are, however, required prior to this shifting procedure in order to account for the temperature change during the SIM experiment, as described schematically in Fig. 27.1. The deformation caused by thermal expansion while heating the sample must first be subtracted from the measurement data (see Fig. 27.1a) to obtain the deformation solely related to the creep behaviour. A core feature of SIM is to consider the creep behaviour for each temperature step as if the measured deformation results of an independent isothermal creep test starting at the virtual start time t' (see Fig. 27.1b). The independent creep tests are rescaled in the virtual time scale ($t-t'$) (see Fig. 27.1c) and can then be shifted to a master curve the same way as in conventional TTSP (see Fig. 27.1d). The resulting master curve describes the creep behaviour at the start temperature—labelled here as the reference temperature—for the applied load level.

SIM was mainly applied for product testing of geosynthetics. Several investigations for various geosynthetics proved a good agreement of SIM master curves with conventional long-term creep tests [8–10]. Therefore, SIM meanwhile becomes a well-established method for the accelerated product testing of geosynthetics; standards have been published for both tensile creep (ASTM D 6992) and compressive creep (ASTM D 7361).

Despite the advantages of SIM, only sparse attempts have been made to extend the application range of this method to other polymeric products. Alwis and Burgoyne [11] applied SIM successfully to creep testing of aramid yarns. Like geosynthetics, high-performance yarns mostly feature a very small cross-sectional area and can thus be rapidly heated. More recently, first attempts were made with thicker samples: Thomas et al. investigated PE-HD under tensile load with respect to plastic pipes [12]; Bozorg-Haddad and Iskander focused on compressive loading of PE-HD [13]. Previously published work of the authors [14] shows that SIM can be also used for accelerated measurement of the long-term creep behaviour of polypropylene with conventional dumbbell specimens.

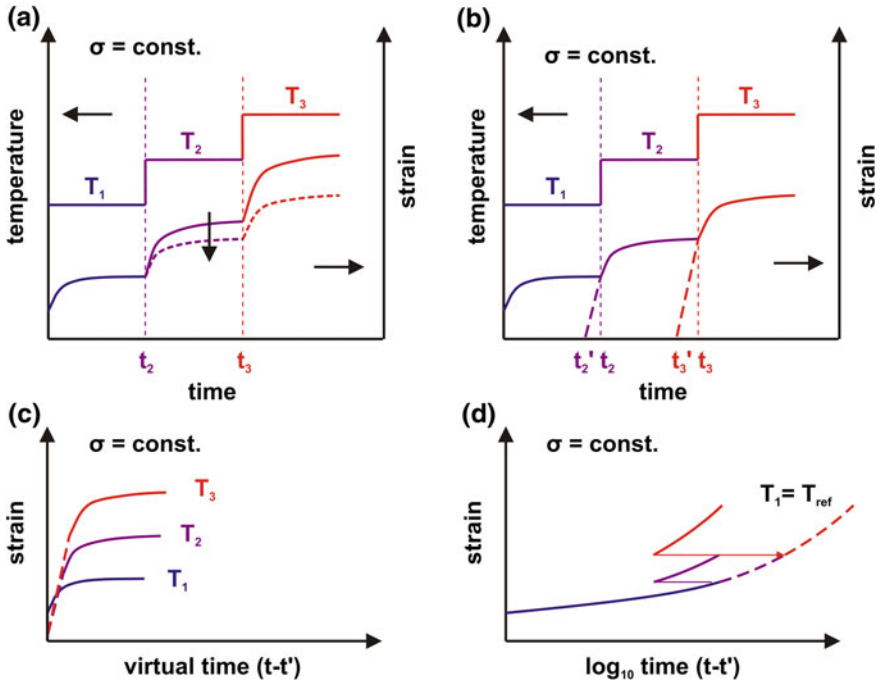


Fig. 27.1 Principle of the SIM procedure: correction of measured data due to thermal expansion (a), determining virtual start time t' (b), rescaling (c), curve shifting according to TTSP (d), reprinted from [14] with permission from Elsevier

27.3 Creep Testing Using SIM

Like in previous work of the authors [14], polypropylene is used here as an example for creep testing because of its widespread use in engineering applications with long-term static loading. The investigations do not focus on testing components but on characterising the material behaviour in general. Therefore, creep testing was performed following ISO 899-1 on standard dumbbell specimens (ISO 527-2). They were injection-moulded with a thickness of 4 mm using several commercially available polypropylene homopolymer types and stored under standard climate conditions (23 °C/50% relative humidity) before testing.

Short-term creep tests were performed on a creep test rig developed together with Coesfeld GmbH & Co. KG, Dortmund (Germany), providing 5 measuring stations with electro-mechanical drive and closed-loop load control (see Fig. 27.2). The tests were conducted in an insulated chamber, which maintains a stable temperature (± 0.5 K) over many hours but also allows a quick heating (>5 K min^{-1}). The creep strain was measured optically. All SIM experiments were started at 23 °C and lasted up to 3 days. The load was maintained constant all the time but the temperature was gradually increased in 10 K steps. Between two heating steps the

Fig. 27.2 Creep test rig for SIM measurements

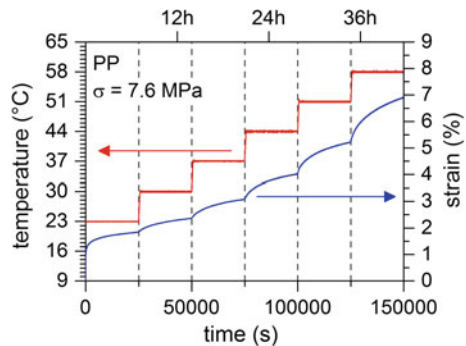


temperature was maintained constant for a dwell time of at least 10,000 s. The raw data of an exemplary SIM test are displayed in Fig. 27.3.

The experimental setup for SIM was also used to perform short-term isothermal creep tests for 7 different temperature levels using 3 specimens per temperature. Altogether, 21 single creep experiments each lasting at least 10,000 s were necessary to generate a master curve for a reference temperature of 23 °C according to conventional TTSP. Reference long-term measurements were performed for up to one year at 23 °C using a dead-weight loading setup.

Due to the specific analysis approach of SIM, the change of temperature has to be quick enough so that the transition phase with undefined creep behaviour can be considered as negligible. Due to the poor thermal conductivity of polymers the bulk temperature of a 4 mm thick tensile specimen increases indeed slower than its surface temperature. However previous investigations showed for a temperature increase of 10 K that the target temperature can be reached in the bulk within max. 600 s [14]. Hence, compared to the dwell time at constant temperature, the heating of the sample can be considered as stepwise (see Fig. 27.4).

Fig. 27.3 Example of raw SIM data for a polypropylene dumbbell specimen tensile loaded at 30% of the yield stress



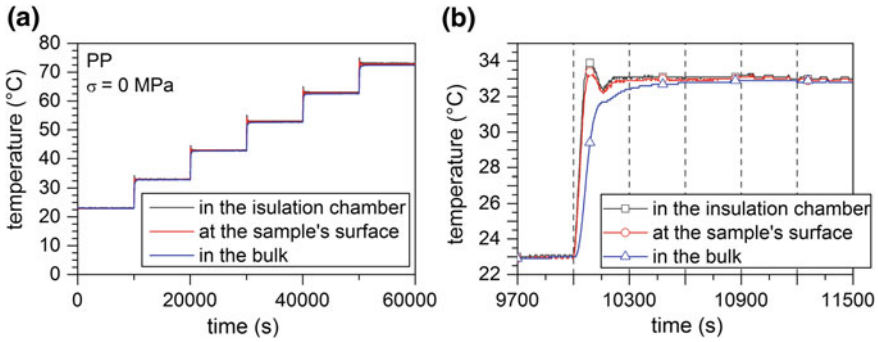


Fig. 27.4 Temperature of the sample during a complete SIM test (a) and during the first heating step (b), reprinted from [14] with permission from Elsevier

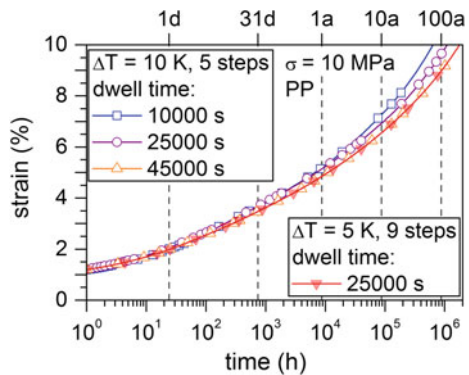
The actual test procedure is fairly straightforward and can be fully automated, so that SIM testing does not involve high personnel costs. However, it requires thorough test planning, since four major test parameters can influence both the testing time and the quality of the results:

- the start temperature
- the temperature increase per step
- the number of steps
- the dwell time at constant temperature

The maximum testing temperature is determined by the first three parameters and represents a major limitation of SIM. This temperature primarily defines the maximal shift factor and, thus, the predictable range for long-term creep. However, the maximal temperature must be carefully chosen, so that the creep mechanism remains unchanged over the whole temperature range of the SIM test.

Figure 27.5 shows that SIM tests using many small temperature steps yield similar creep master curves as SIM tests using higher but less temperature steps. Due

Fig. 27.5 Influence of the dwell time of SIM experiments on the resulting master curve



to the iterative analysis procedure, small errors add up with each step. Thus, limiting the number of steps may help reducing potential errors. However, it increases the requirements for the experimental setup with respect to the speed of heating.

Furthermore, the creep master curves only match when adjusting the dwell time as well. For a given temperature increase per step, the creep prediction for times longer than one year clearly varies with the chosen dwell time for the SIM experiment (see Fig. 27.5). On the other hand, for a given dwell time the master curves depend significantly on the temperature increase per step. Altogether, short dwell times and high temperature steps lead to higher strains than the actual long-term creep behaviour, which means that the inadequacy of poorly chosen testing conditions is conservative [6].

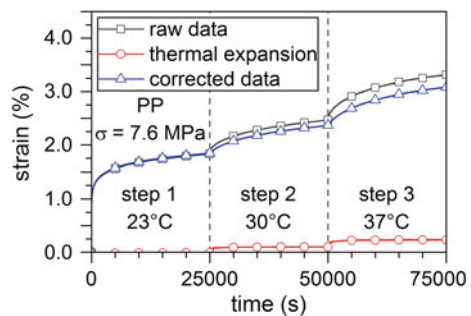
Long dwell times and small temperature steps result in a higher accuracy to the detriment of testing duration and costs. Therefore, sensible planning always involves a compromise between the quality of creep prediction and the practicability of the test method, depending on the purpose of the specific experiment. In addition, optimal conditions may depend on the testing material and on the experimental setup.

27.4 Construction of a Master Curve

As previously mentioned, the specific testing procedure requires a precise analysis in order to obtain a smooth master curve. In the following the implementation of the four analysis steps described schematically in Fig. 27.1 will be shown in detail using the SIM raw data displayed in Fig. 27.3.

The correction of the raw data to account for thermal expansion can be done using the coefficient of thermal expansion (CTE) or directly by recording the deformation resulting from the temperature increase with a controlled load set to 0 N. Since the experimental setup allows investigating up to 5 specimens simultaneously, the direct measurement of thermal expansion was performed for each experiment for one measuring station and then deducted from the deformation measured for higher loads on the other stations as displayed in Fig. 27.6. The

Fig. 27.6 Correction of raw data by subtracting thermal expansion



resulting corrected data describes exclusively the deformation caused by the creep behaviour.

The core feature of SIM analysis is to consider this corrected data separately for each temperature step as if the creep deformation results of an independent isothermal creep test starting at the virtual time t' . This application of the Boltzmann superposition principle beyond the linear viscoelastic range (small strains) is an approximation for engineering purposes, though proven appropriate in numerous investigations for geosynthetics [7–10].

The empirical procedure to determine the starting time of such independent creep tests is based on the specificity of SIM: since creep is measured using a single sample, the physical state at the junction between two steps is unique. Two independent isothermal creep experiments can only reflect this specificity when the creep rate for this unique creep strain is identical for both creep curves. Therefore, the slope at the beginning of a temperature step is determined in the logarithmical time scale ($t-t'$) using an estimated value of t' . This value is then varied iteratively until the calculated slope matches the slope at the end of the previous step, as shown in Fig. 27.7a. This procedure is repeated for all temperature steps and the rescaled SIM data (see Fig. 27.7b) can be used to generate a master curve by means of horizontal shifting according to TTSP.

However, SIM data correspond to continuous creep deformation and the creep curves do not overlap like in the conventional TTSP procedure. Furthermore, due to the non-isothermal conditions leading to undefined creep behaviour, the transition region at the beginning of each temperature step should be excluded from the analysis. The creep strain of the previous step is thus extrapolated according to Findley's equation [15] until it reaches the strain level immediately after the excluded data as displayed in Fig. 27.8a. Therefore, the creep curve of the current step can so be appended directly to the previous curve, hence building a smooth master curve. Each master curve describes the long-term creep behaviour only for one reference temperature and one load level, but the SIM experiments can be repeated for different load levels (see Fig. 27.8b) or different starting temperatures.

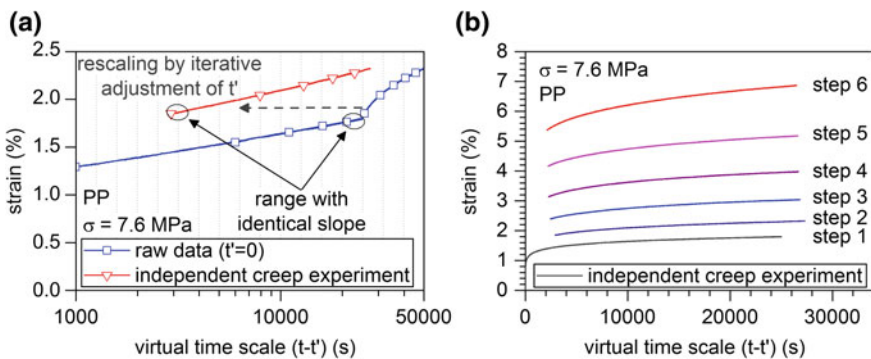


Fig. 27.7 Determining the virtual start time t' (a) in order to rescale the temperature steps into virtually independent isothermal creep tests (b)

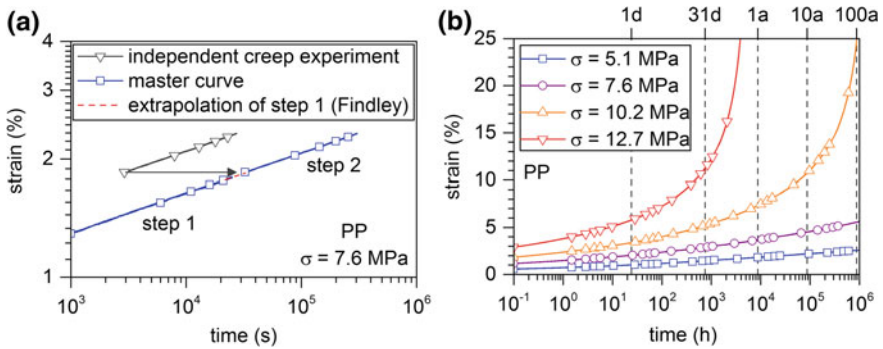


Fig. 27.8 Shifting procedure according to TTSP (a) in order to generate a creep master curve for one load level or more if several SIM experiments are performed (b)

27.5 Assessment of the Method

Since some of the analysis steps, particularly the determination of the virtual start time t' , are rather time intensive and operator sensitive, a computer-based routine was employed for the automated analysis of all SIM measurements presented in this work. The consistency of the curve shifting can be evaluated by displaying the shift factors a_T in an Arrhenius plot as described in previous work [14]. This procedure is particularly useful when the testing parameters were poorly chosen and the creep mechanism is not constant over the whole temperature range.

Thanks to the automated processing of the creep data, the master curves resulting from SIM experiments on various samples all match very well, regardless of whether they are obtained during the same experiment at different measuring stations or during various experiments at the same measuring station. Figure 27.9 displays the good reproducibility of the SIM master curves for two different polypropylene types.

Since SIM master curves always result from one single experiment, the specimen variability need to be assessed separately. Due to the good reproducibility of the SIM analysis, this can be limited to short creep times.

The SIM results were compared with the conventional TTSP procedure based on several isothermal short-term creep experiments. As displayed in Fig. 27.10, the comparison of TTSP and SIM master curves shows a perfect match. This confirms the initial hypothesis that SIM data can be split into virtual independent creep experiments. SIM analysis is indeed appropriate and the method can be regarded as a fully functional alternative to conventional TTSP procedure.

The actual creep data was also measured directly in long-term experiments up to 1 year and then extrapolated according to Findley's equation. Both SIM and TTSP master curves basically match actual creep data; however, long-term comparison shows a clear divergence. Physical ageing is presumed to be responsible for this discrepancy, since the short-term creep tests offer only a snapshot of the ageing

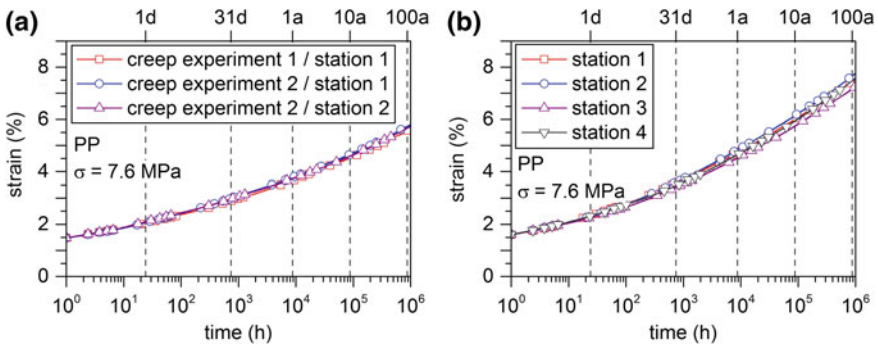
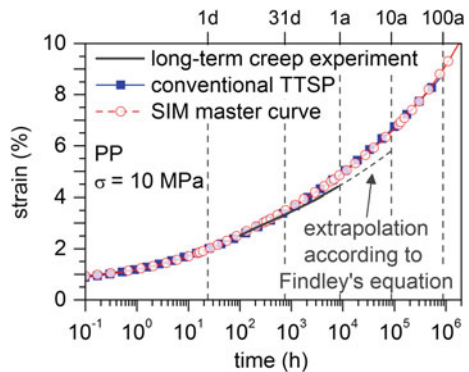


Fig. 27.9 Comparison of master curves at 23 °C resulting from SIM experiments on various samples of two different polypropylene types, obtained during various experiments at the same measuring station (a) or during the same experiment at different measuring stations (b)

Fig. 27.10 Comparison of SIM, conventional TTSP and long-term creep experiments at 23 °C, reprinted from [14] with permission from Elsevier



state and do not reflect that the sample continues ageing while it creeps, leading to a stiffening of the material with increasing time [16]. Creep prediction based on TTSP or SIM is therefore conservative.

27.6 Applications of SIM

Beside some specific requirements to the experimental setup, the implementation of SIM is rather straightforward and can be automated to a very large extent. Therefore, SIM allows reducing the experimental effort to a minimum, compared to the classical TTSP procedure, while still providing the same accuracy of the master curves. Since one single experiment accounts for the long-term creep behaviour up to 100 years, it saves both time and money, which makes SIM a very attractive accelerated testing method, especially for applications where quick results are

decisive like investigations during the product development stage or for an at-line quality assessment during production.

The good reproducibility of the construction of master curves indicates that SIM is a suitable comparative method which can be applied as a useful tool, e.g. for quick screening of material formulations. Figure 27.11 displays SIM master curves for 3 polypropylene types with different formulations. It shows that one of these formulations lead to a clearly higher long-term creep than the others for the same applied load and, thus, would not be suitable for a product where creep is an issue.

For applications reaching beyond comparative purposes, SIM can also be useful but additional long-term measurements are required to validate the SIM master curves, especially with regard to the influence of physical ageing. Such validation should preferably be done each time a new material is investigated in order to estimate the possible error. Since the required experimental effort is reduced to a minimum, it is possible to measure in a very short time the long-term creep of a material for various load levels as displayed in Fig. 27.8b. This provides enough creep data to build isochronous stress–strain curves as required for the calibration of material models for FEM structure simulation.

SIM focusses on the accelerated measurement of long-term creep deformation. However, SIM experiments can be also used in addition to standard isothermal short-term creep tests for accelerating the prediction of long-term creep failure (see Fig. 27.12). Ductile failure requires to choose some failure criterion, based on which the time-to-failure can be directly read off the creep curves and displayed in a creep rupture curve as shown in Fig. 27.13.

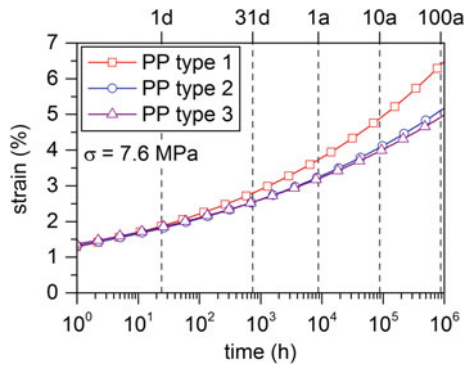


Fig. 27.11 Comparison of SIM master curves at 23 °C for 3 polypropylene types with different formulations

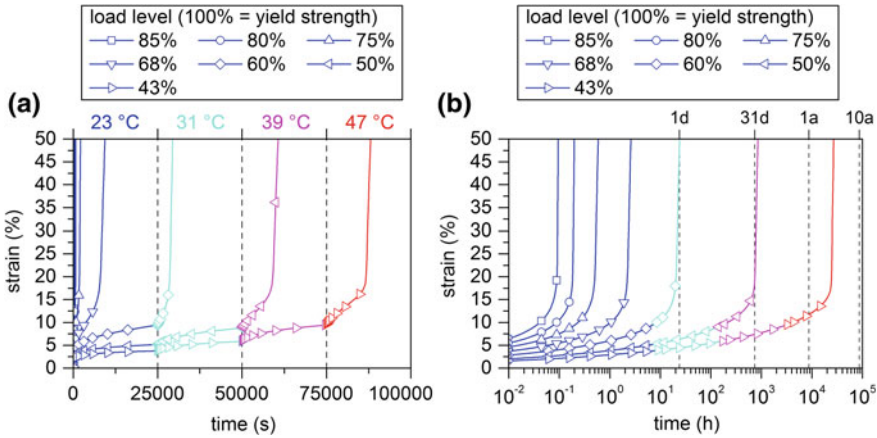
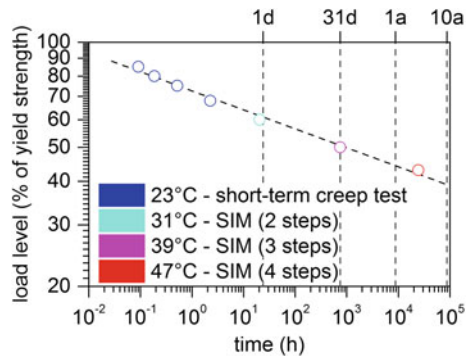


Fig. 27.12 Creep data resulting from standard isothermal short-term creep tests and from SIM tests for several load levels (a) and the resulting master curves (b)

Fig. 27.13 Time-to-rupture curve at 23 °C based on short-term isothermal creep tests and SIM tests performed on polypropylene dumbbell specimens



27.7 Conclusions

The Stepped Isothermal Method (SIM), a short-term creep experiment during which the temperature is elevated stepwise was originally developed for product testing of geosynthetics. This method was here successfully applied to characterise the long-term creep behaviour of polypropylene tensile specimens, using an adequate experimental setup to perform a quick heating of these thick samples.

The actual test procedure is fairly straightforward and can be automated. However, it requires thorough test planning, since four major test parameters can influence both the testing time and the quality of the results. The measured strain was analysed in successive steps to generate a master curve. The core feature of SIM analysis is the rescaling of the measured data to account for virtually

independent isothermal creep tests, which can be shifted to a master curve according to the time–temperature superposition principle (TTSP).

Using an automated analysis procedure, SIM proved to have good reproducibility. Compared to the classical TTSP procedure, SIM allows reducing the experimental effort to a minimum while still providing the same accuracy of the master curves. The results show that SIM is a suitable comparative method which can be applied as a useful tool, e.g. for a quick screening of material formulations during the early development stages or the at-line assessment of resins as part of quality assurance.

Quantitative applications such as the determination of isochronous stress–strain curves are possible. However, the predictions are limited by the snapshot effect of short-term tests which prevent for considering the physical ageing phenomenon. Furthermore, SIM experiments can be performed until creep failure and, thus, be employed in addition to standard isothermal short-term creep tests to accelerate the determination of the creep strength and the construction of a creep rupture curves.

References

1. Ferry, J.D.: *Viscoelastic Properties of Polymers*, 3rd edn. Wiley, New York (1980)
2. Leaderman, H.: Creep and creep recovery in plasticized polyvinyl chloride. *Ind. Eng. Chem.* **35**, 374–378 (1943)
3. Tobolsky, A.V., Andrews, R.D.: Systems manifesting superposed elastic and viscous behavior. *J. Chem. Phys.* **13**, 3–27 (1945)
4. Seitz, J.T., Balazs, C.F.: Application of time–temperature superposition principle to long term engineering properties of plastic materials. *Polym. Eng. Sci.* **8**, 151–160 (1968)
5. Williams, M.L., Landel, R.F., Ferry, J.D.: The temperature dependence of relaxation mechanisms in amorphous polymers and other glass-forming liquids. *J. Am. Chem. Soc.* **77**, 3701–3707 (1955)
6. Thornton, J.S., Allen, S.R., Thomas, R.W., Sandri, D.: The stepped isothermal method for time–temperature superposition and its application to creep data on polyester yarn. In: Rowe, R.K. (ed.) *Proceedings of the 6th International Conference on Geosynthetics* (Atlanta, 25.–29.03.1998). Industrial Fabrics Association International, Roseville (1998), pp. 699–706
7. Thornton, J.S., Paulson, J.N., Sandri, D.: Conventional and stepped isothermal methods for characterizing long term creep strength of polyester geogrids creep of product. In: Rowe, R.K. (ed.) *Proceedings of the 6th International Conference on Geosynthetics* (Atlanta, 25.–29.03.1998). Industrial Fabrics Association International, Roseville (1998), pp. 691–698
8. Zornberg, J.G., Byler, B.R., Knudsen, J.W.: Creep of geotextiles using time–temperature superposition methods. *J. Geotech. Geoenvironmental Eng.* **130**, 1158–1168 (2004)
9. Bueno, B.S., Costanzi, M.A., Zornberg, J.G.: Conventional and accelerated creep tests on nonwoven needle-punched geotextiles. *Geosynthetics Int.* **12**, 276–287 (2005)
10. Yeo, S.-S., Hsuan, Y.G.: Evaluation of creep behavior of high density polyethylene and polyethylene-terephthalate geogrids. *Geotext. Geomembr.* **28**, 409–421 (2010)
11. Alwis, K.G.N.C., Burgoyne, C.J.: Accelerated creep testing for aramid fibres using the stepped isothermal method. *J. Mater. Sci.* **43**, 4789–4800 (2008)
12. Thomas, R., Nelson, J., Cuttino, D.: The use of the stepped isothermal method for estimating the long-term creep modulus, creep strain and strength of polyethylene pipe resins. In: *Proceedings of Plastic Pipes XV* (Vancouver, 20.–22.09.2010). Vancouver (2010), p. 10

13. Bozorg-Haddad, A., Iskander, M.: Predicting compressive creep behavior of virgin HDPE using thermal acceleration. *J. Mater. Civ. Eng.* **23**, 1154–1162 (2011)
14. Achereiner, F., Engelsing, K., Bastian, M., Heidemeyer, P.: Accelerated creep testing of polymers using the stepped isothermal method. *Polym. Test.* **32**, 447–454 (2013)
15. Findley, W.N., Lai, J.S., Onaran, K.: *Creep and Relaxation of Nonlinear Viscoelastic Materials with an Introduction to Linear Viscoelasticity*. Applied Mathematics and Mechanics 18, North-Holland Publishing, Amsterdam New York Oxford (1976)
16. Brinson, H.F., Brinson, L.C.: *Polymer Engineering Science and Viscoelasticity—An Introduction*. Springer, US, New York (2008)

Part VI
**Influence of Ageing on Mechanical
and Fracture Mechanics Performance
of Thermoplastics and Elastomers**

Chapter 28

Hygrothermal Ageing of Injection-Moulded PA6/GF Materials Considering Automotive Requirements

T. Illing, M. Schoßig, C. Bierögel, B. Langer and W. Grellmann

Abstract Short-glass fibre-reinforced polyamide 6 (PA6/GF) materials have been used for many decades successfully in the automotive industry, especially for components in exterior and interior area. Due to the required product qualification testing in the automotive field, components are exposed to, among others, a hygrothermal stress of 1000 h or more during the development phase. This work aims to contribute to enhanced understanding of the mechanical properties of stiffness, tensile strength, hardness and fracture toughness of short-glass fibre-reinforced polyamide 6 materials at hygrothermal aging. The results show a decrease in properties, which is more characterised by the absorption of moisture and less than by other aging processes.

28.1 Introduction

Short-glass fibre-reinforced polyamide 6 (PA6/GF) materials have been used for many decades successfully in the automotive industry, especially for components in exterior and interior area. The advantageous combination of mechanical and thermal properties and a favorable production by injection moulding enables a wide operational range of applications and variable shaping. Due to the required product qualification testing in the automotive field, components are exposed to, among others, a hygrothermal stress of 1000 h or more during the development phase. The current trend towards lightweight and less material consumption leads to thinner

T. Illing (✉)

Valeo Schalter und Sensoren GmbH, Bietigheim-Bissingen, Germany

M. Schoßig · C. Bierögel · B. Langer · W. Grellmann

Polymer Service GmbH Merseburg, Merseburg, Germany

C. Bierögel · W. Grellmann

Centre of Engineering, Martin Luther University Halle-Wittenberg, Halle/Saale, Germany

B. Langer

Department of Engineering and Natural Sciences,

University of Applied Sciences Merseburg, Merseburg, Germany

© Springer International Publishing AG 2017

W. Grellmann and B. Langer (eds.), *Deformation and Fracture Behaviour of Polymer Materials*, Springer Series in Materials Science 247,

DOI 10.1007/978-3-319-41879-7_28

walls in automotive components at the same time increasing demands for accuracy, tolerance and ageing stability. This work aims to contribute to enhanced understanding of the mechanical properties of stiffness, tensile strength, hardness and fracture toughness of short-glass fibre-reinforced polyamide 6 materials at hygrothermal ageing. The mechanical behaviour of semi-crystalline polymers in general and in particular of glass fibre-reinforced polyamide materials as a function of glass fibre content, of fibre length and fibre diameter in consideration of the orientation as well as absorption of moisture, under thermal and hydrothermal ageing, is widely known [1–11]. Thus, the *E*-modulus and the tensile strength can be calculated by different models, wherein the fibre orientation is taken into account as a factor in current models. The orientation of the short-glass fibres, which is generated mainly by the injection moulding process, influences not only the geometric change in hygrothermal ageing but also the level of mechanical properties. It can be determined visually or by X-ray microstructure analysis. Further, it can also be analysed by a tool filling study of injection moulding process. At a hygrothermal load of PA6/GF material chemical and physical ageing processes are induced due to temperature, relative humidity and a certain time frame which lead to a change of the entire property level [12, 13]. The relevant ageing processes are shown in Fig. 28.1. The absorption of moisture by the diffusion process occurs as a function of the relative humidity which is connected with a decrease of strength and stiffness as well as a relaxation of the polymer matrix [14–16].

This characteristic material behaviour could be supported by chemical ageing processes such as hydrolysis or oxidation (according Becker and Brown [1] and Kohan [2] these processes start to impact PA6 above a temperature of about 80 °C), but could also be impeded by counteracting physical ageing processes such as post-crystallisation.

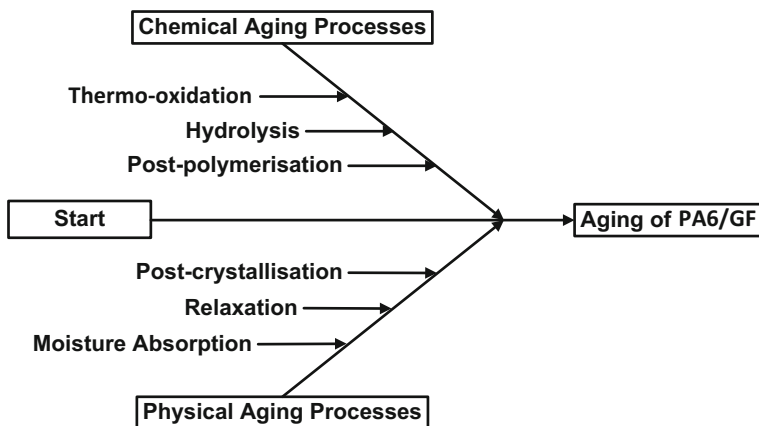


Fig. 28.1 Relevant ageing processes, classified according to DIN 53005 [13]

28.2 Material and Experiments

In this work, short-glass fibre-reinforced polyamide 6 (PA6/GF) were investigated. For the investigations plates with dimensions of $185 \times 160 \text{ mm}^2$ were prepared by injection moulding. Then out of this plate six multipurpose specimen of type 1A according to ISO 3167 were extracted [17]. This was done to assess the influence of both orientations along and transverse to the flow direction of injection moulding. Figure 28.2 shows schematically the sample positions of the multipurpose specimen in the injection moulded plates in longitudinal direction. The film gate is indicated by a red arrow and the fibre orientation is indicated by black dashed lines. The positions of the test specimens in the plate are indicated as L1–L6 in the following diagrams. To evaluate the effect of humidity and temperature on the properties of the PA6/GF materials different climate conditions for ageing were selected. The parameters used together with the underlying standards are listed in Table 28.1 [18–20]. The hygrothermal ageing was carried out in a climate chamber in each case up to 1000 h, at defined time intervals of 24, 48, 96, 480 and 1000 h test specimens were taken out for the characterisation of the ageing by the determination of the change in mechanical and thermal properties. The tensile strength σ_M was determined by tensile test with the device Zwick Z020 universal testing machine according to ISO 527-1 [21] and ISO 527-2 [22] at a test speed of 50 mm min^{-1} and the E -modulus E_t with the device Instron 5507 universal testing machine with a test speed of 5 mm min^{-1} . The ball indentation hardness HB was determined according to ISO 2039-1 [23] with the device Instron-Wolpert K-Testor K2524 and a steel ball with 5 mm diameter as indenter. The evaluation of fracture toughness was carried out according to the standard MPK-IKBV [24] by the instrumented impact test with the pendulum impact tester Zwick HIT25.

The change in the degree of crystallisation X_c was determined with the device Mettler-Toledo DSC 820 according to ISO 11357-1 [25] at a heating rate of

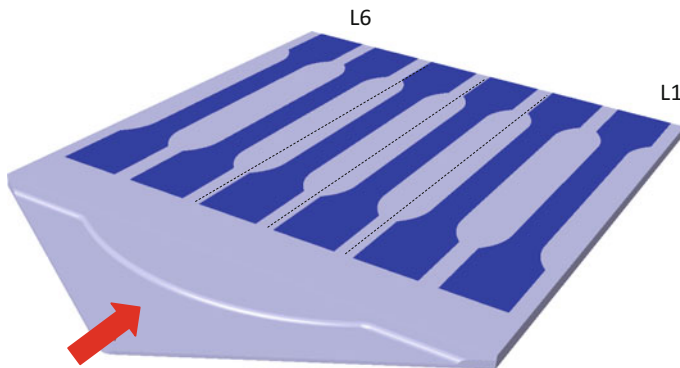


Fig. 28.2 Schematic description of extraction the test specimen off the injection-moulded plate; with a red arrow the film gate is marked, the flow direction is marked by dotted lines, the enumeration of test specimen starts from right (L1) to left (L6)

Table 28.1 Summary of parameters of the climatic tests and the referenced standards

No.	Temperature (°C)	Relative humidity (% RH)	Referenced standard
1	85	10	IEC 60068-2-2: Environmental testing—Part 2-2: Tests—Test B: Dry heat [18]
2	85	50	
3	85	85	IEC 60068-2-78: Environmental testing—Part 2-78: Tests—Test Cab: Damp heat, steady state [19]
4	−40	–	IEC 60068-2-1: Environmental testing—Part 2-1: Tests—Test A: Cold [20]

10 K/min within a temperature range from 0 to 300 °C. The orientation of the glass fibres was determined by micro-CT with the equipment General Electric nanotom m with a voxel size of 4 μm and subsequent software evaluation with Volume Graphics Studio Max V2.2 [26–28]. The mathematical description of the glass fibres orientation are represented by a tensor 2nd order according to Advani and Tucker [29] with a_{xx} for alignment in flow direction, a_{yy} for alignment perpendicular to flow direction and a_{zz} for alignment vertical to flow direction. For determining the average molecular weight, the gel permeation chromatography (GPC) was carried out at 40 °C column temperature in accordance to DIN 55672-1 [30].

28.3 Results and Discussion

The orientation of reinforcing materials such as short-glass fibres in the polymer matrix has a significant influence on the mechanical property level and was the subject of many scientific publications [31–33]. The fibre orientation is mainly influenced by the flow conditions during the filling process of the tool. In this case, the flow velocity v_F effects in dependence on the gate and the component geometry, shear rate $\dot{\gamma}$ and consequently a shear stress, which is responsible for the orientation [34]. Figure 28.3 shows the flow velocities and the shear rates at the positions L1–L3 in the injection-moulded plate (see Fig. 28.1), as well as the fibre orientation in the flow direction out of the filling simulation as orientation tensor component a_{xx} [31, 35, 36].

As can be seen from the diagram, the flow conditions in the cavity cause a slight difference of the shown parameters as a function of plate position. The flow rate influenced by the injection pressure and the film gate increases from the inside to the outside in the plate which is also valid for the shear rate and the fibre orientation. The different fibre orientation is reflected in different stress–strain curves. Figure 28.4 shows these curves for the test specimen of position L1–L6 for PA6/GF30 and which correlate with the position in the plate. The difference in tensile strength between position L1 and L3 is approx. 20 MPa. For the elongation at break the difference between these positions is approx. 0.5%. The difference of

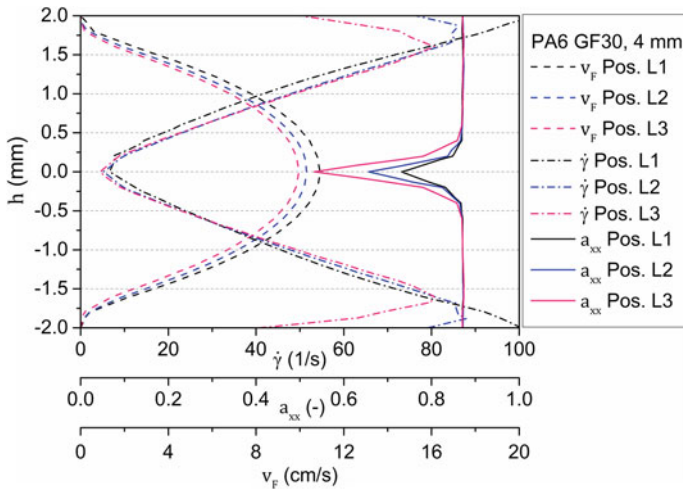
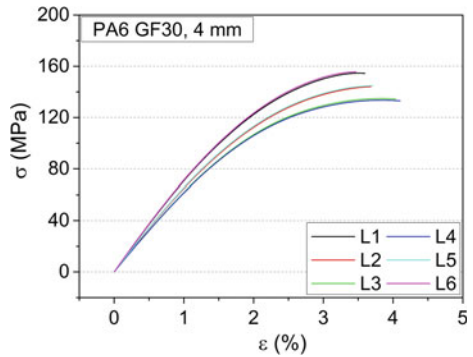


Fig. 28.3 Flow velocity of polymer melt, shear rate and glass fibre orientations out of filling simulation for positions L1–L3

Fig. 28.4 Stress–strain curves of PA6/GF30 in dry-as-moulded state depending on position in the injection-moulded plate (see Fig. 28.2)



the average fibre orientations in the flow direction, as analysed by the micro-CT, for these positions is about 9%. By the similar habitus of the stress–strain curves it can be assumed that between positions L1 and L6, L2 and L5 and L3 and L4, a similar fibre orientation exists, which is caused by the symmetrical pattern of the polymer melt in the flow direction during injection moulding.

If the different fibre orientation is analysed with a filling simulation (see Fig. 28.3), the determined values of the orientation tensors are comparatively less different to each other than the stress–strain diagrams in Fig. 28.4 would identify it. An analysis of the fibre orientation by micro-CT and subsequent software evaluation enables a comparison of orientation values of the filling simulation, which are generated by using the Folgar-Tucker model (FT-model) and based on this the modified model of Wang and Jin (RSC-model), and the values of the micro-CT

[37, 38]. As shown in Fig. 28.5, the calculated orientations of the filling simulation are by an average of about 10–20% higher compared to the micro-CT data. In both methods, the orientation of the glass fibres in the flow direction increases from the inside to the outside of the plate. Furthermore, the filling simulation shows only a slight change of the core zone, whereas the micro-CT data show an increase in the core zone depending on the plate position from inside to outside of the plate. The core zone represents an area in the layer structure of the injection moulded polymer with glass fibres mainly oriented transverse to the flow direction, as it is already described by McNally [39], Bernasconi et al. [40] and Toll and Anderson [41]. The shifted core zone, which can be seen particularly at the position L3 of the micro-CT data, is caused by the eccentric film gate in the tool. The orientation of the glass fibres, which is shown in Fig. 28.5 by a mathematical description, is shown in Fig. 28.6 for the three positions L1–L3 after micro-CT and subsequent software evaluation as cross-sectional images in the flow direction [35, 36]. The orientation angle of the glass fibres are graded by colour. The broadening of the core zone and the decrease of the glass fibre orientation from the outside to the inside of the plate is clearly visible.

If the specimens are exposed to a hot and dry climate (e.g. 85 °C, 10% RH) or a cold climate of –40 °C for duration of 1000 h, the change of the tensile strength σ_M is shown in Fig. 28.7. As expected, the curves show only a slight change in tensile strength. Only from a climate of 95 °C and 10% RH, the effects of the chemical ageing process thermal oxidation can be detected, so that after 1000 h, a decrease in tensile strength by about 9% was recorded. If the same material is exposed to a hot and humid climate of 85 °C, 85% RH, the level of mechanical properties permanently changes. As can be seen in Fig. 28.7, the ageing is dominated by absorption of moisture. Knowingly this leads to a decrease in tensile strength within 96 h up to 50%, which is also the case at a hydrothermal ageing, as reported by Thomason [42].

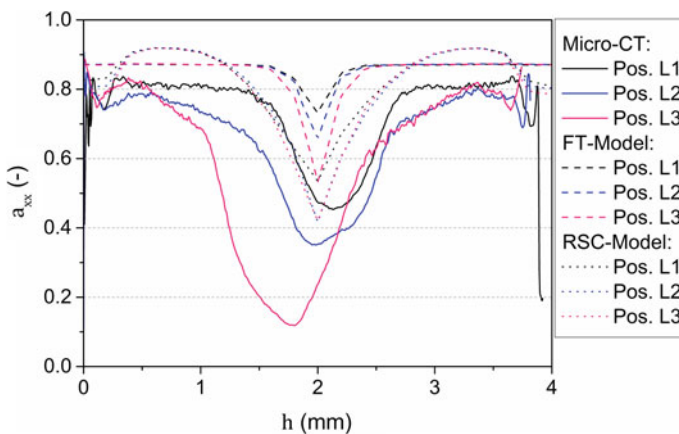


Fig. 28.5 Comparison of different orientation models to the experimental orientation of micro-CT

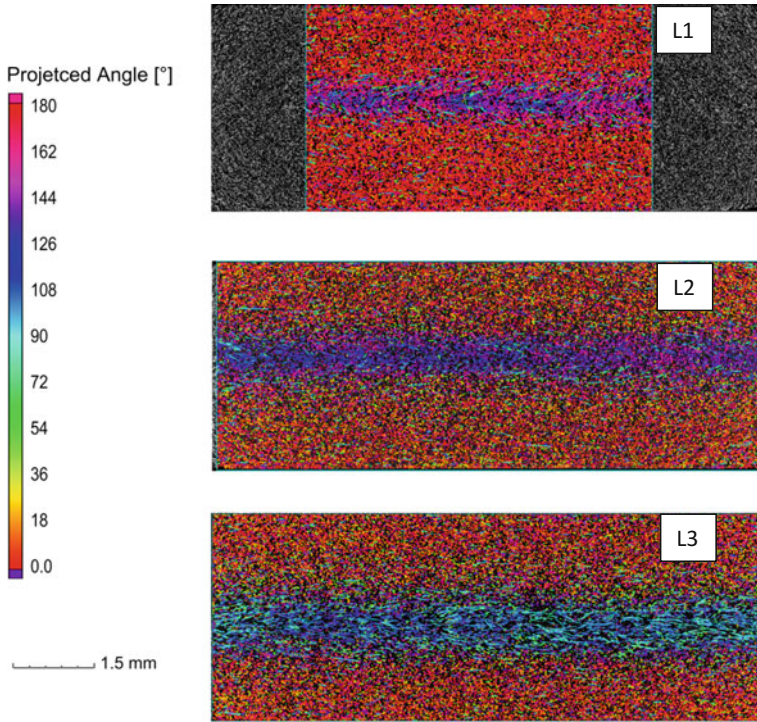
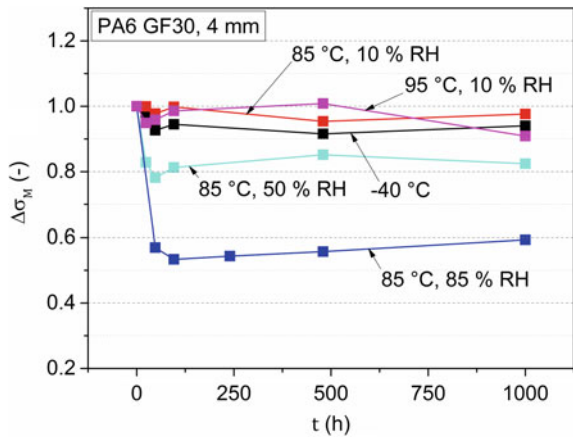


Fig. 28.6 Representation of the glass fibre orientation of the position L1–L3 after micro-CT and software analysis with Volume Graphics Studio Max V2.2

Fig. 28.7 Decrease of normalised tensile strength during due to hygrothermal ageing in different climate tests



In contrast to the ageing in water, where a further reduction of tensile strength takes place, no further reduction in tensile strength after the first 96 h of ageing in climate conditions of 85 °C and 85% RH was detected. The minimum is reached and there is again an increase in tensile strength as a function of temperature by occurring post-crystallisation. The post-crystallisation causes by the higher degree of crystallinity a higher level of tensile strength and also it leads to a displacement of water molecules, which could be observed also as an increase in tensile strength. A climate storage at 85 °C and an average relative humidity of 50% causes a decrease in tensile strength of 18%, in which the effect of increasing tensile strength by post-crystallisation was not detected.

In comparison to the tensile strength σ_M , the tensile modulus E_t reacts more sensitively to the absorption of moisture, as was also found by Jia et al. [43]. The change of tensile modulus as a function of climate test duration is shown in Fig. 28.8 for several climate conditions. In contrast to the tensile strength an influence of a post-crystallisation on the stiffness cannot be observed within 1000 h, if the material is exposed to climatic conditions of 85 °C and 85% RH. The decrease of the tensile modulus as well as the tensile strength depends linearly on the moisture content until certain moisture absorption. After Jia et al. [43] this is valid until the moisture absorption of 1.5%, confirming the recent experimental results. At moisture absorption greater than 1.5%, the decrease in stiffness and tensile strength slows down relatively to moisture absorption.

The change of ball indentation hardness HB at climatic tests with constant 85 °C and different humidity levels and at -40 °C is shown in Fig. 28.9 as a function of time. At climate conditions of 85 °C and 10% RH changes are hardly observed within 1000 h. This material behaviour changes at climatic tests with 50% or 85% relative humidity. By absorbing moisture in the amorphous regions of the hygroscopic polyamide, there is a rapid decrease of the ball indentation hardness. Moisture absorption of 1.1% (see Table 28.2) leads to a decrease of the ball indentation hardness of approx. 36% and moisture absorption of 3.1% (see

Fig. 28.8 Effect of hygrothermal ageing to normalised tensile modulus of PA6/GF30 depending on duration of different climate tests

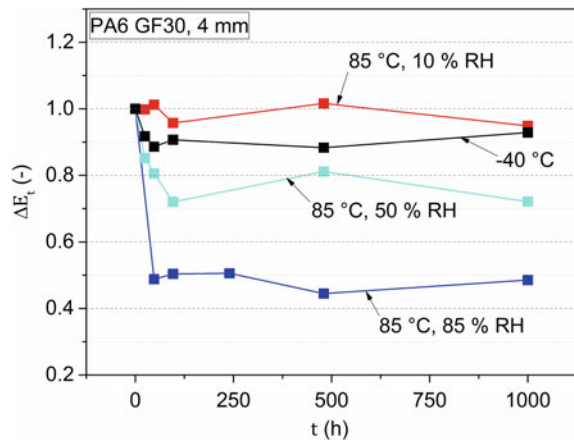


Fig. 28.9 Change of ball indentation hardness due to hygrothermal ageing in different climatic conditions

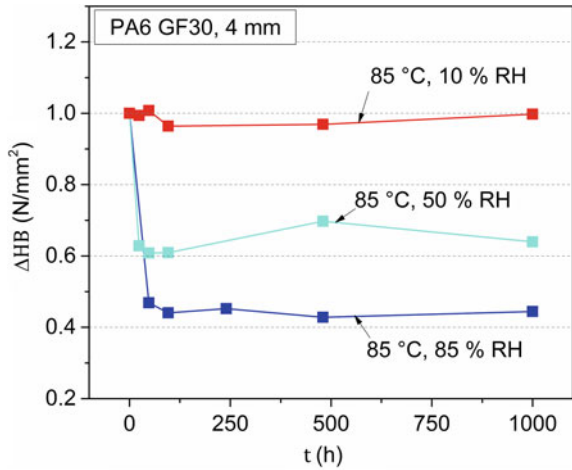


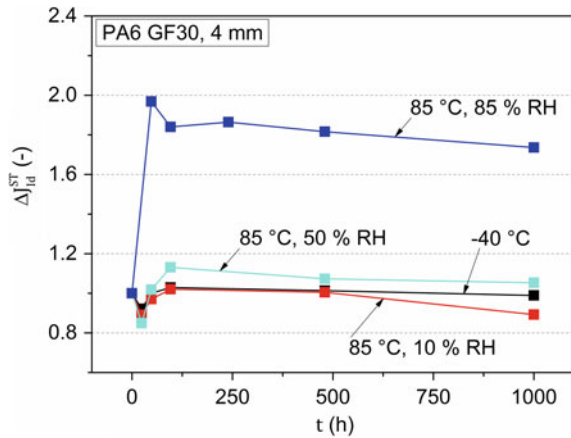
Table 28.2) results in a decrease of the ball indentation hardness of about 56%. This decrease depending on the absorbed moisture content of 3.1% shows the same tendency as described in Brandrup et al. [44], in which for unreinforced PA6 at saturation level (corresponding to a moisture absorption of approx. 3%) a decrease in the ball indentation hardness of 47% was reported.

The changes in the fracture toughness parameters in different climate conditions are exemplified for the J -value according to the evaluation method of Sumpter and Turner in Fig. 28.10. Thereby the concept of the J -integral enables a consideration of the energy of the fracture process of plastics [45]. The shown values for J_{id}^{ST} are considered as geometry independent in dry and in aged state [24, 46]. In dry-hot climate conditions at 85 °C and 10% RH the change of J_{id}^{ST} is small, the decrease amounts after 1000 h approx. -11%. This is also valid for a climate test in -40 °C, where the decrease of 1.1% is negligible. At a climate test at 85 °C and an average humidity of 50% RH, the linear elastic deformation behaviour with dominated unstable crack propagation does not change, despite moisture absorption of about 0.9%. The increase of J_{id}^{ST} is about 5%. Only at a humid-heat climate test at 85 °C and 85% RH, the brittle fracture mechanical behaviour changes into an elastic-plastic material behaviour with dominated unstable crack propagation due to moisture absorption. An increase of J_{id}^{ST} of approx. 74% can be observed here.

Table 28.2 Summary of physical ageing processes as post-crystallisation and moisture absorption, after 1000 h for PA6/GF30

No.	Climate conditions	Absolute change of degree of crystallisation (%)	Relative mass change (%)
1	85 °C, vacuum	+5.4	-0.2
2	85 °C, 10% RH	+5.7	+0.1
3	85 °C, 50% RH	+1.0	+0.9
4	85 °C, 85% RH	+0.8	+3.1

Fig. 28.10 Change of J -value due to hygrothermal ageing in different climatic tests



A post-crystallisation takes place in semi-crystalline PA6 materials depending on time, temperature and relative humidity, as already described. This affects sustainably mechanical, thermal and other physical properties of the material. The calculation of the degree of crystallisation X_c was carried out according to (28.1), where the sample mass was reduced of the moisture-related weight gain and Ψ is the content of glass fibres [47].

$$X_c = \frac{\Delta H_m}{(1 - \Psi)\Delta H_m^0} \cdot 100\% \quad (28.1)$$

As determined by differential scanning calorimetry (DSC) the melting enthalpy ΔH_m is obtained to the value for 100%-crystalline material ΔH_m^0 from the literature with 230 J/g [47, 48]. In Table 28.2 the change in the degree of crystallisation X_c at 85 °C and different moisture levels for the material PA6/GF30 based on the original value after 1000 h are summarised. Due to the high temperature at a climate test with 85 °C and 10% the degree of crystallisation increases of 5.7%. In comparison to that at 85 °C and vacuum the degree of crystallisation increases of 5.4% which is slightly smaller. At an average degree of relative humidity of 50% and the same temperature the increase amounts to 1%. In humid–heat climate test at 85 °C and 85% RH the increase is slightly smaller and amounts approx. 0.8%. The results in dry–hot climate are similar to those of Shu et al. [49], who had reported an increase of 1.7 and 3.3% depending on the PA6 material at a thermal storage at 110 °C. In humid–heat climate conditions of 70 °C and 100% RH Valentin et al. [50] have observed an increase in the degree of crystallisation of PA66/GF40 material of 5.7–6.5%, which is higher than the current results. However, no detailed information on the manufacturing process of the specimens by injection moulding was available on the results of Valentin et al. The small increase of the degree of crystallisation in humid–heat climate conditions and the reduced increase at climate conditions with an average relative humidity of 50% after 1000 h depend most likely on the moisture inside the specimen. In order not to

influence the effects of the injection moulding and the subsequent ageing and to enable an investigation of the glass transition temperature T_g , the DSC samples were not dried. By the water molecules present in the polymer matrix, the distances between the macromolecules are extended and the hydrogen bonds are weakened. A subsequent calorimetric investigation shows a lower value of the enthalpy with wet samples than in the dry state. For the wet samples the degree of crystallinity cannot be determined reliably. This is supported by the observations of Ehrenstein et al. [47] and Hassan et al. [51] in which PA6 and PA66/GF samples were analysed in dry and wet state by DSC and determined in each case a lower degree of crystallisation in the wet state. Furthermore, a correlation of the moisture content to the enthalpy was set-up for PA6 and PA66 from Yue and Chan [52], which was determined by DSC analysis. Due to the moisture dependent enthalpy, also the slightly increasing degree of crystallisation at 85 °C and 50% RH could be explained. The smaller increase of the degree of crystallinity X_c during the climate test correlates with the determined moisture absorption.

The analysis, whether chemical ageing processes, such as hydrolysis, thermal oxidation or post-polymerisation induced by the different climate tests within the required climate area, was performed on the specimens with the GPC method. The study was carried out with test samples which were exposed to 85 °C and different levels of relative humidity. According to Kohan [2] and Becker and Braun [1] chemical ageing processes in PA starts from about 80 °C to impact the material. For the change in the average molar mass at 85 °C a function of relative humidity was determined. Table 28.3 shows the relative change of the average molecular weight of PA6/GF30 depending on the relative humidity at a temperature of 85 °C. For calculating the relative change the number average molecular weight was used. It is observed that, for a dry–hot climate test at 85 °C and 10% RH, a small increase in the average molecular weight occurs, which is suggested to be a post-polymerisation. In a climate test at 85 °C and 50% RH, this effect is amplified, which is due to the increased distances between the molecular chains by diffused water molecules that favor a molecular change. In contrast, a reduction of the average molar mass of 8.2% takes place at humid–heat climate conditions at 85 °C and 85% RH, indicating hydrolysis due to the humidity dependence. A decrease in

Table 28.3 Summary of changing molar mass due to chemical ageing processes after 1000 h in different climate conditions for PA6/GF30

No.	Climate conditions	Δ Molar mass due to hydrolysis (%)	Δ Molar mass due to post-polymerisation (%)
1	85 °C, 10% RH	–	+3.1
2	85 °C, 50% RH	–	+0.9
3	85 °C, 85% RH	–8.2	–

the average molecular weight by hydrolysis was also observed by Bergeret et al. [53] in PA66/GF30 materials. However, the decrease was 28%, because of the climate conditions which were 135 °C and 100% RH.

28.4 Summary and Conclusion

The experimental results show that the fibre orientation of short-glass fibres has a great influence on the mechanical strength. If the fibre orientation is analysed, the used method has a major impact on the results and influences later the usability in integrative simulations. A dry-hot climate test has little effect within 1000 h on the mechanical properties. In contrast, in humid-heat climate tests a decrease in mechanical properties due to water absorption and parallel ageing processes as hydrolysis and post-crystallisation is observed. A comparison of the normalised change in the mechanical properties of tensile strength σ_M , tensile modulus E_t , ball indentation hardness HB and J -integral J_{Id}^{ST} is shown in Fig. 28.11. As it can be seen the decrease in properties is more characterised by the absorption of moisture and less than by other ageing processes. The hardness and tensile modulus are more sensitive to moisture absorption than tensile strength, in contrast to that the value of J_{Id}^{ST} increases by approx. 74% due to moisture absorption. The presented findings allow the consideration of the effects of ageing during the product design.

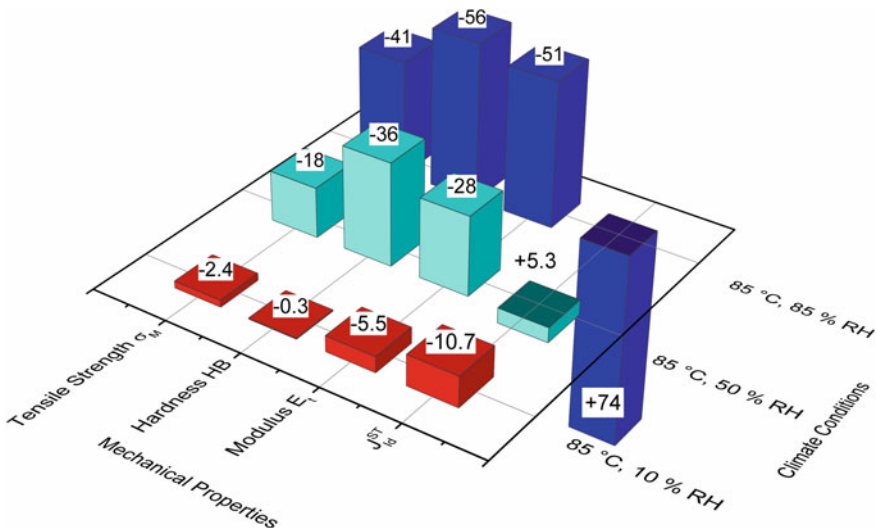


Fig. 28.11 Comparison of normalised change of mechanical properties due to hygrothermal ageing after 1000 h

References

1. Becker, G.W., Braun, D.: *Kunststoff-Handbuch: 3. Thermoplaste, 4. Polyamide*. Carl Hanser, Munich (1998)
2. Kohan, M.I.: *Nylon Plastics Handbook*. Carl Hanser, Munich (1995)
3. Hassan, A., Salleh, N.M., Yahya, R., Sheikh, M.: Fiber length, thermal, mechanical, and dynamic mechanical properties of injection-molded glass-fiber/polyamide 6,6: Plasticization effect. *J. Reinf. Plast. Compos.* **30**, 488–498 (2011)
4. Thomason, J.: The influence of fibre length, diameter and concentration on the modulus of glass fibre reinforced polyamide 6,6. *Compos. A Appl. Sci. Manuf.* **39**, 1732–1738 (2008)
5. Thomason, J.: Micromechanical parameters from macromechanical measurements on glass reinforced polyamide 6,6. *Compos. Sci. Technol.* **61**, 2007–2016 (2001)
6. Thomason, J.: The influence of fibre properties of the performance of glass-fibre-reinforced polyamide 6,6. *Compos. Sci. Technol.* **59**, 2315–2328 (1999)
7. Bergeret, A., Ferry, L., Ienny, P.: Influence of the fibre/matrix interface on ageing mechanisms of glass fibre reinforced thermoplastic composites (PA-6,6, PET, PBT) in a hygrothermal environment. *Polym. Degrad. Stab.* **94**, 1315–1324 (2009)
8. Jia, N., Kagan, V.A.: Effects of time and temperature on the tension–tension fatigue behavior of short fiber reinforced polyamides. *Polym. Compos.* **19**, 408–414 (1998)
9. Mouhmid, B., Imad, A., Benseddqi, N., Benmedakhène, S., Maazouz, A.: A study of the mechanical behaviour of a glass fibre reinforced polyamide 6,6: Experimental investigation. *Polym. Test.* **25**, 544–552 (2006)
10. Ferreno, D., Carrascal, I., Ruiz, E., Casado, J.: Characterisation by means of a finite element model of the influence of moisture content on the mechanical and fracture properties of the polyamide 6 reinforced with short glass fibre. *Polym. Testing* **30**, 420–428 (2011)
11. Langer, B.: *Bruchmechanische Bewertung von Polyamid-Werkstoffen*. Logos-Verlag, Berlin (1998)
12. Ehrenstein, G.W., Pongratz, S.: *Beständigkeit von Kunststoffen*. Carl Hanser, Munich (2007)
13. DIN 50035 (2012): *Begriffe auf dem Gebiet der Alterung von Materialien—Polymere Werkstoffe*
14. El-Rafey, E., Kandill, S., Abdelkader, A.: Auslagern beeinflusst Eigenspannungen. *Kunststoffe* **81**, 710–711 (1991)
15. Illing, T., Schoßig, M., Bierögel, C., Grellmann, W.: Influence of hygrothermal aging on dimensional stability of thin injection-molded short glass-fiber reinforced PA6. *J. Appl. Polym. Sci.* **132**, 42245 (2015)
16. Illing, T., Gotzig, H., Schoßig, M., Bierögel, C., Grellmann, W.: Influence of hygrothermal aging on tensile strength and poisson ratio of thin injection-molded short glass fiber reinforced PA6. *Fibers Issue* **4** (2016) No. 17 (10 pages)
17. ISO 3167 (2014): *Plastics—Multipurpose test specimens*
18. DIN EN 60068-2-2 (2008): *Environmental testing—Part 2-2: Tests—Test B: Dry heat*
19. DIN EN 60068-2-78 (2014): *Environmental testing—Part 2-78: Tests—Test Cab: Damp heat, steady state*
20. DIN EN 60068-2-1 (2008): *Environmental testing—Part 2-1: Tests—Test A: Cold*
21. ISO 527-1 (2012): *Plastics—Determination of tensile properties—Part 1: General principles*
22. ISO 527-2 (2012): *Plastics—Determination of tensile properties—Part 2: Test conditions for moulding and extrusion plastics*
23. ISO 2039-1 (2001): *Plastics—Determination of hardness—Part 1: Ball indentation method*
24. Grellmann, W., Seidler, S., Hesse, W.: *Testing of plastics—Instrumented Charpy impact test (ICIT)—Procedure for determining the crack resistance behaviour using the instrumented impact test (MPK-ICIT): Part I: Determination of characteristic fracture mechanics parameters for resistance against unstable crack propagation; Part II: Determination of characteristic fracture*

- mechanics parameters for resistance against stable crack propagation. Merseburg (2016), http://wiki.polymerservice-merseburg.de/index.php/MPK-Prozedur_MPK-IKBV_englisch
25. ISO 11357-1 (2009): Plastics—Differential scanning calorimetry (DSC)—Part 1: General principles
 26. Precision of 3D CT-Systems. GE Sensing & Inspection Technologies GmbH, Wunstdorf (2014). http://www.armgate.lv/assets/upload/userfiles/files/GEIT-31105_EN_Precision%20Comparison_CT_KMM%2009_10_low.pdf. 1 June 2017
 27. Reinhart, C.: Direkte CT-Datenanalyse mit VGStudio Max 2.0. In: Kastner, J. (ed.) Industrielle Computertomografie Tagung 2008. Reihe: Messtechnik und Sensorik, Shaker Verlag, Herzogenrath (2008)
 28. Phoenix nanotom m. GE Sensing & Inspection Technologies GmbH, Wunstdorf (2013). http://www.ge-mcs.com/download/x-ray/phoenix-x-ray/nanotom_m_s_DE_GEIT-0113.pdf. 1 June 2017
 29. Advani, S.G., Tucker III, C.L.: The use of tensors to describe and predict fiber orientation in short fiber composites. *J. Rheol.* **31**, 751–784 (1987)
 30. DIN 55672-1 (2016): Gelpermeationschromatographie (GPC)—Teil 1: Tetrahydrofuran (THF) als Elutionsmittel
 31. Wyzgoski, M., O’Gara, J.F., Novak, G.E.: Predicting the tensile strength of short glass fiber reinforced injection molded plastics. In: Proceedings of the 10th Annual SPE Automotive Composites Conference & Exhibition, ACCE, Troy, 15–16 Sept 2010. Society of Plastics Engineers, Brookfield (2010), pp. 810–832
 32. Fu, S.-Y., Lauke, B.: Effects of fiber length and fiber orientation distributions on the tensile strength of short-fiber-reinforced polymers. *Compos. Sci. Technol.* **56**, 1179–1190 (1996)
 33. Bernasconi, A., Davoli, P., Basile, A., Filippi, A.: Effect of fibre orientation on the fatigue behaviour of a short glass fibre reinforced polyamide-6. *Int. J. Fatigue* **29**, 199–208 (2007)
 34. Johannaber, F., Michaeli, W.: Handbuch Spritzgießen. Carl Hanser, Munich (2004)
 35. Bay, R.S., Tucker, C.L.: Fiber orientation in simple injection moldings. Part I: theory and numerical methods. *Polym. Compos.* **13**, 317–331 (1992)
 36. Bay, R.S., Tucker, C.L.: Fiber orientation in simple injection moldings. Part II: experimental results. *Polym. Compos.* **13**, 332–341 (1992)
 37. Folgar, F., Tucker, C.L.: Orientation behavior of fibers in concentrated suspensions. *J. Reinf. Plast. Compos.* **3**, 98–119 (1984)
 38. Wang, J., Jin, X.: Comparison of recent fiber orientation models in autodesk moldflow insight simulations with measured fiber orientation data. In: Proceedings of the Polymer Processing Society 26th Annual Meeting, PPS-26, Banff, 04–08 July 2010. Polymer Processing Society, Banff (2010), 6 pages
 39. McNally, D.: Short fiber orientation and its effects on the properties of thermoplastic composite materials. *Polym. Plast. Technol. Eng.* **8**, 101–154 (1977)
 40. Bernasconi, A., Cosmi, F., Dreossi, D.: Local anisotropy analysis of injection moulded fibre reinforced polymer composites. *Compos. Sci Technol.* **68**, 2574–2581 (2008)
 41. Toll, S., Andersson, P.O.: Microstructure of long- and short-fiber reinforced injection molded polyamide. *Polym. Compos.* **14**, 116–125 (1993)
 42. Thomason, J.L.: Structure–property relationships in glass-reinforced polyamide, Part 3: Effects of hydrolysis ageing on the dimensional stability and performance of short glass–fiber-reinforced polyamide 66. *Polym. Compos.* **28**, 344–354 (2007)
 43. Jia, N., Fraenkel, H.A., Kagan, V.A.: Effects of moisture conditioning methods on mechanical properties of injection molded nylon 6. *J. Reinf. Plast. Compos.* **23**, 729–737 (2004)
 44. Brandrup, J., Immergut, E.H., Grulke, E.A.: *Polymer Handbook*. Wiley, New York (1999)
 45. Grellmann, W., Seidler, S. (eds.): *Kunststoffprüfung*, 3rd edn. Carl Hanser, Munich (2015)
 46. Illing, T.: Bewertung von mechanischen und thermischen Eigenschaften glasfaserverstärkter Polyamid-Werkstoffe unter besonderer Berücksichtigung des Alterungsverhaltens von Bauteilen in der Automobilindustrie. Ph.D. thesis, Martin-Luther-University Halle-Wittenberg, Halle (2015)

47. Ehrenstein, G.W., Riedel, G., Trawiel, P.: *Praxis der thermischen Analyse von Kunststoffen*. Carl Hanser, Munich (2003)
48. Xenopoulos, A., Wunderlich, B.: Thermodynamic properties of liquid and semicrystalline linear aliphatic polyamides. *J. Polym. Sci., Part B: Polym. Phys.* **28**, 2271–2290 (1990)
49. Shu, Y., Ye, L., Yang, T.: Study on the long-term thermal-oxidative aging behavior of polyamide 6. *J. Appl. Polym. Sci.* **110**, 945–957 (2008)
50. Valentin, D., Paray, F., Guetta, B.: The hygrothermal behaviour of glass fibre reinforced PA66 composites: A study of the effect of water absorption on their mechanical properties. *J. Mater. Sci.* **22**, 46–56 (1987)
51. Hassan, A., Rahman, N.A., Yahya, R.: Moisture absorption effect on thermal, dynamic mechanical and mechanical properties of injection-molded short glass-fiber/polyamide 6, 6 composites. *Fibers Polym.* **13**, 899–906 (2012)
52. Yue, C., Chan, C.: Assessment of moisture content in nylon using differential scanning calorimetry. *Polym. Test.* **10**, 189–194 (1991)
53. Bergeret, A., Pires, I., Foulc, M., Abadie, B., Ferry, L., Crespy, A.: The hygrothermal behaviour of glass-fibre-reinforced thermoplastic composites: a prediction of the composite lifetime. *Polym. Test.* **20**, 753–763 (2001)

Chapter 29

Ageing of Polymer Materials—Testing, Modelling and Simulation Considering Diffusion

H. Baaser

Abstract The article shows the basics and the fundamental procedure for solving nested calculations of a multistage sequence, taking the example of a compressed O-ring seal influenced by diffusion processes and the ageing of the elastomer component. The mathematical structure of the descriptive equation of diffusion is the same as that of heat transfer. On the other hand, there is the structural-mechanical task for the calculation of mechanical equilibrium. A staggered algorithm solves the referenced problems of “diffusion” and “mechanical equilibrium” independently of each other and takes the results of the other problem as an initial condition. This enables stable solutions of multi-field problems to be achieved which are also dominated by different time scales and processes. We also discuss how to obtain suitable parameters for simulation.

29.1 Introduction

This article focuses on the modelling of diffusion processes and their impact on ageing in elastomer components. Numerical simulation using commercial FEM software packages (FEM—finite element method), such as Abaqus or Ansys, is to be discussed as an example. Depending on temperature and ambient conditions, such diffusion processes are known to influence chemical reactions in the ageing of elastomers and the permeation of fluids in seal applications (Fig. 29.1).

The mathematical structure of the descriptive (differential) equation of diffusion is the same as that of heat transfer. It involves a parabolic differential equation which, in the initially unknown field parameter c for concentration, is only of the

H. Baaser (✉)
Freudenberg Technology Innovation FTI, Weinheim, Germany

H. Baaser
Professor for Engineering Mechanics & FEM, University of Applied Sciences Bingen,
Bingen am Rhein, Germany

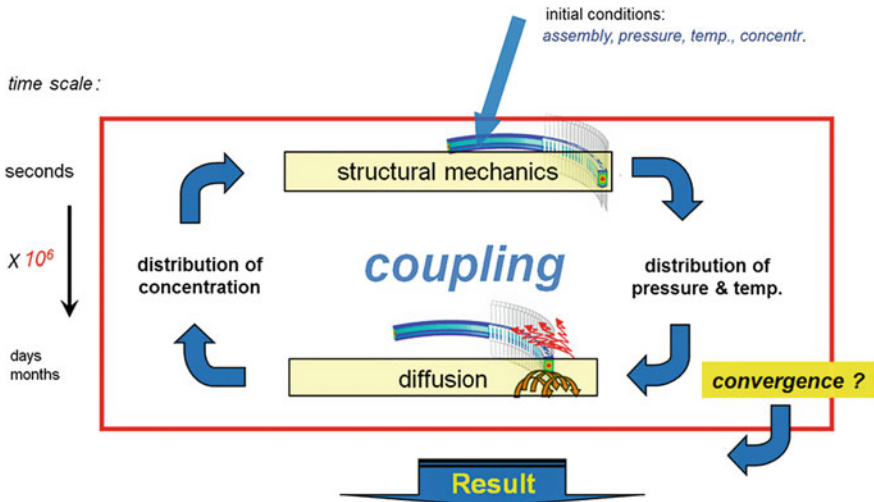


Fig. 29.1 Numerical application—“weak coupling”: Consideration of different time scales in the simulation model

first order in terms of time t . On the other hand, there is the structural-mechanical task for the calculation of mechanical equilibrium for static problems of zero order (elliptic) or of second order in t for dynamic problems (hyperbolic type). In these cases, the second parameter to describe the displacement field \mathbf{u} is of the second order in the spatial directions \mathbf{x} . Furthermore, with regard to the task considered here, a dependence of concentration $c = c(\vartheta, \dots)$ and material stiffness $G = G(\vartheta, \dots)$ on the temperature field ϑ is encountered.

This clearly demonstrates the challenge for such simulation approaches. The “classic” FEM is designed with its solution algorithms for structural mechanics in such a way that it can be used to solve elliptical (or hyperbolic) systems. If first-order derivatives from the parabolic systems are encountered, the selected mathematical approaches are no longer appropriate. A “multi-field problem” is then involved which needs other solution methods. Moreover, in this case we also address other time scales. When describing diffusion, processes exist which continue over “long” periods of time. This too has to be taken into account in simulation as appropriate.

For purposes of computer-aided modelling, a staggered algorithm has proved itself in these cases described. This algorithm solves the referenced problems of “diffusion” and “mechanical equilibrium” independently of each other and takes the results of the other problem as an initial condition or constraint, see Fig. 29.1. In a mathematical sense, this procedure describes a weak coupling of the equations and, after a few nested sequences, generally results in a stable response and thus in a convergent solution [1].

However, the determination of suitable material parameters for such coupled simulations still poses a problem from the author’s point of view. In this article, we would also like to discuss how to suitably determine the individual effects from the

point of view of test engineering in order to describe the respective physical effects. Whereas the numerical simulation of elastomer ageing is based on a phenomenological description of relaxation [2–5], more recent investigations show the necessity of involving diffusion processes which, in rubber materials, are strongly coupled to local temperature and stress [3, 6, 7]. Permeation measurements are available to this effect. In simulation, the coupling of both key phenomena, relaxation and permeation, is applied by means of the algorithm described above, assuming a direct impact of material stiffness from the current local concentration c of a chemical substance in rubber. We demonstrate this by taking the example of a pressed O-ring for sealing a fluid pressure; secondly, we show the influence of surface-volume ratio of specimens typically used to describe the “compression set” resulting in different migration times of media into the core regions of the structure.

29.2 Test Method

29.2.1 *Change in Stiffness Over a Long Period of Time*

The relaxation properties are determined using simple specimens subjected to uniaxial load in a long-term test. Two different types of tests have to be performed in order to distinguish between chain breakdown and crosslinking. During continuous stress relaxation, the specimen is subjected to load through constant expansion, generally 20% strain, see Fig. 29.2, and the time response of force is measured. Due to chain scission caused by ageing, force decreases during the course of time and leads to relaxation. On the other hand, the specimen almost always remains in an unloading condition during discontinuous stress relaxation and is only briefly expanded by the above-referenced value for purposes of measurement. Since chain breakdown and chain build-up are assumed to run in parallel during ageing, the measured force results from the contribution of the still existent original polymer network and the polymer chains which have formed over the course of time [8, 9]. Depending on whether the breakdown or build-up process predominates, a decrease or increase in stiffness can result in the material. This is described in more detail in [5] and is processed for numerical application.

29.2.2 *Diffusion*

In order to determine the permeation properties of the considered materials, we use a test facility as described in [10] and as also available in a similar form in [6]. In

Fig. 29.2 Load cell to measure relaxation; if required, the specimen can be immersed in media such as oil, salt water or gases

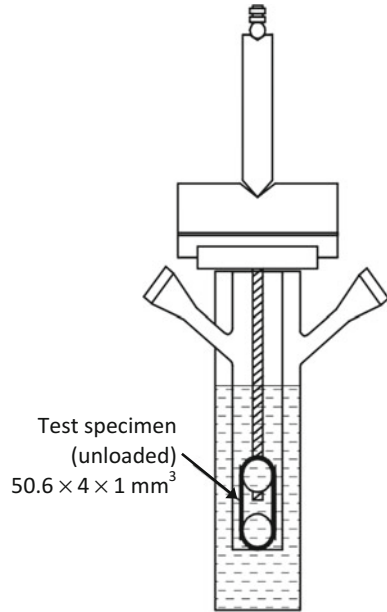
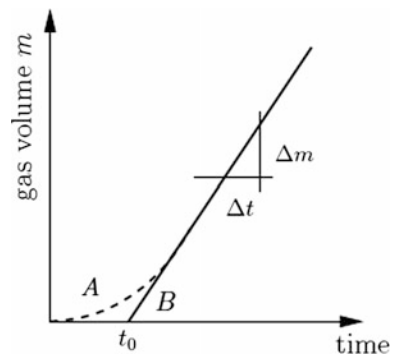


Fig. 29.3 Permeation measurement: t_0 as characteristic induction time for the considered system



this test, a rubber plate is subjected on one side to pressure p at a gas concentration c and the emerging gas volume m is measured at the other side over time.

As shown in Fig. 29.3, on the one hand, this can be used to determine the diffusion coefficient $D = L^2/6t_0$ with L denoting the specimen thickness and t_0 the characteristic time, see “time lag method” in [5]. On the other hand, the permeation coefficient P results from the experimental findings as the gradient $P = \Delta m/\Delta t$ in the linear part of the curve for sufficiently long periods of time t . Solubility for $S = P/D$ continues to be obtained from both these parameters directly. All three parameters are required for this part of diffusion simulation.

29.3 Mechanical Model and Numerical Application

The structural-mechanical part of the model is described by solving the Cauchy momentum equation

$$\text{div}(\boldsymbol{\sigma}) = \mathbf{0} \tag{1}$$

neglecting volume forces and acceleration terms. Stress distribution for $\boldsymbol{\sigma}$ the rubber component is then obtained as a function of the displacement field \mathbf{u} and depending on the constraints from the assembly process and, for example, applied pressure loads. An additional dependence on temperature distribution ϑ can also be taken into account.

The concentration field c inside the body is achieved by solving the diffusion equation in the form of Fick’s second law

$$\frac{\partial c}{\partial t} = D \Delta c = D \text{div}(\text{grad } c) = D \left[\frac{\partial^2 c}{\partial x^2} + \frac{\partial^2 c}{\partial y^2} + \frac{\partial^2 c}{\partial z^2} \right], \tag{2}$$

where the time derivative of c is shown to be a function of the spatial derivative (with Δ as Laplace operator, here denoted in Cartesian coordinates) and the diffusion coefficient D .

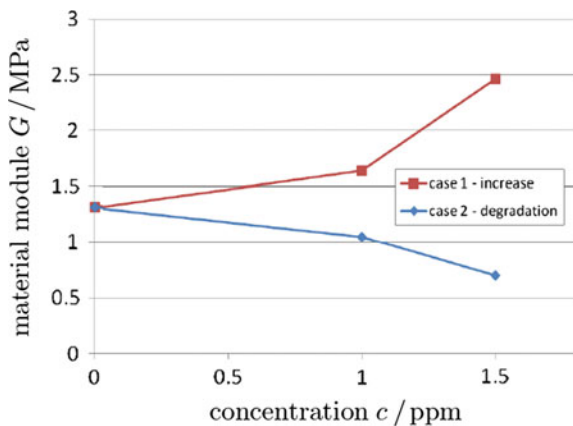
The third field parameter, temperature distribution ϑ , is described by Fourier’s law

$$\mathbf{q} = -\lambda^* \text{grad } \vartheta, \tag{3}$$

where \mathbf{q} is the heat flow (vector) and λ^* is the (thermal) diffusivity. (Note: Fick’s first law has the same structure as Fourier’s law and appears in Fick’s second law as a constitutive assumption here.)

For purposes of simplification, although without restricting the generality of the procedure, we assume here the coupling of the field parameters for displacement

Fig. 29.4 Assumed increase (case 1) and degradation (case 2) of material modulus as a function of the concentration c : $G = G(c)$



u and concentration c via the material model for the elastomer component in the form of the Neo-Hooke law by taking material stiffness as a function of concentration $G = G(c)$ as given in Fig. 29.4 for two cases of material dependency. A dependence on temperature—as mentioned above—can also be readily included here: $G = G(\vartheta, c)$.

29.4 Computational Results

29.4.1 O-Ring Application

As first example, we consider the axi-symmetrical model of an O-ring as a static seal between a rod and a housing. As depicted in Fig. 29.5, this system is subjected on one side to the pressure p_1 of a medium with a concentration c_1 .

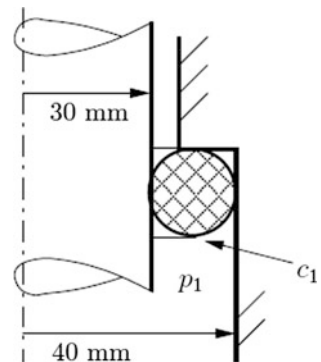
For the purpose of the discussion in this article, we assume two scenarios as depicted in Fig. 29.4 above: an increase in G with c and a decrease in G with increasing concentration c . In both scenarios, we consider the distribution of the sealing ring's contact pressure on the rod and the housing.

This results here in a more sensitive structural response of the pressure-subjected O-ring as given in Fig. 29.7: The contact pressure of the ring on the housing is plotted along the (normalised) path coordinate x/L (see Fig. 29.6), where the contact pressure for the case 2 situation (degradation) is clearly below case 1. Nevertheless, scenario B ($c_1^B = 1.5$ ppm as a boundary condition) in case 2 shows the lowest pressure distribution and thus indicates the most likely point for a possible leakage of the seal.

29.4.2 Compression Test Specimen—Surface–Volume Ratio

As second example of coupled structural and diffusion simulation, we give the geometry of two different specimens for the Compression Set (CS) of typical

Fig. 29.5 Axi-symmetrical model of an O-ring seal subjected to pressure



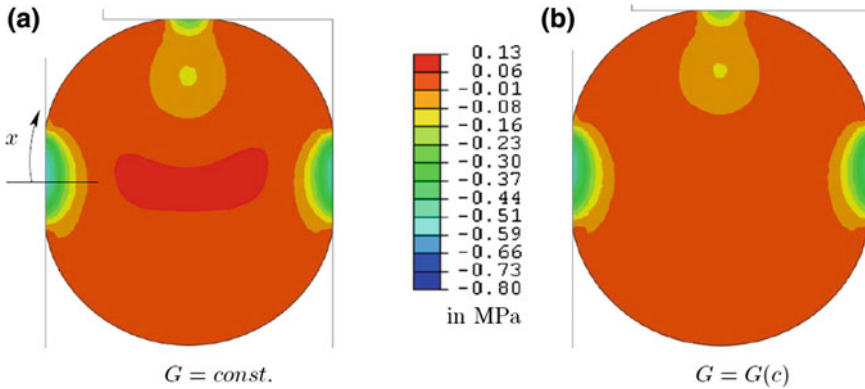


Fig. 29.6 Maximum principle stress in the cross-section of an O-ring as an example for case 2 (degradation): shear modulus $G = \text{const.}$ for the whole component (a), shear modulus as a function of local concentration (b)

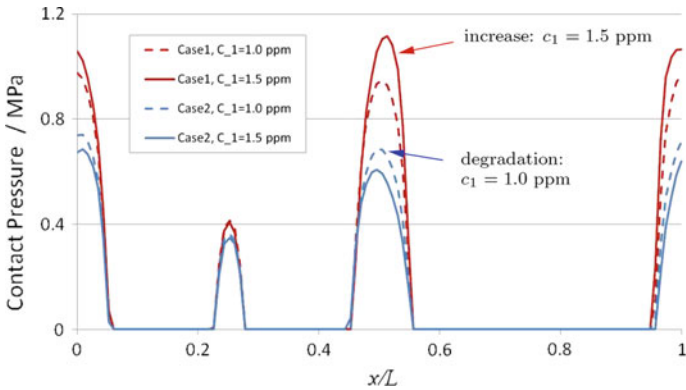


Fig. 29.7 Contact pressure along circumference x/L . For path length x see Fig. 29.6. Scenario A: $c_1^A = 1.0$ ppm (dashed line); scenario B: $c_1^B = 1.5$ ppm (unbroken line)

elastomers. These two specimens are of different surface–volume ratio, subjected to 25% strain (axial compression) and atmospheric gases on their free surfaces.

Very well, we observe the migration of fluid/gas into the bulk material over the time interval. We show in Fig. 29.8 the distribution of concentration after 21 days. Where the small specimen is nearly completely attached during that time (after 28 days, it is completely “filled”), the large test specimen does not see gas loading in its core part. This is the reason for a different behaviour in typical CS tests of these two specimen types.

Again, there is a different and relevant sensitivity of different elastomer types affected by the concentration of air, ozone or generally any gas loading on their

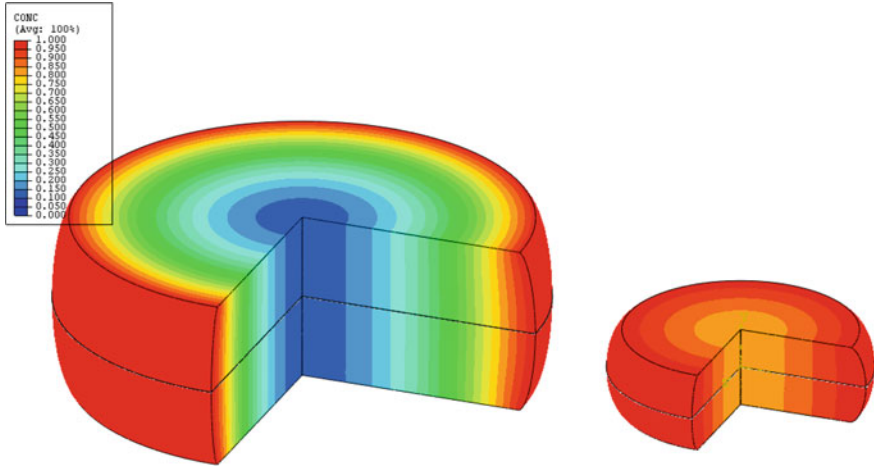


Fig. 29.8 Concentration distribution in a standard specimen for a compression set of 25% for typical elastomers after 21 days. Geometry “large” $h = 12.5$ mm (height), $D = 29$ mm (diameter), “small” $h = 6.3$ mm, $D = 13$ mm

individual material behaviour. These correlations have to be further investigated in future examinations, especially their dependence at least on temperature and additional, external pressure conditions.

29.5 Conclusions and Discussion

In this article, we show the basics and the fundamental procedure for solving nested calculations by means of a multistage sequence, taking the example of a structural-mechanical problem which is influenced by diffusion processes. This procedure enables stable solutions of multi-field problems to be achieved which are also dominated by different time scales and processes.

We also discuss how, in this example, we have succeeded in obtaining suitable parameters for simulation. However, it still has to be definitely clarified to what extent the achieved parameters influence each other and what impact this has on the overall solution. For this purpose, appropriate test programs have to be finalised and harmonised to the numerical solution.

Acknowledgements The author gratefully acknowledges the fruitful discussions and support within the CAE and testing department of FNT, namely to Steffen Bohrmann, Christian Gross, Volkmar Mehling, Christian Ziegler.

References

1. Mehling, V., Baaser, H.: Simulation of self-heating of dynamically loaded elastomer components. In: Heinrich, G., Kaliske, M., Lion, A., Reese, S. (eds.) *Constitutive Models for Rubber VI*. CRC Press, Boca Raton (2009), pp. 119–124
2. Achenbach, M.: Sichere Dichtungen—Alterungsmodell für Gummi. *NAFEMS-Magazin* **18**, 64–78 (2011)
3. Achenbach, M.: Service life of seals—Numerical simulation in sealing technology enhances prognoses. *Comput. Mater. Sci.* **19**, 213–222 (2000)
4. Baaser, H., Gross, C.: Temperature dependent diffusion processes treated by finite elements. In: 10th Rubber Fall Kolloquium (Hanover, 07.–09.11.2012). Deutsches Institut für Kautschuktechnologie, Hanover (2012)
5. Baaser, H., Ziegler, C.: Simulation von Setz- und Relaxationsvorgängen von Elastomer-bauteilen mit Hilfe des mehrachsigen formulierten Freudenberg-Alterungsmodells. in: *Proceedings of the 7th Kautschuk-Herbst-Kolloquium* (Hanover, 08.–11.11.2006). Deutsches Institut für Kautschuktechnologie, Hanover (2006), pp. 393–406
6. Kautz, S., Giese, U.: Characterisation of diffusion limited ageing processes of rubbers. In: *Deutsche Kautschuk-Tagung* (Nuremberg, 02.–05.06.2012). Deutsche Kautschuk-Gesellschaft, Nuremberg (2012), University Session
7. Steinke, L., Weltin, U., Flamm, M., Lion, A., Celina, M.: Numerical analysis of the heterogeneous ageing of rubber products. In: Jerrams, S., Murphy, N. (eds.) *Constitutive Models for Rubber VII*. CRC Press, Boca Raton (2011), pp. 155–160
8. Green, M.S., Tobolsky, A.V.: A new approach to the theory of relaxing polymeric media. *Journal of Chemical Physics* **14**, 80–92 (1946)
9. Tobolsky, A. V.: *Properties and Structures of Polymers*. Wiley Series on the Science and Technology of Materials, Vol. 2. Wiley, New York (1960)
10. Beckmann, W.: Gasdurchlässigkeit von Elastomeren. *KGK—Kautsch. Gummi Kunstst.* **44**, 323–329 (1991)

Chapter 30

Investigations of Elastomeric Seals—Low-Temperature Performance and Ageing Behaviour

M. Jaunich, A. Kömmling and D. Wolff

Abstract Due to their simple and reliable application, elastomers are used for many tasks. Many fields of application like transport, aviation and process technology, entail low temperatures where proper functionality of the employed seals has to be ensured. Therefore, understanding the low-temperature behaviour of elastomeric seals is important for safe seal operation to restrict the temperature application range. For all areas of application, the question of seal lifetime is also important for replacement or maintenance intervals. The lifetime is especially important in applications that allow no seal replacement. Since the seal can determine the lifetime of storage in such cases, reliable lifetime estimation is necessary for these applications, and requires an extensive knowledge of the specific aging behaviour.

30.1 Introduction

The aim of our research is to ensure the safe enclosure of dangerous goods within appropriate vessels (e.g. containers for radioactive waste) under various application conditions and for long-term use. Therefore, fundamental knowledge on material properties is essential to optimise material selection accordingly.

Due to their simple and reliable application, elastomers are used for many tasks [1]. Many fields of application like traffic, aviation and process technology, entail low temperatures where proper functionality of the employed seals has to be ensured. Therefore, understanding the low-temperature behaviour of elastomeric seals is important so that the temperature application range can be restricted in order to ensure safe seal operation. The main findings of the investigations performed are presented here.

For all areas of application the question of seal lifetime is also important for replacement or maintenance intervals. The lifetime is especially important in applications that allow no seal replacement. Since the seal can determine the life-

M. Jaunich (✉) · A. Kömmling · D. Wolff
BAM—Federal Institute for Material Research and Testing, Berlin, Germany

time of storage in such cases, reliable lifetime estimation is necessary for these applications, and requires an extensive database. Respective investigations, started in May 2014, are described and first results are discussed.

30.2 Behaviour at Low Temperatures

The low-temperature limit for the application of elastomeric seals is correlated with the rubber–glass transition during which the material properties change from rubber-like to glass-like behaviour. The properties typical for elastomers, such as high elongation at break, a huge range of elastic behaviour and low stiffness, are lost during cooling when the transition region is crossed. The correlation between the transition temperature range, which usually extends from 10 to 20 K, and seal failure is not trivial, and is strongly influenced by application conditions such as compression and the speed of stress application and release [2]. Therefore a material has to be tested under realistic application conditions and tightness requirements. Some operators demand that the lowest temperature of application must be set above the glass–rubber transition [3], which would give a clearly defined lower temperature limit. This is not required for all applications and might be too restrictive for certain applications. Additionally such a statement could be appropriate only in combination with measurement conditions stipulated to determine the glass–rubber transition. Due to the observed time–temperature equivalence of viscoelastic materials, the temperature range of the glass–rubber transition is strongly dependent on the chosen measurement conditions.

To characterise the material and investigate the sealing performance of different rubber materials, methods of thermal analysis (differential scanning calorimetry (DSC), dynamic-mechanical analysis (DMA)) and a modified method for measuring compression set that employs DMA equipment (CS_{DMA}) were applied, as well as component tests for leakage rate measurements [4–7].

As an example, the glass–rubber transition temperatures for different materials are given in Fig. 30.1. Here results for a nitrile rubber (NBR; designated BAM NBR) and a fluorocarbon rubber (FKM; designated BAM FKM) produced at BAM are shown along with results for two commercial fluorocarbon rubbers (designated FKM 1 and FKM 2) and two ethylene–propylene–diene rubbers (EPDM; designated EPDM 1 and EPDM 2). Different methods were used to determine the glass–rubber transition temperature based on DSC and DMA measurements.

The values show the broad temperature range of the glass–rubber transition. The values determined represent only one point of the transition region depending on the definition applied, and are strongly influenced by measuring conditions and data analysis. The range of the values shown for a single material is about 10 K for EPDM and about 20 K for FKM. The values determined for both EPDM materials are nearly identical.

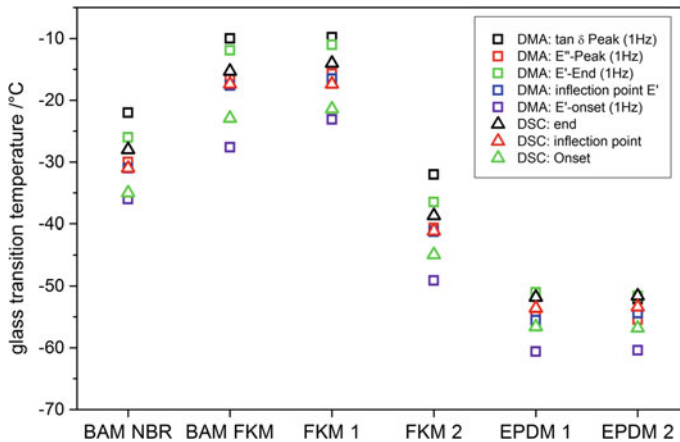


Fig. 30.1 Glass–rubber transition temperatures of six materials determined from DSC (10 K/min) and DMA (1 K/min, 1 Hz) measurements, respectively [6]

The transition region becomes even broader if additional measurement frequencies are considered. The strong time dependence of the material behaviour is also observed in investigations of the compression set [5].

Compression set (*CS*), according to DIN ISO 815-2, is a common method to evaluate the recovery performance of elastomeric seals [8]. A cylindrical sample of height h_0 is compressed along its axis to a defined degree of compression (25%) and a corresponding height h_1 . The compressed sample is heated/cooled to the desired test temperature and stored for a defined time. Afterwards the sample is released at test temperature and the sample height $h(t)$ is measured in dependence of the elapsed time since sample release. Compression set is calculated according to the following (30.1):

$$CS = \frac{h_0 - h(t)}{h_0 - h_1} \cdot 100\% \quad (30.1)$$

A value of 100% means that the sample shows no recovery and remains in a completely deformed condition whereas 0% indicates that the initial sample height is reached again. According to the standard, either the compression set value after a fixed time (typically 30 min) is used, or continuous data recording can be performed. The second option is preferred, as it allows for monitoring the time dependence of the sample recovery.

The standard measurement requires a high amount of handling by the operator and is rather time consuming. For evaluation of the low-temperature behaviour of rubber materials, which is influenced mainly by the physically caused and reversible glass–rubber transition, in our opinion this is not necessary. Therefore an accelerated measurement technique for measuring CS_{DMA} was developed which uses the measurement potential of DMA equipment [7]. With this test the behaviour

of a seal is emulated for the case that the seal compression is released during service, e.g. during an accident by collision or dropped containers. The method and data evaluation are described in more detail in [7, 9].

Figure 30.2 shows compression set values for an NBR compound (28% acrylonitrile, ACN) over time at different temperatures.

The results for NBR show a typical behaviour. The CS_{DMA} curves for temperatures above $-25\text{ }^{\circ}\text{C}$ drop very fast at the beginning. With decreasing temperature the initial drop becomes smaller and finally vanishes. The slight decrease observed for times longer than 10 min shows almost no influence of the test temperature on the slope of the decrease.

The temperature region where CS is close to 100% correlates well with the glass–rubber transition temperature determined as the onset of the storage modulus at a measurement frequency of 1 Hz. By use of an in-depth analysis of the results it is possible to estimate the recovery behaviour as a function of time and temperature [7].

Component behaviour was tested by leakage rate measurements. Here seals were compressed between flanges and the rise in pressure was measured using a vacuum pump and pressure gauges [10]. In the first measurement series shown in Fig. 30.3 the test temperature was decreased stepwise and the leakage rate was measured at every step. Temperature was decreased in this way until a strong increase in the leakage rate was observed. In a second series the temperature was increased stepwise, starting from the lowest temperature of the first series.

The measurements showed that the strong increase in the leakage rate which can be used as criterion for seal failure, lies well below all determined glass–rubber transition temperatures for this static application. In course of the second series, in which the flange initially showing an increased leakage rate is heated stepwise, the

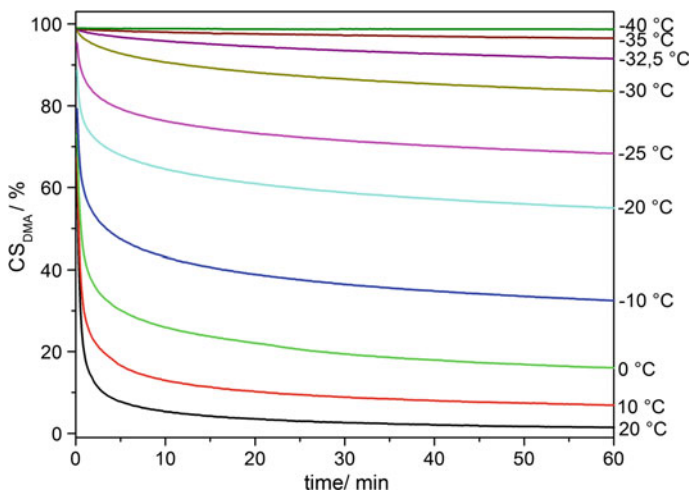


Fig. 30.2 CS_{DMA} of an NBR compound (28% ACN) at different temperatures

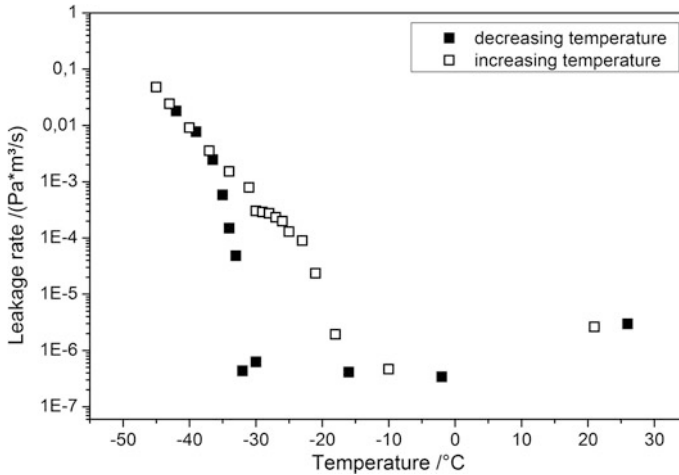


Fig. 30.3 Leakage rate of FKM 1 at different temperatures, taken from [10]

tightness of the seal reaches a value comparable to that at room temperature within the glass–rubber transition temperature range.

These correlations can be explained by considering the differences in the thermal expansion coefficients of elastomer and metal and the material property changes occurring during glass–rubber transition [2].

30.3 Methodology for the Ageing of Elastomeric Seals

The ageing of elastomeric materials is an undesirable but inevitable process that leads to changes in mechanical, thermal and optical properties [11]. For example, a rubber might become brittle and lose gloss. Ageing effects can be caused internally, e.g. by internal stresses or residues of crosslinking agents, but are mostly due to external influences such as heat, oxygen, ozone and radiation. Ageing can be caused by reversible physical processes such as rearrangements of chains, but is mainly a consequence of irreversible chemical reactions. Chemical ageing is characterised by both chain scission reactions and crosslinking reactions, which can occur simultaneously, although one process usually dominates. Chain scission reactions lead to shorter chains, which usually results in a softer material and leads to a decrease in glass transition temperature. On the other hand, crosslinking reactions form additional bonds between chains, which lead to a more brittle behaviour and a higher glass transition temperature [12].

In order to be able to describe the effect of ageing on the operability of elastomeric seals within reasonable time limits, it is necessary to perform accelerated ageing tests. This is described in such standards as ISO 188 [13]. However, the

standard presumes an ageing behaviour, e.g. Arrhenius behaviour, without validating it. In the literature only limited validity of the Arrhenius approach has been reported [14], as the Arrhenius laws refer only to single thermally activated chemical processes, whereas in an ageing polymer, many different complex reactions occur simultaneously. Moreover, when the temperature rises, chemical reactions can be activated that would not occur at room temperature.

What is more, the standard refers to test pieces rather than whole components, which means that the influence of assembly, such as stresses due to compression, cannot be included. Furthermore, lifetime prediction depends greatly on which level of which property is considered as the end-of-lifetime criterion. Some of the criteria frequently employed, such as a 50% decrease in elongation at break, have no direct correlation to the sealing performance.

Another issue that is not addressed in the standard are diffusion-limited oxidation (DLO) effects [15]. As oxidative ageing is a major degradation mechanism, the availability of oxygen is crucial to accelerated ageing. In some materials, especially those with low oxygen permeability and at high temperatures, it is possible that the ageing reactions on the surface are so fast that they consume most of the oxygen and form an oxygen diffusion barrier due to crosslinking reactions. Thus the interior of the sample is protected from oxidation, which leads to heterogeneous ageing of the sample. When testing a bulk property of such a heterogeneously aged sample, such as tensile strength, this property could not be used for lifetime prediction of a rubber that would age slowly and more homogeneously at lower service temperatures (e.g. room temperature). However, surface properties would not be affected by these effects, as oxygen is readily available there independent of the ageing progress.

In order to address all these issues related to accelerated ageing, and to point out that the present procedure given in the standard does not necessarily lead to reliable lifetime predictions, we have devised an accelerated ageing program for elastomeric O-ring seals. The samples are aged uncompressed (see Fig. 30.4) as well as in compression with a deformation of about 25%, corresponding to the actual level of compression during service, to detect the influence of stresses caused by

Fig. 30.4 Undeformed O-rings

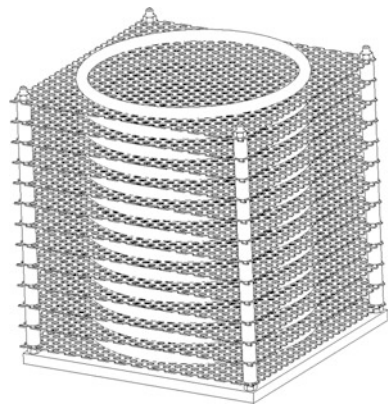


Fig. 30.5 Half O-rings compressed between plates

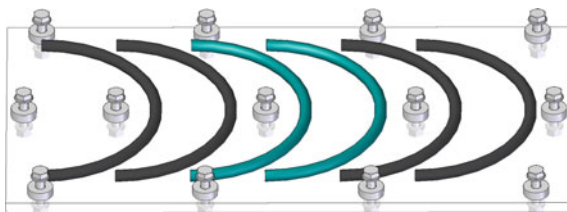
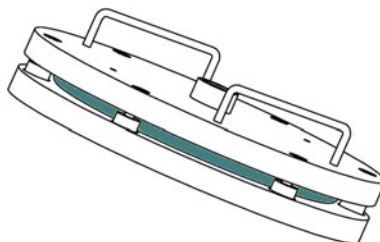


Fig. 30.6 O-ring in flange for leakage rate measurements



compression. Compressed samples are aged as half-O-rings between plates (see Fig. 30.5) and in flanges that allow leakage rate measurements (see Fig. 30.6).

The O-rings have a cord diameter of 10 mm and an inner diameter of 190 mm. On these O-rings, component-specific tests are performed such as compression stress relaxation, compression set, and leakage rate measurements as the ultimate measure of seal functionality. Additionally, polymer analysis methods like dynamic-mechanical analysis (DMA), hardness measurements and infrared (IR) spectroscopy are employed to correlate the changes in the relevant sealing properties to changes in the polymer structure. Microhardness profiles across the O-ring cross section are used to detect DLO effects, similar to the modulus profiling method of Gillen et al. [16]. If inhomogeneities are detected, the samples cannot be used for bulk measurements. The O-rings are aged at 75, 100, 125, and 150 °C, knowing that at 150 °C or even 125 °C DLO effects or non-Arrhenius behaviour may occur. This is to show the limits of ageing studies which do not take these effects into account and age at excessively high temperatures. The ageing periods range from several days up to 5 years and are equally spaced on a logarithmic scale (1, 3, 10 d, ...) until 0.5 a, after which they are examined every six months. In this paper, results for ageing up to 100 d are presented.

The elastomers that were studied are fluorocarbon rubber (FKM), ethylene-propylene–diene rubber (EPDM) and hydrogenated nitrile rubber (HNBR). FKM is typically used for high-temperature applications due to its excellent heat and oxidative stability, whereas EPDM is used when low-temperature leak tightness is required because of its low glass–rubber transition temperature. HNBR is tested for comparative reasons as it is another common sealant material.

When putting a sinusoidal load on a viscoelastic material, it responds with a deformation that is out of phase to the load. A DMA device measures this phase difference δ between stress and strain. The $\tan \delta$ versus temperature curve shows a peak that can be interpreted as a glass transition temperature. When the polymer

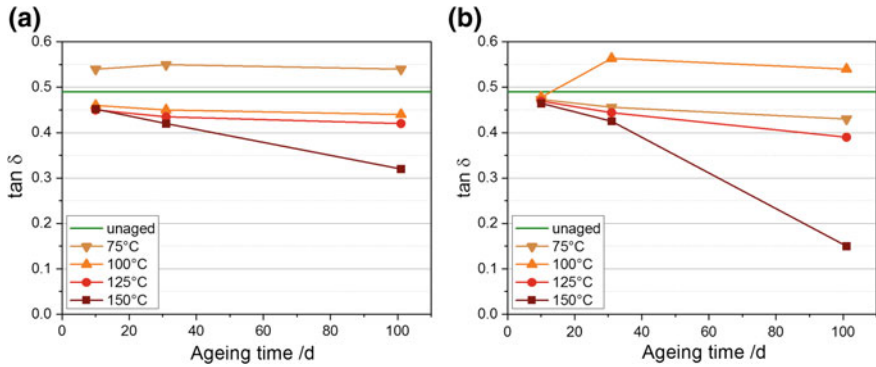
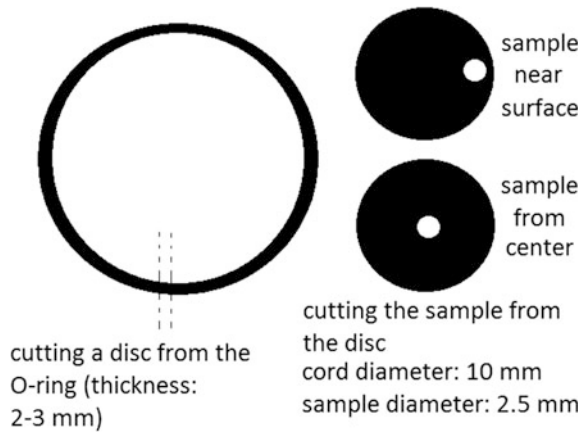


Fig. 30.7 Maximum values of $\tan \delta$ of aged HNBR samples: **a** uncompressed, **b** compressed

Fig. 30.8 Sample preparation from O-ring for DMA measurements



network changes during ageing, $\tan \delta$ changes as well—chain scission reactions lead to an increase in $\tan \delta$, while crosslinking reactions result in a decrease. Thus it is a suitable measure of degradation [17].

Figure 30.7 shows the peak $\tan \delta$ values of HNBR samples aged 10, 30 and 100 d at the four ageing temperatures. A clear difference is visible between uncompressed samples (Fig. 30.7a) and compressed samples (Fig. 30.7b). While it is comprehensible that the higher stresses in a compressed sample lead to faster ageing, as seen in the differences between samples aged for 100 d at 150 °C, it is not so clear why there is a large difference between the samples aged under compression and uncompressed at 75 and 100 °C. However, the behaviour at these lower ageing temperatures is especially important since they are the closest to service temperature. This shows the significance of taking mechanical stresses during ageing into account.

The values shown above were measured on samples that were die-cut near the surface of a disc from an O-ring (see Fig. 30.8). This is to reduce the error

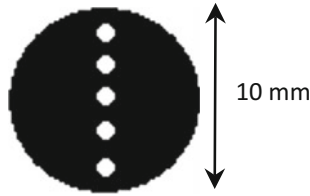


Fig. 30.9 Microhardness measurement positions across O-ring cross section

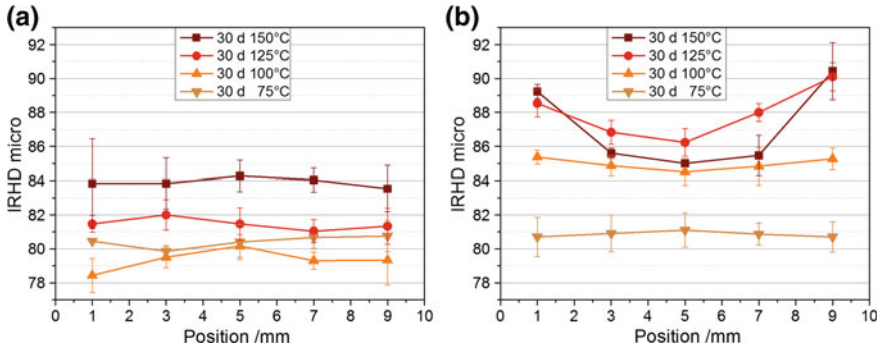


Fig. 30.10 Microhardness profiles across uncompressed O-rings aged for 30 d: a EPDM, b HNBR (IRHD—international rubber hardness degree)

introduced by heterogeneous ageing. Microhardness profiles across an O-ring cord cross section (Fig. 30.9) reveal the extent of heterogeneous ageing as illustrated in Fig. 30.10.

While EPDM shows homogeneous hardness after 30 d of ageing, at all ageing temperatures (see Fig. 30.10a), in HNBR (Fig. 30.10b) the hardness in the center of samples aged at 125 and 150 °C does not increase as much as near the surface, which indicates slower thermo-oxidative ageing in the center due to diffusion-limited oxidation effects [16].

At service conditions and lower temperatures, the samples would age homogeneously, as the reactions would be slower and there would be enough time for the oxygen to diffuse into the sample. Thus only the outer part of the aged samples gives realistic values, while the inside is in a less aged state [16]. Bulk measurements on heterogeneously aged samples give average values of the different ageing states. This becomes clear when looking at compression set (CS) measurements of HNBR and EPDM aged in compression (see Fig. 30.11). The CS is calculated from the measured sample height $h(t)$ several days after release, the initial height h_0 and the compressed height h_1 according to (30.1).

Our procedure applied for aged samples differs from the one outlined in standard ISO 815 [8, 18], as we measure directly on O-rings instead of standard test pieces, and after several days instead of 30 min after release to allow for a recovery close to equilibrium.

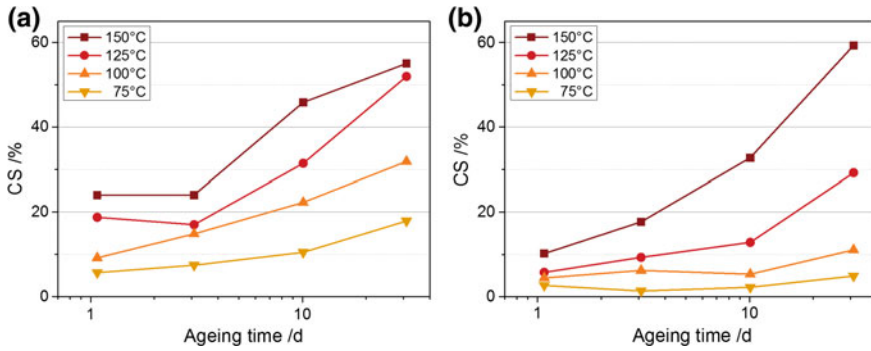


Fig. 30.11 Compression set (CS) of O-rings aged under compression: **a** HNBR, **b** EPDM

While there is a steep increase in CS of HNBR (Fig. 30.11a) aged at 150 °C up to 10 d, the increase becomes flatter after 30 d, which is probably due to a preservation of properties in the less aged sample interior. On the other hand, the CS of EPDM (Fig. 30.11b) aged at 150 °C increases further and overtakes the CS of HNBR after 30 d, as the whole sample has aged homogeneously as shown by microhardness measurements (Fig. 30.10a). The differences between the materials are probably due to a higher oxygen permeability of EPDM, which allows more oxygen to diffuse into the center and cause thermo-oxidative reactions.

The Arrhenius approach [19] for lifetime prediction is based on (30.2), in which t is the time to reach the end of the lifetime at a temperature T , A and C are constants, R is the universal gas constant and E_A is the activation energy of the process leading to the end-of-lifetime criterion.

$$\ln t = A \cdot \exp\left(-\frac{E_A}{RT}\right) + C \tag{30.2}$$

When using the Arrhenius approach, the standard procedure according to ISO 11346 [20] may be used to determine the ageing times t to reach the end-of-lifetime criterion, such as 80% CS, at different ageing temperatures T . A plot of the logarithm of the times vs. the inverse temperature should give a straight line that can be extrapolated to service temperature and yields a corresponding time after which the criterion is reached. Another possibility is to use properties vs. ageing time curves at different temperatures, such as the graphs of CS of EPDM in Fig. 30.11a, and to time–temperature superpose [21] by shifting the curves of higher temperatures along the logarithmic time axis until they superpose with a curve at a lower temperature. In this way all of the measured data points can be used, which makes the extrapolation more accurate. The superposition gives a master curve for the temperature that has not been shifted, usually the lowest temperature (75 °C in this case). This is shown in Fig. 30.12 for the CS of EPDM. According to the shift, the highest measured CS of 60% would be reached at 75 °C after about 1500 d (4 years). However, this plot is only reliable if the reaction mechanisms at the

Fig. 30.12 Time–temperature data from Fig. 30.10a (*CS* of EPDM) shifted to 75 °C

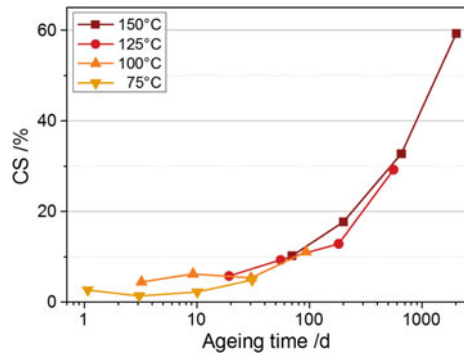
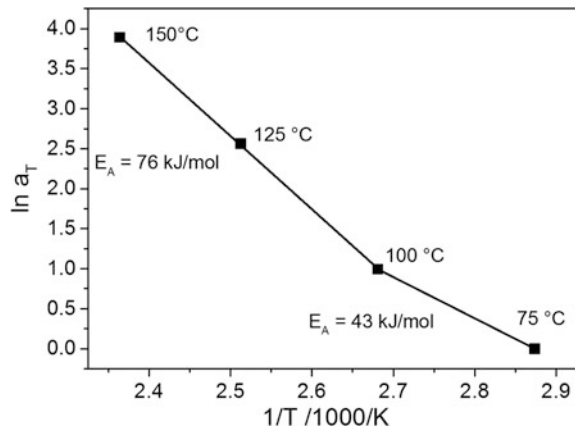


Fig. 30.13 Arrhenius plot of logarithm of shift factors (a_T) versus inverse temperature



higher ageing temperatures are the same as at lower temperatures. The Arrhenius plot of the shift factors a_T vs. the inverse temperature in Fig. 30.13 indicates that this might not be the case, as the slope and thus the activation energy of the ageing mechanism appears to change within the temperature range. Similar results were also obtained by Gillen et al. when ageing EPDM [22].

This would mean that ageing data obtained at 125 and 150 °C cannot be used to predict lifetimes at room temperature, as the ageing mechanism is different and leads to dangerously overestimated lifetimes.

The time–temperature shift and Arrhenius plot of shift factors could also be done for HNBR *CS* data. However, as *CS* is a bulk property and HNBR already shows diffusion-limited oxidation effects after 30 d of ageing at 125 and 150 °C, there is not enough data for a reasonable shift.

FKM did not exhibit significant changes in properties after 30 d of ageing.

One of the first considerations when attempting lifetime predictions is to define a suitable end-of-lifetime criterion. The standard ISO 11346 [20] suggests a decrease by 50% of the original value. However, this is a very general advice and its usefulness depends strongly on the property. For example, while a 50% increase in

hardness or $\tan \delta$ would be a major change, it is only a small effect for CS or leakage rate. For O-ring seals, criteria such as 80% compression set have been postulated without satisfactory physical explanation. As the essential criterion for a seal would be the occurrence of leakage, we measure leakage rate along with physical properties such as CS in order to be able to correlate leakage with the measured physical property, e.g. 95% CS. With the samples presented here, no change in leakage rate occurred during ageing up to 30 d.

30.4 Conclusion

Depending on their application, seals have to fulfill their task at different temperatures and over extended periods of time. For many applications periodic replacement is possible, but for some applications it is not. For both cases knowledge of the specific ageing behaviour is required to either define appropriate replacement intervals or to define an end-of-lifetime criterion. To face the application challenge of elastomeric seals in containers for radioactive materials over timespans of several decades in a temperature range between $-40\text{ }^{\circ}\text{C}$ up to more than $100\text{ }^{\circ}\text{C}$, respective measurement programs are running and methods are in development.

The investigation of low-temperature behaviour allows the seal performance to be estimated from thermoanalytical methods and compression set. The temperature region where no recovery is possible agrees well with the onset of the glass–rubber transition.

First results of the aged samples show the challenges of ageing beyond standard procedures. The influence of compression during ageing as well as DLO effects and non-Arrhenius behaviour have to be taken into account when trying to give reliable lifetime predictions. Our results show that neglecting these factors can lead to dangerously overestimated lifetimes.

References

1. Streit, G., Achenbach, M., Kanters, A.: Sealability of O-rings at low-temperatures 1. Sealability without media influence at low-temperatures. *KGK—Kautsch. Gummi Kunstst.* **44**, 866–870 (1991)
2. Jaunich, M.: Tieftemperaturverhalten von Elastomeren im Dichtungseinsatz. PhD thesis, BAM-Dissertationsreihe Vol. 79, Bundesanstalt für Materialforschung und Prüfung, Berlin (2012)
3. Randler, R.: Tieftemperatureigenschaften von Elastomerwerkstoffen. In: Berger, K.-F., Kiefer, S. (eds.) *Dichtungstechnik Jahrbuch 2013*. ISGATEC, Mannheim (2013), pp. 130–146
4. Jaunich, M., Stark, W., Wolff, D.: Low temperature properties of rubber seals. In: Proceedings of the 9th Fall Rubber Colloquium, Hanover, 03–05 Nov 2010. Deutsches Institut für Kautschuk-technologie, Hanover (2010), pp. 175–178

5. Jaunich, M., Stark, W., Wolff, D.: Low temperature properties of rubber seals. *KGK—Kautsch. Gummi. Kunstst.* **64**, 52–55 (2011)
6. Jaunich, M., Probst, U., Schulz, S., Wolff, D., Stark, W.: Elastomere—Untersuchung des Tieftemperaturverhaltens im Dichtungseinsatz. In: Berger, K.-F., Kiefer, S. (eds.) *Dichtungstechnik Jahrbuch 2014*. ISGATEC, Mannheim (2013), pp. 82–91
7. Jaunich, M., Stark, W., Wolff, D.: A new method to evaluate the low temperature function of rubber sealing materials. *Polym. Test.* **29**, 815–823 (2010)
8. ISO 815-2 (2014): Rubber vulcanized or thermoplastic—Determination of compression set—Part 2: At low temperatures
9. Jaunich, M., Stark, W., Wolff, D.: Comparison of low temperature properties of different elastomer materials investigated by a new method for compression set measurement. *Polym. Test.* **31**, 987–992 (2012)
10. Jaunich, M., Wolff, D., Stark, W.: Low temperature properties of rubber seals—Results of component tests. *KGK—Kautsch. Gummi Kunstst.* **66**, 26–30 (2013)
11. Hofmann, W., Gupta, B.H. (eds.): *Handbuch der Kautschuk-Technologie*. Dr. Gupta Verlag, Ratingen (2001)
12. Ehrenstein, G.W., Pongratz, S.: *Beständigkeit von Kunststoffen, Vol. 1*. Carl Hanser, Munich (2007)
13. ISO 188 (2011): Rubber, vulcanized or thermoplastic—Accelerated ageing and heat resistance tests
14. Celina, M., Gillen, K.T., Assink, R.A.: Accelerated aging and lifetime prediction: review of non-Arrhenius behaviour due to two competing processes. *Polym. Degrad. Stab.* **90**, 395–404 (2005)
15. Wise, J., Gillen, K.T., Clough, R.L.: An ultrasensitive technique for testing the arrhenius extrapolation assumption for thermally aged elastomers. *Polym. Degrad. Stab.* **49**, 403–418 (1995)
16. Gillen, K.T., Clough, R.L.: Polymer aging insights available from modulus profiling data. *Polym. Eng. Sci.* **29**, 29–35 (1989)
17. Kumar, A., Commereuc, S., Verney, V.: Ageing of elastomers: a molecular approach based on rheological characterization. *Polym. Degrad. Stab.* **85**, 751–757 (2004)
18. ISO 815-1 (2014): Rubber, vulcanized or thermoplastic—Determination of compression set—Part 1: At ambient or elevated temperatures
19. Arrhenius, S.: Über die Reaktionsgeschwindigkeit bei der Inversion von Rohrzucker durch Säuren. *Z. Phys. Chem.* **4**, 226–248 (1889)
20. ISO 11346 (2014): Rubber, vulcanized or thermoplastic—Estimation of life-time and maximum temperature of use
21. Ferry, J.D.: *Viscoelastic Properties of Polymers*, 3rd edn. Wiley, New York (1980)
22. Gillen, K., Wise, J., Celina, M., Clough, R.: Evidence that Arrhenius high-temperature aging behavior for an EPDM O-ring does not extrapolate to lower temperatures. In: Sandia National Laboratories. Albuquerque (1997), 5 pages

Part VII
Mechanical Properties and Fracture
of Elastomers—Influence of Composition,
Reinforcement and Crosslinking

Chapter 31

Mechanical Reinforcement in a Polyisoprene Rubber by Hybrid Nanofillers

S. Agnelli, V. Cipolletti, S. Musto, M. Coombs, L. Conzatti, S. Pandini,
M.S. Galimberti and T. Riccò

Abstract Melt blending of hybrid nanofillers with rubber matrices could make rubber nanocomposites more attractive for industrial applications. In this work, the low-amplitude dynamic shear modulus of polyisoprene rubber filled with carbon nanotubes or nano-graphite, individually or in combination with carbon black, was measured. A rationalisation of the results highlighted interactive effects of carbon allotropes on the mechanical reinforcement of rubber nanocomposites. The filler–matrix interfacial area was identified as a parameter able to correlate the moduli values of different fillers, by reducing them to a common master curve.

31.1 Introduction

The continuous improvement of filled rubbers is pushing toward the use of nanofillers. Such nanoparticles have attracted great attention in the research of the last decades on polymer- and rubber-based nanocomposites. Provided that a good filler dispersion is achieved, the nanometric dimensions of such particles allow extensive interaction with the matrix and the formation of networks at lower concentration in comparison with conventional fillers, with large influence on nanocomposite properties. However, a single filler or nanofiller rarely fulfills all the numerous requirements of a specific application. A recent strategy to tailor a

S. Agnelli (✉) · S. Pandini · T. Riccò
University of Brescia, Brescia, Italy

V. Cipolletti · S. Musto · M.S. Galimberti
Polytechnic University of Milan, Milan, Italy

M. Coombs
Pirelli Tyre, Milan, Italy

L. Conzatti
Institute for Macromolecular Research, National Research Council, Genova, Italy

suitable profile of properties is the combination of different fillers in the same rubber matrix. Since this strategy is defined in [1] as “hybridisation of composite materials at a macroscopic scale”, in this work the mix of different fillers in the same matrix is termed “hybrid”. In particular, the obtainment of hybrid nanofillers by mixing a filler and a nanofiller, and their addition to a rubber matrix by melt blending, should make rubber nanocomposites more attractive for industrial applications. The filler particles used in this work are all carbon-based, with different shape and characteristic length: carbon black (CB), carbon nanotubes (CNT) and nano-graphite (nanoG).

Carbon nanotubes, graphene, and graphitic nanofillers are the most recently investigated nanofillers. Several literature works have shown synergistic effects between such carbon nanofillers and the so-called nano-structured filler, i.e. carbon black, on mechanical and electrical properties of the ensuing polymer-based nanocomposites [2–6].

The authors of this work highlighted synergistic effects promoted by hybrid fillers in systems based on poly(1,4-cis-isoprene) (IR) matrix containing a prevailing amount of CB (N326, 60 phr) and small contents of either CNT [4] or nano-graphite, i.e. particles made of few stacked layers of graphite with a high shape anisotropy [5, 6]. In both cases, hybrid networks of nanofillers and CB (i.e. CNT–CB and nanoG–CB) were observed by transmission electron microscopy (TEM) analysis already at low nanofiller contents. Moreover, the initial modulus values of the nanocomposites with the hybrid-filler network were found to be much higher than those calculated through the simple addition of the initial moduli of the composites containing only CB and only the nanofiller, which was interpreted as a synergism between the different fillers.

For a further understanding of such effects, in this work a more systematic investigation on the interaction between CB and either CNT or nanoG in IR matrix was performed. The attention is focused on two issues:

- quantification of the strength of interaction between different fillers in the same rubber matrix,
- identification of the filler parameters that promote filler network formation and thus increase the stiffness at small deformation in the considered hybrid-filler systems.

Different IR based composites were prepared by melt blending: single-filler systems, obtained by adding only CB, CNT or nanoG, and hybrid-filler systems, obtained by adding CB with CNT or with nanoG. Mechanical characterisation was focused on stiffness at small deformation, which was measured by dynamic-mechanical tests in the torsion mode. The results were elaborated according to micro-mechanical models proposed in literature, and were supported by the findings of structural analyses carried out by TEM analysis.

31.2 Experimental

The matrix of the investigated composites was a synthetic poly(1,4-cis-isoprene) (IR), SKI3, from Nizhnekamskneftechim Export, with 70 Mooney units (MU) as Mooney viscosity (test method used: ML(1 + 4)100 °C, see ISO 289-1).

Carbon black (CB) was N326 from Cabot, a medium-high reinforcing CB characterised by spherical primary particles diameter of 30 nm. Multiwall carbon nanotubes (CNT) were Baytubes C150 P from Bayer Material Science, characterised by a chemical purity >95 wt%, length of 1–10 µm before dispersion in the matrix and outer diameter of 10–16 nm. NanoGraphite (nanoG) was Synthetic Graphite 8427 from Asbury Graphite Mills Inc., characterised by a carbon content >99 wt%.

A structural characterisation of the three fillers was performed and the results are reported in Table 31.1. Surface area was measured by the method based on the Brunauer, Emmett, and Teller theory (BET) according to ASTM D 6556 and filler structure was measured by the dibutyl phthalate (DBP) oil absorption according to ASTM D 2414 method. Filler density was measured by a helium pycnometer for N326 and nanoG, whereas the density of CNT was calculated from the density of the composite by the rule of mixture.

Rubber compounds were prepared by adding to the matrix only the fillers and the peroxide that was selected in place of a sulphur based system, in order to limit the influence of the ingredients of the crosslinking system.

The recipe of each compound, expressed in parts per hundred rubber (phr), contains 100 phr of IR matrix, 1.4 phr of dicumylperoxide and the filler, with the contents reported in Table 31.2.

Several rubber composites have been prepared with different filler volume fractions, namely 0, 0.012, 0.024, 0.047, 0.090 and 0.129. Introducing only CB, CNT or nanoG, single-filler composites were realised for each volume fraction. Such composites are labelled with the filler abbreviation followed by a number, indicating the filler content expressed in phr (see Table 31.2). Moreover, hybrid-filler composites have been prepared with the same total filler volume fractions of the single-filler composites: each filler volume fraction is divided into two equal volume fractions, one of CB and the other one of a carbon nanofiller (CNT or nanoG). Such hybrid composites are labelled with CB, a number indicating the CB content expressed in phr and the abbreviation of the nanofiller (see Table 31.2).

Table 31.1 Results of the structural analysis and density measurement of the carbon fillers

Filler	Surface area (ASTM D 6556) (m ² /g)	Oil absorption number (ASTM D 2414) (ml/100 g) ^a	Filler density (kg/dm ³)
N326 (CB)	77	85	1.8
Baytubes C150 P (CNT)	200	316	1.8
Synthetic graphite 8427 (nanoG)	330	162	2.0

^aml of absorbed DBP/100 g of CB

Table 31.2 Label and filler content of the rubber composites^a

Composites with CB						
Label	CB-0	CB-2.5	CB-5	CB-10	CB-20	CB-30
CB content	0 (0.000)	2.50 (0.012)	5.00 (0.024)	10.00 (0.047)	20.00 (0.090)	30.00 (0.129)
Composites with CNT						
Label:	CNT-0	CNT-2.5	CNT-5	CNT-10	CNT-20	CNT-30
CNT content	0 (0.000)	2.50 (0.012)	5.00 (0.024)	10.00 (0.047)	20.00 (0.090)	30.00 (0.129)
Composites with nanoG						
Label:	nanoG-0	nanoG-3	nanoG-6	nanoG-11	nanoG-22	nanoG-33
NanoG content	0 (0.000)	2.78 (0.012)	5.56 (0.024)	11.11 (0.047)	22.22 (0.090)	33.33 (0.129)
Composites with CB and CNT						
Label:	CB-0-CNT	CB-1.25-CNT	CB-2.5-CNT	CB-5-CNT	CB-10-CNT	CB-15-CNT
CB content	0 (0.000)	1.25 (0.006)	2.50 (0.012)	5.00 (0.024)	10.00 (0.045)	15.00 (0.065)
CNT content	0 (0.000)	1.25 (0.006)	2.50 (0.012)	5.00 (0.024)	10.00 (0.045)	15.00 (0.065)
Composites with CB and nanoG						
Label	CB-0-NanoG	CB-1.25-NanoG	CB-2.5-NanoG	CB-5-NanoG	CB-10-NanoG	CB-15-NanoG
CB content	0 (0.000)	1.25 (0.006)	2.50 (0.012)	5.00 (0.024)	10.00 (0.045)	15.00 (0.065)
NanoG content	0 (0.000)	1.39 (0.006)	2.78 (0.012)	5.56 (0.024)	11.11 (0.045)	16.67 (0.065)

^a Amount of fillers is expressed both in phr and in volume fraction (in brackets)

Composites were prepared by a laboratory internal mixer (Brabender) in four phases:

- mastication of 50 g of IR for 1 min, at 90 °C,
- mixing with the filler for 4 min,
- cooling of the rubber mix out of the mixer,
- addition of the peroxide curing agent to the rubber mix in the internal mixer at 50 °C for 2 min.

Finally the composites were further homogenised with a two roll mill, at the following conditions: temperature of 50 °C, nip between the rolls of 1 cm, rolls speed of 30 and 38 rpm.

Each rubber composite was crosslinked and subsequently mechanically characterised with a Monsanto R.P.A. 2000 rheometer, in the torsion mode. Crosslinking was performed at 150 °C, for a time period necessary to obtain the 90% crosslinking of the rubber (t_{90}), determined by a preliminary study of the crosslinking reaction. The samples were mechanically conditioned before the mechanical tests by subjecting them to a strain sweep with the same conditions of the mechanical tests, and then by keeping them in the instrument at the minimum strain amplitude for 10 min. Finally, dynamic-mechanical tests were performed on crosslinked composites, at a shear strain amplitude increasing from 0.1 to 25%, at a temperature of 50 °C, and a frequency of 1 Hz.

TEM analysis was performed with a Zeiss EM 900 microscope on ultrathin sections (about 50 nm thick) obtained with a cryo-ultramicrotome maintained at -130 °C.

31.3 Results and Discussion

31.3.1 Transmission Electron Microscopy Analyses

The microstructure of composites with the highest filler contents was investigated by transmission electron microscopy (TEM). For sake of brevity, only representative images of samples with the hybrid nanofiller system were reported (Fig. 31.1). Those of the samples containing only carbon nanotubes (CNTs), nano-graphite (nanoG) or carbon black (CB) could be found in reference [7].

In CNT-30 sample, an homogeneous distribution of isolated and entangled CNT tubes was observed. In nanoG-33 sample, agglomerates of nano-graphite (nanoG) with a predominantly sub-micrometric size and a disordered structure of the graphitic layers were found homogeneously distributed. In both cases, an almost continuous nanofiller network was identified throughout the IR matrix. Carbon black in CB-30 sample was found to be dispersed in sub-micrometric aggregates, although the filler network was not evenly continuous.

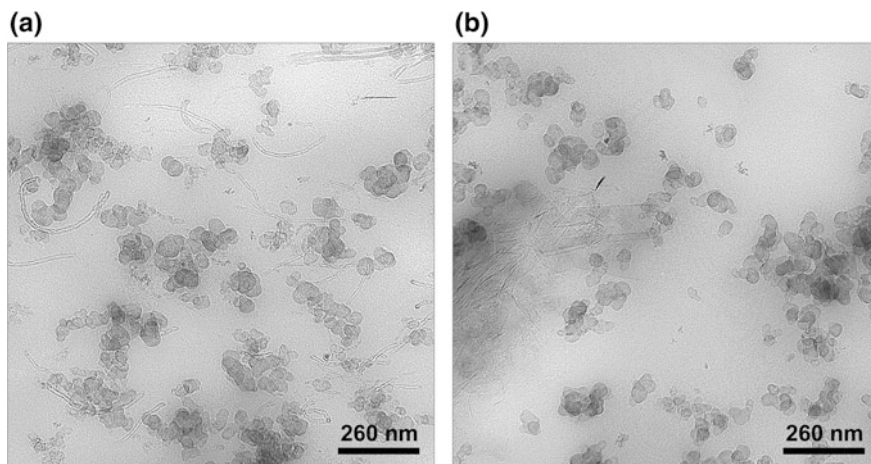


Fig. 31.1 TEM images of hybrid-filler composites with the highest filler content: CB-15-CNT (a) and CB-15-nanoG (b)

The analysis of composites with the highest contents of hybrid nanofiller system showed an homogeneous distribution of filler particles and a good interaction between CB and the nanofillers (see Fig. 31.1). CNTs create a continuous hybrid-filler network with CB (see Fig. 31.1a) being evenly dispersed. Moreover, their high affinity to CB particles together with their high aspect ratio allows CNTs to bridge between separated CB aggregates.

The dispersion of nanoG appeared improved by the presence of CB (see Fig. 31.1b): nanoG particles are smaller and have a lower number of stacked layers with respect to composite with only nanoG at the same total filler amount (nanoG-33). However, no continuous hybrid-filler network is observed (see Fig. 31.1b), although the amount of nanoG is above its mechanical percolation threshold (17 phr, as evaluated in reference [7]). Moreover, nanoG layers tend to remain stacked and appear to be preferentially adhered to CB particles, do not improving the interactions among adjacent CB aggregates, as necessary for building a continuous filler network.

31.3.2 Mechanical Behaviour

The reinforcing effects of fillers were studied by means of dynamic-mechanical tests. Although the storage shear modulus (G') was measured as a function of strain amplitude, in this work the attention is focused on G' values taken at the minimum shear strain amplitude ($G'_{\gamma_{\min}}$).

Figure 31.2 shows $G'_{\gamma_{\min}}$ values as a function of the total filler volume fraction, i.e. $\phi_{\text{nanofiller}}$ or ϕ_{CB} for single-filler systems ($\phi_{\text{nanofiller}} + \phi_{\text{CB}}$) for hybrid-filler

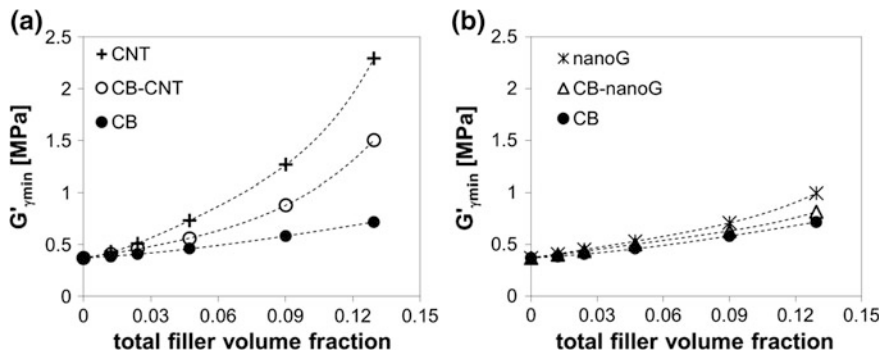


Fig. 31.2 G'_{min} versus total filler volume fraction (nanofiller: CNT (a), nanoG (b))

systems. “Nanofiller” indicates CNT (Fig. 31.2a) or nanoG (Fig. 31.2b). CNT is found to have the highest reinforcing efficiency among the investigated fillers, followed by nanoG and CB. At any total filler volume fraction, the storage modulus of the hybrid-filler composite is lower than that obtained with the nanofiller, but higher than that obtained with CB.

This work shows an attempt to quantify the strength of interaction between different fillers in the same rubber matrix, i.e. the part of modulus enhancement originated by the interaction between different fillers in the hybrid-filler composites. To this aim, the results of Fig. 31.2 were interpreted at the light of an approach proposed by Sternstein et al. [8], who studied the influence of the mutual interaction of two different fillers on the mechanical reinforcement of an elastomeric matrix. Following this approach, we have first evaluated the moduli values of hybrid-filler systems as they can be predicted by an “additive model”, under the hypothesis that no interaction occurs between two different fillers in the same matrix. The additive moduli are obtained as the sum of different contributions: the matrix modulus and the modulus enhancements independently originated by each single filler with respect to the neat matrix, for a given filler content. For example, in case of an incorporation of given volume fractions of nanofiller and CB ($\phi_{nanofiller}$ and ϕ_{CB} , respectively) the modulus of the composite can be predicted by the additive model as follows (31.1):

$$G'_{additive}(\phi_{nanofiller}, \phi_{CB}) = G'_m + [G'_{nanofiller}(\phi_{nanofiller}) - G'_m] + [G'_{CB}(\phi_{CB}) - G'_m] \tag{31.1}$$

where $G'_{additive}$ is the composite modulus predicted by the additive model, G'_m , $G'_{nanofiller}$ and G'_{CB} are the moduli of the neat IR matrix, of composites with only a nanofiller (either only CNT or only nanoG) and of composites with only CB, respectively.

The “additive model” provides a kind of benchmark indicating the lowest moduli values obtainable. The difference between the measured modulus value of the hybrid-filler composite ($G'_c(\phi_{nanofiller}, \phi_{CB})$) and that predicted by the “additive

model” (31.1, $G'_{\text{additive}}(\phi_{\text{nanofiller}}, \phi_{\text{CB}})$) is labelled here interactive term ($\Delta G'_{\text{int}}$). Such term, indicating the strength of interaction between two fillers with each other, is dependent on the type of matrix and fillers, and on the total and relative filler amount. Equation 31.2 shows how $\Delta G'_{\text{int}}$ is calculated:

$$\Delta G'_{\text{int}}(\phi_{\text{nanofiller}}, \phi_{\text{CB}}) = G'_c(\phi_{\text{nanofiller}}, \phi_{\text{CB}}) - G'_{\text{additive}}(\phi_{\text{nanofiller}}, \phi_{\text{CB}}) \quad (31.2)$$

It may be understood that this interaction term may originate not only from actual interaction between the different fillers, but also from an additional contribution given by the interactions of each filler with itself, as a consequence of the higher total filler volume fraction, $\phi_{\text{nanofiller}} + \phi_{\text{CB}}$. In fact, the addition of a second filler to a single-filler composite reduces the volume fraction of the matrix, thus increasing, with respect to the single-filler composite, the concentration of the filler particles within the matrix. It is worth noting that such contributions to the interaction were present also if the two fillers considered were the same.

In order to understand whether the calculated values of the interactive term (see Fig. 31.3) are significant or not, some reference values are needed. These values, labelled “auto-interactive”, were evaluated and used as comparison terms. Such comparison should evidence the contribution to the interaction term due to the peculiarities of the two different fillers. Auto-interactive terms are calculated as done for the interactive term (31.2), but for single-filler composites, considering the total filler amount (ϕ) as made by two equal parts of the same filler ($\phi/2$) rather than two equal parts of different fillers. Therefore, auto-interactive terms indicate the modulus enhancement originated by the interaction between the two parts of the same filler. Auto-interactive terms are calculated by (31.3):

$$\Delta G'_{\text{int}}(\phi/2, \phi/2) = G'_c(\phi) - 2 \cdot G'_c(\phi/2) + G'_m \quad (31.3)$$

In [7] it was analytically shown that such terms are related to the non-linearity of the modulus dependence on the filler amount (see Fig. 31.2). In particular it was

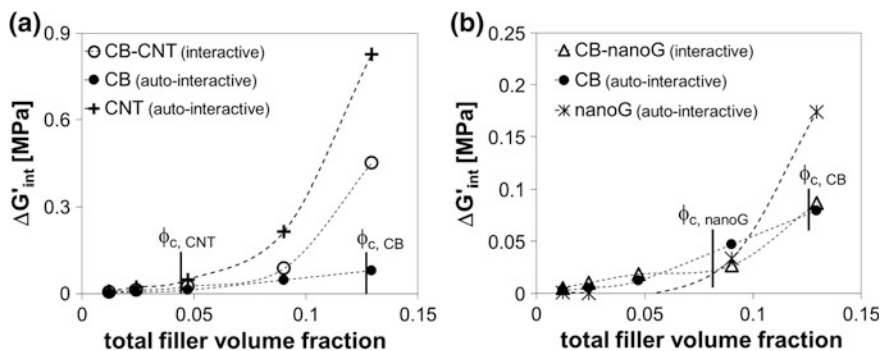


Fig. 31.3 Interactive and auto-interactive terms versus total filler volume fraction for CB and/or CNT (a) CB and/or nanoG (b) the mechanical percolation threshold (ϕ_c) is displayed

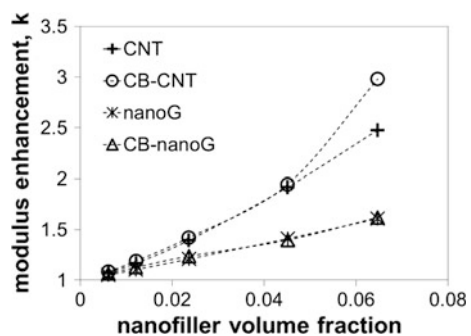
observed that the auto-interactive terms become appreciable only when the nanofiller content is above the mechanical percolation threshold (i.e. 9 phr for CNT; 17 phr for nanoG; 29 phr for CB [7]). Figure 31.3 shows the dependence of both the interactive and auto-interactive terms on the total filler volume fraction; the mechanical percolation threshold (ϕ_c) of the single-filler composites is shown as well.

Figure 31.3 shows two different results for CNT and nanoG. CNT promotes the highest auto-interactive terms, and are responsible for the non-linearity of filler reinforcement of the hybrid-filler system as well: in fact, the interactive terms of the hybrid-filler composites with CNT are between those of the single-filler composites, while CB exerts a moderate contribution. On the other hand, nanoG shows a significant auto-interactive term only at the highest filler content (33 phr). The non-linear effect is not significant in the hybrid nanoG-CB composite. In fact interactive terms of composites with both nanoG and CB are overlapped to the $\Delta G'_{int}$ values of the systems containing only CB.

Modulus reinforcement has been evaluated also by another approach, i.e. as the ratio of the composite modulus versus the matrix modulus. The relative modulus enhancement is expressed by a k -factor, defined as follows: for single-nanofiller composites, $k = G'_{nanofiller}(\phi_{nanofiller})/G'_m$, whereas for hybrid-filler composites $k = G'_c(\phi_{nanofiller}, \phi_{CB})/G'_{CB}(\phi_{CB})$. The last definition of k is obtained by ideally considering as matrix not only the neat IR, but the elastomer filled with CB, at the same volume fraction as in the hybrid-filler composite considered.

The k -factors for both single- and hybrid-filler composites are shown in Fig. 31.4 as a function of the nanofiller volume fraction. The k -factor is evidently higher for CNT than for nanoG, thus confirming the results obtained by the interactive term. Interestingly, k -factors of single- and hybrid-filler composites of the same nanofiller are overlapped, except for the composites with the highest CNT content. This result was obtained also for other systems investigated by the authors [4], in which CB content was much higher (60 phr). Although the authors could not yet provide a physical motivation for this finding, it is apparent that nanofillers enhance the “matrix” modulus by a multiplication factor (k) that depends only on the nanofiller type and content, independently of the “matrix” composition, which can be both a

Fig. 31.4 Relative modulus enhancement (k -factor) versus nanofiller volume fraction



neat elastomer and a CB filled polymer. This result corresponds to the following equivalence (31.4):

$$k = G'_{\text{nanofiller}}(\phi_{\text{nanofiller}})/G'_m = G'_c(\phi_{\text{nanofiller}}, \phi_{\text{CB}})/G'_{\text{CB}}(\phi_{\text{CB}}) \quad (31.4)$$

which, rearranged, gives the following expression for the modulus of a hybrid-filler composite:

$$G'_c(\phi_{\text{nanofiller}}, \phi_{\text{CB}}) = G'_{\text{nanofiller}}(\phi_{\text{nanofiller}}) \cdot G'_{\text{CB}}(\phi_{\text{CB}})/G'_m \quad (31.5)$$

Equation 31.4 indicates that the modulus of a hybrid-filler composite can be calculated as a product of the moduli of the single-filler composites over the matrix modulus, provided that k -factors of single- and hybrid-filler composites overlap (i.e. 31.4 is experimentally verified).

Finally, the role played by filler–polymer interfacial area in determining the initial modulus of the composite was investigated. In fact, the filler–polymer interfacial area is known to be a key parameter governing the modulus reinforcement in filled rubber, not only with CB, according to the basic theory of elastomer reinforcement [9], but also with nanofillers, as recently shown in literature [10, 11].

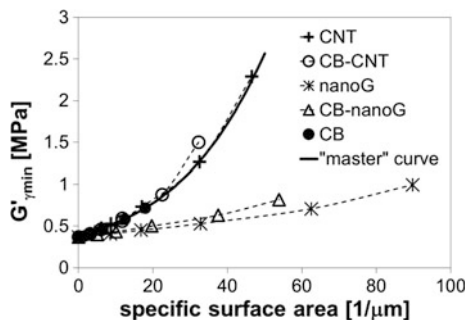
Thus in this work an attempt was done to evaluate the filler–polymer interfacial area of the different rubber composites, in order to see whether such parameter could correlate the modulus values of composites with different types of (nano-) fillers. The filler–polymer interfacial area was tentatively evaluated from surface area measurements, although the authors are aware that the area actually available to the contact with polymer could be smaller, depending on the dispersion and morphology of the filler particles. Furthermore, the total amount of filler–polymer interfacial area in a rubber composite depends on the concentration of the filler, therefore a specific filler surface area is evaluated, in order to take into account the filler surface area per unit volume of composite. The specific filler surface area of single-filler composites is obtained as $A \cdot \rho \cdot \phi$, where A is assumed to be equal to BET surface area (area per unit of filler weight), ρ is the filler density (see Table 31.1) and ϕ is the filler volume fraction (see Table 31.2). For hybrid-filler composites, the specific surface area of each of the two fillers is evaluated, and the results are simply added to give the overall area, as follows (31.6):

$$\text{Specific surface area(for hybrid fillers)} = A_{\text{CB}} \cdot \rho_{\text{CB}} \cdot \phi_{\text{CB}} + A_{\text{nanofiller}} \cdot \rho_{\text{nanofiller}} \cdot \phi_{\text{nanofiller}} \quad (31.6)$$

Figure 31.5 shows the moduli data versus the specific surface area for composites with CB and/or CNT and with CB and/or nanoG.

Surprisingly, the modulus data with CNT and/or CB in Fig. 31.5 at the same specific surface area are very close and seem to follow a common increasing trend,

Fig. 31.5 G'_{min} versus specific filler surface area; the “master” curve (see text) is also displayed



as evidenced by the so-called “master” curve traced in Fig. 31.5 (solid line). The existence of such a “master” curve indicates that the reinforcing efficiency of CNT, CB or a mixture of both is governed by the specific surface area. This confirms the role attributed to the filler interfacial area by the literature [9–11], however, for the first time, a common elaboration seems to be possible for nano- (CNT) and nano-structured (CB) fillers. Such finding could indicate that the surface area of the CB and CNT investigated mostly coincides with the filler–polymer interfacial area, i.e. the surface area is mostly accessible to the elastomeric matrix, and that the difference between the chemistry of the interactions between matrix and filler for both fillers is not relevant to the reinforcing effects.

On the other hand, modulus values referred to systems with nanoG are lower than those of the “master” curve. This could be attributed to two factors: the different chemistry of interaction of IR with nanoG, with respect to CB and CNT, or, more probably, the surface area of filler not completely accessible to the polymer matrix. The second hypothesis is in fact sustained by the oil absorption data, which are related to the structure of the filler, i.e. to its bulkiness. As can be seen from Table 31.1, although nanoG has a surface area higher than that of CNT, its DBP absorption is lower, indicating that not all the surface area reached by the gas molecules used for the BET measurement is accessible to the viscous oil used for DBP absorption. The surface area necessary to shift the modulus data of nanoG on the “master” curve was calculated and is about $90 \text{ m}^2/\text{g}$, which is lower than the actual, experimentally measured value (Table 31.1). Another result supporting this hypothesis is the analysis of the nanoG structure, formed by stacked layers. X-ray diffraction (XRD) analysis performed on the hybrid-filler composite CB-15-nanoG [7] showed that the layers of nanoG form crystalline aggregates relatively thick, with a calculated number of layers stacked in a crystalline domain of about 72. This number is even higher than the one detected in the pristine nanoG sample [5], probably due to the high pressure applied in the curing phase. The layered structure of nanoG could clarify the fact that most of the surface area of the nanoG layers, i.e. the surface of the layers internal to the nanoG particles, is precluded to the polymer chains.

31.4 Conclusions

This work aims at quantifying the interactive effects of carbon allotropes on the mechanical reinforcement of poly(1,4-cis-isoprene) from Ziegler-Natta catalysts. Single fillers, both nano- (CNT and nanoG) and nano-structured fillers (CB), and hybrid fillers, i.e. a mix of two equal volume fractions of CB and a nanofiller, are used.

Low amplitude dynamic shear modulus of the composites was interpreted on the basis of a simple model for binary filler mixtures, and the part of such modulus related to the interaction between the different fillers in the same rubber matrix could be quantified by an interaction term. Due to the high aspect ratio of CNT and to their ability to wrap around and bridge between CB aggregates, the interaction term of both single- and hybrid-filler composites with CNT was higher than those of the other rubber composites.

A multiplication factor (k) was identified for the carbon (nano-)fillers: the modulus of the hybrid-filler composite was related to the product of the moduli of single-filler composites.

Finally, the reinforcing efficiency of both a nano- (CNT) and a nano-structured (CB) filler was found to be dependent on the same parameter: the filler-polymer interfacial area. A “master” curve was found, which relates the modulus values of different rubber (nano)composites to the specific filler surface area by a unique function, provided that the surface area is mostly accessible to the polymer. The definition of such a “master curve” could be seen as a tool to investigate the filler surface area actually accessible to the polymer.

The results of this work disclose two of the reasons of the outstanding reinforcing ability of CNT, related to their shape: the high aspect ratio and the high, accessible surface area.

References

1. Nanko, M.: Definitions and categories of hybrid materials. *Adv. Technol. Mater. Mater. Process.* **11**, 1–8 (2009)
2. Lorenz, H., Fritzsche, J., Das, A., Stoeckelhuber, K.W., Jurk, R., Heinrich, G., Klüppel, M.: Advanced elastomer nano-composites based on CNT-hybrid filler systems. *Compos. Sci. Technol.* **69**, 2135–2143 (2009)
3. Malas, A., Das, C.K., Das, A., Heinrich, G.: Development of expanded graphite filled natural rubber vulcanizates in presence and absence of carbon black: Mechanical, thermal and morphological properties. *Mater. Des.* **39**, 410–417 (2012)
4. Galimberti, M., Coombs, M., Cipolletti, V., Riccio, P., Riccò, T., Passera, S., Pandini, S., Conzatti, L., Ravasio, A., Tritto, I.: The role of CNTs in promoting hybrid filler networking and synergism with carbon black in the mechanical behavior of filled polyisoprene. *Macromol. Mater. Eng.* **298**, 241–251 (2012)
5. Mauro, M., Cipolletti, V., Galimberti, M., Longo, P., Guerra, G.: Chemically reduced graphite oxide with improved shape anisotropy. *J. Phys. Chem. C* **116**, 24809–24813 (2012)

6. Galimberti, M., Kumar, V., Coombs, M., Cipolletti, V., Agnelli, S., Pandini, S., Conzatti, L.: Filler networking of a nanographite with a high shape anisotropy and synergism with carbon black in poly(1,4-cis-isoprene) based nanocomposites. *Rubber Chem. Technol.* **87**, 197–218 (2014)
7. Agnelli, S., Cipolletti, V., Musto, S., Coombs, M., Conzatti, L., Pandini, S., Riccò, T., Galimberti, M.: Interactive effects between carbon allotrope fillers on the mechanical reinforcement of polyisoprene based nanocomposites. *Express Polym. Lett.* **8**, 436–449 (2014)
8. Sternstein, S.S., Ramorino, G., Jang, B., Zhu, A.-J.: Reinforcement and nonlinear viscoelasticity of polymer melts containing mixtures of nanofillers. *Rubber Chem. Technol.* **78**, 258–270 (2005)
9. Mark, J.E., Erman, B., Eirich, F.R. (eds.): *Science and Technology of Rubber*, 2nd edn. Academic Press, San Diego (1994)
10. Heinrich, G., Klüppel, M.: Recent advances in the theory of filler networking in elastomers. *Adv. Polym. Sci.* **160**, 1–44 (2002)
11. Kalfus, J., Jančář, J.: Elastic response of nanocomposite poly(vinylacetate)–hydroxyapatite with varying particle shape. *Polym. Compos.* **28**, 365–371 (2007)

Chapter 32

Structure–Property Correlations of SSBR/BR Blends

K. Reincke, W. Grellmann, S. Ilisch, S. Thiele and U. Ferner

Abstract During the reported project work, ca. 200 different SSBR and SSBR/BR vulcanisates were produced and investigated. During compounding, for each mixture, various processing-related parameters were recorded. Afterwards, the vulcanisation behaviour was characterised by using vulcametry and the last step was to quantify the mechanical and fracture mechanical properties by selected methods. The general aim was to optimise the material properties regarding a possible application in car tires. Mainly, the type of polymer, type and content of filler as well as the surface modification of the used alternative filler TROVO[®] powder were varied to get a preferably balanced property level. It could be stated that the different main components of the rubber mixture (polymer, filler, coupling agent) have a large influence on the physical properties. Basing on the results, most promising combinations of polymer and filler were defined and further investigated. It was found that the silica filler can be replaced by maximal 10 phr TROVO[®] powder BK3 without loss in application-related properties or to get an increase in properties, respectively. From the processing-related properties, it could be concluded that due to the reduced polymer filler interaction, the processing requires less energy to get a homogeneous mixture. This can be an advantage. Further, for some application-related properties such as tear strength, an increase due to the substitution of small amounts of silica by TROVO[®] powder BK3 was observed. This means, TROVO[®] powder BK3 can contribute to an enhancement of the processing behaviour. Due to the large particle size and the low specific surface

K. Reincke (✉) · W. Grellmann
Polymer Service GmbH Merseburg, Merseburg, Germany
e-mail: katrin.reincke@psm-merseburg.de

W. Grellmann
e-mail: wolfgang.grellmann@iw.uni-halle.de

W. Grellmann
Centre of Engineering, Martin Luther University Halle-Wittenberg, Halle/Saale, Germany

S. Ilisch · S. Thiele
Trinseo Deutschland GmbH, Schkopau, Germany

U. Ferner
Trovotech GmbH, Bitterfeld-Wolfen, Germany

area, only small amount of polymer–filler interaction as a basis of reinforcement can be expected. However, the surface modification of TROVO[®] powder with silane or zinc for example is an elegant way, to transport critical substances into the mixture and distribute them very well.

32.1 Introduction

The composition of a raw rubber mixture and the processing are known to influence very strongly the resulting properties of the vulcanisate (elastomeric material). Generally, active—this means reinforcing—fillers are used to enhance the mechanical property level of the elastomer. Thus, reinforcing components of the mixture may increase tensile strength σ_M , storage modulus E' , crack resistance or abrasion resistance. For the optimisation of an elastomeric material, the basic step is the variation of the composition of the mixture in this way that the properties are changed so that a good fit to the application field of the material is given. For example, by the selection of the polymer and the crosslinking system basic properties such as heat stability or achievable mechanical property level of the final elastomer are fixed. “Fine tuning” comprises the selection of plasticiser and plasticiser content, filler type and content, processing aids, ageing protection, ozone protection aids and so on. The challenge here can be the possible interaction between all these single components of the mixture. Therefore, the optimisation of the properties can require extensive modifications of the mixture composition of the application of statistical design of experiments.

This contribution bases on work within a project having the aim to develop new rubber–filler composites for the production of energy-efficient car tires. The experimental work comprised the compounding (production of a homogeneous mixture), the characterisation of the vulcanisation behaviour and the determination of mechanical and fracture mechanical parameters for the resulting elastomer materials. The variation of the mixture composition mainly covered the polymer type as well as the type and the content of the used filler. Additionally, for selected materials, ageing tests with thermo-oxidative loading were performed.

32.2 Experimental

The aim of the work was the development of a tire-tread material with optimised properties, especially regarding the rolling resistance in the sense of the enhancement of the energy-efficiency of car tires. Therefore, the starting point of the investigations was a typical mixture for a passenger car tire tread basing on solution styrene–butadiene rubber (SSBR) with precipitated silica (SiO_2) as filler. Starting from this mixture, variations of the polymer, the filler content, filler type, content of zinc oxide as well as the silane type and content were realised. Overall 82 elastomers basing on a homopolymer (single) and 124 elastomers basing on blends of 2 polymers (blends) were prepared and examined.

Beside new polymers by Trinseo Deutschland GmbH, different standard SSBR polymers by Trinseo were used: Sprintan™ SLR-4602—Schkopau and Sprintan™ SLR-4630—Schkopau. Within the blends, varying SSBR and polybutadiene (BR) Buna™ Cis 132—Schkopau were used as the polymeric matrix.

As fillers, silica Ultrasil® GR7000 by Evonik as well as newly developed fillers TROVO® powder produced by Trovotech GmbH were used. The TROVO® powder bases on borosilicate glass and is here named BK1 and BK3. Beside the pure BK1 and BK3, respectively, modified versions of these fillers were added to the mixture in different contents as substitution of silica and additionally to silica. The modifications of the fillers were done according to the results of the previous tests. Details on the filler modification can be found in [1].

Compounding was realised with a two-step mixing regime by using the lab kneader Brabender Plasticorder PL 2000 N50. After mixing, the raw mixture was homogenised by using a two-roll mill before sample plates were vulcanised. Because the used kneader has only a small chamber with a volume of 75 cm³, for each recipe, three single mixtures were prepared and afterwards mixed and homogenised by using the two roll lab mill.

During the compounding within the kneader, torque and temperature were recorded to observe the mixing process and to calculate the energy input for mixing, what is highly relevant for large-scale mixing. Beside the characteristics of the mixing behaviour, also the vulcanisation behaviour plays an important role for the processing. For example, too early starting of the crosslinking reaction (vulcanisation) is not allowed for practical application similar to incomplete or too long-lasting crosslinking. All this can be assessed on the basis of vulcanisation isotherms (vulcameter curves). Such curves were recorded by using the rotor less shear vulcameter Elastograph of the company Göttfert and the vulcameter SIS-V50 of the company Scarabaeus. The parameters were temperature $T = 160$ °C and rotation angle 0.5°. Beside the scorch time t_{s2} , characterising the start of the crosslinking reaction, the time t_{90} and the difference in torque ΔM were determined. The time t_{90} characterises this time where 90% of the crosslinking reaction has occurred, this means, the material can be seen as crosslinked. the difference in torque ΔM calculated from the maximum and the minimum torque $M_{\max} - M_{\min}$ is often used as a measure of the crosslink density.

The basic mechanical characterisation contained the tensile test according to DIN 53504 [2], the Shore A hardness testing according to DIN 53505 [3] and the tear test according to ISO 34-1 [4]. Furthermore, for more than 50% of the materials, the DIN abrasion test was performed according to ISO 4649 [5].

For the tensile and tear tests, the universal testing machine Zwick Z020 was used. The specimens for the tensile test were S2 specimens, for each material 5 single measurements were done. From the stress–strain diagrams, the tensile strength σ_{\max} (here this value equals with the rupture strength σ_R), the rupture strain ϵ_R as well as the different stress values σ_{100} , σ_{200} , σ_{300} and σ_{400} (stress at x % strain) were determined. From the tear tests, the tear resistance T_s was determined. This value is a technological material parameter and characterises the behaviour of the material when a cut or a crack is existent. For the tests, 2 mm thick trouser

specimens were used. From the load–elongation diagrams, the maximum load or the median of the load was determined and afterwards by using this value, the tear strength T_s is calculated by normalisation to the thickness. Abrasion resistance was determined by using the well-known “DIN abrasion” method according to ISO 4649 [5]. The abrasion values can be used for a ranking of different materials, but they are not really related to the usual abrasion of a car tire. For the tests, a drum tester of the company Zwick was used. Specimens with 10 mm diameter were taken out of plates of 6 mm thickness. For each material, three single measurements were done. The analysis of the tests resulted in the determination of the relative volume loss in mm^3 .

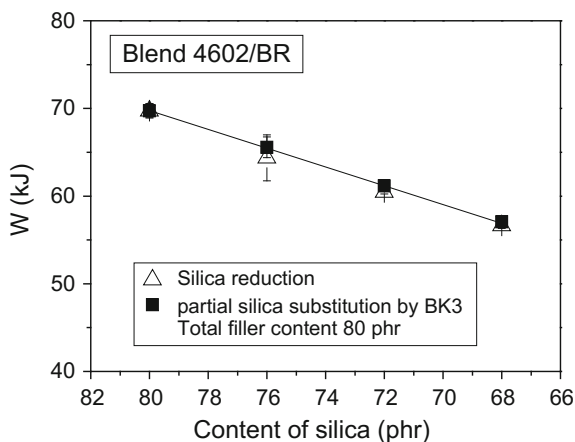
For selected materials, the instrumented tensile-impact test [6, 7] was performed to characterise the fracture behaviour. For this purpose, double-edge-notched tension (DENT) specimens were used. The performance and analysis of the experiments followed the own procedure “Testing of polymers—Instrumented notched tensile impact test” [8]. During the experiment, the load–time signal (F – t signal) is recorded, which is converted to a load–deformation (F – l diagram) through double integration. Afterwards, these diagrams were analysed with the aim of the determination of the measuring values maximum load F_{\max} and deformation at the maximum load l_{\max} as well as different energies A_{\max} and A_p . According to [8], finally crack toughness values J_d were calculated. By using all of this information, one is able to assess the deformation and fracture behaviour in a structure-related manner.

32.3 Results

32.3.1 *Influence of the Composition on the Processing-Related Properties*

Exemplarily, in Fig. 32.1 one can see the work W which is necessary for the production of a homogeneous rubber mixture on the basis of the polymeric blend 4602/BR (ratio 80/20). From the figure it arises that the decrease in silica content—due to the reduction as well as the substitution by BK3 at constant total filler content—leads to a decrease in mixing work. This is traced back to the reducing interactions between filler and polymer. If the silica content is reduced, less surface area is available. Further, by using BK3 as a filler with a decreased specific surface area, the area for polymer–filler interactions is smaller. Because there is no difference between the two series investigated (reduction and substitution of silica), it can be concluded that between non-modified TROVO[®] powder BK3 and the polymeric matrix no or only less interactions take place. The decrease in work W is due to the reduction in silica content.

Fig. 32.1 Work for mixing during the first mixing step in dependence on the silica content for mixtures on the basis of blends with 4602/BR



If modified TROVO[®] powder is used, this means the surface of the BK3 particles is increasingly endowed with zinc, the mixing work increases. Due to this result, more polymer–filler interactions can be expected.

Generally, the substitution of silica by TROVO[®] powder leads to a decrease in the energy necessary for the homogenisation of the rubber mixture. Regarding the energy costs, this is a positive effect of the use of TROVO[®] powder, because it contributes to an economic point balance. However, the reduced polymer–filler interactions can be connected with changes in application-related properties. This must be clarified in detail for each single mixture.

Beside the mixing behaviour, also the vulcanisation behaviour is influenced by changes in the filler type and content. Following Fig. 32.2a shows results of vulcameter experiments with mixtures on the basis of 4602 (single). Again, TROVO[®] powder BK3 substituted certain parts of silica. The decrease in the initial torque M_L is due to the reduced silica content because of a reduction in polymer–filler interactions. The filler BK3 contributes only by hydrodynamic reinforcement. With the exception of the material with 50 phr BK3, it can be concluded that there is only a little influence of the BK3 content on the vulcanisation behaviour. The difference in torque ΔM (see Fig. 32.2b) depends on the filler content.

Firstly, an increasing BK3 content leads to an increase in ΔM and then a strong drop of this value is observed. This means, by the use of small contents of BK3, a slightly increasing crosslink density can be expected. If higher loadings of BK3 are realised, the crosslink density seems to be negatively influenced. As a consequence, the results in Fig. 32.2 show that the BK3 content should be maximum 25 phr. Otherwise, the vulcanisation behaviour and the result of the crosslinking reaction are not optimal.

Beside the influence of the BK3 and silica content, respectively, the influence of the amount of silane on the vulcanisation behaviour was investigated. Silan is a necessary ingredient in a rubber mixture containing silica as a filler. Precipitated silica tends to agglomerate, depending on the type of silica, and without a coupling

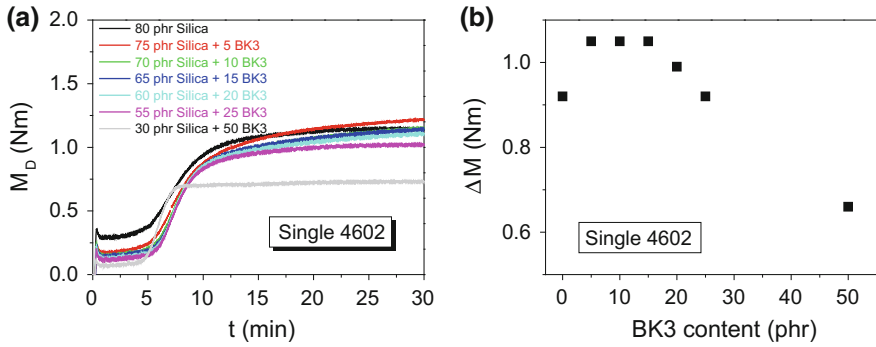
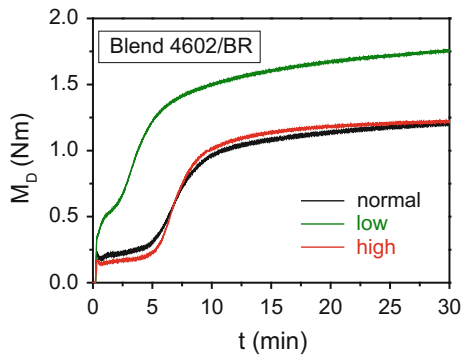


Fig. 32.2 Isothermal vulcanisation curves of mixtures on the basis of 4602 (single) with different contents of BK3 (a) and difference in torque ΔM (b)

Fig. 32.3 Influence of the silane content on the crosslinking behaviour of the reference mixture on the basis of the SBR/BR blend with 4602



agent it cannot be act as a reinforcing filler due to the lacking polymer–filler bonding. Therefore, silane is used in silica compounds. In Fig. 32.3, the isothermal vulcanisation curves of the reference mixture with different contents of the silane NXT can be seen. Clearly, a low dosage of silane leads to an oversized increase in torque within the rubber before the crosslinking reaction starts. This is due to flocculation and can influence the mechanical properties in a negative kind. If the concentration of the silane is high, no difference in the vulcanisation curve is visible in comparison to the normal dosage. In conclusion, a minimum content of silane is needed to get a suitable vulcanisation behaviour.

32.3.2 Influence of Composition of the Rubber Mixture on the Physical Properties

32.3.2.1 Influence of Silane Type and Content on the Mechanical and Fracture Mechanical Properties

To get an optimal result regarding the application-related mechanical properties of a silica-filled elastomer, the content of the coupling agent—here silane—must be optimised. For this reason, the silane content was varied, as mentioned above. Figure 32.4 shows selected results of mechanical tests with the vulcanisates.

In Fig. 32.4a, one can see the tensile strength σ_{\max} and the fracture strain ε_R from tensile tests; Fig. 32.4b contains the tear resistance T_s from tear tests. It can be seen that the content of silane has an impact on the selected properties strength, deformation ability and tear strength. If the concentration of silane is too low (NXT_LOW), the strength is comparable, but the fracture strain is decreased to a value below 400%. This is not sufficient for the application in a car tire. Further, when the silane content is high (NXT_HIGH), the effect is more positive, which is concluded from the high value of the tear resistance. However, the subsequent investigations within the project were performed with the “normal” (mean) silane content.

The project partner Merseburger Spezialchemikalien developed silanes which can be used for the modification of the TROVO[®] powder fillers. The following Table 32.1 contains selected results of mechanical and fracture mechanical tests demonstrating the influence of the silanes on the resulting properties. For both types of modified BK3, the level of the mechanical parameters is constant or higher, compared to the reference. This shows the potential of the development of special silanes.

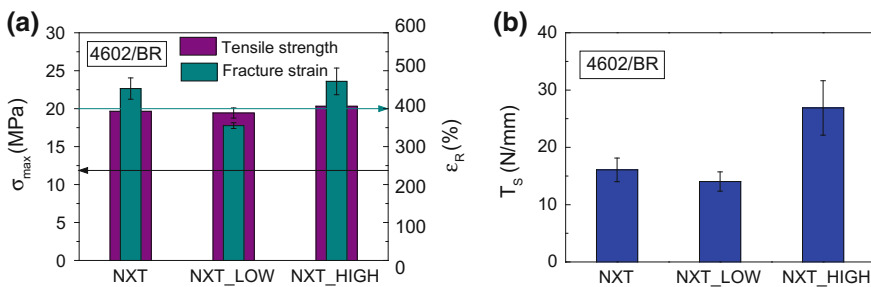


Fig. 32.4 Influence of the silane content on the tensile strength σ_{\max} and the fracture strain ε_R (a) as well as the tear resistance T_s (b) of the SBR/BR vulcanisates on the basis of 4602/BR

Table 32.1 Selected mechanical and fracture mechanical parameters of two blend materials B178 (4602/BR + 80 phr Silica + 5 BK3 modified with 12% silan type A) and B 329 (4602/BR + 80 phr silica + 5 BK3 with bifunctional silane) in comparison to the reference

Parameter	Reference	B178	B329
σ_{300} (MPa)	10.7 ± 0.88	10.5 ± 0.5	11.6 ± 0.2
σ_{\max} (MPa)	19.2 ± 0.29	17.8 ± 2.3	20.7 ± 1.7
ε_R (%)	447 ± 28	431 ± 27	440 ± 22
Shore A	66 ± 0.6	66 ± 0.7	66 ± 0.4
T_s (N/mm)	18.7 ± 1.3	24.2 ± 4.4	21.4 ± 2.3
DIN abrasion (mm^3)	105 ± 12.3	–	119
J_d (N/mm)	229 ± 66	175 ± 16	205 ± 19

32.3.2.2 Influence of the TROVO[®] Powder Content on the Mechanical Properties

One of the most important steps during the project work was the investigation of the influence of the filler content on the resulting properties. For this purpose, vulcanisates on the basis of homopolymers and blends were produced containing different amounts of different fillers. The BK3 content was varied between 5 and 25 phr, at the same time the silica content was changed too, so that a constant filler content of 80 phr was given. Figure 32.5 shows the tensile strength σ_{\max} as well as the fracture strain ε_R in dependence on the BK3-content for single and blend materials with the SBR type 4602. The horizontal lines in the diagrams mark the minimum values of the parameters.

Firstly, the use of 20 phr BR in the polymer matrix (blend) leads to a significant increase in strength and deformability. The substitution of silica results in a changing of the properties: for the homopolymer-based materials (Fig. 32.5a), the fracture strain increases with the BK3 content up to 20 phr, while the strength is influenced only less when the standard deviation is regarded. For the technically more relevant blend materials (Fig. 32.5b), a maximum of strength and deformability can be seen at 10 phr BK3. The hardness reacts in another way to the silica substitution by BK3 (see Fig. 32.6). By using only SBR as matrix, the hardness decreases continuously with the BK3 content, for the blend materials there is a maximum again at 10 phr. The minimum of the hardness is reached up to 20 phr BK3.

In Fig. 32.6b, the tear resistance is shown. Here it becomes very clear that the blend material has a much higher resistance to further tearing of an existent cut or crack. Additionally, by using a small amount of BK3, the tear resistance increases for the blend, while for the single materials, this material property decreases with increasing BK3 content. This means, if a blend of solution SBR and BR is used, the TROVO[®] powder has as certain reinforcement potential up to 5 or 10 phr filler content.

Because the abrasion resistance is one of the most important properties for tire tread materials, also abrasion tests were performed. However, this test characterises the material's abrasion resistance during a very sharp abrasive power reached comparably seldom, e.g. during full braking. At the same time, this test is widely

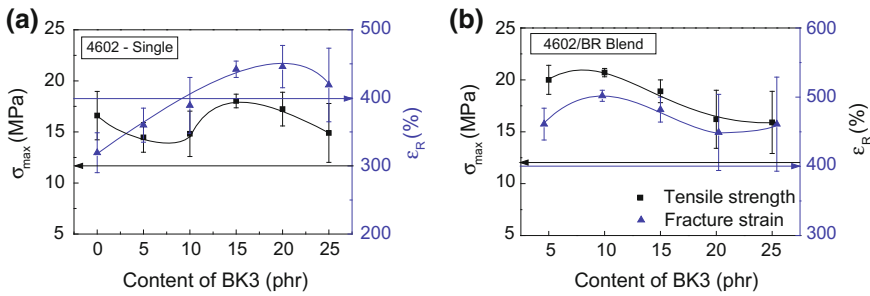


Fig. 32.5 Tensile strength σ_{max} and fracture strain ϵ_R in dependence on the BK3 content (silica substitution) for single (a) and blend materials (b) with SBR type 4602

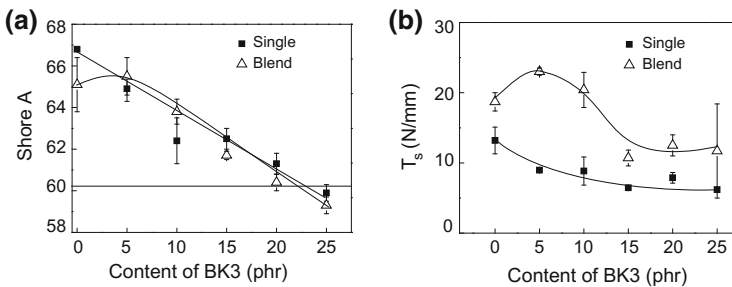
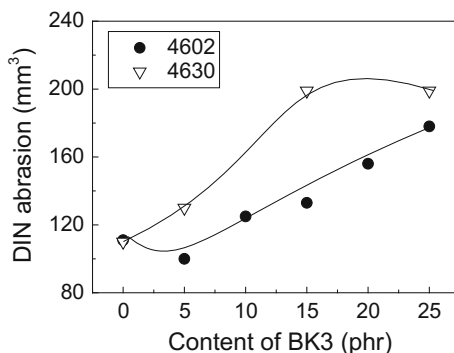


Fig. 32.6 Influence of the TROVO[®] powder BK3 content on the Shore-A hardness (a) and the tear resistance T_s (b) of the materials based on SBR 4602

spread and relatively fast, so that it is used to get a first impression about the abrasion resistance. Generally, the higher the value of relative volume loss, the lower the abrasion resistance. Selected results are shown in Fig. 32.7 for blend materials based on SBR type 4602 and 4630. Again, due to the increase in BK3 content, the material property is influenced strongly. Adding 5 and 10 phr respectively to a 4630 and 4602/BR blend, the abrasion resistance increases. With high filler contents, the volume loss is very high. This is due to the comparably large filler particle size of the TROVO[®] powder and an increasing agglomeration of the particles at high filler contents. These agglomerates act as inhomogeneity and crack initiation sites. So, during the abrasion test, large particles of the elastomer can be pulled out leading to a high volume loss.

Following conclusion of all the tests regarding the influence of the TROVO[®] powder content can be drawn: a maximum substitution of 10 phr silica by BK3 is possible. The level of the mechanical properties characterised within this study can be enhanced partly with small contents of BK3, but also a slight decrease in certain properties can arise. This is mainly due to the large particle size of the

Fig. 32.7 Influence of increasing BK3 content on the DIN abrasion (relative volume loss) of SBR/BR blend materials based on SBR types 4602 and 4630



TROVO[®] powder contributing to a comparably small specific surface area. Latter is combined with a smaller number of polymer–filler interactions. This effect is especially pronounced when larger amounts of the TROVO[®] powder are used.

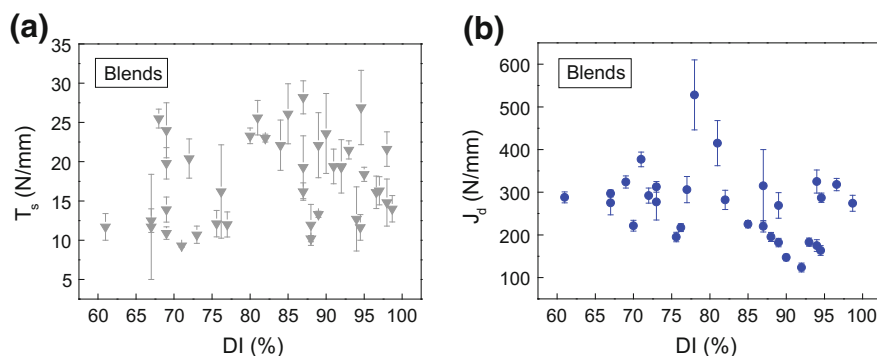
32.4 Structure–Property Correlation

The knowledge of quantitative relationships between the structure and the resulting properties is of great importance. For a material, the structure and morphology arise from the composition of the mixture, the mixing process and the vulcanisation. This means, it is a very complex situation. Furthermore, the characterisation of the structure and morphology of an elastomeric material can be difficult and time-consuming. Table 32.2 gives some examples of possible methods/parameters for the structural characterisation of elastomers.

Partly, the relationship between the characteristics of mixture components and the resulting properties are generally known, so that no further effort is done to investigate it again. One example here is the use of carbon black as a filler. It is well-known and generally accepted that die size of the primary particles and their structure determine the reinforcement efficiency. For the materials here reported having a new filler combination (silica and TROVO[®] powder), the relationship between the macro dispersion index and mechanical and fracture mechanical parameters were investigated. Usually, it is assumed that an elastomer property becomes “better” with increasing macro dispersion index e.g. due to the better homogeneity of the mixture. Figure 32.8 shows the tear resistance T_s and the J_d -value in dependence on the macro dispersion index determined by using light microscopy. The materials based on homopolymers and blends of SBR 4602 and 4630 resp. as well as BR. After an adequate sample preparation, all filler agglomerates larger than the wavelength of the visible light can be seen during a light microscopic investigation and can be analysed. The higher the macro dispersion index, the lower is the number of agglomerates larger than ca. 3 μm . As can be seen in Fig. 32.8, there is no correlation between the parameters. This means,

Table 32.2 Possible methods and parameters for structural characterisation of elastomers

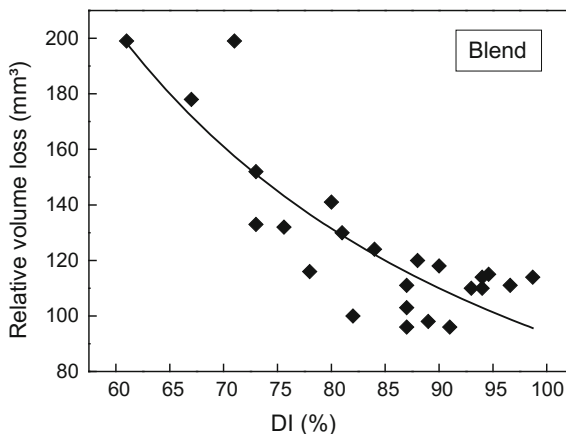
Method	Parameter (examples)	Possibly information regarding
Microscopy (light microscopy, SEM, TEM)	Size of primary particles, size of filler agglomerates, macro dispersion index	Filler distribution and dispersion
Equilibrium swelling measurements	Swelling degree, chemical and physical crosslink density, molecular weight between two crosslinks	Network (crosslink density)
NMR	Relaxation time	Network (crosslink density)
Vulcameter testing	Torque, torque difference	Crosslink density
Gel permeation chromatography (GPC)	Distribution of molecular weight	State of the network (completely crosslinked, damaged...), existence of softening substances

**Fig. 32.8** Tear resistance T_s (a) and fracture mechanics values J_d (b) plotted versus macro dispersion index DI

although there is a good macro dispersion of the filler, the tear strength T_s and the resistance against unstable crack propagation J_d are not higher compared to vulcanisates with low dispersion index [9].

However, as Fig. 32.9 shows, for the abrasion resistance (relative volume loss) there is a correlation visible. With increasing macro dispersion, the relative volume loss decreases, this means, the abrasion resistance becomes better. There is a direct connection between the number of large agglomerates acting as crack initiation sites as described above and the results of the abrasion test. From this result, one can conclude that the mechanical properties of such materials are not necessarily dependent on the macro dispersion index.

Fig. 32.9 Relative volume loss from DIN abrasion tests of SBR/BR blend materials in dependence on the macro dispersion index



32.5 Conclusions

The reported project work contains ca. 200 different vulcanisates which were produced and investigated. During compounding, for each mixture, various processing-related parameters were recorded. Afterwards, the vulcanisation behaviour was characterised by using vulcametry and the last step was to quantify the mechanical and fracture mechanical properties by selected methods. The general aim was to optimise the material properties regarding a possible application in car tires. Mainly, the type of polymer, type and content of filler as well as the surface modification of the used alternative filler TROVO[®] powder were varied to get a preferably balanced property level. It could be stated that the different main components of the rubber mixture (polymer, filler, coupling agent) have a large influence on the physical properties. Basing on the results, most promising combinations of polymer and filler were defined and further investigated. It was found that the silica filler can be replaced by maximal 10 phr TROVO[®] powder BK3 without loss in application-related properties or to get an increase in properties, respectively.

From the processing-related properties, it could be concluded that due to the reduced polymer–filler interaction, the processing requires less energy to get a homogeneous mixture. This can be an advantage. Further, for some application-related properties such as tear strength, an increase due to the substitution of small amounts of silica by TROVO[®] powder BK3 was observed. This means, TROVO[®] powder BK3 can contribute to an enhancement of the processing behaviour. Due to the large particle size and the low specific surface area, only small amount of polymer–filler interaction as a basis of reinforcement can be expected. However, the surface modification of TROVO[®] powder with silane or zinc for example is an elegant way, to transport critical substances into the mixture and distribute them very well.

Acknowledgements The authors thank the Country of Saxony-Anhalt for the financial support of the project “Neue Füllstoff-Kautschuk-Komposite zur Verbesserung der Energieeffizienz von Reifen” by the Ministerium für Wirtschaft und Arbeit of Saxony-Anhalt within the “Innovationscluster Polymertechnologie Halle-Leipzig” with the focus on “Neue Kautschuktypen and innovative Syntheseverfahren”. All of the project partners we would like to thank for the fruitful cooperation and discussion.

References

1. Keller, M.: Einfluss funktionalisierter Borosilikatglaspartikel auf das Vulkanisationsverhalten and die Eigenschaften von SSBR/BR-Kompositen. Ph.D. thesis, Martin-Luther-University Halle-Wittenberg, Halle (2015)
2. DIN 53504 (2009): Prüfung von Kautschuk and Elastomeren—Bestimmung von Reißfestigkeit, Zugfestigkeit, Reißdehnung und Spannungswerten im Zugversuch
3. ISO 7619-1 (2010): Rubber, vulcanized or thermoplastic—Determination of indentation hardness—Part 1: Durometer method (Shore hardness)
4. ISO 34-1 (2015): Rubber, vulcanized or thermoplastic—Determination of tear strength—Part 1: Trouser, angle and crescent test pieces
5. ISO 4649 (2010): Rubber, vulcanized or thermoplastic—Determination of abrasion resistance using a rotating cylindrical drum device
6. Grellmann, W., Reincke, K.: Quality improvement of elastomers. Application of instrumented notched tensile-impact testing for assessment of toughness. *Materialprüfung* **46**, 168–175 (2004)
7. Grellmann, W., Bierögel, C., Reincke, K. (eds.) Wiki “Lexikon Kunststoffprüfung and Diagnostik”. Merseburg. <http://wiki.polymerservice-merseburg.de> (2014). Accessed 1 June 2017
8. Grellmann, W., Reincke, K.: Testing of plastics—Instrumented tensile impact test (ITIT). Procedure for determining the crack resistance behaviour using the instrumented tensile-impact test (MPK-ITIT). Merseburg. http://wiki.polymerservice-merseburg.de/index.php/MPK-Prozedur_MPK-IKZV_englisch (2012)
9. Reincke, K.: Elastomere Werkstoffe—Zusammenhang zwischen Mischungsrezeptur. Struktur and mechanischen Eigenschaften sowie dem Deformations- and Bruchverhalten. Shaker Verlag, Aachen (2016)

Chapter 33

Comparison Between Peroxide and Radiation Crosslinking of Nitrile Rubber

K. Bandzierz, D.M. Bielinski, G. Przybytniak, M. Jaszczak and A. Marzec

Abstract In the present study, two methods of nitrile rubber curing were compared: peroxide and radiation crosslinking. Both methods lead to formation of carbon–carbon crosslinks, directly between the polymer chains. The nitrile rubber samples were unfilled, and filled with silica, carbon black, organoclay and graphene nanoplatelets. The chain scission to crosslinking ratio was calculated on the basis of the Charlesby-Pinner equation. It was demonstrated that radiation curing results in lower number of chain scission events than peroxide thermal curing. Mechanical properties tests showed that the radiation-cured samples generally show better tensile strength and larger elongation at break than the peroxide-cured samples with the same values of crosslink density. It was proved that radiation curing can be successfully used to alter the properties of the composite materials based on nitrile rubber.

33.1 Introduction

Peroxide crosslinking is the most common method leading to formation of carbon–carbon (C–C) crosslinks. They characterise themselves with short length and high bond energy (approx. 350 kJ/mole), what makes them durable and resistant to thermo oxidative ageing. C–C crosslinks provide good elastic properties, but due to limited extensibility, they are not good for dynamic loading application.

K. Bandzierz (✉) · D.M. Bielinski · M. Jaszczak · A. Marzec
Faculty of Chemistry, Institute of Polymer & Dye Technology,
Lodz University of Technology, Lodz, Poland

D.M. Bielinski
Institute for Engineering of Polymer Materials & Dyes,
Division of Elastomers & Rubber Technology, Piastow, Poland

G. Przybytniak
Institute of Nuclear Chemistry and Technology, Warsaw, Poland

The basic mechanism of peroxide crosslinking involves three steps. In the first step, thermal energy causes homolytic cleavage of oxygen–oxygen (O–O) bond, which has a very low bond energy (approx. 150 kJ/mole), into two radicals. The generated radicals remove hydrogen atom from macromolecular chain, what leads to formation of a polymer radical. This step is called radical abstraction. Then, two polymer radicals recombine (radical coupling), forming a covalent C–C crosslink. The general three-step mechanism is relatively simple and well understood, but in polymer systems, numerous side reactions can occur, making the whole process much more complex [1].

One of the side reactions, which accompanies crosslinking and is counterproductive to this process, is chain scission. The chain scission occurs, when macro-radical is broken, leaving a double bond and a radical, what leads to polymer degradation. It lowers the crosslinking effectiveness and causes deterioration of mechanical properties. Polymer structure is the main factor, which determines the occurrence of scission reactions, but temperature and peroxide concentration can also contribute to the process [1].

An interesting alternative for peroxide crosslinking, which leads to formation of the same crosslink type (C–C) is radiation crosslinking. This curing process has been successfully transferred from research laboratories into industrial applications [2–4] and is gaining increasing popularity. In this method, activation energy, required for crosslinking initiation, is not transferred in a form of heat (like in thermal peroxide crosslinking), but as high-energy ionising radiation, which carries enough energy to generate radicals directly on polymer chains. These radicals, recombining with each other, form C–C crosslinks between the polymer chains, and, as a result, a durable three-dimensional structure is developed. The radiation crosslinking occurs via free radical process and its mechanism is often compared to peroxide crosslinking [5, 6]. However, ionising radiation is able to initiate itself particular reactions and processes in the modified material. The radiation crosslinking does not require initiators nor high temperature—the process of crosslinking initiation is therefore regarded to be of physical nature, not chemical, like in peroxide curing.

The crosslink density is an increasing linear function of absorbed dose, what makes the process and material properties easy to control [7].

Radiation crosslinking is known to considerably improve, among others, thermal stability, comparing to peroxide and sulphur vulcanisates [8, 9]. Additionally, according to Bik [10] the presence of oxygen during irradiation does not influence the crosslinking density and radiation yield. However, the reactions occurring during irradiation are highly complicated and the process is very sensitive to additives incorporated into polymer matrix. The reason of this phenomenon is the fact, that ionising radiation affects all components of the material, which can also undergo chemical changes and influence the process [11–13]. During the crosslinking processes—radiation curing and thermal treatment in peroxide method, both crosslinks formation and chain scission occur. To calculate the ratio between these two competing processes, Charlesby-Pinner equation can be implemented [14].

The acrylonitrile–butadiene rubber (NBR) samples, unfilled, and filled with silica, carbon black, organoclay and graphene nanoplatelets, were the object of study. The NBR was chosen due to the fact, that it effectively crosslinks upon irradiation, rather than degrades. The rubber samples were crosslinked to the same crosslink density, by either dicumyl peroxide (DCP) or irradiation with electron beam (EB). The ratio between crosslinking and chain scission was calculated for unfilled samples. The mechanical properties were determined in static tensile tests. The samples, characterised by the same crosslink type and crosslink density, obtained by the above-described different methods, were compared.

33.2 Experimental

33.2.1 *Materials and Samples Preparation*

Acrylonitrile–butadiene rubber Europrene N3325 (bound acrylonitrile (ACN) content: 33%) was supplied by Polimeri Europa (Italy). Fumed silica Aerosil was obtained from Evonik Industries (Germany), carbon black HAF N-330 from Kunshan Jasmine Intl Trading (China), organoclay Cloisite 93A (montmorillonite modified with a quaternary ammonium salt) from Southern Clay Products (USA) and graphene nanoplatelets Grade 4 from Cheap Tubes (USA). Dicumyl peroxide ($\geq 98\%$) was provided by Merck (Germany).

Rubber mixes were prepared with the use of Brabender Plasticorder internal micromixer (Germany) at temperature of mixing chamber of 100 °C. To the plastified NBR, the fillers in appropriate quantity were incorporated with rotors speed of 20 min^{-1} , and 60 min^{-1} , during 25 min lasting homogenisation process. In case of samples with DCP in composition, the curative was incorporated after cooling a mixing chamber to 60 °C and homogenised for 10 min. The samples compositions and their designations are given in Table 33.1.

33.2.2 *Radiation Crosslinking*

For radiation crosslinking, 1 mm rubber mixes (0', 0'', 0''', 0, S, N, CB and G) sheets were compression moulded in an electrically heated press at temperature of 110 °C under pressure of 150 bar for 4 min. The moulded rubber sheets were subjected to electron beam (EB) irradiation at Elektronika 10/10 linear electron accelerator (Russia), located at the Institute of Nuclear Chemistry and Technology (Poland). The absorbed dose was 150 kGy. Irradiation process was carried out in air atmosphere at room temperature. The rubber sheets were placed horizontally in the front of pulsed, scanned beam. The total doses were obtained by multi-pass exposure (approx. 25 kGy per pass).

Table 33.1 Compositions and designations of the samples given for 100 phr of NBR

Rubber mix	Irradiation dose (kGy)	DCP (phr)	Silica (phr)	Organoclay (phr)	Carbon black (phr)	Graphene nanoplatelets (phr)
0'	75	–	–	–	–	–
0	150	–	–	–	–	–
0''	200	–	–	–	–	–
0'''	250	–	–	–	–	–
0/DCP'	–	0.50	–	–	–	–
0/DCP	–	1.00	–	–	–	–
0/DCP''	–	1.50	–	–	–	–
0/DCP'''	–	2.00	–	–	–	–
S	150	–	40	–	–	–
S/DCP	–	1.84	40	–	–	–
N	150	–	–	10	–	–
N/DCP	–	1.24	–	10	–	–
CB	150	–	–	–	40	–
CB/DCP	–	1.18	–	–	40	–
G	150	–	–	–	–	10
G/DCP	–	1.06	–	–	–	10

0, S, N, CB and G stands for rubber mix without filler (0) and for composite filled with silica (S) or organoclay (N) or carbon black (CB) or graphene nanoplatelets (G), respectively. The samples designated with ', '' and ''' are auxiliary ones, for chain scission and crosslinking ratio determination.

33.2.3 Peroxide Thermal Crosslinking

The corresponding samples with DCP in composition (0/DCP', 0/DCP'', 0/DCP''', 0/DCP, S/DCP, N/DCP, CB/DCP and G/DCP), characterised with the same crosslink density as samples obtained by irradiation of rubber mixes without DCP, were prepared by calculation of DCP amount, needed to form the same amount of crosslinks in polymer network. The samples with DCP were crosslinked thermally in an electrically heated press at temperature of 160 °C under pressure of 150 bar. The crosslinking time was determined rheometrically, using Monsanto vulcameter with oscillating disc rotor, according to ISO 3417. The crosslinking time $\tau_{0.9}$ was 38 min for 0/DCP', 0/DCP'', 0/DCP''' and 0/DCP, 18 min for S/DCP, 20 min for N/DCP, 33 min for CB/DCP and 35 min for G/DCP.

33.2.4 Crosslink Density Determination

Total crosslink density of the samples was determined using method of equilibrium swelling in toluene and calculated on the basis of Flory-Rehner equation [15]. The

swelling time was 3 days and following drying time to constant weight was 24 h at 60 °C. The Flory-Huggins interaction parameter used in the calculations for toluene–NBR rubber was 0.435 [16].

33.2.5 Chain Scission and Crosslinking Ratio Determination

The chain scission and crosslinking ratio was calculated on the basis of gel–sol analysis, taking advantage of equilibrium swelling in methyl ethyl ketone at room temperature for 3 days, followed by drying for 24 h at 60 °C.

The gel content (33.1) was calculated as:

$$g = \frac{W_2}{W_1} \text{ and } s = 1 - g, \quad (33.1)$$

where g , s , W_1 and W_2 are the gel or sol fraction (g and s) and the weight of sample before swelling (W_1) or the weight of dried sample after swelling (W_2), respectively.

Assuming that crosslinking and chain scission occur at random and proportionally to the radiation dose, to determine to what extent chain scission, beside crosslinking, occurs during irradiation, Charlesby-Pinner equation [14] can be used (33.2). This simple equation relates sol fraction to the ratio between chain scission and crosslinking.

$$s + \sqrt{s} = \frac{p_0}{q_0} + \frac{1}{q_0 \cdot u \cdot r}, \quad (33.2)$$

where p_0 , q_0 , u and r are the chain scission per radiation unit dose (p_0), the crosslink density per radiation unit dose (q_0), the average degree of polymerisation of the primary polymer chains (u) and the radiation dose (r), respectively.

The ratio between chain scission and crosslinking p_0/q_0 can be then determined by plotting $s + \sqrt{s}$ versus $1/r$.

To calculate the p_0/q_0 for peroxide cured samples, Barton [17] modified the Charlesby-Pinner equation (33.3):

$$s + \sqrt{s} = \frac{p_0}{q_0} + \frac{1}{2M_n \cdot [I] \cdot \varepsilon}, \quad (33.3)$$

where M_n , $[I]$ and ε are the number average molar mass (M_n), the peroxide concentration ($[I]$) and the crosslinking efficiency (ε), respectively.

To obtain the p_0/q_0 ratio for peroxide cured systems, $s + \sqrt{s}$ versus $1/[I]$ has to be plotted.

33.2.6 Mechanical Properties Test

Mechanical tests were carried out with the use of Zwick 1435 universal mechanical testing machine (Germany), according to ISO 37. The crosshead speed was 500 mm/min and the temperature was 23 ± 2 °C. Five dumbbell specimens were tested for each sample and the average is reported here.

33.3 Results and Discussion

In Figs. 33.1 and 33.2, $s + \sqrt{s}$ versus the reciprocal radiation dose and reciprocal peroxide concentration is plotted, for unfilled samples cured with radiation and peroxide, respectively. The ratio between chain scission and crosslinking acts (p_0/q_0), is determined as the intercept of the linear function with ordinates.

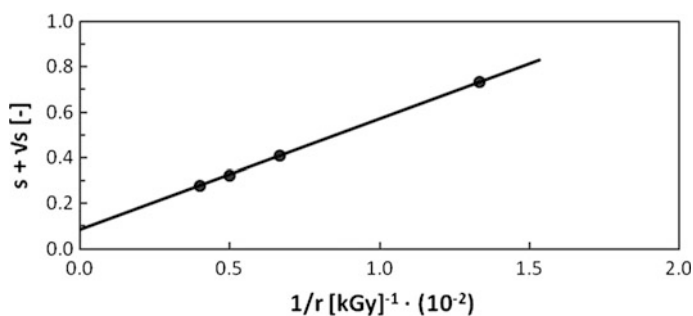


Fig. 33.1 $s + \sqrt{s}$ versus the reciprocal radiation dose for unfilled, radiation cured samples

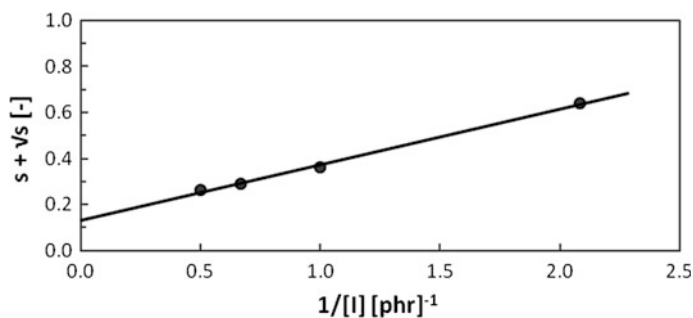


Fig. 33.2 $s + \sqrt{s}$ versus the reciprocal peroxide concentration for unfilled, peroxide cured samples

For the electron beam irradiated and peroxide cured samples, the p_0/q_0 is 0.08 and 0.13, respectively. The difference between the ratios shows, that although the mechanisms of crosslinking are considered to be very similar and they both lead to C–C crosslinks formation, different processes can occur beside the crosslinking reactions induced by either high-energy radiation, or chemical processes initiated with DCP radicals. Another reason of this phenomenon can be the fact, that radiation crosslinking was carried out at room temperature, whereas peroxide curing had to be performed at high temperature (160 °C). The thermal curing time in the experimental work was relatively long—38 min for the unfilled samples. High temperature action during this time probably gave contribution to increased chain scission in case of peroxide curing.

The data representing mechanical properties of all the samples are presented in Table 33.2. Tensile strength of the samples studied is presented in Fig. 33.3.

As can be seen from Fig. 33.3, tensile strength of the samples crosslinked with ionising radiation is in general slightly higher than for the peroxide cured samples. Only in case of composite with carbon black, the determined respective TS value is lower, but the difference is not large. It can be the result from the fact, that carbon black is an effective scavenger of free radicals. The differences between the mechanical properties of radiation and peroxide cured samples, can be caused by increased chain scission acts in the latter. Apart from that, side reactions of DCP, such as addition and oxygenation, or partial embedment of the DCP on the filler surface could occur. Additionally, presence of crosslinks clusters, which result from poor solubility of DCP in the rubber matrix and higher localised concentration of DCP, could also negatively influence the rubber structure. This all could give contribution to slightly lower mechanical properties of peroxide cured samples.

Table 33.2 Mechanical properties (TS , S_{E100} , S_{E200} , S_{E300} , E_b) of all the samples studied

Sample	Crosslink density (10^{-4} mol/cm ³)	Mechanical properties				
		TS (MPa)	S_{E100} (MPa)	S_{E200} (MPa)	S_{E300} (MPa)	E_b (%)
0	2.0	3.5	1.1	1.5	2.1	424
0/DCP	2.0	2.5	1.1	1.4	1.9	290
S	4.4	27.4	5.0	8.2	12.6	451
S/DCP	4.3	21.2	3.6	7.5	14.0	360
N	2.0	10.3	2.7	4.1	5.4	519
N/DCP	2.1	8.1	2.2	3.6	5.0	453
CB	2.7	20.5	4.3	10.7	17.6	327
CB/DCP	2.7	21.3	2.6	7.7	15.8	365
G	2.1	5.4	1.5	2.7	3.8	418
G/DCP	2.1	4.8	1.6	3.1	4.4	341

TS —Tensile strength, S_E —Stress at a given elongation (100, 200 and 300%), E_b —elongation at break

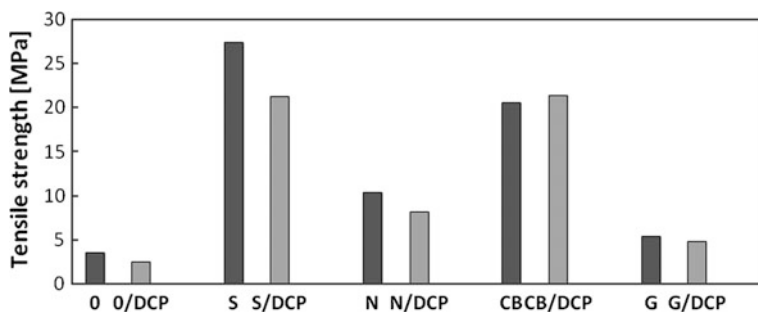


Fig. 33.3 Tensile strength of the samples crosslinked radiationally and thermally

33.4 Conclusion

The object of study were nitrile rubber samples, unfilled, and filled with silica, carbon black, organoclay and graphene nanoplatelets. For the unfilled samples, crosslinked by either dicumyl peroxide or ionising radiation and having the same crosslink density, the ratio between chain scission and crosslinking (p_0/q_0) was calculated using Charlesby-Pinner equation. The results showed that the p_0/q_0 is 0.08 and 0.13 for radiation and peroxide cured samples, respectively. The mechanical properties of the samples crosslinked radiationally are in general slightly higher than for the corresponding, peroxide cured samples.

Due to the fact, that the process of radiation crosslinking of elastomers is gaining increasing popularity in industrial applications, these results are noteworthy. The radiation crosslinking does not require elimination of oxygen during curing, additional heat treatment (postcuring), incorporation of curatives, which are often expensive, give an unpleasant odour and have volatile decomposition products. This is particularly important in case of e.g. seals working under high vacuum, which requires very high purity and can suck in the residues of curatives, or in case of rubber products which have contact with food. Moreover, the radiation crosslinking can ensure very good mechanical properties. This all makes radiation crosslinking “green technology”.

References

1. Dlużneski, P.R.: Peroxide vulcanization of elastomers. *Rubber Chem. Technol.* **74**, 451–492 (2001)
2. Bohm, G.G.A., Tveekrem, J.O.: The radiation chemistry of elastomers and its industrial applications. *Rubber Chem. Technol.* **55**, 575–668 (1982)
3. Clough, R.L.: High-energy radiation and polymers: a review of commercial processes and emerging applications. *Nucl. Instrum. Methods Phys. Res., Sect. B* **185**, 8–33 (2001)

4. Cleland, M.R.: Industrial applications of electron accelerators. In: Brandt, D. (ed.) Proceedings of CERN Accelerator School (CAS) (Zeegse, 24.05.–02.06.2005). Yellow reports, CERN, Geneva (2006), pp. 383–416
5. Loan, L.D.: Peroxide crosslinking reactions of polymers. *Pure Appl. Chem.* **30**, 173–180 (1972)
6. Manaila, E., Stelescu, M.D., Craciun, G.: Aspects regarding radiation crosslinking of elastomers. In: Boczkowska, A. (ed.) *Advanced Elastomer Technology, Properties and Applications*, pp. 3–34. InTech, Rijeka (2012)
7. Bandzierz, K., Bielinski, D., Korycki, A., Przybytniak, G.: Radiation crosslinking of acrylonitrile–butadiene rubber: The influence of sulphur and dibenzothiazole disulphide on the process. In: Bielinski, D.M., Kozłowski, R., Zaikov, G.E. (eds.) *High Performance Elastomer Materials*, pp. 129–141. Apple Academic Press, Waretown (2014)
8. Basfar, A.A., Silverman, J.: Improved ozone resistance of styrene butadiene rubber cured by a combination of sulfur and ionizing radiation. *Polym. Degrad. Stab.* **46**, 1–8 (1994)
9. Ahmed, S., Abdel Aziz, A.A., Basfar, M.M.: Comparison of thermal stability of sulfur, peroxide and radiation cured NBR and SBR vulcanizates. *Polym. Degrad. Stab.* **67**, 319–323 (2000)
10. Bik, J.M., Rzymiski, W.M., Gluszewski, W., Zagorski, Z.P.: Electron beam crosslinking of hydrogenated acrylonitrile–butadiene rubber. *KGK—Kautsch. Gummi Kunstst.* **57**, 651–655 (2004)
11. Gluszewski, W., Zagorski, Z.P.: Radiation sterilization of healthcare products. *Contemp. Oncol.* **7**, 787–790 (2003)
12. Panta, P.P., Gluszewski, W.: Dosimetric control of high energy EB. *Contemp. Oncol.* **8**, 342–346 (2004)
13. Podrez-Radziszewska, M., Gluszewski, W.: Radiation modification of polyethylene surgical implants. *Contemp. Oncol.* **9**, 357–365 (2005)
14. Charlesby, A., Pinner, S.H.: Analysis of the solubility behaviour of irradiated polyethylene and other polymers. *Proc. Roy. Soc. London A* **249**, 367–386 (1959)
15. Flory, P.J., Rehner, J.: Statistical mechanics of crosslinked polymer networks II Swelling. *J. Chem. Phys.* **11**, 521–526 (1943)
16. Hwang, W.-G., Wei, K.-H., Wu, C.-M.: Mechanical, thermal, and barrier properties of NBR/organosilicate nanocomposites. *Polym. Eng. Sci.* **44**, 2117–2124 (2004)
17. Barton, J.: Peroxide crosslinking of poly(n-alkyl methacrylates). *J. Polym. Sci., Part A: Polym. Chem.* **6**, 1315–1323 (1968)

Chapter 34

Wood Flour as a Filler of Natural and Epoxidised Natural Rubber

A. Smejda-Krzewicka, W.M. Rzymiski and P. Dmowska-Jasek

Abstract It was found that the wood flour (WF; both from coniferous trees and deciduous trees) can be used as the fillers of natural rubber (NR) or epoxidised natural rubber (ENR). It was confirmed by the decrease of the curing time, especially in the case of ENR. The incorporation of WF into rubbers positive effects on the crosslinking density, wherein the wood flour derived from coniferous trees influences more those properties, that are associated with a greater surface area of this filler. Both types of WF weaken the tensile strength and elongation at break, but clearly improved stress at 100, 200 and 300% elongation. The presence of epoxy groups in the ENR does not lead to a greater reinforcement of this elastomer with wood flour in relation to natural rubber without functional groups on the surface. Additionally it was found that the WF content in NR or ENR vulcanisates leads to the formation of more amount of disulfide crosslinks and simultaneously causes lower friction coefficient of obtained vulcanisates.

34.1 Introduction

Carbon black and silica are commonly used as reinforcing fillers in elastomers. There are also many materials showing reinforcing properties in elastomers, such as glass and carbon fibres or nanofillers as well. However, these materials are synthetic and expensive products, therefore inexpensive, natural fillers that improve the properties of elastomers and reduce the cost of rubber products, are constantly searched. Ecological factors would be taken into account too. Thus, the interest in organic substances, such as wood flours, slate nuts, hemp fibres, as fillers of polymeric materials has significantly increased recently [1–6].

Compared to inorganic fillers, natural fillers present some well-known advantages such as lower density and lower price. They are harmless, biodegradable, renewable, and their mechanical properties can be comparable to those of inorganic fibres [1, 7–9].

A. Smejda-Krzewicka (✉) · W.M. Rzymiski · P. Dmowska-Jasek
Institute of Polymer & Dye Technology, Łódź University of Technology, Łódź, Poland

The aim of our study was to investigate the effect of the wood flour (WF) on the crosslinking and properties of natural (NR) and epoxidised natural rubber (ENR) cured with conventional system.

34.2 Materials and Methods

34.2.1 Materials

The natural (NR) and epoxidised natural rubber (ENR, epoxidation degree: 25 mol%) were chosen to study.

The wood flour derived from coniferous trees (CF; brand LIGNOCEL S150 TR, particle diameter 70–150 μm) and from deciduous trees (DF; brand LIGNOCEL HB120 TR, particle diameter 40–120 μm) were used as the fillers of chosen elastomers, in the amount of 15 phr (see Fig. 34.1). Both types of WF are made by J. Rettenmaier & Söhne GmbH & Co. KG (Rosenberg, Germany).

Such filled elastomers were cured with conventional system, e.g. with sulphur (S) in the presence of N-cyclohexyl-2-benzothiazolesulfenamide (CBS) as an accelerator at $T = 433\text{ K}$ for 15 min.

34.2.2 Sample Preparation

NR or ENR compounds were prepared in 8 min on two-roll mill at the temperature 300–310 K. The curing ability of compounds was determined on the basis of vulcanometric measurements according to the PN ISO 3417 (1994) standard. Test samples were prepared using a hydraulic press at the temperature of 433 K.

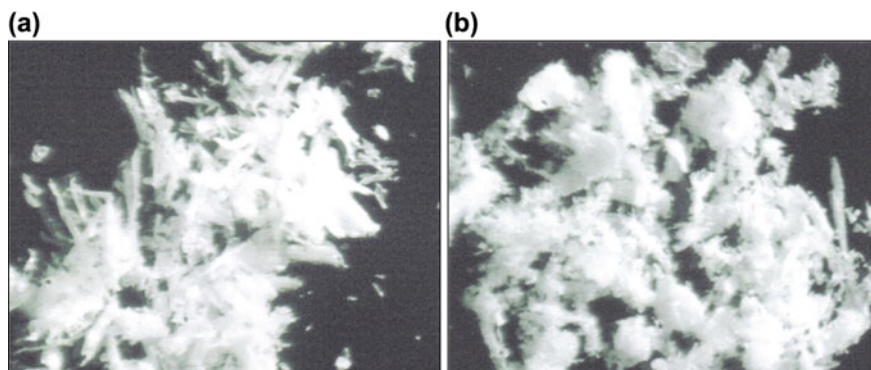


Fig. 34.1 Micrograph of the wood flour derived from coniferous trees (a) and derived from deciduous trees (b); magnification: 40 \times

34.2.3 Testing Methods

The crosslinking degree was determined on the basis of the equilibrium swelling and Mooney-Rivlin elasticity constants ($2C_1$) [10].

The equilibrium swelling was determined in toluene. Four samples (40–60 mg) were cut from vulcanisates; they were placed in the solvent for 72 h in a thermostatic chamber at 293 K. The swollen samples, before weighing, were washed with ether and their surfaces were dried on filter paper.

The tensile strength (TS_b) and elongation at break (E_b) were determined using the tensile tester Zwick 1435 according to the PN ISO 37 (2007) standard.

34.3 Results and Discussion

In our work NR and ENR were investigated. The aim of our study was to assess how the wood flour will affect the properties of NR and ENR. We have expected that the interactions between hydroxyl groups on the surfaces of WF and epoxy groups present in ENR are possible and will lead to better reinforcement of obtained products.

The wood flour (WF) used in our studies is a mixture of soft fibres obtained by accurate fragmentation of the woods. This product is characterised by a very low moisture content (up to 2%) and very high purity, and WF is completely devoid of metallic and mineral impurities. The wood flour derived from coniferous or deciduous trees, thus these two types of WF differ in the structure and properties arising from differences in the structure of deciduous and coniferous trees, particularly in the content of the lignin and cellulose.

34.3.1 Effect of Wood Flour Derived from Coniferous Trees (CF) on Properties of NR and ENR

It has found that the incorporation of 15 phr of CF to NR or ENR does not affect the scorch time (τ_{02}) and curing time (τ_{90}) of NR and ENR, excluding ENR filled with CF. In this case the curing time reduces from 432 s (unfilled ENR) to 253 s. Additionally we have observed that the filling of both elastomers with CF leads to significantly reduction of minimum vulcanometric torque (L_{\min}) from 9.2 (without a filler) to 5.4 dNm for NR filled with CF and from 17.5 (without a filler) to 14.1 dNm for ENR filled with CF. This indicates a decrease in viscosity of studied blends after the incorporation CF as the filler and the better processability of the filled compounds. As expected, the incorporation of CF into mentioned elastomers causes the increase of vulcanometric torque after heating for 15 (ΔL_{15}) and 30 (ΔL_{30}) minutes (see Table 34.1).

Table 34.1 Effect of wood flour derived from coniferous trees on properties NR or ENR unfilled and filled with CF, cured at 433 K for 15 min

Component	Component amount (phr)			
NR	100	100	–	–
ENR	–	–	100	100
Paraffin	1	1	1	1
ZnO	5	5	5	5
Stearic acid	1	1	1	1
S	2.5	2.5	1	1
CBS	1	1	2	2
CF	–	15	–	15
Vulcamic parameters, 433 K				
τ_{02} (s)	278	268	121	123
τ_{90} (s)	484	486	432	253
L_{\min} (dNm)	9.2	5.4	17.5	14.1
ΔL_{15} (dNm)	60.6	74.0	62.3	73.9
ΔL_{30} (dNm)	58.5	6.5	62.0	71.0
Properties of vulcanisates				
S_{100} (MPa)	0.71	0.96	0.73	2.31
S_{200} (MPa)	1.14	1.57	1.12	3.03
S_{300} (MPa)	1.33	1.99	1.62	3.69
TS_b (MPa)	15.11	10.18	14.15	6.87
E_b (%)	663	597	589	480
Q_w^T (g/g)	4.87	3.58	3.63	2.73
$2C_1$ (kg/cm ²)	2.15	3.06	2.68	3.27
$2C_2$ (kg/cm ²)	3.54	2.35	2.87	4.60

τ_{02} —scorch time, τ_{90} —curing time, L_{\min} —minimum vulcamic torque, ΔL_{15} and ΔL_{30} —increase of vulcamic torque after heating for 15 or 30 min, S_{100} , S_{200} , S_{300} —stress at 100, 200, 300% elongation, TS_b —tensile strength, E_b —elongation at break, Q_w^T —equilibrium swelling in toluene, $2C_1$, $2C_2$ —Mooney-Rivlin elasticity constants

The conclusions from vulcamic measurements were also confirmed by the determination of the equilibrium swelling in toluene and values of the elasticity constants ($2C_1$), which shows that the curing degree of studied blends increases with the using of CF as the filler. This fact was confirmed by the decreasing value of the equilibrium swelling (Q_w) following with the rubber filling (Table 34.1). In the case of cured NR, Q_w in toluene decreases from 4.87 (without filler) to 3.58 g/g (after the filling with CF) and in the case of cured ENR, these values equal 3.63 and 2.73 g/g, respectively. The filling of NR with CF and curing leads to the increase of $2C_1$ about 40% and in the case of cured ENR the increase of this value is more than 20% (see Table 34.1).

We have found that stress–strain properties of CF-filled and cured NR or ENR were changed significantly (Fig. 34.1). The tensile strength of cured, unfilled NR reached $TS_b = 15.1$ MPa, while for the cured NR, filled with 15 phr of CF, TS_b is

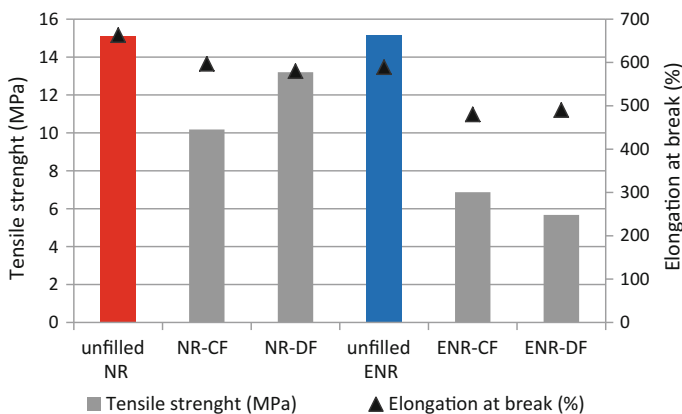


Fig. 34.2 Effect of the wood flour (15 phr) on the stress–strain properties of cured NR and ENR; CF—wood flour derived from coniferous trees, DF—wood flour derived from deciduous trees

10.2 MPa. And TS_b of cured, unfilled ENR equals 14.2 MPa, while for the filled and cured ENR TS_b is 6.9 MPa, only (Fig. 34.2). The influence of CF on the properties of ENR vulcanisates was different than our expectations, however it is worth noting, that values of stress at 100, 200 and 300% elongation increase greatly after the introduction of CF into investigated elastomers. The filling of NR and ENR with CF decreases the elongation at break slightly (see Table 34.1).

34.3.2 *Effect of Wood Flour Derived from Deciduous Coniferous Trees (DF) on Properties of NR and ENR*

Our studies showed that it is also possible to use wood flour (15 phr) derived from deciduous trees (DF) as the filler of NR and ENR. It follows from the observed increase of vulcanometric torque (ΔL_{15} , ΔL_{30}), the measured equilibrium swelling (Q_w) and stress–strain properties, and the values of Mooney–Rivlin elasticity constants as well.

As in the case of CF we have found a small effect of DF on the scorch time (τ_{02}) and curing time (τ_{90}) and marked decrease of minimum vulcanometric torque (L_{min}). These relationships are shown for both NR and ENR (Table 34.2). The filling of these elastomers with DF leads to higher increase of vulcanometric torque after heating for 15 (ΔL_{15}) and 30 (ΔL_{30}) minutes. The value of ΔL_{15} increases from 60.6 for unfilled NR to 69.6 dNm for NR filled with DF and from 62.3 for unfilled ENR to 72.4 dNm for ENR filled with DF. The values of ΔL_{30} change in a similar way, for NR from 58.5 to 67.8 dNm and for ENR from 62.0 to 71.1 dNm, respectively.

Table 34.2 Effect of wood flour derived from deciduous trees on properties NR or ENR unfilled and filled with DF, cured at 433 K for 15 min

Component	Component amount (phr)			
	NR	100	100	–
ENR	–	–	100	100
Paraffin	1	1	1	1
ZnO	5	5	5	5
Stearic acid	1	1	1	1
S	2.5	2.5	1	1
CBS	1	1	2	2
DF	–	15	–	15
Vulcanometric parameters, 433 K				
τ_{02} (s)	278	275	121	118
τ_{90} (s)	484	540	432	290
L_{min} (dNm)	9.2	4.8	17.5	14.9
ΔL_{15} (dNm)	60.6	69.6	62.3	72.4
ΔL_{30} (dNm)	58.5	67.8	62.0	71.1
Properties of vulcanisates				
S_{100} (MPa)	0.71	1.11	0.73	1.76
S_{200} (MPa)	1.14	1.62	1.12	2.47
S_{300} (MPa)	1.33	2.06	1.62	3.05
TS_b (MPa)	15.11	13.20	14.15	5.67
E_b (%)	663	580	589	490
Q_w^T (g/g)	4.18	3.99	3.46	2.97
$2C_1$ (kg/cm ²)	2.15	4.02	2.68	2.81
$2C_2$ (kg/cm ²)	3.54	4.25	2.87	4.94

We have found that mechanical properties of DF-filled and cured NR or ENR were changed significantly (see Table 34.2, Fig. 34.2), similarly to the filling with CF. The tensile strength of cured, unfilled ENR reached $TS_b = 15.1$ MPa, while for the DF-filled and cured ENR it is 5.7 MPa, only. An exception is the tensile strength of filled and cured NR which changes slightly from 15.1 MPa (unfilled NR) to 13.2 MPa only. But, the filling of NR and ENR with DF leads to the significant increase of stress at 100, 200 and 300% elongation which indicates increased hardness of the vulcanisates.

It is worth noting that unfilled ENR has a large tensile strength due to the possible crystallisation caused by the deformation. It is related to a very good orientation of rubber macromolecules due to applied strain. But the incorporation of filler particles into ENR causes the orientation of its macromolecules is significantly inhibited, which leads to a decrease in crystallisation or its total absence. Therefore, the tensile strength of ENR filled with wood flour clearly decreases.

34.4 Conclusion

It was found that the wood flour (both from coniferous trees and deciduous trees) can be used as the fillers of natural or epoxidised natural rubber. It was confirmed by the decrease of the curing time, especially in the case of ENR. The incorporation of WF into rubbers positive effects on the crosslinking density, wherein the wood flour derived from coniferous trees (CF) influences more those properties, that are associated with a greater surface area of this filler. Both types of wood flour weaken the tensile strength and elongation at break, but clearly improved stress at 100, 200 and 300% elongation. The presence of epoxy groups in the ENR does not lead to a greater reinforcement of this elastomer with wood flour in relation to NR without functional groups on the surface.

References

1. Bledzki, A.K., Gassan, J.: Composites reinforced with cellulose based fibres. *Prog. Polym. Sci.* **24**, 221–274 (1999)
2. Plackett, D., Logstrup, A.T., Batsberg, P.W., Nielsen, L.: Biodegradable composites based on L-poly lactide and jute fibres. *Compos. Sci. Technol.* **63**, 1287–1296 (2003)
3. Kuciel, S., Liber, A.: Ocena skuteczności wzmacniania polietylenów mączką drzewną. *Polimery* **50**, 436–440 (2005)
4. Zajchowski, S., Ryszkowska, J.: Kompozyty polimerowo-drzewne—Charakterystyka ogólna oraz ich otrzymywanie z materiałów odpadowych. *Polimery* **54**, 674–682 (2009)
5. Pach, J., Kaczmar, J.W.: Wpływ chemicznej modyfikacji włókien konopnych na wybrane właściwości mechaniczne kompozytów na osnowie polipropylenowej. *Polimery* **56**, 385–389 (2011)
6. Sobczak, L., Brüggemann, O., Putz, R.F.: Polyolefin composites with natural fibres and wood-modification of the fiber/filler-matrix interaction. *J. Appl. Polym. Sci.* **127**, 1–17 (2013)
7. Bledzki, A.K., Reihmane, S., Gassan, J.: Thermoplastics reinforced with wood fillers: A literature review. *Polym. Plast. Technol. Eng.* **37**, 451–468 (1998)
8. Ratajska, M., Boryniec, S.: Biodegradation of some natural polymers in blends with polyolefines. *Polym. Adv. Technol.* **10**, 625–633 (1999)
9. Plackett, D., Logstrup, A.T., Batsberg, P.W., Nielsen, L.: Biodegradable composites based on L-poly lactide and jute fibres. *Compos. Sci. Technol.* **63**, 1287–1296 (2003)
10. Mooney, M.: A theory of large elastic deformation. *J. Appl. Phys.* **11**, 582–592 (1940)

Chapter 35

Characterisation of the Ultimate Tensile Properties of Elastomers by a Dimensionless Hooke Number—A New Approach to Failure Envelopes

N. Rennar and P. Kirchner

Abstract The ultimate tensile properties of polymeric materials can be described by different kinds of master curves. Attention is focused mainly on the dimensionless Hooke number He fairly unknown in the literature. This quantity is defined and its utility to characterise the fracture mechanical properties of chemically uncrosslinked thermoplastics as well as very slightly crosslinked rubbers is discussed in detail. Pronounced differences were observed in a double logarithmic plot of the Hooke number versus the elongation at break ε_b for these two types of polymeric materials. The reasons of these discrepancies are explained on a molecular level. Furthermore, the effect of carbon black as reinforcing filler and its influence on the Hooke number is analysed. The presented test results support the idea that the Hooke number is adequate to characterise the fracture mechanical behaviour of polymers in a similar manner as do the well-known failure envelope representations.

35.1 Introduction

The outstanding properties of elastomers are their high reversible extensibility exerted by relatively small external forces and their ability to regain the original state after removal of the external forces. The ultimate properties of polymeric materials are of great importance from both practical and theoretical considerations. The ultimate mechanical property σ_b^0 is the nominal tensile stress at break, i.e. the retractive force of the sample just before rupture divided by the cross-sectional area A_0 of the undeformed specimen. It should not be confused with the true stress which is related to the cross-section of the deformed sample. The breaking stress σ_b^0 , the elongation at break ε_b , and the energy density at break U_b of a rubber matrix are

N. Rennar (✉) · P. Kirchner
Plastics and Elastomer Technology, University of Applied Sciences Würzburg-Schweinfurt,
Würzburg, Germany

influenced strongly by a great number of parameters. Test conditions (temperature, strain rate), chemical structure of polymers, crystallisation effects, type and amount of filler particles have to be mentioned, for example. Because of such a great number of influence parameters, yet it is not possible to calculate and predict these fracture mechanical properties with sufficient precision.

Primary objective of this study is to point out different kinds of master curve representations in order to characterise the failure behaviour of polymers. To gain statements of general validity, it is imperative to vary a great number of test parameters systematically. Attention is focussed mainly on the dimensionless Hooke number fairly unknown in the technical literature. This quantity will be defined and its utility to describe the fracture mechanical properties of uncrosslinked thermoplastics and crosslinked rubbers will be discussed in details.

35.2 Theoretical Background

Experiments on crosslinked rubbers without filler particles reveal that ε_b and the reduced quantity $[\sigma_b^0 \cdot (T_0/T)]$ can be represented over several orders of magnitude of strain rates by two separate master curves. Combining these curves and replotting $\lg [\sigma_b^0 \cdot (T_0/T)]$ versus $\lg \varepsilon_b$ results in a typical failure envelope curve, originally introduced by Smith [1–5]. It describes ultimate properties in creep or stress relaxation as well as in constant rate of strain, respectively, by a single curve with parabolic shape. Following around the curve in an anticlockwise sense corresponds to increasing rate of extension and/or decreasing temperature while both variables do not appear explicitly. It is common practice to correct the measured values σ_b^0 by a factor (T_0/T) when test temperature T and reference temperature T_0 do not coincide. In a first approximation, failure envelopes generated in this way should be independent of strain rate and test temperature because they are based on the time–temperature superposition principle and the applicability of the method of reduced variables. But more accurate studies reveal that the method is only valid in a restricted range of temperatures and strain rates [6]. Even for non-crystallisable elastomers containing moderate amounts of reinforcing fillers, the principle seems to be applicable leading to separate failure envelopes with constant amount of filler (Fig. 35.1) [6–8].

Further generalisation can be made if the breaking stress σ_b^0 is reduced not only to a common reference temperature T_0 but also to unit crosslink density ν_c . Then, at sufficient high temperatures compared to the glass transition temperature, failure envelopes obtained from samples differing in ν_c will superpose to a common response curve independent of chemical structure of the polymer when $[\sigma_b^0 \cdot (T_0/T)]$ is normalised to unit crosslink density. Despite the universal character of this reduced failure envelope, deviations are observed at low temperatures because of different polymer chain flexibilities [9, 10].

An alternative approach to describe the failure data independently of time and temperature is to plot the reduced energy density at break versus the elongation at break in a double logarithmic plot [11]. Again, for the unfilled crosslinked rubber

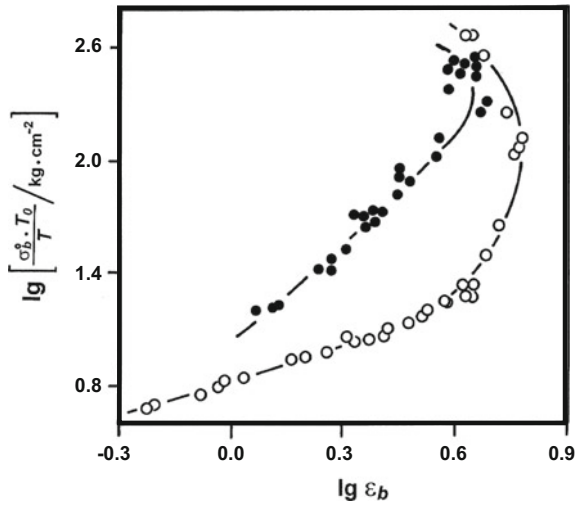


Fig. 35.1 Double logarithmic plot of the reduced nominal breaking stress $[\sigma_b^0 \cdot (T_0/T)]$ versus the ultimate strain ε_b for SBR vulcanisates (data according to Halpin [8]). ●: 30 phr carbon black, ○: without carbon black

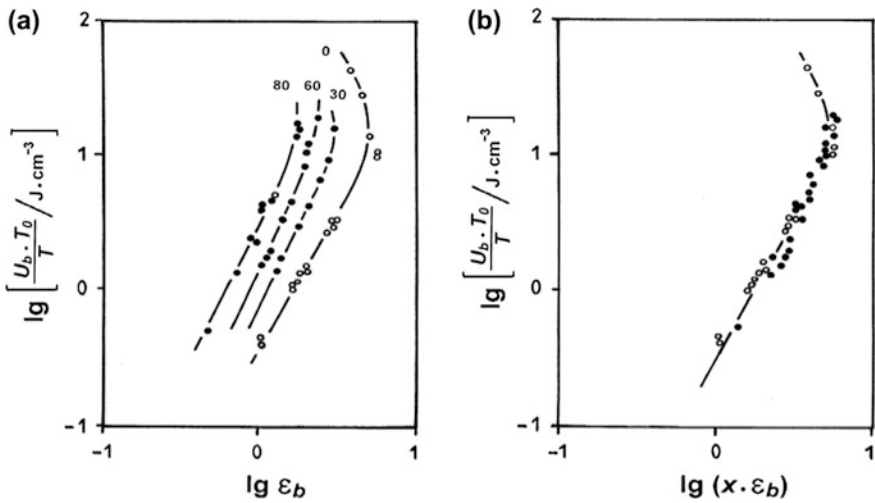


Fig. 35.2 Double logarithmic plot of the normalised energy at break $[U_b \cdot (T_0/T)]$ versus the elongation at break ε_b for SBR vulcanisates (data according to Harwood [11]); as a function of carbon black content (in phr) (a), master curve (b). ●: 30/60/80 phr carbon black, ○: without carbon black

matrix as well as for vulcanisates loaded with different amounts of filler, a set of separate failure curves is obtained. They can be shifted along the $\lg \varepsilon_b$ -axis to coincide with the failure data for the gum vulcanisates, finally resulting in a single master curve to describe the whole failure envelope behaviour (Fig. 35.2).

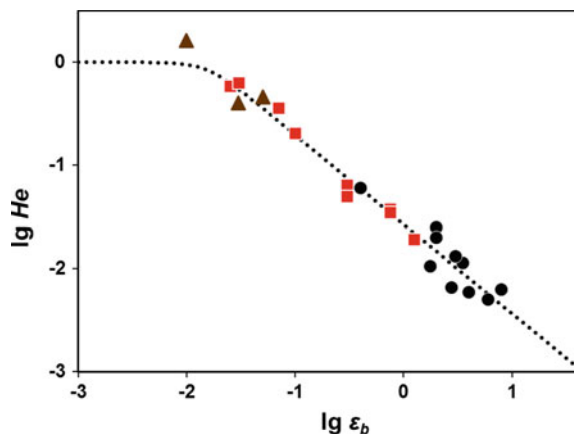
As was first demonstrated by Elias [12–14], ultimate tensile properties of thermoplastic polymers without additives also can be characterised by a Hooke number $He = \sigma_b^0 / (\varepsilon_b \cdot E)$ with the ultimate tensile strength σ_b^0 , the elongation at break ε_b , and Young's modulus E . He can be identified as the ratio of the slope of the secant at ultimate elongation to the slope of the tangent of the stress–strain curve at infinitely small extensions. For quite a large number of uncrosslinked thermoplastic polymers, amorphous or crystalline in nature, the rupture properties can be presented in a typical $\lg He$ – $\lg \varepsilon_b$ plot by a single master curve with empirically adjustable parameters (Fig. 35.3).

The fact that all data points of a great number of different polymers fall on a single master curve in a $\lg He$ – $\lg \varepsilon_b$ plot only differing in their positions on the line—despite great variations in chemical structures and morphologies—can be seen as an indication that Hooke numbers in this linear range are mainly controlled by shear flow processes before rupture. It seems to be obvious that these processes are becoming more significant with increasing ε_b and decreasing He . Three distinct regions can be distinguished in this plot:

- A Hookeian region with $He = 1$ at very low ε_b ($\varepsilon_b < \varepsilon_{crit}$),
- A non-Hookeian region with linear relation between $\lg He$ and $\lg \varepsilon_b$ at $\varepsilon_b > \varepsilon_{crit}$,
- A transition region between these two regimes ($\varepsilon_b \approx \varepsilon_{crit}$).

A question that requires careful exploration is whether or not the above defined Hooke number is also adequate to describe the observed rupture behaviour of slightly crosslinked rubbers, i.e. elastomers without fillers or containing moderate amounts of particulate fillers, or is it mainly restricted to thermoplastics. The effect of testing speed on the exact value of the Hooke number and its position in a $\lg He$ – $\lg \varepsilon_b$ plot needs further clarification, too.

Fig. 35.3 Double logarithmic plot of Hooke number He versus elongation at break ε_b for amorphous (■) and semi-crystalline (●) thermoplastics as well as for thermosets (▲) according to Elias [12]



35.3 Experimental Part

35.3.1 Selection of Polymers and Recipes of Test Compounds

In order to proof the applicability of the Hooke number concept to rupture mechanics of elastomers and to support the general conclusions of our study, a series of different rubbers were tested. Chemical structure, polarity, glass transition temperature, crystallisability, crosslink density, crosslinking temperature, and type of crosslinking were varied over a wide range [15]. In a first test series, the ultimate tensile properties of gum vulcanisates were investigated. In a second test series, the focus was mainly on the rupture behaviour of non-crystallisable rubbers (e.g. styrene-butadiene rubber) containing finely divided fillers (e.g. carbon black). The test recipes of the rubber compounds are described in Table 35.1. A compilation and characterisation of the tested polymers is given in Table 35.2.

As can be seen in Table 35.2, the glass transition temperatures of the selected polymers cover a temperature range of approximately 100 K. Included are also materials of partially crystalline character under the chosen test conditions.

35.3.2 Mixing Procedure, Crosslinking and Testing

All compound ingredients were incorporated on a two roll mill. Sheets of 2 mm thickness were prepared by pressure moulding of the final mixtures at specified cure temperatures ranging from $T_c = 140\text{--}160$ °C. Additionally, a variation in cure time t_c gave the opportunity for elastomers of different crosslink densities. Standard dumbbell-shaped test specimens were cut from the sheets (S1, S2 standard test pieces).

The stress-strain curves of the test samples were measured at different temperatures by a commercially available tensile tester with an optical device. Extension rates v covered a wide range ($v = 0.5\text{--}500$ mm min⁻¹). Normally, the crosshead of the tester attached to the sample traveled at constant velocity till rupture. This

Table 35.1 Recipes of the tested rubber compounds (concentrations in phr)

Rubber	100	Test compound A
Dicumyl peroxide (DCP)	0.3–3.0	
Rubber	100	Test compound B
Carbon black (CB)	0–80	
Zinc oxide	3.0	
Stearic acid	2.0	
Accelerator CBS	1.5	
Accelerator DPG	0.3	
Sulphur	1.8	

Table 35.2 Compilation and characterisation of the tested polymers

Abbreviation	Polymer name	Specification	T_g (°C)
PDMS	Polydimethylsiloxane	SiH endgroups	-123
Cis-BR	Butadiene rubber	98% cis-1,4-BR	-109
BIIR	Brominated poly (isobutylene-co-isoprene)	<2% brominated isoprene units	-73
EPDM	Ethylene-propylene-diene rubber	ca. 50% ethylene content	-55
S-SBR	Solution styrene-butadiene rubber	25% styrene, 25% 1,2-BR	-49
NBR	Nitrile-butadiene rubber	18, 28, 39% ACN	-38, -29, -17
Trans-PNR	Trans-polynorbornene	with 150 phr oil extended	-25
ENR	Epoxidised natural rubber	50% epoxidised isoprene units	-24
NR	Natural rubber	100% cis-1,4-IR (pale crepe)	-63 ($T_m = 40$ °C)
TOR	Polyoctenamer	80% trans-octenamer units	-75 ($T_m = 55$ °C)
TPE-S	Thermoplastic elastomer (styrene type)	Hard segment: polystyrene	-68 ($T_m = 124$ °C)
TPE-U	Thermoplastic elastomer (urethane type)	Hard segment: polyurethane	-41 ($T_m = 164$ °C)

ACN—acrylonitrile, T_g —glass transition temperature, T_m —softening temperature, BR—butadiene rubber, IR—isoprene rubber

procedure gave by no means constant strain rates of the sample because of extrusion effects of the specimen tabs from the grips. Nevertheless, the retractive force and the extension of the sample were recorded simultaneously in dependence of time. Because of the low reproducibility of the so-called ultimate tensile properties σ_b^0 and ε_b caused by statistical fluctuations, it was stringent to characterise the mechanical rupture process by adequate mean values. e.g. median values. Young's moduli E of the elastomers were estimated by different evaluation procedures to check for their reproducibility. These experimentally accessible data were necessary to calculate the dimensionless Hooke number He .

35.4 Results and Discussion

For a correct evaluation of the Hooke number it was imperative to measure σ_b^0 and ε_b of the sample simultaneously and with high precision. It was common practice to record σ_b^0 by a force transducer and to measure ε_b by an optical transducer without any contact between specimen and extensometer. The estimation of ε_b by measuring the distance of the grips moving at constant speed would result in quite inaccurate data because the strain in the specimen does not increase in direct proportion to the crosshead velocity. This can be seen in Fig. 35.4 where the elongation of the sample and the elongation of the crosshead are compared. There is a direct

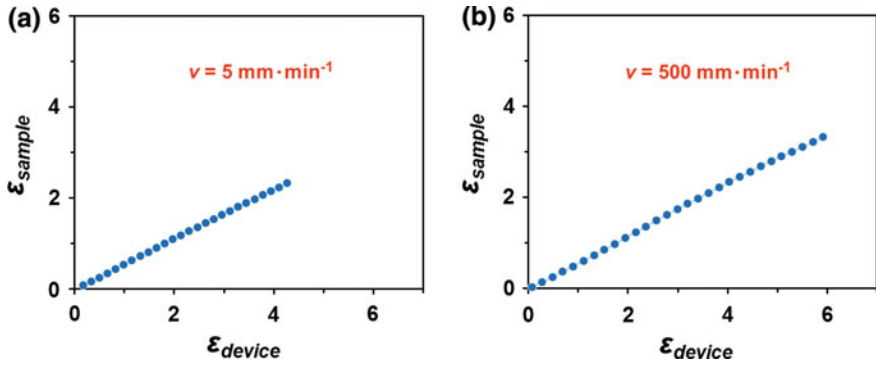


Fig. 35.4 Actual elongation ϵ_{sample} of the rubber sample plotted against the distance ϵ_{device} of the grips; $v = 5 \text{ mm min}^{-1}$ (a), $v = 500 \text{ mm min}^{-1}$ (b)

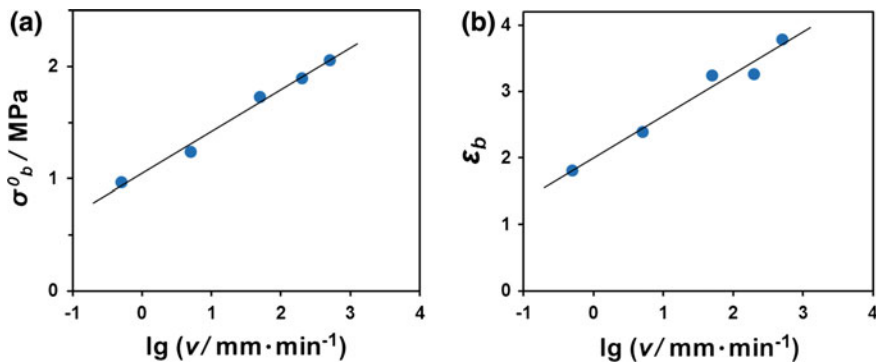


Fig. 35.5 Effect of testing speed v on the ultimate tensile strength σ_b^0 (a) and the ultimate tensile strain ϵ_b (b) for slightly crosslinked NBR

proportionality between ϵ_{sample} and ϵ_{device} whatever is the actual extension speed. But in all cases, at any time, ϵ_{sample} gives always smaller values than ϵ_{device} because of extrusion effects in the skin zones of the sample.

Nevertheless, with increasing extension velocity also an increase in breaking stress σ_b^0 , elongation at break ϵ_b , work-to-break U_b , and Young's modulus E is observed (Fig. 35.5). Because of the same trend of the ultimate tensile properties with increasing extension rate and probably in dependence on structural parameters, it seems quite plausible that some compensation can occur if dimensionless Hooke numbers are considered.

Indeed, plotting the Hooke number He of several crosslinked rubbers versus the elongation at break ϵ_b in a double logarithmic plot reveals that the data can be represented by a single master curve which seems to be quite independent of the chemical structures of the tested polymers and their physical structures inherent in their chain-lengths and chain-length distributions. However, the exact position of

the individual data points on this master curve can be changed by the actual polymer flexibility and the actual test conditions. e.g. strain rate and temperature.

The fact that in a first approximation the Hooke numbers of several uncrosslinked thermoplastic polymers as well as the Hooke numbers of a variety of slightly crosslinked rubbers can be represented by master curves is quite surprising. In a typical $\lg He - \lg \varepsilon_b$ plot below $\varepsilon_b < \varepsilon_{crit}$, the Hooke number is nearly constant corresponding to $He \approx 1$. Far above $\varepsilon_b > \varepsilon_{crit}$, the Hooke number decreases monotonically with increasing ε_b resulting in a more or less extended transition region in the vicinity of ε_{crit} . But the range where He decreases linearly with ε_b in a $\lg He - \lg \varepsilon_b$ plot is more pronounced for thermoplastics than for very slightly crosslinked rubbers. Additionally, a few elastomers show an upturn of He versus ε_b . This behaviour is totally missing for uncrosslinked plastics (Fig. 35.6).

Furthermore, it seems quite evident that the Hooke numbers of the two series of polymers, i.e. uncrosslinked thermoplastics (data from Elias) and slightly crosslinked rubbers (this study), can be represented only by separate master curves characterised by different values of ε_{crit} . The lower ε_{crit} for thermoplastic materials is inherent in the fact that plastomers deviate from linear Hookeian behaviour even at very small elongations (Fig. 35.7). The extraordinary position of the Hooke number of trans-poly(octenamer) requires further discussion given below.

The distinct differences of the master curve representation in a $\lg He - \lg \varepsilon_b$ plot are serious indications that there is a basic difference whether the polymer chains have the opportunity to change their conformations before rupture or are restricted in their backbone conformations by neighbouring chains or domains of crosslinks. The chain mobility seems to be the key parameter which can be restricted to a great extent by chemical or physical crosslinks giving rise to higher values of ultimate tensile strength σ_b^0 and Hooke numbers He . This is consistent with calculated plots based on non-Gaussian chain statistics demonstrating the limited extensibility of

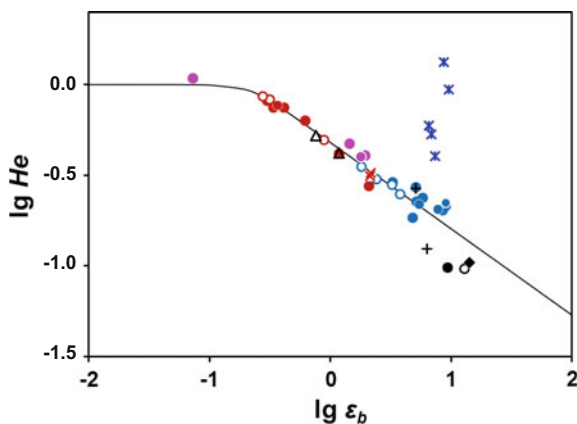


Fig. 35.6 Hooke number He versus ultimate strain ε_b for crosslinked rubbers. ●, ○: NBR, ●, ○, ×: SBR, ●, ○, +, ◆, △: TPE-U, EPDM, ENR, BIIR, BR, ●: PDMS, *: NR, PNR, TPE-S

Fig. 35.7 Master curve representations of the Hooke number He versus elongation at break ϵ_b for typical thermoplastic and rubber elastic materials. ●, ○: NBR, ●, ○, ×: SBR, ●, ○, +, ◆, △: TPE-U, EPDM, ENR, BIIR, BR, ●: PDMS, *: NR, PNR, TPE-S, ▲: thermoplastics, thermosets

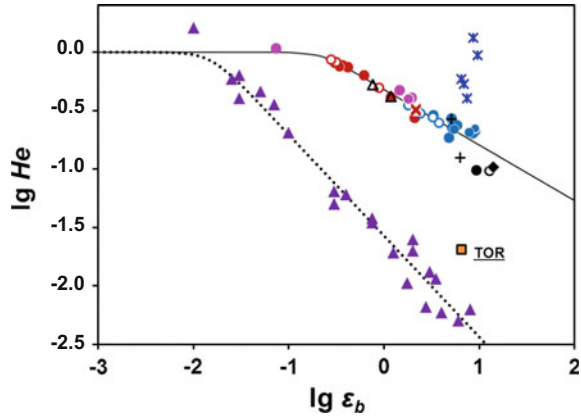
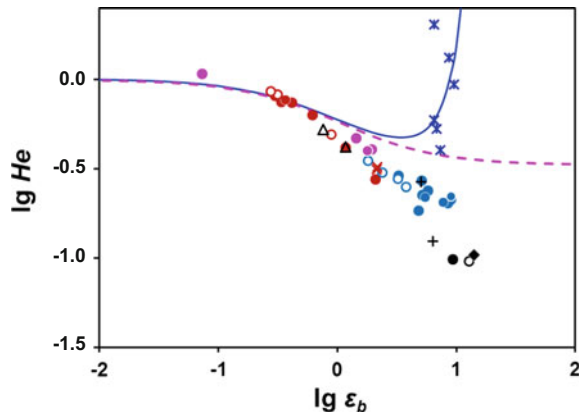


Fig. 35.8 Comparison of the experimentally observed Hooke numbers He with theoretical predictions for slightly crosslinked rubbers (legend and explanation of the symbols as in Fig. 35.6). - - -: Gaussian chain statistics, —: non-Gaussian chain statistics



network strands (Fig. 35.8). A closer look at the data reveals that the upturn of He versus ϵ_b is observed for a few vulcanisates only. Especially NR and TPE-S show this behaviour. It seems quite obvious that crystalline domains inherent in these polymers contribute to a reinforcement of the material resulting in higher Hooke numbers; in some cases $He > 1$ is found.

The majority of the tested rubbers are only slightly crosslinked. During the elongation of the macroscopic specimen, uncrosslinked portions consisting of polymer chains not connected to the three-dimensional polymer network slide away by reptation. Therefore, very slightly crosslinked rubbers and chemically uncrosslinked thermoplastics show similar behaviour in a typical tensile test. Their internal interactions are controlled to a great extent by the existence of entanglements. Glassy or crystalline domains interact as physical crosslinks provided they really exist and the deformation process is not accompanied with the evolution of enormous heat giving rise to a destruction of the reinforcing domains.

Considering the original stress–strain curves gives further insight into the fracture mechanical properties. The theoretical predictions of the stress–strain relation

Fig. 35.9 Theoretical predictions of the stress–strain relation for uniaxial extension according to the statistical theory of rubber elasticity. — — —: Gaussian chain statistics, —: non-Gaussian chain statistics

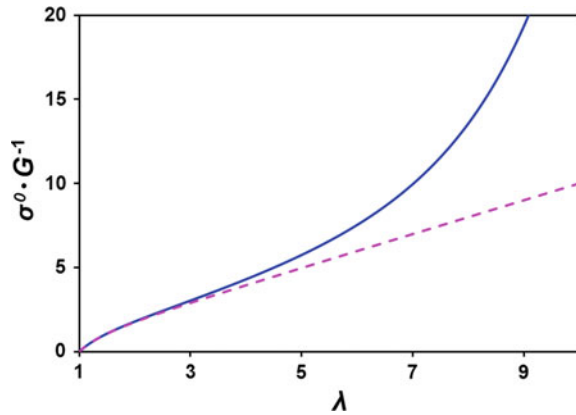
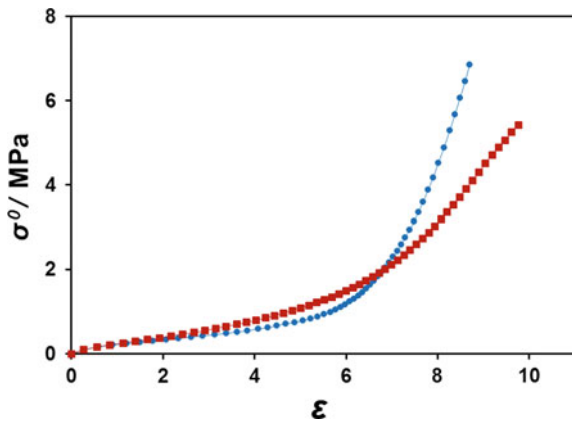


Fig. 35.10 Nominal stress σ^0 versus tensile strain ε for chemically crosslinked NR and TPE-S physically crosslinked by secondary bonds. ●: NR, ■: TPE-S



for uniaxial elongation are visualised in Fig. 35.9. Indeed, the statistical theory of rubber elasticity based on non-Gaussian chain statistics [16] is able to predict the sigmoidal stress–strain behaviour while the failure of the Gaussian chain statistics is obvious. For comparison with experiments, tensile properties of NR and TPE-S vulcanisates are shown in Fig. 35.10. The predicted sigmoidal stress–strain behaviour as well as the upturn of He versus ε_b are peculiarities of these rubbers. The characteristic inflection of the force–extension curve at high strains can be explained by the limited extensibility of network strands. Crystalline domains inherent in these rubbers under test conditions can amplify the effect to a certain extent [17].

The majority of the tested vulcanisates gave stress–strain curves as shown in Fig. 35.11. In some cases, however, the inflection at high elongations could also be observed, even if to a minor extent, although homogeneous elastic phases of non-crystallising synthetic rubbers were present. Additionally, the effect of crosslink density on the force–extension behaviour of slightly crosslinked SBR is

Fig. 35.11 Stress–strain curves of SBR crosslinked to various extents ($T_c = 150\text{ }^\circ\text{C}$). ●: 0.5 phr DCP/ $t_c = 15\text{ min}$, ■: 0.5 phr DCP / $t_c = 20\text{ min}$, ▲: 1.0 phr DCP/ $t_c = 20\text{ min}$

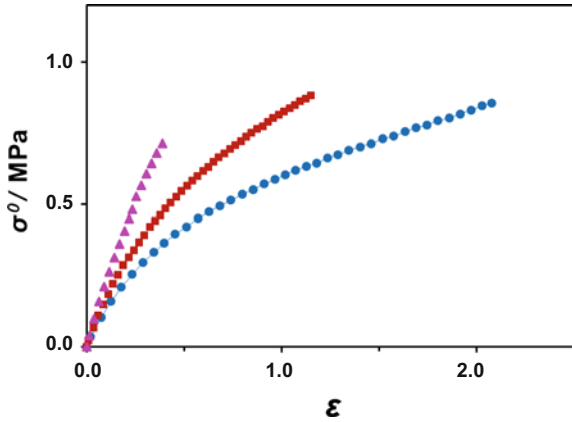
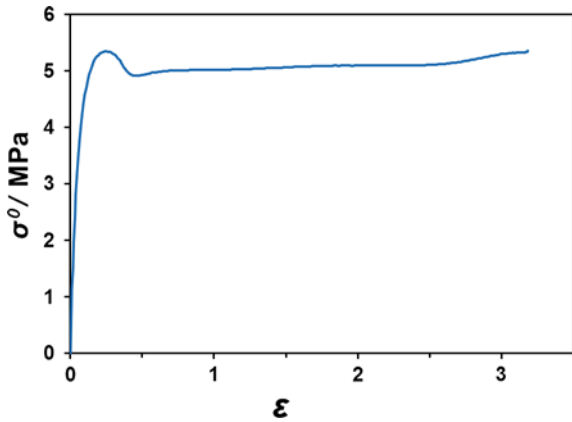


Fig. 35.12 Nominal tensile stress σ^0 versus tensile strain ϵ for semi-crystalline, slightly crosslinked TOR



demonstrated in Fig. 35.11. An increase in crosslinking always results in smaller values of ϵ_b and U_b as well as in slightly reduced σ_b^0 . In a typical $\lg He - \lg \epsilon_b$ plot all these samples are characterised by Hooke numbers He decreasing with increasing ϵ_b but lying on a single master curve.

The extraordinary tensile behaviour of TOR needs some comment. Although this polymer is chemically crosslinked, its stress–strain curve resembles the corresponding plot of a typical thermoplastic material with distinct yield point (Fig. 35.12). It seems that the crosslink density is of minor importance because of the high crystalline content of this material. But under the actual test conditions these domains are partly molten resulting in weak interactions between the slim polymer chains. Therefore, this polymer shows a typical hybrid behaviour between uncrosslinked thermoplastics and slightly crosslinked rubbers (see also Fig. 35.7).

Even for elastomers containing a certain amount of finely divided filler particles, the observed dependence of He on ϵ_b shows the same trend. Moreover, the

Fig. 35.13 Hooke number He versus ultimate strain ϵ_b for SBR vulcanisates loaded with the same amount of finely divided carbon blacks of increasing specific surface area (indicated by the arrow)

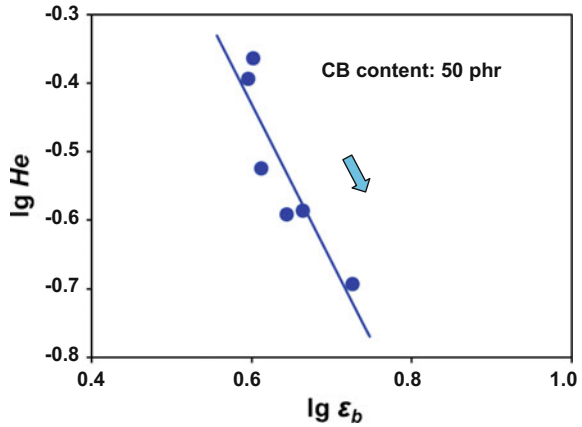
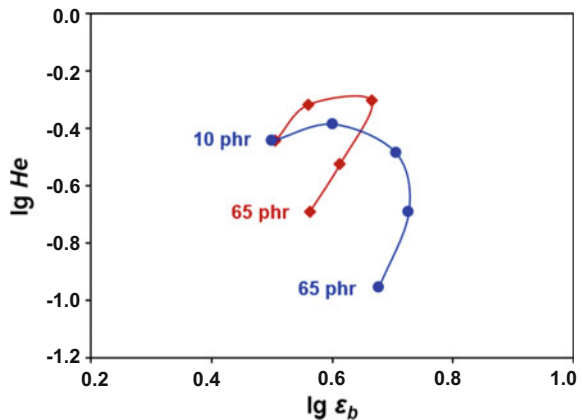


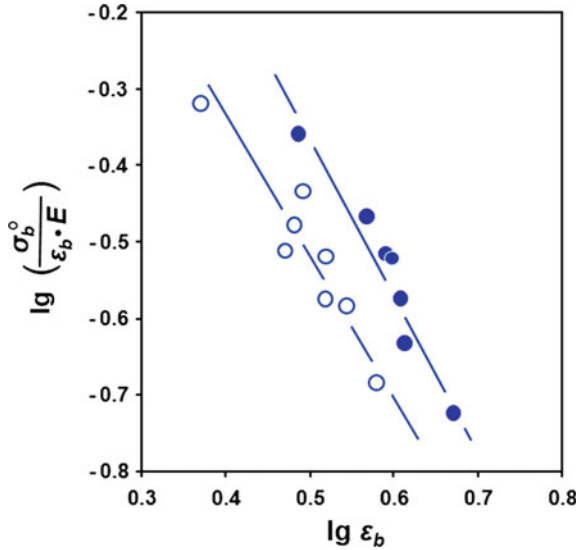
Fig. 35.14 Hooke number He versus elongation at break ϵ_b for SBR vulcanisates loaded with increasing amounts of carbon black ($T = 23\text{ }^\circ\text{C}$) (BET —values of nitrogen absorption, method by Brunauer, Emmet and Teller). ●: CB 1 with $BET = 195\text{ m}^2\text{ g}^{-1}$, ◆: CB 2 with $BET = 84\text{ m}^2\text{ g}^{-1}$



Hooke number can be identified as a measure to quantify the filler reinforcement. At constant loading, a reduction of He with increasing ϵ_b can be found when carbon blacks of increasing specific surface areas and nearly constant structure are incorporated into the rubber matrix (Fig. 35.13). At constant test conditions, increasing the amount of filler in the rubber matrix yields curves of parabolic shape when the corresponding data points of the Hooke number and the elongation at break are connected in a clockwise sense (Fig. 35.14).

Furthermore, when tensile tests are performed at different temperatures, parallel curves are obtained in a typical $\lg He - \lg \epsilon_b$ plot. It seems quite obvious that they can be superimposed by vertical or horizontal shifting as it is common practice for the well-known failure envelope representation (Fig. 35.15).

Fig. 35.15 Double logarithmic plot of Hooke number as function of ultimate elongation ε_b for carbon black loaded (50 phr) SBR elastomers. ●: $T = 23\text{ }^\circ\text{C}$, ○: $T = 40\text{ }^\circ\text{C}$



35.5 Summary and Conclusions

The ultimate mechanical properties of rubber elastic materials are of great importance from both practical and theoretical considerations. Very often the experimentally observed data have much lower values than the calculated ones. Under certain circumstances, it is possible to describe the observed phenomena under different test conditions by the method of reduced variables.

Objective of this study was to point out the different kinds of master curve representations to describe the ultimate tensile properties. Attention was focussed mainly on the dimensionless Hooke number He largely unknown in the technical literature. This quantity was defined and its utility to characterise the fracture mechanical properties of chemically uncrosslinked thermoplastics and very slightly crosslinked rubbers was discussed in detail. Pronounced differences were observed in a double logarithmic plot of the Hooke number versus the elongation at break ε_b for these two types of polymeric materials. The reasons of these discrepancies were explained on the basis of their chain mobilities and the limited extensibility of network strands. Furthermore, the effect of carbon black as reinforcing filler and its influence on the Hooke number were analysed.

The presented test results support the idea that the Hooke number is adequate to characterise the fracture mechanical behaviour of polymers in a similar manner as do the well-known failure envelope representations, e.g. σ_b^0 versus ε_b or U_b versus ε_b .

Acknowledgements The authors would like to express their gratitude to Dr. S. Seibold from ContiTech MGW GmbH for financial support and the permission to publish the results of this study.

References

1. Smith, T.L.: Dependence of the ultimate properties of a GR-S rubber on strain rate and temperature. *J. Polym. Sci. Part A: Polym. Chem.* **32**, 99–113 (1958)
2. Smith, T.L.: Ultimate tensile properties of elastomers. I. Characterization by a time and temperature failure envelope. *J. Polym. Sci. Part A: Polym. Chem.* **1**, 3597–3615 (1963)
3. Bueche, F.: *Physical Properties of Polymers*. Interscience Publishers, New York (1962)
4. Landel, R.F., Fedors, R.F.: Rupture behavior of elastomers: effect of statistical variability and crosslink density. *J. Polym. Sci. Part C: Polym. Lett.* **1**, 539–544 (1963)
5. Halpin, J.C.: Fracture of amorphous polymer solids: time to break. *J. Appl. Phys.* **35**, 3133–3141 (1964)
6. Ecker, R.: Der Einfluß verstärkender Ruße auf die viskoelastischen Eigenschaften von amorphen Elastomeren. *KGK—Kautsch. Gummi Kunstst.* **21**, 304–317 (1968)
7. Halpin, J.C., Bueche, F.: Fracture of amorphous polymeric solids: reinforcement. *J. Appl. Phys.* **35**, 3142–3149 (1964)
8. Smith, T.L.: Strength and extensibility of elastomers. In: Eirich, F.R. (ed.) *Rheology—Theory and Applications*, Vol. 5. Academic Press, New York (1969), pp. 127–222
9. Landel, R.F., Fedors, R.F.: Fracture of amorphous polymers. In: *Proceeding of the 1st International Conference on Fracture (Sendai, 12.–17.09.1965)*. Japanese Society for Strength and Fracture of Materials, Tokyo (1966), Vol. 2, pp. 1247–1256
10. Landel, R.F., Fedors, R.F.: Fracture of amorphous polymers. *Rubber Chem. Technol.* **40**, 1049–1059 (1967)
11. Harwood, J.A.C., Payne, A.R., Smith, J.F.: A new approach to rubber reinforcement. *KGK—Kautsch. Gummi Kunstst.* **22**, 548–553 (1969)
12. Elias, H.-G.: A master curve for tensile properties of thermoplastics. *Macromol. Chem. Phys.* **195**, 3117–3131 (1994)
13. Nielsen, L.E., Landel, R.F.: *Mechanical Properties of Polymers and Composites*, 2nd edn. Marcel Dekker, New York (1994), p. 253
14. Richard, R.M.: A Study of Structural System Having Nonlinear Elements. PhD thesis, Purdue University, Lafayette (1961)
15. Kirchner, P.: Synthese thermischer und mechanischer stabiler, gummielastischer Polymer-netzwerke sowie Untersuchung ihrer mechanischen Eigenschaften. Master thesis, Hochschule Würzburg-Schweinfurt, Würzburg (2014)
16. Treloar, L.R.G.: The photoelastic properties of short-chain molecular networks. *Trans. Faraday Soc.* **50**, 881–896 (1954)
17. Smith, K.J., Greene, A., Ciferri, A.: Crystallization under stress and non-Gaussian behavior of macromolecular networks. *Kolloid-Zeitschrift und Zeitschrift für Polymere* **194**, 49–67 (1964)

Chapter 36

Thermomechanical Analysis Strategies for Elastomer Components Under Dynamic Loading

R. Behnke and M. Kaliske

Abstract In the form of bearings, seals, conveyors, V-belts and pneumatic tires, elastomers are commonly used to transmit or handle time-dependent (dynamic) loadings. Dissipative effects in cyclically loaded elastomer components lead to a steady loss of mechanical input energy. The transformation of mechanical energy to thermal energy results in an increase of the temperature of the elastomer component. In this contribution, finite element (FE) solution schemes for the computation of the displacement and temperature field are discussed. First, a simultaneous solution scheme is used to analyse a cyclically loaded elastomer specimen (strong coupling of the displacement and temperature field). Second, a sequentially coupled solution scheme (weak coupling of the displacement and temperature field) is presented for the modelling of steady state dynamic systems. Subsequently, the sequential analysis is used to predict the thermo-mechanical behaviour of steady state rolling tires.

36.1 Introduction and Overview

Elastomers are used in many industrial applications due to their distinct properties, which are large deformations upon rupture (hyperelasticity), damping of mechanical excitations (inelasticity) and outstanding frictional behaviour on various surface types to name only few of them. Typical elastomer products, consisting fully or partially of one or several elastomer compounds in combination with reinforcing elements, are depicted in Fig. 36.1. In the form of bearings, seals, conveyors, V-belts and pneumatic tires, elastomers are commonly used to transmit or handle time-dependent (dynamic) loadings. While for short-time loading (e.g. shock and impact loading) energy absorption is desired to counterbalance the mechanical overload, dissipative effects in cyclically loaded elastomer components lead to a steady loss of mechanical input energy. The transformation of mechanical energy to

R. Behnke (✉) · M. Kaliske

Institute for Statics and Dynamics of Structures, Faculty of Civil Engineering,
Dresden University of Technology, Dresden, Germany

© Springer International Publishing AG 2017

W. Grellmann and B. Langer (eds.), *Deformation and Fracture Behaviour of Polymer Materials*, Springer Series in Materials Science 247,
DOI 10.1007/978-3-319-41879-7_36

507

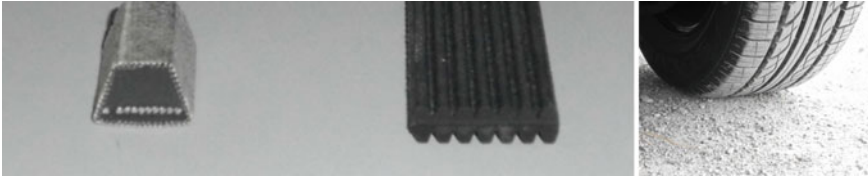


Fig. 36.1 Dynamically loaded elastomer components: V-belt, fan belt, tire

thermal energy results in an increase of the temperature of the elastomer component. This phenomenon can become even critical in case of cyclic loading conditions applied to compact components (size effect) causing a monotonic rise of its core temperature. In consequence, heat build-up in the component can (A) affect the mechanical response by changing the material properties at higher temperature, (B) lead to accelerated chemical reactions (e.g. ozone or oxygen) or other irreversible material alteration (growth of gas bubbles or other defects) which is undesired and (C) even trigger ultimate failure of the component by accumulated thermal degradation [1]. In addition, the temperature increase affects negatively the crack growth resistance of the material since for non-crystallising elastomers, a drop of the fracture resistance is observed in general [2].

On the one hand, the combined study of the mechanical field (displacement) and the thermal field (temperature) of the elastomer component and their interaction is promising in order to improve its durability characteristics. On the other hand, the thermomechanically coupled numerical analysis of dynamically loaded elastomer components requires appropriate solution strategies and is theoretically as well as computationally challenging. First, besides the mechanical balance of momentum, the energy balance and its evolution has to be captured by the simulation approach. Second, thermal boundary conditions have to be qualitatively and quantitatively taken into account in addition to the kinematic boundary conditions which are often easier to define. Third, adequate numerical solution schemes are required to solve the thermomechanical problem which is nonlinear in general.

In this contribution, finite element (FE) solution schemes for the computation of the displacement and temperature field are discussed. In Sect. 36.2, a simultaneous solution scheme is used to analyse a cyclically loaded elastomer specimen. The simultaneous solution scheme is characterised by the fact that the numerical time discretisation for the displacement and temperature field coincides. The update of the solution fields is simultaneously accomplished at the same points in time. Hence, a strong coupling of the displacement and temperature field can be studied. As simplest example, a rubber cube is subjected to cyclic loading and its temperature evolution is computed using different time discretisations (time steps). In Sect. 36.3, a sequentially coupled solution scheme is presented for the modelling of steady state dynamic systems. The sequential analysis is based on the weak coupling of the displacement and temperature field. Numerical solutions are obtained

with the help of a distinct time discretisation for the mechanical and the thermal response to steady state loading. The coupling of both fields is accomplished by common solution crosspoints in time. Subsequently, the sequential analysis is used to predict the thermomechanical behaviour of steady state rolling tires.

36.2 Simultaneous Solution Scheme

In this section, the simultaneous solution of a thermomechanically coupled problem is addressed. The same numerical time discretisation is used to obtain an update of the displacement and temperature field and strong coupling between each solution field is considered.

In (36.1), the fully coupled equation system of the thermomechanical problem is given. After linearisation of the weak form of the balance of linear momentum (first equation line) and the linearisation of the weak form of the balance of energy (second equation line), the fully coupled equation system

$$\begin{bmatrix} \mathbf{K}_{uu} & \mathbf{K}_{u\Theta} \\ \mathbf{K}_{\Theta u} & \mathbf{K}_{\Theta\Theta} \end{bmatrix} \begin{bmatrix} \Delta \mathbf{u} \\ \Delta \Theta \end{bmatrix} = \begin{bmatrix} \Delta \mathbf{f} \\ \Delta \mathbf{q} \end{bmatrix} \quad (36.1)$$

is obtained with tangent terms \mathbf{K}_{ij} representing dynamic (time-dependent) nodal stiffness matrices and the right hand side with entries $\Delta \mathbf{f}$ (residual nodal force vector) and $\Delta \mathbf{q}$ (residual nodal heat flux vector). At a given time t , the update of the solution quantities in form of $\Delta \mathbf{u}$ (increment in nodal displacement vector) and $\Delta \mathbf{q}$ (increment in nodal heat flux vector) is computed by solving (36.1) with respect to the solution increments $\Delta \mathbf{u}$ and $\Delta \mathbf{q}$. Since two different solution fields are considered, the off-diagonal terms $\mathbf{K}_{u\Theta}$ and $\mathbf{K}_{\Theta u}$ are not identical. Hence, the tangent matrix is unsymmetrical and numerical equation solvers for unsymmetrical matrices have to be used during the solution process. The latter fact induces an additional increase of computational cost besides the computational cost caused by considering four degrees of freedom per node (three nodal displacements and one nodal temperature) at each node of the complete FE mesh as illustrated in Fig. 36.2.

In the following, a numerical study on a viscoelastic elastomer cube with a side length of $l = 10$ mm is carried out. In Fig. 36.2, the undeformed configuration and the deformed configuration of the elastomer cube at maximum tensile stretch are depicted. In the numerical simulation, inertia effects are taken into account and the sides of the cube are perfectly insulated. In consequence, it is assumed that the dissipated energy contributes completely to the uniform temperature rise. For a loading frequency of $f = 1$ Hz, the uniform temperature change $\Delta \Theta$ of the elastomer cube and the reaction force in loading direction are computed. The excitation consists of a sinusoidal displacement-controlled uniaxial loading in tension–compression mode with a strain amplitude of $\hat{\varepsilon} = \pm 25\%$. The thermomechanical material properties of the elastomer material are represented by the material model proposed in [3].

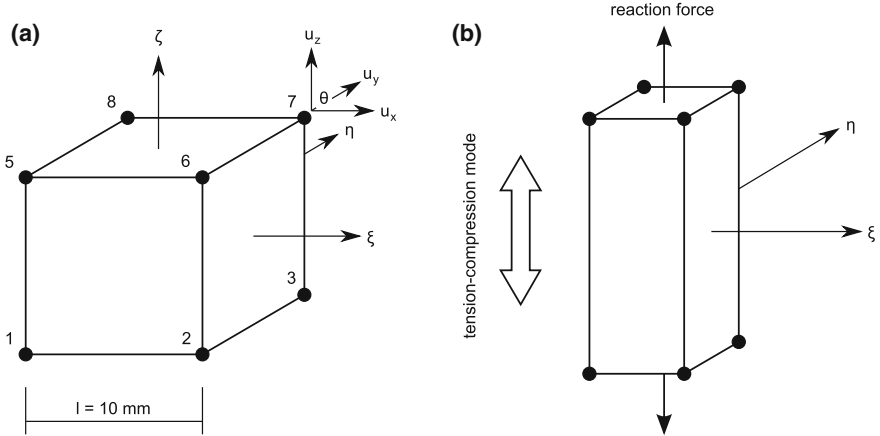


Fig. 36.2 Completely thermally insulated elastomer cube with a side length of $l = 10$ mm and model parameters $\rho = 1.12 \text{ g/cm}^3$, $\kappa_0 = 1000 \text{ MPa}$, $G_c = 0.1867 \text{ MPa}$, $\delta = 0.09693$, $G_e = 0.2169 \text{ MPa}$, $\beta = 0.20$, $G'_v = 1.45 \text{ MPa}$, $\gamma_0/\dot{\gamma}^m = 0.00145 \text{ s}^{-1} \text{ MPa}^{-m}$, $c = 957$, $m = 1.094$, $a = 1$, $b = 1$, $\Theta_0 = 298 \text{ K}$, $c_v = 1.68 \text{ N mm}^{-2} \text{ K}^{-1}$, $\alpha_0 = 0.0 \text{ K}^{-1}$ with creep rate expression $\gamma = \gamma_0 \lambda_e^c (\tau_v/\hat{\tau})^m$, see [3]: undeformed configuration (a); deformed configuration (cyclic uniaxial loading tension–compression) with strain amplitude $\hat{\epsilon} = \pm 25\%$ (b)

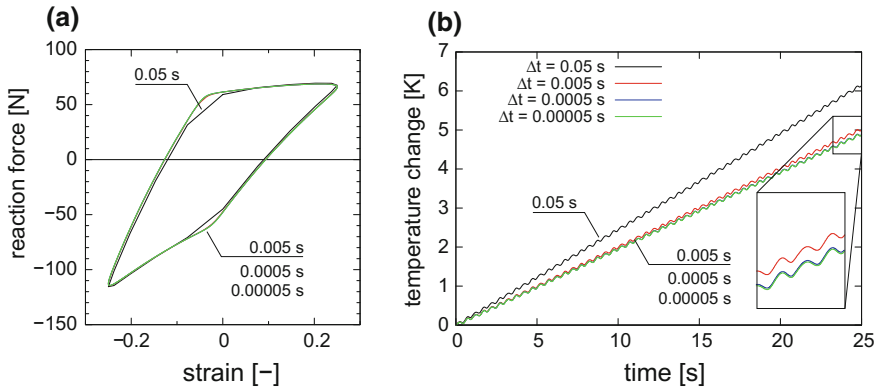


Fig. 36.3 Reaction force and temperature change as function of time t and time discretisation Δt : reaction force forming hysteresis loop for $24 \text{ s} \leq t \leq 25 \text{ s}$ (a); internal temperature change $\Delta\Theta$ (b)

The computed reaction force and the simulated temperature variation due to mechanical energy dissipation are depicted in Fig. 36.3 for a total simulation time of $t = 25 \text{ s}$. Hysteresis loops are observable in the force–strain response. With decreasing time step Δt , the shape of the hysteresis is more detailed and the computed total dissipated energy per cycle slightly changes but the overall envelop of the hystereses remains unaffected. The solution of the temperature variation is

Table 36.1 Computational aspects: required CPU time (machine-dependent) for a total simulation time of $t = 25$ s and relative solution error as function of time discretisation Δt of the thermomechanical problem with cycle duration $T = 1$ s

Time discretisation Δt (s)	Total CPU time (s)	Relative temperature solution error (%)
0.05 = $T/20$	44.44	26.00
0.005 = $T/200$	924.92	2.72
0.0005 = $T/2000$	6866.91	0.25
0.00005 = $T/20,000$	50,069.82	0 ^a

^aReference solution

more sensitive to the time step and converges for decreasing time steps Δt . For the present analysis, a backward Euler scheme (implicit Euler method) with linear interpolation between the points in time is used. To obtain a faster convergence of the temperature response for decreasing time steps Δt , special energy conserving time integration schemes can be employed.

By using larger time steps, the numerically computed dissipation is overestimated by the applied time integration method which leads to a steeper increase of the temperature change (heat build-up) depicted in Fig. 36.3. Due to the fact that the energy loss is computed based on a time-discretised solution quantity itself [4–6], the computed temperature field is sensitive to the time step even for standard, fully implicit and numerically stable solution schemes as employed in the present example. In Table 36.1, the total CPU time and the relative error of the final cube temperature variation in comparison to the converged solution are given. It can be concluded that a small time step Δt is required in general (A) to correctly compute the energy dissipation from the mechanical field (size and shape of the hysteresis) and (B) to accurately predict the core temperature of the component. However, the use of a small time step Δt will result in an increase of computational cost since for each time step, an update of the displacement and temperature field has to be computed.

36.3 Sequential Solution Scheme

In this section, the fully coupled equation system given in (36.1) is reduced to its decoupled form (36.2–36.4)

$$\begin{bmatrix} \mathbf{K}_{uu} & \mathbf{0} \\ \mathbf{0} & \mathbf{K}_{\Theta\Theta} \end{bmatrix} \begin{bmatrix} \Delta \mathbf{u} \\ \Delta \Theta \end{bmatrix} = \begin{bmatrix} \Delta \mathbf{f} \\ \Delta \mathbf{q} \end{bmatrix} \quad (36.2)$$

with zero off-diagonal terms. Hence, each equation line will be treated as separate subproblem, i.e. a purely mechanical problem

$$[\mathbf{K}_{uu}]_{\Theta=\text{const}} [\Delta \mathbf{u}] = [\Delta \mathbf{f}]_{\Theta=\text{const}} \tag{36.3}$$

at fixed current temperature Θ and a purely thermal problem

$$[\mathbf{K}_{\Theta\Theta}]_{\mathbf{u}=\text{const}} [\Delta \Theta] = [\Delta \mathbf{q}]_{\mathbf{u}=\text{const}} \tag{36.4}$$

at constant deformation \mathbf{u} . Note that the subproblems are still linked to each other by their dependencies $\mathbf{K}_{uu}(\Theta)$ and $\Delta \mathbf{f}(\Theta)$ as well as $\mathbf{K}_{\Theta\Theta}(\mathbf{u})$ and $\Delta \mathbf{q}(\mathbf{u})$. However, in the case of a weak coupling, the thermo-elastic coupling (oscillating temperature variation around mean temperature for cyclic loading) is neglected and only the mean temperature rise is considered by (A) solving (36.3) at constant temperature Θ for an entire cycle duration using time steps Δt_u , (B) deriving the energy dissipation rate, (C) using the computed dissipation rate as heat source term in (36.4) and solving (36.4) for a time step $\Delta t_{\Theta} > \Delta t_u$. In consequence, it is assumed that the time scale of the mechanical subproblem is much smaller than the time scale of the thermal subproblem.

As structural example of a sequential analysis, a steady state rolling tire on a drum test rig is numerically analysed and simulation results for rolling resistance and temperature evolution are compared to experimental measurements. Several approaches for the thermomechanical analysis of rolling tires have been developed during the last decades, see e.g. [7–9]. In this contribution, the thermomechanical analysis scheme illustrated in Fig. 36.4 is characterised by an Arbitrary Lagrangian

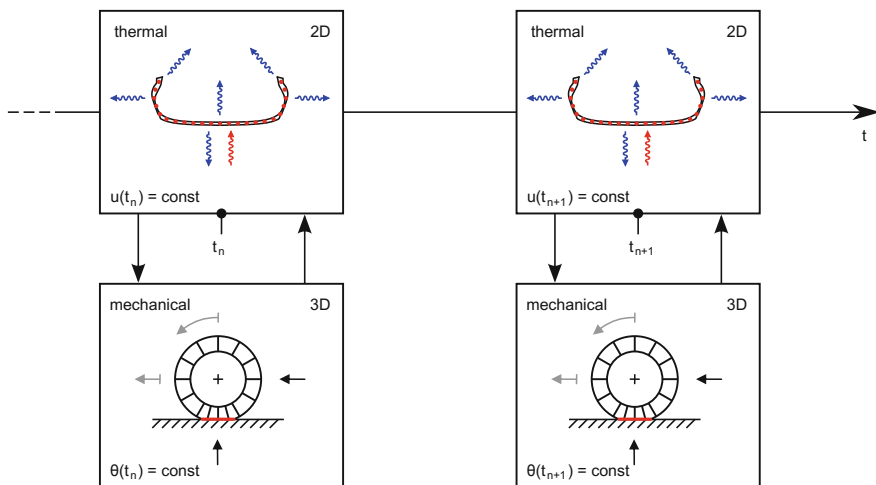


Fig. 36.4 Representation of the computation scheme for the thermomechanically sequential analysis: Mechanical and thermal module and interactions

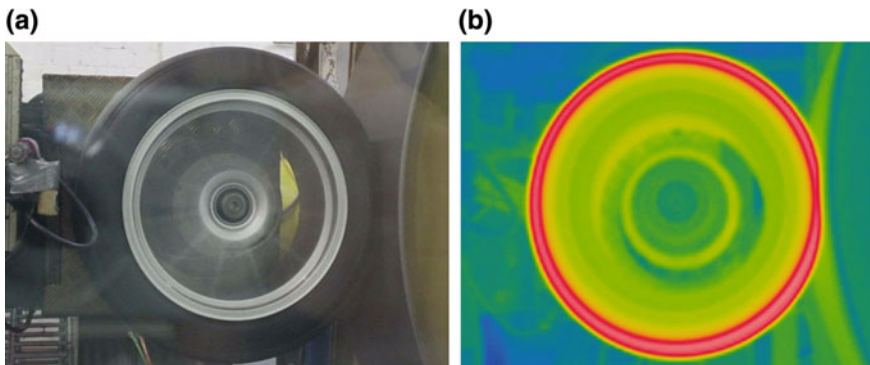


Fig. 36.5 Tire on drum test rig to reveal rolling resistance and surface temperature evolution during rolling: photo of the rolling tire on the drum (a); infrared image of the tire's side profile (b)

Eulerian (ALE) formulation which takes into account the inelastic properties of the elastomer compounds during steady state rolling. In addition, heat generation due to friction in the tire-drum interface is incorporated.

Experimental measurements with respect to rolling resistance (force method) and surface temperature evolution (infrared measurement) are available for comparison as exemplarily depicted in Fig. 36.5. The tire is placed on a drum test rig of diameter $d = 1.707$ m. Via infrared measurement of the tire's side profile, the temperature evolution of the surface temperature has been recorded during the test. The tire is subjected to a constant vertical load of 5260 N and a constant rotational velocity corresponding to a translational velocity of $v = 80$ km/h. The inner pressure $p = 2.45$ bar of the tire has been measured at the beginning of the test.

The simulation approach consists of a mechanical module and a thermal module. In the mechanical module, the deformation of the rotating, viscoelastic tire is computed at constant temperature using an ALE-framework. From an internal time measure and the history of a material point travelling on a streamline (one loading cycle), an average dissipation rate is computed per cross-sectional point of the tire. In the thermal module, the average dissipation rates are used as heat source terms to compute a new temperature profile for the cross-section in its reference (undeformed) configuration where the temperature in circumferential direction of the tire is assumed to be constant (instantaneous thermo-elastic and thermo-viscoelastic coupling are neglected). With the new temperature profile of the tire cross-section, the mechanical response is updated to give finally an updated dissipation rate. For more details, the reader is referred to [10].

An axisymmetric 3D FE model of the tire has been obtained by revolving the cross-sectional FE mesh of the tire around its rotation axis. In the potential contact zone with the rigid drum (rigid surface), the FE mesh in circumferential direction is

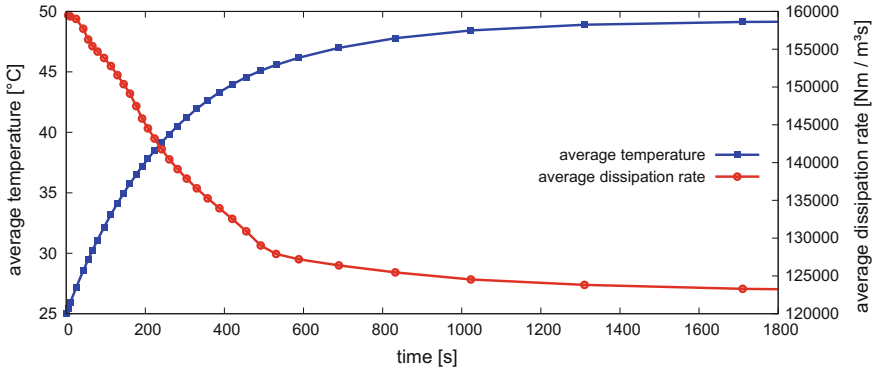


Fig. 36.6 Crosspoints of mechanical and thermal analyses, controlled by a sensitivity measure based on the average dissipation rate and the average cross-sectional temperature

refined. The ground state elastic response of the elastomer compounds (hyperelasticity at finite deformation) has been identified based on multistage tests in tension, compression and planar tension mode at different temperatures. The time-dependent material properties of the elastomer compounds have been identified based on dynamic-mechanical analysis (DMA) to reveal their viscoelastic response over a wide frequency and temperature range.

In Fig. 36.6, the adaptive time discretisation of the sequentially coupled thermal subproblem is highlighted by depicting the evolution of the average dissipation rate and the average cross-sectional temperature of the tire. The crosspoints of mechanical and thermal analysis are marked by points. From the sensitivity of the thermomechanical problem with respect to the average dissipation rate and the average cross-sectional temperature, a sensitivity measure is derived to compute the adaptive time step ΔT_{Θ} of the thermal subproblem.

In Fig. 36.7, the simulated cross-sectional temperature variation is depicted for different points in time. The measured surface temperature of the tire has been compared to the simulation outcome and shows good agreement. For more details, it is referred to [10]. As already mentioned, the thermal boundary conditions are hard to determine experimentally in situ and, in consequence, are hard to correctly capture within the numerical model. In the present study, thermal boundary conditions depending on the rotational speed (enforced heat convection due to the rotation of the tire) are assumed.

In Table 36.2, the results for the load radius of the deformed tire and the converged value of the rolling resistance (heated tire) are compared to their simulated counterparts.

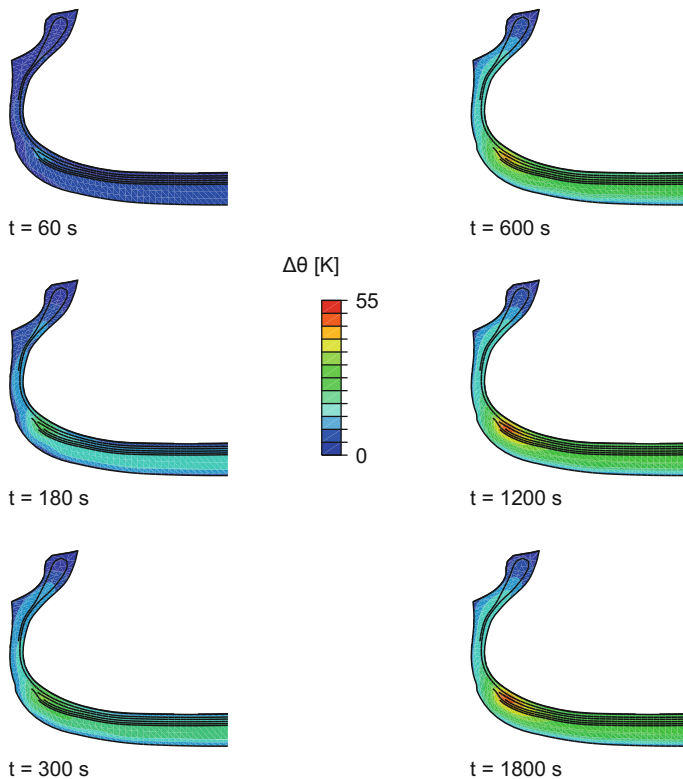


Fig. 36.7 Numerically simulated evolution of temperature change in the tire cross-section for tire rolling on drum test rig (corresponding translational velocity $v = 80$ km/h)

Table 36.2 Comparison of experimental and numerical simulation results for tire on drum test rig (corresponding translational velocity $v = 80$ km/h)

	Load radius (m)	Rolling resistance (N)
Measurement	0.2968	48.46
Simulation	0.2956	47.79
Relative error (%)	0.40	1.40

36.4 Conclusion and Outlook

The examples of the previous sections highlight that the thermomechanically coupled numerical analysis of dynamically loaded elastomer components requires appropriate solution strategies. Although the simultaneous solution of the fully coupled problem is rigorous and offers the most detailed response of the system under investigation, it is numerically too time consuming for most of the engineering applications and demands for a large computational effort (unsymmetrical

tangent matrix, increase of the nodal degrees of freedom of each node in the FE mesh). With the help of distinct time discretisations (different time scales for each solution field) combined with a sequentially coupled analysis of a purely mechanical and a purely thermal subproblem, the numerical investigation of large scale FE models is enabled.

Nevertheless, the engineer's expertise is required in all the cases to first set up the correct model, e.g. with respect to the model boundaries and the thermal boundary conditions, and solve it in an adequate and still efficient way.

Acknowledgements This contribution has been presented at the conference PolyMerTec 2014 (25th to 27th of June 2014, Merseburg). We thank the organisers and editors Prof. Wolfgang Grellmann from Martin Luther University Halle-Wittenberg (Germany) and Prof. Beate Langer from University of Applied Science Merseburg (Germany) for the possibility to contribute to the present book on deformation and fracture behaviour of polymer materials. Parts of the research outlined in this contribution have been financially supported by the Deutsche Forschungsgemeinschaft (DFG) under grant KA 1163/16. The authors gratefully acknowledge the support by Hankook Tire Co.

References

1. Behnke, R., Kaliske, M.: Thermo-mechanical finite element analysis of steady state rolling off-the-road tires with respect to thermal damage. In: Proceedings of the International Rubber Conference 2014 (IRC2014; Beijing, 16.–18.09.2014). Beijing (2014), pp. 1455–1460
2. Gent, A. (ed.): Engineering with Rubber: How to Design Rubber Components. Carl Hanser, Munich (1992)
3. Behnke, R., Dal, H., Kaliske, M.: An extended tube model for thermo-viscoelasticity of rubberlike materials: Theory and numerical implementation. In: Jerrams, S., Murphy, N. (eds.) Constitutive Models for Rubber, Vol. VII. CRC Press, Taylor & Francis Group, London (2011), pp. 87–92
4. Armero, F., Simo, J.: A new unconditionally stable fractional step method for non-linear coupled thermomechanical problems. *Int. J. Numer. Meth. Eng.* **35**, 737–766 (1992)
5. Groß, M., Betsch, P.: Stable long-term simulation of dynamically loaded elastomers. *Proc. Appl. Math. Mech.* **8**, 10501–10502 (2008)
6. Romero, I.: Thermodynamically consistent time-stepping algorithms for non-linear thermo-mechanical systems. *Int. J. Numer. Meth. Eng.* **79**, 706–732 (2009)
7. Ebbott, T., Hohman, R., Jeusette, J.-P., Kerchman, V.: Tire temperature and rolling resistance prediction with finite element analysis. *Tire Sci. Technol.* **27**, 2–21 (1999)
8. Suwannachit, A., Nackenhorst, U.: A novel approach for thermomechanical analysis of stationary rolling tires within an ALE-kinematic framework. *Tire Sci. Technol.* **41**, 174–195 (2013)
9. Wang, Y., Wei, Y., Feng, X., Yao, Z.: Finite element analysis of the thermal characteristics and parametric study of steady rolling tires. *Tire Sci. Technol.* **40**, 201–218 (2012)
10. Behnke, R., Kaliske, M.: Thermo-mechanically coupled investigation of steady state rolling tires by numerical simulation and experiment. *Int. J. Non-Linear Mech.* **68**, 101–131 (2015)

Chapter 37

Influence of Selected Silica Fillers on the Properties of Vulcanised Rubber Blends

W.M. Rzymiski, A. Smejda-Krzewicka, J. Rogoża
and A. Ochenduszko

Abstract It has been found that the use of selected precipitated silica fillers (80 phr; BET surface 130–235 m²/g) in SBR–BR blends (3:1 by weight) containing coupling agent (CA in the amount of 6.4 phr) and thermomechanical treatment (TMT) at selected temperature (up to 160 °C) of the rubber–silica filler–CA premixes leads to cured compounds showing increased ice and wet grip (IG, WG), and acceptable rolling (RR) and abrasion resistance (AR) as well. Better results (IG, WG, AR) were obtained using in chain with ester groups–functionalised styrene–butadiene rubber (CF-SBR) instead of standard SBR. The best results were found using silica filler having BET surface of 130–160 m²/g.

37.1 Introduction

Since 1980, the year in which the “Green Tyre Concept and Technology” [1] was introduced on an industrial scale, the use of silica fillers, in particular precipitated nano-silica, has increased significantly in the tyre industry. The use of these fillers as a key component of the rubber in the tyre tread—connected with the use of an adequate amount of a coupling agent of sufficient quality and a much lower amount of activated carbon black—offered the opportunity to produce tyres with reduced rolling resistance and acceptable ice and wet traction. This also made it possible to lower the fuel consumption of passenger cars and heavy goods vehicles considerably [2–4]. In addition to an appropriate amount and quality of these fillers, it is necessary to use an elastomer matrix with an appropriate property profile, which in passenger car tyres is usually a mix of styrene–butadiene rubber (SBR) and butadiene rubber (BR) [5, 6].

With the aim of achieving strong interaction between the elastomer mix and the silanol group on the surface of silica filler particles and, in doing so, between rubber

W.M. Rzymiski (✉) · A. Smejda-Krzewicka
Institute of Polymer and Dye Technology, Łódź University of Technology, Łódź, Poland

J. Rogoża · A. Ochenduszko
Synthos S.A., Oświęcim, Poland

qualities and the desired property profiles of tyres, the use of emulsion and solution SBR, which were functionalised on the chain ends or within the chain with select side groups [5–10], or the use of SBR with different chain microstructures [11] has been attracting great attention in the past few years. However, the starting point of current approaches is that there are no authoritative results of comparative investigations into the effect of silica fillers with a different specific surface (with or without the use of a coupling agent and with or without thermomechanical treatment of the rubber/filler/coupling agent premixes) on the property profile. The publications in this area often present contradictory results. These refer to, among others, the amount and kind of the coupling agents to be used in connection with the quality and amount of the filler mixed in and the conditions of the thermomechanical treatment of premixes composed of rubber, filler and coupling agent [10, 12–18].

Using precipitated silica as filler with various BET surfaces (130, 160, 175 and 235 m²/g; primary particle size <25 nm; BET = Brunauer-Emmett-Teller), the aim of our investigations was to determine the effect of the selected coupling agent (CA) and the thermomechanical treatment (TMT) of rubber, filler and coupling agent premixes on the properties of vulcanisates composed of SBR/BR mixes (that is, viscosity, vulcanisation process, tensile strength, elongation at break and abrasion resistance), which are essential during the production of tyres. Another focus of the investigations was the analysis of the mechanical dissipation factor $\tan \delta$ at temperatures of -10 and +60 °C; $\tan \delta$ is the measure for the ice and wet traction (the higher the better) and the rolling resistance (the smaller the better). Furthermore, the influence of the functionalisation of the SBR chains with ester side groups on the abovementioned properties was examined.

37.2 Materials and Methods

The rubber mixes were composed of standard styrene–butadiene rubber (Kralex 1500 by the company Synthos S.A., in the following referred to as SBR), a test product functionalised with ester side groups by the company Synthos S.A. (styrene–butadiene–butyl acrylate emulsion mix polymer, in the following referred to as FSBR; with mass ratios of the monomer blended in the product of ca. 60:20:20) and a cis-butadiene rubber (Synteca 44 of the company Synthos S.A., in the following referred to as BR). Ultrasil VN2 GR, Zeosil 1165 MP, Ultrasil 7000 GR and Ultrasil 9000 GR with a BET surface of 130, 160, 175 or 235 m²/g (in the following referred to as S130, S160, S175 and S235; primary particle size <28 nm) were used as silica fillers. Bis-triethoxysilylpropyl tetrasulfide (C₂H₅O)₃Si(CH₂)₃S₄(CH₂)₃Si(OC₂H₅)₃, a product of the company Evonic Industries AG, traded under the name Si 69, was chosen as the coupling agent (CA). Other components of the mixes (antioxidant, vulcanisation accelerator and activator, sulphur, carbon black N234, plasticiser oil Quantilus 50 TDAE) were standard materials used in the rubber industry. The premixes and mixes were produced in a laboratory roller mill with chilled rollers within an appropriate time. In the roller mill, the coupling agent (CA) was added to

the premixes composed of rubber, antioxidants, fillers and plasticisers, but not including accelerator and sulphur. Subsequently, these premixes were treated subjected to thermomechanical treatment (TMT) in the Plasti-Corder laboratory kneader at a temperature of 138–145 °C for 4–5 min. After cooling, the accelerator and sulphur were added in the roller mill.

The curemetric testing of the premixes was done by using the curemeter WG-02 according to ISO 3417 (1994). The test specimens needed for further investigations were produced by vulcanisation of discs in a closed mould under pressure at a temperature of 433 K within a specific cure time. Typical mechanical properties were determined under the conditions described in the corresponding ISO standards. The values of dissipation angle δ (and thus those of the mechanical dissipation factor $\tan \delta$) were determined under dynamic shear stress of test specimens measuring 2 mm in thickness at temperatures of -10 and $+60$ °C. The measurements were done using the DMTA apparatus (DMTA—dynamic-mechanical-thermal analysis; Metravib DMA + 450 DMA Analyser) at a relative strain amplitude and frequency of 3% and 10 Hz as well as a temperature increase of 2.5 K/min.

37.3 Results and Discussion

At first we investigated how the addition of the coupling agent (CA) only and afterwards the thermomechanical treatment (TMT) of the premixes composed of rubber, filler and plasticiser with the coupling agent influenced the properties of the mixes and the vulcanisates (Table 37.1). The analysis of the determined values indicates that the increase in the liquid coupling agent (Si 69) without the thermomechanical treatment of the premixes leads to a slight reduction of the time of vulcanisation, a significant decrease in viscosity and thus improved plasticity of the mixes as well as a considerable increase in the attainable degree of crosslinking, the stiffness, tensile strength and abrasion resistance of the linked system, but not to a significant improvement of the ice and wet traction and the rolling resistance of the vulcanisates (see data for SBR-S130, SBR-S130-CA and Fig. 37.1).

The thermomechanical treatment of the premix with the coupling agent (see SBR-S130-CA-TMT) leads to a further, unwanted reduction of the time of vulcanisation, a desired increase in stiffness and tensile strength, which is connected, however, with an unwanted deterioration in ice and wet traction, and a considerable positive effect on the rolling resistance of the vulcanisates (see Fig. 37.1). This means that the tetrasulfide groups of the coupling agent contribute to the formation of the network and the development of chemical bonds between the silica particle surface and the rubber, as was expected according to [2, 4, 11, 13–16]. In conclusion it can be stated that through the use of the coupling agent and the thermomechanical treatment of the premix on the basis of standard SBR, some of the desired results could be achieved.

Next we analysed whether or not the replacement of standard SBR with rubber functionalised with ester side groups (FSBR)—with the same amount and kinds of

Table 37.1 Properties of mixes and vulcanisates of standard SBR/BR blends; silica filler with a BET surface of 130 m²/g

Property	Sample		
	SBR-S130	SBR-S130-CA	SBR-S130-K-CA-TMT
L_{\min} (dNm)	24.2	12.2	14.3
t_{02} (min)	3.8	3.2	2.8
t_{vul} (min) at 433 K	15	15	15
S_{300} (MPa)	4.3 (± 0.2)	12.8 (± 0.5)	16.9 (± 0.5)
TS_b (MPa)	14.6 (± 0.3)	18.8 (± 2.0)	19.7 (± 2.8)
E_b (%)	660 (± 21)	402 (± 26)	340 (± 43)
ARI (%)	60.2	119.7	125.9
Q_v (ml/ml)	2.93	2.11	2.12
$\tan \delta$ at -10 °C (ice grip)	0.534	0.560	0.483
$\tan \delta$ at 0 °C (wet grip)	0.462	0.503	0.372
$\tan \delta$ at 60 °C (rolling resistance)	0.225	0.246	0.152

Compound recipe (in phr): SBR: 75; BR: 25; stearin: 2.0; ZnO: 3.0; antioxidant 6PPD: 2.0; accelerators (TBBS + DGP): 3.7; sulphur: 1.5; S130: 80; carbon black N234: 10; poly(ethylene glycol) PEG 4000S: 2.6; oil Quantilus 50 TDAE: 37.5; Si69: 6.4

Explanation of the symbols: SBR-S130—without coupling agent; SBR-S130-CA—with coupling agent, but without thermomechanical treatment; SBR-S130-CA-TMT—all ingredients and thermomechanical treatment of the preblend; L_{\min} —minimum vulcanometric torque, t_{02} —scorch time, t_{vul} —vulcanisation time, S_{300} —stress at 300% elongation, TS_b —tensile strength, E_b —elongation at break, ARI —abrasion resistance index, Q_v —equilibrium swelling in toluene

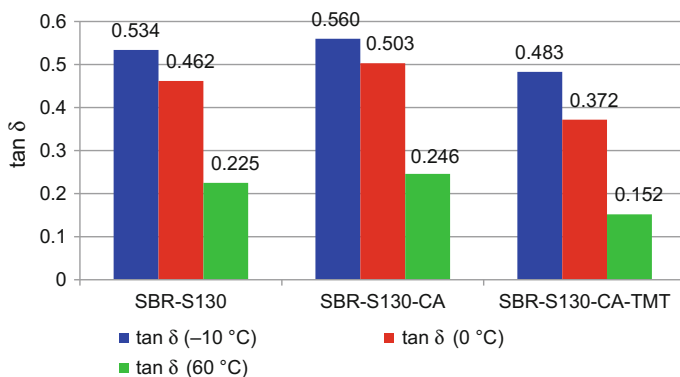


Fig. 37.1 Mechanical loss factor $\tan \delta$ at -10 and 0 °C as measure of the ice or wet grip (greater is better) and $\tan \delta$ at 60 °C as measure of the rolling resistance (lower is better) of the cured blends containing standard SBR; silica filler with BET surface of 130 m²/g; SBR-S130: only filler; SBR-S130-CA: with coupling agent, but without thermomechanical treatment; SBR-S130-CA-TMT: with coupling agent and thermomechanical treatment; compare Table 37.1

the other components of the mix—leads to a desired result (Table 37.2). Compared to the mix with SBR, we found that the mix containing FSBR showed the same viscosity but had a longer time of vulcanisation. Independent of the kind of rubber used (SBR or FSBR), the vulcanisates of both mixes show the same degree of crosslinking and the same values for elongation at break, stiffness, tensile strength and abrasion resistance.

An advantage of FSBR is that its use led to products that have improved ice and wet traction but a slightly higher rolling resistance (Fig. 37.2). This behaviour can be attributed to additional, strong interactions between the polar ester side groups of the FSBR and the polar $\equiv\text{Si}-\text{OH}$ groups on the surface of the silica filler. This indicates that the use of rubber functionalised with ester side groups is advantageous in relation to the desired properties of tyre treads.

Because of the abovementioned results, we decided to investigate the influence of silica fillers with various BET surfaces (130, 160, 175 and 235 m^2/g)—and the different strengthening effect to be thus expected—on the properties of the produced mixes and vulcanisates (Table 37.3). The mixes, which were produced under the same conditions, show, independent of the kind of added silica filler, the same viscosity but a slightly different time of vulcanisation, in particular in case of the fillers with BET surfaces of 160 and 175 m^2/g , and a reduced vulcanisation speed. The vulcanisates of the mixes with the corresponding fillers also show a reduced degree of crosslinking as well as reduced stiffness and abrasion resistance but higher elongation at break. This behaviour can most likely be explained by a specific higher adsorption of the components of the network system on the surface of these fillers, which is connected with a lower degree of crosslinking. According

Table 37.2 Comparison of the properties of mixes and vulcanisates containing standard SBR or rubber functionalised with ester side groups (FSBR); silica filler with a BET surface of 130 m^2/g

Property	Sample	
	FSBR-S130-CA-TMT	SBR-S130-CA-TMT
L_{\min} (dNm)	15.8	14.3
t_{02} (min)	3.7	2.8
t_{vul} (min) at 433 K	15	15
S_{300} (MPa)	16.1 (± 0.9)	16.9 (± 0.5)
TS_{b} (MPa)	19.9 (± 0.9)	19.7 (± 2.8)
E_{b} (%)	360 (± 17)	340 (± 43)
ARI (%)	117.2	125.9
Q_{v} (ml/ml)	2.12	2.11
$\tan \delta$ at -10 °C (ice grip)	0.525	0.483
$\tan \delta$ at 0 °C (wet grip)	0.427	0.372
$\tan \delta$ at 60 °C (rolling resistance)	0.194	0.152

Explanation of the symbols: FSBR-S130-CA-TMT—mix an cured blend containing the by ester groups in-chains functionalised rubber, all ingredients, thermomechanical treatment; SBR-S130-CA-TMT—mix an cured blend containing standard SBR, all ingredients, thermomechanical treatment; for recipe and other symbols see Table 37.1

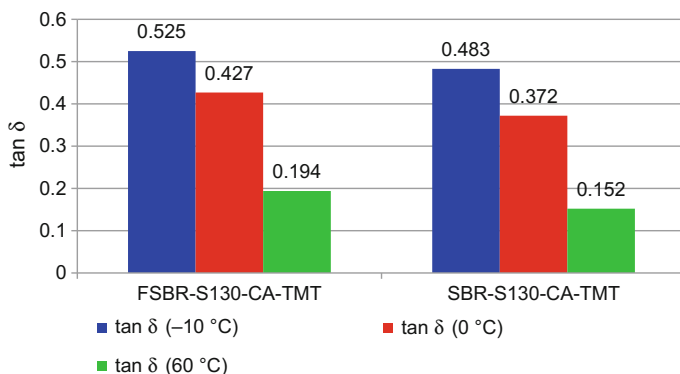


Fig. 37.2 Mechanical loss factor $\tan \delta$ at -10 and 0 °C as measure of the ice or wet grip (greater is better) and $\tan \delta$ at 60 °C as measure of the rolling resistance (lower is better) of the cured blends containing in-chains functionalised (FSBR) or standard rubber (SBR); silica filler with BET surface of $130 \text{ m}^2/\text{g}$; coupling agent and thermomechanical treatment of the preblends; compare Table 37.2

Table 37.3 Effect of various BET surfaces of silica fillers on the properties of mixes composed of BR and FSBR functionalised with ester side groups as well as corresponding vulcanisates; mixes and vulcanisates with coupling agent; premixes with thermomechanical treatment

Property	Sample			
	FSBR-S130	FSBR-S160	FSBR-S175	FSBR-S235
L_{\min} (dNm)	15.8	13.5	13.0	18.1
t_{02} (min)	3.7	2.6	3.4	3.9
t_{vul} (min) at 433 K	15	30	30	15
S_{300} (MPa)	16.1 (± 0.9)	3.9 (± 0.4)	6.2 (± 0.9)	11.0 (± 0.5)
TS_b (MPa)	19.9 (± 0.9)	18.2 (± 1.8)	15.5 (± 2.8)	17.1 (± 2.8)
E_b (%)	360 (± 17)	795 (± 43)	562 (± 43)	423 (± 43)
ARI (%)	117.2	106.2	73.7	97.0
Q_v (ml/ml)	2.33	3.13	3.17	2.61
$\tan \delta$ at -10 °C (ice grip)	0.525	0.505	0.547	0.513
$\tan \delta$ at 0 °C (wet grip)	0.427	0.468	0.485	0.422
$\tan \delta$ at 60 °C (rolling resistance)	0.194	0.231	0.240	0.215

Explanation of the symbols: FSBR-S130; FSBR-S160; FSBR-S175; FSBR-S235—compound and cured compound containing rubber functionalised in-chains with ester groups rubber and silica filler with different BET surface of 130, 160, 175 und 235 m^2/g ; compounds with coupling agent and thermomechanical treatment; for recipe and other symbols see Table 37.1

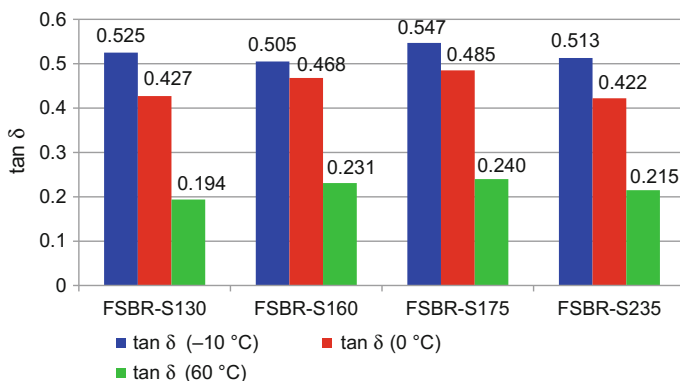


Fig. 37.3 Influence of the silica BET surface (130, 160, 175 or 235 m^2/g) on the mechanical loss factor $\tan \delta$ as the measure of ice (at $-10\text{ }^{\circ}\text{C}$) and wet grip (at $0\text{ }^{\circ}\text{C}$) as well as rolling resistance (at $60\text{ }^{\circ}\text{C}$) for the cured blends containing in-chains functionalised rubber (FSBR); blends with coupling agent and thermomechanical treatment

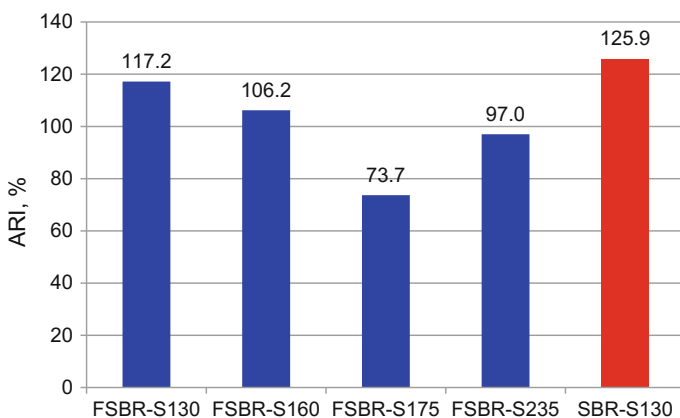


Fig. 37.4 Abrasion resistance index *ARI* (greater is better) of the cured compounds containing in-chains functionalised (FSBR) or standard (SBR) rubber; blends with coupling agent and thermomechanical treatment; silica filler with BET surface of 130, 160, 175 or 235 m^2/g ; compare Tables 37.1, 37.2 and 37.3

to [19], another explanation could be a change in the chemical structure of the bonds caused by the effect of the coupling agent–silica systems.

We found that the increased BET surface of the silica fillers investigated does not have any significant influence on the ice and wet traction and the rolling resistance of the vulcanisates (Fig. 37.3). Therefore, it is not advisable to use silica fillers with very high BET surfaces ($>160\text{ m}^2/\text{g}$) in the mixes for tyre treads (compare Fig. 37.4).

37.4 Conclusion

The results of our investigations presented in this paper clearly show that it is advisable to replace the standard SBR with butadiene–styrene rubber (FSBR) functionalised with ester side groups. The use of this rubber (FSBR) in the mixes contacting silica fillers, in connection with the coupling agent and a thermomechanical treatment of the premixes, results in vulcanisates with improved ice and wet traction as well as acceptable abrasion resistance and rolling resistance. With the conditions chosen for the production of the rubber mixes, it is not advisable to use silica fillers with a very large BET surface, that is, a BET surface of $>160 \text{ m}^2/\text{g}$.

Acknowledgements The investigations presented in this paper were done in cooperation with the Institute of Polymer and Dye Technology of Lodz University of Technology and the company SYNTHOS S.A., with special thanks to SYNTHOS S.A. for their financial support.

References

1. Flanigan, C.M., Bezer, L., Klekamp, D., Rohweder, D.: Comparative study of silica, carbon black and novel fillers in tread compounds. *Rubber World* **243**, 15–30 (2012)
2. Jacobson, M., Cameron, P., Neilsen, J., Nikiel, L., Wampler, W.: Improving hysteresis through filler modifications and smart compounding. *Rubber World* **244**, 22–26 (2013)
3. Gersler, M., Faguori, C., Peregi, E.: Novel coupling agents for silica-filled rubbers with superior processing safety and improved hysteresis of the vulcanizates. *Tire Sci. Technol.* **38**, 80–98 (2010)
4. Chakraborty, S., Shah, D.: Precipitated silica in tires. *Rubber World* **244**, 37–41 (2013)
5. Kloppenburg, H., Gross, T., Hardy, D., Kheirandish, S., Lucassen, A., Runzi, T., Zhang, Y.: Standard and modified NdBR for high-performance tires. *Rubber World* **244**, 24–27 (2013)
6. Douglas, J.E., Crossley, S., Hallett, J., Curtis, J., Hardy, D., Gross, T., Steinhauser, N., Lucassen, A., Kloppenburg, H.: The use of a surface-modified carbon black with an in-chain functionalized SSBR as an alternative to higher cost green tire technology. In: Proceedings of the 180th Technical Meeting of the ACS Rubber Division (Cleveland, 11.–13.10.2011). American Chemical Society (ACS), Cleveland (2011), Vol. 1, pp. 634–675
7. Steinhauser, N., Lucassen, A.: New functionalised S-SBRs to meet future tire performance demands. In: Belgian Plastics and Rubber Institute (BPRI) Conference (Brussels, 25.11.2009). Brussels (2009)
8. Hardy, D., Steinhauser N., Gross, T.: Compounding Functionalized Carbon Black with Along-The-Chain Functionalized SSBR. *Tire Technol. Int.*, 96–98 (2011)
9. Thiele, S., Knoll, S.: SSBR chain and structure determination and cured silica formulation properties. In: 180th Technical Meeting of the ACS Rubber Division, Cleveland, 11–13 Oct 2011. American Chemical Society (ACS), Cleveland (2011)
10. Martin, J.J., Okel, T.A.: Functionalized silicas for improved natural rubber truck tire vulcanisates. *Rubber World* **244**, 19–24 (2013)
11. Agrawal, S.L., Parmar, B.S.: SBR structure properties with reference to rolling resistance, wet grip, and mileage. *Tire Technol. Int.*, 54–60 (2011)
12. Reuvekamp, L.A.E.M., ten Brinke, J.W., van Swaaij, P.J., Noordermeer, J.W.M.: Effect of the time and temperature on the reaction of TESPT silane coupling agent during mixing with silica filler and tire rubber. *Rubber Chem. Technol.* **75**, 187–198 (2002)

13. Morris, M.D.: Fillers for reduced thread hysteresis. In: 176th Technical Meeting of the ACS Rubber Division (Pittsburgh, 13.–15.10.2009). Pittsburgh (2009)
14. Miyatake, K., Ohama, O., Kawahara, Y., Urano, A., Kimura, A.: Study on analysis method for reaction of silane coupling agent on inorganic materials. *SEI Tech. Rev.* **65**, 21–24 (2007)
15. Ren, H., Qu, Y., Zhao, S.: Reinforcement of styrene–butadiene rubber with silica modified by silane coupling agents: Experimental and theoretical chemistry study. *Chin. J. Chem. Eng.* **14**, 93–98 (2006)
16. Blume, A., El-Roz, M., Thibault-Starzyk, F.: Infrared studies of the silica–silane reaction. *KGK—Kautsch. Gummi Kunstst.* **66**, 63–70 (2013)
17. Okel, T.A.: Improvements in tire productivity and performance with performance silicas. *Rubber World* **242**, 30–40 (2011)
18. Wang, L., Zhao, S.: Study on the structure-mechanical properties relationship and antistatic characteristics of SSBR composites filled with SiO₂/CB. *J. Appl. Polym. Sci.* **118**, 338–345 (2010)
19. Choi, S.-S., Choi, S.-J.: Influence of silane coupling agent content on crosslinking type and density of silica-filled natural rubber vulcanizates. *Bull. Korean Chem. Soc.* **27**, 1473–1476 (2006)

Index

A

- Abrasion resistance, 189, 264, 462, 464, 468–471, 517, 519–521, 523, 524
- Abrasion test, 463, 468, 469, 471, 472
- Acoustic emission, 139–141, 145, 147, 148, 150, 151, 155, 157, 160, 161
- Acrylonitrile–butadiene–copolymer (ABS), 3, 4, 12, 104
 - blends with thermoplastic polyurethane (TPU/ABS), 3, 4, 5, 12
- Adhesion, 29, 147, 173, 223, 244, 250, 277, 278, 284, 285, 292, 298
- Ageing, 165, 181, 197, 298–307, 351–353, 356–362, 406, 407, 410, 412–416, 423, 431, 435–442
- Arc-shaped specimens, 213–217
- Atomic force microscopy (AFM), 106, 113, 166

B

- Ball indentation test, 407, 412, 413, 416
- Biaxial deformation, 335, 339
- Biaxial testing, 335, 336, 338
- Biax Test Stand, 336, 338, 348
- Brominated poly(isobutylene-co-isoprene) (BIIR), 498, 500, 501

C

- Cellulose fibres, 96, 97
- Chain statistics, 500–502
- Cling test, 283, 287, 289, 295
 - instrumented peel cling test, 287, 289
- Compact Tension (CT) specimen, 27, 33, 44–48, 213, 215–218
- Composites
 - conventional, 8, 83, 121, 160, 297, 315
 - nanocomposites, 23–31, 447, 448
- Compression set (CS), 423, 426, 429, 432–434, 437, 439, 440, 442

- Crack deflection, 24, 25, 29–31
- Cracked round bar (CRB) specimen, 33, 36, 44–48, 179, 185, 198, 199
- Crack growth, 39
 - environmental, 33, 36
 - fatigue, 23–25, 27, 30, 41, 42, 351
 - slow, 34, 35, 37, 39, 177–179, 182, 186, 197–199, 204–206, 208, 233, 239, 240
 - stable, 3–5, 7–12, 15–18, 23, 29, 30, 76, 78, 80, 122, 124–126, 129, 132, 205, 214–216, 290, 294, 361
 - Unstable, 15, 17, 30, 74, 87, 261, 264
- Crack initiation, 3–5, 12, 16, 25, 30, 31, 37, 40, 55, 67, 76, 78, 89, 109, 124, 134–136, 160, 165–169, 198, 199, 234, 236, 285, 286, 288, 289, 293–295, 323, 352, 360, 368, 469
- Crack resistance curve (R-curve), 3–10, 16–18, 73, 80, 122, 124, 131–133, 214–216, 219, 224, 286, 289, 290, 292–295
- Crack Round Bar (CRB) Test, 33, 36, 45, 48, 179, 185–187, 198
- Crack speed, 4, 10, 11, 14, 15, 18, 219, 291
- Crack-(tip)-opening displacement (C(T)OD), 4, 5, 10, 18, 148, 205
- Creep testing, 121, 181, 316, 387, 391, 392
- Crosslink density, 248, 249, 463, 465, 471, 475–478, 481, 482, 485, 491, 494, 503, 521
- Crosslinking
 - using radiation or peroxide thermal, 478
- Crystallinity, 57, 73–75, 77, 80, 147, 215, 220, 230, 284, 412
- Crystal modification, 73–75, 191
- C specimens, 213–215, 217

D

- 3D digital microscopy, 121, 125, 215

- Debonding, 139, 140, 148, 149, 151, 152, 154, 161
- Detergent, 179–182, 184, 187
- Differential Scanning Calorimetry (DSC), 57, 407, 414, 432, 433
- Diffusion, 279, 352, 380, 406, 421–426, 428, 436, 439
- Digital image correlation, 315, 328, 330, 337, 343
- 3D image correlation analysis, 246
- Double-edge-notched tension (DENT) specimens, 258, 259, 464
- 3D reconstruction, 95, 103, 105, 106, 109, 111, 115–117
- Dynamic-mechanical analysis (DMA), 19, 57, 123, 243, 245, 247, 352–354, 378, 379, 381, 432, 437, 519
- Dynamic-thermomechanical analysis, 299, 300, 377, 507, 512, 519
- E**
- Elastic–plastic fracture mechanics (EPPM), 76, 125, 212, 224, 290
- Elastomer
 - chemically crosslinked, 435, 449, 451, 462, 478, 481, 491, 497, 502
 - magnetorheological (MRE), 365, 370–373
 - thermoplastic (TPE), 287, 289, 498, 500–502
- Elastomeric seals, 431–433, 435, 442
- Elastomer-modified polypropylene, 172
- Electron microscopy, 96, 103, 105, 109, 114, 121, 129, 166, 448, 451
- Energy-Dispersive X-ray Spectrometry (EDS), 113
- Energy dissipation, 16, 18, 60, 68, 71, 133, 192, 288, 291, 328–331, 510
- Energy-Filtered Transmission Electron Microscope (EFTEM), 26
- Energy release rate, 74, 86, 154, 263, 271, 274–280, 286, 288–292, 295, 355
- Environmental crack growth, 33, 36
- Environmental Scanning Electron Microscopy (ESEM), 95, 106, 111, 139, 140, 145–147, 149, 150, 152, 153, 160, 161
- Epoxy–clay nanocomposites, 26
- Epoxy nanocomposites
 - with clay as nanofiller, 26
 - with silica as nanofiller, 23, 24, 26
- Epoxy resins
 - modified, 244, 248, 297
 - rubber modified, 244
 - nanocomposites, 23–31
- Epoxy–silica nanocomposites, 26
- Ethylene–propylene–diene rubber (EPDM), 243, 245, 247, 249, 251, 252, 365, 368, 369, 371–374, 437, 498, 500, 501
 - blends with natural rubber, particle filled, 365
- Ethylene-propylene rubber (EPR), 103, 104, 106, 109, 117, 123, 129
- Ethylene vinyl acetate (EVA), 171, 273–280
- Exposure to chemical agents, 266
- F**
- Failure analysis, 165, 166, 173
- Fatigue crack growth, 23–25, 27, 30, 41, 42, 351
- Fatigue crack propagation, 23, 25, 27, 28, 355
- Fatigue loading conditions, 23, 40–42, 197, 223, 330, 331, 335
- Fatigue testing, 316, 323, 326–328, 330, 336, 345, 370, 372
- Fibre fracture, 139–141, 143, 144, 148, 152, 154–157, 161
- Fibre–matrix adhesion, 173, 317, 318
- Fibre orientation, 83, 85, 86, 91, 315, 317, 318, 322–324, 328, 406–411, 416
- Fibre pull-out, 86, 98, 140, 141, 148–157, 161
- Fibre-reinforced thermoplastics, 3, 42, 83, 85, 91, 98, 139–141, 161, 213, 315–317, 319, 325, 378, 406, 407
- Film
 - peel film, 99, 267, 272, 273, 275, 278, 279, 292
 - stretch film, 284–286, 291–295
- Finite element method (FEM), 19, 38, 89, 223, 225, 340, 341, 399, 421, 422, 508
- Fixed-arm peel test, 262, 263, 268, 275, 276
- Fluorescence Adsorption-Contrast Method (3D-FAC), 121, 129, 130, 136
- Fluorescent dye colouring, 125, 127, 129, 130
- Fluorocarbon rubber (FKM), 432, 437
- Fourier transform infrared spectroscopy (FTIR), 102
- Fractography, 95, 106, 152, 165, 166, 171, 173
- Fracture mechanics
 - Elastic–plastic fracture mechanics (EPPM), 76, 125, 212, 224, 290
 - Linear Elastic Fracture Mechanics (LEFM), 36, 39–41, 44, 45, 48, 74, 135, 198
- Fracture mechanics parameters
 - crack-(tip)-opening displacement, 3–5, 10, 18, 148, 205
 - energy release rate, 74, 86, 154, 263, 271, 274–280, 288–292, 295, 355

- J-integral, 4, 6, 9, 15, 16, 121, 122, 135, 340, 346, 413, 416
- stress intensity factor, 15, 23, 24, 27, 36–39, 46, 74, 185, 198, 223, 229, 234–237, 239, 240
- tearing energy, 345–347, 355, 357, 361
- Fracture mechanics specimens
 - arc-shaped specimens, 213–217
 - Compact Tension (CT) specimens, 27, 33, 44–48, 213, 215–218
 - Cracked round bar (CRB) specimens, 33, 44–48, 177, 185, 198, 199
 - C specimens, 213–215, 217
 - Double-edge-notched tension (DENT) specimens, 258, 259, 464
 - pure-shear specimens, 345, 347, 355
 - Single-edge-notched bending (SENB) specimens, 76, 124, 126, 148, 213–221, 225
 - Single-Edge-Notched Tension (SENT) specimens, 205, 213–217, 219, 225, 343, 344
- Fracture (mechanics) tests
 - accelerated Full Notch Creep Test (aFNCT), 177, 179, 181, 182, 184
 - Crack Round Bar Test (CRB), 33, 34, 36, 45, 48, 179, 185–187, 198
 - Full Notch Creep Test (FNCT), 36, 179, 204–206, 208, 212
 - instrumented peel cling test, 287, 289
 - Pennsylvania Edge Notch Tensile Test (PENT), 203–206, 208, 209
 - pipe falling weight test, 192, 193, 196, 199
 - pure-shear test, 345, 347, 355
 - Strain Hardening Test (SHT), 36, 177, 179, 182, 183, 203, 204, 206, 212
- Full Notch Creep Test (FNCT), 36, 179, 204–206, 208, 212
 - accelerated Full Notch Creep Test (aFNCT), 177, 179, 181, 182, 184
- G**
- Gel Permeation Chromatography (GPC), 408, 415, 471
- Glass fibre-reinforced composites, 8, 117, 129, 135, 139, 157, 166, 172, 315, 325, 378, 380, 382, 384
- Glass fibres, 84, 86, 98, 122, 123, 125, 146, 160, 319, 322, 379
- Glass rubber transition, 432–435, 442
- Glass transition temperature, 55, 57, 123, 243, 245, 246, 249, 252, 298, 299, 379, 381, 384, 390, 415, 435, 437, 494, 497, 498
- H**
- Hardness, 113, 147, 155, 215, 220, 231, 245, 264, 267, 369, 406, 407, 412, 413, 416, 437, 439, 440, 442, 463, 468, 469, 490
- High-density polyethylene (PE-HD), 12, 33, 34, 42, 43, 45–48, 139, 147, 157, 183, 204, 205, 207–209, 212, 213, 215, 230, 238, 391
 - reinforced with short-glass fibres, 147, 157–161
- Hooke number, 493–505
- Hygrothermal ageing, 405–407, 409, 411, 416
- Hysteresis, 286, 291, 294, 316, 328, 329, 352, 510, 511
- I**
- Ice traction, 517–519, 521, 523, 524
- Impact-loading conditions, 12, 74, 76, 122, 139, 147, 161, 214, 258
- Infrared spectroscopy, 102, 248, 299
- In situ peel test, 99–101, 106
- In situ tensile test, 96, 99, 100, 106, 139, 145–147, 149, 152, 160
- In situ ultramicrotomy, 103, 106, 111
- Instrumented impact test, 76, 78, 80, 125, 129, 139, 140, 147, 161, 407
 - instrumented puncture impact test, 260, 261, 265
 - instrumented tensile impact test, 258, 259, 264, 464
- Instrumented peel cling test, 283, 287, 289, 295
- J**
- J-integral, 4, 6, 9, 15, 16, 121, 122, 135, 340, 346, 347, 413, 416
- L**
- Leakage rate, 432, 434, 435, 437, 442
- Lifetime estimation, 33, 34, 40, 41, 45, 46, 48, 204, 206, 208, 229, 240, 298, 328, 330, 431, 432
- Light microscopy, 76, 106, 121, 135, 166, 322, 471
- Linear Elastic Fracture Mechanics (LEFM), 33, 36, 39–41, 44, 45, 48, 74, 135, 198
- Linear low-density polyethylene (PE-LLD), 109, 111, 112, 115–117, 216, 273, 275, 277, 278, 284, 286, 287, 292
- Loading conditions
 - fatigue, 23, 40, 42, 197, 223, 330, 331, 335, 355
 - impact, 3, 4, 12, 74, 76, 122, 139, 147, 161, 214, 219, 258

- Loading conditions (*cont.*)
 quasi-static, 3, 10–12, 139, 161, 166, 212, 214, 216, 219, 261, 316, 335, 353
 static, 36, 41, 43, 47, 99, 212, 390, 392
 Loading rate, 60, 61, 62, 69, 152, 214, 218, 220
 Long-glass fibre-reinforced composites, 83
 Long-glass fibre-reinforced polypropylene, 83
 Long-term mechanical performance, 23, 40, 177, 189, 191, 197, 198, 205, 208, 219, 223, 297, 377–379, 387, 389–397, 423
 Low-density polyethylene (PE-LD), 99, 273–275, 279, 285
- M**
- Macro dispersion index (DI), 470–472
 Master curve construction, 379, 385–387, 389–391, 393–401, 440, 447, 457, 493–496, 499–501, 503, 505
 Matrix yielding, 139, 148, 152, 154–157, 161
 Maximum tangential stress (MTS) criterion, 234
 Medium-density polyethylene (PE-MD), 207, 216
 Micro-Bond Test, 86, 87
 Micro Computer Tomography (micro-CT), 408–411
 Microindentation test, 211, 215, 220, 225, 232
 Microscopy
 3D digital microscopy, 121, 125, 215
 electron microscopy
 energy-filtered transmission electron microscopy, 26
 Environmental Scanning Electron Microscopy (ESEM), 95–103, 106, 111, 139, 140, 145–147, 149, 150, 152, 153, 160, 161, 281, 286
 Scanning Electron Microscopy (SEM), 29, 77, 79, 80, 95–98, 101, 103, 106, 110, 112, 113, 117, 121, 129, 133, 135, 136, 146, 166, 192, 281, 296, 471
 transmission electron microscopy (TEM), 103, 114, 279, 448, 451
 light microscopy
 3D digital microscopy, 124, 125, 215
 reflected-light microscopy, 322
 transmitted-light microscopy, 220
 Moisture absorption, 122, 123, 406, 412–414, 416, 419
 Multi-layer pipes, 169–171, 212, 214, 222
 Multiple-specimen technique, 214
- N**
- Nanocomposites
 with epoxy as matrix, 23–31
 Natural rubber (NR)
 epoxised (ENR), 485, 486
 with wood flour, 490
 with carbon black (CB), 368
 with micron-sized carbonyl iron powder (CIP), 365, 367–369, 371, 373
 with wood flour, 490
 Necking, 65, 291
 Nitrile–butadiene rubber (NBR), 341, 342, 432, 434, 477–479, 498–501
 hydrogenated (HNBR), 341, 342, 347, 437–441, 477–479
 with carbon black (CB), 341
 Notched impact strength, 193
 notched tensile impact test, 259
 Nucleation, 191, 194, 352
 Nucleation agent, 73–75
- O**
- Orientation, 29, 68, 70, 83, 85, 86, 91, 106, 140, 142, 150, 172, 211, 213–215, 217, 218, 220, 224, 225, 315–318, 320, 322, 324–326, 328, 331, 365, 367, 371, 373, 374, 406–411, 416, 490
- P**
- Paris law, 24, 36
 Particle debonding, 23, 29, 30
 Peel film, 99, 267, 268, 272, 273, 275, 278, 279, 283, 292
 Peel system
 adhesive, 271–273, 275–279, 285
 cohesive, 271–274, 277–279, 285
 Peel test, 99, 262, 263, 268, 275–277, 288, 295, 298–300, 304, 306, 307
 fixed-arm peel test, 262, 263, 268, 275, 276
 T-peel test, 99, 262, 263, 275, 276, 285, 298–300, 304, 306, 307
 Pennsylvania Edge Notch tensile (PENT) Test, 36, 179, 203–205, 212, 233
 Pipe falling weight test, 192, 193, 196, 199
 Pipes
 joints, 243
 plastic pipes, 33, 35, 197, 204, 211–213, 216, 219–221, 224, 259, 389, 391
 rehabilitation of pipes, 243, 244
 Plastic deformation, 9, 11, 13, 18, 34, 55, 66–68, 70, 122, 125, 129, 133, 136,

- 141, 147, 149, 150, 156, 157, 166,
168–170, 199, 222, 223, 225, 286, 291
 - Plastic void growth, 24, 29, 30
 - Plastic zone size, 23, 24, 30
 - Polyamide (PA)
 - high impact, 168
 - polyamide 6 (PA6), 121, 122, 405–407
 - polyamide 66 (PA66), 123, 377, 378, 380,
382–384, 414–416
 - polyphthalamide (PPA), 377–387
 - reinforced with short-glass fibres, 377–387,
405–416
 - Polybutadiene (BR), 3, 463
 - blends with styrene-butadiene rubber, 461,
463
 - with silica or glass powder, 461–472
 - Polybutene-1 (PB-1), 99, 147, 212, 267, 271,
273, 274, 285, 296
 - Polycarbonate (PC), 3, 11–16, 19, 42, 55–57,
66, 68, 71
 - Poly(ethylene terephthalate) (PET), 55–57,
59–63, 65–69, 71, 273, 275, 277–279
 - Polyethersulfone (PES), 100, 101–104
 - Polyethylene (PE)
 - high-density (PE-HD), 12, 33, 34, 42, 43,
45–48, 139, 147, 157–161, 183, 204,
205, 207–209, 212, 213, 215, 230, 238,
391
 - reinforced with short-glass fibres, 147,
157–161
 - linear low-density (PE-LLD), 109, 111,
112, 115–117, 216, 273, 275, 277, 278,
284, 286, 287, 292
 - low-density (PE-LD), 99, 273, 275, 279,
285
 - medium-density (PE-MD), 207
 - Polyisoprene (IR), 447–449, 451, 453, 455,
457–458
 - with carbon black (CB), carbon nanotubes
(CNTs) and/or nanographite, 448–458
 - Polymer composites, 297, 316
 - Poly(methyl methacrylate) (PMMA), 15, 166,
167
 - Polynorbornene (PNR), 498, 500, 501
 - Polyoctenamer (TOR), 498
 - Polypropylene (PP)
 - blends, 10, 12
 - with ethylene-propylene rubber, 103,
104, 106, 109–118
 - with linear low-density polyethylene
(PE-LLD), 109, 111, 112, 115–117
 - elastomer-modified, 122, 172
 - layered-particle reinforced, 213
 - mineral-filled, 172
 - with talc, 103, 104, 172
 - neat
 - homopolymer (PPH), 118, 193, 194,
196, 198–199
 - random copolymer (PPR), 75, 193, 194,
196, 197
 - short-glass fibre-reinforced (PP/GF), 6, 13,
150, 160, 315
 - talc-filled, 104, 172
 - Poly(styrene-divinylbenzene), 103, 104
 - Polyvinylchloride (PVC), 19, 56, 97, 190, 265,
266
 - Powder X-ray Diffraction, 26, 27
 - Polypropylene-talc nanocomposites, 104, 172
 - Pure-shear specimen, 345, 347, 355
 - Pure-shear test, 345
- ## Q
- Quasi-static loading conditions, 3, 10–12, 139,
161, 166, 212, 214, 216, 219, 261, 316,
335, 353
- ## R
- Raman spectroscopy, 298, 299, 304
 - Reflected-light microscopy (optical
microscopy), 322
 - Rolling resistance, 462, 512–515, 517–524
 - Rubber
 - acrylonitrile–butadiene–rubber, 341, 342,
347, 477
 - with silica, carbon black (CB),
organoclay or graphene, 477, 478,
482
 - brominated poly(isobutylene-co-isoprene)
(BIIR), 498
 - ethylene–propylene–diene rubber (EPDM),
243, 245, 247, 249, 251, 252, 365, 368,
369, 371–374, 432, 437, 439–441, 498,
500, 501
 - blends with natural rubber, particle
filled, 352, 353
 - ethylene–propylene–rubber (EPR), 3, 5–8,
10–12, 16, 103, 104, 109–117, 123,
124, 129, 133–136
 - fluorocarbon rubber (FKM), 432, 435, 437,
441
 - natural rubber (NR), 341–343, 345, 351,
352, 356, 365–368, 485–487, 489, 491,
498
 - epoxised, with wood flour, 490
 - epoxised (ENR), 485, 486
 - with carbon black (CB), 368
 - with wood flour, 490

- Rubber (*cont.*)
- nitrile–butadiene rubber (NBR), 341, 342, 432, 434, 477–479, 498–501
 - hydrogenated (HNBR), 341, 342, 347, 437–441
 - hydrogenated, with carbon black (CB), 341
 - polybutadiene (BR), 352, 353, 463, 517
 - polydimethylsiloxane (PDMS), 498
 - polyisoprene, 447, 449, 458
 - with carbon black (CB), carbon nanotubes (CNTs), 448–458
 - polynorbornene (PNR), 498, 500, 501
 - polyoctamer (TOR), 498
 - styrene–butadiene rubber/polybutadiene blends (SBR/BR), 461, 467, 470, 472, 518, 520
 - with glass powder, 463
 - with silica, 475, 477, 478, 482
 - styrene–butadiene rubber (SBR), 262, 264, 341, 351, 352, 517, 522, 523
 - with carbon black (CB), 262, 264, 341, 352, 356, 495, 497, 504, 505
 - with glass powder, 463
 - with silica, 475, 477, 478, 482
- S**
- Scanning Electron Microscopy (SEM), 27, 29, 77, 79, 95–97, 101, 103, 105, 109, 110, 112, 113, 117, 121, 129, 133, 135, 136, 146, 166, 192, 471
 - Short-glass fibre-reinforced composites, 139, 140, 157, 161, 315, 405, 406
 - Short-glass fibres reinforced high-density polyethylene (PE-HD/GF), 147, 157–160, 161
 - Short-glass fibres reinforced polyamide 6 (PA6/GF), 405–419
 - Short-glass fibres reinforced polyamide 66 (PA66/GF), 378–387
 - Short-glass fibres reinforced polybutene-1 (PB-1/GF), 160
 - Short-glass fibres reinforced polyphthalamide, 380
 - Single-Edge-Notched Bending specimens (SENB), 76, 124, 126, 148, 213–221, 225
 - Single-Edge-Notched Tension specimens (SENT), 205, 213–217, 219, 225, 343, 344
 - Short-glass fibre reinforced polypropylene (PP/GF), 6, 13, 150, 160, 315
 - Short-glass fibre reinforced composites, 139, 140, 157, 161, 315, 405, 406
 - Single-fibre unit cell model, 87, 88
 - Single-specimen method/technique, 4, 5, 214, 290, 292, 293
 - Slow crack growth (SCG), 33–35, 37, 39, 177–179, 182, 186, 189, 197–199, 204–206, 208, 229, 233, 235, 239, 240
 - Specimen geometry, 44, 47, 180, 184, 185, 206, 217, 340, 341, 355
 - Stable crack growth, 12, 17, 24, 29, 166
 - Static loading conditions, 12, 36, 41, 43, 47, 316, 353, 392
 - Stepped Isothermal Method (SIM), 377, 379, 385, 387, 389–401
 - Stiffness, 13, 25, 28, 55, 74, 75, 140, 147, 220, 221, 223, 225, 244, 262, 265, 267, 315, 339, 366, 378, 405, 406, 412, 422, 423, 426, 432, 448, 509, 519, 521
 - Strain field analysis, 331, 340
 - Strain hardening modulus, 183–185
 - Strain hardening test (SHT), 36, 177, 179, 182, 183, 203, 204, 206, 212
 - Stress cracking, 33, 40, 41, 48, 177–187, 208
 - Stress intensity factor, 15, 23, 24, 27, 36–39, 46, 74, 185, 198, 223, 229, 234–237, 239, 240
 - Stress–strain curve, 59, 60, 65, 87–91, 207, 383, 399, 408, 409, 496, 497, 501–503
 - Stretch film, 283–287, 289, 291, 293–295
 - Structural mechanics, 422
 - Styrene–butadiene–butylacrylate mix polymer, 518
 - Styrene–butadiene copolymer, 3, 20
 - Styrene–butadiene rubber (SBR), 262, 341, 342, 351, 352, 356, 497, 517, 522, 523
 - blends with polybutadiene, 463
 - with silica or glass powder, 463
 - with carbon black (CB), 262, 264, 341, 352, 356, 495, 497, 504, 505
 - with silica, 475, 477, 478, 482
 - with silica or glass powder, 463
- T**
- Tearing energy, 345–347, 355, 357, 361
 - Tear resistance, 261, 262, 267, 463, 467–471
 - Tear test, 261, 262, 264–266, 269, 463, 467
 - Tensile lap-shear test, 298–300, 306, 307
 - Tensile test, 67, 98–100, 103, 106, 109–112, 114–117, 123, 124, 139, 140, 145–147, 152, 160, 161, 179, 183, 187, 203–205, 207, 208, 215, 222, 223, 246, 247, 249, 250, 252, 257, 265, 266, 288, 323, 326, 370, 371, 377, 379, 382–384, 387, 407, 463, 467, 477, 487, 497, 501, 504
 - Thermography, 56, 71

- Thermogravimetric Analysis (TGA), 26, 246, 298, 300, 305
- Thermo-mechanical behaviour, 507
- Thermomechanical treatment, 518–523
- Thermoplastic elastomer (TPE), 287, 289, 498, 500–502
- Threshold of crack growth, 23, 28
- Time-temperature superposition principle (TTSP), 389–393, 396–398, 401
- Time to crack initiation, 37
- Time to failure, 37, 180–182, 184, 186, 204, 208, 209, 239, 399
- Toughening, 23–25, 29–31, 121, 135, 194, 195
- Toughening mechanisms
- crack deflection, 23–25, 29–31, 246
 - crack pinning, 24, 29
 - particle debonding, 23, 29, 30
 - plastic void growth, 24, 29, 30
- T-peel test, 99, 262, 263, 275, 276, 285, 298–300, 304, 306, 307
- Transmission Electron Microscopy (TEM), 103, 114, 279, 448, 451
- Transmitted-light microscopy, 220
- Trouser specimen, 261
- Tyre, 517, 518, 521, 523
- V**
- Vulcametry, 461, 472
- W**
- Water absorption, 243, 249, 252, 377–385, 387, 416
- Wavelet analysis, 144, 145, 148, 152, 155, 158, 159
- Welding, 211, 213–215, 219–221, 224, 225, 229–233, 235, 239, 240
- Wet traction, 517–519, 521, 523, 524
- Wöhler curves, 326, 327, 370, 372
- X**
- X-ray computed tomography, 315, 316
- Y**
- Yield point, 56, 59–61, 64–66, 68–71, 170, 171, 207, 222, 299, 503
- Yield temperature, 60–63, 65